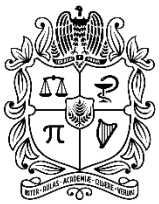

UNIVERSIDAD
NACIONAL
DE COLOMBIA

Modelamiento numérico de la producción masiva de arena durante la producción en frío de crudo pesado

Alejandra Arbeláez Londoño

Universidad Nacional de Colombia
Facultad de Minas, Departamento de Procesos y Energía
Medellin, Colombia
2023

Numerical modeling of massive sand production during cold heavy oil production

Alejandra Arbeláez Londoño

A thesis submitted in partial fulfillment of the requirements for the degree of:

Doctor of Philosophy in Engineering – Energy Systems

Director:

José Gildardo Osorio Gallego, Ph.D.

Co-director:

Guillermo A. Alzate Espinosa, M.Sc.

Research area:

Applied geomechanics to reservoir engineering

Research Group:

Research Group in Applied Geomechanics - GIGA

Universidad Nacional de Colombia

Facultad de Minas, Departamento de Procesos y Energía

Medellin, Colombia

2023

Dedicated to my lovely husband.

Acknowledgments

This thesis would not have been possible without encouragement and support from many people. I would foremost like to express gratitude to my research supervisors, Dr. Gildardo Osorio and Guillermo Alzate, for their time and patience during this decade.

I am thankful to Dr. Marisela-Nagel, Dr. Gonzalo Zambrano, and Dr. Pedro Benjumea, my defense committee members, who generously provided knowledge and expertise.

Special thanks to Dr. Rick Chalaturnyk and Dr. Gonzalo Zambrano for their time, discussion, and contributions during my internship at the University of Alberta, an enlightening experience.

I wish to acknowledge the financial support from Ecopetrol and Minciencias.

I am extremely grateful to Elvis Higuita, for his devoted dedication and for having spent so much time in the programming work related to this project.

I am also grateful to colleagues and officemates for their long feedback sessions and unconditional support.

Last, and most importantly, I would like to express my deepest gratitude and love to my husband for providing unconditional love, encouragement, and moral support. His belief in me has kept my spirits and motivation high during this agony process.

Abstract

Cold heavy oil production with sand (CHOPS) is a single well technology that involves the deliberate initiation and sustaining of sand inflow into the wells using progressive cavity pumps (PCP) to produce at oil high rates with a subsequent high-pressure drawdown around the wellbore and improvement in oil well productivity. CHOPS is a primary recovery method extensively used in the world as a profitable and simple technology. Foamy-oil flow and wormhole formation are the main mechanisms of CHOPS, where aggressive sand production is a consequence of geomechanical issues such as elastoplastic behavior, stress redistribution, failure criteria, pressure gradient, erosion, and sand liquefaction.

The general objective of this thesis is to build a numerical model to predict and explain massive sand production during cold heavy oil production by coupling fluid flow with geomechanics and considering stress redistribution and erosional processes. This research also identifies the relevant phenomena of massive sand production and describes the interaction between geomechanical and erosional processes. A methodology is proposed to model the initiation and propagation of wormholes based on geomechanical behavior.

A 3D-single well model is built to understand the cold heavy oil production with sand, considering relevant dynamics such as stress redistribution and the interaction between geomechanical and erosional processes, by coupling fluid flow with geomechanics. This model couples a three-phase fluid flow model and an elastoplastic model and integrates other models: a sand production model, a foamy-oil module, and a conceptual model for wormhole formation. This coupled model is verified and validated firstly by components and lately integrating step by step the different components using commercial software such as ABAQUS® and CMG®. Field cases are run to calibrate the parameters of the sand production model resulting in low sand levels, a case with the main characteristics of a CHOPS well is run and its results are analyzed, and a sensitive study is performed to evaluate the impact of variables such as pressure drawdown, cohesion, internal friction angle, and stress regime. Finally, a special case is built combing all variables and looking to promote sand production with successful results.

Keywords: cold heavy oil production with sand, CHOPS, sand production, heavy oil.

Resumen

La producción en frío de crudo pesado con arena (CHOPS) es una tecnología de un solo pozo que involucra el inicio deliberado y el mantenimiento del flujo arena a los pozos utilizando bombas de cavidad progresiva (PCP) para producir petróleo a altas tasas con un subsiguiente alto gradiente de presión alrededor del pozo. y mejora en la productividad de los pozos de petróleo. CHOPS es un método de recuperación primaria ampliamente utilizado en el mundo como una tecnología rentable y sencilla. El flujo de crudo espumoso y la formación de agujeros de gusano son los principales mecanismos de CHOPS, donde la producción agresiva de arena es consecuencia de problemas geomecánicos como el comportamiento elastoplástico, la redistribución de esfuerzos, los criterios de falla, el gradiente de presión, la erosión y la licuefacción de la arena.

El objetivo general de esta tesis es construir un modelo numérico para predecir y explicar la producción masiva de arena durante la producción en frío de crudo pesado acoplando el flujo de fluidos con la geomecánica y considerando la redistribución de esfuerzos y los procesos de erosión. Esta investigación también identifica los fenómenos relevantes de producción masiva de arena y describe la interacción entre los procesos geomecánicos y erosivos. Se propone una metodología para modelar la iniciación y propagación de agujeros de gusano basada en el comportamiento geomecánico.

Se construye un modelo de pozo único en 3D para comprender la producción en frío de crudo pesado con arena, considerando dinámicas relevantes como la redistribución de esfuerzos y la interacción entre los procesos geomecánicos y erosivos, al acoplar el flujo de fluidos con la geomecánica. Este modelo combina un modelo de flujo de fluido trifásico y un modelo elastoplástico e integra otros modelos: un modelo de producción de arena, un módulo de crudo espumoso y un modelo conceptual para la formación de agujeros de gusano. Este modelo acoplado es verificado y validado primeramente por componentes y posteriormente integrando paso a paso los diferentes componentes utilizando software comerciales como ABAQUS® y CMG®. Se corren casos de campo para calibrar los parámetros del modelo de producción de arena resultando en bajos niveles de arena, se corre un caso con las principales características de un pozo CHOPS y se analizan sus resultados, y se realiza un estudio de sensibilidad para evaluar el impacto de variables como como el gradiente de presión, la cohesión, el ángulo de fricción interna y el régimen de esfuerzos. Finalmente, se construye un caso especial combinando todas las variables y buscando promover la producción de arena con resultados exitosos.

Palabras clave: Producción en frío de crudo pesado con arena, CHOPS, producción de arena, crudo pesado.

Table of Contents

Nomenclature

Latin symbols

A	=	Cross-sectional area, [ft^2].
a	=	Experimental parameter (Detournay sand production criterion), $[dimensionless]$.
B	=	Formation volume factor (FVF) – Liquid FVF, [RB/STB]; Gas FVF,[RB/scf].
C	=	Concentration of sand grains (Vardoulakis sand production criterion), $[fraction]$.
$\mathbb{C}$	=	Stiffness matrix (constitutive – elastic)
c	=	Compressibility $[psi^{-1}]$
c	=	Coefficient of equivalent plastic strain for the associated flow of Drucker & Prager.
d	=	Derivative function.
∂	=	Partial derivative function.
det	=	Determinant.
$diam$	=	Diameter.
div	=	Divergence.
E	=	Young modulus, $[psi]$
$\boldsymbol{e}$	=	Canonical vector.
F	=	Function.
F	=	Yield function.
f	=	Right side of the stress-strain constitutive system.
f	=	Failure or entrained-gas volume fraction (foamy oil).
G	=	Shear modulus (second Lame's constant), $[psi]$
g	=	Gravitational acceleration, $[32.174\ \mathrm{ft}/s^2]$ – shear potential function.
H	=	Finite dimensional subspace.
h	=	Plasticity function
i	=	Experimental parameter (sand production).
I	=	Stress invariants or identity matrix.
J	=	Deviator stress invariants or Jacobian
K	=	Bulk modulus, $[psi]$
K	=	Global stiffness matrix.
$\widehat{K}$	=	Reference element -8-node hexahedron.
k	=	Permeability (scalar), $[mD]$.
$\boldsymbol{k}$	=	Permeability tensor.
M	=	Molecular weight
m	=	Mass, [lbm] or viscosity constant (foamy oil).
N	=	Number
n	=	Normal unit vector.
n	=	Number of blocks.
p	=	Phase pressure, pressure, $[psi]$.
q	=	Volumetric flow rate. – Liquid flow rate[STB/D], Gas flow rate, [scf/D]

q	=	Volumetric discharge (sand production).
q_φ	=	Drucker and Prager material constant (coefficient of pressure sensitivity).
R	=	Gas universal constant.
Rs	=	Solution GOR, [scf/STB].
S	=	Saturation [fraction] or boundary surface (sand production) or salinity, [%]
$\boldsymbol{s}$	=	Deviator stress tensor.
T	=	Temperature, [°F] or transmissibility.
t	=	Time, $[D]$
tr	=	Trace function.
$\mathbf{u}$	=	Displacement tensor.
v	=	Real velocity scalar [ft/s] or test functions (FEM).
$\mathbf{v}$	=	Real velocity vector.
V	=	Volume, [ft^3].
x	=	Foamy oil mass fraction, [fraction].
y	=	Free gas mass fraction, [fraction].
z	=	Depth, [ft]
Z	=	Gas compressibility factor, [dimensionless].
∇	=	Divergence function.

Greek symbols

α	=	Biot's coefficient, $[dimensionless]$ or entrained gas fraction (foamy oil)
α_c	=	Volume conversion factor.
β_c	=	Transmissibility conversion factor.
Γ	=	Polyhedral boundary.
γ	=	Phase gravity, $[psi/\text{ft}]$– shear stress, $[psi]$.
γ_c	=	Gravity conversion factor.
δ	=	Kronecker's delta function.
Δ	=	Gradient function.
ϵ	=	Strain, [dimensionless].
$\boldsymbol{\varepsilon}$	=	Strain tensor.
ξ	=	Internal variable.
η	=	Node.
κ	=	Constant of yield function.
κ_φ	=	Drucker and Prager material constant (shearing cohesion).
$\mathcal{M}$	=	Mesh.
μ	=	Phase viscosity, $[cP]$
ν	=	Poisson ratio, [dimensionless]
λ	=	Experimental sand production parameter (Detournay sand production criterion).
λ	=	First Lame's constant, $[psi]$
Λ	=	Plasticity scale multiplier.
ρ	=	Density, [lbm/ft^3].
Φ	=	Phase potential, $[psi]$.
φ	=	Mohr-Coulomb internal friction angle, [°].
ϕ	=	Effective porosity, [fraction] or Flash fraction (foamy oil), [fraction].
ψ	=	Dilation angle, [°].

σ	=	Stress, normal stress, $[psi]$.
$\mathcal{T}$	=	Finite family of polygons.
τ_o	=	Cohesion, $[psi]$.
τ	=	Normal stress, $[psi]$.
Ω	=	Lipschitz domain.
ω	=	Integration parameter.

Subscripts

API	=	API (American Petroleum Institute).
B	=	Bottom.
b	=	Bulk (volume) or bubble point(pressure).
bc	=	Bulk volume change due to mean stress pressure (compressibility).
bp	=	Bulk volume change due to pore pressure (compressibility).
c	=	Capillary (pressure) or connate (saturation).
cr	=	Critical.
do	=	Dead oil
E	=	East.
e	=	Element.
ego	=	Entrained gas.
end	=	End.
f	=	Fluid or cavity (sand production)
fo	=	Foamy oil.
go	=	Gas – oil.
H	=	Maximum horizontal (stress).
h	=	Minimum horizontal (stress) or subspace of H
HC	=	Hydrocarbon gas mixtures.
i	=	Phase index (oil, water, gas, or foamy oil).
i, j, k	=	Direction index.
ir	=	Irreducible
L	=	Local.
l	=	liquid
m	=	Mean or Corey exponent for free gas
max	=	Maximum.
N	=	North.
n	=	Normal to the wellbore wall for discharge rate or Corey exponent
o, w, g	=	Oil, water, gas phase.
ow	=	Oil – water.
p	=	Pore (pressure) or porous (volume), or producing (gas-oil ratio).
p	=	Pseudo bubble-point (foamy oil).
pc	=	Pore volume change due to mean stress (compressibility) or pseudo-critical (p or T).
pp	=	Pore volume change due to pore pressure (compressibility).
pr	=	Pseudo-reduced.
r	=	Real for velocity, residual (saturation or frictional angle), or relative (permeability).
r, θ, z	=	r, θ, z direction, respectively.
ref	=	Reference.
RC	=	Reservoir conditions.

S	=	South.
s	=	Solid or sand.
sp	=	Separator conditions.
SC	=	Standard Conditions.
T	=	Top.
v	=	Volumetric.
v	=	Vertice or vertical (stress).
vp	=	Viscoplastic.
x, y, z	=	x, y, z direction, respectively.
W	=	West.
Wb	=	Wellbore (boundary).
w	=	Wellbore (radius).
wf	=	Wellbore flowing (pressure).
0	=	Initial.

Superscripts

$'$	=	Effective, derivative (capillary pressure or solution GOR).
$\bar{}$	=	Mean (pressure).
$\dot{}$	=	Rate.
$\tilde{}$	=	Source/sink term as mass rate per total volume per time unit.
e	=	Elastic.
I	=	Elastic guess.
m	=	Corey exponent for free gas.
N	=	New.
n	=	Corey exponent for foamy oil or other phases.
p	=	Plastic.
O	=	Old.
ps	=	Plastic strain.
ref	=	Reference.
s	=	Shear.
t	=	Tensile.
T	=	Total or transpose matrix.

Chapter 1. Introduction

1.1 Overview

Heavy oil reservoirs are the largest hydrocarbon reserves of the world's total oil resources of 9 to 13 trillion barrels, being essential in worldwide oil production (Shafiei & Dusseault, 2013). Presently, the abundance of oil resources and the prospect of reducing oil demand promote a change in global oil supplies. Mainly, low-cost producers may use their competitive advantage to rising market share. So, heavy oil reservoirs compete with feasibility and low cost to supply energy demand. The challenges are still about extracting, recovering, producing, and selling heavy oils under shifting economic rules and with minimal environmental impact.

To get these challenges, there are technical difficulties in heavy oil extraction because of the characteristics of the formation, weak and unconsolidated sandstones, and the contained fluids, in terms of density and viscosity. The production of sand grains from unconsolidated sandstones under viscous fluid flow is inevitable. Sand production has been found to increase effectively productivity in heavy oil reservoirs, but it can also lead to geomechanical problems.

Cold Heavy Oil Production with Sand (CHOPS) is the principal heavy oil production technology, which is a primary and non-thermal recovery method that implies the deliberate initiation and sustaining of sand influx into the wells using progressive cavity pumps (PCP) to enhance production rates and to assurance operating reliability (Dusseault, 2002, 2009). CHOPS has become a profitable mainstream strategy for heavy oil reservoirs due to its low operational costs and relatively high recovery factors, compared to the thermal recovery methods and horizontal wells (Dusseault & El-Sayed, 2000; Young, Mathews, & Hulm, 2011; Bybee, 2011).

Colombia is framed in the mid-moon that connects the heavy oil basins from Venezuela and Ecuador. Colombia, according to this location, appears to be a sedimentary basin with similar characteristics and large heavy oil reserves. Hence, despite the challenges of the exploitation of heavy oil reservoirs and the previous experience in this technology, cold heavy oil production with sand is projected as an attractive and rentable alternative to the exploitation of heavy oil reservoirs in Latin America, especially in Colombia.

1.2 Problem statement

This work is part of a research project Ecopetrol – Colciencias 264: "Geomechanical Aspects of the Production and Recovery of Heavy and Extra Heavy Oils," which is framed in the theme of technological tools to optimize the production and increase the recovery factor in heavy oil reservoirs, and so reducing the technological gap of the oil and gas industry of Colombia.

Applied geomechanics to reservoir simulation is a modern strategy in modeling for some oil and gas reservoirs, where stresses and strains play an important role in reservoir performance and productivity.

Heavy oil development is far more geomechanical demanding than conventional oil development. Cold heavy oil production with sand involves different physical mechanisms that require geomechanical handling to model the phenomena' complexity. The literature review reveals the successful applications of this technique at a field scale and indicates that understanding the fundamentals of sand production is a key factor in successful production involving massive continuous sanding. These processes include foamy oil behavior, wormhole formation, stress redistribution, and complex fluid flow. Inter-relating their physical mechanisms requires coupling fluid flow and geomechanical processes (Young, Mathews, & Hulm, 2011; Guo, Gao, Ai, & Qu, 2012; Sanyal & Al-Sammak, 2011; Rangrizshokri, 2015).

Advanced numerical models have been applied to predict the onset of sand production during cold heavy oil production, but most of them are unable to give a reliable estimation of sand production and its response to oil production. Other attempts have been used in conventional numerical reservoir simulators to model cold production with sand, but do not incorporate capabilities to model the complex geomechanical processes responsible for the failure of poorly consolidated formations in cold heavy oil production with sand (Rivero, Coskuner, Asghari, Law, Pearce, Newman, Birchwood, Zhao, & Ingham, 2010).

Because of the large amounts of sand and water produced in processes such as cold heavy oil production, realistic simulation models are required to ensure safe operations and optimize complex large-scale production. Understanding the dominant mechanisms governing these phenomena will help include additional components in a more robust model for CHOPS.

1.3 Background

Cold production with sand involves different physical mechanisms like foamy oil behavior, wormhole formation, massive stress redistribution, sand liquefaction, and complex fluid flow (oil, gas, water, and sand). Specifically, aggressive sand production has been modeled as responding to foamy oil flow and wormhole formation.

Foamy oil behavior is responsible to reduce in-situ oil viscosity and high apparent critical gas saturation due to trapped gas bubbles in heavy oil, resulting in solution gas drive. This process is still a discussion issue because the small quantities of gas are not necessarily significant to be a reservoir drive mechanism (Ruifeng, Xintao, Xueqing, Xianghong, Xinzheng, Li, & Xiaoling, 2011).

During cold heavy oil production, sand will be produced by the interaction between geomechanical and erosional processes; sand grains are removed from the solid matrix due to fluid and stress gradients, both resulting from high-pressure drawdown (Wang, Yale, & Dasari, 2011).

If the pressure drawdown is great enough to destroy the internal binding forces of sand particles, sand tends to produce together with oil, thus generating wormholes. A wormhole is a space or cavity in the formation that continually increases in size and creates regions of enhanced permeability and porosity, which contribute to oil productivity (Ruifeng *et al.*, 2011). The formation and growth of wormholes have been modeled in terms of the disturbed zone to incorporate permeability and porosity dynamics. Three

mathematical models have been applied in different commercial simulators: skin factor, mobile permeability, and wormhole spreading. Alternative methods use probabilistic models to describe the wormholes' network and its propagation in the reservoir. However, these techniques do not couple accurately the geomechanical issues (Pan, Chen, Sun, Bao, Xiao, & Wang, 2010; Istchenko, & Gates, 2011; Du, Jiang & Chen, 2009; Foo, Chee, Zain, & Mamora, 2011).

Understanding how the wormholes will initiate and how they will propagate gives us the capacity to predict more economical and producible zones, adjust the completion program, decrease costs by not completing sands that will not produce, and finally improve the well placement.

The altered regions can be considered damaged zone due to changing permeability and porosity. The stress field, which has a significant impact, changes at two different scales, one around the wellbore and the other in the reservoir itself. For some researchers, stress redistribution is what governs oil and sand production, affecting directly geomechanical stability (Wang, Yale, & Dasari, 2011; Rivero et al., 2010).

Sand production phenomena are governed by the interaction between geomechanical and erosional processes with three relevant components: erosion, stresses, and pore pressure (Wang, Yale, & Dasari, 2011).

Modeling sand production presents significant numerical challenges because it is coupled geomechanical and fluid flow process, and also because the productions are from weakly consolidated reservoirs where the material behavior is very complex (Guo, Gao, Ai, & Qu, 2012; Young, Mathews, & Hulm, 2011).

Thus cold heavy oil production with sand requires a numerical model coupling fluid flow with geomechanics, considering the relevant mechanisms such as stress redistribution and the interaction between geomechanical and erosional processes, to predict sand production and optimize oil productivity.

The construction of a numerical simulator coupling fluid flow and geomechanics and including the effect of stress redistribution and erosional processes, and the massive sand production during cold heavy oil production constitutes a powerful tool to predict and understand the complex phenomena, and to optimize the oil recovery.

This research investigates the phenomena associated with cold heavy oil production with sand, in the simplest possible way with academic rigor, including the interaction between geomechanical and erosional processes to model the sand production, the effect of the stress redistribution on the formation and propagation of wormholes and the effect of the conditions of the massive sand production on production performance. With this understanding, a 3D single well model is built that couples a fluid flow model that includes foamy oil with an elastoplastic model. This model also includes an alternative methodology for wormhole initiation and propagation to simulate different scenarios for cold heavy oil with sand.

1.4 Objectives

1.4.1 General objective

To investigate the massive sand production during cold heavy oil production by coupling fluid flow with geomechanics and considering stress redistribution and erosional processes. This objective is achieved by building a numerical model that simulates the physics associated with cold heavy oil production processes.

1.4.2 Specific objectives

The specific objectives of this research can be stated as follows:

i. To identify the relevant phenomena of massive sand production during cold heavy oil production.

ii. To investigate the interaction between geomechanical and erosional processes, during sand production in cold heavy oil production.

iii. To develop a methodology to define the initiation and propagation of wormhole paths based on geomechanical behavior during massive sand production in cold heavy oil production.

iv. To investigate the reservoir geomechanical stability for cold heavy oil production with sand, considering the impact of stress redistribution on sand production and oil productivity.

1.5 Outline

This thesis has been divided into seven (7) main chapters. Following the introduction contained in Chapter 1, a summary of the basics of cold heavy oil production with sand and the state of the art are presented in Chapter 2. The basics include the mechanisms associated with CHOPS, foamy oil, and wormholes. The state of the art is performed to find out what has been published concerning the cold production process itself, foamy oil, wormhole formation, and elastoplasticity and to gain knowledge from the experience cumulative on massive sand production in the last few decades. Chapter 3 presents the general model as a 3D single well model coupling a fluid flow model to a geomechanical model, including for both models the initial and boundary conditions. Chapter 4 contains the CHOPS model, which consists of independent modules such as the foamy oil, sand production, and wormholes models to integrate into the general model. The validation for each one of the components of the modules is included in Chapter 5. Chapter 6 presents the results of applying the model to some field cases. Chapter 7 contains the conclusions and recommendations of this research.

Chapter 2. State of the art

This chapter consists of two parts, the first one presents the basics and terminology of cold heavy oil production (CHOPS) to have a common language to use throughout the next sections and the second one presents the state of the art of the CHOPS itself and each one of components: sand production, foamy oil, wormhole formation, and elastoplasticity.

2.1 Basics of cold heavy oil production with sand – CHOPS

This preliminary section describes the basics of cold heavy oil production with sand (CHOPS) based on Dusseault (2002, 2009), who describes in detail the features of this technology and the mechanisms governing the associated phenomena.

Cold heavy oil production with sand is used in heavy oil exploitation where sand delivery improves the oil well productivity. This single-well technology is a non-thermal recovery method that implicates the deliberate initiation and sustaining of sand influx into the wells using progressive cavity pumps (PCP) to increase production rates and guarantee operating reliability (Dusseault, 2002, 2009). The last version of this technology consists of cold production of a foamy extra-heavy oil field using horizontal wells in the Carabobo Area, the eastern Orinoco Belt (Yang, Li, Xu, Shen, & Shi, 2021).

This technology is functional in unconsolidated sandstone reservoirs to raise the production rate by the massive sand influx. CHOPS is defined as the primary recovery method because it exploits natural energy sources in the reservoir: energy from gas dissolution and expansion and energy from the downward motion of the overburden. Unconsolidated sandstone reservoirs exhibit porosities of around 30% containing heavy oils with high viscosities in the range of 500 to 15,000 cP. The mean characteristics of these reservoirs are listed in Table 2 – 1.

Table 2 – 1. Mean characteristics of unconsolidated sandstones (Dusseault, 2002).

PARAMETER	RANGE
Depth (ft)	1200 – 2800
Porosity (%)	28 – 32%
Permeability (D)	0.5 – 4.5
Oil Viscosity (*cP*)	500 – 15000
Oil Saturation	0.72 – 0.88
Gas Saturation	0.0
Pore Pressure (psi)	378 – 1160
Grain size (μm)	120
Clay content (%)	< 5% in oil-saturated zone
Asphaltene content (%)	12% (11°API) – 5% (17°API)
Gas in solution	> 90% CH_4 and <10% CO_2

However, CHOPS implicates massive sand influx that responds mostly to two main mechanisms: foamy-oil flow defined as solution gas drive with entrained bubbles that maintains the pore pressure and

therefore the flow rate and increases the fluid mobility, and wormholes that are cavities or spaces generated during the massive sand production improving permeability and porosity. This last mechanism is the consequence of geomechanics aspects such as elastoplastic behavior, stress state redistribution, and sand liquefaction.

Sand output increases oil production. To apply the principle that massive sand production would increase the well productivity, it would be necessary to initiate and maintain sand influx using progressive cavity pumps (PCP) to get high oil rates. CHOPS can increase oil production from 5 to 20 times and oil recovery from 12% to 20% OOIP. Then, sand is seen as an asset because more sand means more oil. Cold heavy oil production with sand is about to produce massive sand while producing oil. This means sanding at critical flow conditions, that is, high flow rates.

Sanding remains the dominant mechanism, which is associated and sustained due to the continuous yielding of the formation around the wellbore under the combined effects of overburden stress and lateral unloading, gas evolution, and drag forces. The sand production starts typically at the wellbore sand face, where a disturbed zone is formed during drilling and completion operations. The sand grains and oil flow together to decrease the in-situ stresses and cause the disturbed zone to grow into piping channels filled with slurry formed by the foamy oil and sand. So, the slurry flow increases fluid mobility and the process is cyclically repeated, rising well productivity because of enhanced fluid conductivity and the zone around the wellbore with improved porosity and improved permeability. The continuous sanding process reduces progressively the well production because of the gradual depletion of the reservoir. These combined effects give a peak production followed by a gradual decline as the depletion effects begin to dominate with time. Figure 2 – 1 presents the oil and sand production rates for a well under CHOPS technology.

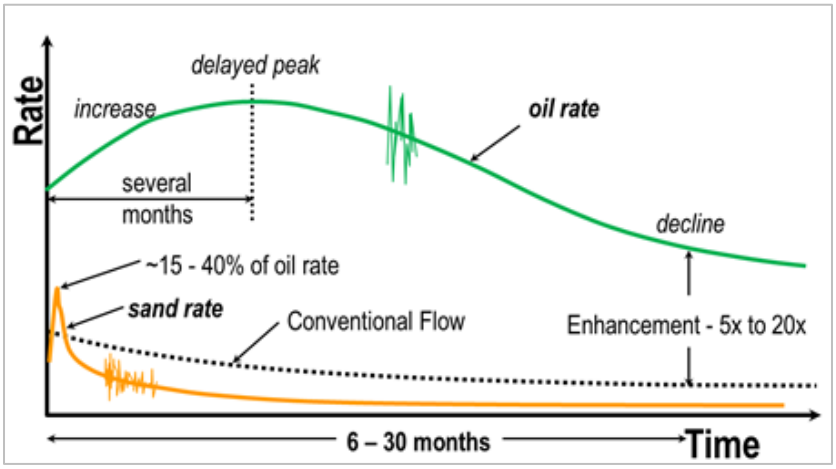

Figure 2 – 1. Oil and sand production rates for a typical CHOPS well (Modified after Dusseault, 2002).

The oil production rate increases at a maximum of several months after placing the well on production, and then it slowly decays as the reservoir depletion effects begin to dominate and there is less reservoir energy available to drive well productivity. This is considered a production cycle for a CHOPS well with a duration from six to thirty months. Table 2 – 2 presents the mean production characteristics of CHOPS wells.

Each production cycle finishes with production declination that is recovered by a workover operation. A successful workover operation can partly reestablish the oil and sand rate but generally not to levels as high as the first cycle. CHOPS wells may experience several workovers during their life, and each workover usually results in a surge of oil and sand production, although diminishing in magnitude with each cycle. These continuing cycles extend the production life of CHOPS wells from 2 to 10 years. Figure 2 – 2 presents the production cycles separated by workover to maintain sand influx for a typical CHOPS well.

Table 2 – 2. Production characteristics for a typical CHOPS well (Dusseault, 2002).

PARAMETER	RANGE
Sand production before CHOPS (%)	0.5 – 10%
Initial sand production – peak (%)	10 – 40%
Sand production per year (TON)	500 – 800
Oil production (bbl/d)	100 – 250
Oil Recovery Factor (%)	12 – 20%
Productivity	5 – 20X
Production time (years)	5 – 12

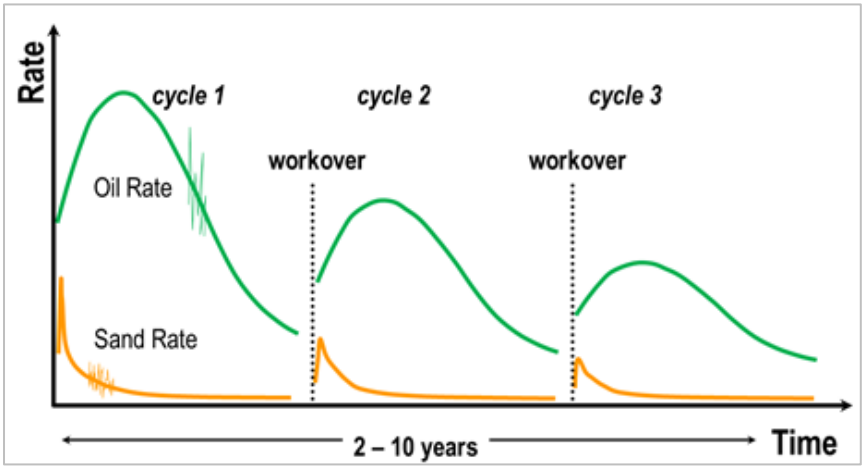

Figure 2 – 2. Production cycles for a typical CHOPS well (Modified after Dusseault, 2002).

2.1.1 Mechanisms of cold production with sand

As mentioned earlier, cold production with sand is governed by foamy oil and wormhole formation. However, in CHOPS technology, a set of driving forces is responsible for the continued sand production that generates higher oil production rates (Dusseault, 2002):

- Gravitational forces as vertical stresses increase from overburden that causes yielding and dilating of the formation.

- The reservoir pressure decreases up the bubble-point pressure because of the bottom-hole pressure reduction. At this pressure level, the fluid behaves as foamy oil, which appears as a solution gas drive with entrained bubbles that maintain the pore pressure and the flow rate, liquefy, and keep sand on suspension, forming a slurry that increases the flow velocity and mobility.

These mechanisms operate at different scales with different effects. Gravitational forces act at the scale of the entire reservoir and overburden. The sand liquefaction and sand suspension happen at the grain scale. At an intermediate scale, a wellbore scale, the generation of a foamy bubble phase in the moving slurry has an important effect on the pressure gradient and thus on the sand suspension and the flow velocity to the well.

Also, these drive forces generate other effects that complement the cold production and raise the flow rate (Dusseault, 2002):

- Aggressive and continuous sand influx increases fluid mobility and grows the disturbed zone around the wellbore that is characterized by enhanced properties: high porosity and high permeability.

- Solution gas behavior in the form of entrained-gas bubbles destabilizes sand, maintains fluid pressure, and improves the production rate.

- Skin effect removal because the massive sand influx maintains the wellbore region without blockage by precipitated asphaltenes, fine-grained particles, or mineral deposits.

Although the main mechanisms for massive sand influx are foamy oil and wormhole formation, sand production has influenced several geomechanical processes arising from changes in petrophysical and mechanical properties, which involve a continuous dynamism in the stress state around the well and in the reservoir itself. Important reservoir properties change during the CHOPS process. Figure 2 – 3 presents the mechanisms governing the CHOPS processes.

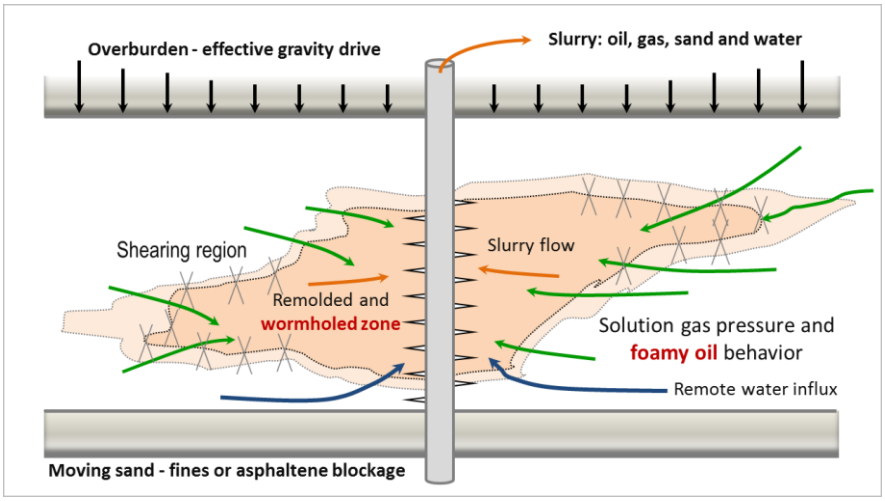

Figure 2 – 3. Mechanisms of CHOPS (Modified after Dusseault, 2002).

2.1.2 Foamy oil

Heavy oils differ considerably from conventional oils in viscosities and thermodynamic properties, especially in some cases, in which heavy oils display a foamy-oil behavior. The gas-oil interface stabilizes due to the presence of asphaltenes and the crude oil behaves as a gas-oil emulsion (Tang, Temizel & Kovscek, 2006).

In conventional oils, the gas evolves from solution when the formation pressure reaches the bubble-point pressure; these bubbles coalesce with each other to form a free gas phase and the number of gas bubbles increases in the liquid phase as pressure goes down. The generation and coalescence of these bubbles are usually instantaneous. The gas starts to flow once the critical gas saturation is achieved. However, in heavy oils, the gas bubbles that evolve from solution do not coalesce with each other easily, and stay as entrained gas in the solution; and the fraction of entrained gas increases as pressure decreases and initiates flowing as a free gas phase only at a pressure notably less than the conventional oil's bubble-point pressure (Kraus, McCaffrey & Boyd, 1993; Joseph, Kamp & Bai, 2002).

Foamy oil is a mixture of oil, water, and small gas bubbles that is related to the release mechanism of dissolved gas. This is a type of solution gas drive, in which the entrained gas bubbles in the solution delayed the bubble coalescence and the free gas formation. Foamy oils have gas in solution, more than 90% is methane (CH_4) and less than 10% is carbon dioxide (CO_2) (Dusseault, 2002).

The gas is close to saturation in dissolved form in the liquid phase because the bubble point usually is at or near the pore pressure. The gas release starts as small bubbles due to the high drawdown, but these bubbles do not coalesce rapidly to form a continuous phase, keeping as entrained bubbles during flow to the wellbore and rising in size as the pressure declines. Then, these bubbles act as an internal drive force, expanding and driving the slurry into the wellbore at a velocity greater than the one predicted by conventional liquid flow theories.

The foamy oil is formed in an induction zone, where the bubble nucleation occurs in response to pressure decline. Part of the gas bubbles is trapped in the solution in the oil into a pore due to a pressure gradient. This foam (entrained gas in the oil) tries to move but gets blocked in the pore and impedes the flow through the pore throat, thus reducing the flow capacity in the porous media and raising the local gradient pressure. This leads to destabilizing sand from the formation matrix because of an increment of the drag force on the grains. At some point deeper in the induction zone, the pressure gradient becomes high enough and the friction forces are low enough to achieve detachment and discharge of individual grains from the matrix, in what is known as sand liquefaction. This removal of sand grains occurs simultaneously at many sites around the well.

Although bubbles move with the fluid and discrete gas channels are developed in these wells, there is no direct drainage mechanism to deplete gas pressures far within the reservoir. Thus, gas-oil ratios (GOR) remain constant, often for years, and virgin pressures are sustained. Hence, solution gas in the form of bubbles destabilizes sand, maintains pressure in the fluids, and accelerates the flow to the wellbore. Another important point for foamy-oil behavior is the reduction of in-situ oil viscosity (Dusseault, 2002; Wang, Yale & Dasari, 2011).

To summarize, the foamy oil retards the formation of a continuous mobile gas phase, enhancing fluid compressibility and providing a natural pressure maintenance mechanism. The existence of a non-equilibrium foam of oil and gas requires some adjustment of the typical fluid property data used in a simulator to capture the fluid compressibility effects of foamy oils. The gas-oil ratio (GOR) remains stable typically for years and virgin pressures stay constant because there is no direct drainage mechanism to deplete gas pressures far within the reservoir. Consequently, gas release displaces sand, retains the fluid pressure, and accelerates the flow to the wellbore (Dusseault, 2002; Wang *et al.*, 2011). Another way to explain the performance of foamy-oil reservoirs is that the oil entrains the solution gas liberated when the reservoir pressure falls below the thermodynamic equilibrium bubble-point pressure forming a

foam (Kraus *et al.*, 1993).

2.1.3 Wormholes formation

As mentioned previously, the massive sand influx during cold heavy oil with sands creates zones of high porosity and high permeability known as wormholes. A wormhole is a cavity that is not precisely empty or a volume in which there is no grain-to-grain contact, and it is full of slurry (fluidized sand and foamy oil). The wormholes initiate around the perforating that is dilated and tend to develop and grow in the weakest sand and towards the highest-pressure gradient. The wormholes are generated at the early stage of aggressive sanding and then tend to be stable. Figure 2 – 4 presents a sketch of the wormhole formation.

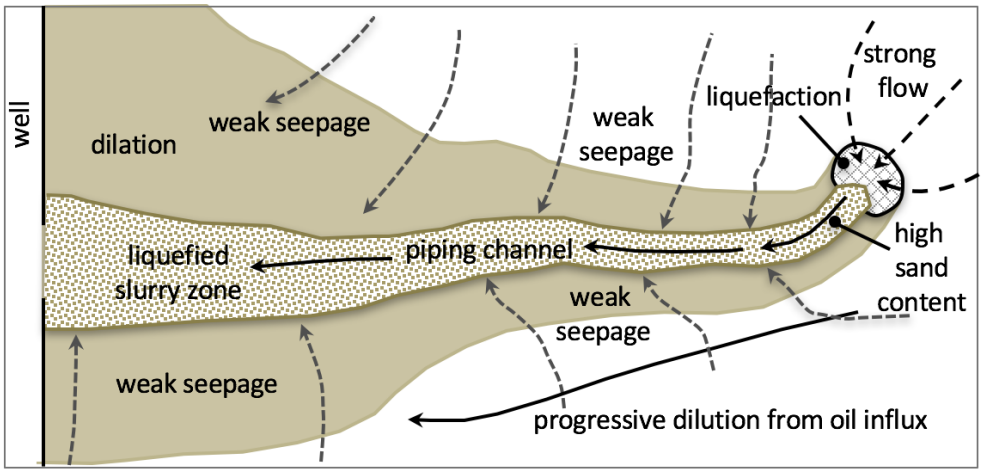

Figure 2 – 4. Wormhole formation (Modified after Dusseault, 2002).

As sand grains detach from the matrix, create spaces, which are not void, and form a remolded zone of higher porosity that is filled with a slurry (sand, oil, water, and gas). The growth of this zone causes an increment of the apparent permeability around the wellbore; because this zone grows with continuous sanding, the well behaves as if it has a rising radius with time. The near-wellbore region is filled with high porosity slurry (>50%) where the permeability is huge, but for the most part, the remolded zone is viewed as a dilated, partly remolded region with diffuse gradational boundaries (Dusseault, 2002).

The piping channels initiate usually at the wellbore sand face because this zone is weakened during drilling and completion operations. The oil that flows towards the production well generates pressure gradients large enough to overcome cohesion forces that hold the sand grains together, leaving them free to be moved. Two conditions seem to be necessary for wormholes to maintain growth: the pressure gradient at the tip of the wormhole, which must be high enough to dislocate the sand grain as well as the pressure gradient along the wormhole to transport the sand from the tip to the wellbore (Tremblay, 2005). Wormholes tend to grow in preferential layers (highest porosity and oil saturation) within the formation, in the weakest sand, and towards the highest-pressure gradient.

While sand is removed from the formation matrix, the gravitational loading (overburden) causes shear and dilation around the well, because this zone is also weakened and dilated. The pore pressure stays mostly unaltered in the yielding and intact zones due to the high oil viscosity.

The vertical stresses and fluid pressures both act upon cavity walls. Around the cavity, the radial stress decreases, and the tangential increases, causing the shear stress increases, and the confining stress declines, bringing the intact zone to a shear yield condition. This shearing induces dilation in the weak formation around the cavity, and destroys the cohesion, so the sand is deformed and remolded. The rock changes intensely from intact sand (densely packed) to sheared sand with higher porosity. In other words, the porosity increases from an initial value of around 30% to high values of 35% – 38%, but the matrix remains as a solid mass held together by compressive stress and has frictional behavior. This change in porosity increases the absolute and relative permeability and changes the phase saturations. As sand is dilating and yielding, the stresses must be redistributed at different scales: reservoir scale, wellbore scale, and channel or cavity scale.

At the reservoir scale, the wormholes help to prolong a yielded region of softer material that is weaker and can hold less of the overburden stress. However, the total overburden load must still be carried to preserve the overall stress equilibrium, so the vertical stress increases around the wellbore. At the same time, the lateral stresses within the reservoir decrease all over due to the continuous sand withdrawal. Whereas the reservoir is thin compared to its length, the stress equilibrium is reached by the horizontal stress redistribution into the overlying and underlying strata and the vertical stress redistribution into the cavity flanks. Accordingly, the main impact of the sanding in the reservoir is the reduction of the horizontal stresses (Dusseault, 2002).

At the cavity scale, both the radial and tangential effective stresses are low because there is no cohesion. The stress reduction due to the cavity formation should be compensated by redistribution further from the opening where the confining stress effect leads the intact rock to hold up to higher shear stresses.

A wide zone around the wormholes is affected by their propagation with softening or partial loss of structural rigidity, and this can be a zone of dilation and improved permeability. The existence of many channels in the reservoir should so have an overall softening effect, leading to large-scale stress redistributions between intact reservoir zones and zones with channels, which, at a large scale, look quite similar to the compact growth model. This zone also has a decrease in high frictional resistance on dense sand packings at the natural state, making it more ductile and vulnerable to plastic deformation and easy to be dragged into the slurry flow that contains sand in suspension. This process of weakening, dilation, and increased ductility remains dynamic by overburden that stays driving pressure on the reservoir. No matter what happens in the reservoir, the weight of the overlying rocks exerts stresses, which also provide energy to sustain pressure.

The remolded zone may not extend over the all-vertical height of the reservoir. Near the wellbore, the porosity values are around 42% – 45%. Values around 45% are close to the maximum porosity for loose sands in grain-to-grain contact under very low stress. Whatever the geometrical details of the zone around the wellbore, the effect of continued sanding is evident propagation of a zone or channels of high permeability, so the flow capacity of the well stays to gradually rise (Dusseault, 2002).

The continuous sanding causes changes in petrophysical properties that also imply changes in mechanical properties and stresses around the wellbore and in the reservoir, itself. These changes define dynamic zones with diffused boundaries that drive the performance of CHOPS. Figure 2 – 5 displays these zones during massive sanding. These zones are defined in terms of their characteristics as follows(Dusseault, 2002):

- ***Intact zone:*** This is the reservoir zone, where porosity continues at around 30% and the sand has not yet suffered shear distortion, cohesion loss, dilation, and shear yield, while the stresses are altered. In this zone, the ratio of effective stresses (σ_1'/σ_3') is as high as 5 or 6 before yielding, but after the failure occurs, it gradually reduces as the sand continues yielding and weakening. Hence, the vertical stress increases to support part of the overburden load causing higher shear stress than in the virgin state and lower lateral stress due to the sand production but saving all properties of intact virgin rock.

- ***Transition zone:*** It is the weakening zone with cohesion loss. It is an intermediate zone between yielded and intact zones, where the stresses change as the rock undergoes shear and loses strength and cohesion. As an extension of the yielded zone, the vertical stress is high and the radial stress is low due to the continuous sand withdrawal.

- ***Yielded zone:*** This is the shear zone. Hence, this zone has high shear stresses and so loses strength and cohesion. This fully remolded plastic flow zone is not yet liquefied. In this zone, the ratio of effective stresses (σ_1'/σ_3') after shearing and dilation is demarcated by the residual friction angle for sands ($\approx 30°$) and it is around 3. Furthermore, the maximal principal stress tends to be the vertical stress because of the gravitational force from overburden, and the minimum principal stress is the radial stress because of the lateral unloading from sand production. Moreover, the porosity range is from 40% to 45%.

- ***Liquefied zone:*** It is the slurry zone around the wellbore, where sand liquefaction occurs and the mixture of foamy oil and fluidized sand flows. The porosity here must be greater than 50%, which assures the existence of a liquefied state. The permeability is extremely high. This is the zone, in which the wormholes are created.

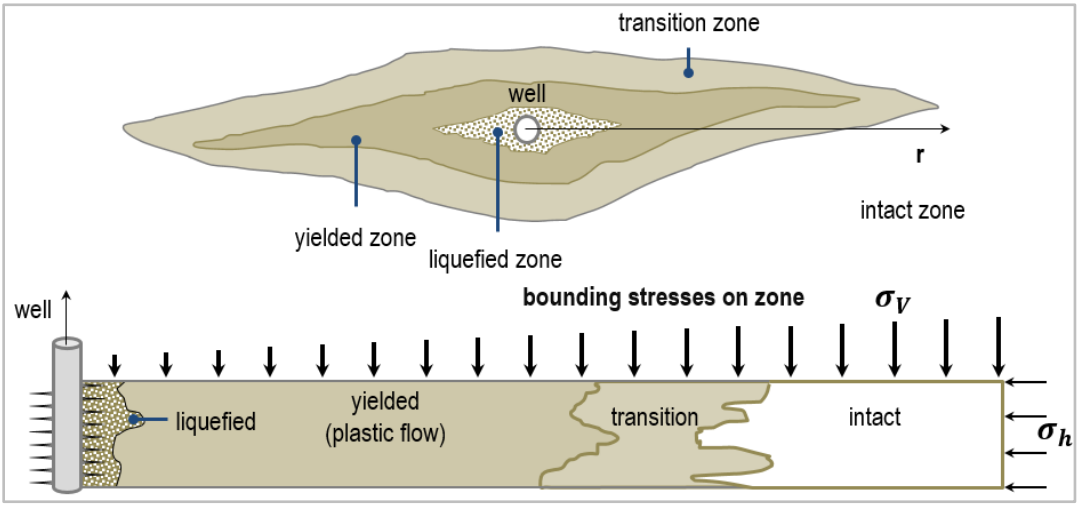

Figure 2 – 5. Zones around the wellbore during massive sand production. (Modified after Dusseault, 2002)

The growth of these areas is smooth and managed by stress redistribution. Vertical stress plays a major role in destabilization and dilation processes. The yielded and liquefied zones can support a small part of the vertical stress, but the rest of the stress should be redistributed around the well, added to the other forces that cause yield and dilation. The shale layer over the producing formation behaves like a beam

with high stiffness that homogenizes the geometry of the deformation and yield zone. Thus, the outer region of the altered zone loads stresses lower than vertical stress, while the more rigid zones as intact zone must support higher stress.

Intact regions located between yielded zones are most affected by the stresses than others, and if this stress concentration cannot be sustained, then shear, dilation, and weakening will occur in these zones. Thus, stiffness of overburden causes a flattening due to deformation, leading to the continuous stress redistribution towards the periphery of the yielded zones, which tends to homogenize the yield strength in the area with smooth growth, maintaining the circular or elliptical bounds and removing the shaped fingers of the plastic flow zone within the perimeter intact zones.

Understanding the wormhole's formation and its effect on production is essential to describe an additional component: sand liquefaction. Sand liquefaction is the process in which the saturated sand loses shear strength and stiffness due to dynamic loading. In other words, liquefaction is the loss of strength of weak sands that causes flow slides due to a slight disturbance (Robertson & Fear, 1997; Terzaghi, Peck, & Mesri, 1996).

While the wormhole's initiation and propagation is the dominant sanding mechanism, it seems probable that the sand is liquefied at the advancing tip at about the same rate at which the crude oil is flowing into the channel tip. Hence, at the channel tip, the sand concentration in the liquid is still high as the channels grow into the formation. As the slurry with high sand concentration flows to the wellbore through the channel, it is gradually diluted by slow liquid influx from the closest reservoir zones.

At the grain scale, the sand liquefaction and entrainment effect occur because of the foamy-oil behavior, in which locally high-pressure gradients pluck almost unconfined sand grains from the weak and dilated matrix to discharge the sand grains into the slurry. Sand liquefaction is controlled by grain buoyancy, changes in the bulk density of the sand, high-pressure gradient around the wellbore, weak cohesive cement between sand grains, and low internal friction angle (Hayatdavoudi, 1999).

When a well produces at a high production rate, the shear stresses around the wormholes cause the build-up of high pore pressure very fast. Consequently, the decrease in shear strength and the pore pressure increase are favorable conditions for sand liquefaction. If sand is free to shear, dilate, and suffer liquefaction, as in CHOPS wells, then pore throat blockages and the local pressure gradient increase, so continuously clean themselves up by sand movement and liquefaction. The main outcome of sand liquefaction is the complex multiphase fluid flow stated as a mixture of foamy oil and fluidized sand flows, and then the fluid flow is combined by four components: oil, gas, water, and sand. As a result, sand grains can flow easily like a liquid (Hayatdavoudi, 1999).

2.2 State of the art

Dusseault (2002, 2009) presents in detail the physical mechanisms acting in CHOPS wells, defining dynamic zones where mechanical and petrophysical properties change due to stress distribution during massive sand production. The stress distribution may be calculated from a combination of non-linear elastic theory in the intact zone, and plasticity or damage theory in the weakening and plastic flow zones.

Generally speaking, the range of models runs from idealized analytical models based on cylindrical geometry to very general coupled fluid-flow and geomechanical models based on the strength, damage, and failure characteristics of the unconsolidated sand. Simple models are quite useable but not fully general while the complex full-physics models provide generality and extensibility in principle but in practice require extensive computational resources.

Wang, Chen & Dusseault (2001) propose an integrated model for sand production coupling a 3D black-oil model for three-phase with foamy oil with an elastoplastic geomechanical model with a wormhole model. This seems to be the first approach to model CHOPS wells.

Rivero *et al.* (2010) present a coupled flow/geomechanics simulator with non-equilibrium foamy-oil reactions, representing the wormholes as a homogeneous damage zone. This simulator has some limitations such as the sand production rates are calculated using an empirical correlation that depends on pressure gradients and it needs a relationship between damage (porosity change) induced by sand failure and its corresponding increase in permeability.

Xiao (2012) simulates CHOPS using a combined model: a transient pressure and production analysis to determine the wormholes coverage quantitatively using a semi-analytical approach based on source and sink function methods, and a composite model with PVT properties discontinuity between foamy oil and heavy oil zones to model foamy oil behavior.

Rangrizshokri (2015) presents a workflow for CHOPS modeling to investigate efficient EOR/IOR (enhanced/improved oil recovery) methods after CHOPS. A partial-dual porosity approach coupled with algorithms for wormhole generation as Diffusion Limited Aggregation (DLA) is used for the fractal wormhole patterns, and a 3D geomechanical model is used to calculate the stress distribution. After validation of the models using field data, several post-CHOPS scenarios are simulated, including thermal, solvent, and thermal/solvent hybrid applications. As overall findings, the heavy oil recovery is achieved using combined light and heavy solvents, and steam has a positive role in solvent retrieval.

Fan, Yang, & Li (2020) propose a robust simulator with a technique to determine the three-phase relative permeability of the CHOPS processes considering contributions of the dynamic wormhole growth and the foamy oil flow with an improved IES (iterative ensemble smother) algorithm, which is achieved by normalizing both model parameters and measured production profiles. The dynamic wormhole propagation is characterized by a sand failure criterion based on pressure gradient and the evolution of the foamy oil is achieved through kinetic reactions.

Mohamad-Hussein, Mendoza, Delbosco, Sorgi, De Gennaro, Subbiah, ... & Daniels (2021) propose a coupled model of fluid flow model and elastoplastic damage model to simulate production in CHOPS well including foamy oil and wormholes.

Given the nature of this research, the state of the art presented here is oriented to CHOPS modeling, starting with sand production and incorporating elements such as foamy oil and wormholes to get the different components to simulate massive sand during cold heavy oil production.

2.2.1 Sand production

Salama & Venkatesh (1983) present a predictive sand production method based on empirical relation that depends on fluid velocity, the strength of the formation, and grain size. This model is considered a specific case and not a general predictive method.

Many other researchers have also investigated the mechanisms for the prediction of sand production. Bratli & Risnes (1981) and Risnes, Bratli & Horsrud (1982) propose a theoretical model for stability and sanding of a perforation opening with a tensile failure criterion. Perkins & Weingarten (1988) propose a sanding criterion in terms of the pressure gradient. Veeken, Davies, Kenter, & Kooijman (1991), Ramos, Katahara, Gray, & Knox (1994), and Van den Hoek, Hertogh, Kooijman, De Bree, Kenter, & Papamichos (2000) identify compressive shear failure, tensile failure, and erosion as the three main mechanisms of sand production.

Morita, Whitfill, Fedde, & Lovik (1989) present an analytical approach to predict the onset of sand production in terms of critical drawdown pressure at the high flow rate, considering two factors: well pressure and local pressure gradient around a cavity.

During the last three decades, finite element methods have also been used to predict limited sand production. Morita, Whitfill, Massie, & Knudsen (1989) present a numerical approach for sand production prediction based on drawdown pressure and using two finite element models: a transient fluid flow model that calculates pore pressure distribution around perforation holes for given boundary conditions, and a geostructural model coupled with the fluid force that calculates stress state, deformation, and plastic deformation from the calculated pore pressure.

Burton, Davis, Morita, & McLeod (1998) postulate a methodology for sand production prediction using a similar numerical approach as Morita *et al.* (1989) for sand production prediction based on pressure drawdown for gas reservoirs.

Vardoulakis, Stavropoulou, & Papanastasiou (1996) propose a 1D model implemented by the finite differences method that couples fluid flow and erosion. The theoretical basis of the hydrodynamic erosion of sandstones is based on filtration theory and three phases mixture theory for a continuum consisting of skeleton solids, fluidized solids, and fluid. Later on, Papamichos & Stavropoulou (1998) present a sand prediction model in finite elements that combines the evolution of localized deformation with hydrodynamic erosion. Papamichos, Vardoulakis, Tronvoll, & Skjærstein (2001) develop a sand production model for volumetric sand production predictions that take into account the effects of the external stresses and fluid flow rate.

Yi (2001) proposes a coupled single-well geomechanical-gas/sand flow simulator for gas wells, in which the gas can flow either Darcy or non-Darcy flow, porosity and permeability can vary during sanding, and sand particles move at the gas velocity. The geomechanical model uses the Mohr-Coulomb failure criterion and the sand is produced from the failure region once the formation around the wellbore is yielded.

Wang *et al.* (2001) and Wang & Chen (2004) introduce a 3D integrated model incorporating a three-phase, black oil model coupled with a geomechanics model. This model is featured an elastoplastic

constitutive model with a slurry flow model.

Wan & Wang (2004a) present a sand production model that couples an erosional model with a stress model through bulk volumetric strains to include the effect of the deformation of porous media. The erosional model is developed based on the mixture theory to define the porosity considering a three-phase system composed of solid, crude, and fluidized sand. This couple model attempts to evaluate the enhanced production and cumulative sand production in cold production wells.

Wang & Xue (2004) propose a fully coupled reservoir-geomechanics model to simulate production in heavy oil reservoirs, which couples a two-phase flow model with solution gas behavior and an elastoplastic geomechanical model with dilation and erosion. A sand erosion model is proposed after the onset of sand production, based on the degree of plastic deformation inside the reservoir formation. This is the first attempt to properly model massive sand production.

Wang, Walters, Settari, Wan, & Liu (2004) present a fully coupled black oil/geomechanics sand production model with erosion and multiphase flow of three components (gas, water, oil) using the mixture theory. This model can be used for wellbore stability analysis, design in open-hole completions, perforation designs as well as a volumetric sand prediction for different production strategies.

Wang, Settari, Wan, & Walters (2005) apply the coupled reservoir/geomechanical model to predict the volumetric sand production and associated wellbore stability for two types of completion schemes: open-hole completion and perforated casing.

Wang, Walters, Settari, & Wan (2006) extend their earlier coupled model for sand production (Wang, Settari, Wan, & Walters, 2005) to CHOPS incorporating the foamy-oil effect and integrating a modular approach to quantitatively predict volumetric sand production and enhanced oil recovery.

Wan, Liu, & Wang (2006) present a simplified sand production model that involves the coupling of geomechanics with hydrodynamics and erosion to predict volumetric sand production using the mixture theory. This model is applied to compute the axial and radial viscous flow in a thick wall cylinder test.

Du, Jiang & Chen (2009) propose an integrated spread erosion model, in which a wormhole spreading model and an erosion model are combined to describe the sanding behavior and oil production, both in wormhole tips and in the sand wall of the wormhole. This sand production model combines three models: a skin factor, a mobile permeability, and a wormhole spreading model to describe the dynamic performance of sanding and oil production in CHOPS.

Wang, Yale, & Dasari (2011) propose a geomechanics and fluid flow coupled model using the finite element method with an Arbitrary Lagrangian-Eulerian (ALE) formulation with automatic adaptive re-meshing, Eulerian Boundary, and an explicit dynamic relaxation solution scheme for massive sand production. The numerical platform of this coupled model is ELFEN™ (Rockfield Software Ltd.). These features allow the modeling of large deformation and highly nonlinear geomechanical behavior. Also, it considers stress study and wormholes as damage zone.

Cerasi & Vardoulakis (2012) present a sand production model based on episodic functions, in which the sand rate is proportional to the fluid drag force if exceeds a certain grain transport threshold, that is moderated by the solid friction between sand grains and a porosity evolution law, where the natural result

of losing sand grains under sand production depends on the stress level, above sandstone failure stress.

Kim & Sharma (2012) present a sand production model to predict the stability of wellbores and perforation tunnels as well as the mass of sand produced, incorporating two-phase flow, formation failure, and flow-driven sand erosion mechanisms.

Rahmati, Jafarpour, Azadbakht, Nouri, Vaziri, Chan, & Xiao (2013) present an in-depth review of the different approaches and models for sanding prediction, which most of these models are based on the continuum assumption, while a few of them are based on discrete element model, some models evaluate the conditions that lead to the onset of sanding, while others make volumetric predictions, some models use analytical approaches to estimate the onset of sanding while others use numerical models to calculate the sanding rate. This review concludes that although major improvements have been reached, sanding tools are still unable to predict the sand mass and the sand rate for all field problems in a reliable form, a conclusion that can still be said to hold.

Araujo Guerrero, Alzate, Arbelaez-Londono, Pena, Cardona, & Naranjo (2014) and Araujo-Guerrero, Alzate-Espinosa, Arbelaez-Londoño, & Morales-Monsalve (2018) present the main variables (but not unique) involved in the sand production issue and an analytical geomechanical model considering the stress state regime, the pressure drawdown, and well completion (open-hole and cased-hole) to predict the production onset and select the adequate sand control technique.

Araujo-Guerrero (2015) presents a sand production model that consists of a fluid flow module, a geomechanics module, and a sand production module with the calibration of parameters from experimental data.

Wu, Choi, Denke, Barton, Viswanathan, Lim, ... & Madon (2016) present a numerical model based on laboratory experiments to quantify the sand production for weak sandstones. The experiment program is conducted on large samples under realistic effective stress and drawdown conditions with oil and gas flow to calculate the cumulative amount of sand produced. The numerical model used discrete element and finite difference methods to calculate the critical plastic volume. The sand production quantification model was developed by correlating the critical plastic volume with the cumulative amount of sand produced and is applied to a field case study aiming for model validation with consistent results.

Wang & Sharma (2016) propose a coupled model for sand production prediction with the multi-phase fluid flow, geomechanical stress, and sanding criteria, in which the sanding criteria are based on a combination of tensile and shear failure from Mohr-Coulomb theory and strain-hardening/softening; the sand erosion is predicted once the failure criteria are met using hydrodynamic and other forces and the cohesion and residual strength resulting from relative permeability and capillary pressure. The sanding onset and the sand production rate have both been simulated for open-hole and cased-hole completions under different flow conditions.

Olatunji & Micheal (2017) propose a prediction model based on the Support Vector Machines (SVMs) classification approach to evaluate the sanding onset in petroleum reservoirs of the Niger Delta Region, taking into account different parameters such as the rock and fluid properties, and geotechnical data, among others. This robust model is verified using field data.

Eshiet & Sheng (2021) provide a review of the historical progress in experimental and analytical models

to understand the nature of sanding and its mechanisms. The models are classified based on the onset of sanding, rate and amount of sand as well as the failure criterion used. This review confirms that there are still some features of sand production requiring further study, and maybe a hybrid approach that combines experimental, analytical, and numerical methods could be the best solution.

2.2.2 Foamy oil

Heavy oil reservoirs under solution gas drive as foamy-oil behavior have shown anomalous primary performance: high oil production rates, low production GOR, and high oil recovery.

The earliest model for foamy oil is proposed by Smith (1988), which involves a highly compressible mobile liquid phase, consisting of a true oil liquid and tiny entrained gas. The model defines a pseudo-pressure form from Darcy's law and the radial diffusivity equation is used to account for the effects of the compressibility of the enhanced liquid phase. Thus, the compressibility of the foamy oil is $c_{fo} = \kappa/p$, where κ is an empirical constant that depends on the amount of entrained gas, and p is the mixture pressure; a solution gas drive model is obtained to define the pressure-dependent multiphase flow properties and define the flow of the foamy oil. The features of this model are too simple.

The first attempt to simulate the foamy-oil effect uses empirical adjustments to conventional solution gas drive models. The key parameters to be adjusted are critical gas saturation, oil/gas relative permeability, fluid and/or rock compressibility, pressure-dependent oil viscosity, absolute permeability, and the bubble-point pressure as proposed by Loughead & Saltuklaroglu (1992), and do not expect to capture many important features of foamy-oil behavior.

Maini, Sarma, & George (1993) try to verify the high dispersion mobility in the laboratory but find that the presence of freshly nucleated gas bubbles decreased the oil mobility, establishing that the dispersed-gas flow is indeed possible under conditions of solution gas drive.

Maini (1996) explains the high recovery factor found in heavy oil as the answer to foamy oil, which is in the range of 5% to 15% compared to light oil in the range of 1% to 5%. In heavy oils, this range can be attributed to the higher-pressure drawdown imposed during cold production because of the high oil viscosity, leading to the breakup and entrainment of pore throat-sized gas bubbles through the porous medium.

Some of the most interesting attempts to model foamy oil are mechanistic models based on how the gas comes out of the solution and what happens to the released gas. Such models can be divided into two broad categories: equilibrium and kinetic models. The equilibrium models assume complete local equilibrium between different phases and that the fluid mobility is independent of the capillary number, and then they cannot account for the thermodynamically unstable nature of foamy dispersions. Kinetic models attempt to capture the time-dependent changes in the foamy-oil behavior considering that the gas dispersion in oil is not thermodynamically stable and will separate into free gas and oil phases. While the natural tendency of the dispersion is to move toward the segregation of phases, such segregation can be detained by imposing flow conditions that help the regeneration of the dispersed bubbles.

Kraus, McCaffrey & Boyd (1993) propose a pseudo-bubble-point model for primary depletion in foamy oil reservoirs as an adjustable parameter of the fluid properties. Below this pseudo-bubble-point pressure,

only a fraction of the released gas remains entrained, and the gas fraction decreases linearly to zero with declining pressures. The entrained gas is treated as a part of the oil phase, but its molar volume and compressibility are evaluated as free gas.

Other models such as Lebel (1994) intend to match the production behavior by modifying fractional-flow curves obtained from the gas and oil relative permeabilities. The models vary in function of the assumption of the entrained-gas fraction, which converts into a match parameter of the model, and the fractional flow increases linearly with saturation until the limiting entrained gas saturation is reached, departing from a zero-gas saturation. Beyond the limiting volume fraction of gas in the foamy oil, any further increase in gas saturation results in free gas. The gas begins to collect and flow as its saturation increases. For foamy oil, the effective viscosity decreases slightly from that of the oil as the volume fraction of gas increases, the density is taken as a volume-weighted average of the densities of the oil and gas components, and a gas-oil PVT is an equilibrium relationship. This fractional flow model only captures a feature of foamy-oil behavior in that some fraction of the evolved gas is entrained in the oil phase, and requires only modified relative permeability and component properties to be implemented in a reservoir simulator, but time-dependent changes and pressure gradient changes are not considered, and so finding the right fractional flow curve may require a trial and error process.

Other models suggest a viscosity reduction to model foamy-oil flow. Claridge & Prats (1995) propose a reduced viscosity model to emulate foamy oil flow considering that the asphaltenes present in the crude oil adhere to the gas bubbles, while the latter is still very tiny. The bubble surfaces are coated by the asphaltenes stabilizing the bubbles at small sizes. This concept of asphaltenes adsorption leading to viscosity reduction has not been experimentally verified (Sheng, Maini, Hayes, & Tortike, 1999a).

Sheng, Maini, Hayes, & Tortike (1999a; 1999c) and Sheng, Hayes, Maini, & Tortike, (1999b) describe a dynamic-flow model considering two rate processes: a rate process that controls the transfer from solution gas to evolved gas and a process that controls the transfer rate from evolved gas to free gas, and two phases of foamy-oil and gas using the conventional two-phase relative permeabilities. The dispersed gas flows with the oil as a part of the liquid phase with the compressibility and density of the gas phase and the viscosity of the liquid-oil phase. An empirical correlation describes the bubble growing exponentially and the disengagement of dispersed-gas bubbles from the oil decaying exponentially.

Pooladi-Darvish & Firoozabadi (1999) and Firoozabadi (2001) propose a relative permeability approach similar to the approach suggested by Sheng, Maini, Hayes, & Tortike (1999a; 1999c). The improved recovery results primarily from the reduction of the gas's relative permeability as well as the increase of the oil viscosity due to the oil pressure gradient that causes the movement of the dispersed bubbles.

Wang *et al.* (2001) and Wang & Chen (2004) propose a three-phase model to simulate the oil/gas/water flow and to address reservoir mobility changes arising from sanding, and pressure drive changes arising from the foamy-oil flow.

Dynamic-flow models account for the dispersion characteristics with time-dependent changes using simple rate processes, controlled by the rock and fluid properties and the capillary number. The constant rates affect the history matching at a known-depletion rate and are not valid for predicting the outcome of a new reservoir under different flow properties.

Maini (1996) suggests a model that accounts for the kinetics of physical changes occurring during the

gas in oil dispersion, defining three non-volatile components in the oil phase: dead oil, dissolved gas, and gas dispersed in the forms of micro-bubbles. The dissolved gas changes to dispersed gas due to a rate process dominated by the existing local super-saturation and the dispersed gas changes into free gas by a second-rate process. Both rate processes are modeled as chemical reactions.

Some researchers such as Sheng *et al.* (1999a; 1999c) and Sheng *et al.* (1999b) observe during solution gas drive experiments an oil recovery increment with increasing pressure depletion rates due to the increasing super-saturation of the oil leading to a greater number of gas bubbles and higher gas saturation. They model the rate of release of solution gas using the exponential decay of local super-saturation and assuming that the gas released from solution stayed as dispersed gas in the oil. The dispersed gas separates from the oil. Then, two sequential rated processes describe the kinetics of the transfer of the solution gas to the free gas.

Maini (2001) finds two types of non-equilibrium processes involved in solution gas drive in heavy oils. There is a non-equilibrium process between solution gas and free gas that leads to the super-saturation of dissolved gas in the oil phase and another non-equilibrium is related to fluid distribution in the rock.

Joseph, Kamp & Bai (2002) present a foamy-oil model that depends only on the velocity through Darcy's law, the pressure, and the dispersed gas fraction. This simple model uses an empirical relation for the derivation of solubility isotherms obtained from PVT data and the modeling of nucleation, coalescence, bubble drag laws, and transfer functions are avoided.

Bayon, Cordelier, Coates, Lillico, & Sawatzky (2002) compares two foamy-oil models: one model with two kinetic equations for mass transfer that describes how one type of gas is transformed into another: solution gas, dispersed gas, and free gas; while a second model with six kinetic equations for mass transfer identifies four types of gas, including two types of dispersed gas. Each model defines originally the mobility of each type of gas, which leads to different relative permeability models. These models are applied to two sets of long-core depletion experiments with significantly different depletion rates and different results.

Sahni, Gadelle, Kumar, Tomutsa, & Kovscek (2004) and Tang, Sahni, Gadelle, Kumar, & Kovscek (2006) present a mechanistic model and experiments to study the gas saturation behavior, which suggests a greater number of nucleation sites and bubbles nucleated are generated at higher-pressure depletion rates, resulting in greater gas saturation. Most heavy oil depletion experiments evidence some non-equilibrium characteristics, which depend on viscosity and depletion. Analysis of field pressure gradients and flow rates suggests that dispersed gas flow occurs close to the wellbore or near wormholes if they are present. This model captures overall heavy oil solution gas drive behavior in the field using a suitable critical gas saturation and gas relative permeability curve.

Uddin (2005) proposes a kinetic model coupled with a thermal reservoir simulator via a set of pseudo-kinetic reactions that simulate the dynamics of gas ex-solution and transport processes in a heavy oil reservoir. In this model, two relatively simple types of mass transfer equations predict bubble nucleation and growth in a live heavy reservoir.

Wang, Walters, Wan, & Settari (2005) incorporate the foamy-oil drive into their sand production model. Foamy oil is modeled as a dispersion of gas bubbles trapped in the oil, where these gas bubbles maintain higher reservoir pressure and the gas bubble never forms a free phase as the reservoir pressure drops

below the bubble point pressure and moves with the same velocity as the oil phase. Essentially, foamy oil is treated as a single-phase flow with a modified formation volume factor.

Chen & Maini (2005) simulate several depletion experiments carried out in long sand packs and compare the results with the black oil model from IMEX® and a reaction rate-based foamy oil model from STARS®. This study evidences that the foamy oil model provides a more accurate matching of the experimental results compared to the black oil model, and concludes that the relative permeabilities to gas and oil and the reservoir fluids properties as mole fraction or ratio of original dissolved gas to dead oil, the viscosity of the fluids (dead oil and the liquid-phase of gas) have significant effects on oil production, and the distributions of oil, dissolved gas, free gas and pressure along the sand-pack changes significantly with depletion rates.

Adil & Maini (2007) presents an experimental study to evaluate the role of asphaltenes in foamy-oil behavior using sand packs. The results show that the presence of asphaltenes appears to facilitate bubble nucleation and decreases critical super-saturation, and seem to help in sustaining the dispersed gas flow by suppressing bubble coalescence. This study concludes that the presence of asphaltenes significantly promotes foamy-oil flow and revives the concept of viscosity reduction by asphaltenes adsorption.

Rivero *et al.* (2010) implement in their model a foamy-oil model developed by Uddin (2005) at Alberta Research Council (ARC). This model employs a sophisticated treatment of fluid PVT behavior based on kinetic reactions and uses a total of three oil phase pseudo-components (dead oil, dissolved CH_4 gas, dispersed CH_4 bubbles), one gas phase pseudo-component (connected CH_4 gas bubbles), and one aqueous component (water).

Wang, Chen, Qin, & Zhao (2008) and Chen, Sun, Wang & Wu (2015) propose a foamy-oil model based on the pseudo-bubble-point pressure concept from an experimental study, which can be adjusted for different cases to capture the foamy-oil PVT data for a corresponding production process.

Kumar & Mahadevan (2012) develop an expression for inflow performance as a function of properties of foamy oils such as density, viscosity, solution gas-oil ratio, and formation volume factor, defining two parameters such as the endpoint entrained-gas fraction and the apparent bubble point, adapted from previous studies, to account for the entrained-gas fraction in the liquid.

The direct approach to model foamy oil is to adjust some parameters in conventional solution gas drive. These parameters include absolute permeability, oil and gas relative permeabilities, fluid and rock compressibilities, critical gas saturation, and oil viscosity (Chen *et al.,* 2015). The conventional models cannot capture the atypical features of dispersed flow such as the dynamic processes involved in the generation and collapse of dispersion.

Liu, Mu, Li, Wu, & Li (2017) develop three depletion experiments to model foamy-oil flow, in which the foamy oil is treated as a pseudo-single-phase flow with the dispersed bubbles as a part of the oil, where the effective permeability varies with the changes of pressure depletion rate, oil viscosity, and gas saturation. A new foamy-oil model is proposed considering foamy-oil supersaturation, in which the effective permeability is redefined assuming that the foamy-oil viscosity is equal to the saturated oil under equivalent conditions and the compressibility coefficient of foamy oil is treated as a volume-weighted compressibility coefficient of that of oil and gas, obtaining good matching with the experimental data, when is compared to the conventional black-oil model and the pseudo-bubble-point

model.

Similarly, Lu, Zhou, Luo, Zeng, & Peng (2019) simulates lab tests for both gas/oil production data and pressure distribution along sand packs in a heavy oil/methane system using two different models: an equilibrium black oil model with two sets of gas/oil relative permeability curves and a four-component nonequilibrium kinetic model. The black oil model has good matching results on production data but not good matching on pressure distribution along the sand-pack, and the four-component nonequilibrium kinetic model with two reactions to capture gas bubbles status presents better matching with production data and pressure distribution simultaneously. This study indicates that a higher pressure drop rate could cause stronger foamy oil flow, but the excessive pressure drop rate could shorten the lifetime of foamy oil flow.

Recently, the foamy oil flow is considered the common drive mechanism of not only the primary production (depletion of naturally methane-saturated heavy oil) but also of the secondary stage (cyclic gas -mostly methane- injection after primary production). Basilio & Babadagli (2020) review the optimal conditions for secondary recovery as a cyclic solvent injection (CSI), taking into account mainly the foamy oil stability, and evidencing that the pressure depletion rate is the most crucial parameter to control the process.

Chen & Leung (2021) simulates the nonequilibrium foamy oil for cyclic solvent injection (CSI) in reservoirs after cold heavy oil production with sand using a field-scale model to analyze the impacts of pressure depletion strategies, single-stage pressure depletion involving three oil solvent systems, as well as two cycles of production processes, involving various propane-based and carbon dioxide-based solvent mixtures. The simulation model is calibrated against detailed experimental data and upscaled from a core-scale model, including a fractal wormhole network and kinetic reactions for the nonequilibrium gas dissolution and exsolution for foamy oil flow. The results prove that both propane-based and carbon dioxide-based solvents exhibit significant nonequilibrium foamy oil characteristics, enabling the oil viscosity to remain close to its value with dissolved solvent during pressure depletion, and the amount of nonequilibrium foamy oil flow is strongly dependent on the pressure depletion rate, i.e., a faster depletion rate is beneficial for higher oil recovery.

2.2.3 Wormholes formation

Several field studies in Canada have shown evidence of the development of channels of high permeability in fields produced under cold heavy oil production with sand. Squires (1993) shows evidence of a wormhole network during a well tracer program performed at the Elk Point Field in Alberta by Amoco Canada, reporting that the tracer traveled through a channel system of two kilometers long at speeds of about 7 m/min. Later, Yeung (1995) presents tracer tests conducted at the Burnt Lake Field in Alberta that evidence high permeability channels known as wormholes caused by sand production. Smith (1998) evidences the existence of high permeability channels or large-scale wormholes inside the reservoir formations.

Tremblay, Sedgwick & Vu (1999) conducted laboratory experiments to illustrate the wormhole evolution, in which oil flows through a horizontal sand pack. The formation and growth of a wormhole are visualized using a computerized tomography (CT) scanner, revealing high permeability channels that grow predominantly within areas of higher porosity.

Yang, Tremblay & Babchin (1999) propose a Probabilistic Active Walker (PAW) to describe wormhole growth, in which the wormhole diameter is a function of the distance from the wellbore. The model calculates the mobility of the slurry of sand and oil that is used to calculate the oil and sand production rates. The wormhole network is developed using the pressure field as a potential function and the wormhole direction has a certain degree of randomness due to cohesive strength variation.

Denbina, Baker, Gegunde, Klesken, & Sodero (2001) propose a transmissibility multiplier function to model wormhole growth, which is a function of decreasing reservoir pressure. The transmissibility is a function of grid block geometry and permeability, allowing a dynamic and implicit permeability that increases due to sand fluidization and production.

Wang *et al.* (2001) propose a wormholes model assuming that the wormholes are developed from perforations when pressure gradients exceed the residual cohesion of the sandstones and a 1D slurry flow model that includes the solid phase as the fourth phase. For the wormhole propagation model, a material balance equation is provided to characterize the slurry production, balancing the combined mass of displaced sand from the wormhole tip and the volume of sand produced due to wormhole propagation. A slurry transport model is used to describe the flow inside the wormholes and the slurry transport zone is represented as a wormhole network that is defined statistically from fractal theory defining a wormhole number that initially depends on the perforation density, increases with wormhole length and its size decreases with the length. Last, a complement of this model is presented by Wang & Chen (2004).

The concept of a remolded zone to model wormholes has difficulties describing the initial mechanism by which cavities would hypothetically form around the perforations. Walton, Atwood, Halleck, & Bianco (2002) present an experiment to design a perforating strategy for unconsolidated sandstones, which consists of a single shot-perforation in a cylindrical sample placed under highly effective stress in a pressure vessel, and using a video probe and computerized tomography (CT) scanner to observe post-shot sand production and to map the geometry of the cavity. A theoretical model of failure mode has been developed to support the experimental results. This study concludes that the perforating does not generate a tunnel in unconsolidated sands but instead a dilated zone around the tunnel entrance that grows as the flow rate increases to a critical value, in which a large volume of sand is produced affecting the sand cohesion.

Tan, Slevinsky, & Jonasson (2003) propose a fractal geostatistical model to pre-generate the wormhole network, which is incorporated into a full field thermal simulation model with a dual porosity-dual permeability grid (one for the reservoir pay and one for the wormhole network) to match a steam injection pilot.

Tremblay & Oldakowski (2003) perform lab experiments to investigate the effect of producing large quantities of sand on the overall permeability in two sand packs with different cohesive strengths, in which a large high porosity channel or wormhole is created from the perforation. A model of wormhole growth simulates the experimental tests, in which the produced volumes of oil, sand, and gas, the pressure distribution along the pack, and the final length of the wormholes are well predicted. This study concludes that the sand strength did not have a significant effect on the growth of the wormholes, while the weakening of the sand generates tensile failure bands with lower pressure gradients compared to the critical pressure gradient predicted by other authors.

Wan & Wang (2004b) present a coupled erosional-stress-deformation model for sand production analysis, which is formulated within the framework of mixture theory with porosity as one of the main field state variables. Numerical results show the wormholes as regions of very high porosities and the wormhole propagation is captured around a perforated wellbore by localization of erosion in the vicinity of the perforations, where high fluxes existed. It is also found that permeability anisotropy dictates the wormhole propagation that follows the direction of greatest permeability.

Wang & Xue (2004) propose a fully coupled geomechanical model with a two-phase reservoir model, including a sand erosion model based on the degree of plastic deformation. Besides, the fluid flow affects the pressure gradient and the residual cohesion of the formation due to capillary pressure change, which is also critical for sand control. So, the sand model displays the wormholes as a geomechanical dilation zone that is characterized by a higher permeability region in the plastic-yielding zone due to porosity enhancement. Also, the solid flow is considered a continuous moving phase throughout the transient multi-phase-fluid flow.

Liu & Zhao (2004) propose a comprehensive semi-analytical model coupling the reservoir/wormhole flow and using Source and Green's functions method to solve the transient flow problems through the wormhole. This model incorporates a wormhole-hydraulic model with foamy oil and sand flow in terms of the pressure drop along the wormholes. A sensitivity analysis results in a significant effect on the well performance of the wormhole patterns, scales, diameters, and branching and relatively less effect of the pressure drop along the wormhole.

Liu & Zhao (2005) propose a Diffusion-Limited Aggregation (DLA) fractal model to describe wormhole growth, which naturally relates a wide variety of branching growth patterns through the phenomena using a fractal model and including the growth of a drainage network, the formation of cavities, the dissolution of the porous media and the growth of random dendrites in thin films. The wormhole diameter distribution along the wormhole is modeled using the Area Version of Gaussian Function fixing with the experimental results obtained from the computerized tomography (CT) X-Ray scanner.

Tremblay (2005) proposes an analytical Bingham Mohr-Coulomb model as a sand transport model to describe the laminar flow of sand and oil along the wormholes. This model is part of a cold production field model, which predicts reasonable cumulative oil and sand volumes. As a result, a sharp decrease in the oil rate is obtained when the wormholes are stopped and the diameter of the channel within the wormholes suddenly increased from 5 cm to 24 cm after 10 years.

Du, Jiang, & Chen (2009) integrate an erosion model into a wormhole-spreading model, in which the sand is produced from the disturbed zone and its performance depends on the wormhole spreading, determined by the cohesion and the pressure gradient between the tip and the reservoir. An erosion parameter and sand concentration are two components of the model that help to represent the sand withdrawal from the wormhole wall. Laboratory data validates reasonably the results of the model.

Rivero et al. (2010) propose a coupled reservoir and geomechanical model with an approach to contain the wormholes, which is based on a homogenized damage model where the heterogeneous and discrete wormholes are defined by an equivalent continuous damaged zone with changes in porosity and permeability during sand production. The onset and propagation of the wormholes in this damaged area are calculated by coupling a finite-element geomechanical simulator with a finite-difference numerical reservoir simulator, and the geomechanical simulator uses the pressure gradients calculated by the

reservoir simulator to determine changes in the stress regime of the reservoir. If these changes are large enough, the rock will fail and the wormholes will be created.

Sanyal & Al-Sammak (2011) analyze the performance of a CHOPS pilot in Kuwait using analysis of pressure transient data, in which the productivity index increases gradually during the initial production due to the increment of negative skin effect caused by the sand production around the wellbore due to the wormhole growth that contributes to the negatives skin effect. In this way, the wormhole growth is modeled using negative skin.

Xiao & Zhao (2012) propose a novel approach using the concept of effective wormhole coverage with results that show variation in the transient pressure and production responses due to the different wormhole structures and reservoir areas. This model provides quantitative information about wormholes by analysis of the transient pressure, production rate, and sand production data for wells produced by cold, neglecting the sand transport within the wormholes. Later, Xiao & Zhao (2013) propose a radial-composite CHOPS well model, integrating a foamy-oil flow and complex wormhole configurations to investigate how wormholes and foamy-oil can affect the pressure responses of CHOPS wells simultaneously.

VanderHeyden, Jayaraman, Ma, & Zhang (2013) propose a multi-scale approach to model the wormhole growth with live oil including the effect of foamy oil and sand failure and based on the multi-phase material point method (MMPM). This model uses a Lagrangian-Eulerian methodology that permits the simulation of multiphase flow with fluid-structure interaction that includes material deformation, damage, and failure. Also, an up-scaled pressure-field-driven scheme has been developed to predict the wormhole network structure. The simulations of a CHOPS pilot are performed using a CartaBlanca simulation tool from Los Alamos National Laboratory.

Istchenko & Gates (2011, 2014) introduces an approach to model the wormholes as a series of multi-lateral wells using CMG STARS™. This set of wells models the open channels within the wormholes, where the slurry flow occurs, with further dilation around the wells creating the channels through sand erosion and dilation. This approach incorporates wormhole growth in the reservoir considering foamy-oil flow, failure, and sand production without modifying the intrinsic reservoir properties. The wormholes are modeled as an extension of a production well and grow dynamically within the reservoir according to a growth criterion set by the fluidization velocity of sand along the existing well/wormhole. If the growth criterion is satisfied, the wormhole extends in the appropriate direction, otherwise, production continues from the existing well/wormhole until the criterion is met.

Fan & Yang (2016) develop a wormhole dynamic growth model and incorporate it into the CMG® reservoir simulator to characterize the wormhole network for CHOPS processes. The model includes a geomechanics analysis associated with a collapsed pore and its throat structure to quantify the sand production, a sand failure criterion, and a four-direction pressure difference analysis to determine the sand production rate and the potential direction of wormhole generation and growth. A history matching is conducted to reduce the uncertainties in estimating the critical breakdown pressure, superficial area of collapse throats, and permeability-porosity correlation. The wormhole network model is validated using a synthetic model.

Again, Xiao & Zhao (2017) propose an enhancement of their model using the boundary-element method (BEM) to account for various boundary conditions, wormhole morphologies, and effects of wormhole

dynamic growth, which results that effective wormhole coverage and wormhole intensity within the region dominantly affect the characteristics of pressure and rate/time behaviors, regardless of the detailed wormhole morphologies.

Yu & Leung (2020) present a novel dynamic wormhole growth model to generate a set of realistic fractal wormhole networks during the CHOPS operations using an improvement to the Diffusion-Limited Aggregation (DLA) algorithm with a sand-arch stability criterion, in which the wormhole would still expand following the fractal pattern, provided that the pressure gradient at the tip exceeds the limit corresponding to a sand-arch stability criterion. Also, the model includes foamy oil and sand-arch failure.

2.2.4 Elastoplasticity

An elastoplastic material model can simulate the behavior of unconsolidated sandstones more realistically than elastic models. Many researchers have implemented elastoplastic models in sand production analysis as described in the following paragraphs:

Morita, Whitfill, Fedde, & Løvik (1989) in their sand production prediction implement plastic strain with two types of plastic behavior: compaction with high mean stress and volumetric expansion with a high deviatoric stress state and uses a modified kinematic model with a cap as yield surface to simulate accurately the behavior of weak sandstones.

Morita *et al.* (1989) propose an analytical model with a Mohr-Coulomb-type plastic constitutive relation with a Mohr-Coulomb yield surface and a linear work hardening stress-strain. Additionally, a parametric sensitivity study is conducted with analytical solutions for poroelastic and strain-hardening plastic materials.

Wan, Chan & Kosar, (1991) propose an elastoplastic model at different thermal conditions using the Ramberg-Osgood function to describe the hardening/softening law, and the Matsouka-Nakai failure criterion, and Rowe's stress dilatancy equation to describe the mechanical behavior of soil sand.

Papanastasiou & Vardoulakis (1992) apply the Cosserat continuum formulation for a strain-softening cohesive-frictional material to model cavity failure around boreholes. This is the beginning to implement the hardening/softening behavior of sandstones in sand production models and the use of the localization parameter.

Geilikman, Dusseault & Dullien (1994, February; 1994, April) propose a continuum model of sand production coupling the fluid flow and rate-sensitive plastic flow of granular matrix (viscoplastic), in which the initial granular matrix yielding is reached as a result of pressure drawdown below some critical level with front propagation away from the wellbore as the process of sanding continues, and the mass balance analysis relates the cumulative sand production and the current yielding front location.

Wan & Wang (2004a, 2004b) propose its coupled stress erosional model including a more adequate constitutive law based on plasticity and incorporating stress dilatancy aspects. The model is defined from the elastoplasticity theory with a yield function based on Mohr-Coulomb and combined with a plastic flow rule to describe yield condition and plastic strains respectively. The porosity changes are divided into two components: one related to volume changes due to sand grains erosion, and the other one due to

matrix deformation under stress field.

Walton, Atwood, Halleck, & Bianco (2002) and Wang & Chen (2004) propose an elastoplastic constitutive model that is extended to describe the reservoir material before seepage forces liquefy and suspend the sand particles at the advancing tips of wormholes.

Han, Stone, Liu, Cook, & Papanastasiou (2005) propose a 3D elastoplastic approach solved with the Finite Element Method in Corner Point Geometry grid cells and apply it to a commercial reservoir simulator. The model uses both Mohr-Coulomb and Drucker-Prager as yield criteria, where rock behaves elasto-plastically. A work-hardening rule is used for plasticity calculations, which is implemented through the shear cohesive strength that includes two hardening relations, a hyperbolic law, and a power law.

Many coupled models to simulate oil and sand production for CHOPS wells use elastoplastic models using the Mohr-Coulomb failure criterion and strain-hardening/softening as Wang & Sharma (2016). The Mohr-Coulomb is the conventional and practical criterion used to represent a shear failure on sand production prediction. However, this criterion produces instability in calculations due to its lack of dependence on the intermediate stress and the corners at the hexagon edges when the derivative of the yield function is required at the edge. This disadvantage leads to considering other criteria as the Drucker-Prager criterion to model the yielding during sand production (Han *et al.*, 2005).

Mohamad-Hussein *et al.* (2021) formulate an elastoplastic damage model to simulate sand production in CHOPS wells due to rock dilation and wormhole development, using the Drucker-Prager failure surface to describe the mechanical behavior of unconsolidated sand material. The damage is defined as the change of total average porosity due to rock dilation and shearing during plastic flow.

Chapter 3. General Model

This chapter describes the main components of the general model to simulate cold heavy oil production with sand including the physical model, the fluid flow model, and the geomechanical model. The physical model represents a 3D single well model to simulate the governing mechanisms that occur around the well, the fluid flow model is a 3-phase fluid flow that includes the fluid composed of oil, water, and gas, and the geomechanical model or material constitutive model that is defined as an elastoplastic stress-strain relation.

3.1 Physical model

The oil production in heavy oil reservoirs generates changes in the reservoir in terms of the pore pressure and the stress state, inducing a volume change in the fluid and rock of the reservoir. The volumetric behavior of the reservoir fluids depends on the fluid composition and the pore pressure change. The volumetric behavior of the reservoir rock depends on the mechanical properties and the combined effect of the pore pressure and stress state changes, which is the effective stress. The physical model is a single well model that represents the reservoir behavior of the flow in the region around the well where the elastoplastic deformation occurs. Figure 3 – 1 presents schematically the physical model.

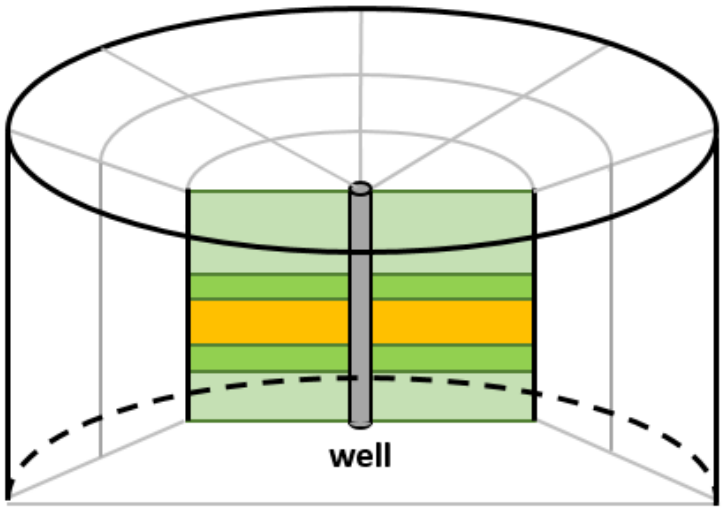

Figure 3 –1. Physical model.

The rock deformation is governed by the effective stress change that acts on the rock-solid skeleton. The pore pressure change in the reservoir is a combined effect of two different processes: (i) expansion/compression of the reservoir fluids because of production/injection operations, and (ii) expansion/compression of the porous medium because of the local stress state change.

The physical model represents a heavy oil reservoir as a cylinder with a specific height that is divided in

its vertical axis by strata and its horizontal plane is divided by angles with a constant length arc, with a producer vertical well located in the center. This geometric representation suggests using a cylindrical coordinates system.

The general model is based on the simultaneous solution of five sets of no linear differential equations. The governing equations describe the interaction between the pressure field and the stress field, resulting from the coupling of two different types of models: (i) a fluid flow model that describes the pore pressure distribution, and (ii) a stress-strain model that describes the elastoplastic deformation of the porous medium in each direction r, θ y z.

These governing equations for coupling rock elastoplastic deformation with fluid pressure for porous media are established through several publications in the rock mechanics literature. In recent years, reinterpretations of these equations and extensions to different oil reservoir studies have been published in the petroleum literature. The general model proposed here closely follows the interpretation given by Chen, Teufel & Lee, (1995), and Osorio (1999) with two exceptions, which are the 3-phase fluid for the fluid flow model and the geomechanical governing equations that take into account the elastoplastic behavior characteristic of heavy oil reservoirs.

The development of the governing equations is based on the following assumptions: (i) isothermal and 3-phase fluid flow (oil, gas, and water); (ii) isotropic rock mechanical properties; (iii) deformation of the solid part of the rock behaves as an elastoplastic medium with small deformations, and; (iv) permeability is assumed to be a function of porosity that changes as a function of the total strain and mean effective stress.

3.2 Fluid flow model

The reservoir or fluid flow model assumes isothermal and 3-phase fluid composed of oil, gas, and water in a deformable porous medium. Four basic relations constitute this model: fluid mass conservation, solid mass conservation, Darcy's law, and the equation of state. The combination of these four relations yields 3-phase fluid flow equations. This flow model gives rise to one of the following three fluid-flow equations depending on the nature of the fluid: compressible, slightly compressible, or incompressible fluid. The governing equations describing the fluid flow model are presented below. A detailed development can be found in Annex A and is based on the multiphase fluid flow model presented by Abou-Kassem, Rafiqul Islam, & Farouq Ali (2020).

Difference Finite Method (DFM) is the numerical method selected for solving the differential equations of the fluid flow model by approximating them with difference equations, in which finite differences approximate the derivatives.

3.2.1 Fluid mass conservation

The fluid mass conservation equation is obtained from a mass balance based on the infinitesimal volume element of a porous media as represented in Figure 3 –2.

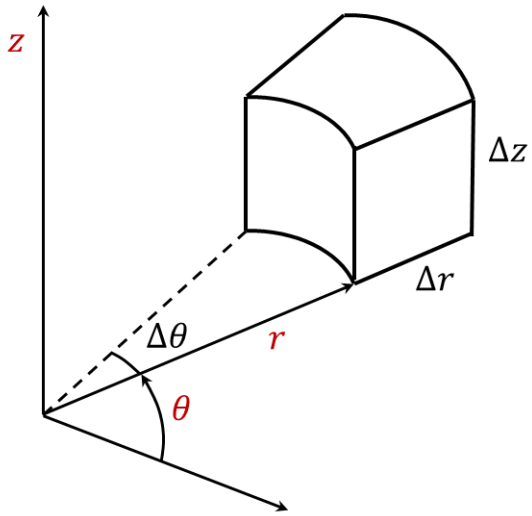

Figure 3 –2. Infinitesimal volume element of a porous media in cylindrical coordinates.

Fluid mass conservation can be expressed as follows (Annex A, Section A1.1),

$$-\nabla\cdot\left(\phi\mathbf{v}_{osc}\right)=\frac{1}{\alpha_c V_b}\frac{\partial}{\partial t}\left(\frac{\phi V_b S_o}{B_o}\right)+q_{osc} \tag{3-1}$$

$$-\nabla\cdot\left(\phi\mathbf{v}_{wsc}\right)=\frac{1}{\alpha_c V_b}\frac{\partial}{\partial t}\left(\frac{\phi V_b S_w}{B_w}\right)+q_{wsc} \tag{3-2}$$

$$-\nabla\cdot\left(\phi\mathbf{v}_{gsc}+R_{so}\phi\mathbf{v}_{osc}+R_{sw}\phi\mathbf{v}_{wsc}\right)=\frac{1}{\alpha_c V_b}\frac{\partial}{\partial t}\left(\frac{\phi V_b S_g}{B_g}+R_{so}\frac{\phi V_b S_o}{B_o}+R_{sw}\frac{\phi V_b S_w}{B_w}\right)+q_{gsc} \tag{3-3}$$

3.2.2 Solid mass conservation

Solid mass conservation can be expressed as follows (Annex A, Section A1.2):

$$-\nabla\cdot\left[\rho_s(1-\phi)\mathbf{v}_s\right]=\frac{1}{\alpha_c V_b}\frac{\partial}{\partial t}\left[\rho_s V_b(1-\phi)\right]+\widetilde{q_s} \tag{3-4}$$

where $\mathbf{v}_s$ is the solid real velocity vector.

3.2.3 Darcy's law

Darcy's law can be expressed as follows (Annex A, Section A1.3):

- **Oil-phase**

The oil real velocity at standard conditions in terms of oil pressure gradient considering gravity is given by:

$$\mathbf{v}_{oSC}-\mathbf{v}_s=-\beta_c\frac{\boldsymbol{k}_o}{\phi B_o\mu_o}\left(\nabla p_{\mathrm{o}}-\rho_{osc}\gamma_c g\nabla z\right) \tag{3-5}$$

Where $\mathbf{v}_{roSC}$ is the oil real velocity vector at standard conditions, $\mathbf{v}_{oSC}$ is the oil volumetric velocity vector at standard conditions, $\mathbf{v}_s$ is the solid velocity vector, $\boldsymbol{k}_o$ is the oil permeability tensor, μ_o is the oil viscosity, B_o is the oil volume factor, g is the gravitational acceleration ($g = 32.174\ \mathrm{ft/s^2}$) and γ_c is the gravity conversion factor ($\gamma_c = 0.21584 \times 10^{-3}$). The z direction is positive in the vertically downward direction.

Solving for the oil real velocity, at standard conditions, in each direction:

$$\mathrm{v}_{or_{SC}} = \mathrm{v}_{sr} - \beta_c \frac{k_{or}}{\phi B_o \mu_o}\left(\frac{\partial p_o}{\partial r} - \rho_{o_{SC}} \gamma_c g \frac{\partial z}{\partial r}\right)$$

$$\mathrm{v}_{o\theta_{SC}} = \mathrm{v}_{s\theta} - \beta_c \frac{k_{o\theta}}{\phi B_o \mu_o}\left(\frac{\partial p_o}{r\partial \theta} - \rho_{o_{SC}} \gamma_c g \frac{\partial z}{r\partial \theta}\right)$$

$$\mathrm{v}_{oz_{SC}} = \mathrm{v}_{sz} - \beta_c \frac{k_{oz}}{\phi B_o \mu_o}\left(\frac{\partial p_o}{\partial z} - \rho_{o_{SC}} \gamma_c g \frac{\partial z}{\partial z}\right) \quad (3-6)$$

- **Water-phase**

Similar to the oil phase, the water real velocity at standard conditions in terms of water pressure gradient considering gravity is given by:

$$\mathbf{v}_{rw_{SC}} = \mathbf{v}_{w_{SC}} - \mathbf{v}_s = -\beta_c \frac{\boldsymbol{k}_w}{\phi B_w \mu_w}\left(\nabla p_w - \rho_{w_{SC}} \gamma_c g \nabla z\right) \quad (3-7)$$

Similar to the oil phase, the water real velocity, at standard conditions, in each direction can be written as:

$$\mathrm{v}_{wr_{SC}} = \mathrm{v}_{sr} - \beta_c \frac{k_{wr}}{\phi B_w \mu_w}\left(\frac{\partial p_w}{\partial r} - \rho_{w_{SC}} \gamma_c g \frac{\partial z}{\partial r}\right)$$

$$\mathrm{v}_{w\theta_{SC}} = \mathrm{v}_{s\theta} - \beta_c \frac{k_{w\theta}}{\phi B_w \mu_w}\left(\frac{\partial p_w}{r\partial \theta} - \rho_{w_{SC}} \gamma_c g \frac{\partial z}{r\partial \theta}\right)$$

$$\mathrm{v}_{wz_{SC}} = \mathrm{v}_{sz} - \beta_c \frac{k_{wz}}{\phi B_w \mu_w}\left(\frac{\partial p_w}{\partial z} - \rho_{w_{SC}} \gamma_c g \frac{\partial z}{\partial z}\right) \quad (3-8)$$

- **Gas-phase**

Similar to the oil and water phases, the gas real velocity at standard conditions in terms of gas pressure gradient considering gravity is given by:

$$\mathbf{v}_{rg_{SC}} = \mathbf{v}_{g_{SC}} - \mathbf{v}_s = -\beta_c \frac{\boldsymbol{k}_g}{\phi B_g \mu_g}\left(\nabla p_g - \rho_{g_{SC}} \gamma_c g \nabla z\right) \quad (3-9)$$

The water real velocity at standard conditions in each direction for the gas phase can be written as:

$$\mathrm{v}_{gr_{SC}} = \mathrm{v}_{sr} - \beta_c \frac{k_{gr}}{\phi B_g \mu_g}\left(\frac{\partial p_g}{\partial r} - \rho_{g_{SC}} \gamma_c g \frac{\partial z}{\partial r}\right)$$

$$\mathrm{v}_{g\theta_{SC}} = \mathrm{v}_{s\theta} - \beta_c \frac{k_{g\theta}}{\phi B_g \mu_g}\left(\frac{\partial p_g}{r\partial \theta} - \rho_{g_{SC}} \gamma_c g \frac{\partial z}{r\partial \theta}\right)$$

$$\mathrm{v}_{gz_{SC}} = \mathrm{v}_{sz} - \beta_c \frac{k_{gz}}{\phi B_g \mu_g}\left(\frac{\partial p_g}{\partial z} - \rho_{g_{SC}} \gamma_c g \frac{\partial z}{\partial z}\right) \quad (3-10)$$

3.2.4 Equation of state

The equation of state (isothermal fluid compressibility) can be expressed as follows (Annex A, Section A1.4):

$$c_f = \frac{1}{\rho_f}\frac{\partial \rho_f}{\partial p} \quad (3-11)$$

On the other hand, in terms of the fluid formation volume factor:

$$c_f = -\frac{1}{B_f}\frac{\partial B_f}{\partial p} \quad (3-12)$$

The oil and water phases are handled as slightly compressible fluids and the gas phase is handled as real gas. The compressibility for the oil, water, and gas phases can be expressed, respectively, as:

$$c_o = -\frac{1}{B_o}\frac{\partial B_o}{\partial p_o} = constant$$

$$c_w = -\frac{1}{B_w}\frac{\partial B_w}{\partial p_w} = constant$$

$$c_g = -\frac{1}{B_g}\frac{\partial B_g}{\partial p_g} \quad (3-13)$$

3.2.5 Compressibility of the formation

Four different compressibilities are associated with porous media according to Zimmerman, Somerton, & King (1986). Each of these rock compressibilities relates to changes in either the pore volume V_p or the bulk volume V_b concerning changes in the pore pressure, p or the mean stress, σ_m. Annex A, Section A1.5 presents the definitions of formation compressibilities.

The compressibilities of a porous medium that express the effect of total mean stress and pore pressure variations on pore volume denote as c_{pc} and c_{pp}, respectively, are defined as:

$$c_{pc} = -\frac{1}{V_p}\frac{\partial V_p}{\partial \sigma_m}\Big|_p$$

$$c_{pp} = \frac{1}{V_p}\frac{\partial V_p}{\partial p}\Big|_{\sigma_m} \quad (3-14)$$

The compressibilities of a porous medium that express the effect of total mean stress and pore pressure variations on bulk volume denote as c_{bc} and c_{bp}, respectively, are defined as:

$$c_{bc} = -\frac{1}{V_b}\frac{\partial V_b}{\partial \sigma_m}\Big|_p$$

$$c_{bp} = \frac{1}{V_b}\frac{\partial V_b}{\partial p}\Big|_{\sigma_m} \quad (3-15)$$

Zimmerman *et al.* (1986) found the relations among these four compressibilities, the porosity, ϕ, and solid compressibility, c_s, defined as the compressibility of the rock matrix material. These relations for pore and bulk compressibilities are given by Equations (3 – 16) and (3 – 17) respectively.

$$c_{bc} = c_{bp} + c_s$$

$$c_{pc} = c_{pp} + c_s \quad (3-16)$$

$$c_{bp} = \phi c_{pc}$$

$$c_{pc} = \frac{c_{bc} - c_s}{\phi} \quad (3-17)$$

3.2.6 Other relations

This section presents other relations that complement the model. (Annex A, Section A1.6).

- **Saturations**

The oil, water, and gas saturations must satisfy the following constraint:

$$S_o + S_w + S_g = 1 \quad (3-18)$$

with: $0 \leq S_o, S_w, S_g \leq 1$

- **Capillary Pressures**

The oil, water, and gas pressures p_o, p_w and p_g can be related to the concept of capillary pressure:

$$p_{cwo} = p_o - p_w \quad (3-19)$$

$$p_{cgo} = p_g - p_o \quad (3-20)$$

And the derivates of these equations can be expressed as:

$$\frac{\partial p_w}{\partial t} = \frac{\partial p_o}{\partial t} - \frac{\partial p_{cwo}}{\partial t} = \frac{\partial p_o}{\partial t} - p'_{cwo}\frac{\partial S_w}{\partial t} \quad (3-21)$$

where:

$$p'_{cwo} = \frac{\partial p_{cwo}}{\partial S_w}$$

$$\frac{\partial p_g}{\partial t} = \frac{\partial p_o}{\partial t} - \frac{\partial p_{cgo}}{\partial t} = \frac{\partial p_o}{\partial t} + p'_{cgo}\frac{\partial S_g}{\partial t} \quad (3-22)$$

where:

$$p'_{cgo} = \frac{\partial p_{cgo}}{\partial S_g}$$

The terms p'_{cwo} and p'_{cgo} can be obtained by using the capillary pressure curves of each set of two-phase systems.

- **Mean Pore Pressure**

Considering three phases (oil, water, and gas) in the porous media, the mean pore pressure can be defined by:

$$\bar{p} = S_o p_o + S_w p_w + S_g p_g \quad (3-23)$$

3.2.7 Governing equations

Equations (3 – 1) through (3 – 23) can be combined resulting in the following fluid-flow equation (Annex A, Section A1.7):

- **Oil-phase**

The governing equation of the fluid flow for the oil phase is given:

$$\nabla \cdot \left(\beta_c \frac{\boldsymbol{k}_o}{B_o \mu_o}\left(\nabla p_o - \rho_{o_{SC}} \gamma_c g \nabla z\right)\right) = F_o + G_o \frac{\partial S_o}{\partial t} + H_o \frac{\partial S_g}{\partial t} + I_o \frac{\partial p_o}{\partial t} + J_o\left(\alpha \frac{\partial \epsilon_v^e}{\partial t} + \frac{\partial \epsilon_v^p}{\partial t}\right) + q_{o_{SC}} \quad (3-24)$$

where:

$$F_o = \frac{q_s \phi}{(1-\phi)}$$

$$G_o = \frac{\phi}{\alpha_c B_o}$$

$$H_o = 0$$

$$I_o = \frac{\phi}{\alpha_c B_o} S_o \left[c_{pc}(1-\alpha) - c_s + c_o \right]$$

$$J_o = -\frac{S_o}{\alpha_c B_o}$$

- **Water-phase**

The governing equation of the fluid flow for the water phase is given:

$$\nabla \cdot \left(\beta_c \frac{\boldsymbol{k}_w}{B_w \mu_w} \left(\nabla p_o - \rho_{w_{SC}} \gamma_c g \nabla z \right) \right) + \nabla \cdot \left(\beta_c \frac{\boldsymbol{k}_w}{B_w \mu_w} p'_{cwo} \nabla S_o \right) + \nabla \cdot \left(\beta_c \frac{\boldsymbol{k}_w}{B_w \mu_w} p'_{cwo} \nabla S_g \right) = F_w + G_w \frac{\partial S_o}{\partial t} + H_w \frac{\partial S_g}{\partial t} + I_w \frac{\partial p_o}{\partial t} + J_w \left(\alpha \frac{\partial \epsilon_v^e}{\partial t} + \frac{\partial \epsilon_v^p}{\partial t} \right) + q_{w_{SC}} \quad (3-25)$$

where:

$$F_w = \frac{q_s \phi}{(1-\phi)}$$

$$G_w = \frac{\phi}{\alpha_c B_w} \left\{ \left(1 - S_o - S_g\right) \left[c_{pc}(1-\alpha) - c_s + c_w \right] p'_{cwo} - 1 \right\}$$

$$H_w = \frac{\phi}{\alpha_c B_w} \left\{ \left(1 - S_o - S_g\right) \left[c_{pc}(1-\alpha) - c_s + c_w \right] p'_{cwo} - 1 \right\}$$

$$I_w = \frac{\phi}{\alpha_c B_w} \left(1 - S_o - S_g\right) \left[c_{pc}(1-\alpha) - c_s + c_w \right]$$

$$J_w = -\frac{1}{\alpha_c B_w} \left(1 - S_o - S_g\right)$$

- **Gas-phase**

Similarly, the governing equation of the fluid flow for the gas phase is given:

$$\nabla \cdot \left[\beta_c \frac{\boldsymbol{k}_g}{B_g \mu_g} \left(\nabla p_o - \rho_{g_{SC}} \gamma_c g \nabla z \right) + \beta_c R_{so} \frac{\boldsymbol{k}_o}{B_o \mu_o} \left(\nabla p_o - \rho_{o_{SC}} \gamma_c g \nabla z \right) + \beta_c R_{sw} \frac{\boldsymbol{k}_w}{B_w \mu_w} \left(\nabla p_o - \rho_{w_{SC}} \gamma_c g \nabla z \right) \right] + \nabla \cdot \left[\left(\beta_c \frac{\boldsymbol{k}_g}{B_g \mu_g} p'_{cgo} + R_{sw} \beta_c \frac{\boldsymbol{k}_w}{B_w \mu_w} p'_{cwo} \right) \nabla S_g \right] + \nabla \cdot \left(R_{sw} \beta_c \frac{\boldsymbol{k}_w}{B_w \mu_w} p'_{cwo} \nabla S_o \right) = F_g + G_g \frac{\partial S_o}{\partial t} + H_g \frac{\partial S_g}{\partial t} + I_g \frac{\partial p_o}{\partial t} + J_g \left[\alpha \frac{\partial \epsilon_v^e}{\partial t} + \frac{\partial \epsilon_v^p}{\partial t} \right] + q_{g_{SC}} \quad (3-26)$$

where:

$$F_g = (1 + R_{so} + R_{sw}) \frac{q_s \phi}{(1-\phi)}$$

$$G_g = \frac{\phi}{\alpha_c}\left\{R_{so}\frac{1}{B_o} + R_{sw}\frac{1}{B_w}\left[\left(1 - S_o - S_g\right)\left(R'_{sw} + c_w\right)p'_{cwo} - 1\right]\right\}$$

$$H_g = \frac{\phi}{\alpha_c}\left\{\frac{1}{B_g}\left[1 + S_g p'_{cgo}\left[c_{pc}(1-\alpha) - c_s + c_g\right]\right] + R_{so}\frac{1}{B_o}S_o p'_{cgo}\left[c_{pc}(1-\alpha) - c_s\right] + R_{sw}\frac{1}{B_w}\left[\left(1 - S_o - S_g\right)\left[\left(R'_{sw} + c_w\right)p'_{cwo} + \left[c_{pc}(1-\alpha) - c_s\right]p'_{cgo}\right] - 1\right]\right\}$$

$$I_g = \frac{\phi}{\alpha_c}\left\{\frac{S_g}{B_g}\left[c_{pc}(1-\alpha) - c_s + c_g\right] + R_{so}\frac{S_o}{B_o}\left[R'_{so} + c_{pc}(1-\alpha) - c_s + c_o\right] + R_{sw}\frac{\left(1-S_o-S_g\right)}{B_w}\left[R'_{sw} + c_{pc}(1-\alpha) - c_s + c_w\right]\right\}$$

$$J_g = -\frac{\phi}{\alpha_c}\left[\frac{S_g}{B_g} + R_{so}\frac{S_o}{B_o} + R_{sw}\frac{\left(1-S_o-S_g\right)}{B_w}\right]$$

3.2.8 Boundary conditions

The governing equations of the phases (oil, water, and gas) at the boundaries are affected by pressure and saturation, the main variables. Annex A, section A2.3 presents in detail the boundary conditions and their discretization.

- **Radial direction**

– For the wellbore boundary – internal radial boundary, $(i = 1)$

Pressure condition

The well production is defined as a bottom-hole pressure-constrained well, which states that the wellbore pressure is constant (Dirichlet boundary condition type) and its discretization at the boundary can be expressed by:

$$p_{o_{0,j,k}} = {p_{wf_{z_{1,j,k}}}}^n = {p_{wf_{ref}}}^n + \gamma_o\left(z_{1,j,k} - z_{ref}\right) \qquad (3-27)$$

Saturation conditions

The well production condition is defined as a non-flow condition, i.e., there is no radial flow between $i = 0$ and $i = 1$, then oil saturation at the radial boundary has no change (Neumann boundary condition type) and its discretization at the boundary can be expressed by:

$$S_{o_{0,j,k}} = S_{o_{1,j,k}} \qquad (3-28)$$

Similarly, for gas saturation (Neumann boundary condition type), its discretization at the boundary can be expressed by:

$$S_{g_{0,j,k}} = S_{g_{1,j,k}} \quad (3-29)$$

– For the external radial boundary, $(i = n_r)$

Pressure condition

The external radial pressure condition is defined as a non-flow condition, i.e., there is no radial flow between $i = n_r$ and $i = n_r + 1$ (Neumann boundary condition type) and its discretization at the boundary can be expressed by:

$$p_{o_{n_r+1,j,k}} = p_{o_{n_r,j,k}} \quad (3-30)$$

Saturation conditions:

The external radial oil saturation condition is defined in terms of the non-flow condition, i.e., there is no radial oil saturation change between $i = n_r$ and $i = n_r + 1$ (Neumann boundary condition type) and its discretization at the boundary can be expressed by:

$$S_{o_{n_r+1,j,k}} = S_{o_{n_r,j,k}} \quad (3-31)$$

Similarly, for the gas saturation (Neumann boundary condition type), its discretization at the boundary can be expressed by:

$$S_{g_{n_r+1,j,k}} = S_{g_{n_r,j,k}} \quad (3-32)$$

- **Tangential direction**

– For the first angular boundary, $(j = 1)$

Pressure condition

The pressure at the first angular boundary is a Dirichlet boundary condition type that is stated as:

$$p_{o_{i,0,k}} = p_{o_{i,n_\theta,k}} \quad (3-33)$$

Saturation conditions

The oil saturation at the first angular boundary is stated as (Dirichlet boundary condition type):

$$S_{o_{i,0,k}} = S_{o_{i,n_\theta,k}} \quad (3-34)$$

Similarly for the gas saturation (Dirichlet boundary condition type):

$$S_{g_{i,0,k}} = S_{g_{i,n_\theta,k}} \quad (3-35)$$

– For the final angular boundary, $(j = n_\theta)$

Pressure condition

The pressure at the final angular boundary is also a Dirichlet boundary condition type that is stated as:

$$p_{o_{i,n_\theta+1,k}} = p_{o_{i,1,k}} \quad (3-36)$$

Saturation conditions

The oil saturation at the final angular boundary is stated as (Dirichlet boundary condition type):

$$S_{o_{i,n_\theta+1,k}} = S_{o_{i,1,k}} \quad (3-37)$$

Similarly for the gas saturation (Dirichlet boundary condition type):

$$S_{g_{i,0,k}} = S_{g_{i,n_\theta,k}} \quad (3-38)$$

- **Vertical direction**

– For the top boundary, $(k = 1)$

Pressure condition

The vertical pressure condition at the top is defined as a no-flow condition, i.e., there is no vertical flow between the blocks $k = 0$ and $k = 1$ (Neumann boundary condition type) and its discretization at the boundary can be expressed by:

$$p_{o_{i,j,0}} = p_{o_{i,j,1}} + \gamma_o z_{i,j,0} \quad (3-39)$$

Saturation conditions

The vertical oil saturation condition at the top is defined in terms of the no-flow condition, i.e., there is no vertical oil saturation change between $i = n_r$ and $i = n_r + 1$ (Neumann boundary condition type) and its discretization at the boundary can be expressed by:

$$S_{o_{i,j,0}} = S_{o_{i,j,1}} \quad (3-40)$$

Similarly, for the gas saturation (Dirichlet boundary condition type), its discretization at the boundary can be expressed by:

$$S_{g_{i,j,0}} = S_{g_{i,j,1}} \quad (3-41)$$

– **For the bottom boundary,** $(k = n_z)$

Pressure condition

The vertical pressure condition at the bottom is defined as a no-flow condition, i.e., there is no vertical flow between the blocks $k = n_z$ and $k = n_z + 1$ (Neumann boundary condition type) and its discretization at the boundary can be expressed by:

$$p_{o_{i,j,n_z+1}} = p_{o_{i,j,n_z}} - \gamma_o z_{i,j,n_z+1} \quad (3-42)$$

Saturation conditions

The vertical oil saturation condition at the bottom is defined in terms of the non-flow condition, i.e., there is no vertical oil saturation change between $i = n_r$ and $i = n_r + 1$ (Neumann boundary condition type) and its discretization at the boundary can be expressed by:

$$S_{o_{i,j,n_z+1}} = S_{o_{i,j,n_z}} \quad (3-43)$$

Similarly, for the gas saturation (Dirichlet boundary condition type), its discretization at the boundary can be expressed by:

$$S_{g_{i,j,n_z+1}} = S_{g_{i,j,n_z}} \quad (3-44)$$

3.2.9 Initial conditions

The usual initial conditions of a reservoir consist to define the initial values of the primary variables of the model such as pressure and saturation to begin the simulation. At the initial time ($t_0 = 0$), all reservoir unknowns must be specified considering that the fluids are in hydrodynamic equilibrium.

The model requires that the user defines some preliminary data to describe the case to run such as the grid specifications (well radius, reservoir radius, and reservoir height), initial mean pressure and bubble-point pressure at reference depth, initial saturations in the reservoir (oil, water, and gas), capillary pressure curves and relative permeability curves (oil and water system and/or oil and gas systems), layers open to production, the production log that consists to the wellbore hole pressure on time, among others.

The bubble-point pressure and the initial mean pressure are defined at the top of the reservoir, this last pressure lets to calculate each phase pressure using the initial saturation values and capillary pressure curves, and the vertical distribution of all these pressures is done considering the hydrostatic gradient.

The initial saturation values are stated for all the reservoirs, i.e., for each block of the grid. There is no gas cap or aquifer to have saturation distribution with gravity.

3.2.10 Ternary model for the three-phase system

Direct experimental measurement of three-phase relative permeability is really difficult and implicates rather complex techniques to establish the fluid saturation distribution along the core. Experimentally, it is easier to measure the two-phase relative permeability. For this reason, the strategy consists to estimate the three-phase relative permeability from two sets of two-phase data and using a correlation. The same strategy is used for capillary pressures.

• Two-phase systems

Figure 3 – 3 presents the relative permeability and capillary pressure curves for the two sets of two-phase systems.

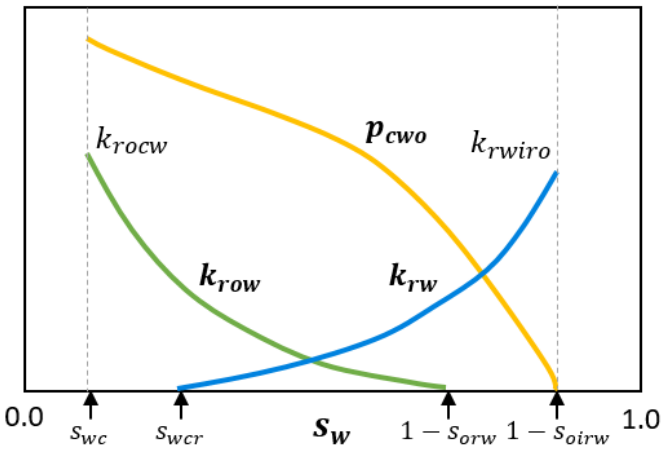

a.

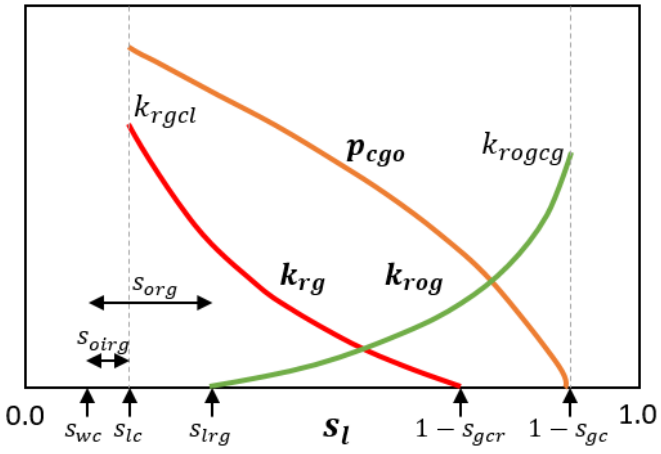

b.

Figure 3 – 3. Relative permeability and capillary pressure curves. a) Oil and water system. b) Oil and gas system.

– Relative permeability

To replace the two sets of two-phase data, Corey's correlation is used to estimate the relative permeability

of each one of the two-phase systems (Ahmed, 2010).

Oil and water system

For an oil-water system,

$$k_{row} = k_{row}|_{S_{wc}} \left(\frac{1-S_w-S_{orw}}{1-S_{wc}-S_{orw}}\right)^{n_{ow}}$$

$$k_{rw} = k_{rw}|_{S_{oirw}} \left(\frac{S_w-S_{wcrit}}{1-S_{wcrit}-S_{oirw}}\right)^{n_w} \quad (3-45)$$

In Equations (3 – 45), k_{row} and k_{rw} are oil and water relative permeability in the oil-water system, respectively; S_w is the water saturation, S_{wc} is the connate water saturation, S_{wcrit} is the critical water saturation, S_{orw} is the residual oil saturation and S_{oirw} is the irreducible oil saturation in the oil-water system, and n_{ow} and n_w are the oil and water exponents on relative permeability curves.

Oil and gas system

For an oil-gas system,

$$k_{rog} = k_{rog}|_{S_{gc}} \left(\frac{1-S_g-S_{lrg}}{1-S_{gc}-S_{lrg}}\right)^{n_{og}} \quad (3-46)$$

$$k_{rg} = k_{rg}|_{S_{lc}} \left(\frac{S_g-S_{gcrit}}{1-S_{lc}-S_{gcrit}}\right)^{n_g} \quad (3-47)$$

with

$$S_{lrg} = S_{wc} + S_{org}$$

$$S_{lc} = S_{wc} + S_{oirg}$$

In Equations (3 – 46) and (3 – 47), k_{rog} and k_{rg} are oil and gas relative permeability in the oil-gas system, respectively; S_g is the gas saturation, S_{gc} and S_{wc} are the connate gas and water saturation, respectively; S_{gcrit} is the critical gas saturation, S_{oirg} is the irreducible oil saturation in the oil-gas system, and S_{org} is the residual oil saturation in the oil-gas system, and n_{og} and n_g are the oil and gas exponents on relative permeability curves.

– Capillary pressure

To replace the two sets of two-phase data, a potential law is used to estimate capillary pressure.

Oil and water system

Taking into account an oil-water system with $S_{wcr} \geq S_{wc}$ and $S_{orw} \geq S_{oirw}$, the oil-water capillary pressure in the drainage curve can be expressed as:

$$p_{cwo_D} = \left(p_{cwo}|_{S_{wc}} - p_{cwo}|_{1-S_{oirw}}\right)\left(\frac{1-S_w-S_{oirw}}{1-S_{wc}-S_{oirw}}\right)^{n_{p_{cow}}} + p_{cwo}|_{1-S_{oirw}} \quad (3-48)$$

with:

$S_{wc} \leq S_w \leq 1 - S_{oirw}$

In Equation (3 – 48), p_{cwo} and p_{cwo_D} are oil-water capillary pressure and dimensionless oil-water capillary pressure, respectively; and $n_{p_{cwo}}$ is the oil-water exponent on capillary pressure.

And the capillary pressure derivative for the oil-water system:

$$\frac{\partial p_{cwo}}{\partial S_w} = \frac{-n_{p_{cow}}\left(p_{cwo}|_{S_{wc}} - p_{cwo}|_{1-S_{oirw}}\right)(1-S_w-S_{oirw})^{n_{p_{cow}}-1}}{(1-S_{wc}-S_{oirw})^{n_{p_{cow}}}} \quad (3-49)$$

Oil and gas system

Taking into account an oil-water system with $S_{lcr} \geq S_{lc}$ and $S_{gcr} \geq S_{gc}$, the gas-oil capillary pressure in the drainage curve can be expressed as,

$$p_{cgo_D} = \left(p_{cgo}|_{S_{lc}} - p_{cgo}|_{1-S_{gc}}\right)\left(\frac{1-S_{gc}-S_l}{1-S_{lc}-S_{gc}}\right)^{n_{p_{cog}}} + p_{cgo}|_{1-S_{gc}} \quad (3-50)$$

where,

$S_{lc} = S_{wc} + S_{org}$

$S_{lc} \leq S_l \leq 1 - S_{gc}$

In Equation (3 – 50), p_{cgo} and p_{cgo_D} are oil-gas capillary pressure and dimensionless oil-gas capillary pressure, respectively; S_{lc} and S_{gc} are the connate liquid and gas saturation, respectively; and $n_{p_{cgo}}$ is the oil-gas exponent on capillary pressure.

And the capillary pressure derivative for the oil-gas system:

$$\frac{\partial p_{cgo}}{\partial S_g} = \frac{n_{p_{cog}}\left(p_{cog}|_{S_{lc}} - p_{cog}|_{1-S_{gc}}\right)(S_g-S_{gc})^{n_{p_{cog}}-1}}{(1-S_{lc}-S_{gc})^{n_{p_{cog}}}} \quad (3-51)$$

- **Three-phase system**

According to the selected strategy, the relative permeability of water in a three-phase system is the same as that in a two-phase water-oil system and is a function of water saturation only. The relative permeability of gas in the three-phase system is equal to the gas relative permeability in the two-phase liquid-gas system and is a function of gas saturation only. Stone's model II is a normalized method with a reasonable approximation to calculate the three-phase oil relative permeability, k_{ro}, using k_{row} and k_{rog} from the two sets of two-phase permeability systems (Aziz & Settari, 2002; Ahmed, 2010).

$$k_{ro} = k_{ro}|_{S_{wc}} \left[\left(\frac{k_{row}}{k_{ro}|_{S_{wc}}} + k_{rw} \right) \left(\frac{k_{rog}}{k_{ro}|_{S_{wc}}} + k_{rg} \right) - \left(k_{rw} + k_{rg} \right) \right] \quad (3-52)$$

Equation (3 – 52) allows computing the values of oil relative permeability k_{ro} for the three-phase system, which can be represented in the ternary diagram as shown in Figure 3 – 4.

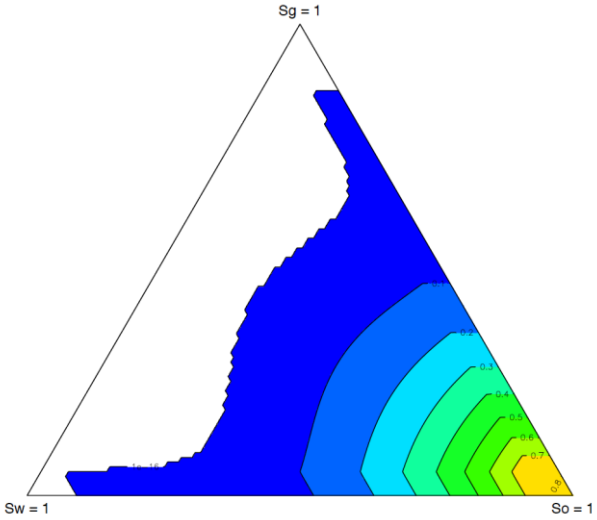

Figure 3 – 4. Ternary diagram for oil relative permeability for a three-phase system using Stone's model II.

3.3 Geomechanical model

The geomechanical model is a 3D elastoplastic stress-strain relationship that assumes that the solid phase behaves as an elastoplastic medium with small strains. The basic assumptions for this geomechanical model are that the total strain increment may be decomposed into elastic and plastic parts, with the elastic part contributing to the stress increment using an elastic law. The elastoplastic calculations include an incremental stress-strain relation, a yield surface, a flow rule, and a hardening/softening law.

The numerical method selected for solving the geomechanical model is the Finite Element Method (FEM) in cartesian coordinates, which requires the solution to a boundary value problem for partial differential equations. The FEM formulation of the problem results in a system of algebraic equations and the method yields approximate values of the unknowns at a discrete number of points over the domain. The approach to solving the problem consists to divide a large problem into smaller considering

simpler parts that are called finite elements. The simple equations that model these finite elements are then assembled into a larger system of the equation that models the entire problem, using variational methods from the calculus of variations to approximate a solution by minimizing an associated error function (Sherif, 2012). Annex B presents detailed mathematical development for implementing this numerical solution.

3.3.1 Basic relations

• Stress Tensor

Using indicial notation to reduce the expressions of equations, the stress tensor is given by:

$$\sigma_{ij} = \begin{bmatrix} \sigma_{11} & \sigma_{12} & \sigma_{13} \\ \sigma_{21} & \sigma_{22} & \sigma_{23} \\ \sigma_{31} & \sigma_{32} & \sigma_{33} \end{bmatrix} \quad (3-53)$$

• Principal stresses

If the axes of the coordinate system are aligned with the principal stress directions, the stress tensor will be having this simple form:

$$\sigma_{ij} = \begin{bmatrix} \sigma_1 & 0 & 0 \\ 0 & \sigma_2 & 0 \\ 0 & 0 & \sigma_3 \end{bmatrix} \quad (3-54)$$

where σ_1, σ_2 and σ_3 are the principal stresses. These are the proper values of the matrix and are obtained as:

$$\det(\sigma_{ij} - \sigma\delta_{ij}) = 0 \quad (3-55)$$

• Principal stress invariants

The invariants of the principal stress tensor can be written as:

$$I_1 = tr(\sigma_{ij}) = \sigma_1 + \sigma_2 + \sigma_3$$

$$I_2 = \frac{1}{2}\left[\left(tr(\sigma_{ij})\right)^2 - tr(\sigma_{ij}^2)\right] = \sigma_1\sigma_2 + \sigma_2\sigma_3 + \sigma_1\sigma_3$$

$$I_3 = \det(\sigma_{ij}) = \sigma_1\sigma_2\sigma_3 \quad (3-56)$$

The mean stress is equivalent to the first invariant divided by 3:

$$\sigma_m = \frac{1}{3}(\sigma_1 + \sigma_2 + \sigma_3) \quad (3-57)$$

• Deviator stress tensor

The deviator stress tensor can be obtained by subtracting the mean stress from the stress tensor:

$$s_{ij} = \sigma_{ij} - \sigma_m \delta_{ij} = \begin{bmatrix} \frac{2\sigma_{11}-\sigma_{22}-\sigma_{33}}{3} & \sigma_{12} & \sigma_{13} \\ \sigma_{21} & \frac{2\sigma_{22}-\sigma_{11}-\sigma_{33}}{3} & \sigma_{23} \\ \sigma_{31} & \sigma_{32} & \frac{2\sigma_{33}-\sigma_{11}-\sigma_{22}}{3} \end{bmatrix} \quad (3-58)$$

• Invariants of the deviator stress tensor

In the same way, the invariants of the deviator stress tensor are obtained as:

$$J_1 = 0 \quad (3-59)$$

$$J_2 = \frac{1}{2}\left(tr^2(s_{ij}) - tr(s_{ij})\right) = s_{11}s_{22} + s_{22}s_{33} + s_{11}s_{33} - {s_{12}}^2 - {s_{13}}^2 - {s_{23}}^2$$

$$J_3 = \det(S_{ij}) = s_1 s_2 s_3$$

• Strain tensor

The strain tensor, ϵ_{ij}, can be expressed as:

$$\epsilon_{ij} = \begin{bmatrix} \epsilon_{11} & \epsilon_{12} & \epsilon_{13} \\ \epsilon_{21} & \epsilon_{22} & \epsilon_{23} \\ \epsilon_{31} & \epsilon_{32} & \epsilon_{33} \end{bmatrix} \quad (3-60)$$

The volumetric strain, ϵ_v, can be expressed as:

$$\epsilon_v = \epsilon_{11} + \epsilon_{22} + \epsilon_{33} = \epsilon_1 + \epsilon_2 + \epsilon_3 = \nabla \cdot u \quad (3-61)$$

where u is the displacement vector.

• Stress-strain model

The stress-strain model is based on three basic relations (Chen & Baladi,1985):

- The equilibrium equation or the stress equilibrium equation.
- The strain-displacement equation is related to the geometry conditions of the compatibility of strains and displacements.
- The constitutive relation of the material to be modeled, elasticity, or elastoplasticity, which defines the strain-stress-pressure relations.

– Stress-equilibrium equations

$$\sigma_{ij,j} + F_j = 0 \quad (3-62)$$

where,

$\sigma_{ij} = \sigma_{ji}$

– Strain-displacement equations

$$\epsilon_{ij} = \frac{1}{2}\left[\frac{\partial u_i}{\partial x_j} + \frac{\partial u_j}{\partial x_i}\right] \quad (3-63)$$

where u is the displacement tensor, and,

$\epsilon_{ij} = \epsilon_{ji}$

3.3.2 Elasticity

In physics, elasticity is the ability of a material to resist distorting stress and to return to its original size and shape when the stress is removed. Then, if the material is elastic, it will return to its initial shape and size when these forces are removed (Chen *et al.*, 1995).

For the model implementation, compressive stresses are positive and the principal stresses are used considering that $\sigma_1 \geq \sigma_2 \geq \sigma_3$.

• Stress-strain relation

Hooke's law defines the elastic behavior of materials relating the stresses and strains with isotropic elastic properties, and it can be defined as:

$$\epsilon_{ij} = \frac{1}{2G}\sigma_{ij} + \left(\frac{1}{9K} + \frac{1}{6G}\right)\sigma_{kk}\delta_{ij}$$

$$\sigma_{ij} = 2G\epsilon_{ij} + \left(K - \frac{2G}{3}\right)\epsilon_{kk}\delta_{ij} \quad (3-64)$$

In Equation (3 – 64), K is the bulk modulus and G is the shear modulus, and δ_{ij} is the Kronecker's delta function $\left(\delta_{ij} = 1 \text{ for } i = j\ ,\ \delta_{ij} = 0 \text{ for } i \neq j\ \right)$.

• Stiffness matrix

The Equations (3 – 62) can be reduced to the following equation:

$$\sigma_{ij} = \mathbb{C}_{ijkl}\epsilon_{ij} \quad (3-65)$$

In Equation (3 – 65), $\mathbb{C}_{ijkl}$ is known as the stiffness matrix or constitutive matrix.

• Elastic strain increment

The elastic strain increment, ϵ_{ij}^{e}, can be defined as:

$$d\epsilon_{ij}^{e} = \frac{1}{9K} dI_1 \delta_{ij} + \frac{1}{2G} ds_{ij} \quad (3-66)$$

In Equation (3 – 66), s is the stress tensor, K is the bulk modulus and G is the shear modulus.

Also:

$$d\varepsilon_{kk}^{e} = \frac{1}{3K}\ dI_1 \quad (3-67)$$

And increment of the deviator elastic strain:

$$d\epsilon_{ij}^{e} = \frac{1}{2G} ds_{ij} \quad (3-68)$$

In Equation (3 – 68), ϵ_{ij}^{e} is the elastic deviator strain tensor.

• Strain-stress-pressure equations

The constitutive relation of an elastic material defines strain-stress-pressure relations:

$$\epsilon_{ii} = \frac{1}{E}\left[\sigma_{ii} - \nu\left(\sigma_{jj} - \sigma_{kk}\right)\right] - \frac{\alpha c_b}{3} p_p \quad (3-69)$$

In Equation (3 – 69), E is Young's modulus, ν is Poisson's ratio, p_p is the fluid pore pressure, α is Biot's poroelastic constant and c_b is bulk compressibility.

Also:

$$\epsilon_{ij} = \frac{\sigma_{ij}}{2G}; i \neq j \quad (3-70)$$

Equations (3 – 69) and (3 – 70) can be solved to state the stresses in terms of the strains:

$$\sigma_{ij} = 2G\epsilon_{ij} + \left(\lambda\epsilon_v + \alpha p_p\right)\delta_{ij} \quad (3-71)$$

where λ is the Lame's constant that can be expressed as $\lambda = K - 2G/3$.

Effective stress, σ'_{ij}, is defined in terms of the total stress and the pore pressure as:

$$\sigma'_{ij} = \sigma_{ij} - \alpha p_p \delta_{ij} \quad (3-72)$$

Effective stress is a measure of the actual stress carried by the solid skeleton of the rock.

3.3.3 Elastoplasticity

Elastoplasticity is the condition of the material to show both elastic and plastic behavior, typically as a result of being stretched beyond an elastic limit. Thus, the material behavior is elastic up to a transition point called the yield point, in which the material changes from elastic behavior to plastic behavior.

In physics, plasticity describes the deformation of a material undergoing permanent or non-reversible changes of shape and size in response to applied stresses. The elastoplastic calculations include an incremental stress-strain relation, a yield surface, a flow rule, and a hardening / softening law (Davis & Selvadurai, 2002).

• Basic relation

To carry out strain calculations, the incremental strain is assumed linearly divided into two parts, an elastic part, and a plastic part,

$$d\epsilon_{ij} = d\epsilon^e_{ij} + d\epsilon^p_{ij} \quad (3-73)$$

• Yield surface

If the stress exceeds a critical value, the material will undergo plastic or irreversible deformation. This critical stress can be tensile or compressive. This critical value is known as the yield point and refers to the onset of plastic behavior or the stress at which a material begins to deform plastically. The yield criteria define the mathematical conditions for yielding (Davis & Selvadurai, 2002).

$$f(\sigma_{ij}) = \kappa \quad (3-77)$$

In Equation (3 – 77), f is the yield function and κ is a constant.

The yield criterion often expressed as yield surface is a hypothesis concerning the limit of elasticity under any combination of stresses. The yield criterion defines a surface where plastic deformation occurs.

The yield surface or failure envelope determines the plastic behavior of the material: perfectly plastic material or plastic material with hardening/softening. So that the stress state reaches the failure envelope, the afterload generates plastic strains. For perfectly plastic materials, the failure envelope is a function of the stresses and does not change with time. For plastic materials with hardening/softening, the failure envelope is also a function of stresses and plastic strains, thus this implies that the failure envelope change with the load history (Han *et al.*, 2005).

$$f = f(\sigma_{ij}, \epsilon^p_{ij}) \quad (3-78)$$

where ϵ_{ij}^{p} is the plastic strain.

Shear o tensile processes can generate failure or yield. For this reason, the yield criteria can be defined in terms of shear or tensile.

• Drucker and Prager yield criterion

There are different yield criteria to apply in elastoplasticity as Tresca, Von Mises, Mohr-Coulomb, and Drucker-Prager, among others.

Although the Mohr-Coulomb criterion is the conventional criterion used to represent a shear failure in soils and rocks, its disadvantages are the lack of dependence on the intermediate stress and the corners at the hexagon edges that lead to instability on calculations when the derivative of the yield function is required at the edge. For these disadvantages, other criteria such as Drucker and Prager criterion are considered to model the yielding during sand production (Han *et al.*, 2005).

The Drucker and Prager criterion is a three-dimensional pressure-dependent model to estimate the stress state at which the rock reaches its ultimate strength, determining whether a material has failed or undergone plastic yielding. Its advantages are its simplicity and its smooth and, symmetric failure surface in the stress space, which facilitate its implementation into numerical codes (Cividini, 1993). The criterion gives as much weight to each one of the three stresses (Alejano & Bobet, 2012). For this advantage, it is established as a generalization of the Mohr-Coulomb criterion for soils (Drucker & Prager, 1952).

The Drucker and Prager failure criterion naturally represents the frictional relation between shear and normal stresses through a yield stress criterion (Klar, Gast, Pradhana, Fu, Schroeder, Chenfanfu, & Teran, 2016). This criterion is used to model frictional materials, which are typically granular-like soils and rock, and exhibit pressure-dependent yield (the material becomes stronger as the pressure increases) and has been applied to rock, concrete, polymers, foams, and other pressure-dependent materials (Dassault Systémes Simulia Corporation, 2014).

Rock failure and degradation are mostly accepted as requisite for sand production. However, several mechanisms are well-known as responsible for sand production, which is mainly based on the shear and tensile failure, critical pressure gradient, critical drawdown pressure, critical plastic strain, and erosion criteria (Rahmati *et al.*, 2013). This is how the yield criterion is an important consideration for sand production. It is also proved that the problem of sanding onset prediction cannot be well solved by using strength criteria that are not influenced by the intermediate principal stress because laboratory test data indicate rock failure is dependent on intermediate principal stress (Yi, Valkó & Russell, 2005).

The Drucker and Prager criterion can be expressed as:

$$\sqrt{J_2} = \kappa_\varphi + q_\varphi I_1' \qquad (3-79)$$

In Equation (3 – 79), I_1' is the first invariant of the effective stress tensor, J_2 is the second invariant of the deviator tensor, and κ_φ and q_φ are material constants usually defined from experiments.

In terms of the principal effective stresses:

$$\sqrt{\frac{1}{6}[(\sigma_1' - \sigma_2')^2 + (\sigma_2' - \sigma_3')^2 + (\sigma_3' - \sigma_1')^2]} = \kappa_\varphi + B(\sigma_1' + \sigma_2' + \sigma_3') \quad (3-80)$$

The Drucker and Prager yield surface is a smooth version of the Mohr-Coulomb yield surface. Figure 3 – 5 presents a view of the Drucker and Prager yield surface in the 3D space of principal stresses.

Since the Drucker and Prager yield surface is a smooth version of the Mohr-Coulomb yield surface, it is often expressed in terms of cohesion, τ_o, and the angle of internal friction, φ, that are used to describe the Mohr-Coulomb yield surface. If it is assumed that, the Drucker and Prager yield surface circumscribes the Mohr-Coulomb yield surface then:

$$q_\varphi = \frac{2\sin\varphi}{\sqrt{3}(3-\sin\varphi)}$$

$$\kappa_\varphi = \frac{6\tau_o\cos\varphi}{\sqrt{3}(3-\sin\varphi)} \quad (3-81)$$

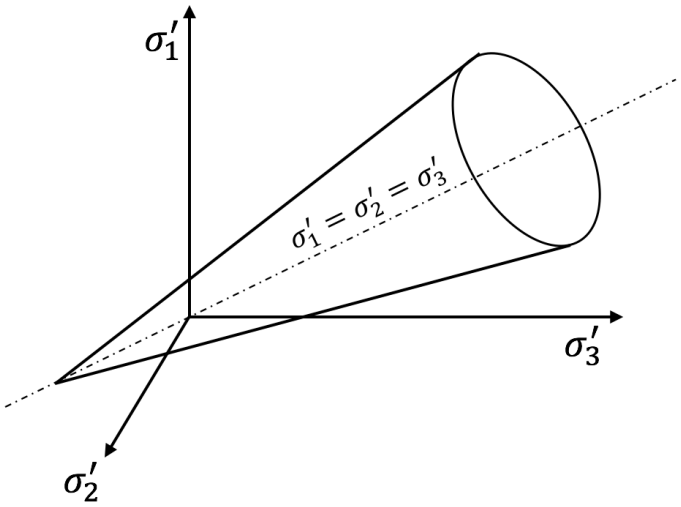

Figure 3 – 5. Drucker and Prager yield surface in 3D space of principal stresses.

The Drucker and Prager criterion produces a failure surface with tension cutoff, in which the shear flow rule is non-associated, and the tensile flow rule is associated (Chen & Han, 1988; Itasca Consulting Group Inc., 2005). Then, this criterion is expressed in terms of two generalized stress components: the tangential stress, τ, and mean normal stress, σ, defined as:

$$\tau = \sqrt{J_2} = \sqrt{\frac{1}{6}[(\sigma_1' - \sigma_2')^2 + (\sigma_2' - \sigma_3')^2 + (\sigma_3' - \sigma_1')^2] + (\sigma_{12}')^2 + (\sigma_{23}')^2 + (\sigma_{31}')^2}$$

$$\sigma_m = \frac{1}{3}I_1' = \frac{1}{3}(\sigma_1' + \sigma_2' + \sigma_3') \quad (3-82)$$

The shear strain increment, $\Delta\gamma$, and volumetric strain increment, $\Delta\epsilon_v$, associated with τ, and σ_m respectively, have the form:

$$\Delta\gamma = 2\sqrt{\Delta J_2'}$$

$$\Delta\epsilon_v = \Delta\epsilon_{11} + \Delta\epsilon_{22} + \Delta\epsilon_{33} \quad (3-83)$$

where $\Delta J_2'$ is the second invariant of the incremental strain deviator tensor that is given by:

$$\Delta J_2' = \frac{1}{6}[(\Delta\epsilon_{11} - \Delta\epsilon_{22})^2 + (\Delta\epsilon_{22} - \Delta\epsilon_{33})^2 + (\Delta\epsilon_{33} - \Delta\epsilon_{11})^2] \quad (3-84)$$

The total strain increments are decomposed:

$$\Delta\gamma^T = \Delta\gamma^e + \Delta\gamma^p$$

$$\Delta\epsilon^T = \Delta\epsilon^e + \Delta\epsilon^p \quad (3-85)$$

where the superscripts e and p refer to elastic and plastic parts, respectively, and the plastic components are nonzero during plasticity only. The incremental expression of Hooke's law in terms of generalized stresses and strains is:

$$\Delta\tau = G\Delta\gamma^e$$

$$\Delta\sigma_m = K\Delta\epsilon^e \quad (3-86)$$

where G and K are the shear and bulk modulus, respectively.

• Yield functions

The Drucker and Prager criterion consists of two failure functions: the shear function, f^s, and the tensile failure function, f^t. This criterion in the $\sigma_m - \tau$ plane is sketched in Figure 3 – 6. The failure envelope is defined from point A to B by the yield function,

$$f^s = \tau - q_\varphi\sigma_m - \kappa_\varphi \quad (3-87)$$

and from B to C by the tension yield function,

$$f^t = \sigma_m + \sigma_m^t \quad (3-88)$$

where q_φ and κ_φ are constant material properties, and σ_m^t is the tensile strength for Drucker & Prager model. Note that this strength is defined as the maximum value of the mean normal stress for the material under consideration. For a material whose property q_φ is not equal to zero, the tensile strength cannot exceed the value σ_{max}^t given by,

$$\sigma_{max}^t = \frac{\kappa_\varphi}{q_\varphi} \quad (3-89)$$

It is clear that when the stress state has overcome the Drucker and Prager failure criterion by shear: $f^s \leq 0$, and similarly by tensile failure: $f^t \leq 0$.

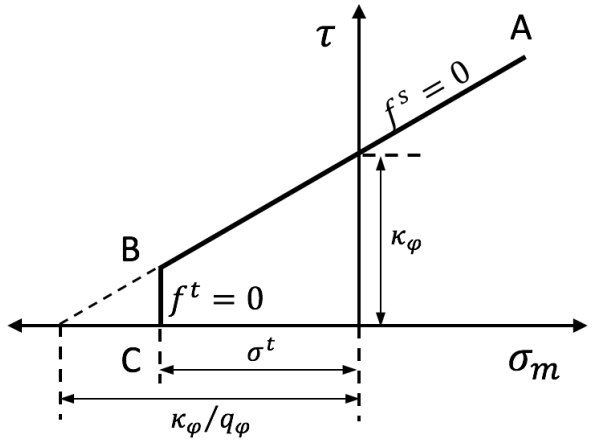

Figure 3 – 6. Drucker and Prager failure criterion.

• Plastic potential functions

The shear potential function g^s relates in general to a non-associated flow rule, and has the form:

$$g^s = \tau - q_\psi \sigma_m \tag{3 – 90}$$

where q_ψ is a material constant equal to q_φ if the flow rule is associated.

The flow rule for tensile failure is associated and the tensile potential function g^t is given by,

$$g^t = -\sigma_m \tag{3 – 91}$$

The flow rules are given a unique definition in the vicinity of an edge of the composite yield function using the following technique. A function, $h(\sigma_m, \tau) = 0$, which is represented by the diagonal between the failure criteria $f^s = 0$ and $f^t = 0$ in the $\sigma_m - \tau$ plane. Figure 3 – 7 represents the domains of the flow rule and the definition of function h.

The function h can be expressed as:

$$h = \tau + \tau^P + \alpha^P(\sigma_m^t - \sigma_m) \tag{3 – 92}$$

where:

$$\tau^P = \kappa_\varphi - q_\varphi \sigma_m^t$$

$$\alpha^P = \sqrt{1 + q_\varphi^2} - q_\varphi$$

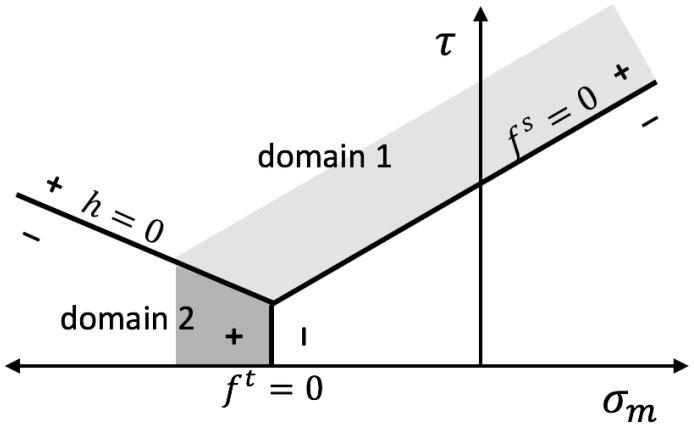

Figure 3 – 7. Domains of the flow rule in the Drucker and Prager criterion.

An elastic guess violating the failure criterion is represented by a point in the $\sigma - \tau$ plane, placed either in domain 1 or 2, corresponding to positive or negative domains of $h(\sigma_m, \tau) = 0$, respectively. If in domain 1, shear failure takes place, and the stress point is brought back to the curve $f^s = 0$ using a flow rule derived using the potential function g^s. If in domain 2, tensile failure takes place, and the stress point is brought back to $f^t = 0$ using a flow rule derived using g^t.

• Flow rules and plastic corrections

The flow rule specifies the direction of the plastic strain increment vector as that normal to the potential surface. It is called associated if the potential and yield function coincides, non-associated otherwise (Chen & Han, 1988). In general, the plastic strain increment can be defined as:

$$d\epsilon_{ij}^p = \Lambda \frac{dg}{d\sigma_{ij}} \tag{3 – 93}$$

where g is the plastic potential surface and Λ is the plasticity scale multiplier. For associated flow, g is set equal to the yield criterion f, which is a function of both stresses and strains, Equation (3 – 93).

– For shear failure

For the shear failure, the flow rule has the form:

$$\Delta\gamma^p = \Lambda^s \frac{\partial g^s}{\partial \tau}$$

$$\Delta\epsilon^p = \Lambda^s \frac{\partial g^s}{\partial \sigma_m} \tag{3 – 94}$$

where the magnitude of the shear plastic multiplier Λ^s must be determined. Using Equation (3 – 90) that defines g^s and after its partial differentiation, Equations (3 – 94) can be expressed as:

$$\Delta\gamma^p = \Lambda^s$$

$$\Delta\epsilon^p = \Lambda^s q_\psi \qquad (3-95)$$

Taking Equations (3 – 85) in Equations (3 – 95):

$$\Delta\tau = G\Delta\gamma^T - G\Lambda^s$$

$$\Delta\sigma_m = K\Delta\epsilon^T - \Lambda^s q_\psi \qquad (3-96)$$

Defining the stress increments in terms of new and old stress states by the subscripts N and O,

$$\Delta\tau = \tau^N - \tau^O$$

$$\Delta\sigma_m = \sigma_m^N - \sigma_m^O \qquad (3-97)$$

Substituting Equations (3 – 95) into Equations (3 – 97):

$$\tau^N = \tau^I - G\Lambda^s$$

$$\sigma_m^N = \sigma_m^I - K\Lambda^s q_\psi \qquad (3-98)$$

where the superscript I represents the elastic guess obtained by adding to the old stresses, elastic increments computed using the total stain increments:

$$\tau^I = \tau^O + \Delta\gamma^T$$

$$\sigma_m^I = \sigma_m^O - K\Delta\epsilon^T \qquad (3-99)$$

The shear plastic multiplier Λ^s can now be defined by requiring that the new stress point be placed on the shear yield surface. Replacing τ^N and σ_m^N for τ and σ_m in Equation (3 – 87) doing $f^s = 0$, which after some manipulations gives:

$$\Lambda^s = \frac{f^s(\tau^I, \sigma_m^I)}{G + Kq_\varphi q_\psi} \qquad (3-100)$$

Noting that the new deviator stresses may be obtained by multiplying the corresponding deviator elastic guesses with the ratio τ^N/σ_m^I, and the new stresses can be written as:

$$\sigma_{ij}^N = \left(\sigma_{ij}^I - \sigma_m^I \delta_{ij}\right)\frac{\tau^N}{\sigma_m^I} + \sigma_m^N \delta_{ij} \qquad (3-101)$$

where δ_{ij} is the Kronecker delta symbol.

- **For tensile failure:**

For the tensile failure, the flow rule has the form:

$$\Delta\gamma^p = \Lambda^t \frac{\partial g^t}{\partial \tau}$$

$$\Delta\epsilon^p = \Lambda^t \frac{\partial g^t}{\partial \sigma_m} \quad (3-102)$$

where the magnitude of the tensile plastic multiplier Λ^t stays to be defined. Using Equation (3 – 91) that defines g^t and after its partial differentiation, Equations (3 – 102) can be expressed as:

$$\Delta\gamma^p = 0$$

$$\Delta\epsilon^p = \Lambda^t \quad (3-103)$$

Applying a similar reason to that described above:

$$\tau^N = \tau^I$$

$$\sigma_m^N = \sigma_m^I - K\Lambda^t \quad (3-104)$$

And the tensile plastic multiplier can be expressed as:

$$\Lambda^t = \frac{\sigma_m^I - \sigma_m^t}{K} \quad (3-105)$$

Replacing Equation (3 – 105) into Equation (3 – 104):

$$\tau^N = \tau^I$$

$$\sigma_m^N = \sigma_m^t \quad (3-106)$$

For this failure mode, the new deviator stresses correspond to the elastic guess:

$$\sigma_{ij}^N = \sigma_{ij}^I + (\sigma_m^t - \sigma_m^I)\delta_{ij} \quad (3-107)$$

• Implementation procedure

The geomechanical model should be at an initial force-equilibrium state before alterations can be performed. The initial and boundary conditions may often be defined such that the model is just at equilibrium initially. However, it may be necessary to calculate the initial equilibrium state under the given initial and boundary conditions, particularly for problems with complex geometries or multiple layers. The elasticity model allows getting the initial conditions under the boundary conditions.

The implementation of the elastoplastic model using the Drucker and Prager criterion requires first computing the elastic guess σ_{ij}^I by adding the old stress components, and the increments are calculated using Hooke's law to the total strain increment for the step. The generalized stress components (σ_m^I, τ^I) are then derived from σ_{ij}^I using Equations (3 – 82). If these stresses violate the composite yield criterion, a correction must be applied to the generalized stress components to get the new stress state. In this

position, there are two options: $h(\sigma_m^I, \tau^I) > 0$ or $h(\sigma_m^I, \tau^I) \leq 0$ as seen in Figure (3 – 10) represents Equation (3 – 92). In the first option, shear failure takes place and the new generalized stresses components are calculated from Equation (3 – 98) using Equation (3 – 100) for Λ^s, and the stress tensor components are computed from the generalized stress components using Equation (3 – 106). In the second option, tensile failure occurs and the new stresses are computed using Equations (3 – 101) for Λ^t, and the stress tensor components are computed from the generalized stress components using Equation (3 – 107).

3.4 Computer model

The discretized system of equations for both models: the fluid flow model and geomechanical model including their boundary conditions are solved using a program code developed in this study and written in Fortran language. The code can solve each model separately in a full way, which means that the equations of each model can be simultaneously solved for each time step using Pardiso (Alappat, Hager, Schenk, Thies, Basermann, Bischop, Fehske, & Wellein, 2020). Also, the code can solve the system of equations in a fully coupled model. Figure 3 – 8 presents the flow chart for the multi-phase fluid flow model and Figure 3 – 9 presents the flow chart for the geomechanical model.

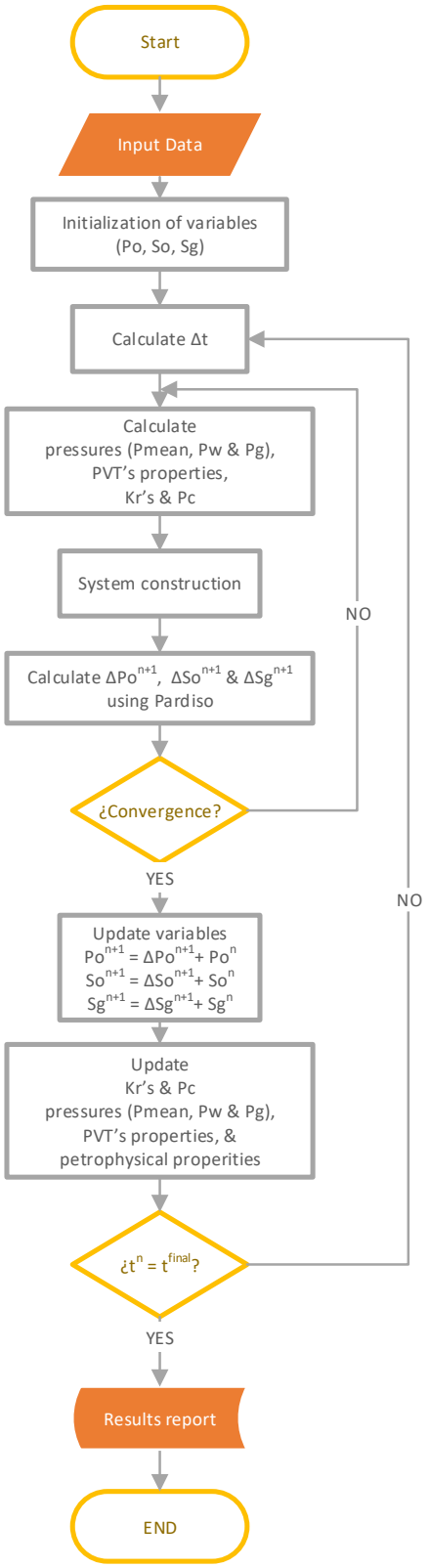

Figure 3 – 8. Flow chart for the multi-phase fluid flow model.

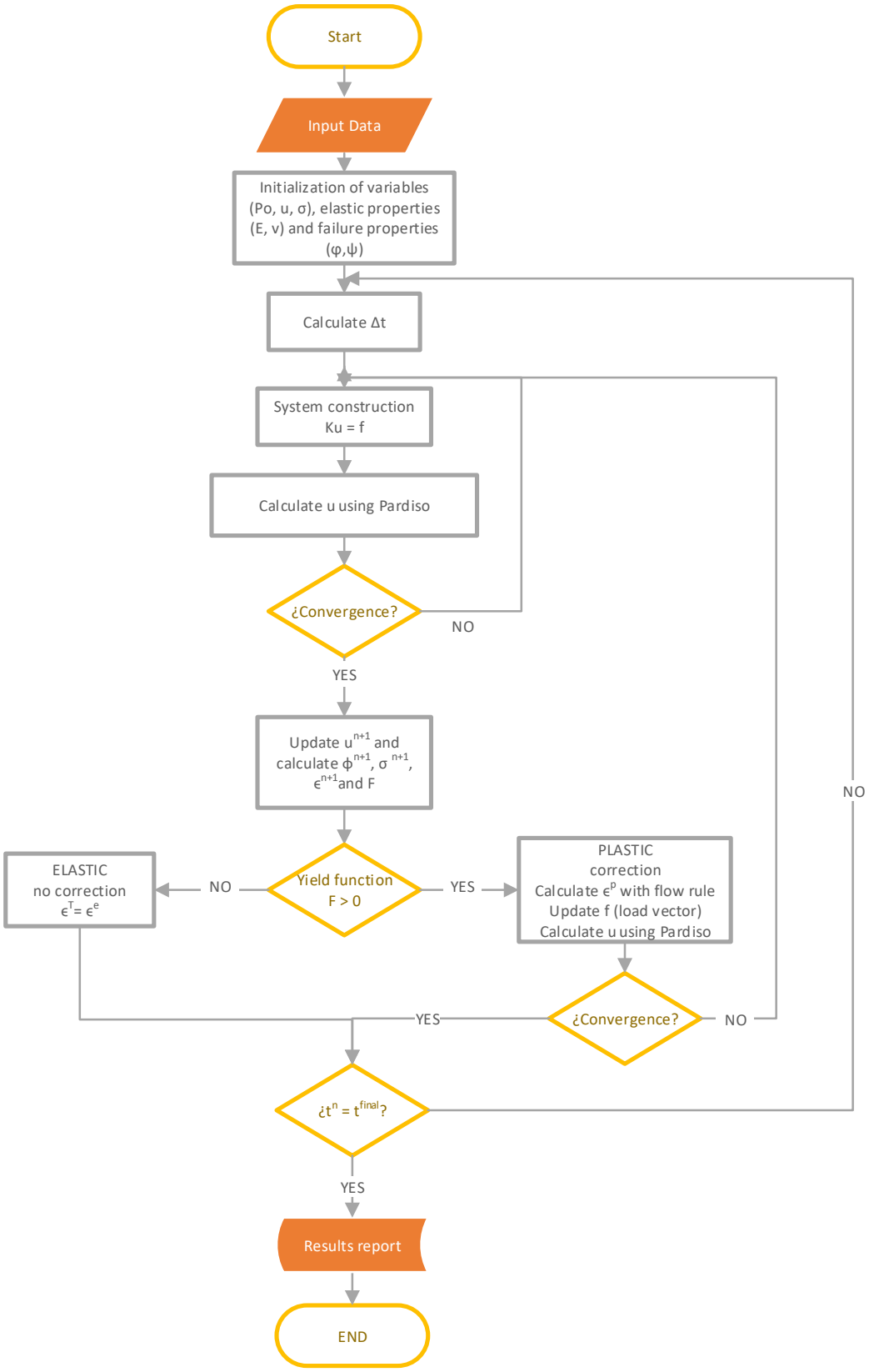

Figure 3 – 9. Flow chart for the multi-phase geomechanical model.

Chapter 4. CHOPS model

This chapter presents the components to complement the general model to simulate cold heavy oil production with sand including the governing mechanisms of this technology as foamy oil, sand production, and wormhole formation.

4.1 Foamy-oil model

The term foamy oil is often used to describe the production fluids from heavy oil reservoirs under solution gas drive. Different from conventional oil reservoirs under solution gas drive, anomalous oil production performances, including high oil production rate, low gas-oil ratio, and high recovery factor, are found in heavy oil reservoirs under solution gas drive. The behavior difference between conventional heavy oil and foamy has been seen during the performance of a Constant Composition Expansion (CCE) test using a visual Pressure/Volume/Temperature (PVT) cell as shown in Figure 4 – 1. Conventional heavy oil behaves under thermodynamic equilibrium conditions at any pressure while foamy oil presents three different processes during pressure depletion: bubble nucleation, bubble growth, and bubble coalescence (Zhou, Yuan, Zeng, Zhang, & Jiang, 2017).

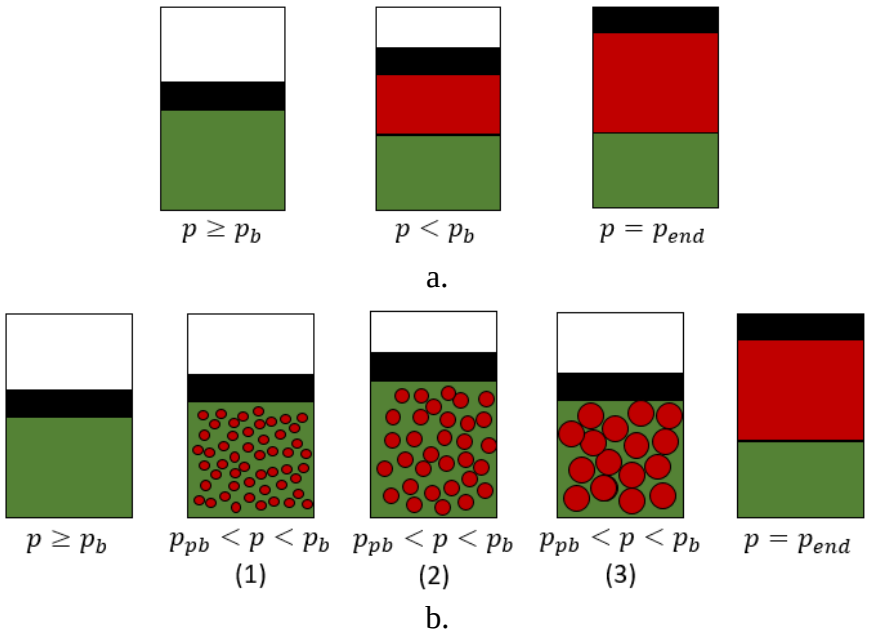

Figure 4 – 1. Schematic characteristics of the gas during the CCE test using a PVT cell. a) Conventional heavy oil. b) Foamy oil including (1) bubble nucleation, (2) bubble growth, and (3) bubble coalescence processes. (Modified after Zhou et al., 2017)

Tiny bubbles start to generate in the crude when pressure declines lower than bubble point pressure, and volume changes of the fluids are discrete due to the bubble size being very small and negligible. In this period, supersaturation status in the crude reaches and volume increment of crude is principally contributed by the liquid phase. When pressure declines to the threshold pressure, which is lower than the bubble point pressure but higher than the pseudo-bubble point pressure, numerous bubbles nucleate and the volume of the foamy oil increases remarkably with the pressure declines, so this process is known as bubble nucleation. Small bubbles are trapped in the crude increasing in size while the pressure declines and the volume changes are dominated by the gas bubbles dispersed in the crude, a process known as bubble growth. When the pressure declines to pseudo-bubble point pressure, dispersed gas bubbles coalescent and starts to evolve out of crude, a process known as bubble coalescence, in which the gas evolution rate relates to pressure depletion rates. During this period, volume changes of total fluids (foamy oil and free gas) are mainly controlled by free gas. If the pressure is maintained for a long time, the system will reach an equilibrium status, indicating that 100% of the dispersed gas transfers to free gas and only solution gas and free gas exist in the gas phase (Zhou *et al*., 2017). These three processes exhibit the presence of another phase known as entrained gas, required to model the foamy oil.

Summarizing, when the reservoir pressure is above the bubble point pressure the gas exists as solution gas in the oil phase being the oil in the saturated state. Once the reservoir pressure is below the bubble-point pressure, the released solution gas is trapped and dispersed in oil, being the oil in a pseudo-undersaturated state as foamy. As the reservoir pressure reaches the pseudo-bubble-point pressure, the dispersed gas in the heavy oil comes off from the oil completely and becomes a movable phase being the oil in some part of the reservoir as dead oil and the gas is produced. In between the pseudo-bubble-point pressure and the bubble-point pressure, the gas bubbles suffer three different processes: nucleation, growth, and coalescence. Figure 6 – 2 represents foamy oil during reservoir depletion.

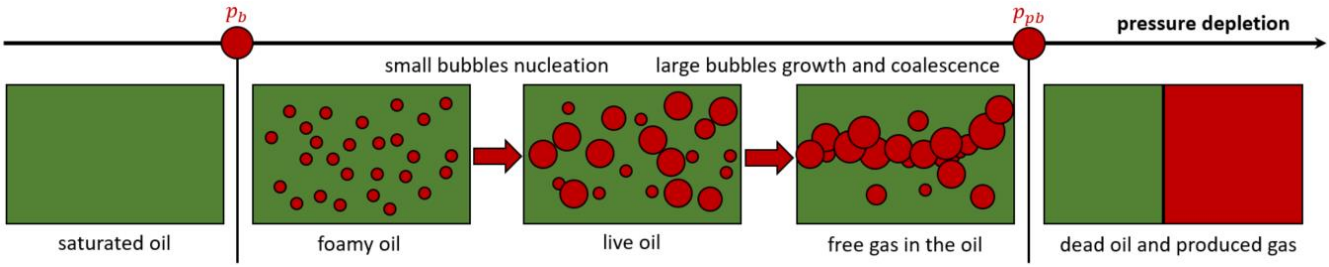

Figure 4 – 2. Foamy oil during reservoir depletion.

The foamy-oil module is integrated following the model proposed by Kumar & Mahadevan (2012). This is the first approach to include foamy-oil behavior during production, i.e., the entrained-gas drive mechanism. This module states two parameters such as the end-point of the entrained-gas fraction and the apparent bubble-point pressure and integrates three elements: (i) the inflow performance as a foamy oil with three phases: dissolved gas, oil component, and entrained gas; (ii) the fluid characterization changing the PVT properties for a foamy-oil crude; and (iii) the relative permeability curves in terms of pressure. This means that the module works by adjusting the fluid flow component. The inflow performance is obtained using Darcy's equation for the flow of each phase (free gas and foamy oil) in the continuity equation and space averaging, assuming pseudo-steady state conditions.

4.1.1 Phases and Components

A heavy oil composed of foamy oil and gas has two phases and three components:

Phases

The heavy oil system is composed of two main phases:

- Free gas (y) is the mass fraction of the free gas phase, and
- Foamy oil (x) is the mass fraction of the foamy-oil phase.

Components

The system has three main components:

- Dissolved gas (y_g, x_g), where y_g and x_g are the mass fractions of dissolved gas in each phase, in the free gas and the foamy-oil phase, respectively.
- Dead oil (y_{do}, x_{do}), where y_{do} and x_{do} are the mass fraction of dead oil in each phase, in the free gas and the foamy-oil phase, respectively.
- Entrained-gas (y_{ego}, x_{ego}), where y_{ego} and x_{ego} are the mass fraction of entrained gas in each phase, in the free gas and the foamy-oil phase, respectively.

Here is important to clarify that $y_g = 0$ and $y_{do} = 0$ because both are components of the free gas phase.

Relationships between components

The components are related to each other:

$$x_{do} + x_g + x_{ego} = 1 \tag{4-1}$$

and

$$y_{do} + y_g + y_{ego} = 1 \tag{4-2}$$

And other relations defined in terms of the solution gas-oil ratio are:

$$R_{sfo} = \frac{(x_g + x_{ego})}{x_{do}} \frac{\rho_{osc}}{\rho_{gsc}} \tag{4-3}$$

$$R_{so} = \frac{x_g}{x_{do}} \frac{\rho_{osc}}{\rho_{gsc}} \tag{4-4}$$

The mass fraction for individual components in the foamy-oil phase can be expressed by:

$$x_{do} = \frac{1}{1+R_{sfo}\frac{\rho_{gsc}}{\rho_{osc}}}$$

$$x_{ego} = \frac{(R_{sfo}-R_{so})\frac{\rho_{gsc}}{\rho_{osc}}}{1+R_{sfo}\frac{\rho_{gsc}}{\rho_{osc}}}$$

and,

$$x_g = \frac{R_{so}\frac{\rho_{gsc}}{\rho_{osc}}}{1+R_{sfo}\frac{\rho_{gsc}}{\rho_{osc}}} \quad (4-5)$$

The mass fraction for individual components in the free gas phase can be expressed by:

$$y_g = 0$$

$$y_{do} = 0$$

and,

$$y_{ego} = 1 \quad (4-6)$$

where ρ_{osc} and ρ_{gsc} are the oil and gas density at standard conditions respectively, and R_{sfo} is the solution gas-oil ratio for the foamy-oil and R_{so} is the solution gas-oil ratio.

4.1.2 Premises and assumptions

The foamy-oil system has two phases: free gas and foamy oil, and three components: dissolved gas, dead oil, and entrained gas. The following are the main assumptions of this model:

- The entrained gas has the same density as the free gas.
- The entrained gas in the foamy-oil phase travels at the same velocity as the foamy-oil phase does.
- The free gas and foamy-oil phases are instantaneously in thermodynamic equilibrium.
- There is no entrained-gas component present above bubble-point pressure.
- The dissolved-gas component does not transfer directly into the free-gas phase.
- The kinetics of gas-bubble nucleation and coalescence is neglected, and the component concentrations are determined only by pressure and temperature at thermodynamic equilibrium.
- The dead-oil component does not contain gas that can be transferred into the free-gas phase.
- The capillary and gravity effects are neglected.

4.1.3 Conceptual parameters

Pseudo-bubble-point

When reservoir pressure drops below the thermodynamic equilibrium bubble-point pressure, the solution gas is liberated. In conventional oil, the gas bubbles coalesce and grow quickly, and form a free mobile

gas phase. In viscous heavy oils, the solution gas is entrained and needs some time to disengage and form a continuous flowing gas phase.

Because of this analysis, Kraus *et al.* (1993) and other authors define an effective or pseudo-bubble-point as the pressure at which free gas flow starts in foamy-oil reservoirs. Even though the bubble coalescence starts at pressures less than the pseudo-bubble-point pressure, not all the bubbles coalesce due to the presence of natural surfactants in the liquid phase, and a fraction of entrained gas is always present in the solution down to a lower pressure, the pressure that could be atmospheric or notably lower than the bubble-point pressure (Tang, Sahni, Gadelle, Kumar, & Kovscek, 2006).

The true bubble-point pressure is the pressure at which bubbles start to generate in the oil phase, i.e., the pressure at which the first small bubbles of free gas evolve from solution and nucleate as a distinct gas phase at reservoir conditions (traditional equilibrium bubble-point pressure). The pseudo-bubble-point pressure is the pressure at which bubbles in the oil phase start to coalesce to form a continuous gas phase. The greater the difference between these two pressures, the greater the contribution to oil recovery from the foamy-oil drive mechanism (Wang, Qin, Chen, & Zhao, 2008).

The entrained gas increases the effective compressibility of the oil phase and inhibits gas liberated below the true bubble-point pressure. Thus, the foamy oil behaves as if it had an effective or pseudo-bubble-point pressure below that measured in a PVT cell in the laboratory. The pseudo-bubble-point works as an adjustable parameter to match field or laboratory performance (Kraus *et al.*, 1993).

Apparent bubble-point and end-point entrained-gas fraction

The apparent bubble-point pressure is termed the pseudo-bubble-point pressure. The fraction of liberated gas, also known as flashed gas, is the entrained gas at the reference condition that is termed as an end-point entrained gas fraction. These two parameters characterize the behavior of the entrained-gas fraction with pressure and define the fluid properties of the foamy oil. (Kumar & Mohadevan, 2012)

When pressure drops below the true bubble point in the foamy oil, the dissolved gas becomes the entrained gas; and when the pressure reduces further, the entrained gas is released to the free-gas phase. That is why there is no direct transfer of the dissolved gas in the foamy-oil phase to the gas in the free-gas phase.

4.1.4 Inflow performance

The presence of entrained gas can alter the oil fluid properties, for this reason, the foamy-oil modeling requires that the fluid properties take it into account as a species in the flow equations for a reservoir at a pseudo-steady state. Many authors such as Mastmann, Moustakis & Benion (2001) and Kumar & Mahadevan (2012) report a significant effect of the entrained gas on the fluid properties such as a reduction of the fluid density and increment of the formation volume factor, both properties have an inflection below the bubble-point pressure and the solution gas-oil ratio stays constant up to the pseudo-bubble pressure and then diminishes.

For modeling the inflow performance of foamy-oil reservoirs, the entrained gas may be considered as a component with its equilibrium concentration determined only by pressure and temperature. Therefore,

foamy oil consists of three components: dissolved solution gas, oil, and entrained gas. Under non-equilibrium conditions, the concentration of the components depends on the bubble coalescence rate and the mass transfer. Sheng, Hayes, Maini & Tortike (1996) used this approach to describe the foamy oil flow.

Joseph *et al.* (2002) present a foamy-oil flow model for porous media, which includes the effect of the entrained gas on the fluid density and viscosity and considers the relaxation of the entrained gas from initial non-equilibrium conditions to equilibrium.

The inflow performance reservoir with foamy-oil behavior is developed including the fluid properties as density, formation volume factor, and solution gas-oil ratio as a function of the entrained-gas fraction. For a conventional oil inflow, the entrained-gas fraction is set equal to zero in the fluid property model. The inflow performance is obtained by using Darcy's equation to model the flow of each phase in the continuity equation, assuming pseudo-steady state conditions. (Kumar & Mahadevan, 2012)

Darcy's law

For the foamy-oil phase,

$$\mathrm{v}_{foSC} = \mathrm{v}_s - \frac{k_{for}}{\phi \mu_{fo} B_{fo}} \nabla p_o \qquad (4-7)$$

In Equation (4 – 7), v_{foSC} is the foamy-oil real velocity vector at standard conditions, v_s is the solid real velocity, ∇p_o is the pressure gradient, ϕ is the porosity, k_{for} is the foamy-oil relative permeability, μ_{fo} is the foamy-oil viscosity, and B_{fo} is the foamy-oil formation volume factor.

For the free-gas phase,

$$\mathrm{v}_{gSC} = \mathrm{v}_s - \frac{k_{gr}}{\phi \mu_g B_g} \nabla p_o \qquad (4-8)$$

In Equation (4 – 8), v_{gSC} is the gas real velocity vector at standard conditions, k_{gr} is the gas's relative permeability, μ_g is the gas viscosity, and B_g is the gas formation volume factor.

The expression for the inflow performance of foamy oils may also be used to model conventional oil inflow by simply setting the entrained gas fraction to zero in the fluid property models.

Fluid properties of foamy-oil

Kumar & Mahadevan (2012) determine the foamy-oil properties in terms of two parameters such as the apparent bubble-point pressure and end-point entrained-gas fraction, i.e., defining the variation of the entrained-gas fraction with pressure.

As mentioned before, the presence of entrained gas alters the fluid properties of oils, specifically the oil density that decreases and the formation volume factor that increases below the bubble-point pressure. This behavior shows an inflection in both properties at the pseudo-bubble-point. Also, the solution gas-

oil ratio is constant up to the pseudo-bubble-point and then decreases. The viscosity behavior is similar to conventional oil (Kumar & Mahadevan, 2012).

– Equations of state of flashed-gas

Flashed-gas fraction ϕ_g is the ratio of the volume of gas flashed to the total solution volume and is given by:

$$\phi_g = \frac{(p_b - p)}{p} \frac{1}{\left[\frac{T_{ref}}{p_{ref}} \frac{p_b}{T R_{sob}} + \frac{(p_b - p)}{p}\right]} \tag{4 – 9}$$

where R_{sob} is the solution gas-oil ratio at bubble-point pressure, p_b is the bubble-point pressure, p_{ref} is the reference pressure, and T_{ref} is the reference temperature.

– Phase-equilibrium relationship

The entrained-gas fraction $\alpha_g = V_{ego}/V_g$ is the fraction of gas volume entrained in foamy oil per unit of gas flashed, V_{ego}, per unit volume of gas flashed, V_g, which varies with pressure and, so, can be defined as (Kraus *et al.*, 1993):

$$\alpha_g(p) = \begin{cases} 1, & p_{pb} \le p \le p_b \\ \frac{1-\alpha_g^{ref}}{p_{pb}-p_{ref}}\left(p - p_{ref}\right) + \alpha_g^{ref}, & p_{ref} < p \le p_{pb} \\ \alpha_g^{ref}, & p = p_{ref} \end{cases} \tag{4 – 10}$$

In Equation (4 – 10), p_{pb} is the pseudo-bubble-point pressure, p_b is the bubble-point pressure, p_{ref} is the reference pressure, and α_g^{ref} is the end-point entrained-gas fraction at the reference pressure (lower than p_{pb}).

All the flashed-gas are entrained between the bubble point and apparent bubble-point pressure. The flashed-gas fraction entrained decreases linearly with pressure below the apparent bubble-point pressure.

– Equation of state

Oil density is a function of pressure. The oil density above the bubble-point pressure varies with the oil compressibility factor, which is constant above the bubble-point pressure. Below bubble-point pressure, gas evolves from oil, and the oil density changes. The density calculation is divided into two stages at distinct pressure ranges, above and below bubble-point pressure.

As the oil phase is under-saturated above the bubble-point pressure, the density change is produced by the oil compressibility factor because there are no gas bubbles in the oil and the foamy oil does not exist. Therefore, the foamy oil density is similar to that of the oil:

$$\rho_{fo} = \rho_o(1-f) + \rho_g f \qquad (4-11)$$

$$f = \frac{\alpha_g \phi_g}{1-\phi_g(1-\alpha_g)}$$

where $f = V_{ego}/V_{fo}$, is the entrained-gas volume fraction in foamy-oil defined as the ratio of entrained-gas volume in foamy-oil, V_{ego}, and the foamy-oil volume, V_{fo}.

- **Gas-oil ratio**

Foamy oil is considered a dispersion of gas in oil stabilized by natural surfactants, in which the evolved gas from the solution stays in the emulsion as an entrained-gas component. The solution gas-oil ratio is generally defined as the volume of dissolved gas at standard conditions in a unit of volume of stock tank oil at specific pressure and temperature. The solution gas-oil ratio for foamy-oil is redefined to include the entrained-gas effect as the ratio of dissolved gas along with entrained-gas volume at standard conditions to stock tank oil volume. The solution gas-oil ratio for foamy oil is related to a conventional solution gas-oil ratio because the volume of gas in oil includes entrained gas and dissolved gas. So, the behavior of the solution gas-oil ratio for foamy-oil displays a constant value up to the apparent bubble-point pressure even though this pressure is less than the bubble-point pressure. The foamy-oil solution gas-oil ratio can be expressed as:

$$R_{sfo} = R_{so} + \alpha_g(R_{sob} - R_{so}) \qquad (4-12)$$

In Equation (4 – 12), R_{sob} is the solution gas-oil ratio at the bubble-point pressure and R_{so} is the solution gas-oil ratio at any pressure p_o.

- **Formation volume factor**

The formation volume factor is the ratio of the volume of phase with the dissolved gas in solution at prevalent temperature and pressure to the volume of phase at standard conditions. The formation volume factor for conventional oil can be defined by applying a material balance approach (Ahmed, 2010):

$$B_o = \frac{62.4\,\gamma_{oSC} + 0.0136\,R_{so}\,\gamma_{gSC}}{\rho_o} \qquad (4-13)$$

In Equation (4 – 13), ρ_o is the conventional oil density at pressure p, R_{so} is the solution gas-oil ratio and γ_{oSC} and γ_{gSC} are the oil and gas specific gravity at standard conditions, respectively.

Similarly, the formation volume factor for foamy oil can be expressed as:

$$B_{fo} = \frac{62.4\,\gamma_{foSC} + 0.0136\,R_{sfo}\,\gamma_{gSC}}{\rho_{fo}} \qquad (4-14)$$

In Equation (4 – 14), ρ_{fo} is the foamy-oil density at pressure p, R_{sofo} is the solution gas-oil ratio for foamy-oil, and γ_{foSC} is the specific gravity for foamy oil at standard conditions.

The specific gravity for foamy oil at standard conditions can be expressed by,

$$\gamma_{foSC} = \frac{\rho_{oSC}\left(1-\alpha_g^{ref}\vartheta_{gSC}\right)+\rho_{gSC}\alpha_g^{ref}\vartheta_{gSC}}{\rho_{wSC}} \quad (4-15)$$

In Equation (4 – 15), ϑ_{gSC} is the flashed-gas volume at standard conditions, ρ_{wSC} and ρ_{gSC} are the water and gas densities at standard conditions, respectively.

- **Viscosity**

Viscosity and density are the major parameters for heavy oil characterization. Several correlations for heavy oil viscosity are available in the literature (Mehrotra, 1991a, b); (Puttagunta, Miadonye, & Singh, 1992); (Puttagunta, Singh, & Miadonye, 1993). These correlations are mainly a function of density (or °API) and temperature. However, when these correlations are used for other oils from other regions with different characteristics, the results are usually not accurate, and certain modifications are needed to obtain satisfactory viscosity predictions.

Another alternative to calculating the viscosity of foamy oil is considering the foam rheology using the Einstein equation (Kumar & Mohadevan, 2012):

$$\mu(\phi_g) = \mu(0)(1 + m\phi_g) \quad (4-16)$$

In Equation (4 – 16), $\mu(\phi_g)$ is the foamy-oil viscosity at a flashed-gas fraction ϕ_g, $\mu(0)$ is the oil viscosity at zero flashed-gas fraction and m is a constant. Therefore, the variation of the foam viscosity depends on the gas fraction linearly, expecting that the viscosity increases as the gas fraction increases.

Goodarzi, Bryan, Mai, & Kantzas (2005) and Mastmann *et al.* (2001) in their investigation consider the foamy oil as foam, i.e., a mixture of gas and liquid, and show that viscosity does not change noticeably under various experimental conditions, and does not follow the Einstein equation.

Abivin, Hénaut, Argillier, & Moan (2008) present results of viscosity measurements for heavy oil crudes using X-ray imaging that determine two main parameters affecting their viscosity: the gas bubbles formation and the heavy oil composition, and conclude that the foamy-oil viscosity increases with the gas bubbles presence. Though the evidence of the dynamic of gas bubbles coalescence, the proposed viscosity correlation is a simple function of pressure.

Generally, all correlations used to calculate the oil viscosity below the bubble-point pressure for heavy and extra-heavy oils are a function of the dead-oil viscosity μ_{od} and solution gas-oil ratio R_{so} (see Annex C). An alternative way to calculate the viscosity of foamy oil is using the selected correlation and replacing the solution gas-ratio R_{so} by the solution gas-oil ratio for foamy oil R_{sfo}.

4.1.5 Relative permeability

The inclusion of the foamy-oil effect requires including the relative permeability variation with pressure to influence the IPR curve. The relative permeability of a phase is not directly a function of pressure but

a function of saturation of the phase and is mostly termed by an exponential relationship. Handy (1957) presents a method to obtain the relationship between the pressure and the relative permeability for solution gas drive at pseudo-steady-state conditions. Applying this method to foamy oil Brill & Mukherjee (1999) find the following equation (Kumar & Mohadevan, 2012):

$$\frac{k_{rg}}{k_{rfo}} = \left(R_{sop} - R_{sfo}\right)\frac{\mu_g B_g}{\mu_{fo} B_{fo}} \qquad (4-17)$$

where R_{sop} is the producing gas-oil ratio, R_{sfo} is the solution gas-oil ratio, μ_g and μ_{fo} are the gas and foamy-oil viscosity, and B_g and B_{fo} are the gas and foamy-oil formation-volume factors, respectively. This equation assumes that the total gas-oil ratio is constant with distance and is nearly equal to the producing gas-oil ratio, which is reasonable because it is a characteristic of CHOPS wells, low and constant gas-oil ratio during the producing life.

So, the producing gas-oil ratio that includes the foamy-oil condition can be calculated by the equation:

$$R_{sop} = R_{sob}\left(\frac{\rho_g}{\rho_{fo}}\right)_{SC}\left(\frac{\rho_{fo}}{\rho_g}\right)_b\left(\frac{B_g}{B_{fo}}\right)_b \qquad (4-18)$$

The relation of k_{rg}/k_{rfo} is usually obtained from experimental measurements of gas and oil relative permeability as a function of saturation, but without experimental data, the Corey correlation can be used to generate the gas and foamy-oil relative permeability curves. The foamy-oil relative permeability can be expressed by:

$$k_{rfo} = k_{rfo}^0\left(1 - \frac{S_g}{1-S_{wc}}\right)^n \qquad (4-19)$$

where n is a Corey exponent and S_{wc} is the connate water saturation

The free gas relative permeability is expressed by:

$$k_{rg} = k_{rg}^0\left(2 - \frac{S_g}{1-S_{wc}}\right)\left(\frac{S_g}{1-S_{wc}}\right)^m \qquad (4-20)$$

where m is a Corey exponent.

And the relative permeability ratio, k_{rg}/k_{rfo}, can be obtained with Equations (4 – 19) and (4 – 20).

$$\frac{k_{rg}}{k_{rfo}} = \frac{{k_{rg}}^0}{{k_{rfo}}^0}\left(2 - \frac{S_g}{1-S_{wc}}\right)\left(\frac{S_g}{1-S_{wc}}\right)^m \qquad (4-21)$$

4.1.6 Module implementation

The implementation of the foamy oil module attempts to integrate the inflow performance, the fluid properties, and the relative permeability of the new fluid as foamy oil. This module interacts basically with the fluid flow model, as a modification of the fluid in the pressure range in between the bubble-

point pressure and the pseudo-bubble-point pressure. Figure 4 – 3 presents a flow chart of the foamy oil model.

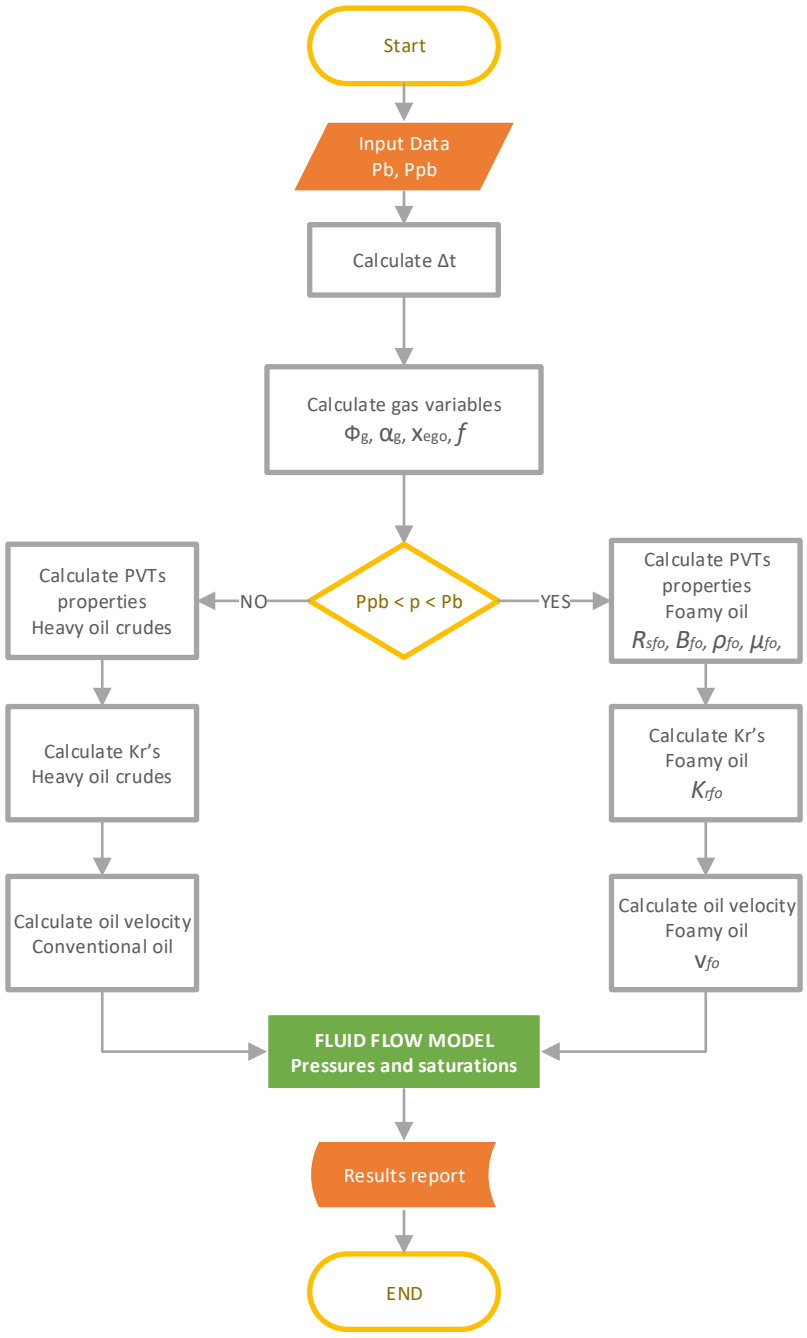

Figure 4 – 3. Flow chart of the foamy oil model.

4.2 Sand production model

Cold heavy oil production with sand requires a sand production model, in which critical conditions can be applied to simulate the massive and continuous sanding. A sand production model based on the

elastoplastic model is proposed integrating two primary components: a sanding onset to determine when the sand production initiates, and a sand production criterion to quantify the produced sand.

4.2.1 Sanding onset

The sanding onset determines the initiation point for sand production in terms of a production criterion such as a pressure gradient or a production rate. The onset sanding prediction consists of evaluating a yield criterion such as Mohr-Coulomb or Drucker and Prager at the stress state to determine the pressure gradient or production rate at which the sand production occurs. In this work, the yield criterion to be used is Drucker and Prager criterion as stated previously in Chapter 3.

4.2.2 Sand production criterion

There are several mechanisms responsible for sand production, which are mainly based on the shear and tensile failure, critical pressure gradient, critical drawdown pressure, critical plastic strain, and erosion criteria. The sand production criterion defines the sand production rate as a function of governing mechanisms such as elastoplastic behavior and erosion. However, it is very difficult to consider all mechanisms for the sand production criterion, and commonly the dominant mechanism is used.

Risnes & Bratli (1979) propose a sand production criterion in terms of the tensile failure for perforation tunnel inner shell collapse. Then, Bratli & Risnes (1981) and Weingarten & Perkins (1995) propose a sanding criterion based on the pressure gradient. Morita, Whitfill, Massie & Knudsen (1989) propose a sanding criterion that can be initiated by either shear failure or tensile failure. Vardoulakis, Stavropoulou & Papanastasiou (1996) present a sanding criterion in terms of surface erosion that is accompanied by high changes in porosity and permeability close to the free surface. This approach based on erosion theory is defined by:

$$\dot{q}_s = \rho_s \lambda (1-\phi) C |\bar{q}_i| \qquad (4-22)$$

where $\dot{q}_s$ is the sand production mass rate, C is the concentration of solid grains in the fluid phase, λ is an experimental parameter, and $\bar{q}_i$ the mixture volume discharge rate. This approach does not consider formation characteristics as the Uniaxial Compressive Strength (UCS).

Detournay (2009) introduced a critical specific discharge q_{cr} as a critical condition for sand production initiation, which depends on the mechanical resistance of the solid as a function of the residual cohesion, τ_{or}, the residual friction angle, φ_r, and the surface tangent effective stress, σ'_θ, tensile o compressive. For tensile stress, it is assumed that particles do not offer any resistance to being produced, and $q_{cr} = 0$. For compressive stress, the critical specific discharge has the following equation:

$$q_{cr} = a_s \frac{k(1-\phi)}{\mathrm{v}_f r_m} (\tau_{or} + |\sigma'_\theta| \tan \varphi_r) \qquad (4-23)$$

where k is permeability, ϕ is porosity, v_f is the dynamic fluid viscosity, r_m is the mean particle radius, and a_s is a dimensionless coefficient determined experimentally.

Finally, Nouri, Vaziri, Belhaj, & Islam (2006) propose a sand production criterion that is quite similar to Vardoulakis' proposal, but the difference is in terms of the critical specific discharge q_{cr} and the local boundary surface S_L.

$$\dot{q}_s = \rho_s(1-\phi)|q_n - q_{cr}|S_L \qquad (4-24)$$

where q_n is the local specific discharge (normal to the wellbore wall) and it must be higher than a critical specific discharge q_{cr} to occur sand production ($q_n < q_{cr}$).

A sand production model is also integrated to determine the sanding onset and sand production criterion. The sand production onset is defined as the initiation point for sand production in terms of a production criterion such as a pressure gradient or wellbore pressure (critical borehole pressure). The onset sanding prediction consists of evaluating a yield criterion at the stress state to determine the pressure gradient or production rate at which the sanding occurs. In this work, the yield criterion to be used is the Drucker-Prager criterion. A sand production criterion is integrated to quantify the sand production rate based on the rock plastic deformation, in which the vertical and radial stresses are increased independently, and a high radial flow rate is produced (Nouri, Vaziri, Belhaj, & Islam, 2006).

Araujo, Alzate-Espinosa & Arbelaez-Londoño (2015) proposed a new criterion to quantify the sand production rate based on the rock plastic deformation using experimental data from a sand production test, in which the vertical and the radial stresses are increased independently, and a high radial flow rate is produced. A function to quantify the level of sand production is presented by Araujo-Guerrero (2015), which is based on the level of plastic failure, e^{ps}. Here, it is proposed that the amount of sand available to produce is proportional to the level of plastic failure caused by the pressure drop and the change of stresses required to have affected the porous medium. To produce sand, a minimum value of flow velocity is defined for which a free grain can be transported by the fluid. In this way, sand production is defined as:

$$\dot{q}_s = \begin{cases} 0 & , \quad \epsilon^{ps} < \epsilon_{cr}^{ps} \\ \frac{i_s}{A_f} A_T \epsilon^{ps} & , \quad \epsilon^{ps} > \epsilon_{cr}^{ps} \quad \& \quad \mathrm{v}_f > \mathrm{v}_{fcr} \end{cases} \qquad (4-25)$$

In Equation (4 – 25), $\dot{q}_s$ is solid mass discharge, ϵ^{ps} is the equivalent plastic strain, ϵ_{cr}^{ps} is the critical plastic strain needed to initiate the sanding, v_{fcr} is the critical fluid velocity required to erode the sand grains, and i_s is an experimental parameter, which relates to the sand production and the plastic strain increments at the cavity surface. The parameter A_f is the sand-producing area perpendicular to the flow direction and A_T is the area perpendicular to flow. The inclusion of the area is important because it allows having a nominal sand production value that can be extrapolated to cases such as open-hole or perforations. The real fluid velocity v_f is calculated from the pressure gradient using Darcy's law as a mean value in terms of saturations. As an improvement of the model, it is proposed that the sand should be produced up to the critical porosity ϕ_{cr}, which is the porosity above which grain-to-grain contact is lost and the rock can exist as a suspension. Remember that porosity is updated with changes in efforts, pressures, strains, and sand production.

The critical fluid velocity responds to an erosion criterion. The yielded sands will stay in the formation until the hydrodynamic force exceeds the frictional resistance force. The kinetic force consists of form

drag and friction drag, while the resistance force is the gravitational force on the sand grains. The equilibrium of force is a balance between the kinetic force and the resistance force on the sand with the critical fluid flow velocity as shown in Equation (4 – 26). Once the fluid velocity is larger than the critical velocity on the failed sand grains during production, sand will be eroded and transported to the well.

$$6\pi\mu_f r_p \mathrm{v}_{fcr} = \frac{4}{3}\pi r_p^3(\rho_s - \rho_f)g \qquad (4-26)$$

In Equation (4 – 26), μ_f and ρ_f are the fluid viscosity and density, the ρ_s is the sand density. r_p is the sand particle radius and g is the gravitational acceleration ($g = 32.174\ \mathrm{ft/s^2}$). The critical fluid can be defined from this equation as:

$$\mathrm{v}_{fcr} = \frac{2}{9}\frac{r_p^2(\rho_s-\rho_f)g}{\mu_f} \qquad (4-27)$$

The sand production model implemented as a module in the coupled model for CHOPS already includes the erosion component. The coupled model itself is an erosional mechanics model because it couples a fluid flow model and geomechanical model, capturing some of the key mechanisms that are involved in sand production. First, sand is assumed to be produced when the material is fully degraded and hydrodynamic forces are high enough to remove the particles and the model shows that sand production initiates from the perforation tip and propagates to the top and sides of the perforation cavity. A dynamic drag force leads to internal and surface erosion that results in the liberation and transport of particles.

4.2.3 Equivalent plastic strain calculation

The equivalent plastic strain is a scalar quantity that describes the degree of work hardening in the material or the plastic history or the shear strain intensity and its calculation is dependent on the chosen yield criterion, in particular its coefficient. Considering that the equivalent plastic strain is a positive quantity and possesses the dimension of strain, the equivalent plastic strain increment can be defined as (Ding, & Zhang, 2017):

$$d\epsilon^{ps} = \mathrm{c}\sqrt{d\epsilon_{ij}^p d\epsilon_{ij}^p} = \mathrm{c}\sqrt{\left(d\epsilon_1^p\right)^2 + \left(d\epsilon_2^p\right)^2 + \left(d\epsilon_3^p\right)^2} \qquad (4-28)$$

In Equation (4 – 28), $d\epsilon^{ps}$ is the equivalent plastic strain increment, c is the coefficient of the equivalent plastic strain, $d\epsilon_{ij}^p$ are components of the plastic strain increment.

When the Mises yield criterion is used, the coefficient of equivalent plastic strain equals $\sqrt{2/3}$. Considering the associated flow of the Drucker-Prager criterion, the coefficient of equivalent plastic strain is no longer a constant and decreases gradually with the plastic deformation, and its value is always less than $\sqrt{2/3}$. If this coefficient based on the associated flow of the Drucker-Prager criterion is taken as $\sqrt{2/3}$, which is a conventional practice and a basis of many finite element software, the computed value of the equivalent plastic strain will significantly deviate from the actual value. Then, the coefficient of equivalent plastic strain based on the associated flow of Drucker and Prager criterion is defined as:

$$c = \frac{\sqrt{1/3} - q_\varphi}{\sqrt{3(q_\varphi)^2 + 1/2}} \qquad (4 - 29)$$

In Equation (4 – 29), q_φ is the coefficient of pressure sensitivity, a Drucker and Prager material constant defined by Equation (3 – 81).

4.2.4 Module implementation

The implementation of the sand production module attempts to integrate the onset and rate of sanding into the general model. That is how the sand production module interacts with the fluid flow model and the geomechanical (elastoplastic) model, which are coupled by the pore pressure and the elastic and plastic deformation and share plastic deformation and sand production rate. Figure 4 – 4 presents a flow chart of the sand production model.

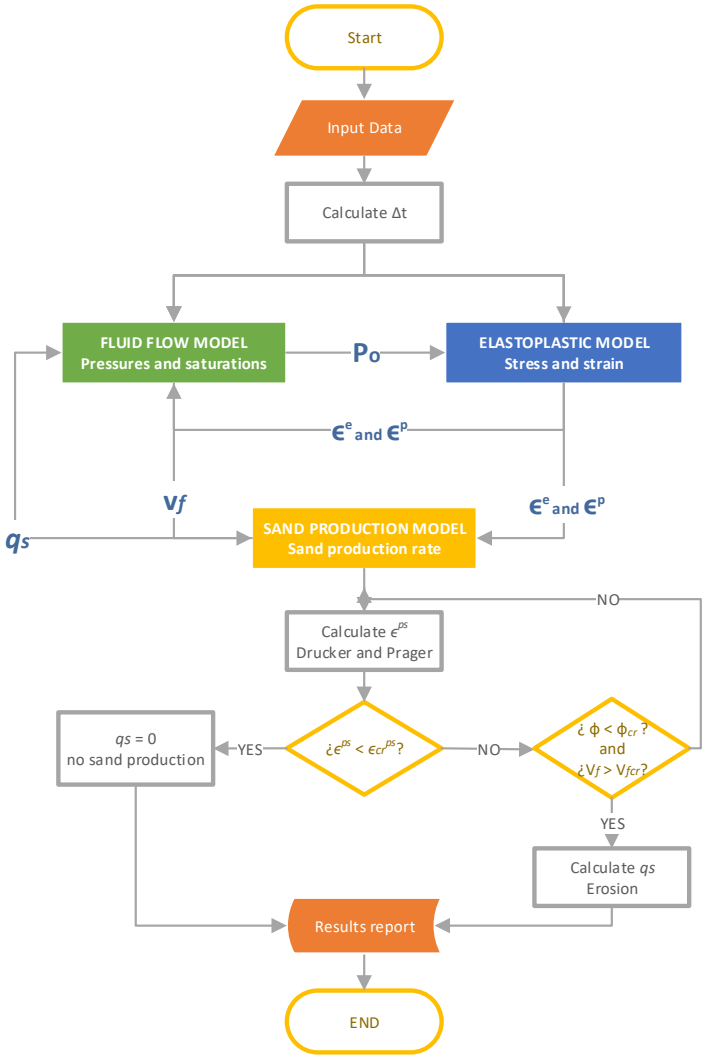

Figure 4 – 4. Flow chart of the sand production model.

4.3 Wormholes methodology

A new methodology is proposed as a conceptual model to take account of the wormhole initiation and propagation, which includes the governing mechanisms such as the elastoplastic behavior of the formation, the dynamic changes in stresses around the well and in the reservoir itself, the failure criteria, the pressure gradient, the hydrodynamic erosion and the changes on petrophysical properties of the formation during the cold heavy oil production with sand.

The dynamic of the massive and continuous sand defines four zones around the well: liquefied zone, yielded zone, transition zone, and intact zone, each one with different mechanical and petrophysical properties, which are changing during the oil and sand production.

It is proposed as a methodology because a 3D-coupled model (3-phase fluid flow model and elastoplastic model) is used as the tool to get the critical conditions to initiate and propagate the wormhole as the natural phenomena, including the different components of CHOPS. However, wormhole growth is the key parameter of this methodology.

This conceptual model states the steps to formate a wormhole defining zones that extend according to the changes suffered by the properties of the reservoir due to the redistribution of efforts and refining during production. During the cold production due to the geomechanical behavior, the formation failed and defines a yielded zone, if this zone passes the sand production criteria then the sanding occurs and the sand grains travel to the wellbore, defining a sanding front and a sanding zone. These geomechanical changes during the production and massive sanding increase petrophysical properties such as porosity and permeability up to the porosity pass the threshold a wormhole or channel is created, defining a liquefaction zone or wormhole zone. Figure 4 – 5 presents the dynamic zones and wormholes during cold production with massive sand.

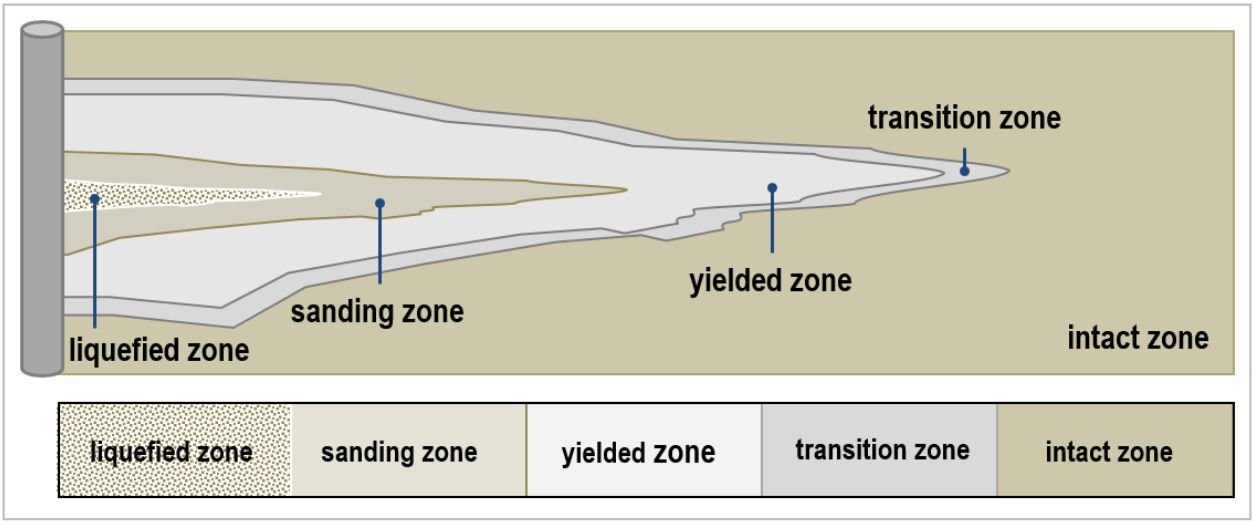

Figure 4 – 5. Dynamic zones and wormhole formation during cold heavy oil production with sands.

Usually, the wormhole growth is modeled using probabilistic methods or a failure criterion at the wormhole's tip such as a critical pressure gradient. The prediction of the wormhole growth is based on a critical pressure gradient at its tip and needs huge and precise information on geomechanical properties such as cohesion of the grains at each point, accurate failure criteria considering the impact of the foamy-oil on strength properties and rock cohesion, and others at the field scale. This complex process requires an additional model to include the wormhole effect on production but using the coupled model (fluid flow and geomechanics), considering the different components such as fluid flow, foamy-oil, and elastoplastic stress-strain behavior.

4.3.1 Module implementation

The dynamic wormhole growth depends on the sand production at critical conditions, in which the pressure gradient and the in-situ stress state drive the initiation and propagation of the wormholes. So, the maximum stress will define the direction of propagation of the wormhole while the effective radial stress in the lateral wall of a wormhole is more compressive with a smaller gradient. Following the sanding process, the wormhole is assumed that initiates usually at the wellbore sand face and will enlarge as long as a critical tip pressure gradient is exceeded radially to its maximum stable cross-sectional area, after which its diameter is assumed stable. And the wormhole only propagates forward from the tip, where pressure gradients are elevated by the three-phase fluid flow and foamy oil behavior.

The oil production generates pressure gradients high enough to overcome cohesion and frictional forces that hold the sand grains together, leaving them free to be transported.

Two conditions to maintain the wormhole growth are that the pressure gradient at the tip may be high enough to displace the solid grains and that the pressure gradient along the wormhole moves toward the wellbore. So, the wormholes are a consequence of massive sanding, and cause a significant improvement in porosity and permeability, resulting in drainage areas increment and production increment. The onset of sand production is assumed to occur when the formation fails according to the yield criterion used (Drucker & Prager).

The elastoplastic model uses the pressure gradient that is calculated by the reservoir model (3-phase fluid flow model) to estimate the changes in the stress state of the reservoir. If these changes are large enough, the rock will fail and the wormhole will be initiated. The yielding zone and the intact zone (reservoir) are defined in terms of plastic deformation, ε^p, using the elastoplastic model with the yield criterion (Drucker & Prager), i.e., the yield zone meets the condition $\varepsilon^p > 0$ and the intact zone meets the condition $\varepsilon^p = 0$. Also, the sand production zone or sanding front is defined inside the yielding zone using the sand production criterion, i.e., where the critical plastic deformation is obtained. Finally, the liquefaction zone or wormhole zone is defined in terms of the critical porosity, ϕ_{cr}, meeting the condition $\phi \geq \phi_{cr}$, where is a slurry flow or no-grain-to-grain contact as defined by Dusseault (2002). The critical porosity for unconsolidated sandstones is 0.52. Following Detournay (2009), when porosity reaches the critical value ($\phi = \phi_{cr}$), the grid block collapses and is removed physically from the model, and the sanding remaining in it is produced instantaneously as follows:

$$\partial q_s = (1 - \phi_{cr})\rho_s V_b \qquad (4-30)$$

As the coupled model does not have an adaptive mesh, the removal of the block occurs only in sand, it provides instantaneous sand and the flow of fluids continues with the critical porosity and its associated permeability.

For a field case, in each time step, the fully coupled model integrates the component of the process and evaluates if a wormhole is created defining the blocks of the grid with failure and critical porosity. A wormhole map is traced with the blocks that meet the conditions for a wormhole.

Figure 4 – 5 presents the flow chart for the wormhole formation model. The previous step to implement the wormhole formation model:

Definition of the critical conditions for CHOPS from the production history of the field cases.

- Definition of study case.
- Drawdown to produce massive sand to generate wormholes.
- A positive value of the dilatancy angle guarantees sand production while the porosity increases.

For $t = n$:

1. Define the yielding zone and the intact zone (reservoir):

   Elastoplasticity model with Drucker & Prager:
   Yielding zone: If $\epsilon^p > 0$
   Reservoir zone: If $\epsilon^p = 0$

2. Define the sand production zone (front) inside the yielding zone: ϵ^{ps}.

3. Define the liquefaction zone (wormholes): $\phi \geq \phi_{cr}$, and when $\phi = \phi_{cr}$ calculate the instantaneous sand production.

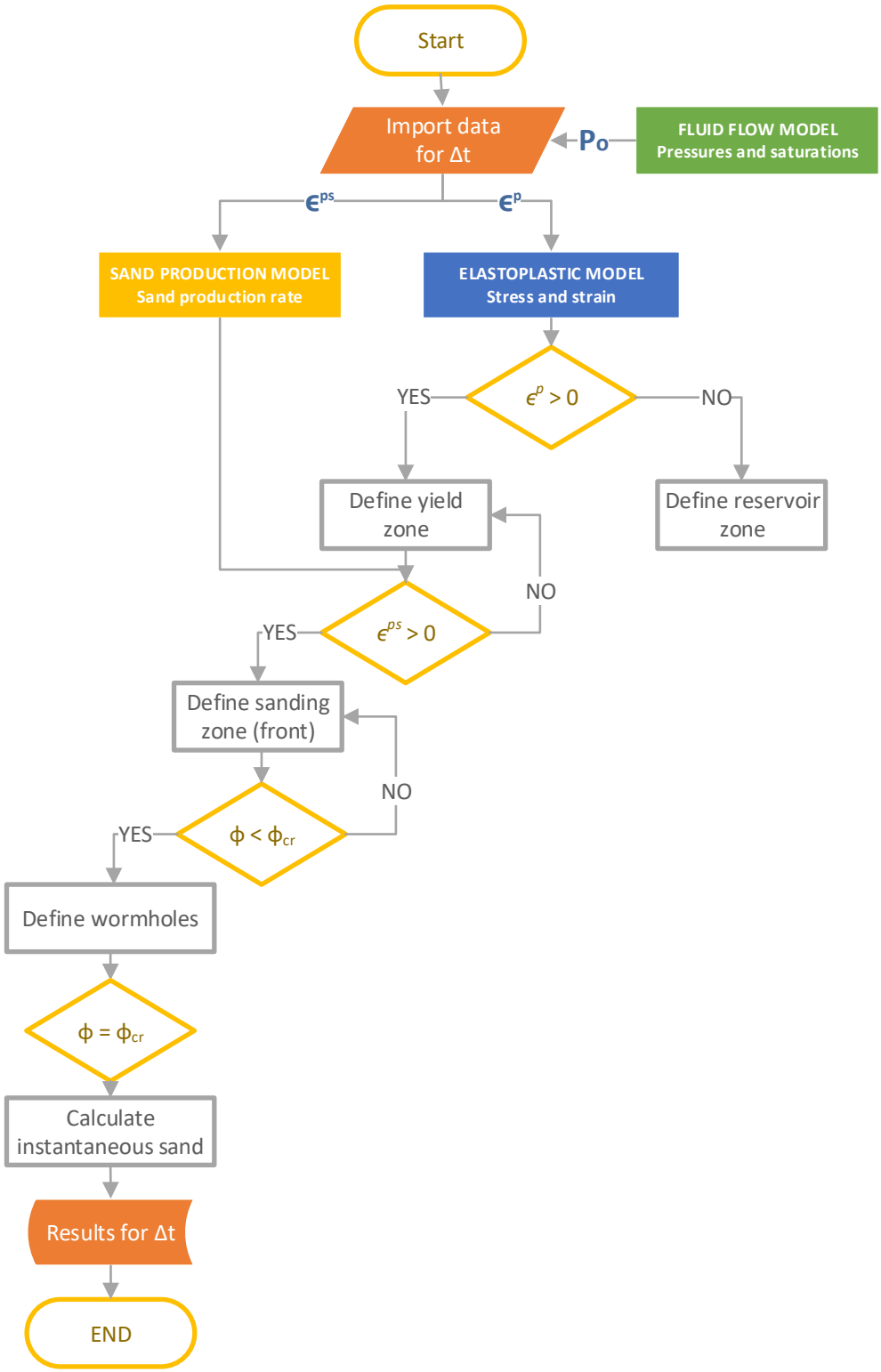

Figure 4 – 6. Flow chart of the wormhole formation model.

Chapter 5. Model Validation

This chapter describes the validation of the coupled model for cold heavy oil production with sand. The strategy for the validation of the coupled model consists to validate separately each one of the components of the model by comparing the results obtained in the numerical simulation with the results obtained with commercial software such as ABAQUS® and CMG®, aligning the models as much as possible and running the several cases. There are two basic components: the fluid flow model and the geomechanical model (elastoplastic).

The validation protocol considers verification as the first step that consists to verify the boundary conditions and the trend of the validation variables for each model. And the second step is the validation step itself, in which the behavior of the main variables is compared for both software, the numerical simulator, and the commercial software. The variables of comparison are selected according to the basic model to be validated and their comparison is done using the graphic behavior and the root mean squared error that quantifies the difference in results between the models.

The fluid flow model is validated using the CMG® software simulator and the geomechanical model is validated using ABAQUS® software. Finally, the coupled model is validated using CMG® as a commercial simulator.

5.1 Fluid flow model

The strategy of validation for the 3D three-phase fluid flow model in cylindrical coordinates consists to compare the results obtained in the numerical model with the results obtained in the commercial simulator CMG®, aligning the models as much as possible and running the same cases. The validation takes into account three basic models: one-phase, two-phase, and three-phase. The foamy-oil model is not included because the CMG® model is in terms of kinetic equations, a very different strategy. First, the one-phase model is validated by considering the two possible cases: oil and gas. Similarly, the validation of the two-phase model considers the two possible cases: oil-water and oil-gas. The validation of the three-phase model considers a basic case with three phases (oil, gas, and water) as a black-oil fluid.

The validation protocol considers verification as the first step that consists to verify the boundary conditions and the trend of the validation variables. And the second step is the validation step itself, in which the main variables of comparison are the oil pressure, the phase saturations, the production rate, and the cumulative production. The comparison of the variables is done using the graphic behavior and the root mean squared error (RMSE) that quantifies the difference in results between the models.

There are significant differences between the CMG® simulator and the numerical model that do not allow for completely aligning these models. For example, the CMG® simulator uses a mean pressure instead of oil pressure and the saturations are not variables per se, while in the numerical model, the

saturations are mean variables. PVT properties are different correlations in both simulators and also the external boundary condition is different.

5.1.1 One-phase model

The validation of the one-phase model takes into account just the oil case as the base case, comparing the results obtained in the numerical model with the results obtained using the CMG® simulator. The variables of validation for these basic cases are the oil pressure, the saturations, the production rate, and the cumulative production.

Oil case

The validation of the one-phase model for oil is performed by comparing the results obtained with the CMG® simulator using a field case. The characteristics of the reservoir of the field case are summarized in Table 5 – 1 and the production schedule to run this case is presented in Table 5 – 2.

Table 5 – 1. Field case for the validation of the one-phase model for the oil case.

RESERVOIR CHARACTERISTICS	VALUE
Depth (ft)	3000
Wellbore radius (in)	2.5
Reservoir radius (ft)	500
Reservoir thickness (ft)	30
Reservoir pressure (psi)	1500
Temperature (°F)	150
Porosity (fraction)	0.30
Horizontal permeability (mD)	300
Vertical permeability (mD)	30
API Gravity (°API)	20
Gas-specific gravity	0.7
Bubble point pressure (psi)	500
Oil saturation (fraction)	0.95
Water saturation (fraction)	0.05
Gas saturation (fraction)	0.00

Table 5 – 2. Production schedule for the validation of the one-phase model for the oil case.

PRODUCTION TIME (days)	WELLBORE PRESSURE (psi)
30	1480
60	1460
90	1440
120	1420
150	1400
180	1380

Figure 5 – 1 presents the relative permeability curve for the oil-water system for the validation of the one-phase model for the oil case using the CMG® simulator and the numerical model.

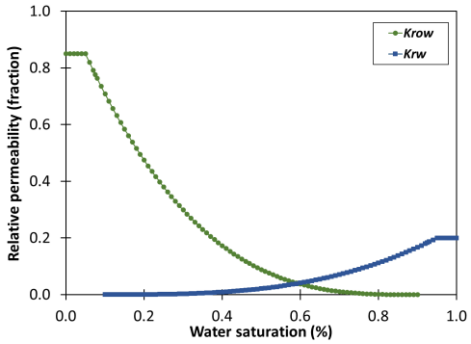

Figure 5 – 1. Relative permeability for the oil-water system for validation.

Figure 5 – 2 presents the results of the radial pressure profile for each production time and Figure 5 – 3 presents the results of the production of oil, water, and gas during simulation time for the oil validation case using the CMG® simulator and the numerical model.

Table 5 – 3 presents the root mean squared error to quantify the oil pressure differences and oil saturation differences between the results of the CMG® simulator and the numerical model for the validation of the one-phase model for the oil case.

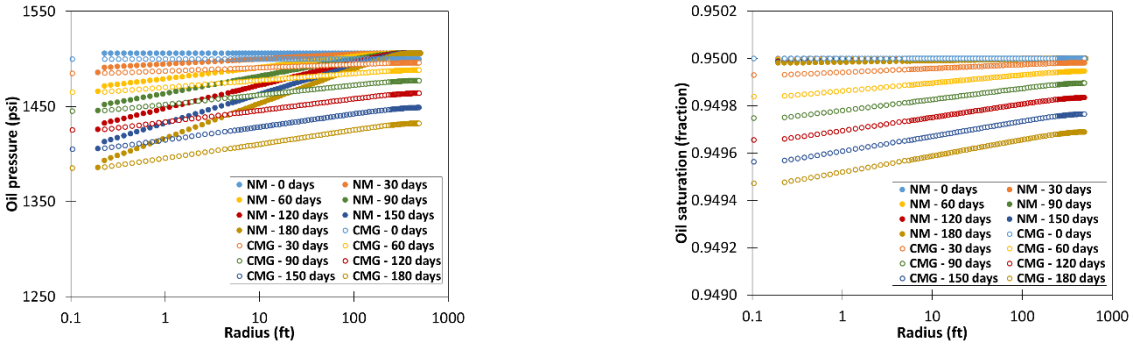

a. b.

Figure 5 – 2. Radial pressure and saturation profiles for each production time for the validation of the one-phase model for the oil case. a) Oil pressure profile. b) Oil saturation profile.

Table 5 – 3. Root mean squared error (RMSE) for oil pressure and oil saturation for each production time for the validation of the one-phase model for the oil case.

PRODUCTION TIME (days)	RMSE	
	Oil pressure (psi)	Oil saturation (fraction)
0	6.32	1.19E-08
30	9.90	3.67E-05
60	16.00	9.08E-05
90	24.39	1.54E-04
120	34.35	2.24E-04
150	45.56	2.99E-04
180	57.67	3.78E-04
Mean	**27.74**	**1.69E-04**

Figure 5 – 3 presents the results of the production of oil, water, and gas during simulation time for the oil validation case using the CMG® simulator and the numerical model.

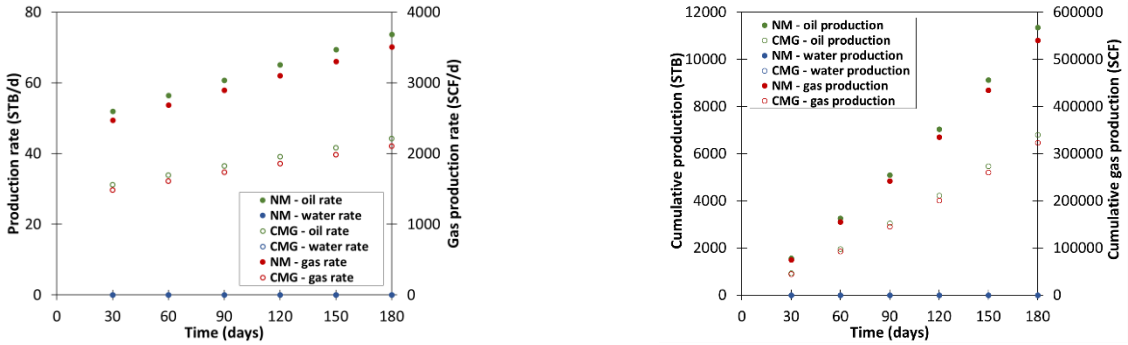

a. b.

Figure 5 – 3. Production (oil, water, and gas) during simulation time for the validation of the one-phase model for the oil case. a) Production rate. b) Cumulative production.

Table 5 – 4 presents the root mean squared error to quantify the differences in production rate and cumulative production between the results of the CMG® simulator and the numerical model for the validation of the one-phase model for the oil case.

Table 5 – 4. Root mean squared error (RMSE) for production rate and cumulative production for oil, water, and gas for the validation of the one-phase model for the oil case.

VARIABLE	RMSE
Oil production rate (STB/d)	25.34
Water production rate (STB/d)	0.00
Gas production rate (SCF/d)	1205.44
Cumulative oil production (STB)	2838.71
Cumulative water production (STB)	0.00
Cumulative gas production (SCF)	135107.38

Remark: For the results of the one-phase model for the oil case, the root mean square error increases with time. In terms of oil pressure are acceptable with a root mean square error of 27.74 psi. In terms of saturation, the results are adequate, and the root mean square errors for saturation are small enough, with a mean value of 1.69E-04. The results in terms of production rate and cumulative production have reasonable differences considering the existing differences between the two models, the behavior trends are similar in both models with no differences in water production, and high differences in oil and gas production. The external boundary conditions manage the trend in terms of pressure affecting significantly production variables. In conclusion, the results of the one-phase model for the oil case are acceptable in terms of oil pressure, saturation, and production variables and allow us to verify and validate the numerical model for this case.

Gas case

The validation of the one-phase model for gas is performed by comparing the results obtained with the CMG® commercial simulator using a field case. The characteristics of the reservoir of the field case are summarized in Table 5 – 5 and the production schedule to run this case is presented in Table 5 – 2.

Figure 5 – 4 presents the relative permeability curve for the oil-gas system for the validation of the one-phase model for the gas case using the CMG® simulator and the numerical model.

Table 5 – 5. Field case for the validation of the one-phase model for the gas case.

RESERVOIR CHARACTERISTICS	VALUE
Depth (ft)	3000
Wellbore radius (in)	2.5
Reservoir radius (ft)	500
Reservoir thickness (ft)	30
Reservoir pressure (psi)	1500
Temperature (°F)	150
Porosity (fraction)	0.30
Horizontal permeability (mD)	300
Vertical permeability (mD)	30
API Gravity (°API)	20
Gas-specific gravity (fraction)	0.7
Bubble point pressure (psi)	1700
Oil saturation (fraction)	0.05
Water saturation (fraction)	0.00
Gas saturation (fraction)	0.95

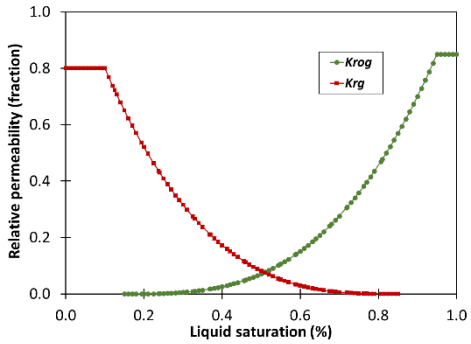

Figure 5 – 4. Relative permeability for the oil-gas system for validation.

Figure 5 – 5 presents the results of the radial pressure profile for each production time and Figure 5 – 6 presents the results of the production of oil, water, and gas during simulation time for the gas validation case using the CMG® simulator and the numerical model.

Table 5 – 6 presents the root mean squared error to quantify the oil pressure differences and gas saturation differences between the results of the CMG® simulator and the numerical model for the validation of the one-phase model for the gas case.

Table 5 – 7 presents the root mean squared error to quantify the differences in production rate and cumulative production between the results of the CMG® simulator and the numerical model for the validation of the one-phase model for the gas case.

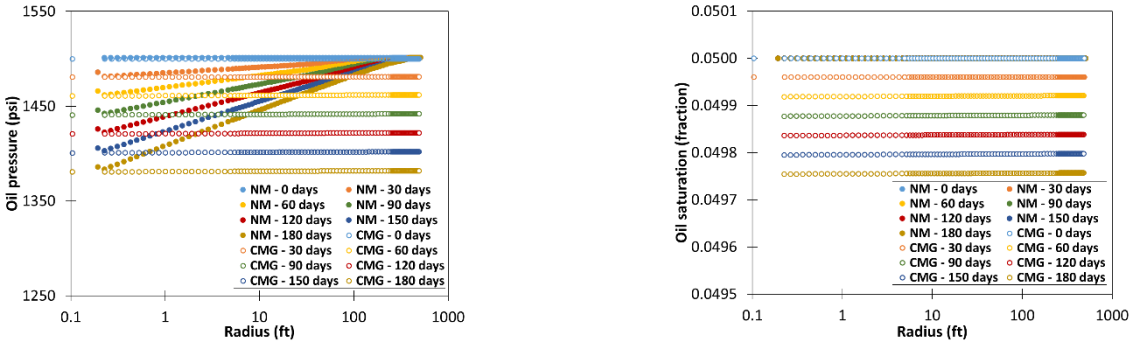

a. b.

Figure 5 – 5. Radial pressure and saturation profiles for each production time for the validation of the one-phase model for the gas case. a) Oil pressure profile. b) Gas saturation profile.

Table 5 – 6. Root mean squared error (RMSE) for oil pressure and gas saturation for each production time for the validation of the one-phase model for the gas case.

PRODUCTION TIME (days)	RMSE	
	Oil pressure (psi)	Gas saturation (fraction)
0	1.32	7.45E-10
30	14.72	3.99E-05
60	29.22	8.00E-05
90	44.42	1.21E-04
120	59.60	1.62E-04
150	74.77	2.03E-04
180	89.89	2.44E-04
Mean	**44.85**	**1.22E-04**

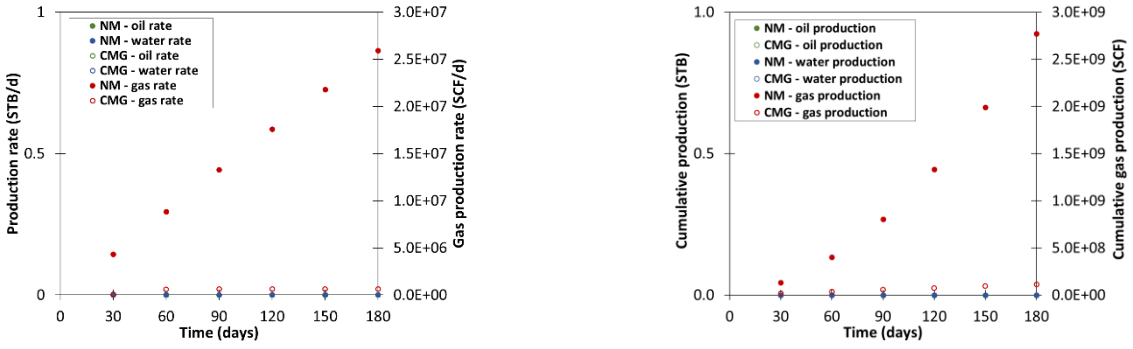

a. b.

Figure 5 – 6. Production (oil, water, and gas) during simulation time for the validation of the one-phase model for the gas case. a) Production rate. b) Cumulative production.

Table 5 – 7. Root mean squared error (RMSE) for production rate and cumulative production for oil, water, and gas for the validation of the one-phase model for the gas case.

VARIABLE	RMSE
Oil production rate (STB/d)	0.0
Water production rate (STB/d)	0.0
Gas production rate (SCF/d)	1.64E07
Cumulative oil production (STB)	0.0
Cumulative water production (STB)	0.0
Cumulative gas production (SCF)	1.47E09

Remark: For the results of the one-phase model for the gas case, the root mean square error increases with time. In terms of oil pressure are acceptable with a root mean square error of 44.85 psi. In terms of saturation, the results are adequate too, and the root mean square errors for saturation are small enough, with a mean value of 1.22E-04. The results in terms of production rate and cumulative production have high differences considering the existing differences between the two models, the behavior trends are similar in both models with no differences in oil and water production, and high differences in gas production. The gas production is significantly low for the CMG® simulator and the gas saturation has a reverse trend, i.e., it is increasing. The external boundary conditions manage the trend in terms of pressure affecting significantly production variables In conclusion, the results of the one-phase model for the gas case are acceptable in terms of oil pressure, saturation, and production variables that allow us to verify and validate the numerical model for this case.

5.1.2 Two-phase model

The validation of the two-phase model takes into account two basic cases: the oil and water case and the oil and gas case, comparing the results obtained in the numerical model with the results obtained using the CMG® commercial simulator. The variables of validation for these basic cases are the oil pressure, the phase saturations, the production rate, and the cumulative production.

Oil and water case

The validation of the two-phase model for the oil and water case is performed by comparing the results obtained with the CMG® simulator using a field case. The characteristics of the reservoir of the field case are summarized in Table 5 – 8, the production schedule to run this case is presented in Table 5 – 2 and the relative permeability curve for the oil-water system is presented in Figure 5 – 1.

Figure 5 – 7 presents the results of the radial pressure profile for each production time and Figure 5 – 8 presents the results of the production of oil, water, and gas during simulation time for the two-phase model for the oil and water case using the CMG® simulator and the numerical model.

Table 5 – 9 presents the root mean squared error to quantify the oil pressure differences and oil saturation differences between the results of the CMG® simulator and the numerical model for the validation of the two-phase model for the oil and water case.

Table 5 – 10 presents the root mean squared error to quantify the differences in production rate and cumulative production between the results of the CMG® simulator and the numerical model for the validation of the two-phase model for the oil and water case.

Table 5 – 8. Field case for the validation of the two-phase model for the oil and water case.

RESERVOIR CHARACTERISTICS	VALUE
Depth (ft)	3000
Wellbore radius (in)	2.5
Reservoir radius (ft)	500
Reservoir thickness (ft)	30
Reservoir pressure (psi)	1500
Temperature (°F)	150
Porosity (fraction)	0.30
Horizontal permeability (mD)	300
Vertical permeability (mD)	30
API Gravity (°API)	20
Gas-specific gravity (fraction)	0.7
Bubble point pressure (psi)	500
Oil saturation (fraction)	0.80
Water saturation (fraction)	0.20
Gas saturation (fraction)	0.00

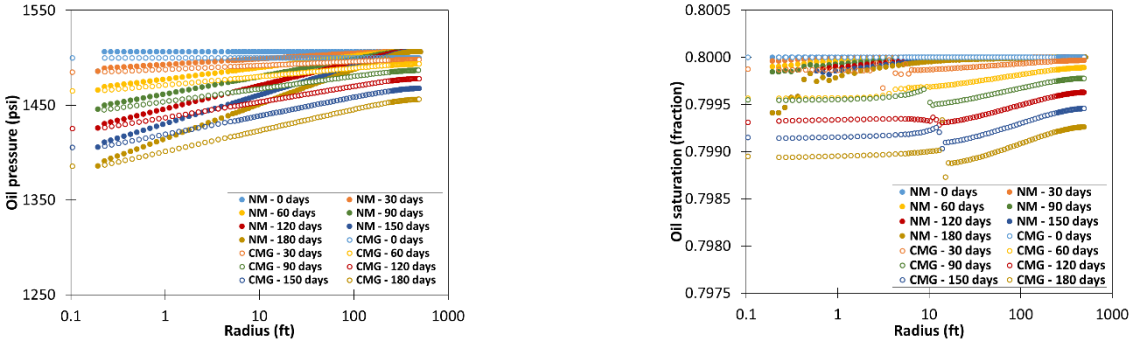

a. b.

Figure 5 – 7. Radial pressure and saturation profiles for each production time for the validation of the two-phase model for the oil and water case. b) Oil saturation profile.

Table 5 – 9. Root mean squared error (RMSE) for oil pressure and oil saturation for each production time for the validation of the two-phase model for the oil and water case.

PRODUCTION TIME (days)	RMSE	
	Oil pressure (psi)	Oil saturation (fraction)
0	6.65	1.19E-08
30	8.01	9.45E-05
60	11.60	2.52E-04
90	16.47	3.46E-04
120	23.09	5.17E-04
150	30.20	6.86E-04
180	38.75	8.81E-04
Mean	**19.25**	**3.97E-04**

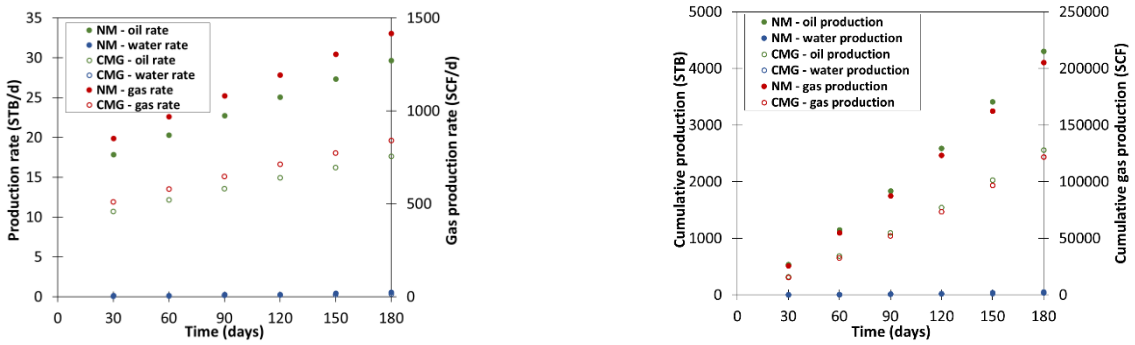

a. b.

Figure 5 – 8. Production (oil, water, and gas) during simulation time for the validation of the two-phase model for the oil and water case. a) Production rate. b) Cumulative production.

Table 5 – 10. Root mean squared error (RMSE) for production rate and cumulative production for oil, water, and gas for the validation of the two-phase model for the oil and water case.

VARIABLE	RMSE
Oil production rate (STB/d)	9.77
Water production rate (STB/d)	1.42E-01
Gas production rate (SCF/d)	466.38
Cumulative oil production (STB)	1070.33
Cumulative water production (STB)	12.67
Cumulative gas production (SCF)	50998.82

Remark: The results of the two-phase model for the oil and water case in terms of oil pressure are acceptable with a root mean square error of 19.25 psi. In terms of saturation, the results are adequate, and the root mean square errors for saturation are small enough, with a mean value of 3.97E-04. The results in terms of production rate and cumulative production are reasonable differences considering the existing differences between the two models, the behavior trends are similar in both models, and differences in oil, water, and gas production. In conclusion, the results of the two-phase model for the oil and water case are adequate in terms of oil pressure, saturation, and production variables that allow us to verify and validate the numerical model for this case.

Oil and gas case

The oil and gas case in the numerical simulator just gets adequate adjustment for low gas saturation, values around the critical gas saturation, so the gas flow is not guaranteed. For the rest of the cases, numerical stability is not achieved, and behavior responds to the high mobility relation of the gas with respect to the liquid and the high aspect ratio of the grid. Then, the validation of the two-phase model for the oil and gas case is not presented.

5.1.3 Three-phase case

The three-phase model in the numerical simulator just gets adequate adjustment for low gas saturation, values around the critical gas saturation, so the gas flow is not guaranteed. For the rest of the cases, numerical stability is not achieved, and behavior responds to the high mobility relation of the gas with respect to the liquid and the high aspect ratio of the grid. Then, the validation of the three-phase model is not presented.

5.2 Geomechanical model

The strategy of validation for the 3D elastoplastic model consists to validate two basic models: the elastic and the elastoplastic model, and considering two well settings: a one-layer set and a multi-layer set, comparing the results obtained in the numerical model with the results obtained with commercial software (ABAQUS® and CMG®), aligning the models as much as possible and running the same cases.

First, the elastic model is validated for a one-layer set considering both isotropic and anisotropic horizontal stress conditions for a mechanical case coupled with the fluid flow; this model is validated by comparing the results obtained from the numerical model with the results obtained from ABAQUS®. Then, a multi-layer set is validated in a similar way to the one-layer case. Second, the elastoplastic model is validated as an extension of the elastic model considering just one model: mechanical case coupled with the fluid flow that allows evaluating the pressure contribution on the strain-stress relationship, considering two cases: one-layer and multi-layer case, both under isotropic and anisotropic horizontal stresses condition. Also, these cases are validated by comparing the results obtained from the numerical model with the results obtained with ABAQUS®.

The validation protocol considers verification as the first step that consists to verify the boundary conditions and the trend of the validation variables. And the second step is the validation step itself, in which the main variables of comparison are the displacements, strains, and stresses in their three directions. The comparison of the variables uses the graphic behavior and the root mean squared error that quantifies the difference in results between the models.

There are significant differences between the geomechanical model and the commercial simulator ABAQUS® that do not allow for completely aligning these two models as the grid features.

Finally, the coupled model is validated by comparing the results with the numerical model with results obtained with a commercial simulator as CMG®, considering two cases: one-layer and multi-layer cases.

5.2.1 Elastic model

For an adequate process, the validation of the elastic model considers two well settings: one-layer set and multi-layer set, both considering a mechanical case coupled with fluid flow, under two different conditions, isotropic and anisotropic horizontal stress conditions. The comparison variables for validation are the displacements, strains, and stresses in three directions, $x, y,$ and z, i.e., under the FEM grid, and evaluating these variables at three different angles: 0º, 45º, and 90º.

One-layer set

The one-layer set consists of a 3D physical model in which the wellbore connects just one lateral layer that works as a reservoir layer and supports the regional stresses.

– Mechanical case coupled with fluid flow under isotropic horizontal stresses condition

A one-layer mechanical case coupled with fluid flow under isotropic horizontal stresses condition evaluates strain and stress behavior in terms of displacement, stress, and strain considering the coupled pressure effect by fluid flow in the porous media.

The validation of the elastic model for a one-layer mechanical case coupled with fluid flow under isotropic horizontal stresses condition is performed by comparing the results obtained with the numerical model with the results obtained with the ABAQUS® software using a field case. The reservoir features of the field case are summarized in Table 5 – 11.

Table 5 – 11. Field case for validation of the elastic model for a one-layer mechanical case coupled with fluid flow under isotropic horizontal stresses condition.

RESERVOIR CHARACTERISTICS	VALUE
Depth (ft)	1000
Reservoir height (ft)	20
Wellbore radius (in)	3
Reservoir radius (ft)	100
Reservoir pressure (psi)	500
Wellbore pressure (psi)	500
Vertical stress gradient (psi/ft)	1
Horizontal stress gradient (psi/ft)	1
Young modulus (psi)	1.0E06
Poisson ratio (fraction)	0.25

Figure 5 – 9 presents the validation results of the elastic model for a one-layer mechanical case coupled with fluid flow under isotropic horizontal stresses condition in terms of the displacements profiles in x, y, and z directions at three different angles: 0º, 45º and 90º, using the ABAQUS® software and the numerical model.

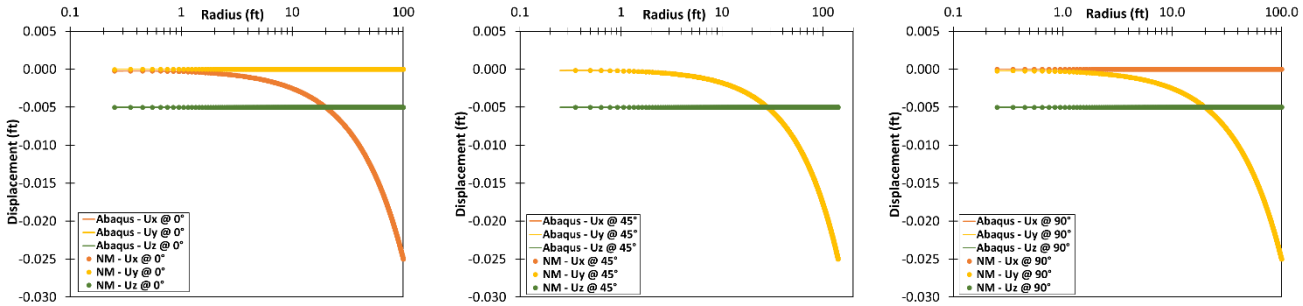

a. b. c.

Figure 5 – 9. Displacement profiles for each direction for the validation of the elastic model for a one-layer mechanical case coupled with fluid flow under isotropic horizontal stresses condition. a) Profiles at 0º. b) Profiles at 45º. c) Profiles at 90º.

Figure 5 – 10 presents the validation results of the elastic model for a one-layer mechanical case coupled with fluid flow under isotropic horizontal stresses condition in terms of the strain profiles in x, y, and z

directions at three different angles: 0º, 45º and 90º, using the ABAQUS® software and the numerical model.

Figure 5 – 11 presents the validation results of the elastic model for a one-layer mechanical case coupled with fluid flow under isotropic horizontal stresses condition in terms of the stress profiles in $x, y,$ and z directions at three different angles: 0º, 45º, and 90º, using the ABAQUS® software and the numerical model.

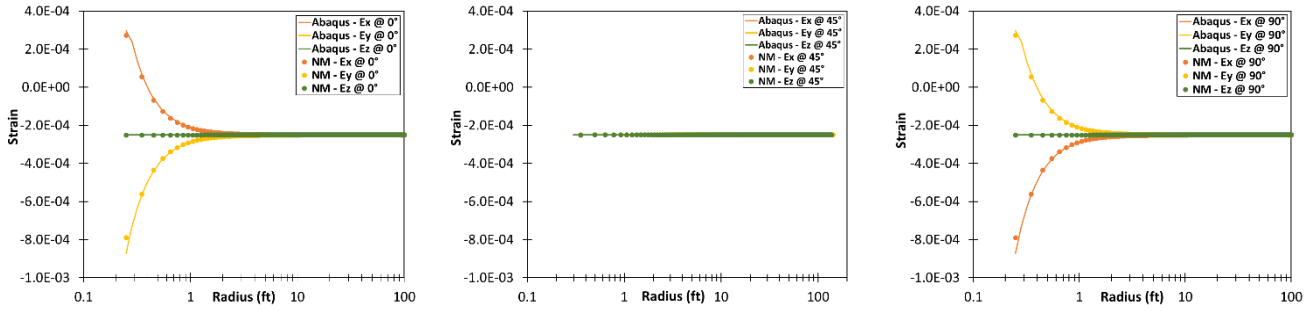

a. b. c.

Figure 5 – 10. Strain profiles for each direction for the validation of the elastic model for a one-layer mechanical case coupled with fluid flow under isotropic horizontal stresses condition. a) Profiles at 0º. b) Profiles at 45º. c) Profiles at 90º.

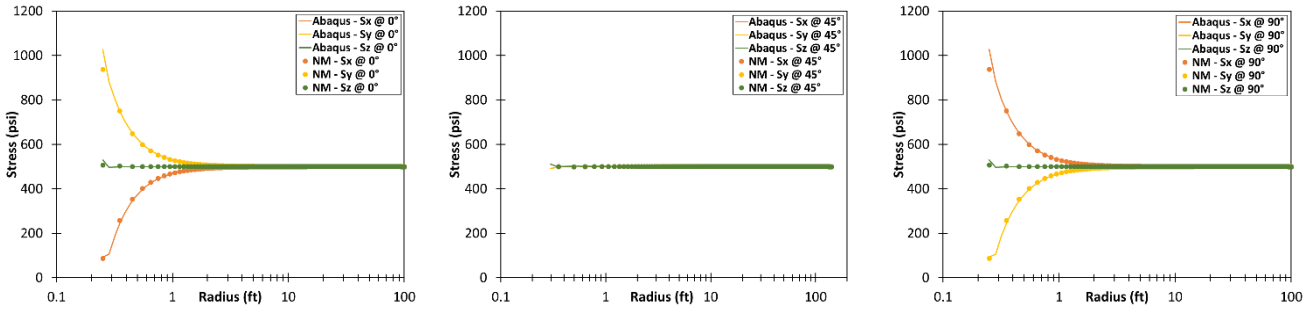

a. b. c.

Figure 5 – 11. Effective stress profiles for each direction for the validation of the elastic model for a one-layer mechanical case coupled with fluid flow under isotropic horizontal stresses condition. a) Profiles at 0º. b) Profiles at 45º. c) Profiles at 90º.

Table 5 – 12 presents the root mean squared error to quantify the differences in displacements, strains, and stresses between the results of the ABAQUS® simulator and the numerical model for the validation of the elastic model for a one-layer mechanical case coupled with fluid flow under isotropic horizontal stresses condition.

Table 5 – 12. Root mean squared error (RMSE) for displacements, strains, and stresses for the validation of the elastic model for a one-layer mechanical case coupled with fluid flow under isotropic horizontal stresses condition.

RMSE		Displacement (ft)	Strain	Stress (psi)
@ 0°	x	2.368E-06	1.019E-06	7.164E-01
	y	1.055E-07	8.531E-06	2.829E-00
	z	4.118E-06	2.074E-07	7.808E-01
@ 45°	x	1.825E-06	1.413E-07	1.923E-01
	y	1.747E-06	1.413E-07	1.923E-01
	z	4.368E-06	2.236E-07	3.696E-01
@ 90°	x	1.055E-07	2.631E-06	2.829E-00
	y	2.368E-06	1.019E-06	7.164E-01
	z	4.118E-06	2.218E-07	7.808E-01

Remark: The results of the elastic model for a one-layer mechanical case coupled with fluid flow under isotropic horizontal stresses condition in terms of displacements follow the expected trend and the root mean square errors for displacement are small enough, errors less than 4.368E-06 ft; in terms of strains also follow the expected trend and the root mean square errors for strains are small enough, errors less than 8.531E-06; and in terms of stresses also follow the expected trend and the root mean square errors for strains are small enough, errors less than 2.829 psi. The results in terms of strain and stress at the boundary conditions, internal and external, are adequate showing that these conditions are well imposed. In conclusion, the numerical model obtains adequate results in terms of displacements, strains, and stresses with a good approach.

– Mechanical case coupled with fluid flow under anisotropic horizontal stresses condition

A one-layer mechanical case coupled with fluid flow under anisotropic horizontal stresses condition evaluates strain and stress behavior in terms of displacement, stress, and strain considering the coupled pressure effect by fluid flow in the porous media. The validation of the elastic model for a one-layer mechanical case coupled with fluid flow under anisotropic horizontal stresses condition is performed by comparing the results obtained with the numerical model with the results obtained with the commercial simulator ABAQUS® using a field case. The reservoir features of the field case are summarized in Table 5 – 13.

Table 5 – 13. Field case for validation of the elastic model for a one-layer mechanical case coupled with fluid flow under anisotropic horizontal stresses condition.

RESERVOIR CHARACTERISTICS	VALUE
Depth (ft)	1000
Reservoir height (ft)	20
Wellbore radius (in)	3
Reservoir radius (ft)	100
Reservoir pressure (psi)	500
Wellbore pressure (psi)	500
Vertical stress gradient (psi/ft)	1.0
Maximum horizontal stress gradient (psi/ft)	1.0
Minimum horizontal stress gradient (psi/ft)	0.9
Young modulus (psi)	1.0E06
Poisson ratio (fraction)	0.25

Figure 5 – 12 presents the validation results of the elastic model for a one-layer mechanical case coupled with fluid flow under anisotropic horizontal stresses condition in terms of the displacements profiles in x, y, and z directions at three different angles: 0º, 45º and 90º, using the ABAQUS® simulator and the numerical model.

Figure 5 – 13 presents the validation results of the elastic model for a one-layer mechanical case coupled with fluid flow under anisotropic horizontal stresses condition in terms of the strain profiles in x, y, and z directions at three different angles: 0º, 45º and 90º, using the ABAQUS® simulator and the numerical model.

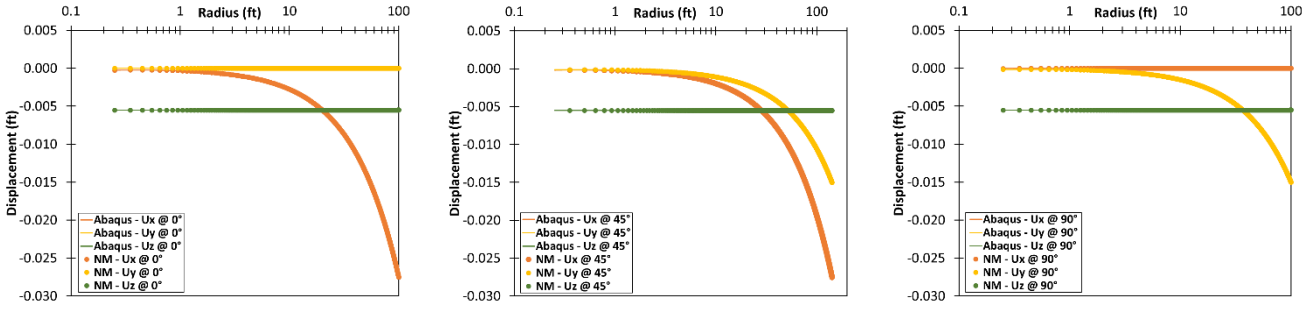

a. b. c.

Figure 5 – 12. Displacement profiles for each direction for the validation of the elastic model for a one-layer mechanical case coupled with fluid flow under anisotropic horizontal stresses condition. a) Profiles at 0º. b) Profiles at 45º. c) Profiles at 90º.

Table 5 – 14 presents the root mean squared error to quantify the differences in displacements, strains, and stresses between the results of the ABAQUS® software and the numerical model for the validation of the elastic model for a one-layer mechanical case coupled with fluid flow under anisotropic horizontal stresses condition.

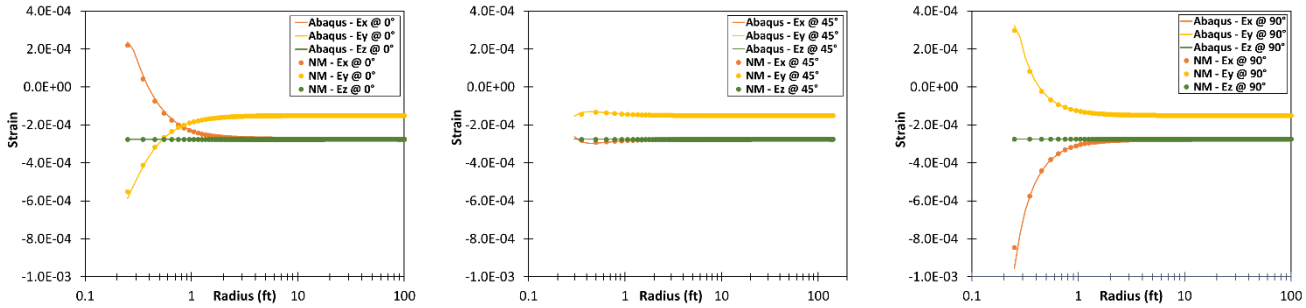

a. b. c.

Figure 5 – 13. Strain profiles for each direction for the validation of the elastic model for a one-layer mechanical case coupled with fluid flow under anisotropic horizontal stresses condition. a) Profiles at 0º. b) Profiles at 45º. c) Profiles at 90º.

Figure 5 – 14 presents the validation results of the elastic model for a one-layer mechanical case coupled with fluid flow under anisotropic horizontal stresses condition in terms of the stress profiles in x, y, and z directions at three different angles: 0º, 45º and 90º, using the ABAQUS® software and the numerical model.

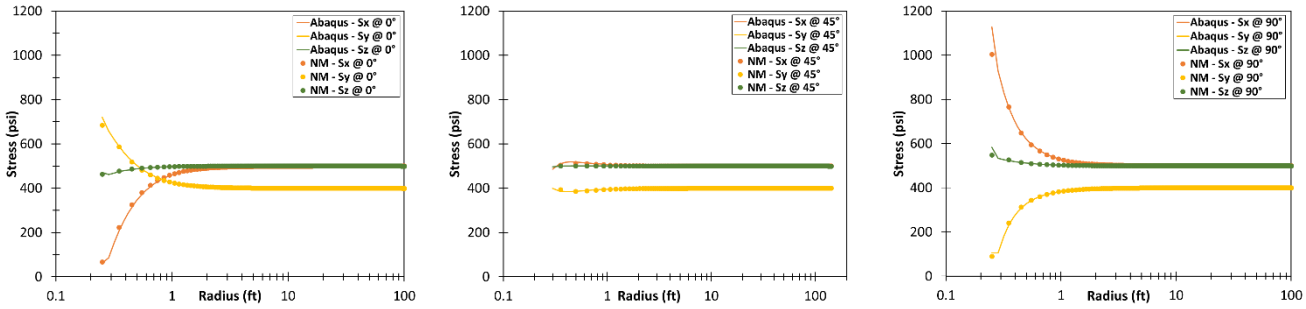

a. b. c.

Figure 5 – 14. Effective stress profiles for each direction for the validation of the elastic model for a one-layer mechanical case coupled with fluid flow under anisotropic horizontal stresses condition. a) Profiles at 0º. b) Profiles at 45º. c) Profiles at 90º.

Table 5 – 14. Root mean squared error (RMSE) for displacements, strains, and stresses for the validation of the elastic model for a one-layer mechanical case coupled with fluid flow under anisotropic horizontal stresses condition.

RMSE		Displacement (ft)	Strain	Stress (psi)
@ 0°	x	2.572E-06	1.009E-06	8.616E-01
	y	6.693E-08	1.249E-06	1.184E00
	z	4.149E-06	2.182E-07	3.673E-01
@ 45°	x	2.128E-06	1.744E-06	2.965E-01
	y	1.105E-06	3.010E-06	2.601E-01
	z	4.427E-06	1.083E-09	2.252E-01
@ 90°	x	1.252E-07	3.545E-06	3.926E00
	y	1.848E-06	9.055E-07	6.445E-01
	z	4.268E-06	2.249E-07	1.112E00

Remark: The results of the elastic model for a one-layer mechanical case coupled with fluid flow under anisotropic horizontal stresses condition in terms of displacements follow the expected trend and the root mean square errors for displacement are small enough, errors less than 4.427E-06 ft; in terms of strains also follow the expected trend and the root mean square errors for strains are small enough, errors less than 3.545E-06; and in terms of stresses also follow the expected trend and the root mean square errors for strains are small enough, errors less than .4 psi. The results in terms of strain and stress at the boundary conditions, internal and external, are adequate showing that these conditions are well imposed. In conclusion, the numerical model obtains results in terms of displacements, strains, and stresses with a good approach.

Multi-layer set

The multi-layer set consists of a 3D physical model, in which the wellbore connects four different lateral layers: the deepest one works as a bottom, the second one is a reservoir or producing layer, the third one is an overlayer and the last one is the top layer that works as a caprock. Each layer has different petrophysical and mechanical properties and all support the regional stresses.

– Mechanical case coupled with fluid flow under isotropic horizontal stresses condition

A multi-layer mechanical case coupled with fluid flow under isotropic horizontal stresses condition evaluates strain and stress behavior in terms of displacement, stress, and strain considering the coupled pressure effect by fluid flow in the porous media. The condition of isotropy of horizontal stresses is stated for all layers.

The validation of the elastic model for a multi-layer mechanical case coupled with fluid flow under isotropic horizontal stresses condition is performed by comparing the results obtained with the numerical model with the results obtained with the commercial simulator ABAQUS® using a field case. The reservoir features of the field case are summarized in Table 5 – 15.

Table 5 – 15. Field case for validation of the elastic model for a multi-layer-mechanical case coupled with fluid flow under isotropic horizontal stresses condition.

RESERVOIR CHARACTERISTICS	LAYER 1	LAYER 2	LAYER 3	LAYER 4
Depth (ft)	1000	1020	1040	1060
Reservoir height (ft)	20	20	20	20
Wellbore radius (in)	3	3	3	3
Reservoir radius (ft)	100	100	100	100
Reservoir pressure (psi)	500	500	500	500
Wellbore pressure (psi)	500	500	500	500
Vertical stress gradient (psi/ft)	1	1	1	1
Horizontal stress gradient (psi/ft)	1	1	1	1
Young modulus (psi)	1.2E06	1.0E06	1.0E06	1.0E06
Poisson ratio (fraction)	0.30	0.30	0.25	0.30

Figure 5 – 15 presents the validation results of the elastic model for a multi-layer mechanical case coupled with fluid flow under isotropic horizontal stresses condition in terms of the displacements profiles in $x, y,$ and z directions at three different angles: 0º, 45º and 90º, using the ABAQUS® software and the numerical model.

Figure 5 – 16 presents the validation results of the elastic model for the multi-layer – mechanical case coupled with fluid flow under isotropic horizontal stresses condition in terms of the strain profiles in $x, y,$ and z directions at three different angles: 0º, 45º and 90º, using the ABAQUS® software and the numerical model.

Figure 5 – 17 presents the validation results of the elastic model for the multi-layer – mechanical case coupled with fluid flow under isotropic horizontal stresses condition in terms of the stress profiles in $x, y,$ and z directions at three different angles: 0º, 45º and 90º, using the ABAQUS® software and the numerical model.

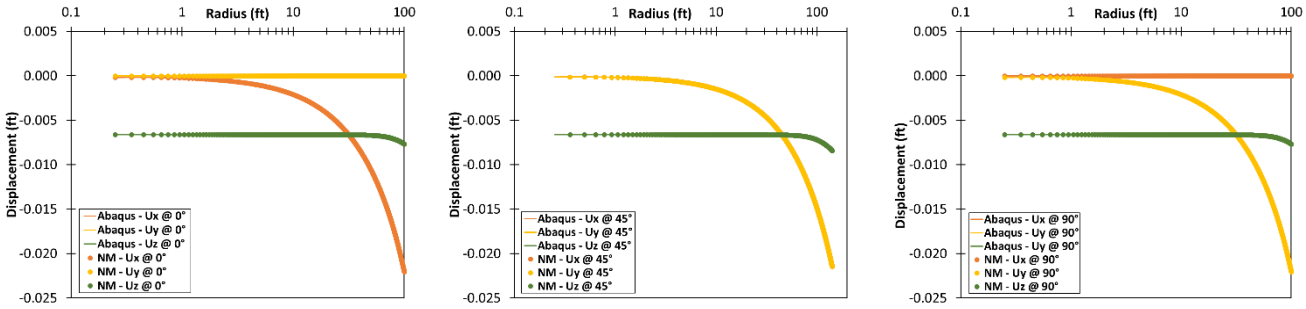

a. b. c.

Figure 5 – 15. Displacement profiles for each direction for the validation of the elastic model for a multi-layer mechanical case coupled with fluid flow under isotropic horizontal stresses condition. a) Profiles at 0º. b) Profiles at 45º. c) Profiles at 90º.

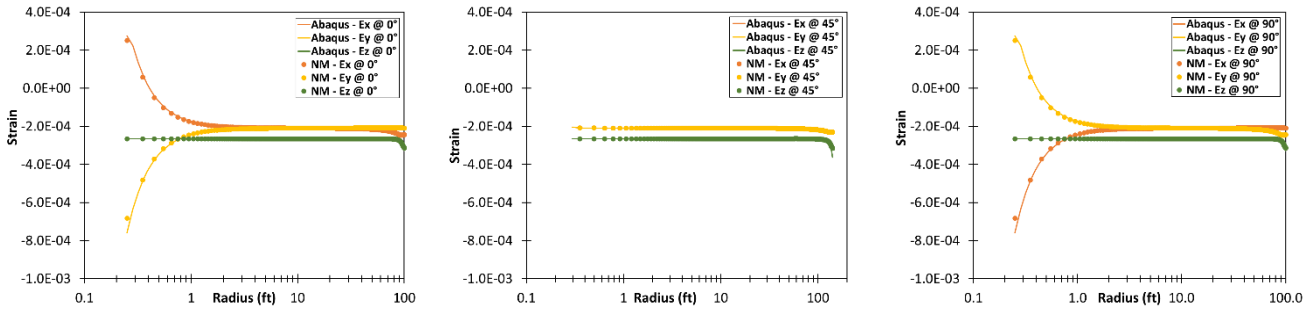

a. b. c.

Figure 5 – 16. Strain profiles for each direction for the validation of the elastic model for a multi-layer mechanical case coupled with fluid flow under isotropic horizontal stresses condition. a) Profiles at 0º. b) Profiles at 45º. c) Profiles at 90º.

Table 5 – 16 presents the root mean squared error to quantify the differences in displacements, strains, and stresses between the results of the ABAQUS® software and the numerical model for the validation of the elastic model for a multi-layer mechanical case coupled with fluid flow under isotropic horizontal stresses condition.

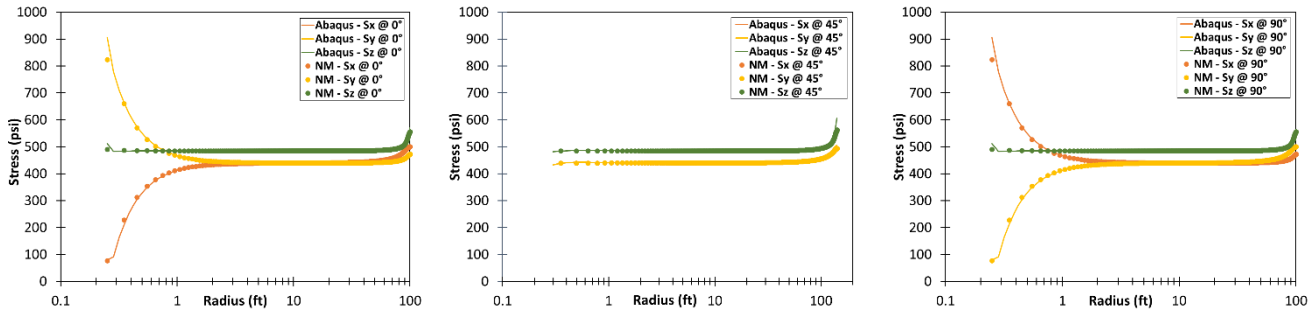

a. b. c.

Figure 5 – 17. Effective stress profiles for each direction for the validation of the elastic model for a multi-layer mechanical case coupled with fluid flow under isotropic horizontal stresses condition. a) Profiles at 0º. b) Profiles at 45º. c) Profiles at 90º.

Table 5 – 16. Root mean squared error (RMSE) for displacements, strains, and stresses for the validation of the elastic model for a multi-layer mechanical case coupled with fluid flow under isotropic horizontal stresses condition.

RMSE		Displacement (ft)	Strain	Stress (psi)
@ 0°	x	5.232E-06	1.434E-06	1.155E00
	y	3.691E-06	2.465E-06	2.642E00
	z	1.095E-05	1.293E-06	1.482E00
@ 45°	x	2.697E-05	2.176E-06	4.661E00
	y	3.031E-05	2.176E-06	4.661E00
	z	4.950E-05	6.747E-06	1.051E01
@ 90°	x	3.691E-06	2.465E-06	2.640E00
	y	5.231E-06	1.434E-06	1.157E00
	z	1.095E-05	1.293E-06	1.108E00

Remark: The results of the elastic model for the multi-layer – mechanic case coupled with fluid flow under isotropic horizontal stresses condition in terms of displacements follow the expected trend and the root mean square errors for displacement are small enough, errors less than 4.950E-05 ft; for strain are small enough, errors less than 6.747E-06 ft; for stress are small enough, errors less than 10.51 psi. The results in terms of strain and stress at the boundary conditions, internal and external, are adequate showing that these conditions are well imposed.

– Mechanical case coupled with fluid flow under anisotropic horizontal stresses condition

A multi-layer mechanical case coupled with fluid flow under anisotropic horizontal stresses condition evaluates strain and stress behavior in terms of displacement, stress, and strain considering the coupled pressure effect by fluid flow in the porous media. The condition of anisotropy of horizontal stresses is stated just for the production layer, and the other layers are stated under the isotropic horizontal stresses condition.

The validation of the elastic model for a multi-layer mechanical case coupled with fluid flow under anisotropic horizontal stresses condition is performed by comparing the results obtained with the numerical model with the results obtained with the commercial simulator ABAQUS® using a field case. The reservoir features of the field case are summarized in Table 5 – 17.

Figure 5 – 18 presents the validation results of the elastic model for a multi-layer mechanical case coupled with fluid flow under anisotropic horizontal stresses condition in terms of the displacements profiles in $x, y,$ and z directions at three different angles: 0º, 45º and 90º, using the ABAQUS® software and the numerical model.

Figure 5 – 19 presents the validation results of the elastic model for a multi-layer mechanical case coupled with fluid flow under anisotropic horizontal stresses condition in terms of the strain profiles in $x, y,$ and z directions at three different angles: 0º, 45º and 90º, using the ABAQUS® software and the numerical model.

Figure 5 – 20 presents the validation results of the elastic model for the multi-layer – mechanical case coupled with fluid flow under anisotropic horizontal stresses condition in terms of the stress profiles in

x, y, and z directions at three different angles: 0º, 45º and 90º, using the ABAQUS® software and the numerical model.

Table 5 – 17. Field case for validation of the elastic model for the multi-layer mechanical case coupled with fluid flow under anisotropic horizontal stresses condition.

VARIABLE	LAYER 1	LAYER 2	LAYER 3	LAYER 4
Depth (ft)	1000	1020	1040	1060
Reservoir height (ft)	20	20	20	20
Wellbore radius (in)	3	3	3	3
Reservoir radius (ft)	100	100	100	100
Reservoir pressure (psi)	500	500	500	500
Wellbore pressure (psi)	500	500	500	500
Vertical stress gradient (psi/ft)	1.0	1.0	1.0	1.0
Maximum horizontal stress gradient (psi/ft)	1.0	1.0	1.0	1.0
Minimum horizontal stress gradient (psi/ft)	1.0	1.0	0.9	1.0
Young modulus (psi)	1.2E06	1.0E06	1.0E06	1.0E06
Poisson ratio (fraction)	0.30	0.30	0.25	0.30

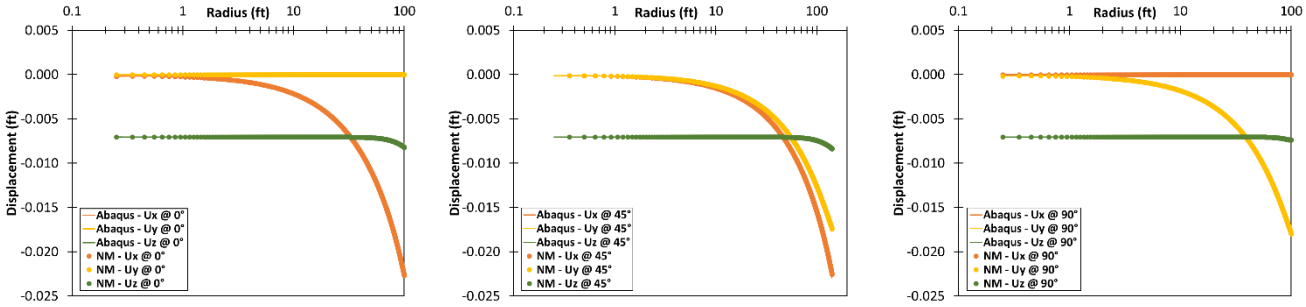

a. b. c.

Figure 5 – 18. Displacement profiles for each direction for the validation of the elastic model for a multi-layer mechanical case coupled with fluid flow under anisotropic horizontal stresses condition. a) Profiles at 0º. b) Profiles at 45º. c) Profiles at 90º.

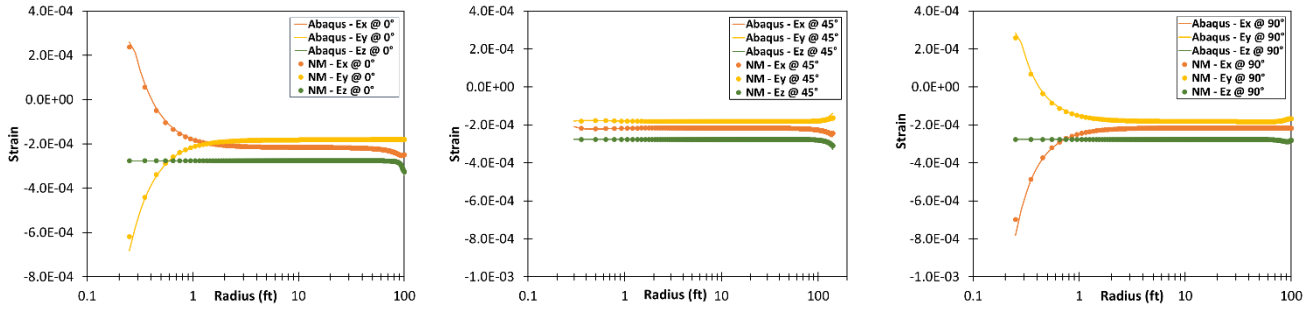

a. b. c.

Figure 5 – 19. Strain profiles for each direction for the validation of the elastic model for a multi-layer mechanical case coupled with fluid flow under anisotropic horizontal stresses condition. a) Profiles at 0º. b) Profiles at 45º. c) Profiles at 90º.

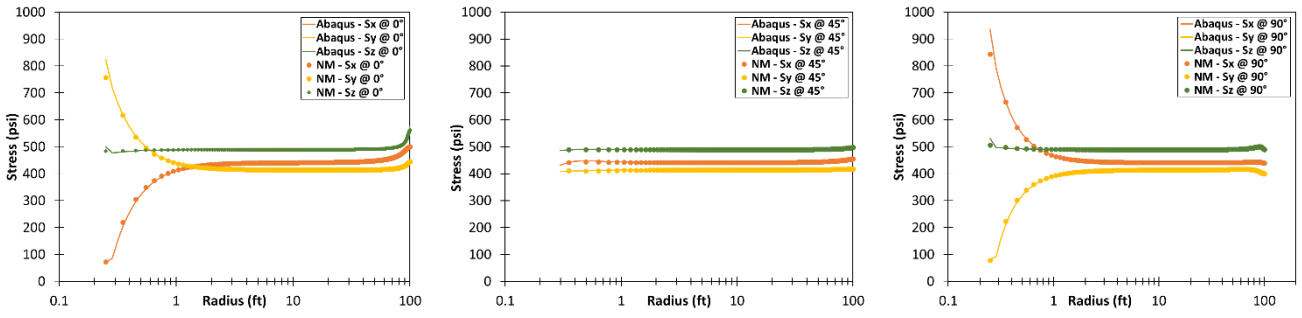

a. b. c.

Figure 5 – 20. Effective stress profiles for each direction for the validation of the elastic model for the multi-layer – mechanical case coupled with fluid flow under anisotropic horizontal stresses condition. a) Profiles at 0º. b) Profiles at 45º. c) Profiles at 90º.

Table 5 – 18 presents the root mean squared error to quantify the differences in displacements, strains, and stresses between the results of the ABAQUS® software and the numerical model for the validation of the elastic model for the multi-layer – mechanical case coupled with fluid flow under anisotropic horizontal stresses condition.

Table 5 – 18. Root mean squared error (RMSE) for displacements, strains, and stresses for the validation of the elastic model for a multi-layer mechanical case coupled with fluid flow under anisotropic horizontal stresses condition.

RMSE		Displacement (ft)	Strain	Stress (psi)
@ 0°	x	5.971E-06	1.415E-06	1.142E00
	y	1.312E-06	2.084E-06	2.192E00
	z	8.656E-06	1.276E-06	1.392E00
@ 45°	x	8.227E-05	6.069E-06	6.436E00
	y	6.790E-05	5.964E-06	3.283E00
	z	3.086E-05	3.923E-06	4.666E00
@ 90°	x	4.019E-06	2.706E-06	2.908E00
	y	3.431E-06	1.084E-06	7.045E-01
	z	7.215E-06	5.064E-07	8.731E-01

Remark: The results of the elastic model for a multi-layer mechanic case coupled with fluid flow under anisotropic horizontal stresses condition in terms of displacements follow the expected trend and the root mean square errors for displacement are small enough, errors less than 8.227E-05 ft; for strain are small enough, errors less than 6.069E-06 ft; for stress are small enough, errors less than 6.5 psi. The results in terms of strain and stress at the boundary conditions, internal and external, are adequate showing that these conditions are well imposed.

5.2.2 Elastoplastic model

For an adequate process, the validation of the elastoplastic model considers the main case: mechanical case coupled with fluid flow under two different conditions: isotropic and anisotropic horizontal stress conditions. The comparison variables for validation are the displacements, strains, and stresses in three directions, $x, y,$ and z, i.e., under the FEM grid, and evaluating these variables at three different angles: 0º, 45º, and 90º.

One-layer set

Similar to the elastic model, the one-layer set consists of a 3D physical model in which the wellbore connects just one lateral layer that works as a reservoir layer and supports the regional stresses.

– Mechanical case coupled with fluid flow under isotropic horizontal stresses condition

The one-layer-mechanical case coupled with fluid flow under isotropic horizontal stresses condition evaluates strain and stress behavior in terms of displacement, stress, and strain including plasticity, and considering the coupled pressure effect by fluid flow in the porous media.

The validation of the elastoplastic model for the one-layer – mechanical case coupled with fluid flow under isotropic horizontal stresses condition is performed by comparing the results obtained with the numerical model with the results obtained with the commercial simulator ABAQUS® using a field case. The reservoir features of the field case are summarized in Table 5 – 19.

Table 5 – 19. Field case for validation of the elastoplastic model for the one-layer – mechanical case coupled with fluid flow under isotropic horizontal stresses condition.

RESERVOIR CHARACTERISTICS	VALUE
Depth (ft)	1000
Reservoir height (ft)	20
Wellbore radius (in)	3
Reservoir radius (ft)	100
Reservoir pressure (psi)	500
Wellbore pressure (psi)	500
Vertical stress gradient (psi/ft)	1
Horizontal stress gradient (psi/ft)	1
Young modulus (psi)	1.0E06
Poisson ratio (fraction)	0.25
Cohesion (psi)	100
Friction angle (°)	15
Dilation angle (°)	15

Figure 5 – 21 presents the validation results of the elastoplastic model for the one-layer – mechanical case coupled with fluid flow under isotropic horizontal stresses condition in terms of the displacements profiles in $x, y,$ and z directions at three different angles: 0º, 45º and 90º, using the ABAQUS® software and the numerical model.

Figure 5 – 22 presents the validation results of the elastoplastic model for the one-layer – mechanical case coupled with fluid flow under isotropic horizontal stresses condition in terms of the elastic strain profiles in $x, y,$ and z directions at three different angles: 0º, 45º and 90º, using the ABAQUS® software and the numerical model.

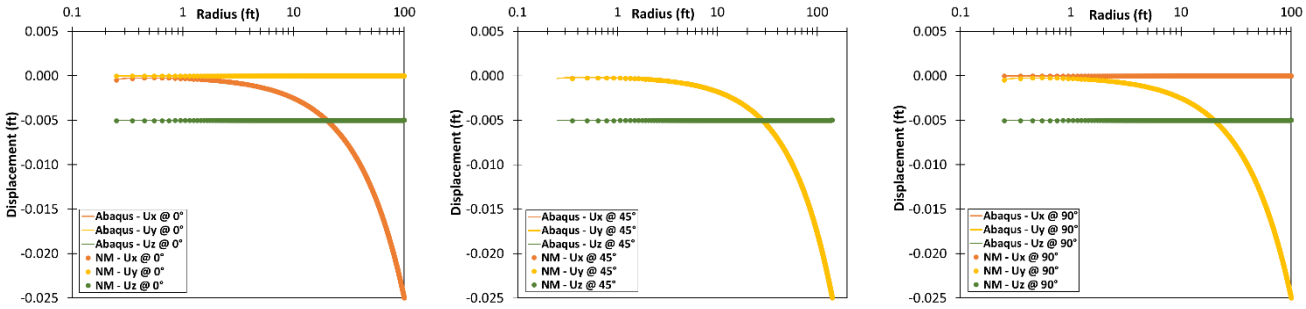

a. b. c.

Figure 5 – 21. Displacement profiles for each direction for the validation of the elastoplastic model for the one-layer – mechanical case coupled with fluid flow under isotropic horizontal stresses condition. a) Profiles at 0º. b) Profiles at 45º. c) Profiles at 90º.

Figure 5 – 23 presents the validation results of the elastoplastic model for the one-layer – mechanical case coupled with fluid flow under isotropic horizontal stresses condition in terms of the stress profiles in $x, y,$ and z directions at three different angles: 0º, 45º and 90º, using the ABAQUS® software and the numerical model.

Figure 5 – 24 presents the validation results of the elastoplastic model for the one-layer – mechanical case coupled with fluid flow under isotropic horizontal stresses condition in terms of the plastic strain profiles in $x, y,$ and z directions at three different angles: 0º, 45º and 90º, using the ABAQUS® software and the numerical model.

Table 5 – 20 presents the root mean squared error to quantify the differences in displacements, strains, and stresses between the results of the ABAQUS® software and the numerical model for the validation of the elastoplastic model for the one-layer – mechanical case coupled with fluid flow under isotropic horizontal stresses condition.

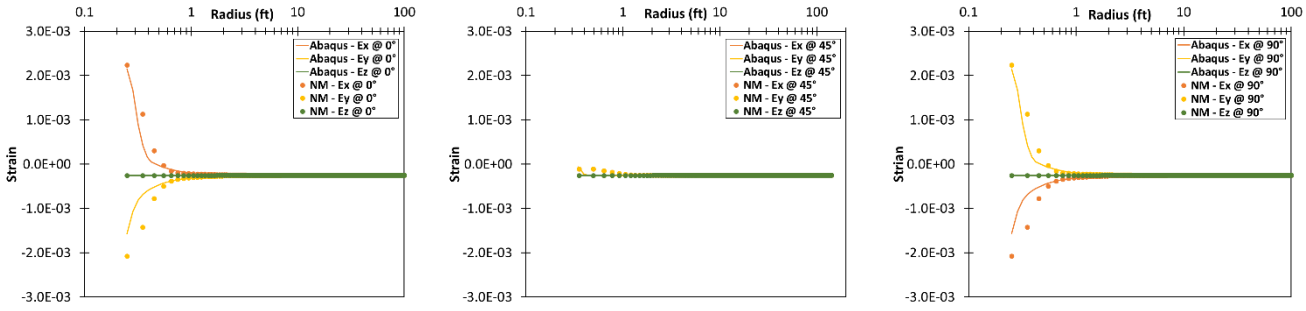

a. b. c.

Figure 5 – 22. Elastic strain profiles for each direction for the validation of the elastoplastic model for the one-layer – mechanical case coupled with fluid flow under isotropic horizontal stresses condition. a) Profiles at 0º. b) Profiles at 45º. c) Profiles at 90º.

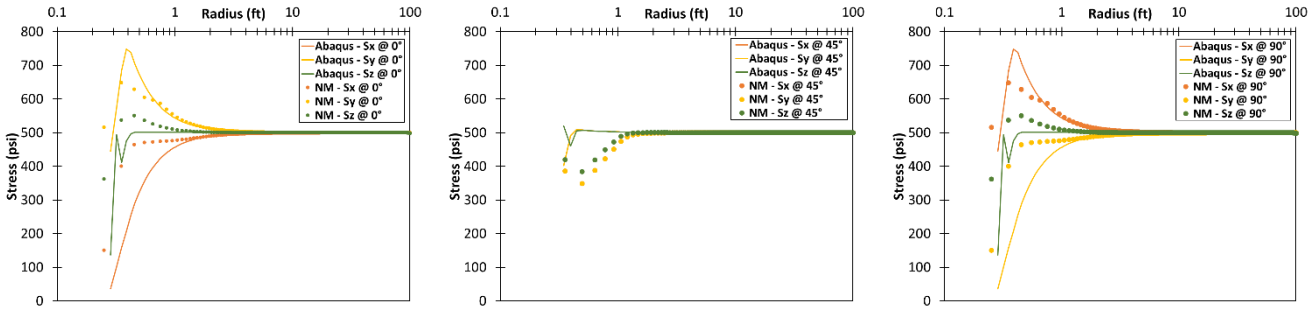

a. b. c.

Figure 5 – 23. Effective stress profiles for each direction for the validation of the elastoplastic model for the one-layer – mechanical case coupled with fluid flow under isotropic horizontal stresses condition. a) Profiles at 0º. b) Profiles at 45º. c) Profiles at 90º.

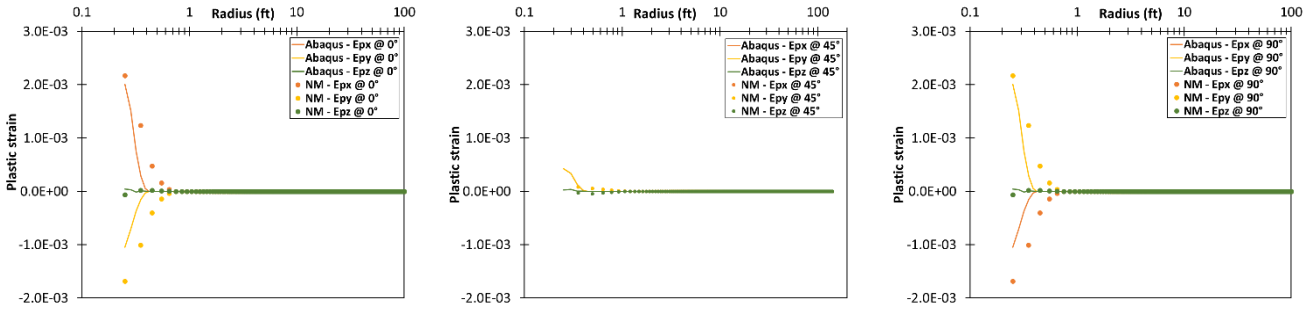

a. b. c.

Figure 5 – 24. Plastic strain profiles for each direction for the validation of the elastoplastic model for the one-layer – mechanical case coupled with fluid flow under isotropic horizontal stresses condition. a) Profiles at 0º. b) Profiles at 45º. c) Profiles at 90º.

Table 5 – 20. Root mean squared error (RMSE) for displacements, elastic strains, and stresses for the validation of the elastoplastic model for the one-layer – mechanical case coupled with fluid flow under isotropic horizontal stresses condition.

RMSE		Displacement (ft)	Elastic strain	Stress (psi)	Plastic strain
@ 0°	***x***	4.480E-06	2.368E-05	1.088E01	3.349E-05
	y	2.566E-07	2.947E-05	6.283E00	3.607E-05
	z	4.723E-06	3.661E-07	6.440E00	3.459E-06
@ 45°	***x***	5.435E-06	6.245E-06	7.074E00	2.431E-06
	y	5.474E-06	6.245E-06	7.074E00	2.431E-06
	z	4.909E-06	4.238E-07	5.876E00	2.239E-06
@ 90°	***x***	2.566E-07	2.947E-05	6.283E00	3.607E-05
	y	4.480E-06	2.368E-05	1.088E01	3.349E-05
	z	4.723E-06	3.661E-07	6.440E00	3.459E-06

Remark: The results of the elastoplastic model for the one-layer – mechanic case coupled with fluid flow under isotropic horizontal stresses condition in terms of displacements follow the expected trend and the root mean square errors for displacement are small enough, errors less than 5.474E-06 ft; in terms of elastic strains also follow the expected trend and the root mean square errors for strains are small enough, errors less than 2.947E-06; in terms of stresses also follow the expected trend and the root mean square errors for strains are small enough, errors less than 11 psi; and in terms of plastic strains also follow the expected trend and the root mean square errors for strains are small enough, errors less than

3.607E-06. The results in terms of strain and stress at the boundary conditions, internal and external, are adequate showing that these conditions are well imposed. In conclusion, although the error grew in magnitude for deformation and stress compared to the elastic case, the numerical model still obtains results in terms of displacements, strains, and stresses with a good approach, even for plasticity.

– Mechanical case coupled with fluid flow under anisotropic horizontal stresses condition

The one-layer-mechanical case coupled with fluid flow under anisotropic horizontal stresses condition evaluates strain and stress behavior in terms of displacement, stress, and strain including plasticity, and considering the coupled pressure effect by fluid flow in the porous media.

The validation of the elastoplastic model for the one-layer – mechanical case coupled with fluid flow under anisotropic horizontal stresses condition is performed by comparing the results obtained with the numerical model with the results obtained with the commercial simulator ABAQUS® using a field case. The reservoir features of the field case are summarized in Table 5 – 21.

Figure 5 – 25 presents the validation results of the elastoplastic model for the one-layer – mechanical case coupled with fluid flow under anisotropic horizontal stresses condition in terms of the displacements profiles in $x, y,$ and z directions at three different angles: 0º, 45º, and 90º, using the ABAQUS® software and the numerical model.

Figure 5 – 26 presents the validation results of the elastoplastic model for the one-layer – mechanical case coupled with fluid flow under anisotropic horizontal stresses condition in terms of the elastic strain profiles in $x, y,$ and z directions at three different angles: 0º, 45º and 90º, using the ABAQUS® software and the numerical model.

Table 5 – 21. Field case for validation of the elastoplastic model for the one-layer – mechanical case coupled with fluid flow under anisotropic horizontal stresses condition.

RESERVOIR CHARACTERISTICS	VALUE
Depth (ft)	1000
Reservoir height (ft)	20
Wellbore radius (in)	3
Reservoir radius (ft)	100
Reservoir pressure (psi)	500
Wellbore pressure (psi)	500
Vertical stress gradient (psi/ft)	1.0
Maximum horizontal stress gradient (psi/ft)	1.0
Minimum horizontal stress gradient (psi/ft)	0.9
Young modulus (psi)	1.0E06
Poisson ratio (fraction)	0.25
Cohesion (psi)	100
Friction angle (°)	15
Dilation angle (°)	15

Figure 5 – 27 presents the validation results of the elastoplastic model for the one-layer – mechanical case coupled with fluid flow under anisotropic horizontal stresses condition in terms of the stress profiles

in $x, y,$ and z directions at three different angles: 0º, 45º and 90º, using the ABAQUS® software and the numerical model.

Figure 5 – 28 presents the validation results of the elastoplastic model for the one-layer – mechanical case coupled with fluid flow under anisotropic horizontal stresses condition in terms of the plastic strain profiles in $x, y,$ and z directions at three different angles: 0º, 45º and 90º, using the ABAQUS® software and the numerical model.

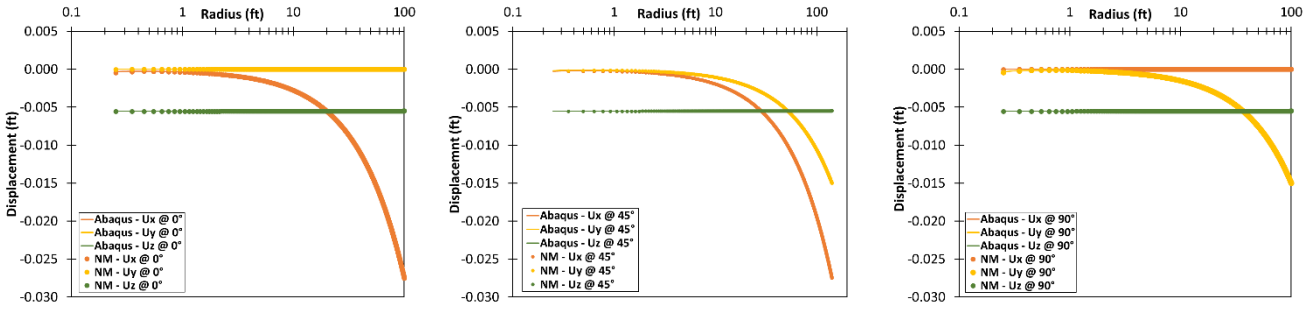

a. b. c.

Figure 5 – 25. Displacement profiles for each direction for the validation of the elastoplastic model for the one-layer – mechanical case coupled with fluid flow under anisotropic horizontal stresses condition. a) Profiles at 0º. b) Profiles at 45º. c) Profiles at 90º.

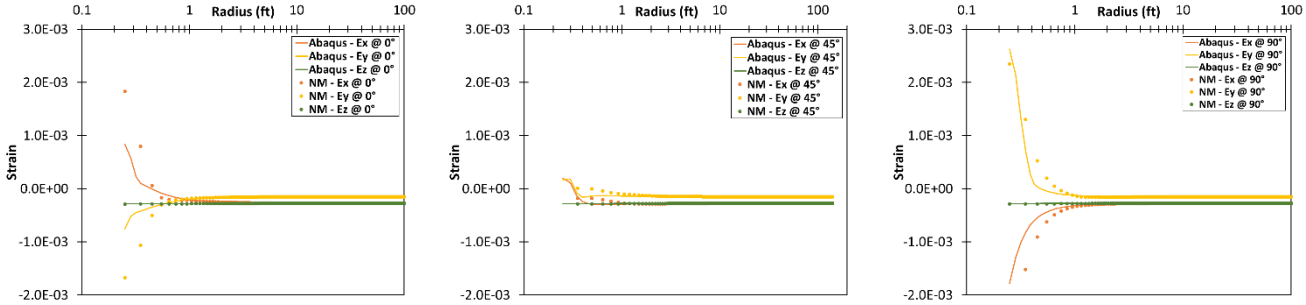

a. b. c.

Figure 5 – 26. Elastic strain profiles for each direction for the validation of the elastoplastic model for the one-layer-mechanical case coupled with fluid flow under anisotropic horizontal stresses condition. a) Profiles at 0º. b) Profiles at 45º. c) Profiles at 90º.

Table 5 – 22 presents the root mean squared error to quantify the differences in displacements, strains, and stresses between the results of the ABAQUS® software and the numerical model for the validation of the elastoplastic model for the one-layer – mechanical case coupled with fluid flow under anisotropic horizontal stresses condition.

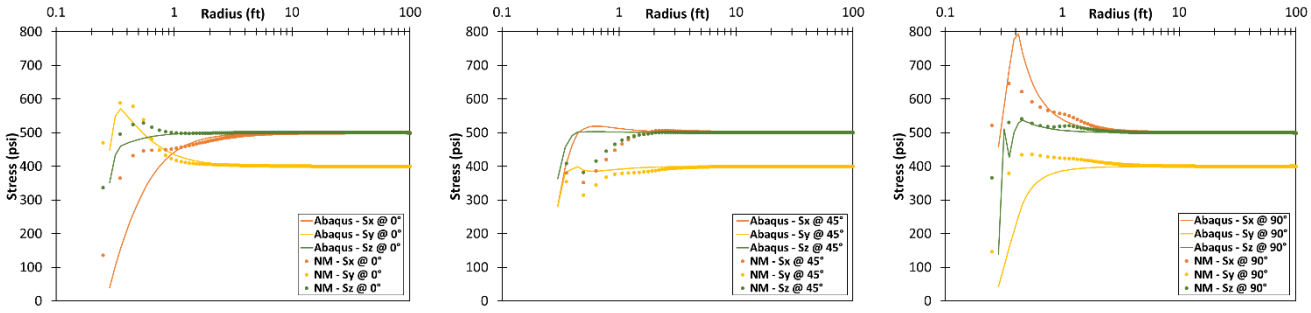

a. b. c.

Figure 5 – 27. Effective stress profiles for each direction for the validation of the elastoplastic model for the one-layer- mechanical case coupled with fluid flow under anisotropic horizontal stresses condition. a) Profiles at 0º. b) Profiles at 45º. c) Profiles at 90º.

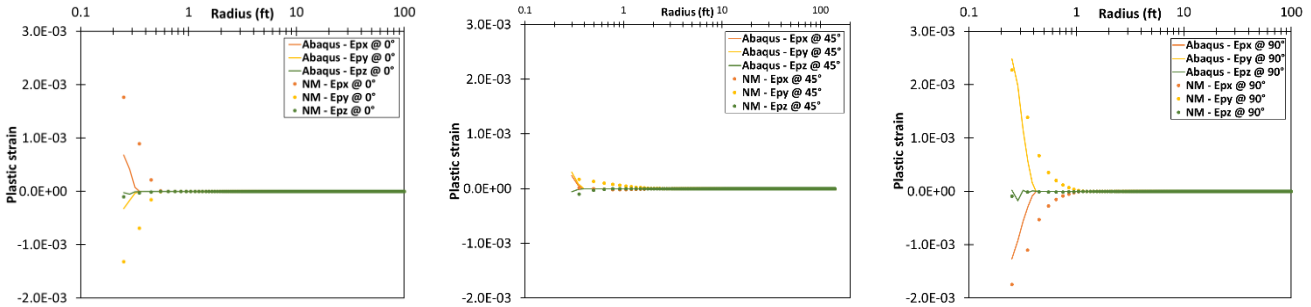

a. b. c.

Figure 5 – 28. Plastic strain profiles for each direction for the validation of the elastoplastic model for the one-layer-mechanical case coupled with fluid flow under anisotropic horizontal stresses condition. a) Profiles at 0º. b) Profiles at 45º. c) Profiles at 90º.

Table 5 – 22. Root mean squared error (RMSE) for displacements, strains, and stresses for the validation of the elastoplastic model for the one-layer – mechanical case coupled with fluid flow under anisotropic horizontal stresses condition.

RMSE		Displacement (ft)	Elastic strain	Stress (psi)	Plastic strain
@ 0°	***x***	8.979E-06	3.856E-05	1.018E01	3.760E-05
	y	2.195E-07	3.589E-05	3.619E00	3.584E-05
	z	7.161E-06	8.075E-07	3.701E00	2.602E-06
@ 45°	***x***	7.493E-06	5.144E-06	7.817E00	1.765E-06
	y	5.213E-06	6.990E-06	3.204E00	7.107E-06
	z	6.242E-06	7.412E-07	5.538E00	3.537E-06
@ 90°	***x***	2.509E-07	2.813E-05	7.147E00	3.536E-05
	y	9.014E-06	2.667E-05	1.027E01	3.602E-05
	z	5.534E-06	6.772E-07	5.684E00	3.592E-06

Remark: The results of the elastoplastic model for the one-layer-mechanical case coupled with fluid flow under isotropic horizontal stresses condition in terms of displacements follow the expected trend and the root mean square errors for displacement are small enough, that errors less than 9.014E-06 ft; in terms of elastic strains also follow the expected trend and the root mean square errors for strains are small enough, errors less than 3.856E-05; in terms of stresses also follow the expected trend and the root mean square errors for strains are small enough, errors less than 11 psi; and in terms of plastic strains also follow the expected trend and the root mean square errors for strains are small enough, errors less than

3.760E-06; the results in terms of strain and stress at the boundary conditions, internal and external, are adequate showing that these conditions are well imposed. In conclusion, although the error grew in magnitude for deformation and stress with respect to the elastic case, the numerical model still obtains results in terms of displacements, strains, and stresses with a good approach, even for plasticity.

Multi-layer set

Similar to the elastic model, the multi-layer set consists of a 3D physical model, in which the wellbore connects four different lateral layers: the deepest one that works as a bottom, the second one is a reservoir or producing layer, and the third one is an overlayer and the last one is the top layer that works as a caprock. Each layer has different petrophysical and mechanical properties and all support the regional stresses.

– Mechanical case coupled with fluid flow under isotropic horizontal stresses condition

A multi-layer mechanical case coupled with fluid flow under isotropic horizontal stresses condition evaluates strain and stress behavior in terms of displacement, stress, and strain including plasticity, considering the coupled pressure effect by fluid flow in the porous media. The condition of isotropy of horizontal stresses is stated for all layers.

The validation of the elastoplastic model for a multi-layer mechanical case coupled with fluid flow under isotropic horizontal stresses condition is performed by comparing the results obtained with the numerical model with the results obtained with the commercial simulator ABAQUS® using a field case. The reservoir features of the field case are summarized in Table 5 – 23.

Table 5 – 23. Field case for validation of the elastoplastic model for a multi-layer-mechanical case coupled with fluid flow under isotropic horizontal stresses condition.

RESERVOIR CHARACTERISTICS	LAYER 1	LAYER 2	LAYER 3	LAYER 4
Depth (ft)	1000	1020	1040	1060
Reservoir height (ft)	20	20	20	20
Wellbore radius (in)	3	3	3	3
Reservoir radius (ft)	100	100	100	100
Reservoir pressure (psi)	500	500	500	500
Wellbore pressure (psi)	500	500	500	500
Vertical stress gradient (psi/ft)	1	1	1	1
Horizontal stress gradient (psi/ft)	1	1	1	1
Young modulus (psi)	1.2E06	1.0E06	1.0E06	1.0E06
Poisson ratio (fraction)	0.30	0.30	0.25	0.30
Cohesion (psi)	1000	1000	100	1000
Friction angle (°)	15	15	15	15
Dilation angle (°)	15	15	15	15

Figure 5 – 29 presents the validation results of the elastoplastic model for a multi-layer mechanical case coupled with fluid flow under isotropic horizontal stresses condition in terms of the displacements profiles in $x, y,$ and z directions at three different angles: 0º, 45º and 90º, using the ABAQUS® software and the numerical model.

Figure 5 – 30 presents the validation results of the elastoplastic model for the multi-layer mechanical case coupled with fluid flow under isotropic horizontal stresses condition in terms of the elastic strain profiles in x, y, and z directions at three different angles: 0º, 45º and 90º, using the ABAQUS® software and the numerical model.

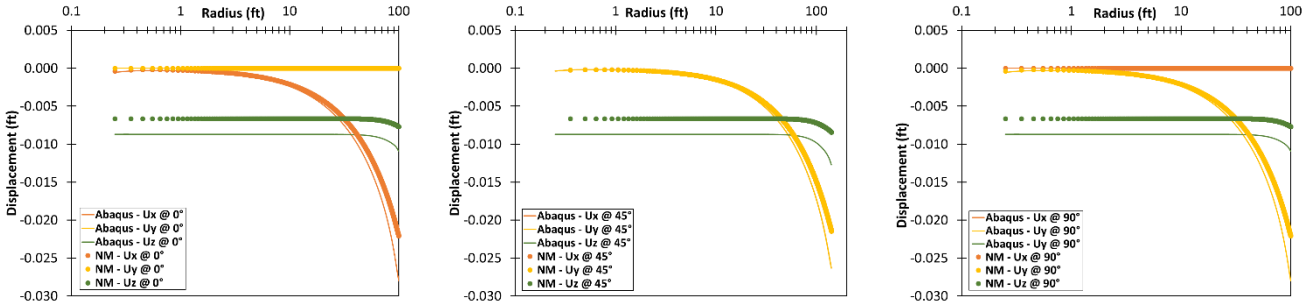

a. b. c.

Figure 5 – 29. Displacement profiles for each direction for the validation of the elastoplastic model for a multi-layer mechanical case coupled with fluid flow under isotropic horizontal stresses condition. a) Profiles at 0º. b) Profiles at 45º. c) Profiles at 90º.

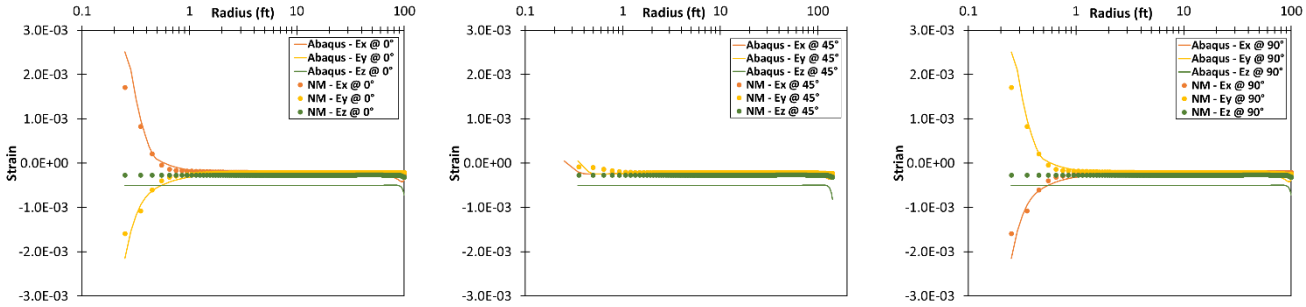

a. b. c.

Figure 5 – 30. Elastic strain profiles for each direction for the validation of the elastoplastic model for a multi-layer mechanical case coupled with fluid flow under isotropic horizontal stresses condition. a) Profiles at 0º. b) Profiles at 45º. c) Profiles at 90º.

Figure 5 – 31 presents the validation results of the elastoplastic model for the multi-layer mechanical case coupled with fluid flow under isotropic horizontal stresses condition in terms of the stress profiles in x, y, and z directions at three different angles: 0º, 45º and 90º, using the ABAQUS® software and the numerical model.

Figure 5 – 32 presents the validation results of the elastoplastic model for the multi-layer mechanical case coupled with fluid flow under isotropic horizontal stresses condition in terms of the plastic strain profiles in x, y, and z directions at three different angles: 0º, 45º and 90º, using the ABAQUS® software and the numerical model.

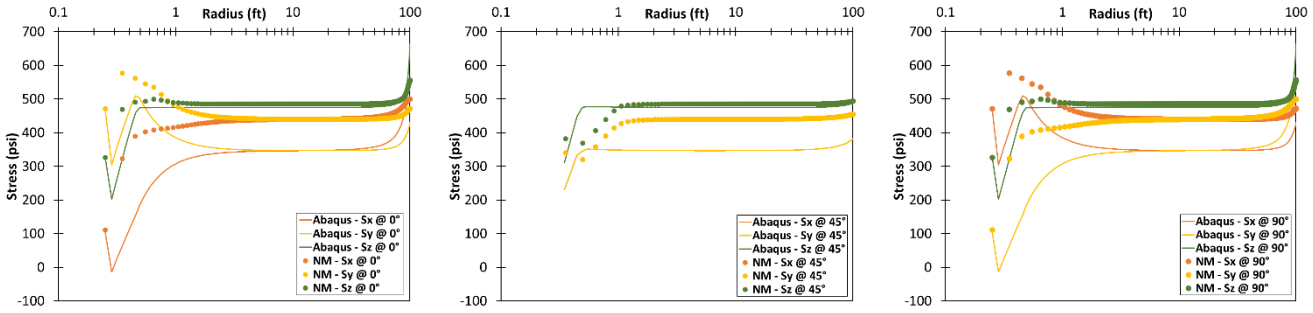

a. b. c.

Figure 5 – 31. Effective stress profiles for each direction for the validation of the elastoplastic model for a multi-layer mechanical case coupled with fluid flow under isotropic horizontal stresses condition. a) Profiles at 0º. b) Profiles at 45º. c) Profiles at 90º.

Table 5 – 24 presents the root mean squared error to quantify the differences in displacements, strains, stresses, and plastic strains between the results of the ABAQUS® software and the numerical model for the validation of the elastoplastic model for a multi-layer mechanical case coupled with fluid flow under isotropic horizontal stresses condition.

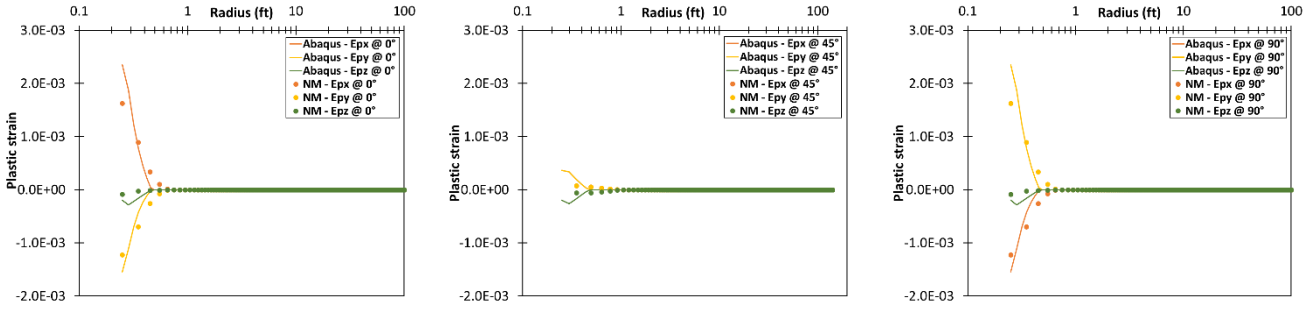

a. b. c.

Figure 5 – 32. Plastic strain profiles for each direction for the validation of the elastoplastic model for the one-layer-mechanical case coupled with fluid flow under isotropic horizontal stresses condition. a) Profiles at 0º. b) Profiles at 45º. c) Profiles at 90º.

Table 5 – 24. Root mean squared error (RMSE) for displacements, elastic strains, stresses, and plastic strains for the validation of the elastoplastic model for a multi-layer mechanical case coupled with fluid flow under isotropic horizontal stresses condition.

RMSE		Displacement (ft)	Elastic strain	Stress (psi)	Plastic strain
@ 0°	***x***	2.049E-03	7.784E-05	8.120E01	0.000E-00
	y	3.696E-06	3.243E-05	8.840E01	1.050E-04
	z	2.292E-03	2.404E-04	1.737E01	0.000E-00
@ 45°	***x***	2.151E-03	6.161E-05	7.857E01	4.255E-06
	y	2.153E-03	6.161E-05	7.857E01	4.255E-06
	z	2.528E-03	2.451E-04	3.051E01	4.234E-06
@ 90°	***x***	1.479E-02	3.243E-05	8.840E01	1.497E-05
	y	1.242E-02	7.784E-05	8.120E01	2.496E-05
	z	2.292E-03	2.404E-07	1.737E01	5.738E-06

Remark: The results of the elastoplastic model for the multi-layer-mechanical case coupled with fluid flow under isotropic horizontal stresses condition in terms of displacements follow the expected trend and the root mean square errors for displacement are small enough, errors less than 1.479E-02 ft; for elastic strain are small enough, errors less than 2.451E-04 ft, however; for stresses, the differences are higher with root mean square errors less than 88 psi; and in terms of plastic strains also follow the expected trend and the root mean square errors for strains are small enough, errors less than 3.760E-06. The higher differences in stress can be explain by the differences in displacements and elastic strains in the z-direction. The results in terms of strain and stress at the boundary conditions, internal and external, are adequate showing that these conditions are well imposed. In conclusion, although the error grew in magnitude for deformation and stress with respect to the elastic case, the numerical model still obtains results in terms of displacements and strains with a good approach, even for plasticity, but the stresses have high differences.

– Mechanical case coupled with fluid flow under anisotropic horizontal stresses condition

A multi-layer mechanical case coupled with fluid flow under anisotropic horizontal stresses condition evaluates strain and stress behavior in terms of displacement, stress, and strain including plasticity, considering the coupled pressure effect by fluid flow in the porous media. The condition of anisotropy of horizontal stresses is stated just for the production layer, and the other layers are stated under the isotropic horizontal stresses condition.

The validation of the elastoplastic model for a multi-layer mechanical case coupled with fluid flow under anisotropic horizontal stresses condition is performed by comparing the results obtained with the numerical model with the results obtained with the commercial simulator ABAQUS® using a field case. The reservoir features of the field case are summarized in Table 5 – 25.

Table 5 – 25. Field case for validation of the elastoplastic model for the multi-layer mechanical case coupled with fluid flow under anisotropic horizontal stresses condition.

RESERVOIR CHARACTERISTICS	LAYER 1	LAYER 2	LAYER 3	LAYER 4
Depth (ft)	1000	1020	1040	1060
Reservoir height (ft)	20	20	20	20
Wellbore radius (in)	3	3	3	3
Reservoir radius (ft)	100	100	100	100
Reservoir pressure (psi)	500	500	500	500
Wellbore pressure (psi)	500	500	500	500
Vertical stress gradient (psi/ft)	1.0	1.0	1.0	1.0
Maximum horizontal stress gradient (psi/ft)	1.0	1.0	1.0	1.0
Minimum horizontal stress gradient (psi/ft)	1.0	1.0	0.9	1.0
Young modulus (psi)	1.2E06	1.0E06	1.0E06	1.0E06
Poisson ratio (fraction)	0.30	0.30	0.25	0.30
Cohesion (psi)	1000	1000	100	1000
Friction angle (°)	15	15	15	15
Dilation angle (°)	15	15	15	15

Figure 5 – 33 presents the validation results of the elastic model for a multi-layer mechanical case coupled with fluid flow under anisotropic horizontal stresses condition in terms of the displacements profiles in

x, y, and z directions at three different angles: 0º, 45º and 90º, using the ABAQUS® software and the numerical model.

Figure 5 – 34 presents the validation results of the elastoplastic model for a multi-layer mechanical case coupled with fluid flow under anisotropic horizontal stresses condition in terms of the elastic strain profiles in x, y, and z directions at three different angles: 0º, 45º and 90º, using the ABAQUS® software and the numerical model.

Figure 5 – 35 presents the validation results of the elastoplastic model for the multi-layer – mechanical case coupled with fluid flow under anisotropic horizontal stresses condition in terms of the stress profiles in x, y, and z directions at three different angles: 0º, 45º and 90º, using the ABAQUS® software and the numerical model.

Figure 5 – 36 presents the validation results of the elastoplastic model for the multi-layer mechanical case coupled with fluid flow under anisotropic horizontal stresses condition in terms of the plastic strain profiles in x, y, and z directions at three different angles: 0º, 45º and 90º, using the ABAQUS® software and the numerical model.

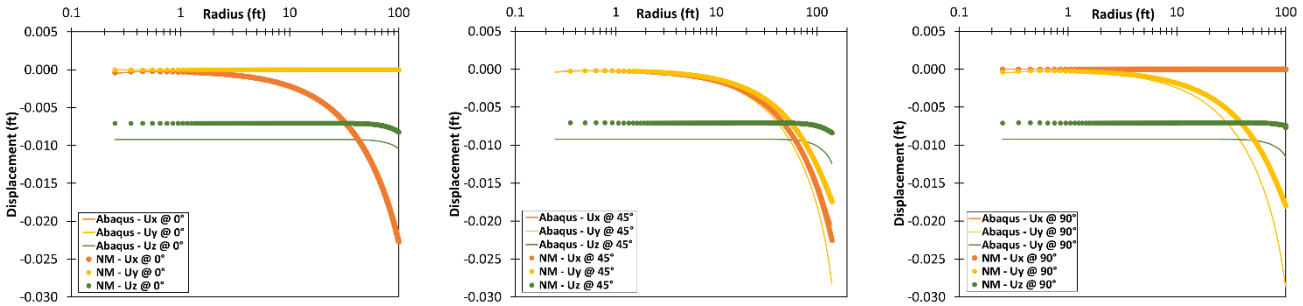

a. b. c.

Figure 5 – 33. Displacement profiles for each direction for the validation of the elastoplastic model for a multi-layer mechanical case coupled with fluid flow under anisotropic horizontal stresses condition. a) Profiles at 0º. b) Profiles at 45º. c) Profiles at 90º.

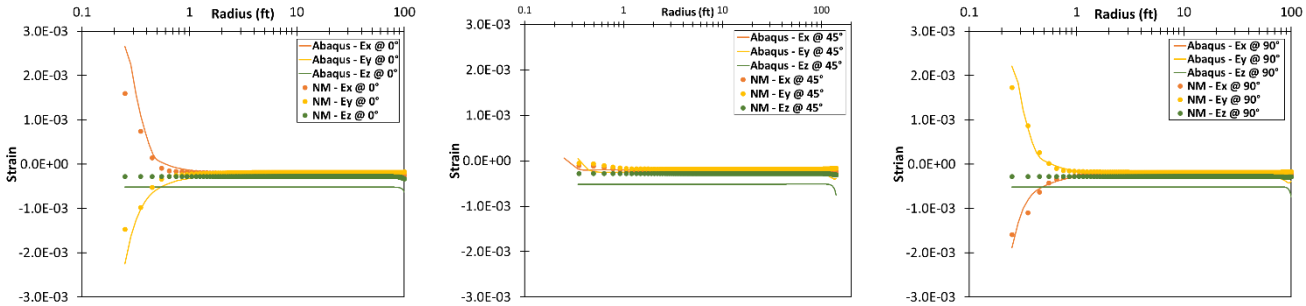

a. b. c.

Figure 5 – 34. Elastic strain profiles for each direction for the validation of the elastoplastic model for a multi-layer mechanical case coupled with fluid flow under anisotropic horizontal stresses condition. a) Profiles at 0º. b) Profiles at 45º. c) Profiles at 90º.

Table 5 – 26 presents the root mean squared error to quantify the differences in displacements, strains, stresses, and plastic strains between the results of the ABAQUS® software and the numerical model for

the validation of the elastoplastic model for a multi-layer mechanical case coupled with fluid flow under isotropic horizontal stresses condition.

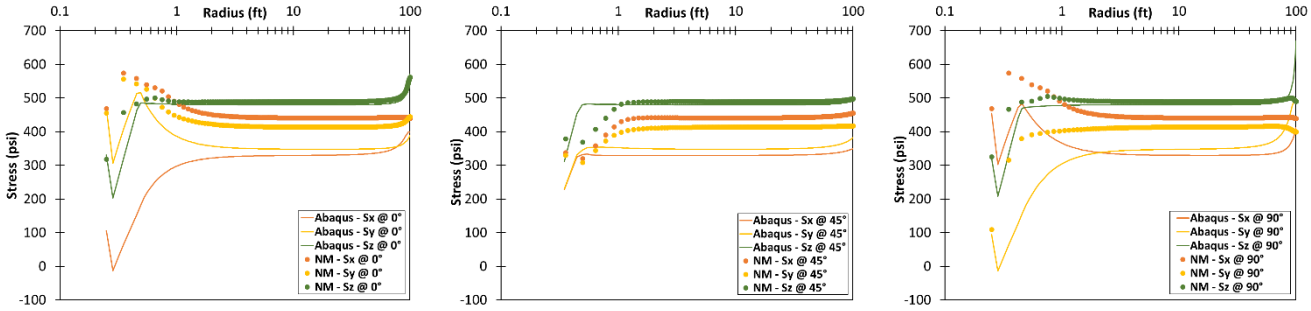

a. b. c.

Figure 5 – 35. Effective stress profiles for each direction for the validation of the elastoplastic model for the multi-layer mechanical case coupled with fluid flow under anisotropic horizontal stresses condition. a) Profiles at 0º. b) Profiles at 45º. c) Profiles at 90º.

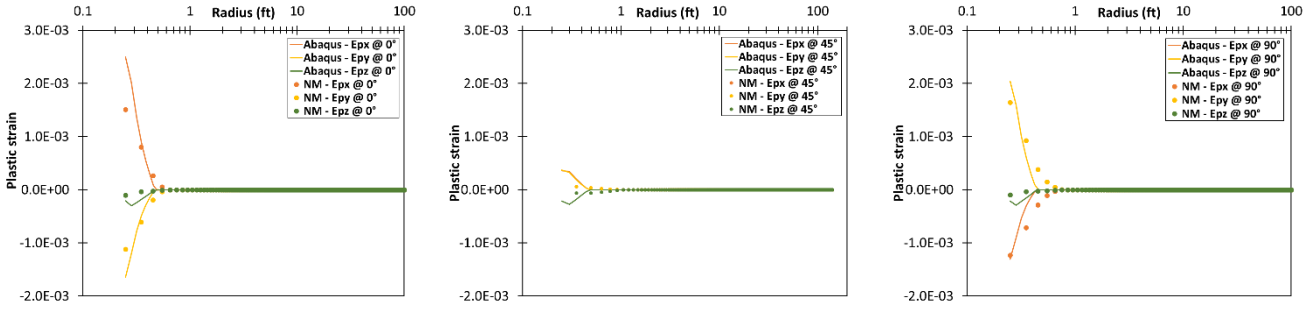

a. b. c.

Figure 5 – 36. Plastic strain profiles for each direction for the validation of the elastoplastic model for the multi-layer mechanical case coupled with fluid flow under anisotropic horizontal stresses condition. a) Profiles at 0º. b) Profiles at 45º. c) Profiles at 90º.

Table 5 – 26. Root mean squared error (RMSE) for displacements, elastic strains, stresses, and plastic strains for the validation of the elastoplastic model for a multi-layer mechanical case coupled with fluid flow under isotropic horizontal stresses condition.

RMSE		Displacement (ft)	Elastic strain	Stress (psi)	Plastic strain
@ 0°	***x***	4.210E-04	3.868E-05	1.032E02	0.000E-00
	y	1.324E-04	6.766E-05	6.485E01	9.556E-05
	z	2.150E-03	2.420E-04	1.164E01	0.000E-00
@ 45°	***x***	8.691E-04	3.868E-05	1.052E02	4.670E-06
	y	4.802E-03	6.766E-05	5.514E01	4.270E-06
	z	2.581E-03	2.420E-04	2.619E01	4.428E-06
@ 90°	***x***	1.241E-02	1.870E-05	1.034E02	3.193E-05
	y	1.048E-02	1.221E-04	5.931E01	1.743E-05
	z	2.345E-03	2.464E-04	2.967E01	5.757E-06

Remark: The results of the elastoplastic model for a multi-layer-mechanical case coupled with fluid flow under anisotropic horizontal stresses condition in terms of displacements follow the expected trend and the root mean square errors for displacement are small enough, errors less than 1.241E-02 ft; for elastic strain are small enough, errors less than 2.464E-04 ft; however; for stresses, the differences are

higher with root mean square errors less than 105 psi; and in terms of plastic strains also follow the expected trend and the root mean square errors for strains are small enough, errors less than 9.956E-05; the results in terms of strain and stress at the boundary conditions, internal and external, are adequate showing that these conditions are well imposed. However, the displacements in the z-direction present high differences, which affects the elastic strain and stresses. The results in terms of strain and stress at the boundary conditions, internal and external, are adequate showing that these conditions are well imposed. In conclusion, although the error grew in magnitude for deformation and stress with respect to the elastic case, the numerical model still obtains results in terms of displacements and strains with a good approach, even for plasticity and horizontal anisotropy, but the stresses have high differences.

5.3 Coupled model

The coupled model that consists of the fluid flow model coupled to the geomechanical model is validated by comparing the results obtained with the numerical model with the results obtained with the CMG® commercial simulator, running the same cases and aligning the models as much as possible. The fluid flow model is a black oil simulator considering a two-phase case for oil and water and while the geomechanical model considers the elastic and the elastoplastic case under isotropic horizontal stress conditions.

5.3.1 Two-phase and elastic case

The validation of the two-phase and elastic case has an oil and water case for the fluid flow model and an elastic case under isotropic and anisotropic horizontal stress conditions for the geomechanical model for a one-layer set, comparing the results obtained in the numerical model with the results obtained using the commercial simulator CMG®. The variables of validation for these basic cases are the oil pressure, the saturations, the production rate, and the cumulative production for the fluid flow model, and the displacements, the strains, and the stresses for the geomechanical model.

– Under isotropic horizontal stresses condition

This section presents the two-phase and elastic case under isotropic horizontal stress conditions. The characteristics of the reservoir of the field case are summarized in Table 5 – 27, the production schedule to run this case is presented in Table 5 – 2 and the relative permeability curve for the oil-water system is presented in Figure 5 – 1.

Figure 5 – 37 presents the results of the radial pressure profile for each production time and Figure 5 – 38 presents the results of the production of oil, water, and gas during simulation time for the two-phase and elastic validation case under isotropic horizontal stress condition using the CMG® software and the numerical model.

Table 5 – 28 presents the root mean squared error to quantify the oil pressure differences and oil saturation differences between the results of the CMG® software and the numerical model for the validation of the two-phase and elastic case under isotropic horizontal stresses condition.

Table 5 – 27. Field case for the two-phase and elastic case under isotropic horizontal stresses condition.

RESERVOIR CHARACTERISTICS	VALUE
Depth (ft)	1000
Wellbore radius (in)	2.5
Reservoir radius (ft)	100
Reservoir thickness (ft)	30
Reservoir pressure (psi)	500
Temperature (°F)	120
Porosity (fraction)	0.30
Horizontal permeability (mD)	300
Vertical permeability (mD)	30
API Gravity (°API)	20
Gas-specific gravity	0.7
Bubble point pressure (psi)	100
Oil saturation (fraction)	0.85
Water saturation (fraction)	0.15
Gas saturation (fraction)	0.00
Vertical stress gradient (psi/ft)	1.0
Horizontal stress gradient	1.0
Biot (fraction)	1.0
Young modulus (psi)	1.0E06
Poisson ratio (fraction)	0.25
Cohesion (psi)	1000
Internal friction angle (°)	15

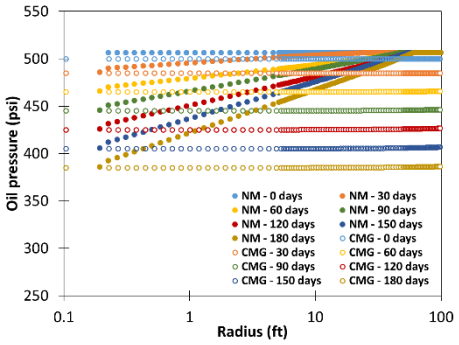

a.

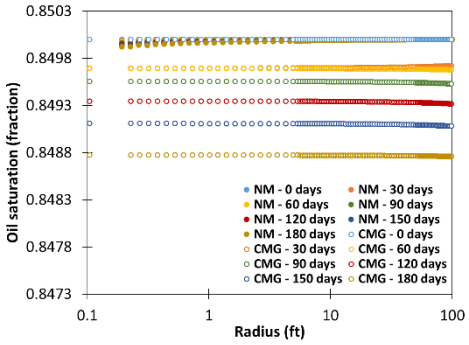

b.

Figure 5 – 37. Radial pressure and saturation profiles for each production time for the two-phase and elastic case under isotropic horizontal stresses. a) Oil pressure profile. b) Oil saturation profile.

Table 5 – 28. Root mean squared error (RMSE) for oil pressure and oil saturation for each production time for the two-phase and elastic case under isotropic horizontal stresses condition.

PRODUCTION TIME (days)	RMSE	
	Oil pressure (psi)	Oil saturation (fraction)
0	6.60	2.38E-08
30	19.25	2.95E-04
60	33.03	3.10E-04
90	49.48	4.48E-04
120	64.05	6.58E-04
150	80.33	8.92E-04
180	94.94	1.22E-03
Mean	**49.67**	**5.46E-04**

Table 5 – 29 presents the root mean squared error to quantify the differences in production rate and cumulative production between the results of the CMG® software and the numerical model for the validation of the two-phase and elastic case under isotropic horizontal stresses condition.

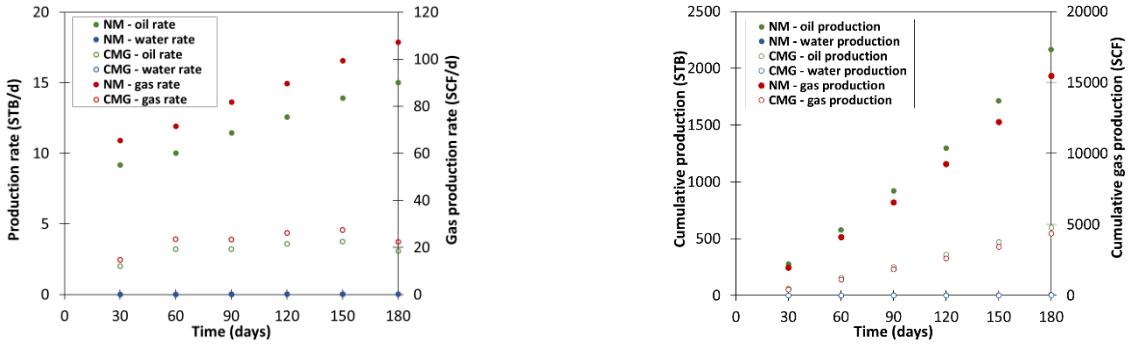

a. b.

Figure 5 –38. Production (oil, water, and gas) during simulation time for the two-phase and elastic case under isotropic horizontal stresses condition a) Production rate. b) Cumulative production.

Table 5 – 29. Root mean squared error (RMSE) for production rate and cumulative production for oil, water, and gas for the two-phase and elastic case under isotropic horizontal stress conditions.

VARIABLE	RMSE
Oil production rate (STB/d)	9.06
Water production rate (STB/d)	1.29E-02
Gas production rate (SCF/d)	64.18
Cumulative oil production (STB)	961.60
Cumulative water production (STB)	0.75
Cumulative gas production (SCF)	6805.95

Remark: The results of the two-phase and elastic validation case under isotropic horizontal stress conditions in terms of oil pressure are acceptable with root mean square errors of 49.67 psi. In terms of saturation, the results are adequate, and the root mean square errors for saturation are small enough, with a mean value of 5.46E-04. The results in terms of production rate and cumulative production have reasonable differences considering the existing differences between the two models, the behavior trends have differences in both models with no differences in water production, and high differences in oil and gas production. In conclusion, the results of the two-phase and elastic validation case under isotropic horizontal stress conditions are acceptable in terms of oil pressure and adequate in terms of saturation, and production variables that allow us to verify and validate the numerical model for this case.

Figure 5 – 39 presents the validation results of the two-phase and elastic validation case under isotropic horizontal stress conditions in terms of the displacements profiles in $x, y,$ and z directions at three different angles: 0º, 45º and 90º, using the CMG® software and the numerical model.

Figure 5 – 40 presents the validation results of the elastic model for the two-phase and elastic case under isotropic horizontal stress conditions in terms of the strain profiles in $x, y,$ and z directions at three different angles: 0º, 45º and 90º, using the CMG® software and the numerical model.

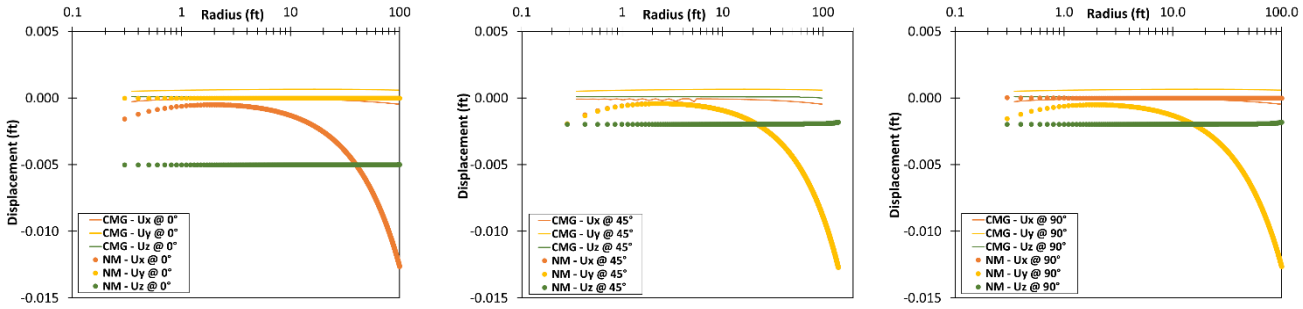

a. b. c.

Figure 5 – 39. Displacement profiles for each direction at the early production for the two-phase and elastic case under isotropic horizontal stress conditions. a) Profiles at 0º. b) Profiles at 45º. c) Profiles at 90º.

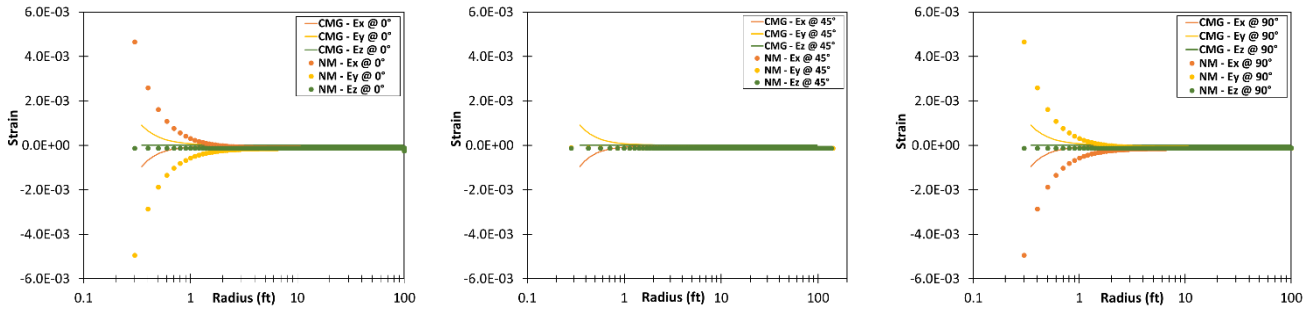

a. b. c.

Figure 5 – 40. Elastic strain profiles for each direction at the early production for the two-phase and elastic case under isotropic horizontal stress conditions. a) Profiles at 0º. b) Profiles at 45º. c) Profiles at 90º.

Figure 5 – 41 presents the validation results of the two-phase and elastic case under isotropic horizontal stress conditions in terms of the stress profiles in $x, y,$ and z directions at three different angles: 0º, 45º, and 90º, using the CMG® software and the numerical model.

Table 5 – 30 presents the root mean squared error to quantify the differences in displacements, strains, and stresses between the results of the CMG® software and the numerical model for the validation of the two-phase and elastic validation case under isotropic horizontal stress conditions.

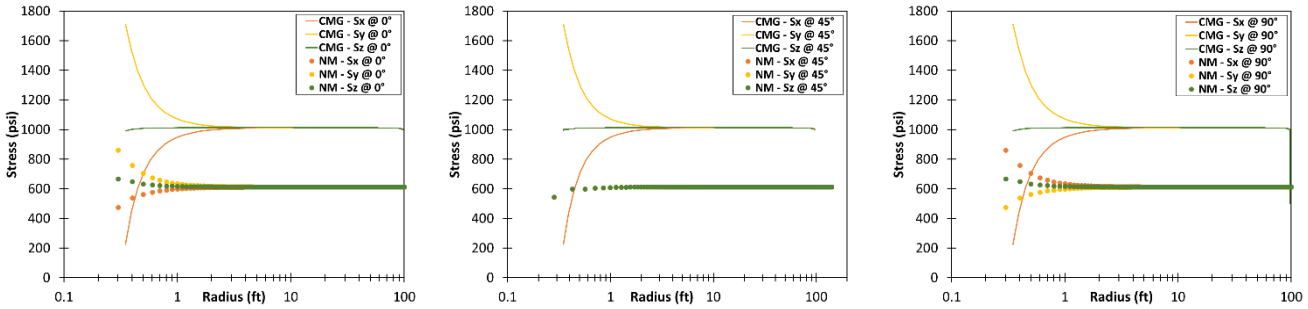

a. b. c.

Figure 5 – 41. Effective stress profiles for each direction at the early production for the two-phase and elastic case under isotropic horizontal stress conditions. a) Profiles at 0º. b) Profiles at 45º. c) Profiles at 90º.

Table 5 – 30. Root mean squared error (RMSE) for displacements, strains, and stresses in the two-phase and elastic case under isotropic horizontal stress conditions.

RMSE		Displacement (ft)	Strain	Effective stress (psi)
@ 0°	x	6.734E-03	2.489E-04	3.908E02
	y	6.238E-04	2.689E-04	3.944E02
	z	5.010E-03	1.329E-04	3.933E02
@ 45°	x	3.942E-03	1.089E-04	3.285E02
	y	4.633E-03	1.138E-04	3.331E02
	z	1.666E-03	2.809E-06	3.311E02
@ 90°	x	2.767E-04	2.152E-04	3.905E02
	y	7.552E-03	1.983E-04	3.966E02
	z	1.974E-03	1.329E-04	3.933E02

Remark: The results of the two-phase and elastic validation case under isotropic horizontal stress conditions in terms of displacements follow the expected trend and the root mean square errors for displacement are small enough, errors less than 7.55E-03 ft; in terms of strains also follow the expected trend and the root mean square errors for strains are small enough, errors less than 2.809E-04; and in terms of stresses also follow the expected trend but present high differences with root mean square errors for stresses less than 397 psi. The results in terms of strain and stress at the boundary conditions, internal and external, are adequate showing that these conditions are well imposed. The displacements in CMG® change insignificantly and their trend is not adequate, different behavior in the numerical simulator with adequate displacement trend; in CMG®, the strains in the x and y direction seem to be changed at 0° and the stresses have the same behavior at 90°. In conclusion, the numerical model obtains results in terms of displacements and strains with a good approach with high differences in stresses.

– Under anisotropic horizontal stresses condition

This section presents the two-phase and elastic case under anisotropic horizontal stress conditions. The characteristics of the reservoir of the field case are summarized in Table 5 – 31, the production schedule to run this case is presented in Table 5 – 2 and the relative permeability curve for the oil-water system is presented in Figure 5 – 1.

Figure 5 – 42 presents the results of the radial pressure profile for each production time and Figure 5 – 43 presents the results of the production of oil, water, and gas during simulation time for the two-phase and elastic validation case under anisotropic horizontal stress condition using the CMG® software and the numerical model.

Table 5 – 32 presents the root mean squared error to quantify the oil pressure differences and oil saturation differences between the results of the CMG® software and the numerical model for the two-phase and elastic validation case under isotropic horizontal stresses condition.

Table 5 – 33 presents the root mean squared error to quantify the differences in production rate and cumulative production between the results of the CMG® software and the numerical model for the two-phase and elastic validation case under anisotropic horizontal stresses condition.

Table 5 – 31. Field case for the two-phase and elastic case under anisotropic horizontal stresses condition.

RESERVOIR CHARACTERISTICS	VALUE
Depth (ft)	1000
Wellbore radius (in)	2.5
Reservoir radius (ft)	100
Reservoir thickness (ft)	30
Reservoir pressure (psi)	500
Temperature (°F)	120
Porosity (fraction)	0.30
Horizontal permeability (mD)	300
Vertical permeability (mD)	30
API Gravity (°API)	20
Gas-specific gravity	0.7
Bubble point pressure (psi)	100
Oil saturation (fraction)	0.85
Water saturation (fraction)	0.15
Gas saturation (fraction)	0.00
Vertical stress gradient (psi/ft)	1.0
Maximum horizontal stress gradient (psi/ft)	1.0
Minimum horizontal stress gradient (psi/ft)	0.9
Biot (fraction)	1.0
Young modulus (psi)	1.0E06
Poisson ratio (fraction)	0.25
Cohesion (psi)	1000
Internal friction angle (°)	15

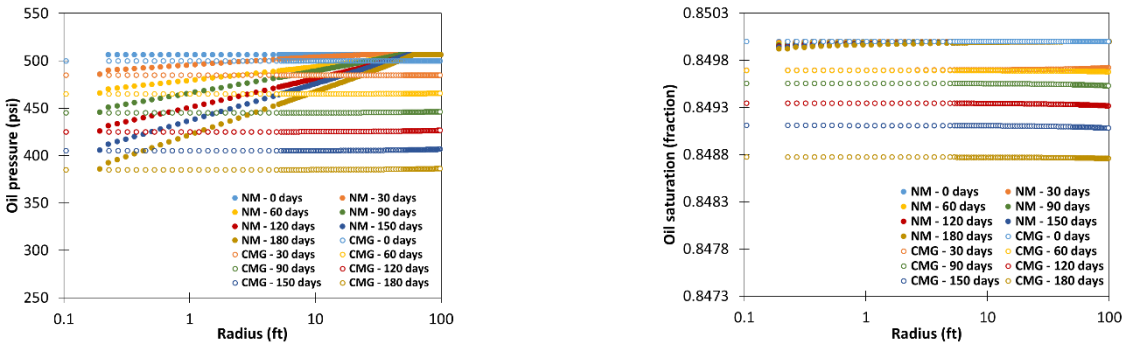

a. b.

Figure 5 – 42. Radial pressure and saturation profiles for each production time for the two-phase and elastic case under anisotropic horizontal stresses. a) Oil pressure profile. b) Oil saturation profile.

Table 5 – 32. Root mean squared error (RMSE) for oil pressure and oil saturation for each production time for the two-phase and elastic case under anisotropic horizontal stresses condition.

PRODUCTION TIME (days)	RMSE	
	Oil pressure (psi)	Oil saturation (fraction)
0	6.60	2.38E-08
30	19.25	2.95E-04
60	33.03	3.10E-04
90	49.48	4.48E-04
120	64.05	6.58E-04
150	80.33	8.92E-04
180	94.94	1.22E-03
Mean	**49.67**	**5.46E-04**

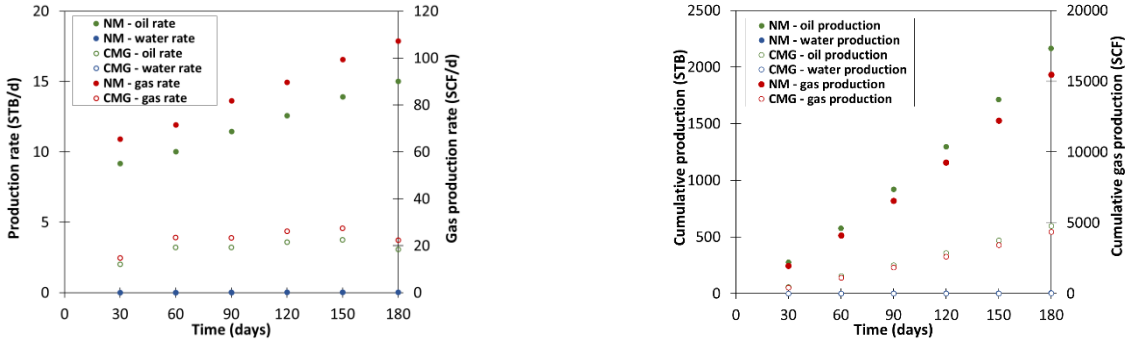

a. b.

Figure 5 –43. Production (oil, water, and gas) during simulation time for the two-phase and elastic case under anisotropic horizontal stresses condition a) Production rate. b) Cumulative production.

Table 5 – 33. Root mean squared error (RMSE) for production rate and cumulative production for oil, water, and gas for the two-phase and elastic case under anisotropic horizontal stress conditions.

VARIABLE	RMSE
Oil production rate (STB/d)	9.06
Water production rate (STB/d)	1.29E-02
Gas production rate (SCF/d)	64.18
Cumulative oil production (STB)	961.60
Cumulative water production (STB)	0.75
Cumulative gas production (SCF)	6805.95

Remark: The results of the two-phase and elastic validation case under anisotropic horizontal stress conditions in terms of oil pressure are acceptable with the root mean square errors for pressure of 49.67 psi. In terms of saturation, the results are adequate, and the root mean square errors for saturation are small enough, with a mean value of 5.46E-04. The results in terms of production rate and cumulative production have reasonable differences considering the existing differences between the two models, the behavior trends have differences in both models with no differences in water production, and high differences in oil and gas production. In conclusion, the results of the two-phase and elastic validation case under anisotropic horizontal stress conditions are acceptable in terms of oil pressure and adequate in terms of saturation, and production variables that allow us to verify and validate the numerical model for this case. There is no difference in terms of production in both simulators for the two-phase and elastic case in both under isotropic and anisotropic horizontal stress conditions.

Figure 5 – 44 presents the validation results of the two-phase and elastic validation case under anisotropic horizontal stress conditions in terms of the displacements profiles in $x, y,$ and z directions at three different angles: 0º, 45º and 90º, using the CMG® software and the numerical model.

Figure 5 – 45 presents the validation results of the elastic model for the two-phase and elastic validation case under anisotropic horizontal stress conditions in terms of the strain profiles in $x, y,$ and z directions at three different angles: 0º, 45º and 90º, using the CMG® software and the numerical model.

Figure 5 – 46 presents the validation results of the two-phase and elastic validation case under anisotropic horizontal stress conditions in terms of the stress profiles in $x, y,$ and z directions at three different angles: 0º, 45º, and 90º, using the CMG® software and the numerical model.

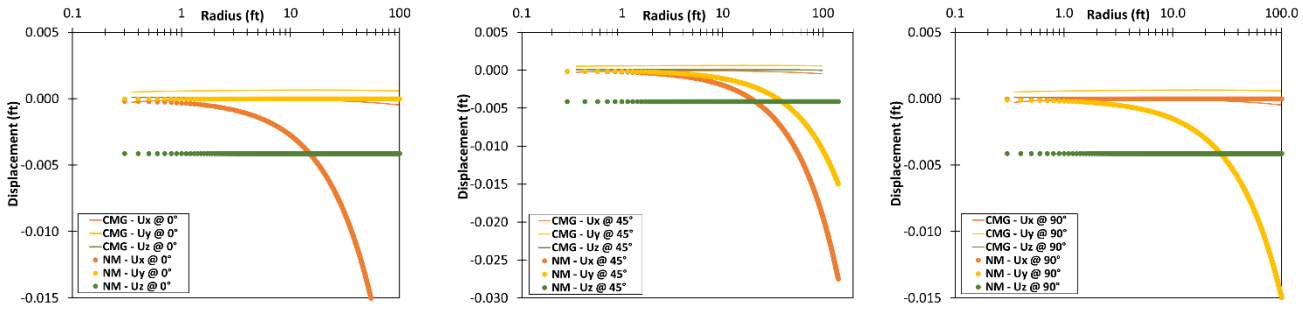

a. b. c.

Figure 5 – 44. Displacement profiles for each direction at the early production for the two-phase and elastic case under anisotropic horizontal stress conditions. a) Profiles at 0º. b) Profiles at 45º. c) Profiles at 90º.

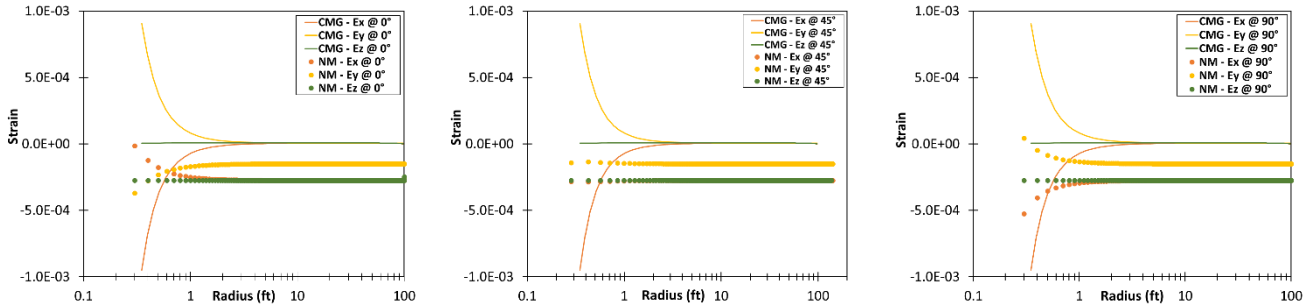

a. b. c.

Figure 5 – 45. Elastic strain profiles for each direction at the early production for the two-phase and elastic case under anisotropic horizontal stress conditions. a) Profiles at 0º. b) Profiles at 45º. c) Profiles at 90º.

Table 5 – 34 presents the root mean squared error to quantify the differences in displacements, strains, and stresses between the results of the CMG® software and the numerical model for the two-phase and elastic validation case under anisotropic horizontal stress conditions.

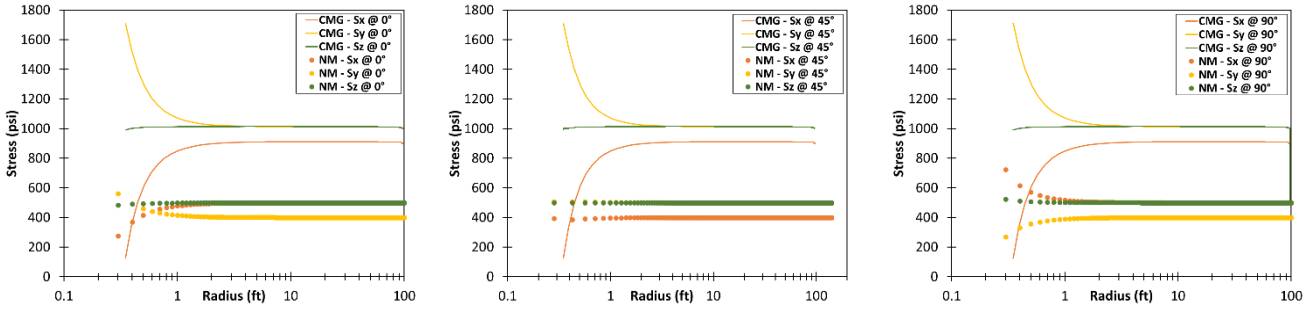

a. b. c.

Figure 5 – 46. Stress profiles for each direction at the early production for the two-phase and elastic case under isotropic horizontal stress conditions. a) Profiles at 0º. b) Profiles at 45º. c) Profiles at 90º.

Table 5 – 34. Root mean squared error (RMSE) for displacements, strains, and stresses for the two-phase and elastic validation case under anisotropic horizontal stress conditions.

RMSE		Displacement (ft)	Strain	Stress (psi)
@ 0°	x	1.505E-02	2.752E-04	4.042E02
	y	6.238E-04	1.619E-04	6.054E02
	z	4.142E-03	2.777E-04	5.055E02
@ 45°	x	8.888E-03	2.309E-04	4.226E02
	y	5.426E-03	2.366E-04	4.269E02
	z	3.485E-03	2.809E-06	4.252E02
@ 90°	x	2.772E-04	2.746E-04	4.038E02
	y	8.893E-03	1.573E-04	6.069E02
	z	4.142E-03	2.777E-04	5.054E02

Remark: The results of the two-phase and elastic validation case under anisotropic horizontal stress conditions in terms of displacements follow the expected trend and the root mean square errors for displacement are small enough, errors less than 1.505E-02 ft; in terms of strains also follow the expected trend and the root mean square errors for strains are small enough, errors less than 2.809E-04; and in terms of stresses also follow the expected trend but present high differences with root mean square errors of 607 psi. The results in terms of strain and stress at the boundary conditions, internal and external, are adequate showing that these conditions are well imposed. Similar to the isotropic case, the displacements in CMG® change insignificantly and their trend is not adequate, different behavior in the numerical simulator, adequate displacement trend; in CMG®, there is no difference between the isotropic and anisotropic case in terms of strains, the strains in the x and y direction seems to be changed at 0° and the stresses have the same behavior at 90°. In conclusion, the numerical model obtains results in terms of displacements and strains with a good approach with high differences in stresses.

5.3.2 Two-phase and elastoplastic case

The validation of the two-phase and elastoplastic case has an oil and water case for the fluid flow model and an elastic case under isotropic and anisotropic horizontal stress conditions for the geomechanical model for a one-layer set, comparing the results obtained in the numerical model with the results obtained using the commercial simulator CMG®. The variables of validation for these basic cases are the oil pressure, the saturations, the production rate, and the cumulative production for the fluid flow model, and the displacements, the strains, and the stresses for the geomechanical model.

– Under isotropic horizontal stresses condition

This section presents the two-phase and elastoplastic case under isotropic horizontal stress conditions. The characteristics of the reservoir of the field case are summarized in Table 5 – 35, the production schedule to run this case is presented in Table 5 – 2 and the relative permeability curve for the oil-water system is presented in Figure 5 – 1.

Figure 5 – 47 presents the results of the radial pressure profile for each production time and Figure 5 – 48 presents the results of the production of oil, water, and gas during simulation time in the two-phase and elastoplastic validation case under isotropic horizontal stress condition using the CMG® software and the numerical model.

Table 5 – 35. Field case for the two-phase and elastoplastic case under isotropic horizontal stresses condition.

RESERVOIR CHARACTERISTICS	VALUE
Depth (ft)	1000
Wellbore radius (in)	2.5
Reservoir radius (ft)	100
Reservoir thickness (ft)	30
Reservoir pressure (psi)	500
Temperature (°F)	120
Porosity (fraction)	0.30
Horizontal permeability (mD)	300
Vertical permeability (mD)	30
API Gravity (°API)	20
Gas-specific gravity	0.7
Bubble point pressure (psi)	100
Oil saturation (fraction)	0.85
Water saturation (fraction)	0.15
Gas saturation (fraction)	0.00
Vertical stress gradient (psi/ft)	1
Horizontal stress gradient (psi/ft)	1
Biot (fraction)	1
Young modulus (psi)	1.0E06
Poisson ratio (fraction)	0.25
Cohesion (psi)	100
Internal friction angle (°)	15
Dilation angle (°)	15

Table 5 – 36 presents the root mean squared error to quantify the oil pressure differences and oil saturation differences between the results of the CMG® software and the numerical model for the two-phase and elastoplastic validation case under isotropic horizontal stress conditions.

Table 5 – 37 presents the root mean squared error to quantify the differences in production rate and cumulative production between the results of the CMG® software and the numerical model for the two-phase and elastoplastic validation case under isotropic horizontal stress conditions.

Table 5 – 36. Root mean squared error (RMSE) for oil pressure and oil saturation for each production time for the two-phase and elastoplastic case under isotropic horizontal stress conditions.

PRODUCTION TIME (days)	RMSE	
	Oil pressure (psi)	Oil saturation (fraction)
0	6.60	2.38E-08
30	19.25	2.95E-04
60	33.05	3.09E-04
90	49.52	4.46E-04
120	64.16	6.54E-04
150	80.59	8.87E-04
180	95.80	1.21E-03
Mean	**49.85**	**5.44E-04**

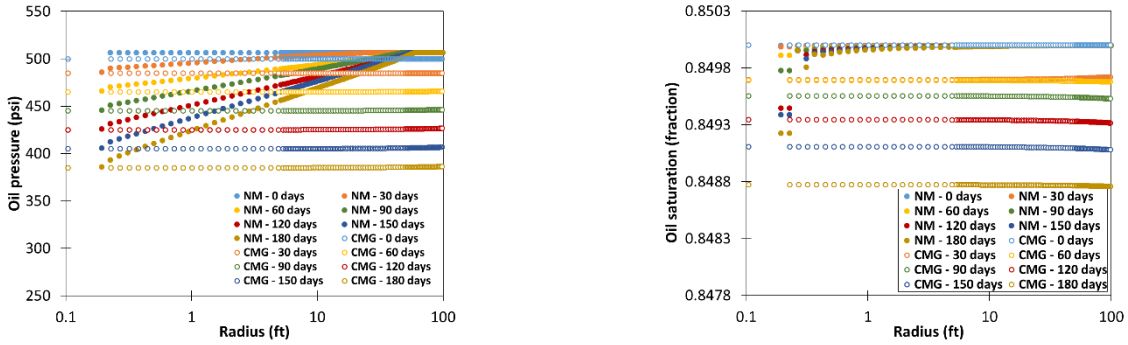

a. b.

Figure 5 – 47. Radial pressure and saturation profiles for each production time for the two-phase and elastoplastic case under isotropic horizontal stress conditions. a) Oil pressure profile. b) Oil saturation profile.

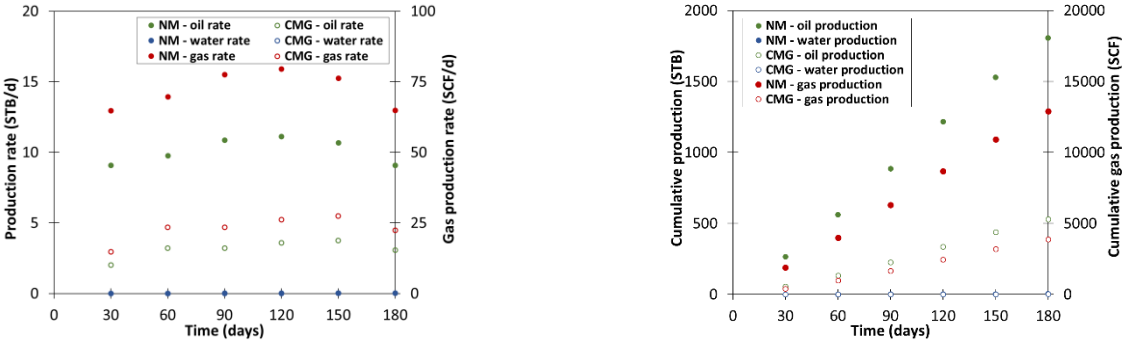

a. b.

Figure 5 –48. Production (oil, water, and gas) during simulation time for the two-phase and elastoplastic case under isotropic horizontal stress conditions. a) Production rate. b) Cumulative production.

Table 5 – 37. Root mean squared error (RMSE) for production rate and cumulative production for oil, water, and gas for the two-phase and elastoplastic case under isotropic horizontal stresses condition.

VARIABLE	RMSE
Oil production rate (STB/d)	6.98
Water production rate (STB/d)	9.03E-03
Gas production rate (SCF/d)	49.33
Cumulative oil production (STB)	819.51
Cumulative water production (STB)	0.56
Cumulative gas production (SCF)	5792.00

Remark: The results of the two-phase and elastoplastic validation case under isotropic horizontal stress conditions in terms of oil pressure are acceptable with root mean square errors of 49.85 psi. In terms of saturation, the results are adequate too, and the root mean square errors for saturation are small enough, with a mean value of 5.44E-04. The oil saturation for the numerical model has a better trend and looks more stable. The results in terms of production rate and cumulative production have reasonable differences considering the existing differences between the two models, the behavior trends have differences in both models with no differences in water production, and high differences in oil and gas production. In conclusion, the results of the two-phase and elastoplastic validation case under isotropic

horizontal stress conditions are acceptable in terms of oil pressure and adequate in terms of saturation, and production variables that allow us to verify and validate the numerical model for this case.

Figure 5 – 49 presents the results of the two-phase and elastoplastic validation case under isotropic horizontal stress conditions at early production (30 days) in terms of the displacements profiles in $x, y,$ and z directions at three different angles: 0º, 45º and 90º, using the CMG® software and the numerical model.

Figure 5 – 50 presents the results of the plastic model for the two-phase and elastoplastic validation case under isotropic horizontal stress conditions at early production (30 days) in terms of the strain profiles in $x, y,$ and z directions at three different angles: 0º, 45º and 90º, using the CMG® software and the numerical model.

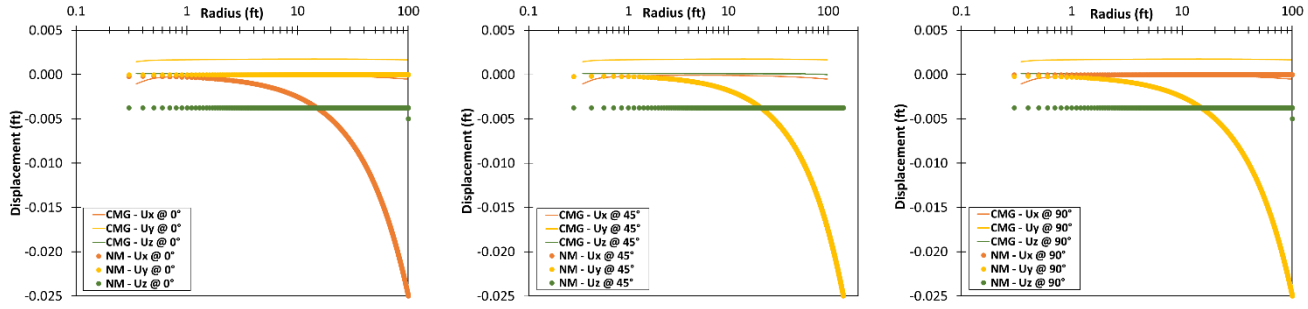

a. b. c.

Figure 5 – 49. Displacement profiles for each direction at the early production for the two-phase and elastoplastic case under isotropic horizontal stress conditions. a) Profiles at 0º. b) Profiles at 45º. c) Profiles at 90º.

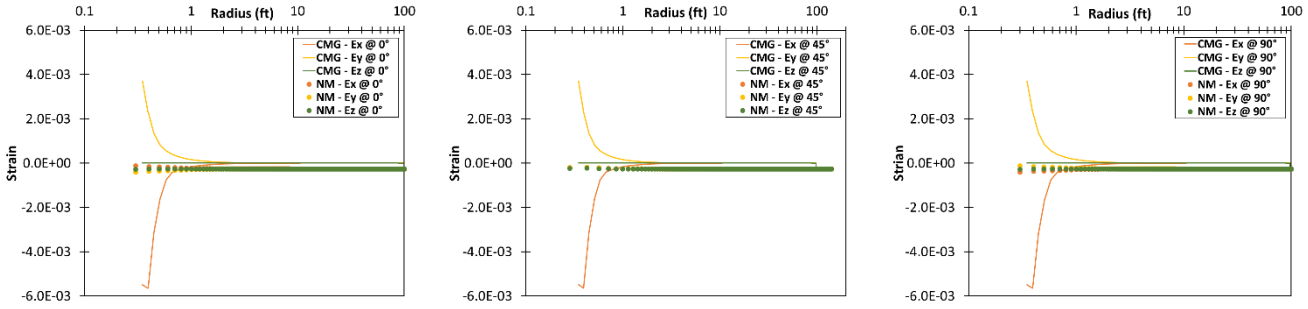

a. b. c.

Figure 5 – 50. Strain profiles for each direction at the early production for the two-phase and elastoplastic case under isotropic horizontal stress conditions. a) Profiles at 0º. b) Profiles at 45º. c) Profiles at 90º.

Figure 5 – 51 presents the results of the plastic model for the two-phase and elastoplastic validation case under isotropic horizontal stress conditions at early production (30 days) in terms of the stress profiles in $x, y,$ and z directions at three different angles: 0º, 45º, and 90º, using the CMG® software and the numerical model.

Figure 5 – 52 presents the results of the plastic model for the two-phase and elastoplastic validation case under isotropic horizontal stress conditions at early production in terms of the mean plastic strain profiles at three different angles: 0º, 45º and 90º, using the CMG® software and the numerical model.

Table 5 – 38 presents the root mean squared error to quantify the differences in displacements, strains, and stresses between the results of the CMG® software and the numerical model for the two-phase and elastoplastic validation case under isotropic horizontal stress conditions.

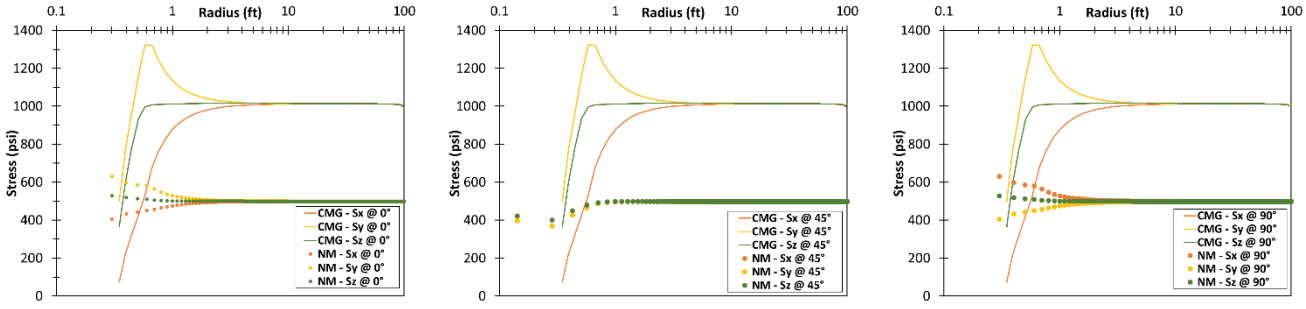

a. b. c.

Figure 5 – 51. Effective stress profiles for each direction at the early production for the two-phase and elastoplastic case under isotropic horizontal stress conditions. a) Profiles at 0º. b) Profiles at 45º. c) Profiles at 90º.

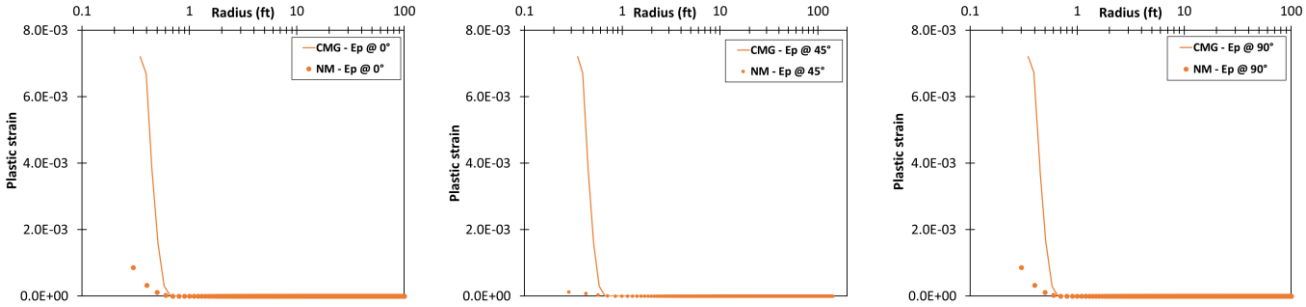

a. b. c.

Figure 5 – 52. Plastic strain profiles at the early production for the two-phase and elastoplastic case under isotropic horizontal stress conditions. a) Profiles at 0º. b) Profiles at 45º. c) Profiles at 90º.

Table 5 – 38. Root mean squared error (RMSE) for displacements, strains, and stresses for the validation of the two-phase and elastoplastic case under isotropic horizontal stress conditions.

RMSE		Displacement (ft)	Strain	Stress (psi)	Plastic strain
@ 0°	***x***	1.362E-02	3.365E-04	5.026E02	2.343E-04
	y	1.689E-03	2.948E-04	5.067E02	
	z	3.780E-03	2.535E-04	5.057E02	
@ 45°	***x***	8.029E-03	2.612E-04	4.225E02	2.411E-04
	y	9.541E-03	2.343E-04	4.270E02	
	z	3.181E-03	2.132E-06	4.254E02	
@ 90°	***x***	3.152E-04	3.290E-04	4.968E02	2.619E-04
	y	1.541E-02	2.872E-04	5.026E02	
	z	3.780E-03	2.535E-04	5.002E02	

Remark: The results of the two-phase and plastic case under isotropic horizontal stresses condition in terms of displacements follow the expected trend and the root mean square errors for displacement are

small enough, errors less than 1.541E-02 ft; in terms of strains also follow the expected trend and the root mean square errors for strains are small enough, errors less than 3.365E-04; and in terms of stresses also follow the expected trend and present high differences with root mean square errors of 507 psi. The results in terms of strain and stress at the boundary conditions, internal and external, are adequate showing that these conditions are well imposed. Similar to the elastic case, the displacements in CMG® change insignificantly and their trend is not adequate, different behavior in the numerical simulator, adequate displacement trend; in CMG®, the strains in the x and y directions seem to be changed at 0° and the stresses have the same behavior at 90°. In general, the trends in geomechanical variables look better in the numerical model than in the CMG® software, with lower values in strains and stresses, especially in the plastic strain. In conclusion, the numerical model obtains results in terms of displacements and strains with a good approach and high differences in stresses.

– Under anisotropic horizontal stresses condition

This section presents the two-phase and elastoplastic case under anisotropic horizontal stress conditions. The characteristics of the reservoir of the field case are summarized in Table 5 – 39, the production schedule to run this case is presented in Table 5 – 2 and the relative permeability curve for the oil-water system is presented in Figure 5 – 1.

Figure 5 – 53 presents the results of the radial pressure profile for each production time and Figure 5 – 54 presents the results of the production of oil, water, and gas during simulation time in the two-phase and elastoplastic validation case under anisotropic horizontal stress condition using the CMG® software and the numerical model.

Table 5 – 39. Field case for the two-phase and elastoplastic case under anisotropic horizontal stresses condition.

RESERVOIR CHARACTERISTICS	VALUE
Depth (ft)	1000
Wellbore radius (in)	2.5
Reservoir radius (ft)	100
Reservoir thickness (ft)	30
Reservoir pressure (psi)	500
Temperature (°F)	120
Porosity (fraction)	0.30
Horizontal permeability (mD)	300
Vertical permeability (mD)	30
API Gravity (°API)	20
Gas-specific gravity	0.7
Bubble point pressure (psi)	100
Oil saturation (fraction)	0.85
Water saturation (fraction)	0.15
Gas saturation (fraction)	0.00
Vertical stress gradient (psi/ft)	1.0
Minimum horizontal stress gradient (psi/ft)	0.9
Maximum horizontal stress gradient (psi/ft)	1.0
Biot (fraction)	1.0
Young modulus (psi)	1.0E06
Poisson ratio (fraction)	0.25
Cohesion (psi)	100
Internal friction angle (°)	15
Dilation angle (°)	15

Table 5 – 40 presents the root mean squared error to quantify the oil pressure differences and oil saturation differences between the results of the CMG® software and the numerical model for the two-phase and elastoplastic validation case under anisotropic horizontal stress conditions.

Table 5 – 41 presents the root mean squared error to quantify the differences in production rate and cumulative production between the results of the CMG® software and the numerical model for the two-phase and elastoplastic validation case under anisotropic horizontal stress conditions.

Table 5 – 40. Root mean squared error (RMSE) for oil pressure and oil saturation for each production time for the two-phase and elastoplastic case under anisotropic horizontal stress conditions.

PRODUCTION TIME (days)	RMSE	
	Oil pressure (psi)	Oil saturation (fraction)
0	6.60	2.38E-08
30	19.25	2.95E-04
60	33.04	3.09E-04
90	49.51	4.47E-04
120	64.12	6.54E-04
150	80.50	8.89E-04
180	95.57	1.21E-03
Mean	**49.80**	**5.44E-04**

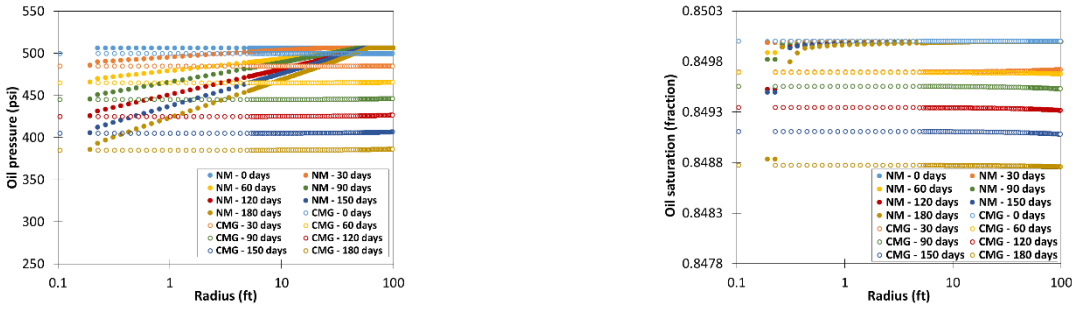

a. b.

Figure 5 – 53. Radial pressure and saturation profiles for each production time for the two-phase and elastoplastic case under anisotropic horizontal stress conditions. a) Oil pressure profile. b) Oil saturation profile.

Table 5 – 41. Root mean squared error (RMSE) for production rate and cumulative production for oil, water, and gas for the two-phase and elastoplastic case under anisotropic horizontal stresses condition.

VARIABLE	RMSE
Oil production rate (STB/d)	7.40
Water production rate (STB/d)	9.68E-03
Gas production rate (SCF/d)	52.32
Cumulative oil production (STB)	854.84
Cumulative water production (STB)	0.60
Cumulative gas production (SCF)	6044.06

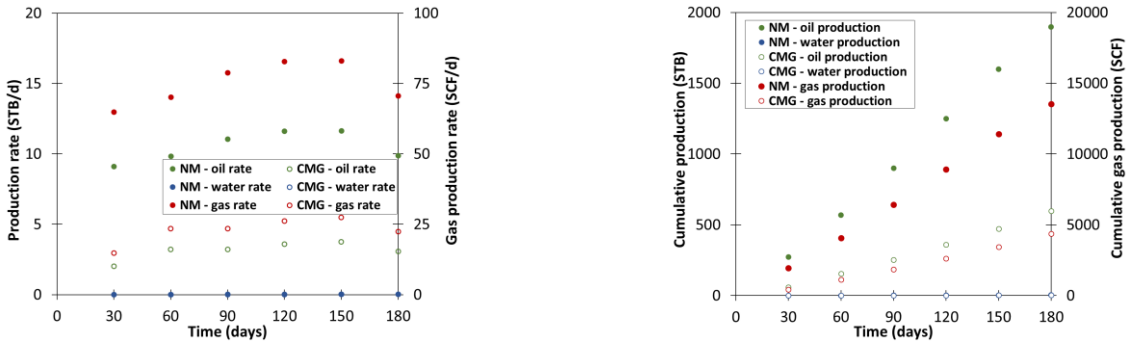

a. b.

Figure 5 –54. Production (oil, water, and gas) during simulation time for the two-phase and elastoplastic case under anisotropic horizontal stress conditions. a) Production rate. b) Cumulative production.

Remark: The results of the two-phase and elastoplastic validation case under anisotropic horizontal stress conditions in terms of oil pressure are acceptable with root mean square errors for oil pressure of 49.85 psi. In terms of saturation, the results are adequate too, and the root mean square errors for saturation are small enough, with a mean value of 5.44E-04. The oil saturation for the numerical model has a better trend and looks more stable. The results in terms of production rate and cumulative production have reasonable differences considering the existing differences between the two models, the behavior trends have differences in both models with no differences in water production, and high differences in oil and gas production. In conclusion, the results of the two-phase and elastoplastic validation case under anisotropic horizontal stress conditions are acceptable in terms of oil pressure and adequate in terms of saturation, and production variables that allow us to verify and validate the numerical model for this case.

Figure 5 – 55 presents the results of the two-phase and elastoplastic validation case under anisotropic horizontal stress conditions at early production (30 days) in terms of the displacements profiles in $x, y,$ and z directions at three different angles: 0º, 45º and 90º, using the CMG® software and the numerical model.

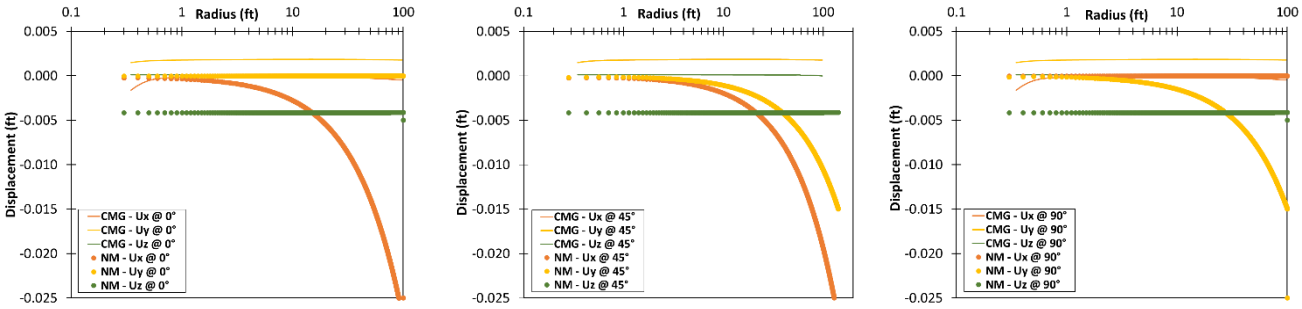

a. b. c.

Figure 5 – 55. Displacement profiles for each direction at the early production for the two-phase and elastoplastic case under anisotropic horizontal stress conditions. a) Profiles at 0º. b) Profiles at 45º. c) Profiles at 90º.

Figure 5 – 56 presents the results of the plastic model for the two-phase and elastoplastic validation case under anisotropic horizontal stress conditions at early production (30 days) in terms of the strain profiles

in x, y, and z directions at three different angles: 0º, 45º and 90º, using the CMG® software and the numerical model.

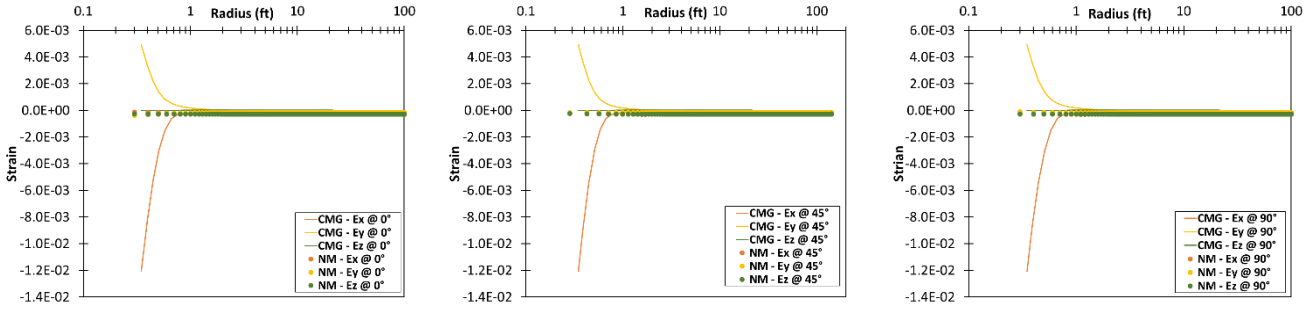

a. b. c.

Figure 5 – 56. Strain profiles for each direction at the early production for the two-phase and elastoplastic case under anisotropic horizontal stress conditions. a) Profiles at 0º. b) Profiles at 45º. c) Profiles at 90º.

Figure 5 – 57 presents the results of the elastoplastic model for the two-phase and plastic validation case under anisotropic horizontal stress conditions at early production (30 days) in terms of the stress profiles in x, y, and z directions at three different angles: 0º, 45º, and 90º, using the CMG® software and the numerical model.

Figure 5 – 58 presents the results of the elastoplastic model for the two-phase and plastic validation case under anisotropic horizontal stress conditions at early production in terms of the mean plastic strain profiles at three different angles: 0º, 45º and 90º, using the CMG® software and the numerical model.

Table 5 – 42 presents the root mean squared error to quantify the differences in displacements, strains, and stresses between the results of the CMG® software and the numerical model for the two-phase and elastoplastic validation case under anisotropic horizontal stress conditions.

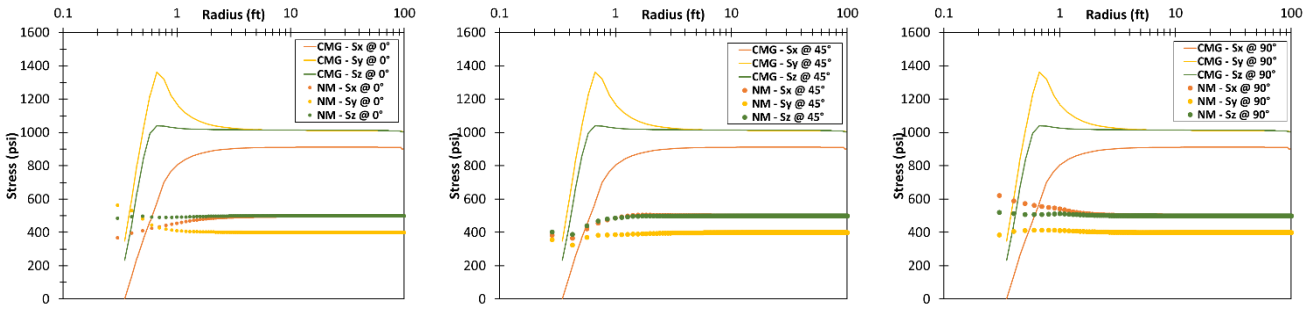

a. b. c.

Figure 5 – 57. Effective stress profiles for each direction at the early production for the two-phase and elastoplastic case under anisotropic horizontal stress conditions. a) Profiles at 0º. b) Profiles at 45º. c) Profiles at 90º.

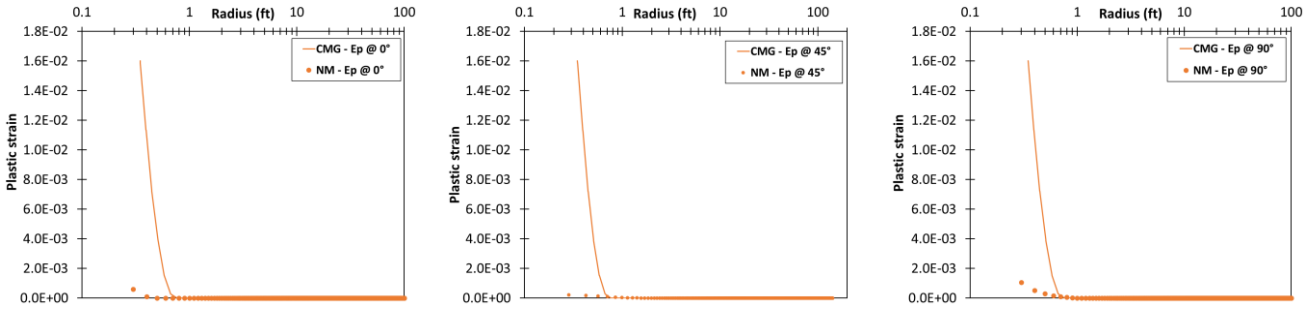

a. b. c.

Figure 5 – 58. Plastic strain profiles at the early production for the two-phase and elastoplastic case under anisotropic horizontal stress conditions. a) Profiles at 0º. b) Profiles at 45º. c) Profiles at 90º.

Table 5 – 42. Root mean squared error (RMSE) for displacements, strains, and stresses for the validation of the two-phase and elastoplastic case under anisotropic horizontal stress conditions.

RMSE		Displacement (ft)	Strain	Stress (psi)	Plastic strain
@ 0°	***x***	1.504E-02	5.049E-04	4.040E02	4.852E-04
	y	1.805E-03	2.508E-04	6.052E02	
	z	4.143E-03	2.777E-04	5.052E02	
@ 45°	***x***	1.046E-02	3.694E-04	3.391E02	4.952E-04
	y	6.325E-03	1.861E-04	5.096E02	
	z	3.486E-03	2.335E-04	4.249E02	
@ 90°	***x***	2.976E-04	5.016E-04	3.990E02	5.363E-04
	y	9.949E-03	2.423E-04	5.985E02	
	z	4.143E-03	2.777E-04	4.994E02	

Remark: The results of the two-phase and elastoplastic case under anisotropic horizontal stresses condition in terms of displacements follow the expected trend and the root mean square errors for displacement are small enough, errors less than 1.504E-02 ft; in terms of strains also follow the expected trend and the root mean square errors for strains are small enough, errors less than 5.049E-04; and in terms of stresses also follow the expected trend and present high differences qut root mean square errors of 605 psi. The results in terms of strain and stress at the boundary conditions, internal and external, are adequate showing that these conditions are well imposed. Similar to the isotropic case, the displacements in CMG® change insignificantly and their trend is not adequate, different behavior in the numerical simulator, adequate displacement trend; in CMG®, there is no difference between the isotropic and anisotropic case in terms of strains, the strains in x and y direction seems to be changed at 0° and the stresses have the same behavior at 90°. In general, the trends in geomechanical variables look better in the numerical model than in the CMG® software, with lower errorr in displacemnts and strains, especially in the plastic strain. In conclusion, the numerical model obtains results in terms of displacements and strains with a good approach and high differences in stresses.

Chapter 6. Results

This chapter presents the analysis of the results for the CHOPS wells using the coupled numerical simulator, a·3D-single well model built by coupling a multi-phase fluid flow model with an elastoplastic model and integrating a sand production model and a wormhole formation model. Field cases are run and their results are analyzed, and a sensitive study is performed to study the effect of massive sand production on production performance, evaluating the variables more implicated during cold production with sands. This section initiates with additional analysis that studies the effect of the foamy oil on production performance using data from a field case. Then, exploratory data analysis of the field data for sand production is presented.

6.1 Foamy-oil analysis

This section presents an analysis of the effect of foamy oil on production. The foamy-oil model adjusts the fluid flow component integrating three elements: (i) the fluid characterization changing the PVT properties for a foamy-oil crude; (ii) the relative permeability curves in terms of pressure; and (iii) the inflow performance as a foamy oil with three phases: dissolved gas, oil component, and entrained gas. The effect of these three elements is studied separately.

6.1.1 Effect of foamy oil on fluid properties

This section presents the analysis of the effect of foamy oil on fluid properties using the proposed model for foamy oil and data from Bare Field in the Hamaca Area located in the Orinoco Belt. This data corresponds to a typical extra-heavy oil reservoir that behaves in some areas as conventional oil and as foamy oil in others (De Mirabal, Rodriguez, & Gordillo, 1997). The purpose of this analysis is to compare the behavior of fluid as foamy oil and conventional oil and see the differences in PVT properties as density, solution GOR, formation volume factor, and viscosity. Table 6 – 1 presents the field case data used for this analysis.

Table 6 – 1. Bare Field data for analysis of the effect of foamy oil on fluid properties.

RESERVOIR PROPERTIES	VALUE
API gravity (°API)	8.1
Initial pressure reservoir (psi)	2000
Bubble-point pressure (psi)	1217.55
Pseudo-bubble-point pressure (psi)	913.16
Temperature (°R)	587
Reference temperature (°R)	520
Reference pressure (psi)	14.7
Gas-specific gravity (fraction)	0.587
Endpoint entrained gas fraction, α^{ref}	0

This study assumes an initial reservoir pressure of 2000 psi. Pseudo-bubble-point pressure and endpoint entrained gas fraction are assumed to be 913.2 psi and zero, respectively. The pseudo-bubble-point pressure is assumed 25% lower than the bubble-point pressure following Kamp, Heny, Andarcia, Lago, & Rodriguez (2001). The reference pressure and temperature are assumed to be at standard conditions.

The analytical model for foamy oil using the field data intends to explain the effect of the entrained gas in the crude. Figure 6 – 1 presents the variation of gas of the foamy oil model with pressure in both foamy oil and conventional oil, including flash gas fraction, entrained gas fraction, entrained-gas mass fraction, and entrained gas volume fraction. The black dashed line marks the pseudo-bubble point pressure.

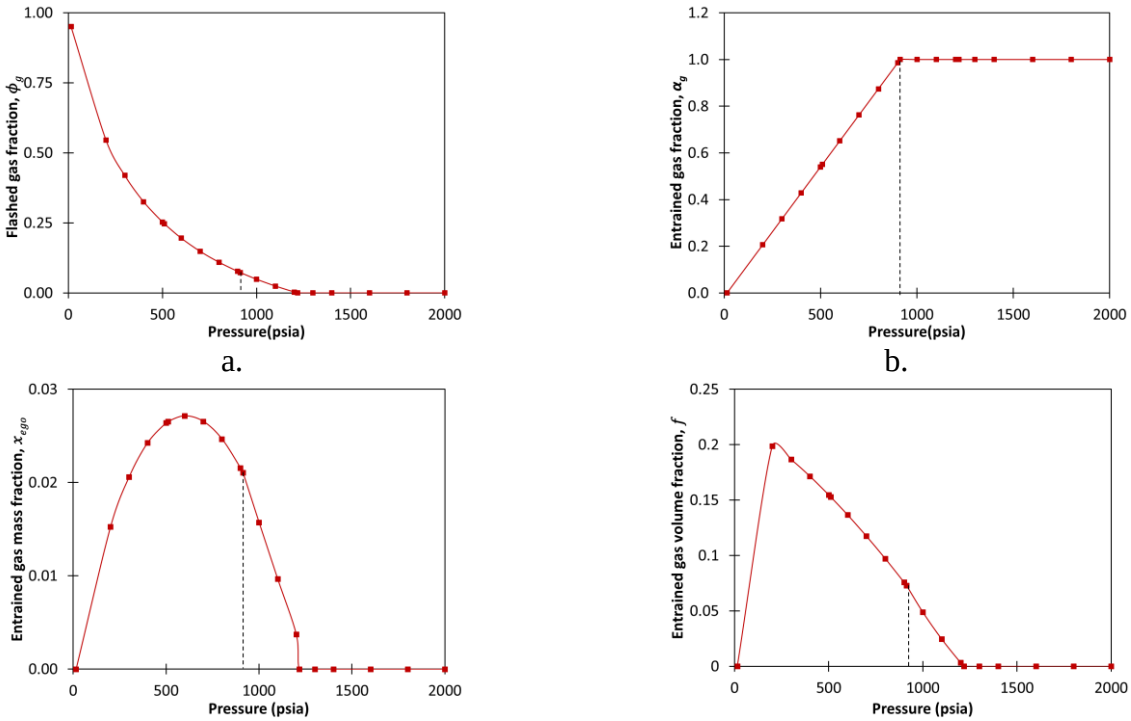

Figure 6 – 1. Variation of gas variables of the foamy oil model with pressure. a) Flashed gas fraction. b) Entrained-gas fraction. c) Entrained-gas mass fraction. d) Entrained-gas volume fraction.

Figure 6 – 1 (a) shows the flashed gas fraction (ϕ_g), in which the gas starts evolving from the solution when the pressure drops below the bubble-point pressure and the flashed gas fraction increases asymptotically. Figure 6 – 1 (b) shows the entrained-gas fraction (α_g), in which all the flashed gas is entrained between the bubble-point pressure and the pseudo-bubble-point pressure and decreases linearly with pressure below the pseudo-bubble-point pressure. Figure 6 – 1 (c) shows the entrained-gas mass fraction (x_{ego}) that starts from zero at bubble-point pressure and gets a maximum value between the pseudo-bubble-point pressure and the standard pressure, i.e., when the pressure drops below the pseudo-bubble-point pressure, the entrained-gas mass fraction decreases because it transfers to the free-gas phase. Figure 6 – 1 (d) shows the entrained gas volume fraction (f) that incrementally below pseudo-bubble point pressure responding to the compressibility of the entrained-gas bubbles, which increase in volume with a decrease in pressure and at lower pressures, the entrained-gas volume decreases while the bubbles transfer from the foamy oil to the free-gas phase. Below pseudo-bubble-point pressure, some fraction of entrained gas starts coalescing and becomes free gas. For conventional oils, the entrained-gas

mass fraction is generally zero because all the gas is liberated/flashed immediately and transfers directly into the free-gas phase.

Remark: Both the conventional oil and the foamy oil reach the bubble-point pressure with the same quantity of gas, the flashed gas, but its release depends on the entrained gas, which appears only in foamy oil delaying the gas transfer to the free-gas phase.

Figure 6 – 2 presents the variation of fluid properties with pressure for conventional oil and foamy oil, including solution gas-oil ratio, density, formation volume factor, and viscosity. The black dashed lines mark the pseudo-bubble point pressure and the bubble-point pressure.

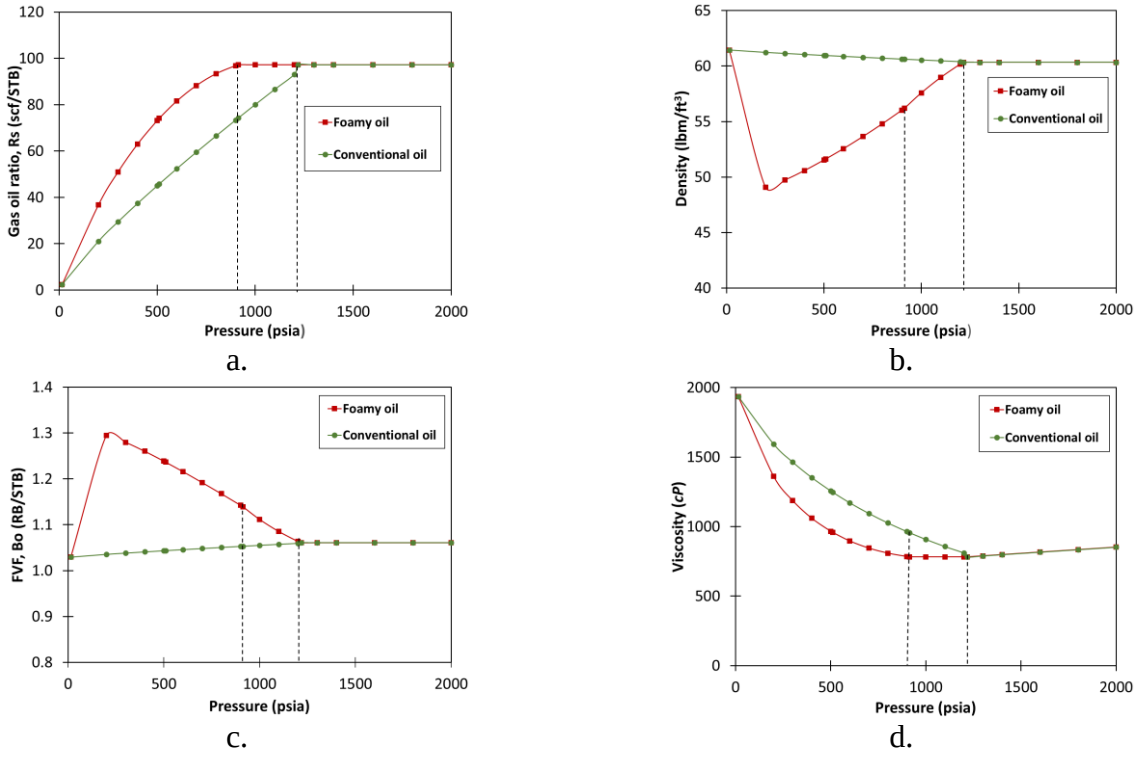

Figure 6 – 2. Fluid properties for conventional oil and foamy oil. a) Solution gas-oil ratio. b) Density. c) Formation volume factor. d) Viscosity.

Figure 6 – 2 (a) shows the solution gas-oil ratio that for foamy oil presents a constant value up to the pseudo-bubble point pressure even though this pressure is less than the bubble-point pressure responding to the delay in gas liberation. Figure 6 – 2 (b) shows density where the foamy-oil densities are lower than conventional-oil densities below the bubble-point pressure because of entrained gas with an inflection between the pseudo-bubble-point pressure and standard pressure responding to the entrained gas behavior in this section. Figure 6 – 2 (c) shows the formation volume factor as a mirror image of density because of the inverse relationship of the formation volume factor with density. Figure 6 – 2 (d) shows viscosity where the foamy-oil viscosities are lower than the conventional-oil viscosities below the bubble-point pressure with a constant value between the bubble-point pressure and the pseudo-bubble-point pressure and a significant reduction below the pseudo-bubble point.

Remark: Fluid properties for foamy oil are significant and positively affected by the presence of the entrained gas, which delays the solution gas up to the pseudo-bubble point, decreasing the density and viscosity and increasing the formation volume factor below the bubble-point pressure.

Knowing that the value of pseudo-bubble point pressure is an assumption for the analysis of this field case, a sensitivity study would allow the evaluation of the impact of this variable on fluid properties. Table 6 – 2 presents the values of pseudo-bubble-point pressure for the sensitivity study of the fluid properties, assuming the values from a percentage below the bubble-point pressure.

Table 6 – 2. Pseudo-bubble-pressure for the sensitivity study of the fluid properties.

% BELOW THE BUBBLE-POINT PRESSURE	VALUE
10 %	1095.795
25 %	913.162
35 %	791.407
50 %	608.775
70 %	365.265

Figure 6 – 3 presents the variation of gas of the foamy oil model with pressure for different pseudo-bubble point pressure, including flash gas fraction, entrained gas fraction, entrained-gas mass fraction, and entrained-gas volume fraction.

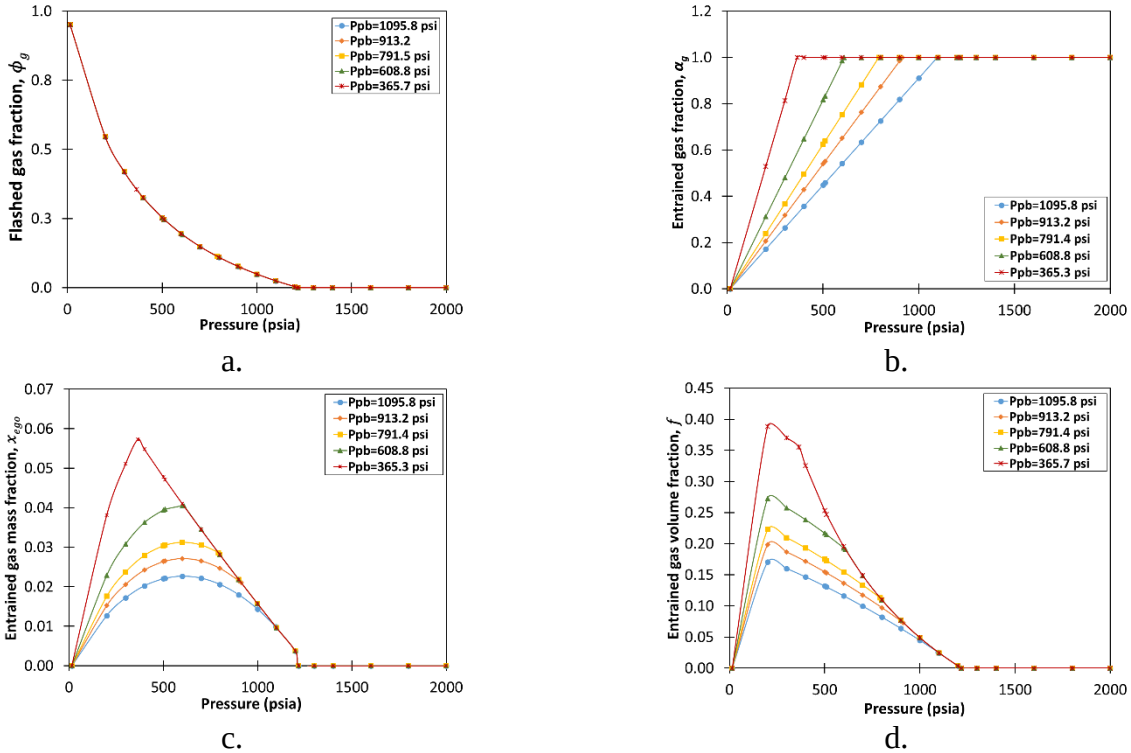

Figure 6 – 3. Variation of gas variables of the foamy oil model with pressure for different pseudo-bubble-point pressures. a) Flashed gas fraction. b) Entrained-gas fraction. c) Entrained-gas mass fraction. d) Entrained-gas volume fraction.

Figure 6 – 3 (a) shows the flashed gas fraction (ϕ_g) with no effect of pseudo-bubble-point pressure. Figure 6 – 3 (b) shows the entrained-gas fraction (α_g) with a lower value as the pseudo-bubble-point pressure is defined with a less percentage below the bubble-point pressure, i.e., this percentage defines the gas release delay: the lower percentage, the lower the gas release delay. Figure 6 – 3 (c) shows the entrained-gas mass fraction (x_{ego}) with a lower value as the pseudo-bubble-point pressure is defined with a less percentage below the bubble-point pressure, i.e., the lower percentage, the lower the entrained-gas mass fraction and the maximum value is less pronounced. Figure 6 – 3 (d) shows the entrained gas volume fraction (f) with a similar trend of the entrained-gas mass fraction, i.e., the lower percentage, the lower entrained gas volume fraction.

Remark: The pseudo-bubble point pressure has no impact on the flashed gas fraction. However, the closer the pseudo-bubble-point pressure is to the bubble-point pressure, the lower the entrained gas fraction will be and the shorter the gas release delay. The difference between the pseudo-bubble-point pressure and the bubble-point pressure defines the period of effect of the entrained gas on the fluid properties.

Figure 6 – 4 presents the variation of fluid properties with pressure for different pseudo-bubble pressure, including solution gas-oil ratio, density, formation volume factor, and viscosity. The black line represents conventional oil.

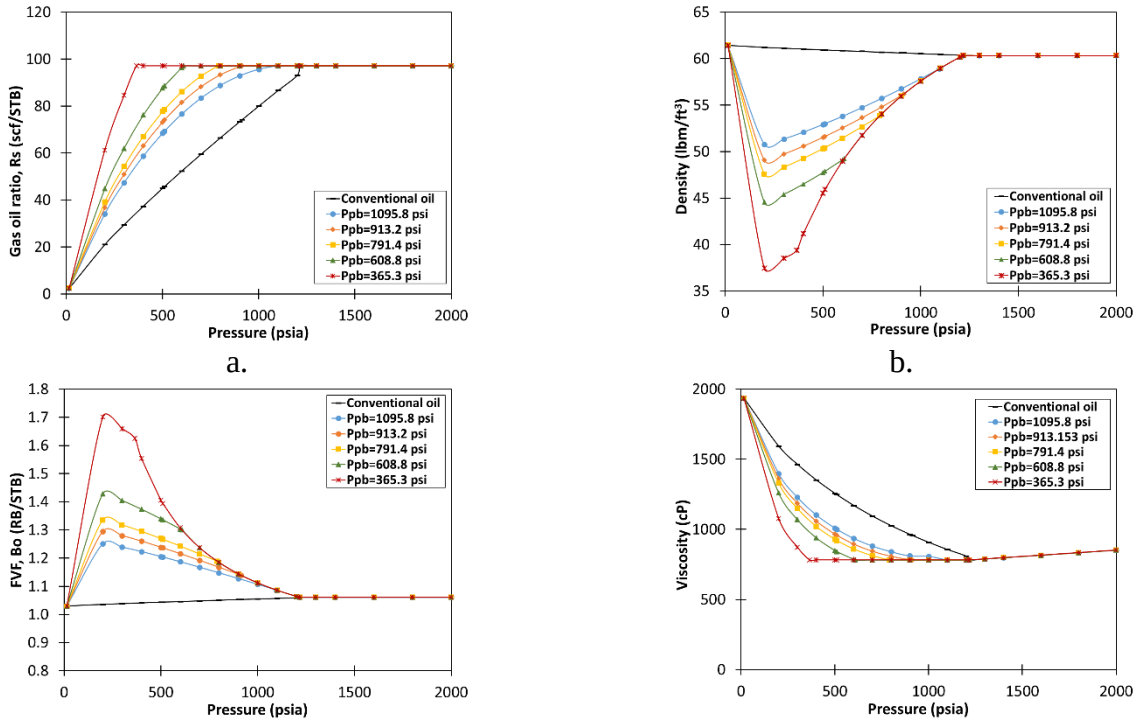

Figure 6 – 4. Fluid properties for conventional oil and foamy oil. a) Solution gas-oil ratio. b) Density. c) Formation volume factor. d) Viscosity.

Figure 6 – 4 (a) shows the solution gas-oil ratio, in which the holding constant value or delay depends on the pseudo-bubble point pressure, the lower gas-oil ratio as the pseudo-bubble-point pressure is defined with a less percentage below the bubble-point pressure, i.e., this percentage defines the gas

release delay: the lower percentage, the lower the gas release delay. Figure 6 – 4 (b) shows density where the higher density as the pseudo-bubble-point pressure is defined with a less percentage below the bubble-point pressure, i.e., the lower percentage, the higher density. Figure 6 – 4 (c) shows the formation volume factor as a mirror image of density because of the inverse relationship of the formation volume factor with density, i.e., the lower percentage, the lower the formation volume factor. Figure 6 – 4 (d) shows viscosity where the higher viscosity as the pseudo-bubble-point pressure is defined with a less percentage below the bubble-point pressure, i.e., the lower percentage, the higher viscosity.

Remark: The trend of the solution gas-oil ratio is very similar to the trend of the entrained gas fraction in terms of pseudo-bubble-point pressure. The closer the pseudo-bubble-point pressure is to the bubble-point pressure, the lower the entrained gas fraction will be and the shorter the gas release delay. The higher the entrained gas fraction, the higher the positive effect on fluid properties: lower densities and viscosities and higher formation volume factor.

6.1.2 Effect of foamy oil on relative permeability

This section presents the analysis of the effect of foamy oil on the relative permeability using the analytical model for foamy oil and compares these results with the results for conventional oil. For both cases, the well-known Corey relationship is used to generate the curve required. The input data for the relative permeability of the oil-gas system is presented in Table 6 – 3.

Table 6 – 3. Input data for relative permeability for the oil-gas system using the Corey relationship.

RESERVOIR PROPERTIES	VALUE
Connate water saturation, S_{wc}	0.00
Connate gas saturation, S_{ac}	0.02
Critical gas saturation, S_{acrit}	0.02
Irreducible oil saturation, S_{oira}	0.20
Residual oil saturation, S_{ora}	0.02
Oil exponent, n_{oa}	3
Gas exponent, n_a	3
Oil relative permeability at S_{ac}, k_{roaca}	1.00
Gas relative permeability at S_{lc}, k_{racl}	0.17

Figure 6 – 5 presents the relative permeability curves for the oil-gas system using the Corey relationship for conventional oil and foamy oil. The green lines represent the oil's relative permeability and the red lines represent the gas's relative permeability. The dark lines represent the relative permeability curves for the conventional oil and the light lines for the foamy oil. The oil relative permeability for foamy oil has higher values than conventional oil, while the gas relative permeability for foamy oil has lower values than conventional oil. These results are projected for production in more oil and less gas during foamy oil due to the entrained gas.

Remark: The effect of relative permeability curves in the production guarantees more oil and less gas between the pseudo-bubble point pressure and the bubble-point pressure, how much depends on how long is the gas release delay, which depends on the difference between these two pressures, the closer they are, the lower the foamy oil delay and lower effect in production.

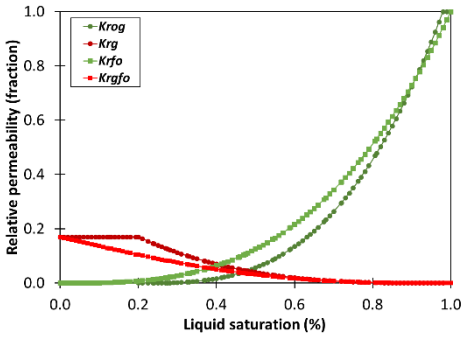

Figure 6 – 5. Relative permeability curves for the oil-gas system for conventional oil and foamy oil.

6.1.3 Effect of foamy oil inflow performance

This section intends to understand the combined effect of entrained gas due to the foamy oil on the fluid properties and the relative permeability curves. This is possible to view using Darcy's equation representing the foamy-oil velocity and the gas velocity as is seen in Equations (4 – 7) and (4 – 8). The oil's relative permeability increases due to the entrained gas and increasing foamy-oil velocity. Then the fluid viscosity decreases and the formation volume factor increases, which in the end implies an increment in the foamy-oil velocity. The gas's relative permeability decreases due to the gas trapping, delaying the gas release and reducing the gas velocity. Both effects enhance the inflow performance during the foamy oil. In conclusion, the presence of entrained gas influences significantly fluid properties such as solution GOR, density, formation volume factor, and viscosity, and a secondary effect is the relative permeability curves.

6.2 Data analysis of field data for sand production

This section presents the results of exploratory data analysis of the field data for sand production. The exploratory data analysis pretends to summarize the main characteristics of the field data using statistical graphics and other visualization methods and obtain relations between the variables and a preliminary understanding of the effect of these variables in sand production during cold heavy oil production with sands. Field data of different CHOPS wells is provided by a Canadian oil company. This data consists of daily and monthly production for oil, water, gas, and sand for 15 wells, and some basic reservoir characteristics such as depth, net pay, porosity, dead oil viscosity, and initial pressure.

6.2.1 Production performance

This section intends to understand the relationship between oil, water, and gas production and sand production using daily and monthly production and cumulative production data. The exploratory data analysis reviews the sanding on production performance using production graphs, boxplots, statistical descriptions, and a heat map. The boxplot is a standardized way of displaying the distribution of data based on a five-number summary: minimum value, first quartile [Q1], median, third quartile [Q3], and maximum value, and includes the outliers. The statistical description includes mean value, standard deviation, minimum and maximum values, and percentiles 25%, 50%, and 75%. A heat map is a data visualization technique that shows the magnitude of a phenomenon as color in two dimensions and determines essential relationships and characteristics amongst different points in a data set as well as the features of those data points; it is an easy way to summarize findings and main components. In this case,

the heat map states the relationships between daily production, monthly production, and cumulative production of oil, water, and gas to understand which would have more incidence on sand production.

Figure 6 – 6 shows the daily production of oil, water, gas, and sand for 15 CHOPS wells, including the boxplots. Table 6 – 4 presents the statistical description of daily production.

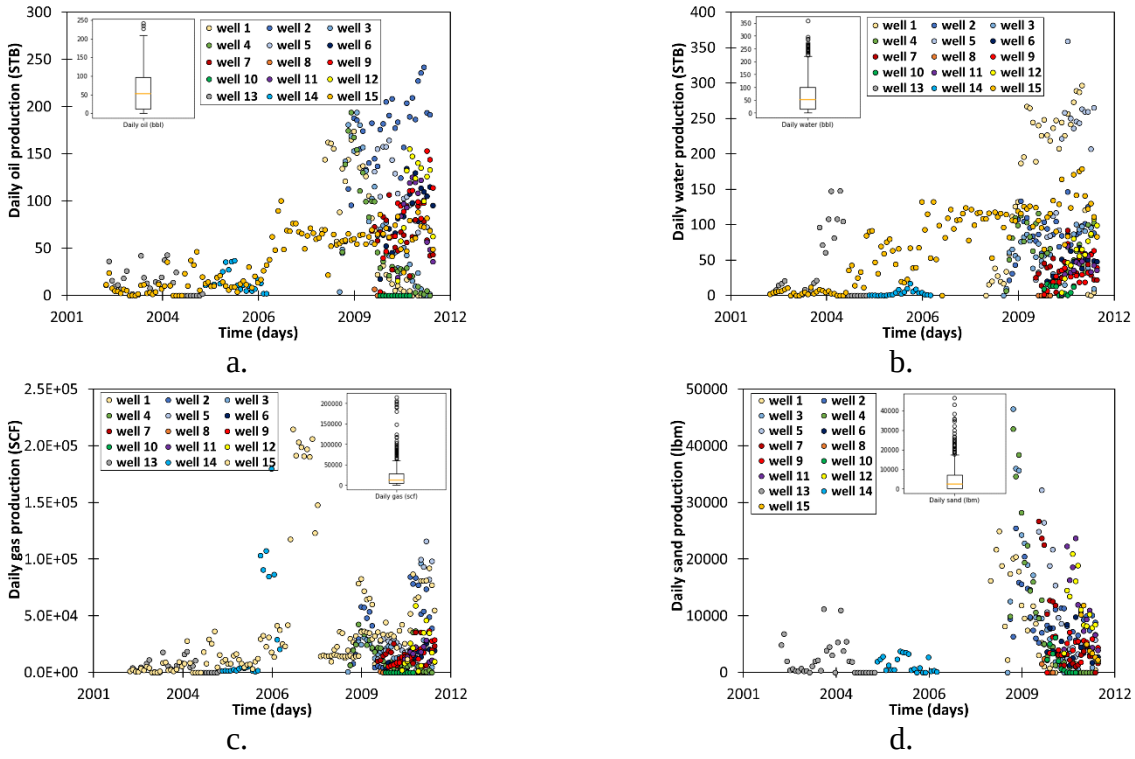

Figure 6 – 6. Daily oil production for CHOPS wells. a) Daily oil production. b) Daily water production. c) Daily gas production. d) Daily sand production.

Table 6 – 4. Statistical description for daily production.

	DAILY OIL (STB)	DAILY WATER (STB)	DAILY GAS (SCF)	DAILY SAND (lbm)
COUNT	424	424	424	424
MEAN	62.55	68.30	23711.12	5094.12
STD	56.81	67.70	35021.83	7574.47
MIN	0.00	0.00	0.00	0.00
25%	11.72	15.78	4540.46	0.00
50%	53.03	51.88	12758.85	2185.91
75%	97.70	99.13	27796.06	7101.35
MAX	241.90	358.80	214595.46	46537.33

Remarks: The daily oil production varies in the range of 0 to 242 STB, with a mean value of 62.55 STB; the daily water production varies in the range of 0 to 359 STB, with a mean value of 68.30 STB; the daily gas production varies in the range of 0 to 214595 SCF, with a mean value of 23711 SCF; and the daily sand production varies in the range of 0 to 45537 lbm, with a mean value of 5094 lbm. The daily production data has a relatively high standard deviation. The daily oil production has fewer outliers than daily water, daily gas, and daily sand production, which can be interpreted with fewer inconsistencies

and errors in the statistical processes. On average, a CHOPS well produces in a day about 63 STB of oil, a little more water, about 68 STB, 214595 SCF of gas, and 5094 lbm of sand.

Figure 6 – 7 shows the mean daily production of oil, water, gas, and sand for 15 CHOPS wells.

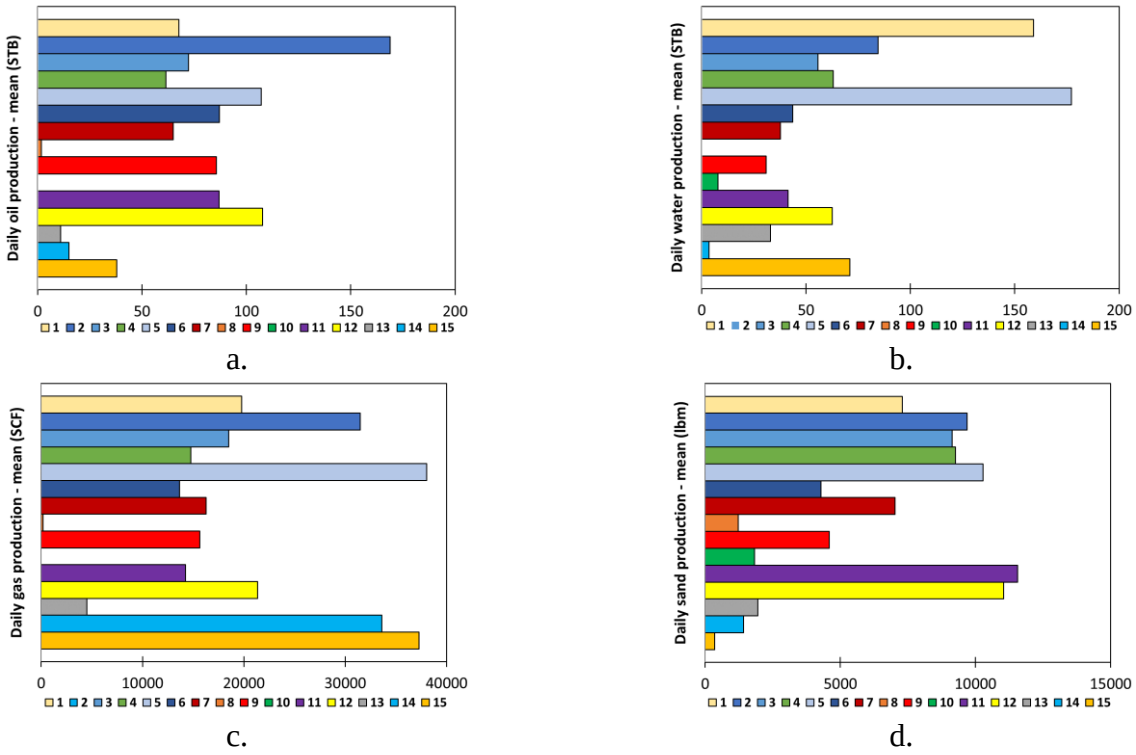

Figure 6 – 7. Mean daily production for CHOPS wells. a) Mean daily oil production. b) Mean daily water production. c) Mean daily gas production. d) Mean daily sand production.

Remarks: In general, the characteristics of the 15 CHOPS wells are very different in terms of the mean daily production. In terms of the mean daily oil production, well 2 is the most oil-producing well with 169 STB and well 10 does not produce any oil; in terms of the mean daily water production, well 5 is the most water-producing well with 177 STB and well 8 does not produce any water; in terms of the mean daily gas production, the well 5 is the most gas-producing well with 38016 SCF and well 10 does not produce any gas; and in terms of the mean daily sand production, the well 11 is the most sand-producing well with 11552 lbm and the well 15 is the less sand-producing well with 346 lbm. Well 10 is a strange case, it does not produce oil and gas, and produces water and sand.

Figure 6 – 8 shows the monthly production of oil, water, gas, and sand for 15 CHOPS wells, including the boxplot. Table 6 – 5 presents the statistical description of monthly production.

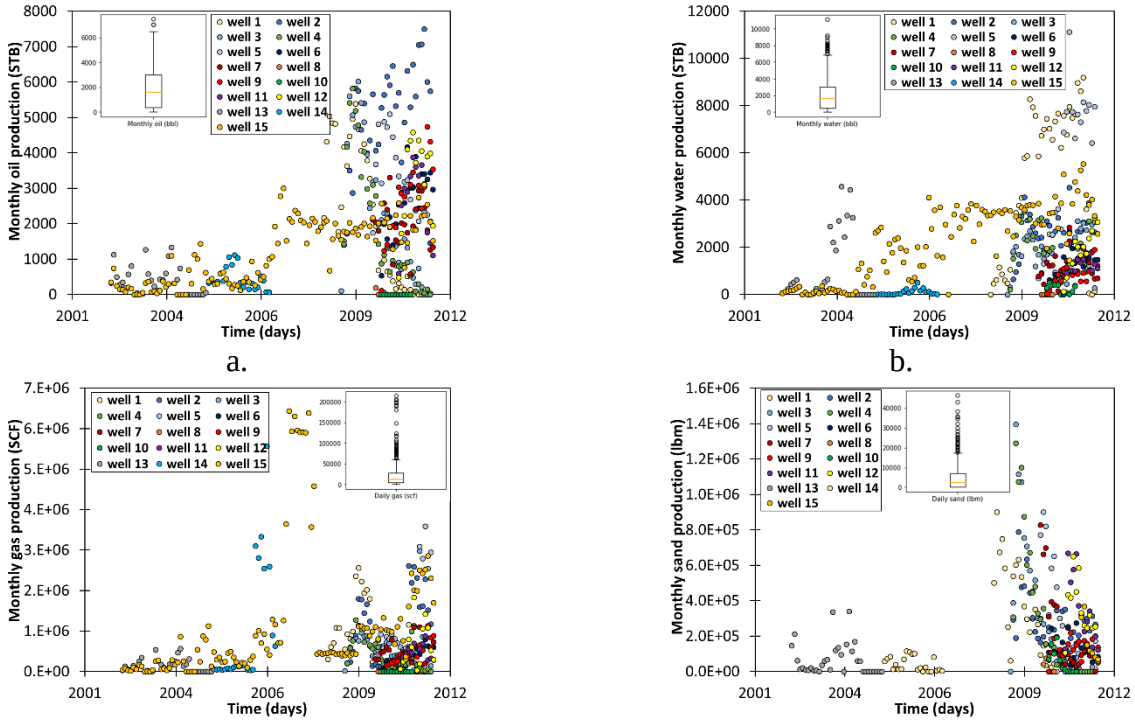

Figure 6 – 8. Monthly production for CHOPS wells. a) Monthly oil production. b) Monthly water production. c) Monthly gas production. d) Monthly sand production.

Table 6 – 5. Statistical description for monthly production.

	MONTHLY OIL (STB)	MONTHLY WATER (STB)	MONTHLY GAS (SCF)	MONTHLY SAND (lbm)
COUNT	424	424	424	424
MEAN	1903.99	2078.35	7.23E05	1.55E05
STD	1732.25	2061.48	1.07E06	2.30E05
MIN	0.00	0.00	0.00	0.00
25%	358.81	473.27	1.34E05	0.00
50%	1569.19	1597.49	3.96E05	6.45E04
75%	2992.16	3044.83	8.41E05	2.20E05
MAX	7498.78	11122.71	6.44E06	1.40E06

Remarks: The monthly oil production varies in the range of 0 to 7499 STB, with a mean value of 1904 STB; the monthly water production varies in the range of 0 to 11123 STB, with a mean value of 2078 STB; the monthly gas production varies in the range of 0 to 6.44 MMSCF, with a mean value of 723 MSCF; and the monthly sand production varies in the range of 0 to 1.4 MMlbm, with a mean value of 155 Mlbm. Similarly to daily production, the monthly production data has a relatively high standard deviation. The monthly oil production has fewer outliers than monthly water, monthly gas, and monthly sand production, which can be interpreted with fewer inconsistencies and errors in the statistical processes. On average, a CHOPS well produces in a month about 1904 STB of oil, a little more water, about 2078 STB, 723 MSCF of gas, and 155 Mlbm of sand.

Figure 6 – 9 shows the mean monthly production of oil, water, gas, and sand on a well basis for 15 CHOPS wells.

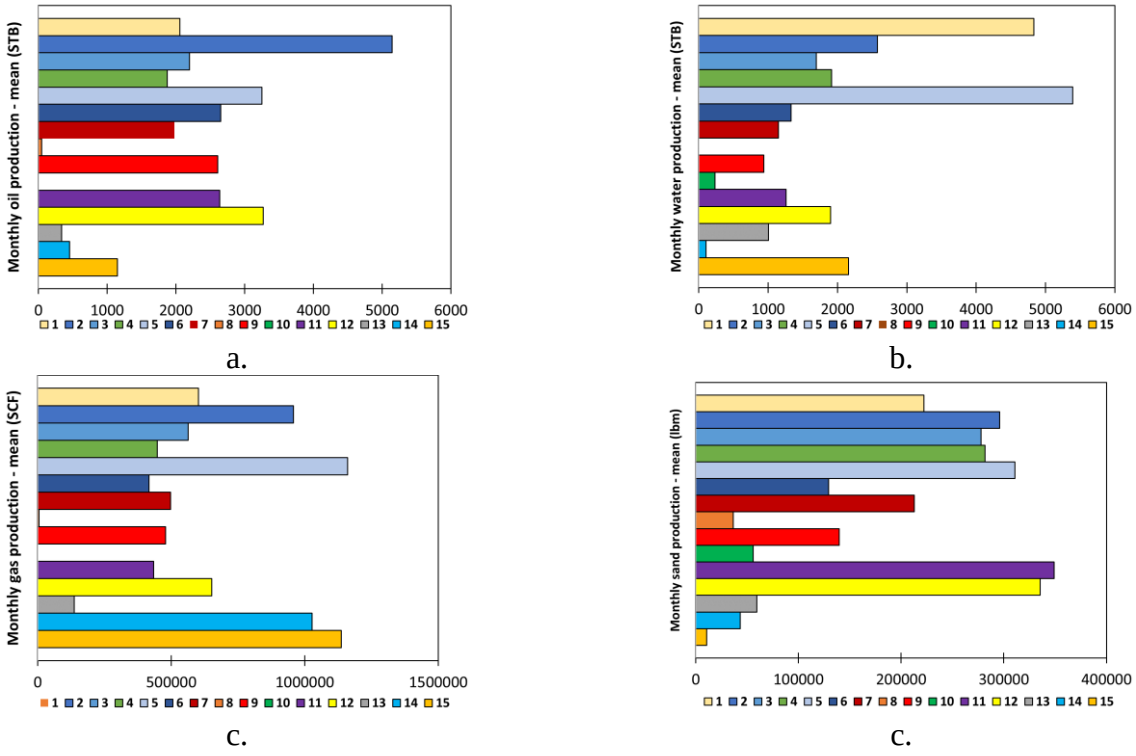

Figure 6 – 9. Mean monthly oil production for CHOPS wells. a) Mean monthly oil production. b) Mean monthly water production. c) Mean monthly gas production. d) Mean monthly sand production.

Remarks: Same as the mean daily production, the characteristics of the 15 CHOPS wells are very different in terms of the mean monthly production. In terms of the mean monthly oil production, well 2 is the most oil-producing well with 5147 STB and well 10 does not produce any oil; in terms of the mean monthly water production, well 5 is the most water-producing well with 5391 STB and well 8 does not produce any water; in terms of the mean monthly gas production, the well 5 is the most gas-producing well with 1.16 MMSCF and well 10 does not produce any gas; and in terms of the mean monthly sand production, the well 11 is the most sand-producing well with 349 Mlbm and the well 15 is the less sand-producing well with 10.58 Mlbm. Well 10 is a strange case, it does not produce oil and gas, and produces water and sand.

Table 6 – 6. Statistical description for cumulative production.

	CUMULATIVE OIL (STB)	CUMULATIVE WATER (STB)	CUMULATIVE GAS (SCF)	CUMULATIVE SAND (lbm)
COUNT	424	424	424	424
MEAN	36095.45	40981.12	1.78E07	2.92E06
STD	34097.87	55604.00	2.93E07	3.15E06
MIN	0.00	0.00	0.00	0.00
25%	7635.11	3040.11	1.92E06	0.00
50%	25796.06	18170.54	7.01E06	1.60E06
75%	57771.56	50691.96	1.53E07	5.27E06
MAX	159544.31	244281.27	1.28E08	9.17E06

The cumulative production is not properly field data but it is easily calculated from monthly production. Figure 6 – 10 shows the cumulative production of oil, water gas, and sand for 15 CHOPS wells. Table 6 – 6 presents the statistical description of cumulative production.

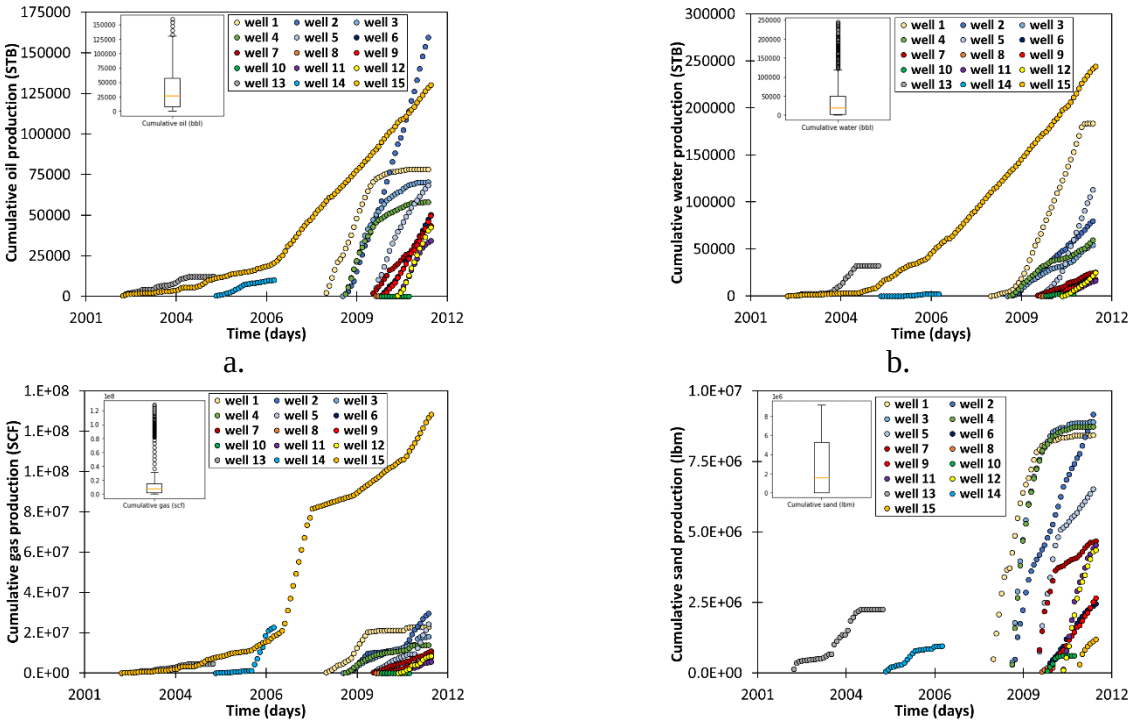

a. b. c. d.

Figure 6 – 10. Cumulative production for CHOPS wells. a) Cumulative oil production. b) Cumulative water production. c) Cumulative gas production. d) Cumulative sand production.

Remarks: The cumulative oil production varies in the range of 0 to 159544 STB, with a mean value of 36095.45 STB; the cumulative water production varies in the range of 0 to 244281 STB, with a mean value of 40981.12 STB; the cumulative gas production varies in the range of 0 to 128 MMSCF, with a mean value of 17.8 MMSCF; and the cumulative sand production varies in the range of 0 to 9.17 MMlbm, with a mean value of 2.92 MMlbm. Similarly to daily and monthly production, the cumulative production data has a relatively high standard deviation. The cumulative sand production and cumulative oil production have fewer outliers than cumulative water and cumulative gas production, which can be interpreted with fewer inconsistencies and errors in the statistical processes. On average, a CHOPS well produces about 36095 STB of cumulative oil, a little more water, about 40981 STB, 17.8 MMSCF of gas, and 2.92 MMlbm of sand.

Figure 6 – 11 shows the cumulative production of oil, water, gas, and sand on a well basis for 15 CHOPS wells. Table 6 – 7 presents the statistical description of cumulative production on a well basis for 15 CHOPS wells.

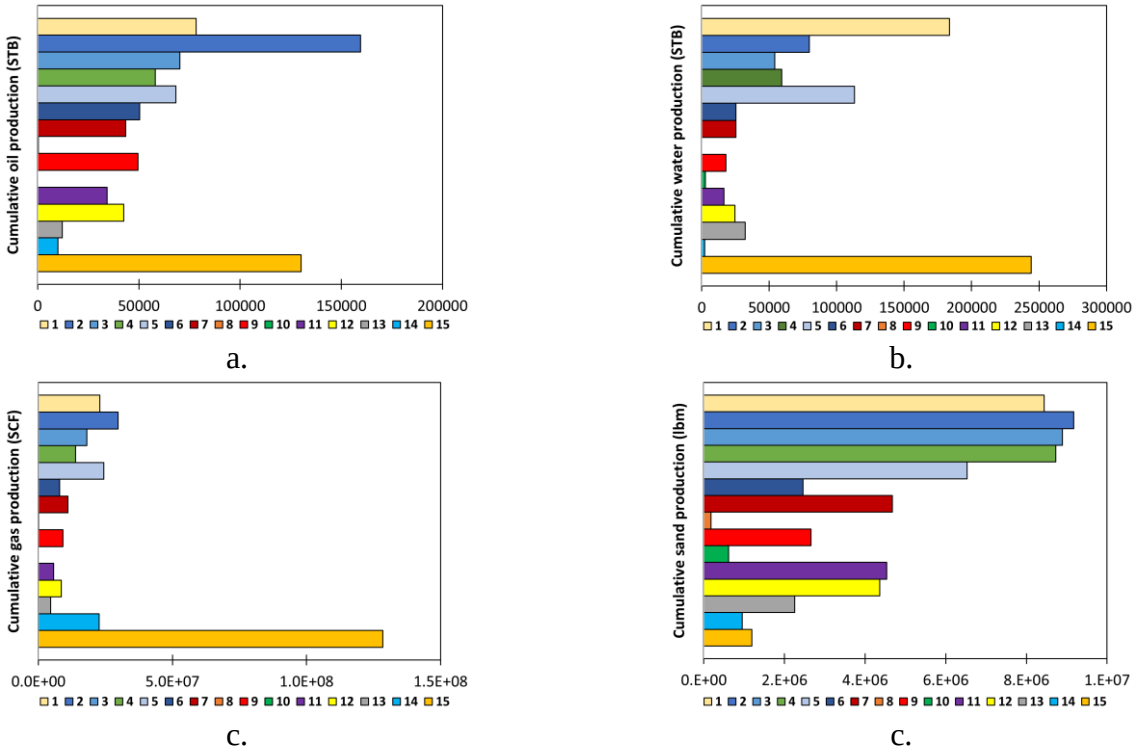

Figure 6 – 11. Cumulative production on a well basis for CHOPS wells. a) Cumulative oil production. b) Cumulative water production. c) Cumulative gas production. d) Cumulative sand production.

Table 6 – 7. Statistical description for cumulative production.

	CUMULATIVE OIL (STB)	CUMULATIVE WATER (STB)	CUMULATIVE GAS (SCF)	CUMULATIVE SAND (lbm)
COUNT	15	15	15	15
MEAN	53819.34	58748.13	2.04E07	4.38E06
STD	44847.47	71113.75	3.12E07	3.26E06
MIN	0.00	0.00	0.00	1.83E05
25%	23262.71	17124.63	6.77E06	1.73E06
50%	49595.88	25297.63	1.1E07	4.36E06
75%	69308.57	69608.26	2.28E07	7.48E06
MAX	159544.31	244281.27	1.29E08	9.17E06

Remarks: Same as the mean daily and monthly production, the characteristics of the 15 CHOPS wells are very different in terms of the cumulative production and all produce massive sand. In terms of cumulative oil production, well 2 is the most oil-producing well with 159544 STB and well 10 does not produce any oil; in terms of cumulative water production, well 15 is the most water-producing well with 244281 STB and well 8 does not produce any water; in terms of the cumulative gas production, the well 15 is the most gas-producing well with 128 MMSCF and well 10 does not produce any gas; and in terms of the mean monthly sand production, the well 2 is the most sand-producing well with 9.17 MMlbm and the well 8 is the less sand-producing well with 182 Mlbm. Well 10 is a strange case, it does not produce oil and gas, and produces water and sand. On average, a CHOPS well has a cumulative oil production of 53819 STB, a cumulative water production of 58.748 STB, a cumulative gas production of 20 MMSCF, and a cumulative sand production of 4.38 MMlbm. Well 2 is the most oil-producing well in terms of the three attributes of oil production (daily, monthly, and cumulative) and is the most sand-producing in terms of cumulative production, and well 15 is the most water and gas-producing in terms of cumulative

production although it is not the most water and gas-producing in terms of daily and monthly production, it is well 5. Well 11 is the most sand-producing well in terms of daily and monthly sand production.

Figure 6 – 12 shows the heat map for the production data. Although the heat map allows us to see all the relationships between the different attributes, sand production is the center of analysis.

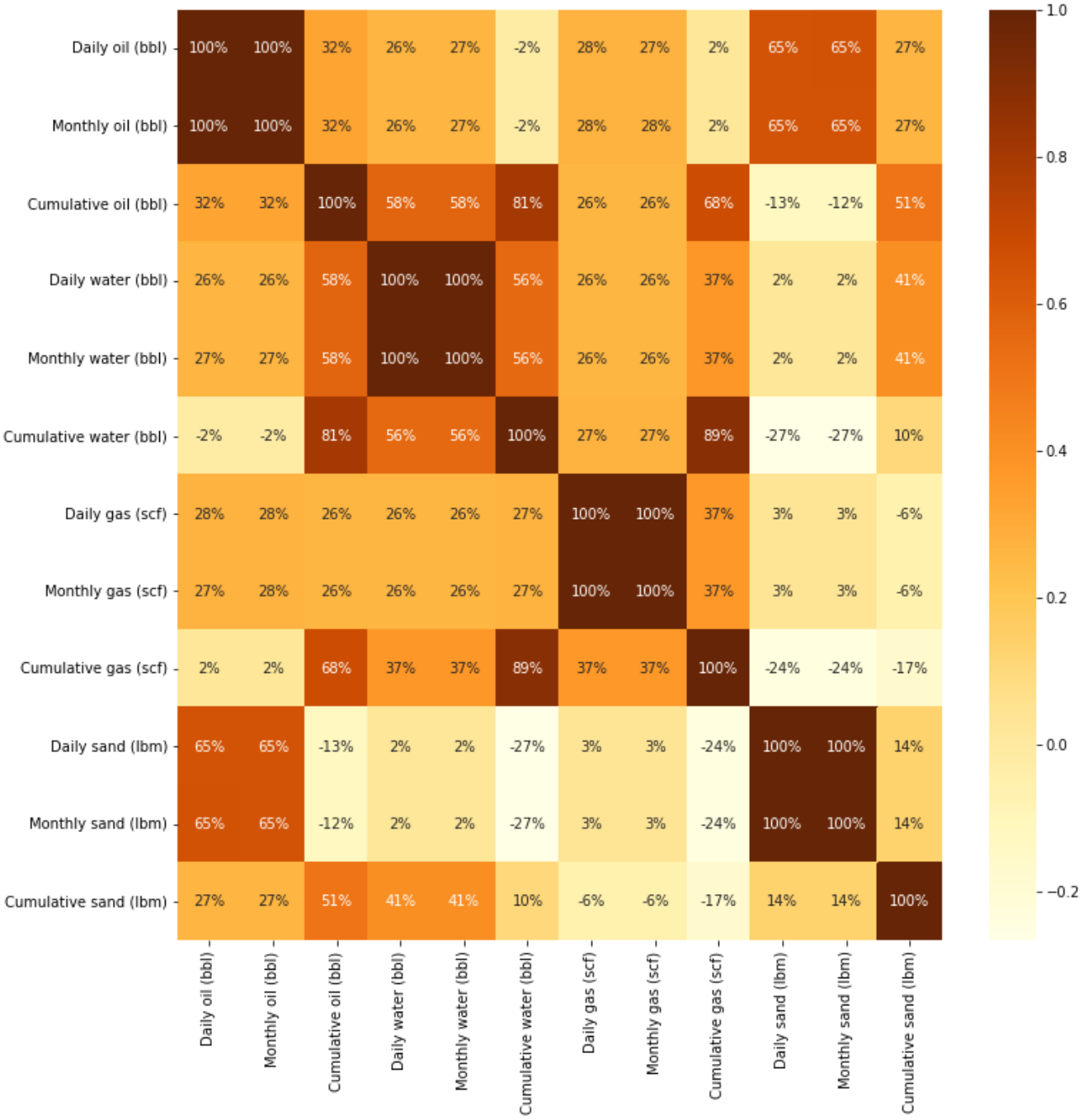

Figure 6 – 12. Heat map of production data for CHOPS wells.

Remarks: Sand production is stated in three attributes: daily, monthly, and cumulative production. The most influential attributes in sand production in terms of daily and monthly sand are daily and monthly oil production (65%), cumulative water production (-27%), and cumulative gas production (-24%), negative values that represent an inversely proportional relationship, the lower the water and gas cumulative production, the higher daily and monthly sand production. The most influential attributes in sand production in terms of cumulative sand production are cumulative oil production (51%) and daily and monthly water production (41%). Minor effects in other attributes such as cumulative water production (10%) and cumulative gas production (-17%). The higher the oil production, the higher the sand production, the oil production is the most influential attribute in sand production with a directly proportional relationship. However, oil production in terms of daily and monthly oil production has a minor influence on water production (26%) and gas production (27%), and in terms of cumulative oil production, the most influential attributes after sand are cumulative water production (81%) and cumulative gas production (68%). In conclusion, the wells with atypical behavior in production are well 10 which does not produce oil and gas, well 15 with the highest gas and water cumulative production and sand production just in the last 7 months, and well 8 with no water production and lowest sand production. Well 2 has the highest oil and highest cumulative sand production and well 11 has the highest daily and monthly sand production. Cumulative production could be the most reliable and more noticeable trend.

6.2.2 Reservoir characteristics

This section intends to understand the effect of the reservoir characteristics on sand production characteristics such as depth, net pay, porosity, oil viscosity, initial pressure, and production time. The exploratory data analysis to review the reservoir characteristics on sanding uses bar plots, statistical descriptions, and a heat map.

Figure 6 – 13 shows the reservoir characteristics on a well basis for 15 CHOPS wells. Table 6 – 8 presents the statistical description of reservoir characteristics on a well basis for CHOPS wells.

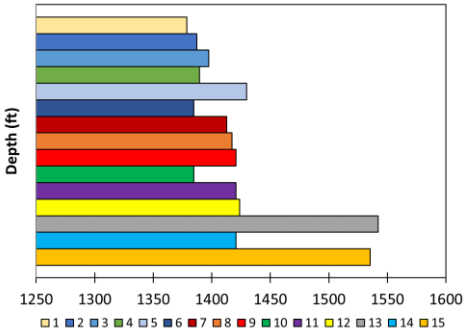

a.

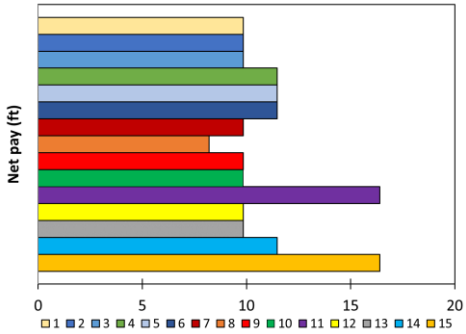

b.

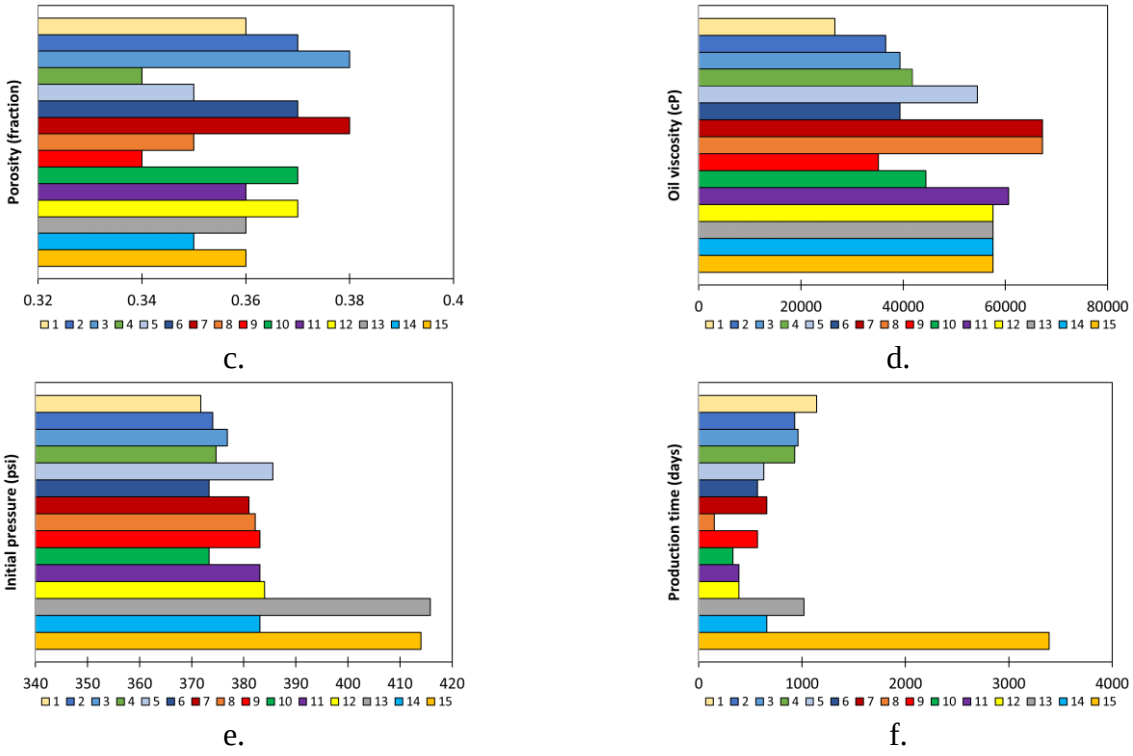

Figure 6 – 13. Reservoir characteristics for CHOPS wells. a) Depth. b) Net pay. c) Porosity. d) Oil viscosity. e) Initial pressure. f) Production time.

Table 6 – 8. Statistical description for reservoir characteristics.

	DEPTH (ft)	NET PAY (ft)	POROSITY (%)	OIL VISCOSITY (cP)	PRESSURE (psi)	PROD. TIME (days)
COUNT	15	15	15	15	15	15
MEAN	1422.97	11.04	36.00	49545.20	383.73	848.00
STD	50.00	2.36	1.31	12602.90	13.48	779.33
MIN	1378.61	8.20	34.00	26630.00	371.76	150.00
25%	1388.29	9.84	35.00	39370.00	374.37	330.00
50%	1417.32	9.84	36.00	54480.00	382.20	570.00
75%	1422.25	11.48	37.00	57560.00	383.53	930.00
MAX	1542.00	16.40	38.00	67240.00	415.82	3390.00

Remarks: In general, the reservoir characteristics of the 15 CHOPS wells are very similar and have low dispersion. In terms of depth, the values vary in the range of 1379 ft and 1542 ft, with a mean value of 1423 ft; the deepest well is well 13 and the shallowest well is well 1. In terms of net pay, the values vary in the range of 8.2 ft and 16.4 ft, with a mean value of 11.02 ft, and 8 wells with a value of 9.84 ft, 4 wells with a value of 11.48 ft and 2 wells with a value of 16.4 ft. In terms of porosity, the values vary in the range of 34% and 38%, with a mean value of 36%, 2 wells with values of 34%, 4 wells with values of 35%, and 3 wells with values of 36%. In terms of oil viscosity, the values vary in the range of 26630 cP and 67240 cP, with a mean value of 49545 cP, and the wells with the highest viscosity are wells 7 and 8 and the well with the lowest viscosity is well 1. In terms of initial pressure, the values vary in the range of 372 psi and 416 psi, with a mean value of 384 psi; the well with the highest pressure is well 13 and the well with the lowest pressure is well 1. In terms of production time, the values vary in the range of 150 days and 3390 days, with a mean value of 776 days, and the well with the longest production time is well 15 and the well with the shortest production time is well 8.

Figure 6 – 14 shows the heat map for the reservoir characteristics data. In this case, the heat map states the relationships between reservoir characteristics and oil, water, and gas cumulative production to understand which would have more incidence in sand production.

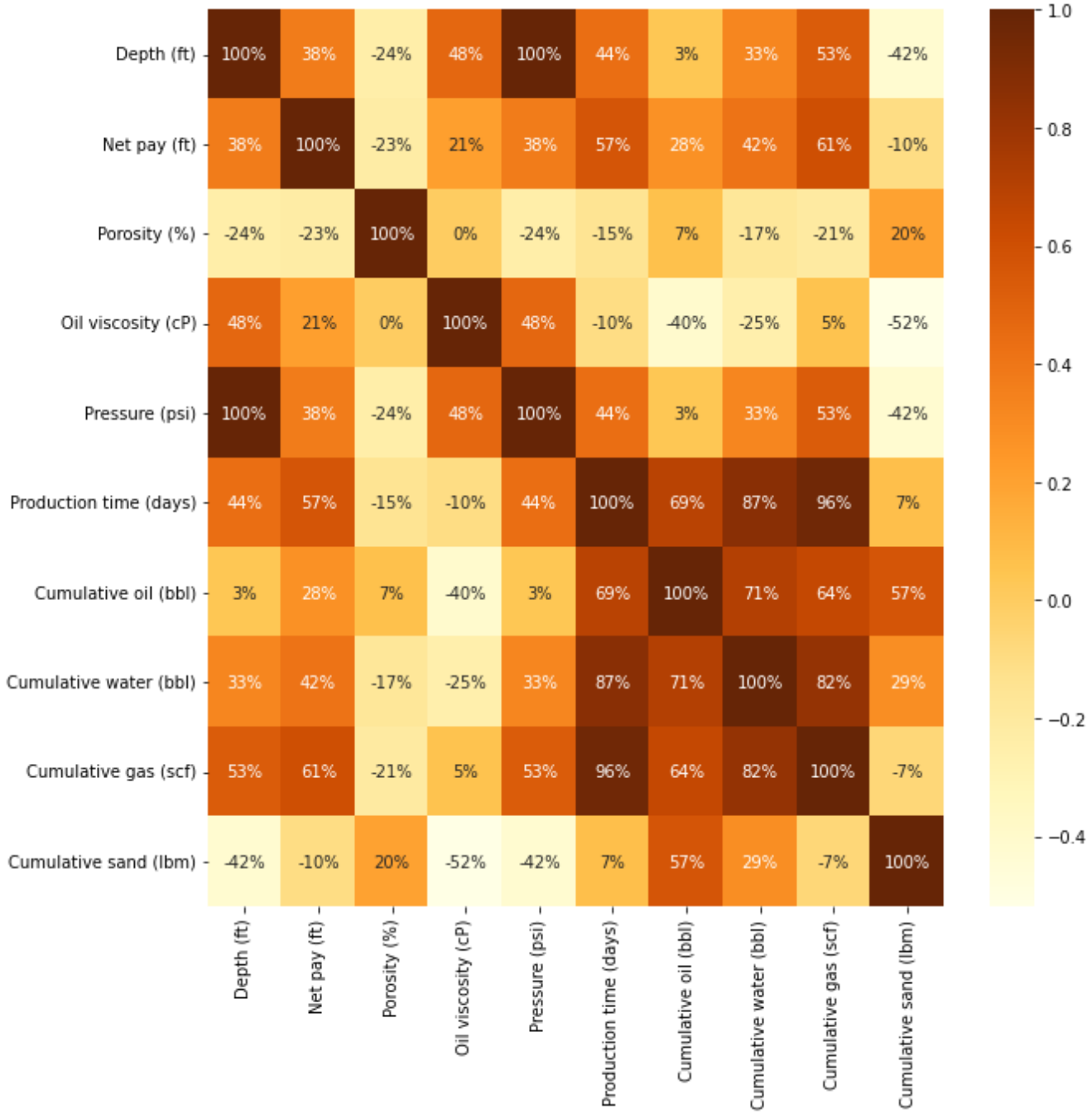

Figure 6 – 14. Heat map of reservoir characteristics for CHOPS wells.

Remarks: Sand production is stated in terms of cumulative sand production. The most influential attributes of sand production are cumulative oil production (57%), oil viscosity (-57%), and depth and pressure (-42%). Minor impact in other attributes such as cumulative water production (29%), porosity

(20%), production time (7%), and net pay (-10%), cumulative gas production (-7%). The higher the oil production, the higher the sand production, and the lower the oil viscosity, the higher the sand production; depth and pressure have an inverse but equal effect, so deeper wells have higher pressure and lower sand production. In conclusion, the oil production and oil viscosity are the most influential attributes on sand production.

6.2.3 Oil production and sand production

This section intends to confirm the strong relationship between oil production and sand production in terms of cumulative production. Figure 6 – 15 shows the cumulative oil production vs. cumulative sand production for the 15 CHOPS wells.

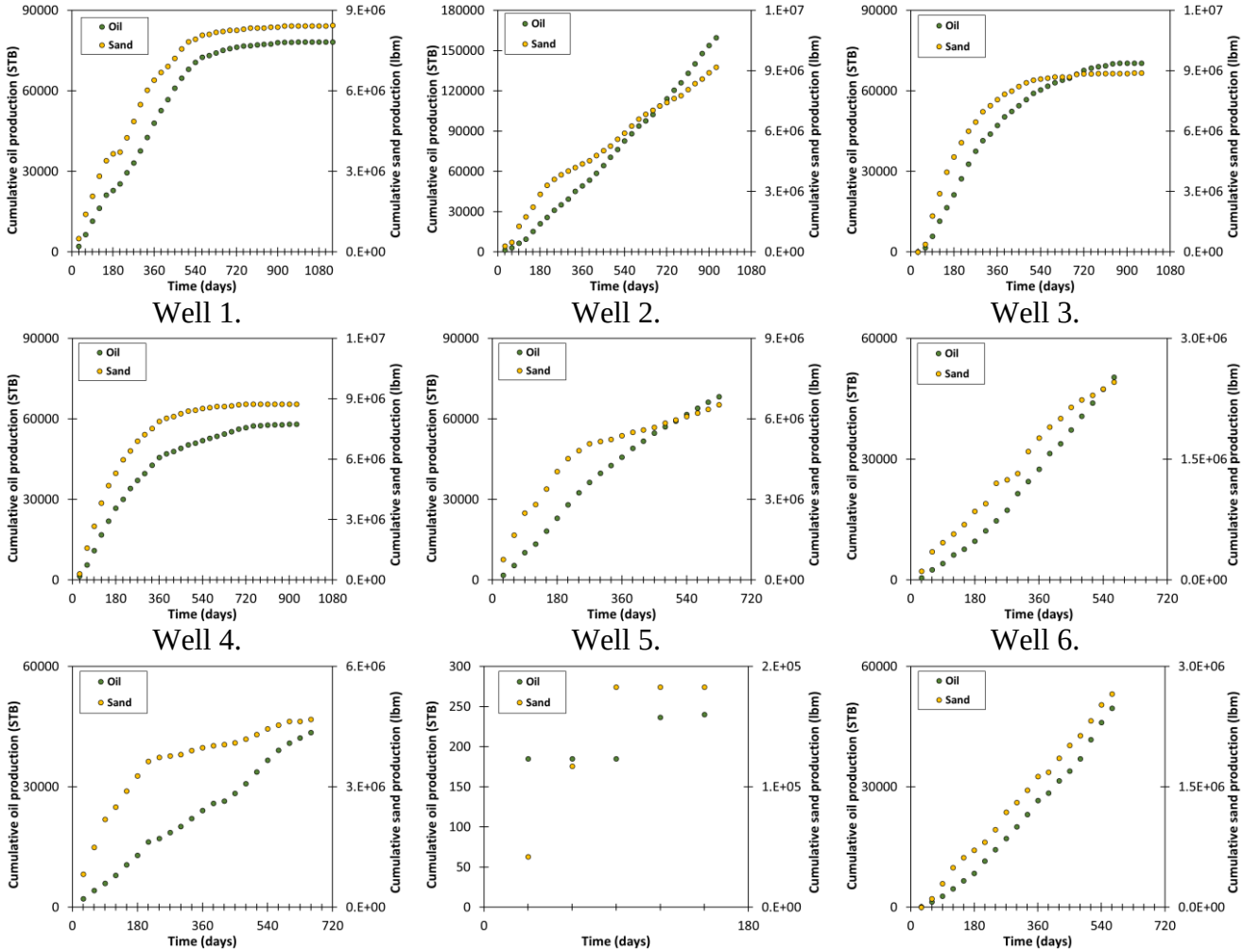

Well 1. Well 2. Well 3.

Well 4. Well 5. Well 6.

Well 7. Well 8. Well 9.

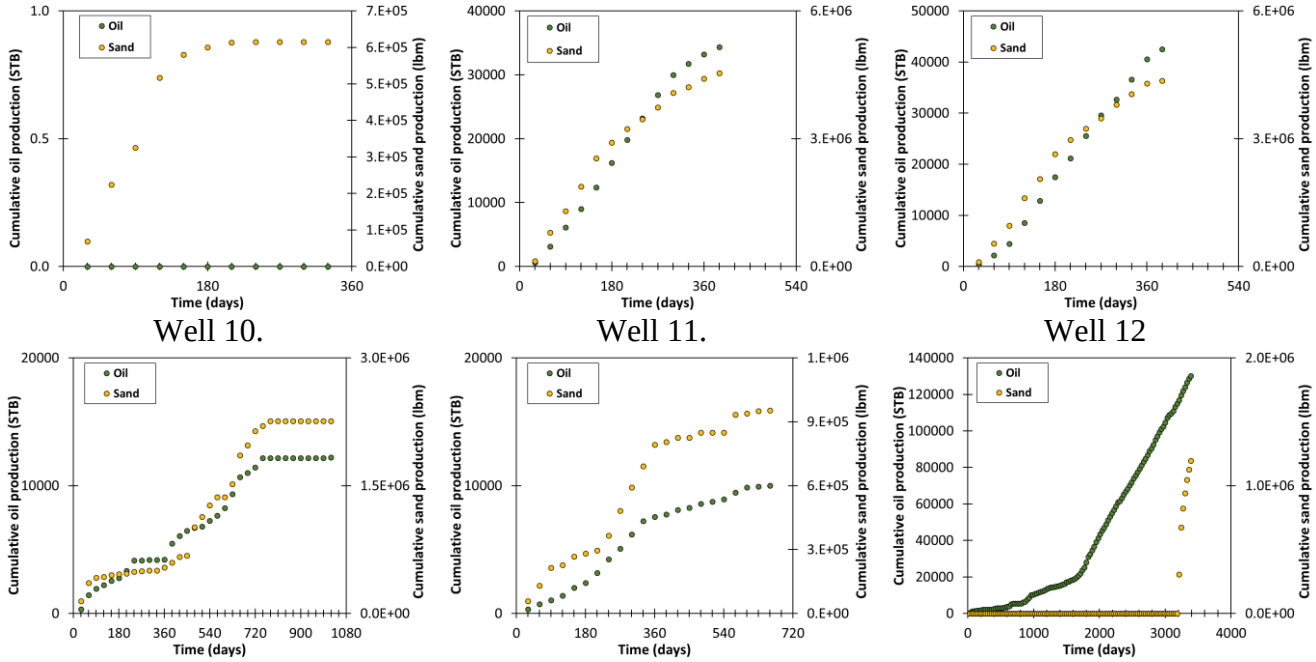

Well 10. Well 11. Well 12

Well 13. Well 14. Well 15.

Figure 6 – 15. Oil production vs. sand production for CHOPS wells.

Remarks: In general, cumulative sand production follows the trend of cumulative oil production. Also, these graphs help to identify the rare behavior in terms of production including sand production of some wells such as well 8, well 10, and well 15, which are not representative of this data of CHOPS wells. These two variables, cumulative oil production, and cumulative sand production are adequate to study the simulation process of wells during cold heavy oil production with sand.

6.3 Sand production on productivity

This section presents the results of the study of sand production during cold heavy oil production with sands on productivity. The study initially with the simulation of sand production using field data comparing in terms of oil production and sand production and then study the effect of the sand production on production performance using a base case and a sensitivity study of the variables with more impact such as the stresses.

6.3.1 Simulation of sand production using the field data

This section tried to calibrate the sand production model using the field data but this data is not complete in terms of the reservoir variables and there would be too many variables to adjust. The permeability is not specifically defined, for all wells are in the range of 0.5 to 4 Darcies. Thus, the strategy consists to run the new simulator with three field cases selected from the exploratory data analysis and compare the results with the field data to have values for the variables of the sand production model: correlation slope and critical values of the equivalent plastic stain.

Three types of CHOPS well are stated from the field data assuming reservoir properties from the mean features of unconsolidated sandstones (Dusseault, 2002) presented in Table 2 – 1. The characteristics of

the reservoir of the three field cases are summarized in Table 6 – 9, the production schedule considers a pressure drawdown of 10 psi every 30 days and is presented in Table 6 – 10, and Figure 6 – 16 presents the relative permeability curve for the oil-water system. The three field cases are set as a three-layer under isotropic horizontal stress conditions.

Table 6 – 9. Field case for calibration.

RESERVOIR CHARACTERISTICS	TYPE 1	TYPE 2	TYPE3
Reference well	13	14	11
Depth (ft)	1542	1421	1421
Wellbore radius (in)	2.5	2.5	2.5
Reservoir radius (ft)	100	100	100
Reservoir thickness (ft)	10	12	16
Reservoir pressure (psi)	416	383	383
Temperature (°F)	150	150	150
Porosity (fraction)	0.36	0.35	0.36
API Gravity (°API)	15	15	15
Gas-specific gravity (fraction)	0.7	0.7	0.7
Bubble point pressure (psi)	100	100	100
Oil saturation (fraction)	0.85	0.85	0.85
Water saturation (fraction)	0.15	0.15	0.15
Gas saturation (fraction)	0.00	0.00	0.00
Biot (fraction)	1.0	1.0	1.0
Young modulus (psi)	1.0E06	1.0E06	1.0E06
Poisson ratio (fraction)	0.25	0.25	0.25
Cohesion (psi)	250	250	250
Internal friction angle (°)	15	15	15
Dilation angle (°)	15	15	15

Table 6 – 10. Production program for calibration.

PRODUCTION TIME (days)	WELLBORE PRESSURE (psi)		
	TYPE 1	TYPE 2	TYPE3
30	406	373	373
60	396	363	363
90	386	353	353
120	376	343	343
150	366	333	333
180	356	323	323
210	346	313	313
240	336	303	303
270	326	293	293
300	316	283	283
330	306	273	273

Figure 6 – 17 presents the cumulative oil production and cumulative sand production for three field cases for a production time of 330 days using a permeability of 0.5 Darcies and different values of the correlation slope according to the field case for three different critical equivalent plastic strain ϵ_{cr}^{ps}. These figures allow the evaluation of the impact of the correlation slope. Table 6 – 11 summarizes the cumulative oil and sand production for the three field cases using different critical equivalent plastic strains and different correlation slopes. When the critical equivalent plastic strain is zero, it is sought to take the sand production to an extreme where the sand is produced where there is plasticity.

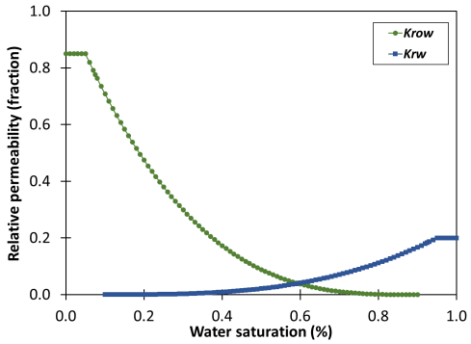

Figure 6 – 16. Relative permeability for the oil-water system for calibration.

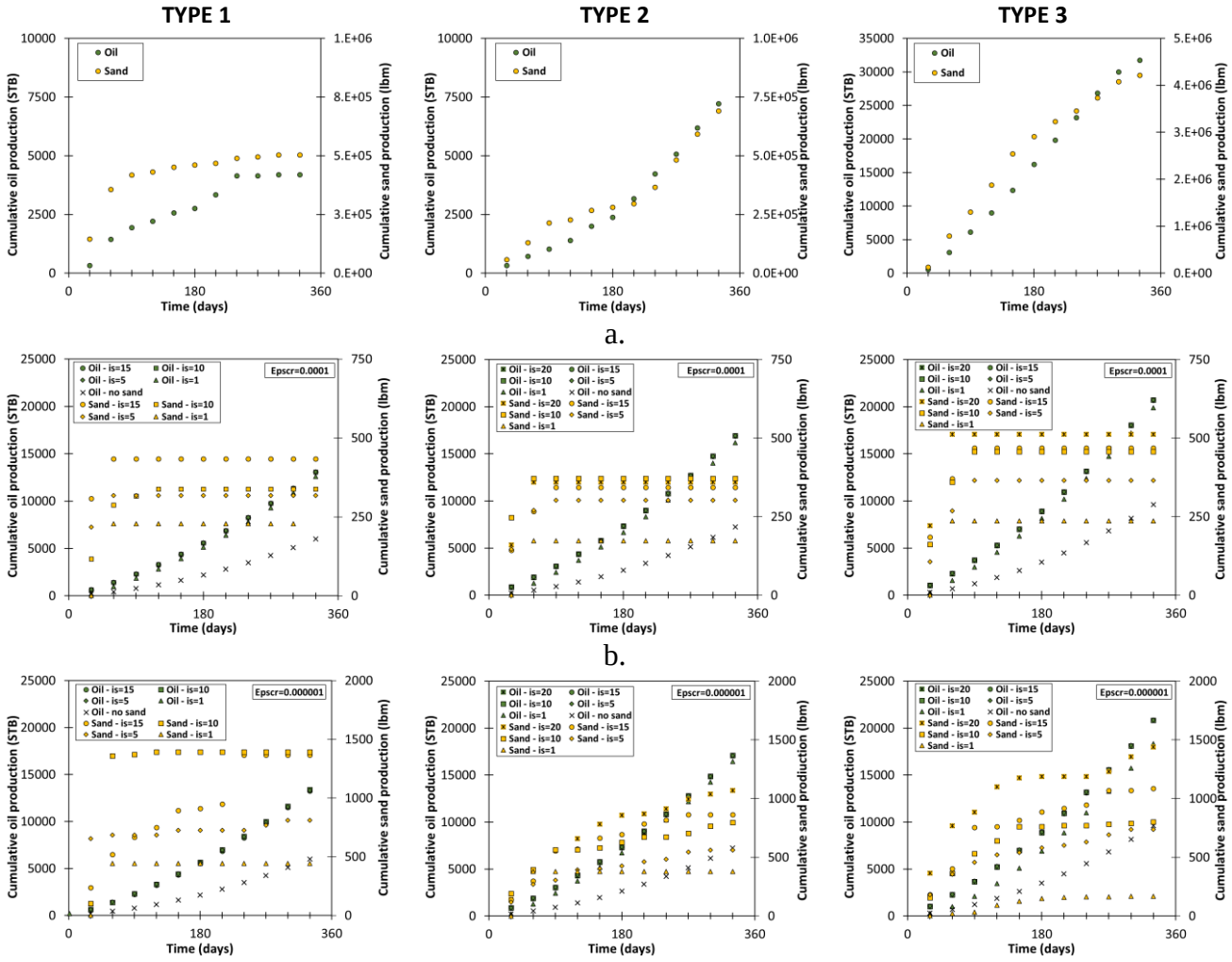

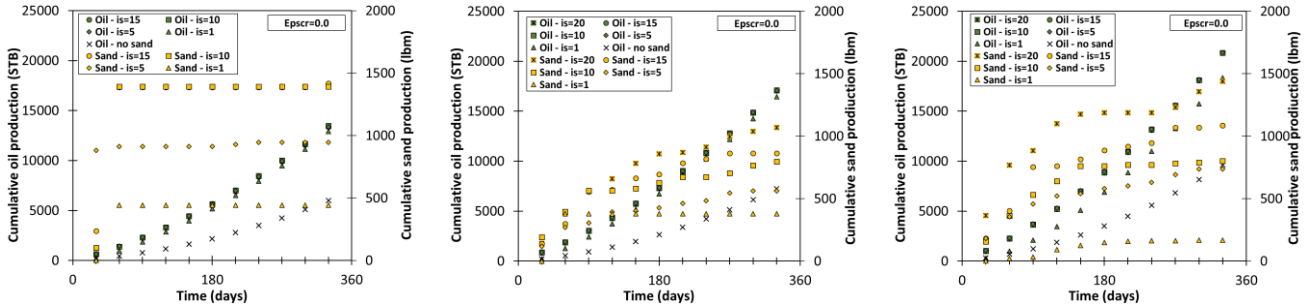

d

Figure 6 – 17. Cumulative oil production and cumulative sand production for the three field cases – sensitivity study for the correlation slope. a) Field data. b) $\epsilon_{cr}^{ps} = 0.0001$. c) $\epsilon_{cr}^{ps} = 0.000001$. d) $\epsilon_{cr}^{ps} = 0.0$.

Remarks: To begin with, it is clear that the sand production model does not allow obtaining the sand level typical of CHOPS wells. It is not possible to use higher values of the correlation slope than those considered because the simulator is not stable and does not guarantee the results, which would be the only thing that would increase the amount of sand produced. However, the results of the model will be reviewed in terms of oil and sand production to evaluate the effect of sand production on oil production.

For well Type 1 (well 13), the cumulative oil production with no sand in simulation is higher at 1811 STB compared to the field data, being the lowest possible permeability for CHOPS wells. The production potential from the simulation is considered to be above the potential from field data. The cumulative oil production is more than double considering sand, so the level of oil production considering sand is similar for the different values of correlation slope and increases slightly as the critical value of equivalent plastic strain is reduced. The produced sand is around 1400 lbm. To get the maximum amount of sand, the correlation slope can be stated in a value of 15 with a critical value of the equivalent plastic strain of 0.000001. This well presents a particular characteristic, which is that the sand production does not increase during the production time, but rather at the second simulation time it reaches its maximum value and stops producing sand.

For well Type 2 (well 14), the cumulative oil production with no sand in simulation is close to the field data. The production potential from the simulation is similar to the potential from field data. The cumulative oil production is more than double considering sand, so the level of oil production considering sand is similar for the different values of correlation slope and increases slightly as the critical value of equivalent plastic strain is reduced. However, the results for the critical value of the equivalent plastic strain in 0.000001 and 0.0 are the same. The produced sand is around 1079 lbm. To get the maximum amount of sand, the correlation slope can be stated in a value of 20 with a critical value of the equivalent plastic strain of 0.000001.

For well Type 3 (well 11), the cumulative oil production with no sand in simulation is lower at 22135 STB compared to the field data, so it should be considered to use a higher value of permeability to get a similar production potential. This cumulative oil production is more than double considering sand, so the level of oil production considering sand is similar for the different values of correlation slope and increases slightly as the critical value of equivalent plastic strain is reduced. However, the results for the critical value of the equivalent plastic strain of 0.000001 and 0.0 are the same. The produced sand is around 1440 lbm. To get the maximum amount of sand, the correlation slope can be stated in a value of 20 with a critical value of the equivalent plastic strain of 0.000001.

Comparing the productivity of the three wells, well Type 3 is the largest oil producer, and well Type 1 is the lowest oil producer. Regarding sand production, well Type 2 and well Type 3 have the same level, while well Type 2 is the lowest sand producer. For all three wells, oil production more than doubles with sand production. The simulation results are consistent with field data. However, the well Type 3 requires approaching the oil potential by increasing its permeability. For the same well, all cases are at the same level of cumulative oil production, although the highest correlation slope obtains the highest sand production, and does not get the highest cumulative oil production. This can be explained by the fact that there is a kind of limit value from which the increase in sand production is not significant.

Table 6 – 11. Cumulative oil and sand production for the three field cases.

	CRITICAL EPS	CORRELATION SLOPE	CUMULATIVE OIL (STB)	CUMULATIVE SAND (lbm)
Type 1 (well 13)	Field data	-	4192	503818
	no sand	no sand	6003	0
	0.001	15	13075	433
		10	13073	338
		5	13101	318
		1	12593	229
	0.000001	15	13261	1365
		10	13400	1392
		5	13304	810
		1	12907	444
	0.0	15	13354	1418
		10	13472	1392
		5	13360	945
		1	12909	444
Type 2 (well 14)	Field data	-	7226	690965
	no sand	no sand	7234	0
	0.001	20	16896	361
		15	16904	343
		10	16934	371
		5	16935	303
		1	16185	174
	0.000001	20	17049	1069
		15	17068	863
		10	17103	796
		5	17073	562
		1	16452	379
	0.0	20	17049	1069
		15	17068	863
		10	17103	796
		5	17073	562
		1	16454	379
Type 3 (well 11)	Field data	-	31741	4214465
	no sand	no sand	9606	0
	0.001	20	20689	512
		15	20704	468
		10	20722	457
		5	20717	366
		1	19899	237
	0.000001	20	20842	1440
		15	20825	1085
		10	20842	802
		5	20869	737
		1	18345	169
	0.0	20	20841	1440
		15	20825	1086
		10	20842	802
		5	20869	737
		1	18345	169

Figure 6 – 18 presents the cumulative oil production and cumulative sand production for three field cases for a production time of 330 days using a permeability of 0.5 Darcies and three different critical equivalent plastic strains for every value of correlation slope. These figures allow the evaluation of the impact of the critical value of the equivalent plastic strain.

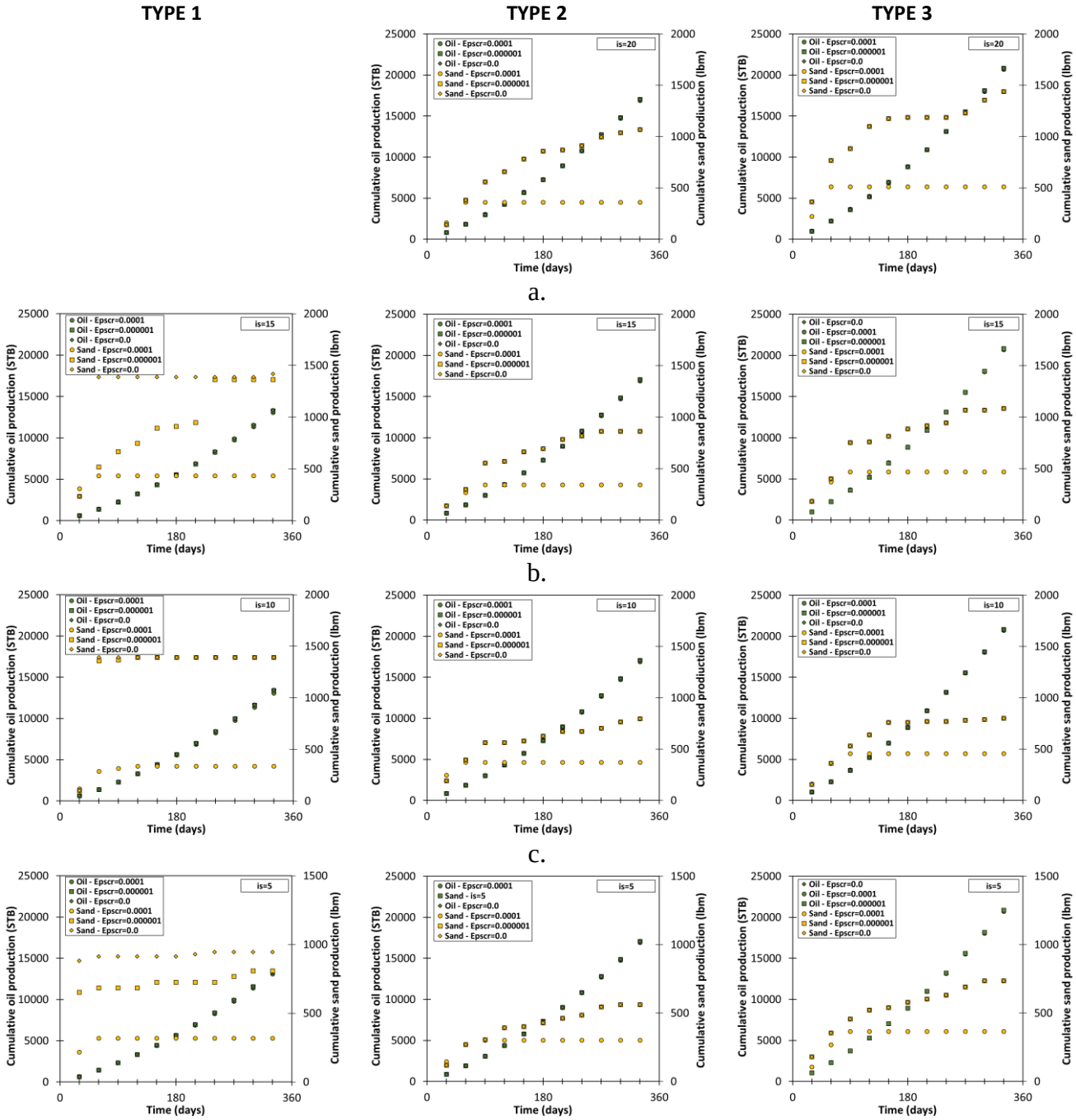

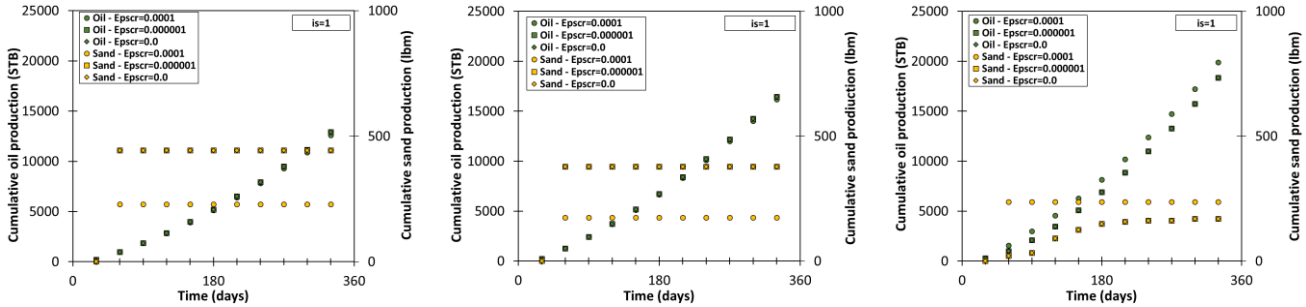

e.

Figure 6 – 18. Cumulative oil production and cumulative sand production for the three field cases – sensitivity study for the critical equivalent plastic stain. a) $i_s = 20$. b) $i_s = 15$. c) $i_s = 10$. d) $i_s = 5$. e) $i_s = 1$.

Remarks: In general, in terms of oil production, the lower the critical value of the equivalent plastic strain, the oil production is slightly higher. For the well Type 3 with a correlation slope of 1, a higher critical value of the equivalent plastic strain (0.0001) generates a higher oil production, which can be justified as this critical value of equivalent plastic strain also generates the highest sand production. It is considered strange, but as mentioned above, the oil potential of this well should be adjusted with a higher value of permeability.

Regarding sand production, the results with the critical value of equivalent plastic strain of 0.000001 and 0.0 are the same, and they differ significantly with a critical value of equivalent plastic strain of 0.0001. However, well Type 1 shows different behavior with higher values of sand production for a critical value of equivalent plastic strain of zero, reflecting lower values of plastic strain that also meet the erosion criterion and contribute to sand production. The lower the critical value of equivalent plastic strain, the lower the sand production.

From the simulation results of these three field wells, it can be said that for maximum oil production, the maximum sand production is required, which can be adjusted from the maximum possible value of correlation slope and a value critical of the equivalent plastic strain of 0.000001.

Figure 6 – 19 presents the cumulative equivalent plastic strain and cumulative sand production for three field cases for a production time of 330 days using a permeability of 0.5 Darcies and different values of the correlation slope for three different critical equivalent plastic strain ϵ_{cr}^{ps}. These figures allow the evaluation of the impact of the critical value of the equivalent plastic strain.

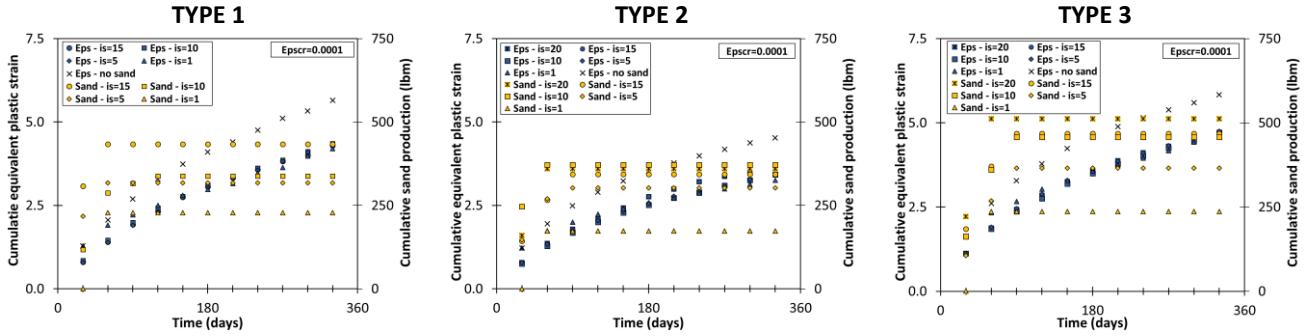

a.

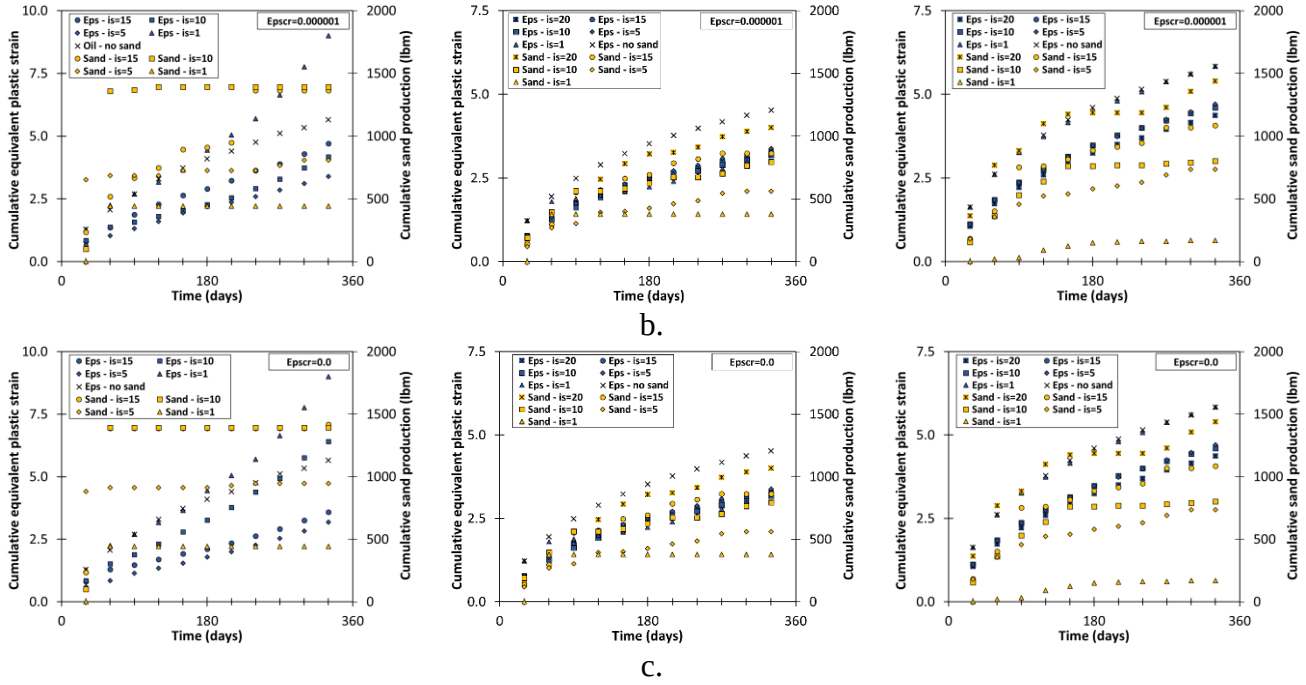

Figure 6 – 19. Cumulative equivalent plastic strain and cumulative sand production for the three field cases. a) $\epsilon_{cr}^{ps} = 0.0001$. b) $\epsilon_{cr}^{ps} = 0.000001$. c) $\epsilon_{cr}^{ps} = 0.0$.

Remarks: In general, the cumulative equivalent plastic strains are higher with no sand than when sand production occurs, except for well Type 1 for critical values of the equivalent plastic strain of 0.000001 and 0.0, where the trend changes to the highest value for a value of 1 for the correlation slope. For the other wells (Type 2 y Type 3) and their cases with sand, the values of equivalent plastic remain in a very close range with no clear tendency in terms of the relation between the correlation slope, the equivalent plastic strain, and the sand production. Comparing the three wells in the cases without the presence of sand, well Type 2 has the highest equivalent plastic strain, while well Type 1 and well Type 3 have a similar level of cumulative equivalent plastic strain.

For well Type 1 (well 13), as said above, there is a particular behavior, for critical values of equivalent plastic strains of 0.000001 and 0.0, the cumulative equivalent plastic strain for a correlation slope of 1 is above the cumulative equivalent plastic strain for no sand, and for the other correlation slopes, which are below, the trend is a wider range of cumulative equivalent plastic strain, in which the higher the correlation slope, the higher equivalent plastic strain. For the critical value of equivalent plastic strain of 0.0, the equivalent plastic strain of the correlation slope of 10 is below the value for the no sand case and exceeds it after 300 days. For the critical value of equivalent plastic strain of 0.0001, the equivalent plastic strain for no sand case is higher than the equivalent plastic strain for sand cases.

For well Type 2 (well 14) for all critical values of equivalent plastic strain, the case with no sand has the highest cumulative equivalent plastic strain, and the rest of the cases with sand have a close range of cumulative equivalent plastic strain with no clear tendency in terms of the relation between the correlation slope, the equivalent plastic strain, and the sand production. However, the results for the critical value of the equivalent plastic strain of 0.000001 and 0.0 are the same.

For well Type 3 (well 11) for critical values of the equivalent plastic strain of 0.000001 and 0.0, the cumulative equivalent plastic strain for the case with no sand is the same as the case with sand production and a value of 1 for the correlation slope, with no clear tendency in terms of the relation between the correlation slope, the equivalent plastic strain, and the sand production. However, the results for the critical value of the equivalent plastic strain of 0.000001 and 0.0 are the same.

For the well Type 3, the previous results recommend increasing the oil potential by increasing its permeability and the chosen value is 1 Darcy. Figure 6 – 20 presents the cumulative oil production and cumulative sand production for well Type 3 (well 11) for a production time of 330 days using a permeability of 1 Darcy and using different values of the correlation slope according to the field case for three different critical equivalent plastic strain ϵ_{cr}^{ps}. These figures allow the evaluation of the impact of the correlation slope. Table 6 – 12 summarizes the cumulative oil and sand production for well Type 3 using different critical equivalent plastic strains and different correlation slopes.

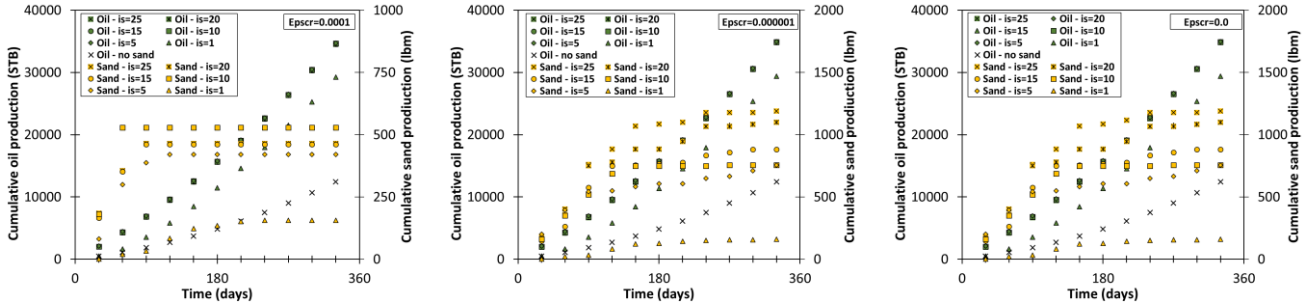

a. b. c.

Figure 6 – 20. Cumulative oil production and cumulative sand production for the well Type 3 – sensitivity study for the correlation slope. a) $\epsilon_{cr}^{ps} = 0.0001$. b) $\epsilon_{cr}^{ps} = 0.000001$. c) $\epsilon_{cr}^{ps} = 0.0$.

Table 6 – 12. Cumulative oil and sand production for well Type 3.

	CRITICAL EPS	CORRELATION SLOPE	CUMULATIVE OIL (STB)	CUMULATIVE SAND (lbm)
Type 3 (well 11)	Field data	-	31741	4214465
	no sand	no sand	12463	0
	0.001	25	34527	464
		20	34529	464
		15	34560	461
		10	34655	528
		5	34697	420
		1	29258	156
	0.000001	25	34808	1189
		20	34830	1100
		15	34847	881
		10	34884	757
		5	34949	755
		1	29383	161
	0.0	25	34808	1189
		20	34830	1100
		15	34846	881
		10	34884	757
		5	34949	755
		1	29383	161

Remarks: For this well, the permeability value of 1 Darcy requires a higher value of correlation slope of 25, entering to be compared with the others previously evaluated. The cumulative oil production with no sand in simulation slightly increases to 12463 STB and is lower at 19278 STB compared to the field

data, which can be considered an adequate value according to previous results that report that in cases with sand, the cumulative oil production will more than double. As expected, the cumulative oil production is more than double producing sand, so the level of oil production with sand is similar for the different values of correlation slope and increases slightly as the critical value of equivalent plastic strain is reduced. However, the results for the critical value of the equivalent plastic strain of 0.000001 and 0.0 are the same. The produced sand is around 1190 lbm. To get the maximum amount of sand, the correlation slope can be stated in a value of 25 with a critical value of the equivalent plastic strain of 0.000001. The sand increases as the critical value of equivalent plastic strain is reduced.

Figure 6 – 21 presents the cumulative oil production and cumulative sand production for three field cases for a production time of 330 days using a permeability of 0.5 Darcies and three different critical equivalent plastic strains for every value of correlation slope. These figures allow the evaluation of the impact of the critical value of the equivalent plastic strain.

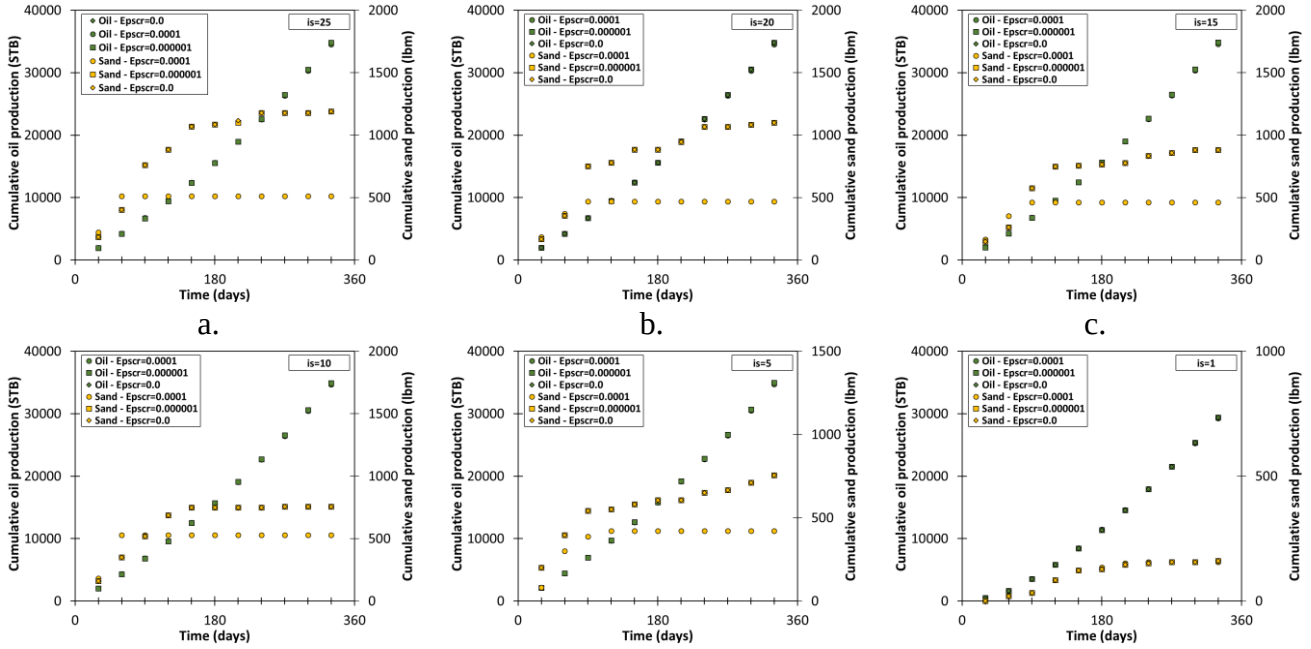

Figure 6 – 21. Cumulative oil production and cumulative sand production for well Type 3 – sensitivity study for the critical equivalent plastic stain. a) $i_s = 25$. b) $i_s = 20$. c) $i_s = 15$. d) $i_s = 10$. e) $i_s = 5$. f) $i_s = 1$.

Remarks: In general, in terms of oil production, the lower the critical value of the equivalent plastic strain, the oil production is slightly higher. For all cases, cumulative oil production remains at the same level that changes slightly according to critical equivalent plastic strain and the slope of correlation. For a value of 1 for the correlation slope, the three values of the cumulative equivalent plastic strain generate the same sand production and the same oil production, which is lower than the obtained with the other values of the correlation slope. Regarding sand production, the results with the critical value of equivalent plastic strain of 0.000001 and 0.0 are the same, and they differ significantly with a critical value of equivalent plastic strain of 0.0001. The higher the correlation slope, the higher the sand production but not necessarily the higher the oil production. For the same critical value of equivalent plastic strain, the lower the correlation slope, the higher the oil production, without considering the value of 1 for the

correlation slope, which implies lower oil and sand production. This can be explained by the interaction of the sand production criteria and the limits of the critical porosity of the sand model and wormhole model.

Figure 6 – 22 presents the cumulative equivalent plastic strain and cumulative sand production for well Type 3 for a production time of 330 days using a permeability of 1 Darcy and different values of the correlation slope for three different critical equivalent plastic strain ϵ_{cr}^{ps}. These figures allow the evaluation of the impact of the critical value of the equivalent plastic strain on oil and sand production.

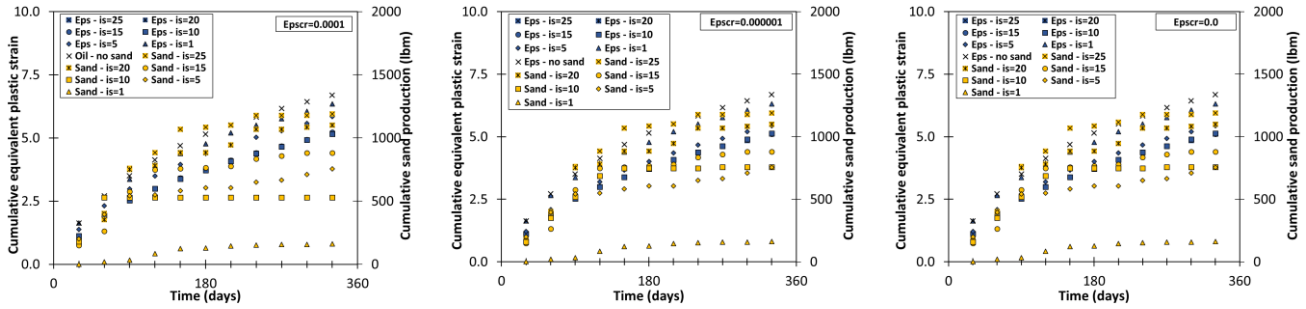

a. b. c.

Figure 6 – 22. Cumulative equivalent plastic strain and cumulative sand production for well Type 3. a) $\epsilon_{cr}^{ps} = 0.0001$. b) $\epsilon_{cr}^{ps} = 0.000001$. c) $\epsilon_{cr}^{ps} = 0.0$.

Remark: To begin with, the cumulative equivalent plastic strains are higher with no sand than when sand production occurs. The behavior here is more clear than before, for cases with sand, the lower the cumulative equivalent plastic strain, the higher the sand production. However, the results for the critical value of the equivalent plastic strain of 0.000001 and 0.0 are the same. In conclusion, this well can be modeled for sand production with a correlation slope of 25 with a critical value of equivalent plastic strain of 0.000001, being at a level of oil production close to the field data.

Figure 6 – 23 shows the heat map for the production data from the simulation for the three CHOPS well. The attributes of this data exploration are permeability, net pay, critical EPS as the critical value for the equivalent plastic strain, correlation slope, production time, cumulative EPS as the cumulative equivalent plastic strain, cumulative oil as the cumulative oil production, and cumulative sand as the cumulative sand production. The sand production model integrates three of these attributes: critical EPS, correlation slope, and cumulative EPS. The purpose of this heat map is to observe all the relationships between the different attributes, in special the attributes from the sand production model with the cumulative oil production, and cumulative sand production.

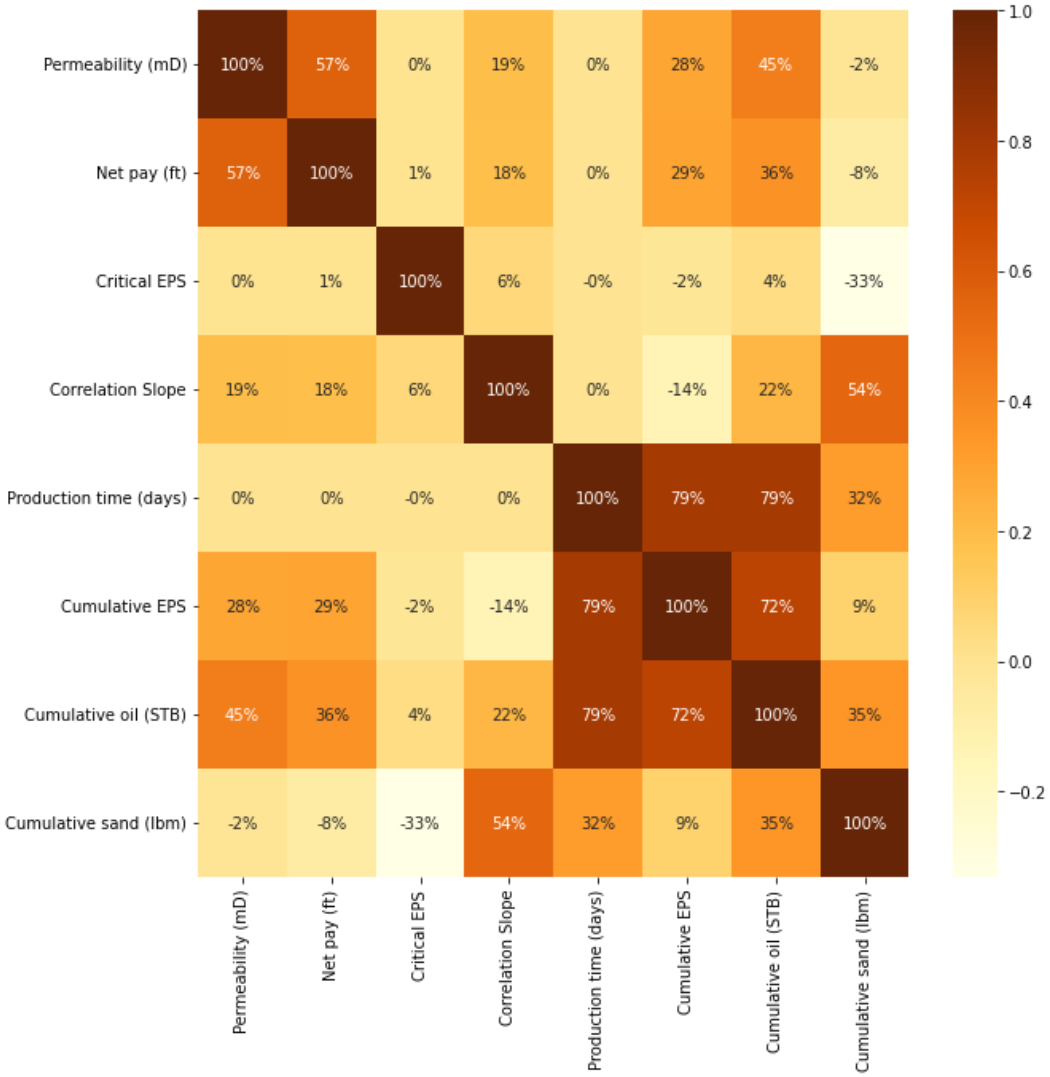

Figure 6 – 23. Heat map of production data from simulation for the three field cases.

Remarks: The most influential attributes in cumulative sand are correlation slope (54%), cumulative oil (35%), production time (32%), and critical EPS (-33%), negative values that represent an inversely proportional relationship, the lower the critical EPS, the higher cumulative sand. The higher the correlation slope, the higher the sand production; and the higher the cumulative oil, the higher the cumulative sand. Minor effects in other attributes such as cumulative EPS (9%), net pay (-8%), and permeability (-2%). The most influential attributes in cumulative oil are production time (79%), cumulative EPS (72%), permeability (45%), net pay (36%), and cumulative sand (35%). The higher the cumulative EPS, the higher the cumulative oil. Minor effects in other attributes such as correlation slope (22%) and critical EPS (4%). The most influential attributes in cumulative EPS are production time (79%), cumulative oil (72%), net pay (29%), and permeability (29%). The higher the net pay and permeability, the higher the cumulative oil, and therefore, the higher the cumulative EPS. Minor effects in other attributes such as cumulative sand (9%), correlation slope (-14%) and critical EPS (-2%), negative values that represent an inversely proportional relationship, the lower correlation slope, the higher cumulative EPS; and the lower the critical EPS, the higher cumulative EPS.

The most dominant attributes in correlation slope are permeability (19%) and net pay (18%). The higher permeability and net pay, the higher the correlation slope. The critical EPS is not impacted by all attributes.

In conclusion, the higher the sand production, the higher the oil production, and also the higher the cumulative EPS, the higher the oil production. In terms of the attributes of the sand production model, the higher the correlation slope, the higher sand and oil production. The critical EPS has no relevant impact on oil production, and the lower critical EPS, the higher sand production.

6.3.2 Simulation of a typical CHOPS well

This section intends to evaluate the behavior of a typical CHOPS well in terms of oil and sand production. A typical CHOPS well is stated as a base case from the field data assuming reservoir properties from the mean features of unconsolidated sandstones (Dusseault, 2002) presented in Table 2 – 1. The characteristics of the reservoir of the typical CHOPS well are summarized in Table 6 – 13 and the geometry and geomechanical characteristics are summarized in Table 6 – 14, the production schedule considers a pressure drawdown of 10 psi every 30 days and is presented in Table 6 – 15 and Figure 6 – 16 presents the relative permeability curve for the oil-water system. The typical CHOPS case is set as a three-layer under isotropic horizontal stress conditions.

Table 6 – 13. Characteristics of a typical CHOPS well.

RESERVOIR CHARACTERISTICS	VALUE
Wellbore radius (in)	2.5
Reservoir radius (ft)	100
Reservoir pressure (psi)	770
Temperature (°F)	150
API Gravity (°API)	15
Gas-specific gravity	0.7
Bubble point pressure (psi)	100
Oil saturation (fraction)	0.85
Water saturation (fraction)	0.15
Gas saturation (fraction)	0.00

Table 6 – 14. Geometry and geomechanical characteristics of a typical CHOPS well.

VARIABLE	LAYER 1	LAYER 2	LAYER 3
Depth (ft)	1680	1700	1720
Formation height (ft)	20	20	20
Porosity (fraction)	0.2	0.3	0.2
Horizontal permeability (mD)	50	1000	50
Vertical permeability (mD)	5	100	5
Vertical stress gradient (psi/ft)	1	1	1
Maximum horizontal stress gradient (psi/ft)	1	1	1
Minimum horizontal stress gradient (psi/ft)	1	1	1
Biot (fraction)	1	1	1
Young modulus (psi)	1.0E06	1.0E06	1.0E06
Poisson ratio (fraction)	0.30	0.25	0.30
Cohesion (psi)	1000	300	1000
Friction angle (°)	15	15	15
Dilation angle (°)	15	15	15

Table 6 – 15. Production schedule for a typical CHOPS well.

PRODUCTION TIME (days)	WELLBORE PRESSURE (psi)
30	760
60	750
90	740
120	730
150	720
180	710
210	700
240	690
270	680
300	670
330	660
360	650
390	640
420	630
450	620
480	610
510	600
540	590

Figure 6 – 24 (a) presents the cumulative oil production and cumulative production sand and Figure 6 – 24 (b) presents the cumulative equivalent plastic strain and cumulative sand for a typical CHOPS case for a production time of 540 days using a permeability of 1 Darcy and different values of the correlation slope according to the field case for a critical equivalent plastic strain of 0.000001. These figures allow stating the value of the correlation slope for the base case.

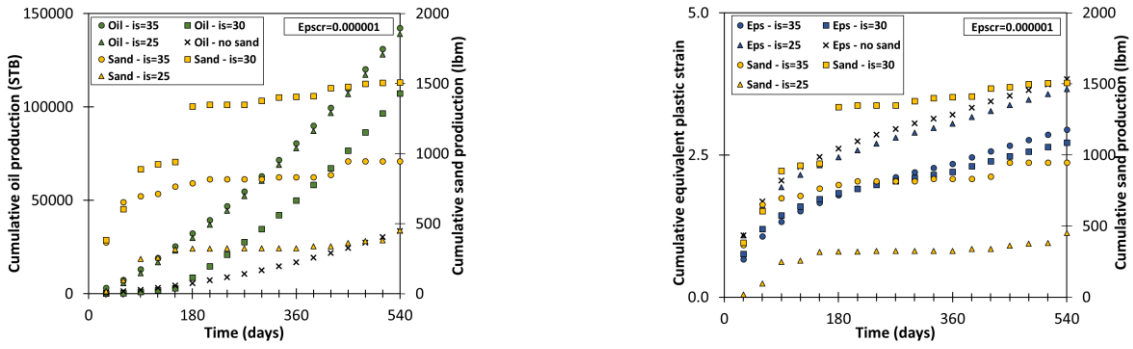

a. b.

Figure 6 – 24. Sand production for a typical CHOPS well. a) Cumulative oil production and cumulative sand production. b) Cumulative equivalent plastic strain and cumulative sand production.

Remarks: The characteristics of the typical CHOPS well with a permeability of 1 Darcy require a higher value of correlation slope, so three values are compared: 35, 30, and 25 with a critical value of equivalent plastic strain of 0.000001 to select the adequate value to produce the maximum amount of sand production. Correlation slopes of 25 and 35 produce higher cumulative oil around 140000 STB but not the highest sand production, but a correlation slope of 30 produces lower oil production (107243 STB) with the highest sand production (1508 lbm). However, the presence of sand implies a significant increase in oil production, much more than double. The cumulative equivalent plastic strain helps to understand the relationships between oil production and sand production for these values of correlation slope. As

expected, the case with no sand gets the maximum cumulative equivalent plastic strain. A value of 30 for the correlation slope generates the minimum equivalent plastic strain producing the maximum sand production. Another point to highlight in this value of correlation slope sand is produced throughout the simulation time while the other slopes it is not.

Sensitivity study

This section intends to perform a sensitivity study of the new simulator to understand the sand production phenomena. This technique studies how various sources of uncertainty in the new simulator contribute to the simulator's overall uncertainty, determining how different values of an independent variable affect a particular dependent variable under a given set of assumptions. In this case, the independent variables are pressure drawdown, cohesion, friction angle, and stress regime and the dependent variables are cumulative oil production and cumulative oil sand. As observed in the previous section, there is a variable in the middle that is associated with sand production, which can help to understand the phenomena and this variable is the cumulative equivalent plastic strain. Also, this study seeks to understand the impact of this variable on cumulative oil production and cumulative sand production.

- Pressure drawdown

The pressure drawdown is an important variable for the evaluation of sand production because is the variable that defines the production schedule and the production itself. The base case defines its production schedule with a pressure drawdown of 10 psi every 30 days and is presented in Table 6 – 16. The sensitivity study for pressure drawdown considers a first case with a pressure drawdown of 20 psi every 30 days and a second case with a high initial pressure drawdown of 30% of reservoir pressure, which for the base case would be 230 psi for the first 30 days, continuing with a pressure drawdown of 10 psi every 30 days for the rest of simulation time. Table 6 – 16 presents the production schedule for the typical CHOPS well for the sensitivity study of pressure drawdown.

Table 6 – 16. Production schedule for a typical CHOPS well – sensitivity study for pressure drawdown.

PRODUCTION TIME (days)	DRAWDOWN=20 PSI	HIGH INITIAL DRAWDOWN
30	750	540
60	730	530
90	710	520
120	690	510
150	670	500
180	650	490
210	630	480
240	610	470
270	590	460
300	570	450
330	550	440
360	530	430
390	510	420
420	490	410
450	470	400
480	450	390
510	430	380
540	410	370

Figure 6 – 25 (a) presents the cumulative oil production and cumulative production sand and Figure 6 – 25 (b) presents the cumulative equivalent plastic strain and cumulative sand for a typical CHOPS case for a production time of 540 days using a permeability of 1 Darcy for the three production schedules defined by the pressure drawdown. These figures allow the evaluation of the impact of the pressure drawdown on oil and sand production.

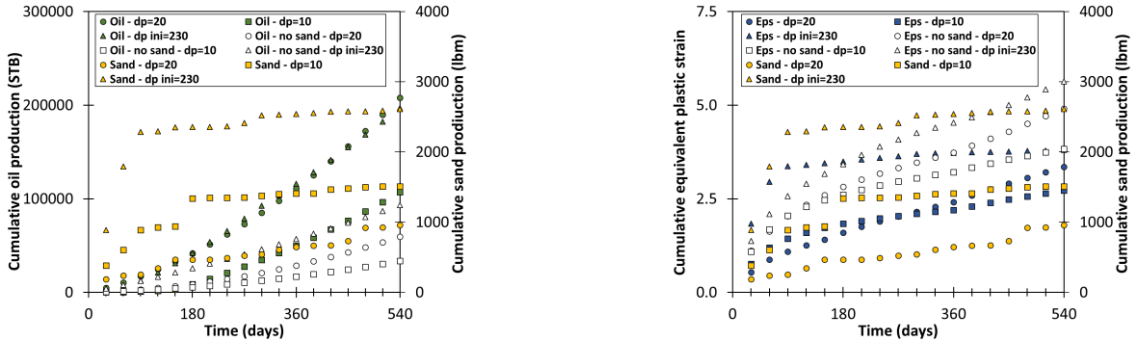

a. b.

Figure 6 – 25. Sand production for a typical CHOPS well – sensitivity study for pressure drawdown. a) Cumulative oil production and cumulative sand production. b) Cumulative equivalent plastic strain and cumulative sand production.

Remark: It is necessary to start with the analysis of the total pressure drawdown of each production schedule to evaluate the effect of the pressure drawdown on oil production separately from the effect on sand production. A drawdown of 10 psi generates a production schedule in which the total drawdown is 230 psi in 540 days, while a drawdown of 20 psi generates a production schedule with a total drawdown is 360 psi in 540 days and the last one, an initial drawdown of 230 psi with a 10 psi every 30 days generates a production schedule with a total drawdown of 400 psi in 540 days. This means that the last one, which has a higher pressure drawdown will produce more oil without considering sand followed by the second production schedule (20 psi) and ending with the base case as is shown in Figure 6 – 25. The presence of sand significantly increases oil production and maintains the trend with very close values for the cases of a drawdown of 20 psi and an initial drawdown of 230 psi. However, sand production changes this tendency, the initial pressure drawdown of 230 produces the highest value of sand around 2614 lbm, followed by a pressure drawdown of 10 psi with 1508 lbm and a pressure drawdown of 20 psi with 958 lbm.

The idea to review the cumulative equivalent plastic strain is to understand the sand production behavior. To begin with, these cases with no sand have a particular trend, the higher the total pressure drawdown the higher the cumulative equivalent plastic strain. As expected, the cases with no sand have higher equivalent plastic strain than the cases with sand. The initial pressure drawdown of 230 psi presents the highest cumulative equivalent plastic strain and the higher cumulative sand production. The pressure drawdown of 20 psi ends the run with higher equivalent plastic strain and lower sand production compared with the pressure drawdown of 10 psi.

- **Cohesion**

The cohesion is another important variable for the evaluation of sand production because is the component of the shear strength of a rock that is independent of the interparticle and participates in the

calculation of the equivalent plastic strain. The base case defines a cohesion value of 300 psi. The sensitivity study for cohesion considers other two cases: a lower value (200 psi) and a higher value (400 psi).

Figure 6 – 26 (a) presents the cumulative oil production and cumulative production sand and Figure 6 – 26 (b) presents the cumulative equivalent plastic strain and cumulative sand for a typical CHOPS case for a production time of 540 days using a permeability of 1 Darcy for the cases defined by cohesion. These figures allow the evaluation of the impact of cohesion on oil and sand production.

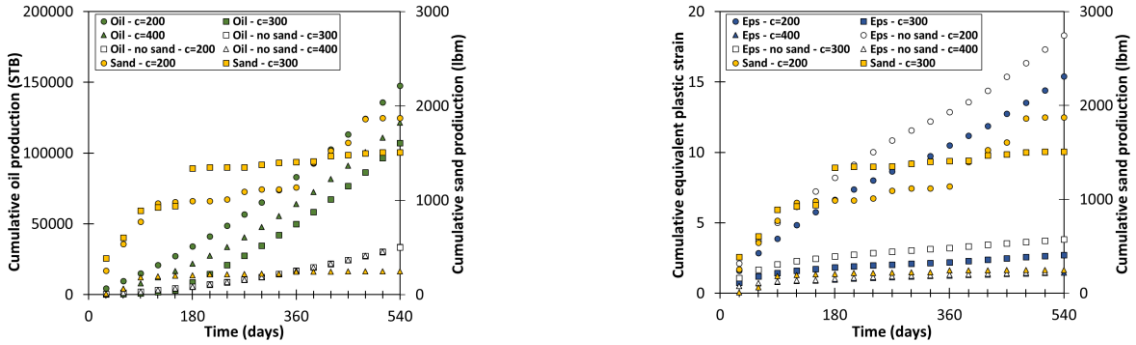

a. b.

Figure 6 – 26. Sand production for a typical CHOPS well – sensitivity study for cohesion. a) Cumulative oil production and cumulative sand production. b) Cumulative equivalent plastic strain and cumulative sand production.

Remark: To begin with, the cohesion does not affect significantly the oil production for the cases with no sand which presents a cumulative oil production of around 33600 STB. However, this situation changes with the presence of sand. The lowest cohesion case (200 psi) presents the highest cumulative oil production with the highest cumulative sand production. The highest cohesion case presents the lowest sand production but an intermediate value of oil production. In terms of cumulative equivalent plastic strain, the cases with no sand have higher values of cumulative equivalent plastic strains than cases with sand. In cases with sand, the lower cohesion, the higher equivalent plastic strain, and the higher equivalent plastic strain, the higher sand production. In general, the lower cohesion, the higher cumulative oil production, and the higher cumulative sand production. Also for sand cases, the lower cohesion the higher the cumulative equivalent plastic strain and the higher the sand production.

- **Internal friction angle**

The internal friction angle helps to quantify the shear strength of a rock and is important for the evaluation of sand production. The base case defines an internal friction angle value of 15°. The sensitivity study for internal friction angles considers other two cases: a lower value (10°) and a higher value (20°).

Figure 6 – 27 (a) presents the cumulative oil production and cumulative production sand and Figure 6 – 27 (b) presents the cumulative equivalent plastic strain and cumulative sand for a typical CHOPS case for a production time of 540 days using a permeability of 1 Darcy for the cases defined by internal friction angle. These figures allow the evaluation of the impact of internal friction angle on oil and sand production.

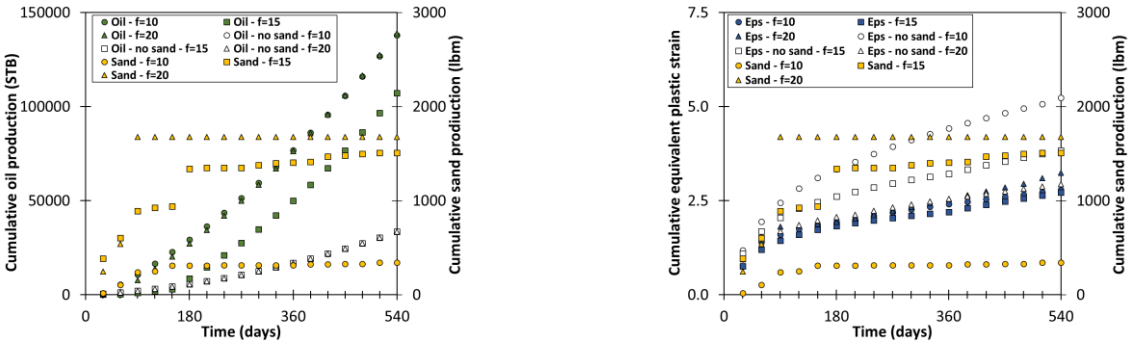

a. b.

Figure 6 – 27. Sand production for a typical CHOPS well – sensitivity study for internal friction angle. a) Cumulative oil production and cumulative sand production. b) Cumulative equivalent plastic strain and cumulative sand production.

Remark: The internal friction angle does not affect significantly the oil production for the cases with no sand which presents a cumulative oil production of around 33600 STB. However, this situation changes with the presence of sand. The sensitivity cases with internal friction angles of 10° and 20° have the same level of cumulative oil production of around 138000 STB with a difference of 1118 STB. The base case with an internal friction angle of 15° has the lowest cumulative oil production (107243 STB). In terms of cumulative sand production, the higher the internal friction angle, the higher the sand production. Regarding presents the highest cumulative oil production with the highest cumulative sand production. The case with the highest internal friction angle (20°) has a particular behavior as to the sand production, it produces sand only at the first three production times, while the other cases produce almost at all production times. In terms of cumulative equivalent plastic strain, the cases with no sand have higher values of equivalent plastic strains than cases with sand with a trend of the lower internal friction angle, the higher cumulative equivalent plastic strain. In cases with sand, the value varies in a very close range with the tendency of the higher equivalent plastic strain, the higher sand production.

- Stress regime

The stress regime for the reservoir layer is another variable for the sensitivity study to evaluate its impact on sand production. The base case states an isotropic condition for all layers, including the reservoir layer. The sensitivity study for stress regime considers two cases: the first one states an anisotropic stress regime in which the minimum horizontal stress gradient for the reservoir layer is 0.9 and the second one states a typical stress regime for CHOPS. Both cases are presented in Table 6 – 17.

Table 6 – 17. Stress regime for a typical CHOPS well – sensitivity study for stress regime.

CASE	VERTICAL (psi/ft)	MIN. HORIZONTAL (psi/ft)	MAX. HORIZONTAL (psi/ft)
Isotropic	1.0	1.0	1.0
Anisotropic	1.0	0.9	1.0
CHOPS	1.0	0.95	1.05

Figure 6 – 28 (a) presents the cumulative oil production and cumulative production sand and Figure 6 – 28 (b) presents the cumulative equivalent plastic strain and cumulative sand for a typical CHOPS case for a production time of 540 days using a permeability of 1 Darcy for the cases defined by the stress regime. These figures allow the evaluation of the impact of stress regime on oil and sand production.

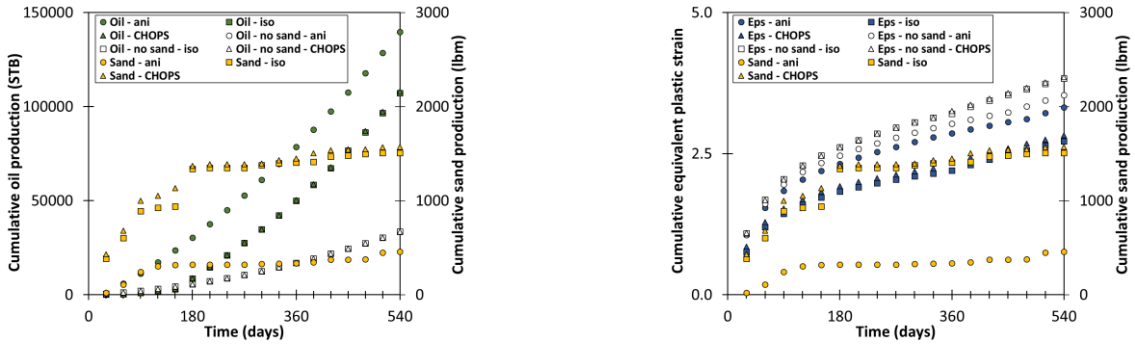

a. b.

Figure 6 – 28. Sand production for a typical CHOPS well – sensitivity study for stress regime. a) Cumulative oil production and cumulative sand production. b) Cumulative equivalent plastic strain and cumulative sand production.

Remark: To begin with, the stress regime does not affect significantly the oil production for the cases with no sand which presents a cumulative oil production of around 33600 STB. However, this situation changes with the presence of sand. The case with stress anisotropy (0.9) has higher cumulative oil production (139.732 STB), and the other two cases are in the same level of cumulative oil production of around 107000 STB with a difference of 894 STB. These cases have also the same level of cumulative sand production of around 1570 lbm. For cases with no sand, the anisotropic case has the highest cumulative oil and the lowest sand production. In terms of the cumulative equivalent plastic strain, the anisotropic case (0.9) has the highest value, and the other two cases have the same level of cumulative equivalent plastic strain. In the cases with sand, the anisotropic case has the highest level of cumulative equivalent plastic strain, and the other two cases have the same level of equivalent plastic strain, lower than the anisotropic case, which can explain the same level of sand, the highest value.

- Results analysis

This section intends to summarize the remarks of the sensitivity study to understand the sand production phenomena. Heat maps of the simulation results are used as a support technique to define the impact of the independent variables on the dependent variables.

Figure 6 – 29 shows the heat map for the production data from the simulation for a typical CHOPS well for the cases of the sensitivity study including sand and no sand cases. The attributes of this data exploration are correlation slope, cohesion, internal friction angle, Pwf as the wellbore flowing pressure, cumulative EPS as the cumulative equivalent plastic strain, cumulative oil as the cumulative oil production, and cumulative sand as the cumulative sand production. The purpose of this heat map is to observe all the relationships between the different attributes, in special the attributes such as cohesion and internal friction angle, drawdown and correlation slope, cumulative EPS with the cumulative oil production, and cumulative sand production. The stress regime cannot be included in this heat map because is a categorical variable.

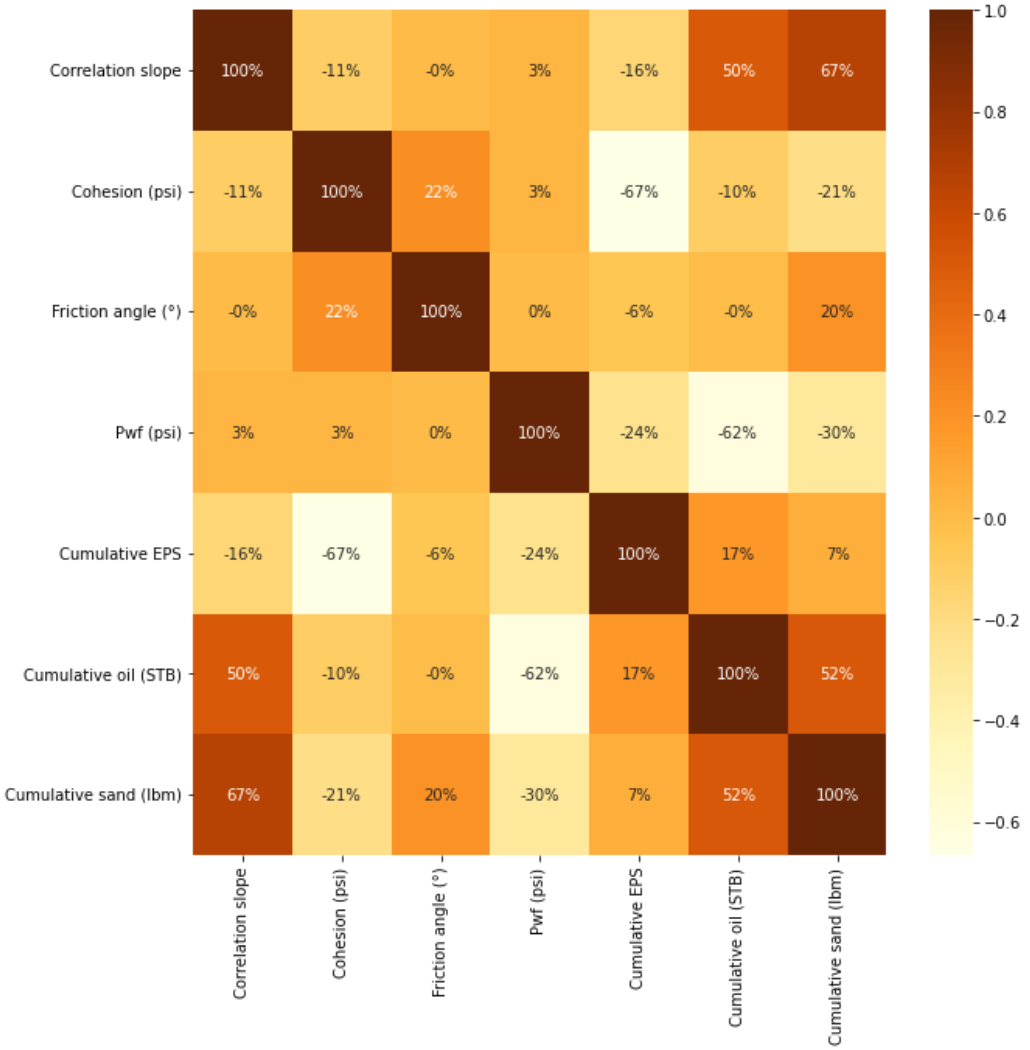

Figure 6 – 29. Heat map of production data from simulation for a typical CHOPS well – sensitivity study – sand and no sand cases.

Remarks: For sand and no sand cases, the most influential attributes on cumulative sand are correlation slope (67%), cumulative oil (52%), friction angle (20%), Pwf (-30%), and cohesion (-21%), negative values that represent an inversely proportional relationship, the lower Pwf, the higher cumulative sand; and the lower cohesion, the higher cumulative sand. The higher the correlation slope, the higher the sand production; and the higher the friction angle, the higher the cumulative sand. A minor effect of cumulative EPS (7%). The most influential attributes of cumulative oil are cumulative sand (52%), correlation slope (50%), cumulative EPS (17%), Pwf (-62%), and cohesion (-10%). The higher the cumulative EPS, the higher the cumulative oil. The lower Pwf, the higher cumulative oil; and the lower cohesion, the higher cumulative oil. The most influential attributes on cumulative EPS are cohesion (-67%) and Pwf (-24%). Minor effects of correlation slope (-16%) and friction angle (-6%).

Figure 6 – 30 shows the heat map for the production data from the simulation for the typical CHOPS well for the cases of the sensitivity study with sand. The attributes of this data exploration are correlation slope, cohesion, friction angle, Pwf as the wellbore flowing pressure, cumulative EPS as the cumulative equivalent plastic strain, cumulative oil as the cumulative oil production, and cumulative sand as the

cumulative sand production. The purpose of this heat map is to observe all the relationships between the different attributes, in special the attributes such as cohesion and friction angle, drawdown and correlation slope, cumulative EPS with the cumulative oil production, and cumulative sand production. The stress regime cannot be included in this heat map because is a categorical variable.

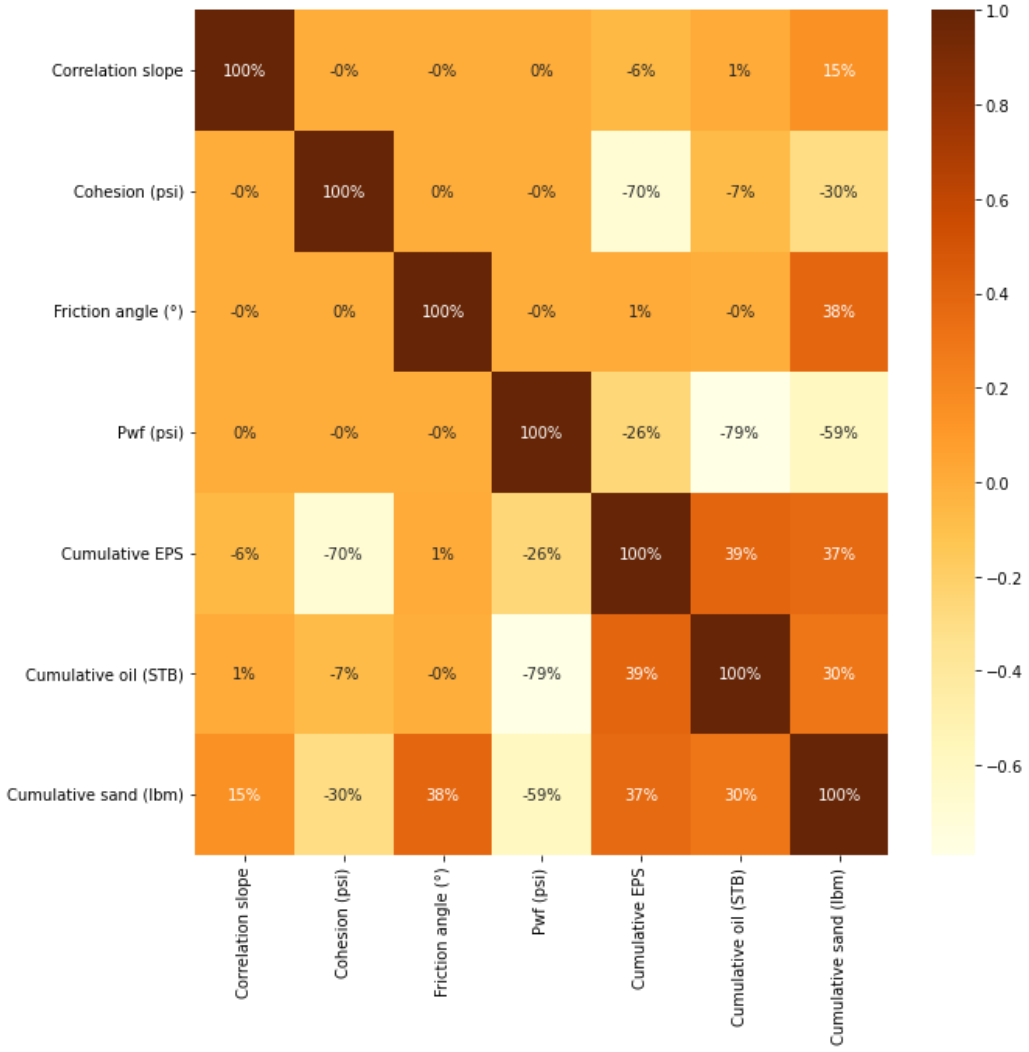

Figure 6 – 30. Heat map of production data from simulation for a typical CHOPS well – sensitivity study – sand cases.

Remarks: For only sand cases, the changes are important. The most influential attributes on cumulative sand are internal friction angle (38%), cumulative EPS (37%), cumulative oil (30%), correlation slope (15%), Pwf (-59%), and cohesion (-30%), negative values that represent an inversely proportional relationship, the lower Pwf, the higher cumulative sand; and the lower cohesion, the higher cumulative sand. The higher the friction angle, the higher the cumulative sand; the higher the cumulative EPS, the higher the cumulative sand; and the higher the correlation slope, the higher the sand production. The impact of correlation slope and cumulative oil decreases and the effect of friction angle, cumulative EPS, Pwf, and cohesion increases compared with the previous heat map (sand and no sand cases). The most influential attributes of cumulative oil are cumulative EPS (39%), and Pwf (-79%). Minor effects of correlation slope (1%) and cohesion (-7%). The higher the cumulative EPS, the higher the cumulative

oil. The lower Pwf, the higher cumulative oil; and the lower cohesion, the higher cumulative oil. The impact of correlation slope, cumulative EPS, and cohesion decreases, and the effect of Pwf and cumulative sand increases compared with the previous heat map (sand and no sand cases). The most influential attributes on cumulative EPS are cohesion (-70%) and Pwf (-26%). Minor effects of correlation slope (-6%) and friction angle (1%). The change in the effect of these variables is less.

- CHOPS well – a special case

Collecting the lessons learned from the sensitivity study, a special case is built with the properties that promote sand production, to determine if together they increase sand production. All previously studied independent variables were considered to build this case. The characteristics of the reservoir of the special case are summarized in Table 6 – 18 and the geometry and geomechanical characteristics are summarized in Table 6 – 19, the production schedule with a high initial pressure drawdown of 30% of reservoir pressure, which for the base case would be 230 psi for the first 30 days, continuing with a pressure drawdown of 10 psi every 30 days for the rest of simulation time, which is presented in Table 6 – 20. The special case for a CHOPS well is set as a three-layer.

Table 6 – 18. Characteristics of the CHOPS well – a special case.

RESERVOIR CHARACTERISTICS	VALUE
Wellbore radius (in)	2.5
Reservoir radius (ft)	100
Reservoir pressure (psi)	770
Temperature (°F)	150
API Gravity (°API)	15
Gas-specific gravity	0.7
Bubble point pressure (psi)	100
Oil saturation (fraction)	0.85
Water saturation (fraction)	0.15
Gas saturation (fraction)	0.00

Table 6 – 19. Geometry and geomechanical characteristics of the CHOPS well – a special case.

VARIABLE	LAYER 1	LAYER 2	LAYER 3
Depth (ft)	1680	1700	1720
Formation height (ft)	20	20	20
Porosity (fraction)	0.2	0.3	0.2
Horizontal permeability (mD)	50	1000	50
Vertical permeability (mD)	5	100	5
Vertical stress gradient (psi/ft)	1.00	1.00	1.00
Maximum horizontal stress gradient (psi/ft)	1.00	1.05	1.00
Minimum horizontal stress gradient (psi/ft)	1.00	0.95	1.00
Biot (fraction)	1	1	1
Young modulus (psi)	1.0E06	1.0E06	1.0E06
Poisson ratio (fraction)	0.30	0.25	0.30
Cohesion (psi)	1000	200	1000
Friction angle (°)	20	15	15
Dilation angle (°)	15	15	15

Figure 6 – 31 (a) presents the cumulative oil production and cumulative production sand and Figure 6 – 31 (b) presents the cumulative equivalent plastic strain and cumulative sand for the CHOPS well – a special case for a production time of 540 days.

Table 6 – 20. Production schedule for the CHOPS well – a special case.

PRODUCTION TIME (days)	WELLBORE PRESSURE (psi)
30	540
60	530
90	520
120	510
150	500
180	490
210	480
240	470
270	460
300	450
330	440
360	430
390	420
420	410
450	400
480	390
510	380
540	370

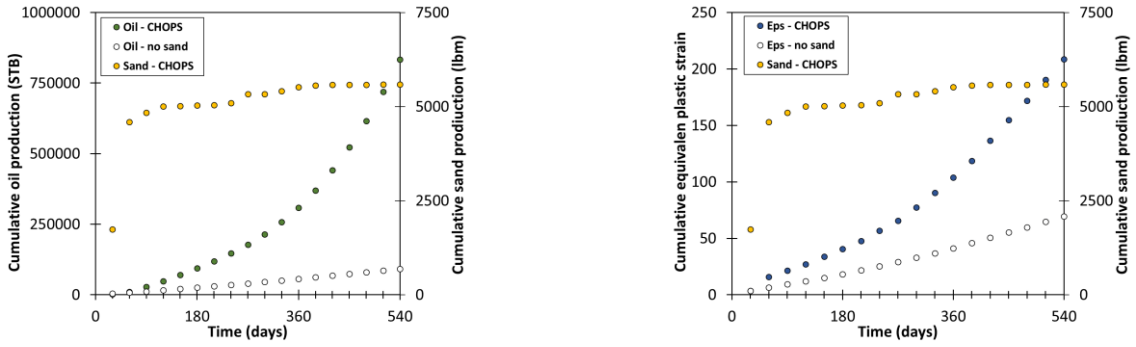

a. b.

Figure 6 – 31. Sand production for the CHOPS well – special case. a) Cumulative oil production and cumulative sand production. b) Cumulative equivalent plastic strain and cumulative sand production.

Remark: The productive response of the CHOPS well – a special case, in which all properties are defined for the promotion of sand production, was successful. The cumulative sand production increases to 92116 STB with no sand and 833262 STB with sand and a cumulative sand production of 5586 lbm. The higher the sand production, the higher the oil production. In terms of cumulative equivalent plastic strain, the case with no sand reaches 69 and the case with sand reaches 208, confirming the previous results of a trend in which the higher the cumulative equivalent plastic strain, the higher cumulative sand production. All properties contributed to sand production. In conclusion, the higher the cumulative equivalent plastic strain, the higher the cumulative sand production and the higher the cumulative oil production.

Chapter 7. Conclusions and Recommendations

7.1 Conclusions

- Cold heavy oil production with sands (CHOPS) is the major technology for heavy oil reservoirs, which involves sand inflow to produce at oil high rates. The literature review states that CHOPS responds to relevant phenomena with three components: massive sand production, foamy oil, and formation wormholes. The main component is the massive sand production because the sand inflow allows more oil production with a porosity increment that implies a permeability increment, while the foamy flow is a short process that works as long as the pressure is between the bubble pressure and the pseudo-bubble pressure. On the other hand, the wormhole formation has been questioned because it does not have sufficient field evidence. At the laboratory level, the formation of flow channels is evident, but not necessarily wormholes, which could be erosion channels or fluidized channels.

- A new 3D single well simulator is built to predict and explain the massive sand production during cold heavy oil production with sands (CHOPS) coupling two main components: a multi-phase fluid flow model and an elastoplastic geomechanical model with Drucker and Prager failure criterion. The simulator integrates a sand production model with two criteria: a plastic criterion and an erosion criterion and a wormhole formation model with a porosity criterion. Although a foamy oil model is integrated into the simulator in some cases including gas the stability of the multi-phase fluid flow is affected. However, the effect of the foamy oil behavior is studied with a proposed analytical model.

- The fluid flow model is solved by the difference-finite method (DFM) and the geomechanical model (elastoplastic) is solved by the finite-difference method (FEM). Each method is quite similar in that it represents a systematic numerical method for solving partial differential equations (PDEs) with some advantages and disadvantages depending on the problem at hand. Some of these advantages and disadvantages became evident during the construction of the new simulator. One important difference is the ease of implementation, the DFM is the easiest to implement and the FEM is the most difficult because requires quite sophisticated mathematics for its formulation. However, the DFM requires choosing the difference scheme according to the PDE at hand and stability and convergence analyses, which are not so simple and available for complex problems such as coupling and high non-linearities. The FEM solves the PDE by a variational model or weak model, resulting easiest to guarantee solution than in a strong model. The current success of the FEM is that is a very general method, solving the resulting equation systems that are the same or very similar to well-known and efficient methods used for other analyses and is easy to increase the order of the elements to get an accurate approximation with polynomials of higher order or increase the element density using an adaptative mesh refinement. Other advantages of FEM over DFM are that general boundary conditions, complex geometry, and variable material properties can be relatively easily handled. In conclusion, both models, fluid flow and geomechanics should be solved by FEM in terms of their complexity, coupling, and high non-linealities.

- The selection of the coordinate system depends upon the problem at hand, based on its symmetry

to find the easiest way to do the maths and simplify a particular problem as some of the constraints or factors may go away in a particular coordinate system by considering symmetry relationships, regardless of physical meaning. A cylindrical system is chosen to model the 3D multi-phase fluid flow around the wellbore using the difference finite method. However, this problem is complex because of its high no linearities and its couples, overloading the model with many mathematical transformations that do not facilitate its solution but instead increase its complexity. The reason for this decision is to focus on the problem of fluid flow coupled with geomechanics in the well vicinity, where geomechanics has a greater incidence. Currently, this can be solved with an automatic mesh or even with an adequate refinement that allows concentrating near the well. A logarithmic distribution in the radial direction is used to enhance this purpose, but the aspect ratio significantly affected the stability of the solution. This situation is solved by three sectors in the radial direction. In conclusion regarding the cylindrical coordinates, it is an unnecessary expense mathematically that does not contribute to the stability of the solution.

- The validation of the new simulator for cold heavy oil production with sands (CHOPS) is done with adequate results in production and geomechanics by comparing the results with the results from commercial software (CMG® and ABAQUS®), aligning the models as much as possible and running the same cases. The validation includes a verification step that consists to verify boundary conditions and the trend of the validation variables. The multi-phase fluid flow model is validated using the CMG® software with production variables such as pressure, saturations, flow rates, and cumulative production and two basic cases: one-phase (oil and gas) and two-phase (oil-water); there are significant differences between the two simulators that do not allow a complete aligning of these models: CMG® software uses a mean pressure instead of oil pressure and the saturations are not variables per se, while in the numerical model, the saturations are mean variables, PVT properties use different correlations and the external boundary conditions are different. For all cases, the results are acceptable in terms of pressure, adequate in saturations, and have reasonable differences in production rate and cumulative rate; the two-phase case presents better results than the one-phase case. The elastoplastic model is validated using ABAQUS® software with two basic models: elastic and elastoplastic under isotropic and anisotropic horizontal stress conditions, and considering two well settings: a one-layer set and muli-layer set, and with mechanical variables such as displacement, strain, and stress; the alignment of the model is considered tight and the results are adequate in all variables and the boundary conditions are well imposed. The coupled model is validated using CMG® software with two basic models: elastic and elastoplastic under isotropic and anisotropic horizontal stress conditions and considering a one-layer set for a two-phase case (oil and water) with production and mechanical variables. For all cases, the results are acceptable in terms of pressure, adequate in saturations, reasonable differences in production rate and cumulative rate, and adequate in terms of displacement, strain, and stress with a good trend and showing that the boundary conditions are well imposed. The elastoplastic case presented lower values in strains and stresses, especially in plastic strains. The sand production could not be valid with the CHOPS field data because it did not produce the typical sand levels of CHOPS.

- The multi-phase fluid flow presents some cases including gas with no stability in the results, particularly in saturations. This instability responds to the presence of the gas or close to the bubble-point pressure because of the high mobility and non-equilibrium flow of this phase and the boundary conditions. The affected cases are the two-phase case with oil and gas and the three-phase model (oil, water, and gas). This situation affects the performance of the foamy oil model.

- The selected correlations for PVT's properties are specific for heavy and extra-heavy oil crudes and

are not representative of the behavior of the crudes studied in the CHOPS field data. In particular, the viscosity values from correlations are very low compared with values from field data.

- The validation of the coupled model lets the analysis of some cases with geomechanics. In these cases using different values of permeability, the coupled model results in a trend in which the higher permeability, the lower pressure drop, and the higher saturation drop, which explains that the pressure disturbance due to a higher permeability took longer to reach the external radius than the lower permeability. Varying the pressure drawdown, the coupled model result in a trend in which the higher drawdown, the higher pressure drop, and the lower saturation drop, which explains that the pressure disturbance due to a higher pressure drawdown reaches the external radius faster than the lower pressure drawdown. Also, the coupled model result in strains that generates an increase in porosity and permeability, which generate a higher effect in saturation than in pressure, which can be explained by the fact that the saturation has the same order of magnitude as the strains, and pressure has a higher order. These results show consistency, which is another important element for validation.

- The foamy-oil behavior occurs in heavy oil reservoirs as a solution gas drive with anomalous high production, in terms of both the production rate and the primary oil recovery under low production gas-oil ratios. This behavior responds to the presence of the entrained gas that delays the gas release up to the pseudo-bubble point and enhances the inflow performance by its effect primarily in fluid properties and in relative permeability affecting positively Darcy's flow. The effect on fluid properties is a reduction in density and viscosity, and an increment in the formation volume factor and the gas-oil ratio between the bubble point and the pseudo-bubble point. The effect of the entrained gas on oil relative permeability is an increment in oil relative permeability and a reduction in gas relative permeability. Both effects increase the foamy oil velocity and reduce in gas velocity. The difference between the bubble-point and the pseudo-point defines the period of entrained gas presence, including its fraction and the gas release delay. The closer the pseudo-bubble-point pressure is to the bubble-point pressure, the lower the entrained gas fraction will be and the shorter the gas release delay. The higher the entrained gas fraction, the higher the positive effect on fluid properties: lower densities and viscosities and higher formation volume factor.

- The foamy oil behavior affects the sand production in heavy oil reservoirs producing by cold heavy oil production with sands. The effect of the entrained gas on fluid properties is a reduction in density and viscosity during the range of pseudo-bubble point pressure and bubble-point pressure. The critical fluid velocity is an erosion criterion included in the sand production model that works as a dynamic threshold to drag the sand grains when hydrodynamic forces exceed the frictional resistance forces. This velocity is affected by the fluid viscosity and fluid density during the foamy oil process. The reduction in fluid viscosity increases the critical fluid velocity generating a delay for the erosion criterion that can result in a stop in sand production if its value becomes greater than the mean fluid velocity. However, the fluid density for the multi-phase fluid flow model is constant because is under standard conditions, the reason why it does not affect the critical fluid velocity.

- The proposed sand production model is a powerful model that quantifies the sand production rate and the cumulative produced sand, in which the onset of sanding is stated with the equivalent plastic strain and the fluid velocity. The equivalent plastic strain passes a threshold value known as a critical equivalent plastic strain that defines a plastic state, in which the sanding initiates and the fluid velocity passes a threshold value known as a critical fluid velocity that responds to an erosion criterion, i.e., the

yielded sand will be eroded and mobilized to the well. The critical equivalent plastic strain is an experimental parameter while the critical fluid velocity is a dynamic variable that depends on fluid viscosity, grain size, and densities (fluid and sand). The sand mass rate depends on the equivalent plastic strain, i.e., the degree of work hardening in the rock. The model is integrated into the coupled simulator including pressures and saturation from the fluid flow and strain and stress for the elastoplastic model. However, this model requires major improvements to simulate massive sand in CHOPS wells but it may be an adequate model to simulate normal levels of sand production. The sand production model underestimates the produced sand because it does not adequately eliminate the blocks that reach the critical porosity and delivery the instantaneous sand, which could be corrected by an adaptative mesh or failing that, by a dynamic wellbore face through which the sand mass rate is quantified, with the support of a mass balance.

- The proposed wormhole model is a conceptual model that defines the steps to formate a wormhole, i.e., the dynamic zones extending from the wellbore into the reservoir. First, the formation failed and defines a yielded zone, if this zone passes the sand production criteria then the sanding occurs and the sand grains travel to the wellbore, defining a sanding front. This geomechanical changes and sanding increases the porosity and permeability; if the porosity passes the threshold a wormhole or channel is created ($\phi \geq \phi_{cr}$), defining a liquefaction zone. When porosity meets the critical porosity ($\phi = \phi_{cr}$), that for unconsolidated sandstones is around 0.52, the block collapses and is removed physically in sand producing the instantaneous sand. The model is integrated into the coupled simulator including pressures and saturation from the fluid flow, strain and stress for the elastoplastic model, and sand rate and cumulative sand from the sand production model. The wormhole model requires additional propagation components of sand production.

- An exploratory data analysis of the field data summarizes the main characteristics of 15 CHOPS wells. In terms of production performance, the results show a strong dependence of oil production on sand production, these two variables have a directly proportional relationship and a minor dependence of water and gas production on sand production with an inversely proportional relationship. Cumulative oil production is the variable with the most reliable and more noticeable trend to study sand production. Regarding the reservoir characteristics, the results show a strong dependence of oil viscosity, depth, and pressure on sand production, these three variables with an inversely proportional relationship with sand production and a minor dependence of porosity, production time, and net pay on sand production, this last variable with an inversely proportional relationship with sand production, and porosity and production time a directly proportional relationship with sand production.

- The simulation of sand production using field data lets to calibrate the parameters to use the sand production model in CHOPS well. The preliminary result is that the sand production model does not allow obtaining the sand level typical of CHOPS well, first because is not possible to use higher values of correlation slope than those considered in this research due to the stability of the simulator, and second, because the equivalent plastic strain does not propagate enough to have a higher amount of sand. From this study, the most influential attributes in sand production are the correlation slope and the critical equivalent plastic strain, the correlation slope with a directly proportional relationship with sand production, and the critical equivalent plastic strain with an inversely proportional relationship with sand production. It is found that for CHOPS well, the correlation slope should use the higher possible value with a critical value for the equivalent plastic should be 0.00001. The permeability, the cumulative equivalent plastic strain, and net pay show a minor effect on sand production.

- The simulation of a typical CHOPS well run a base case and perform a sensitivity study considering independence variables such as pressure drawdown, cohesion, internal friction angle, and stress regime. For sand and no sand cases, the most influential attributes on sand production are correlation slope, friction angle, wellbore flowing pressure, and cohesion, correlation slope and internal friction angle with a directly proportional relationship with sand production and the wellbore flowing pressure and cohesion with an inversely proportional relationship with sand production. In terms of the stress regime, the typical anisotropy for CHOPS wells generates more sand production. The cumulative equivalent plastic strain shows a slight effect on sand production because the cases with no sand show higher values than cases with sand. To clarify these attributes, the sensitivity study considers separately the cases with sand. For sand cases, the most influential attributes are internal friction angle, cumulative equivalent plastic strain, correlation slope, wellbore flowing pressure, and cohesion. Internal frictional angle, cumulative equivalent plastic strain, and correlation slope have a directly proportional relationship with sand production while wellbore flowing pressure and cohesion have an inversely proportional relationship with sand production.

- Gathering the results of the simulation of a typical CHOPS and its sensitivity study, a special case is built with all the properties stated to promote sand production with a successful response, significant values of cumulative oil production, and cumulative sand production. All properties contributed to sand production, confirming previous results, the higher the cumulative equivalent plastic strain, the higher the sand production and the higher the cumulative oil production.

- This study clearly demonstrates that geomechanics is an inherent component of reservoir engineering. A 3D single well simulator coupling multi-phase fluid flow and geomechanics including an elastoplastic behavior and sand production model with appropriate calibration and validation is a viable tool for understanding reservoir behavior and providing CHOPS and post-CHOPS production plans.

7.2 Recommendations

- The results of the fluid flow model in some cases with gas present instability in saturations. It is recommended for these cases to investigate an alternative strategy for the implementation of the boundary conditions in the wellbore and another strategy to drive the high mobility of the gas.

- Once the advantages and disadvantages of the systematic numerical methods for solving partial differential equations (PDEs) have been identified and the drawbacks seen during the development of the new simulator as a coupled model of a multi-phase fluid flow model and an elastoplastic model, it is recommended to implement the fluid flow model by finite element method using adaptative mesh refinement if necessary, thus eliminating the stability problems encountered because of the use of the cylindrical coordinates and the logarithmic radial distribution. The adaptative mesh also allows the cell removal for the coupled model (fluid flow and elastoplastic) with the sand production model when it is reached the critical porosity.

- The coupling of the multi-phase fluid flow model with the elastoplastic demands the variation of permeability with porosity due to the change in the stress state. This investigation uses for simplicity and generality the Kozeny-Carman equation, which should be used under the premise of the elastic

constitutive behavior of the rock. Its lack of accuracy during elastoplastic processes has been widely demonstrated and the sand production model requires calibrating and graduating the porosity effect on permeability that has a direct impact on oil production. It is recommended to include a more suitable alternative for this type of process.

- For the validation of the new simulator for cold heavy oil production with sands (CHOPS), it is recommended to complete the validation for a wider range of cases, including the multi-layer set for the multi-phase fluid flow and the coupled model, and perform the validation of the sand production model using field data for cases with normal sand levels.

- Given that the correlations for PVT's properties do not meet the expected behavior, it is recommended to consider an alternative to include adequate values to model CHOPS well for properties such as viscosity.

- The results from this investigation related to the massive sand during cold heavy oil production with sands (CHOPS) are carried out with field cases considering mean properties that represent a typical CHOPS well, and they may vary significantly for different geomechanical properties. It is recommended to perform a study to find how the variation of the geomechanical properties of the rock affects the results of this investigation.

- Cold heavy oil production with sands is a complex process that includes degradation of elastic and strength properties due to the stress redistribution and sanding during production that has not been included in this coupled simulator. It is recommended to include a model for the degradation of elastic and strength properties including cohesion and friction angle.

- The sand production model requires important improvement to simulate massive sand in CHOPS well, especially in the erosion model, the sand quantification, and the sanding propagation. The erosion model proposed in this research is for one-phase fluid flow and the multi-phase fluid flow should include components such as capillary cohesion that depends on the capillary pressure, water saturation, and internal angle friction. The sand quantification is underestimated because of the inadequate way to remove the wormhole blocks. It is recommended to include an erosion model more robust for multi-phase flow, an adaptive mesh, or failing that, a dynamic wellbore face through which the sand mass rate is adequately quantified and an alternative to increasing the sanding propagation in terms of plasticity. A mass balance could be another component to improve the sand production model.

Annex A. Fluid flow model

The model for cold heavy oil production with sand (CHOPS) requires a robust fluid flow model to be coupled with the elastoplastic model. This section describes the model, which is a 3D multi-phase fluid flow implemented by finite differences methods using cylindrical coordinates, describing the physical model, the mathematical model including the governing equations of each phase (oil, water, and gas), and their boundary conditions and the numerical model.

A1.Mathematical model

The fluid flow model assumes isothermal and multiphase fluid composed of oil, gas, and water in a deformable porous medium. The physical model uses equations in radial-cylindrical coordinates for anisotropic porous media and irregular grid-block distribution (logarithmic) because this geometry fits the behavior of the flow in the region around the well, where the elastoplastic deformation occurs. Four basic relations constitute this model: fluid mass conservation, solid mass conservation, Darcy's law, and the equation of state. The combination of these four relations yields a general fluid flow equation.

A1.1.Fluid mass conservation

The fluid mass conservation equation is obtained from a mass balance based on the infinitesimal volume element of a porous media as represented in Figure A – 1.

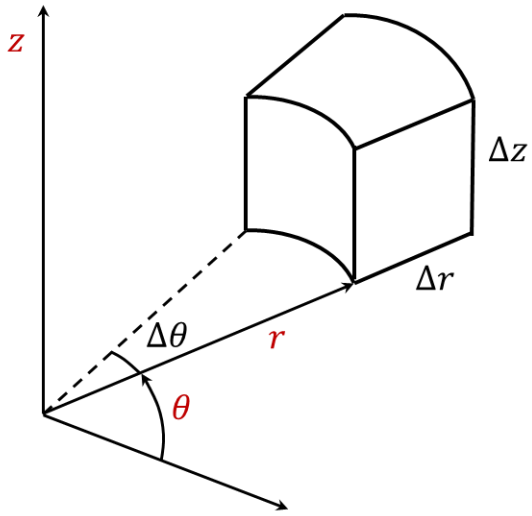

Figure A – 1. Infinitesimal volume element of a porous media in radial-cylindrical coordinates.

A1.1.1. Oil-phase

A mass balance of the oil phase for an infinitesimal volume element (Figure A – 1) leads to:

$$[inflow\ oil\ mass]_{\Delta t} - [\ outflow\ oil\ mass\ ]_{\Delta t} \pm [oil\ source/sink\ mass\ ]_{\Delta t} = [oil\ accumulation]_{\Delta t} \quad \text{(A – 1)}$$

$$[inflow\ oil\ mass\ ]_{\Delta t} = \alpha_c \rho_{o_{SC}} (\phi \mathrm{v}_{or_{SC}}) r \Delta\theta \Delta z \Delta t + \alpha_c \rho_{o_{SC}} (\phi \mathrm{v}_{o\theta_{SC}}) \Delta r \Delta z \Delta t + \alpha_c \rho_{o_{SC}} (\phi \mathrm{v}_{oz_{SC}}) \frac{\Delta\theta}{2} [(r+\Delta r)^2 - r^2] \Delta t \quad \text{(A – 2)}$$

$$[outflow\ oil\ mass\ ]_{\Delta t} = \left[\alpha_c \rho_{o_{SC}} (\phi \mathrm{v}_{or_{SC}}) + \Delta(\alpha_c \rho_{o_{SC}} \phi \mathrm{v}_{or_{SC}})\right](r+\Delta r)\Delta\theta\Delta z\Delta t + \left[\alpha_c \rho_{o_{SC}} (\phi \mathrm{v}_{o\theta_{SC}}) + \Delta(\alpha_c \rho_{o_{SC}} \phi \mathrm{v}_{o\theta_{SC}})\right](r+\Delta r)\Delta z\Delta t + \left[\alpha_c \rho_{o_{SC}} (\phi \mathrm{v}_{oz_{SC}}) + \Delta(\alpha_c \rho_{o_{SC}} \phi \mathrm{v}_{oz_{SC}})\right] \frac{\Delta\theta}{2} [(r+\Delta r)^2 - r^2] \Delta t \quad \text{(A – 3)}$$

In Equations (A – 2) and (A – 3), $\rho_{o_{SC}}$ is the oil density at standard conditions, α_c is the volume conversion factor, ϕ is the porosity of the formation and $\mathrm{v}_{or_{SC}}$, $\mathrm{v}_{o\theta_{SC}}$ and $\mathrm{v}_{oz_{SC}}$ are the oil real velocities at standard conditions in radial, tangential, and vertical directions, respectively. For oilfield units, $\alpha_c = 5.614583$.

The mass of oil through source/sinks, during the time step, Δt, is given by:

$$[oil\ source/sink\ mass\ ]_{\Delta t} = \pm \widetilde{q_o} V_b \Delta t \quad \text{(A – 4)}$$

where V_b is the bulk volume of the infinitesimal element ($V_b = r\Delta r\Delta\theta\Delta z$) and $\widetilde{q_o}$ is the inflow or outflow oil mass through the source/sink per total volume unit per time unit.

The oil accumulation term is given by:

$$[oil\ accumulation]_{\Delta t} = \Delta(\rho_{o_{SC}} V_{o_{SC}})_t^{t+\Delta t} = \Delta\left(\rho_{o_{SC}} \frac{V_{o_{RC}}}{B_o}\right)_t^{t+\Delta t}$$

where $V_{o_{RC}}$ and $V_{o_{SC}}$ are the oil volume at reservoir conditions and standard conditions, respectively, and B_o is the oil formation volume factor. The latter equation can be written as:

$$[oil\ accumulation]_{\Delta t} = \rho_{o_{SC}} \left[\left(\frac{\phi V_b S_o}{B_o}\right)_{t+\Delta t} - \left(\frac{\phi V_b S_o}{B_o}\right)_t\right] \quad \text{(A – 5)}$$

where S_o is the oil saturation.

Replacing Equations (A – 2) to (A – 5) into Equation (A – 1), neglecting infinitesimal terms of higher order, and dividing by $\alpha_c \rho_{o_{SC}} V_b \Delta t$, the mass balance equations can be expressed as:

$$-\left[\frac{\phi \mathrm{v}_{or_{SC}}}{r} + \frac{\Delta(\phi \mathrm{v}_{or_{SC}})}{\Delta r}\right] - \frac{1}{r}\frac{\Delta(\phi \mathrm{v}_{o\theta_{SC}})}{\Delta\theta} - \frac{\Delta(\phi \mathrm{v}_{oz_{SC}})}{\Delta z} = \frac{1}{\alpha_c V_b \Delta t}\left[\left(\frac{\phi V_b S_o}{B_o}\right)_{t+\Delta t} - \left(\frac{\phi V_b S_o}{B_o}\right)_t\right] + q_{o_{SC}} \quad \text{(A – 6)}$$

where $q_{o_{SC}}$ is the oil source/sink term expressed as the oil volumetric flow rate at standard conditions per unit of bulk volume (the convention to follow is: $q_{o_{SC}} < 0$ for oil production and $q_{o_{SC}} > 0$ for oil injection). Taking limits when the infinitesimal increments tend to zero and applying the derivative definition:

$$-\frac{1}{r}\frac{\partial}{\partial r}\left(r\phi \mathrm{v}_{or_{SC}}\right) - \frac{1}{r}\frac{\partial}{\partial \theta}\left(\phi \mathrm{v}_{o\theta_{SC}}\right) - \frac{\partial}{\partial z}\left(\phi \mathrm{v}_{oz_{SC}}\right) = \frac{1}{\alpha_c V_b}\frac{\partial}{\partial t}\left(\frac{\phi V_b S_o}{B_o}\right) + q_{o_{SC}} \quad \text{(A – 7)}$$

Equation (A – 7) is the oil mass conservation equation and it can be expressed in a general form as:

$$-\nabla \cdot \left(\phi \mathbf{v}_{o_{SC}}\right) = \frac{1}{\alpha_c V_b}\frac{\partial}{\partial t}\left(\frac{\phi V_b S_o}{B_o}\right) + q_{o_{SC}} \quad \text{(A – 8)}$$

In Equation (A – 8), $\mathbf{v}_{o_{SC}}$ is the oil real velocity vector at standard conditions and ∇ is the divergence function for a cylindrical coordinates system, which is defined as:

$$\nabla \cdot \boldsymbol{F} = \frac{1}{r}\frac{\partial (rF_r)}{\partial r} + \frac{1}{r}\frac{\partial F_\theta}{\partial \theta} + \frac{\partial F_z}{\partial z} \quad \text{(A – 9)}$$

Considering stress-sensitive reservoirs, V_b and ϕ are time-dependent parameters.

A1.1.2. Water-phase

Similarly to the oil case, the water mass balance is given by:

$$-\nabla \cdot \left(\phi \mathbf{v}_{w_{SC}}\right) = \frac{1}{\alpha_c V_b}\frac{\partial}{\partial t}\left(\frac{\phi V_b S_w}{B_w}\right) + q_{w_{SC}} \quad \text{(A – 10)}$$

where $\mathbf{v}_{w_{SC}}$ is the water real velocity vector at standard conditions, B_w is the water formation volume factor, S_w is the water saturation and q_w is the water source/sink term expressed as the water volumetric flow rate at standard conditions per unit of bulk volume (the convention to follow is: $q_w < 0$ for water production and $q_w > 0$ for water injection).

A1.1.3. Gas-phase

A mass balance of the gas phase leads to:

$$[inflow\ free\ gas\ mass]_{\Delta t} - [outflow\ free\ gas\ mass\ ]_{\Delta t} + [inflow\ gas\ in\ oil\ \ mass]_{\Delta t} - [outflow\ gas\ in\ oil\ \ mass]_{\Delta t} + [inflow\ gas\ in\ water\ \ mass]_{\Delta t} - [outflow\ gas\ in\ water\ mass]_{\Delta t} \pm [gas\ source/sink\ mass\ ]_{\Delta t} = [gas\ accumulation]_{\Delta t} \quad \text{(A – 11)}$$

Expanding each term of Equation (A – 11):

$$[inflow\ free\ gas\ mass]_{\Delta t} = \alpha_c \rho_{g_{SC}}\left(\phi \mathrm{v}_{gr_{SC}}\right) r\Delta\theta\Delta z\Delta t + \alpha_c \rho_{g_{SC}}\left(\phi \mathrm{v}_{g\theta_{SC}}\right)\Delta r\Delta z\Delta t + \alpha_c \rho_{g_{SC}}\left(\phi \mathrm{v}_{gz_{SC}}\right)\frac{\Delta\theta}{2}[(r+\Delta r)^2 - r^2]\Delta t \quad \text{(A – 12)}$$

$$[outflow\ free\ gas\ mass\ ]_{\Delta t} = \left[\alpha_c \rho_{g_{SC}} \left(\phi \mathrm{v}_{gr_{SC}}\right) + \Delta\left(\alpha_c \rho_{g_{SC}} \phi \mathrm{v}_{gr_{SC}}\right)\right](r + \Delta r)\Delta\theta\Delta z\Delta t + \left[\alpha_c \rho_{g_{SC}} \left(\phi \mathrm{v}_{g\theta_{SC}}\right) + \Delta\left(\alpha_c \rho_{g_{SC}} \phi \mathrm{v}_{g\theta_{SC}}\right)\right](r + \Delta r)\Delta z\Delta t + \left[\alpha_c \rho_{g_{SC}} \left(\phi \mathrm{v}_{gz_{SC}}\right) + \Delta\left(\alpha_c \rho_{g_{SC}} \phi \mathrm{v}_{gz_{SC}}\right)\right]\frac{\Delta\theta}{2}[(r + \Delta r)^2 - r^2]\Delta t \quad (A-13)$$

$$[inflow\ gas\ in\ oil\ mass]_{\Delta t} = \alpha_c \rho_{g_{SC}} R_{so}\left(\phi \mathrm{v}_{or_{SC}}\right) r\Delta\theta\Delta z\Delta t + \alpha_c \rho_{g_{SC}} R_{so}\left(\phi \mathrm{v}_{o\theta_{SC}}\right)\Delta r\Delta z\Delta t + \alpha_c \rho_{g_{SC}} R_{so}\left(\phi \mathrm{v}_{oz_{SC}}\right)\frac{\Delta\theta}{2}[(r + \Delta r)^2 - r^2]\Delta t \quad (A-14)$$

$$[outflow\ gas\ in\ oil\ mass]_{\Delta t} = \left[\alpha_c \rho_{g_{SC}} R_{so}\left(\phi \mathrm{v}_{or_{SC}}\right) + \Delta\left(\alpha_c \rho_{g_{SC}} R_{so} \phi \mathrm{v}_{or_{SC}}\right)\right](r + \Delta r)\Delta\theta\Delta z\Delta t + \left[\alpha_c \rho_{g_{SC}} R_{so}\left(\phi \mathrm{v}_{o\theta_{SC}}\right) + \Delta\left(\alpha_c \rho_{g_{SC}} R_{so} \phi \mathrm{v}_{o\theta_{SC}}\right)\right](r + \Delta r)\Delta z\Delta t + \left[\alpha_c \rho_{g_{SC}} R_{so}\left(\phi \mathrm{v}_{oz_{SC}}\right) + \Delta\left(\alpha_c \rho_{g_{SC}} R_{so} \phi \mathrm{v}_{oz_{SC}}\right)\right]\frac{\Delta\theta}{2}[(r + \Delta r)^2 - r^2]\Delta t \quad (A-15)$$

$$[inflow\ gas\ in\ water\ mass]_{\Delta t} = \alpha_c \rho_{g_{SC}} R_{sw}\left(\phi \mathrm{v}_{wr_{SC}}\right) r\Delta\theta\Delta z\Delta t + \alpha_c \rho_{g_{SC}} R_{sw}\left(\phi \mathrm{v}_{w\theta_{SC}}\right)\Delta r\Delta z\Delta t + \alpha_c \rho_{g_{SC}} R_{sw}\left(\phi \mathrm{v}_{wz_{SC}}\right)\frac{\Delta\theta}{2}[(r + \Delta r)^2 - r^2]\Delta t \quad (A-16)$$

$$[outflow\ gas\ in\ water\ mass]_{\Delta t} = \left[\alpha_c \rho_{g_{SC}} R_{sw}\left(\phi \mathrm{v}_{wr_{SC}}\right) + \Delta\left(\alpha_c \rho_{g_{SC}} R_{sw} \phi \mathrm{v}_{wr_{SC}}\right)\right](r + \Delta r)\Delta\theta\Delta z\Delta t + \left[\alpha_c \rho_{g_{SC}} R_{sw}\left(\phi \mathrm{v}_{w\theta_{SC}}\right) + \Delta\left(\alpha_c \rho_{g_{SC}} R_{sw} \phi \mathrm{v}_{w\theta_{SC}}\right)\right](r + \Delta r)\Delta z\Delta t + \left[\alpha_c \rho_{g_{SC}} R_{sw}\left(\phi \mathrm{v}_{wz_{SC}}\right) + \Delta\left(\alpha_c \rho_{g_{SC}} R_{sw} \phi \mathrm{v}_{wz_{SC}}\right)\right]\frac{\Delta\theta}{2}[(r + \Delta r)^2 - r^2]\Delta t \quad (A-17)$$

In Equations (A – 12) and (A – 17), $\rho_{g_{SC}}$ is the gas density at standard conditions, $\mathrm{v}_{wr_{SC}}$, $\mathrm{v}_{w\theta_{SC}}$ and $\mathrm{v}_{wz_{SC}}$ are the water real velocities at standard conditions in the radial, tangential, and vertical direction, respectively; and $\mathrm{v}_{gr_{SC}}$, $\mathrm{v}_{g\theta_{SC}}$ and $\mathrm{v}_{gz_{SC}}$ are the gas real velocities at standard conditions in radial, tangential, and vertical directions, respectively; and R_{so} and R_{sw} are the gas solubility (gas volume at standard conditions/oil volume at standard conditions) in oil and water, respectively.

The mass of gas through sources/sinks during the time step, Δt, is given by:

$$[gas\ source/sink\ mass\ ]_{\Delta t} = \pm\widetilde{q_g} V_b \Delta t \quad (A-18)$$

where $\widetilde{q_g}$ is the inflow or outflow gas mass through the source/sink per total volume unit per time unit.

The gas accumulation term is given by:

$$[gas\ accumulation]_{\Delta t} = \Delta\left(\rho_{g_{SC}} \frac{V_{g_{RC}}}{B_g} + \rho_{g_{SC}} R_{so} \frac{V_{o_{RC}}}{B_o} + \rho_{g_{SC}} R_{sw} \frac{V_{w_{RC}}}{B_w}\right)_t^{t+\Delta t}$$

where $V_{g_{RC}}$, $V_{o_{RC}}$, and $V_{w_{RC}}$ are the volume of gas, oil, and water phases, respectively, at reservoir conditions, B_g is the gas formation volume factor and S_g is the gas saturation.

$$[gas\ accumulation]_{\Delta t} = \rho_{g_{SC}}\left[\left(\frac{\phi V_b S_g}{B_g} + R_{so}\frac{\phi V_b S_o}{B_o} + R_{sw}\frac{\phi V_b S_w}{B_w}\right)_{t+\Delta t} - \left(\frac{\phi V_b S_g}{B_g} + R_{so}\frac{\phi V_b S_o}{B_o} + R_{sw}\frac{\phi V_b S_w}{B_w}\right)_t\right] \quad (A-19)$$

Substituting Equations (A – 12) to (A – 19) into Equation (A – 11), neglecting infinitesimal terms of higher order, and dividing by $\alpha_c \rho_{g_{SC}} V_b \Delta t$, the mass balance equation can be expressed as:

$$-\left[\frac{\phi \mathrm{v}_{gr_{SC}}}{r} + \frac{\Delta\left(\phi \mathrm{v}_{gr_{SC}}\right)}{\Delta r}\right] - \frac{1}{r}\frac{\Delta\left(\phi \mathrm{v}_{g\theta_{SC}}\right)}{\Delta\theta} - \frac{\Delta\left(\phi \mathrm{v}_{gz_{SC}}\right)}{\Delta z} - \left[\frac{R_{so}\phi \mathrm{v}_{or_{SC}}}{r} + \frac{\Delta\left(R_{so}\phi \mathrm{v}_{or_{SC}}\right)}{\Delta r}\right] - \frac{1}{r}\frac{\Delta\left(R_{so}\phi \mathrm{v}_{o\theta_{SC}}\right)}{\Delta\theta} - \frac{\Delta\left(\phi \mathrm{v}_{oz_{SC}}\right)}{\Delta z} - \left[\frac{R_{sw}\phi \mathrm{v}_{wr_{SC}}}{r} + \frac{\Delta\left(R_{sw}\phi \mathrm{v}_{wr_{SC}}\right)}{\Delta r}\right] - \frac{1}{r}\frac{\Delta\left(R_{sw}\phi \mathrm{v}_{w\theta_{SC}}\right)}{\Delta\theta} - \frac{\Delta\left(\phi \mathrm{v}_{wz_{SC}}\right)}{\Delta z} = \frac{1}{\alpha_c V_b \Delta t}\left[\left(\frac{\phi V_b S_g}{B_g} + R_{so}\frac{\phi V_b S_o}{B_o} + R_{sw}\frac{\phi V_b S_w}{B_w}\right)_{t+\Delta t} - \left(\frac{\phi V_b S_g}{B_g} + R_{so}\frac{\phi V_b S_o}{B_o} + R_{sw}\frac{\phi V_b S_w}{B_w}\right)_t\right] + q_{g_{SC}} \quad (A-20)$$

where $q_{g_{SC}}$ is the gas source/sink term expressed as the gas volumetric flow rate at standard conditions per unit of bulk volume (the convention to follow is: $q_{g_{SC}} < 0$ for gas production and $q_{g_{SC}} > 0$ for gas injection). Taking limits, when the infinitesimal increments tend to zero and applying the derivative definition:

$$-\frac{1}{r}\frac{\partial}{\partial r}\left(r\phi \mathrm{v}_{gr_{SC}}\right) - \frac{1}{r}\frac{\partial}{\partial\theta}\left(\phi \mathrm{v}_{g\theta_{SC}}\right) - \frac{\partial}{\partial z}\left(\phi \mathrm{v}_{gz_{SC}}\right) - \frac{1}{r}\frac{\partial}{\partial r}\left(R_{so} r\phi \mathrm{v}_{or_{SC}}\right) - \frac{1}{r}\frac{\partial}{\partial\theta}\left(R_{so}\phi \mathrm{v}_{o\theta_{SC}}\right) - \frac{\partial}{\partial z}\left(R_{so}\phi \mathrm{v}_{oz_{SC}}\right) - \frac{1}{r}\frac{\partial}{\partial r}\left(R_{sw} r\phi \mathrm{v}_{wr_{SC}}\right) - \frac{1}{r}\frac{\partial}{\partial\theta}\left(R_{sw}\phi \mathrm{v}_{w\theta_{SC}}\right) - \frac{\partial}{\partial z}\left(R_{sw}\phi \mathrm{v}_{wz_{SC}}\right) = \frac{1}{\alpha_c V_b}\frac{\partial}{\partial t}\left(\frac{\phi V_b S_g}{B_g} + R_{so}\frac{\phi V_b S_o}{B_o} + R_{sw}\frac{\phi V_b S_w}{B_w}\right) + q_{g_{SC}} \quad (A-21)$$

Equation (A – 21) is the gas mass conservation equation and it can be expressed in a general form as:

$$-\nabla\cdot\left(\phi \mathbf{v}_{g_C} + R_{so}\phi \mathbf{v}_{o_{SC}} + R_{sw}\phi \mathbf{v}_{w_{SC}}\right) = \frac{1}{\alpha_c V_b}\frac{\partial}{\partial t}\left(\frac{\phi V_b S_g}{B_g} + R_{so}\frac{\phi V_b S_o}{B_o} + R_{sw}\frac{\phi V_b S_w}{B_w}\right) + q_{g_{SC}} \quad (A-22)$$

where $\mathbf{v}_{g_{SC}}$ is the gas real velocity vector at standard conditions.

A1.2.Solid mass conservation

The solid mass can be expressed as:

$$m_s = V_s\rho_s = \rho_s(1-\phi)\mathrm{v}_s A_T \Delta t \quad (A-23)$$

where ρ_s is the solid density, A_T is the total area and v_s is the solid real velocity.

By following a similar procedure as the one applied to develop the fluid mass balance, Equations (A – 8), (A – 10), and (A – 22), it can be shown that the solid mass conservation can be expressed as:

$$-\frac{1}{r}\frac{\partial}{\partial r}[r\rho_s(1-\phi)\mathrm{v}_{sr}]-\frac{1}{r}\frac{\partial}{\partial \theta}[\rho_s(1-\phi)\mathrm{v}_{s\theta}]-\frac{\partial}{\partial z}[\rho_s(1-\phi)\mathrm{v}_{sz}]=\frac{1}{\alpha_c V_b}\frac{\partial}{\partial t}[\rho_s V_b(1-\phi)]+\widetilde{q_s} \quad (A-24)$$

where v_{sr}, $\mathrm{v}_{s\theta}$ and v_{sz} are the solid real velocities at standard conditions in the radial, tangential, and vertical direction, respectively, and $\widetilde{q_s}$ is the inflow or outflow of solid mass through the source/sink per total volume unit per time unit (the convention to follow is: $q_s < 0$ for solid production and $q_s > 0$ for solid injection).

Equation (A – 24) can be expressed in a general form as,

$$-\nabla\cdot[\rho_s(1-\phi)\mathbf{v}_s]=\frac{1}{\alpha_c V_b}\frac{\partial}{\partial t}[\rho_s V_b(1-\phi)]+\widetilde{q_s} \quad (A-25)$$

where $\mathbf{v}_s$ is the solid real velocity vector.

Expanding the first term of the left-hand side of Equation (A – 25):

$$-\nabla\cdot[\rho_s(1-\phi)\mathbf{v}_s]=-\mathbf{v}_s\nabla\cdot[\rho_s(1-\phi)]-\rho_s(1-\phi)\nabla\cdot\ \mathbf{v}_s$$

Neglecting the term of the convective component $\mathbf{v}_s\nabla\cdot[\rho_s(1-\phi)]$,

$$-\nabla\cdot[\rho_s(1-\phi)\mathbf{v}_s]=-\rho_s(1-\phi)\nabla\cdot\ \mathbf{v}_s \quad (A-26)$$

Taking Equation (A – 26) into Equation (A – 25),

$$\nabla\cdot\mathbf{v}_s=-\frac{1}{\alpha_c V_b\rho_s(1-\phi)}\frac{\partial}{\partial t}[\rho_s(1-\phi)V_b]+\frac{\widetilde{q_s}}{\rho_s(1-\phi)} \quad (A-27)$$

Differentiating the first term on the right-hand side of Equation (A – 27), applying the porosity definition $\phi = V_p/V_b$ and assuming a constant solid density,

$$\nabla\cdot\mathbf{v}_s=\frac{\widetilde{q_s}}{\rho_s(1-\phi)}=\frac{q_s}{(1-\phi)} \quad (A-28)$$

where q_s is the volumetric sand rate.

A1.3.Darcy's law

From the general form for Darcy's law:

$$\mathrm{v}_x=\frac{q_x}{A_x}=-\beta_c\frac{k_x}{\phi\mu}\frac{\partial\Phi}{\partial x} \quad (A-29)$$

where β_c is the transmissibility conversion factor, k_x is the absolute permeability in the direction of the x-axis, ϕ is the porosity of the rock, μ is the fluid viscosity, Φ is the fluid potential, and v_x is the volumetric velocity of the fluid defined as the fluid flow rate q_x per unit cross-sectional area A_x normal

to flow direction x. For oilfield units, $\beta_c = 0.001127$. The potential Φ is related to pressure through the following relationship:

$$\frac{\partial \Phi}{\partial x} = \frac{\partial p}{\partial x} - \gamma \frac{\partial z}{\partial x}$$

where γ is the phase gravity.

A1.3.1. Oil phase

The oil real velocity at standard conditions in terms of oil pressure gradient considering gravity is given by:

$$\mathbf{v}_{ro_{SC}} = \mathbf{v}_{o_{SC}} - \mathbf{v}_s = -\beta_c \frac{\boldsymbol{k}_o}{\phi B_o \mu_o} \left(\nabla p_{\mathrm{o}} - \rho_{o_{SC}} \gamma_c g \nabla z\right) \quad \text{(A – 30)}$$

Where $\mathbf{v}_{roSC}$ is the oil real velocity vector at standard conditions, $\mathbf{v}_{oSC}$ is the oil volumetric velocity vector at standard conditions, $\mathbf{v}_s$ is the solid velocity vector, $\boldsymbol{k}_o$ is the oil permeability tensor, μ_o is the oil viscosity, B_o is the oil volume factor, g is the gravitational acceleration ($g = 32.174\, ft/\mathrm{s}^2$) and γ_c is the gravity conversion factor ($\gamma_c = 0.21584 \times 10^{-3}$). The z direction is positive in the vertically downward direction.

Solving for the oil real velocity, at standard conditions, in each direction:

$$\mathrm{v}_{or_{SC}} = \mathrm{v}_{sr} - \beta_c \frac{k_{or}}{\phi B_o \mu_o} \left(\frac{\partial p_o}{\partial r} - \rho_{o_{SC}} \gamma_c g \frac{\partial z}{\partial r}\right)$$

$$\mathrm{v}_{o\theta_{SC}} = \mathrm{v}_{s\theta} - \beta_c \frac{k_{o\theta}}{\phi B_o \mu_o} \left(\frac{\partial p_o}{r \partial \theta} - \rho_{o_{SC}} \gamma_c g \frac{\partial z}{r \partial \theta}\right)$$

$$\mathrm{v}_{oz_{SC}} = \mathrm{v}_{sz} - \beta_c \frac{k_{oz}}{\phi B_o \mu_o} \left(\frac{\partial p_o}{\partial z} - \rho_{o_{SC}} \gamma_c g \frac{\partial z}{\partial z}\right) \quad \text{(A – 31)}$$

A1.3.2. Water-phase

Similar to the oil phase, the water real velocity at standard conditions in terms of water pressure gradient considering gravity is given by:

$$\mathbf{v}_{rw_{SC}} = \mathbf{v}_{w_{SC}} - \mathbf{v}_s = -\beta_c \frac{\boldsymbol{k}_w}{\phi B_w \mu_w} \left(\nabla p_w - \rho_{w_{SC}} \gamma_c g \nabla z\right) \quad \text{(A – 32)}$$

The water velocity, at standard conditions, in each direction can be written as:

$$\mathrm{v}_{wr_{SC}} = \mathrm{v}_{sr} - \beta_c \frac{k_{wr}}{\phi B_w \mu_w} \left(\frac{\partial p_w}{\partial r} - \rho_{w_{SC}} \gamma_c g \frac{\partial z}{\partial r}\right)$$

$$\mathrm{v}_{w\theta_{SC}} = \mathrm{v}_{s\theta} - \beta_c \frac{k_{w\theta}}{\phi B_w \mu_w} \left(\frac{\partial p_w}{r \partial \theta} - \rho_{w_{SC}} \gamma_c g \frac{\partial z}{r \partial \theta}\right)$$

$$v_{wz_{SC}} = v_{sz} - \beta_c \frac{k_{wz}}{\phi B_w \mu_w}\left(\frac{\partial p_w}{\partial z} - \rho_{w_{SC}} \gamma_c g \frac{\partial z}{\partial z}\right) \quad (A-33)$$

A1.3.3. Gas-phase

Similar to the oil and water phases, the gas real velocity at standard conditions in terms of gas pressure gradient considering gravity is given by:

$$\mathbf{v}_{rg_{SC}} = \mathbf{v}_{g_{SC}} - \mathbf{v}_s = -\beta_c \frac{\boldsymbol{k}_g}{\phi B_g \mu_g}\left(\nabla p_g - \rho_{g_{SC}} \gamma_c g \nabla z\right) \quad (A-34)$$

Likewise, the gas velocity at standard conditions in each direction for the gas phase can be written as:

$$v_{gr_{SC}} = v_{sr} - \beta_c \frac{k_{gr}}{\phi B_g \mu_g}\left(\frac{\partial p_g}{\partial r} - \rho_{g_{SC}} \gamma_c g \frac{\partial z}{\partial r}\right)$$

$$v_{g\theta_{SC}} = v_{s\theta} - \beta_c \frac{k_{g\theta}}{\phi B_g \mu_g}\left(\frac{\partial p_g}{r\partial \theta} - \rho_{g_{SC}} \gamma_c g \frac{\partial z}{r\partial \theta}\right)$$

$$v_{gz_{SC}} = v_{sz} - \beta_c \frac{k_{gz}}{\phi B_g \mu_g}\left(\frac{\partial p_g}{\partial z} - \rho_{g_{SC}} \gamma_c g \frac{\partial z}{\partial z}\right) \quad (A-35)$$

A1.4.Equation of state (isothermal fluid compressibility)

From the compressibility definition:

$$c = -\frac{1}{V}\left(\frac{\partial V}{\partial p}\right)_T + \frac{1}{V}\left(\frac{\partial V}{\partial T}\right)_p$$

For constant temperature, $T = constant$:

$$c = -\frac{1}{V}\left(\frac{\partial V}{\partial p}\right)_T$$

Taking into account the density definition ($V = m/\rho$) and that the mass is constant:

$$c_f = \frac{1}{\rho_f}\frac{\partial \rho_f}{\partial p} \quad (A-36)$$

On the other hand, in terms of the fluid formation-volume factor:

$$c_f = -\frac{1}{B_f}\frac{\partial B_f}{\partial p} \quad (A-37)$$

A1.4.1. Oil-phase

The oil phase is assumed as a slight compressibility fluid and, therefore, the compressibility is assumed to remain constant over the range of pressure of interest. Thus, Equation (A – 37) takes the following form for the oil phase:

$$c_o = -\frac{1}{B_o}\frac{\partial B_o}{\partial p_o} = constant \tag{A – 38}$$

A1.4.2. Water-phase

Similarly, the water phase is assumed as a slightly compressibility fluid:

$$c_w = -\frac{1}{B_w}\frac{\partial B_w}{\partial p_w} = constant \tag{A – 39}$$

A1.4.3. Gas-phase

Considering the gas phase as a real gas, its compressibility is pressure-dependent:

$$c_g = -\frac{1}{B_g}\frac{\partial B_g}{\partial p_g} \tag{A – 40}$$

Although the compressibility for both slightly compressible fluids and real gases has the same form, the equations used to estimate the fluid properties as B_g, μ_g and c_g are completely different from the equation used to compute the same properties for the oil and water phases.

A1.5.Compressibility of the formation

Following Zimmerman, Somerton, & King (1986), four different compressibilities are associated with porous media. Each of these rock compressibilities relates to changes in either the pore volume V_p or the bulk volume V_b concerning changes in the pore pressure p or the mean normal stress, $\bar{\sigma}$.

The compressibilities that express the effect of total stress and pore pressure variations on pore volume denote as c_{pc} and c_{pp}, respectively, are defined as:

$$c_{pc} = -\frac{1}{V_p}\frac{\partial V_p}{\partial \bar{\sigma}}\Big|_p$$

$$c_{pp} = \frac{1}{V_p}\frac{\partial V_p}{\partial p}\Big|_{\bar{\sigma}} \tag{A – 41}$$

Likewise, the compressibilities that express the effect of total stress and pore pressure variations on bulk volume, denote as c_{bc} and c_{bp}, respectively, are defined as:

$$c_{bc} = -\frac{1}{V_b}\frac{\partial V_b}{\partial \bar{\sigma}}\Big|_p$$

$$c_{bp} = \frac{1}{V_b}\frac{\partial V_b}{\partial p}\Big|_{\bar{\sigma}} \quad (A-42)$$

Zimmerman *et al.* (1986) found the relations among these four compressibilities, the porosity, ϕ, and solid compressibility, c_s, are defined as the compressibility of the rock matrix material. These relations for pore compressibilities are given by:

$$c_{bc} = c_{bp} + c_s$$

$$c_{pc} = c_{pp} + c_s \quad (A-43)$$

These relations for bulk compressibilities are given by:

$$c_{bp} = \phi c_{pc}$$

$$c_{pc} = \frac{c_{bc} - c_s}{\phi} \quad (A-44)$$

A1.6.Other relations

A1.6.1. Saturations

The oil, water, and gas saturations must satisfy the following constraint:

$$S_o + S_w + S_g = 1 \quad (A-45)$$

with: $0 \leq S_o, S_w, S_g \leq 1$

A1.6.2. Capillary pressures

The oil, water, and gas pressures p_o, p_w and p_g can be related to the concept of capillary pressure:

$$p_{cwo} = p_o - p_w \quad (A-46)$$

$$p_{cgo} = p_g - p_o \quad (A-47)$$

On differentiating Equation (A – 46) and applying the chain rule to capillary pressure terms, it can be shown that:

$$\frac{\partial p_w}{\partial t} = \frac{\partial p_o}{\partial t} - \frac{\partial p_{cwo}}{\partial t} = \frac{\partial p_o}{\partial t} - p'_{cwo}\frac{\partial S_w}{\partial t} \quad (A-48)$$

where:

$$p'_{cwo} = \frac{\partial p_{cwo}}{\partial S_w}$$

Similarly, for Equation (A – 47):

$$\frac{\partial p_g}{\partial t} = \frac{\partial p_o}{\partial t} - \frac{\partial p_{cgo}}{\partial t} = \frac{\partial p_o}{\partial t} + p'_{cgo}\frac{\partial S_g}{\partial t} \quad \text{(A – 49)}$$

where:

$$p'_{cgo} = \frac{\partial p_{cgo}}{\partial S_g}$$

The terms p'_{cwo} and p'_{cgo} can be obtained by using the capillary pressure curves of each set of two-phase systems.

A1.7.Governing equations

The fluid flow model consists of three governing equations, one for each fluid phase: oil, water, and gas.

A1.7.1. Oil-phase

Substituting Equations (A – 30) to (A – 31) into Equation (A – 8), is obtained:

$$-\nabla \cdot \left(\phi \mathbf{v}_s - \beta_c \frac{\boldsymbol{k}_o}{B_o \mu_o}\left(\nabla p_o - \rho_{o_{SC}} \gamma_c g \nabla z\right)\right) = \frac{1}{\alpha_c V_b}\frac{\partial}{\partial t}\left(\frac{\phi V_b S_o}{B_o}\right) + q_{o_{SC}} \quad \text{(A – 50)}$$

Therefore,

$$\nabla \cdot \left(\beta_c \frac{\boldsymbol{k}_o}{B_o \mu_o}\left(\nabla p_o - \rho_{o_{SC}} \gamma_c g \nabla z\right)\right) = \nabla \cdot (\phi \mathbf{v}_s) + \frac{1}{\alpha_c V_b}\frac{\partial}{\partial t}\left(\frac{\phi V_b S_o}{B_o}\right) + q_{o_{SC}}$$

$$\nabla \cdot \left(\beta_c \frac{\boldsymbol{k}_o}{B_o \mu_o}\nabla p_o - \beta_c \frac{k_o}{B_o \mu_o}\rho_{o_{SC}} \gamma_c g \nabla z\right) = \mathbf{v}_s \cdot \nabla \phi + \phi \nabla \cdot \mathbf{v}_s + \frac{1}{\alpha_c V_b}\frac{\partial}{\partial t}\left(\frac{\phi V_b S_o}{B_o}\right) + q_{o_{SC}} \quad \text{(A – 51)}$$

The term $\mathbf{v}_s \cdot \nabla \phi$ is a convective component that can be neglected because this product is a small value compared to other terms in Equation (A – 51). The term $\nabla \phi$ represents the variation of ϕ through the path followed by the particle and $\mathbf{v}_s$ represents the instantaneous velocity at a given point. Thus, this term can be ignored because its spatial variation is independent of the trajectory, and physically this means that there is deformation in the reservoir but without rotation or movement. Thus, Equation (A – 51) is simplified to:

$$\nabla \cdot \left(\beta_c \frac{\boldsymbol{k}_o}{B_o \mu_o}\nabla p_o - \beta_c \frac{\boldsymbol{k}_o}{B_o \mu_o}\rho_{o_{SC}} \gamma_c g \nabla z\right) = \phi \nabla \cdot \mathbf{v}_s + \frac{1}{\alpha_c V_b}\frac{\partial}{\partial t}\left(\frac{\phi V_b S_o}{B_o}\right) + q_{o_{SC}} \quad \text{(A – 52)}$$

Differentiating the second term of the right-hand side and applying the porosity definition $\phi = V_p / V_b$

$$\frac{1}{\alpha_c V_b}\frac{\partial}{\partial t}\left(\frac{\phi V_b S_o}{B_o}\right) = \frac{1}{\alpha_c V_b}\frac{\partial}{\partial t}\left(\frac{V_p S_o}{B_o}\right) = \frac{1}{\alpha_c V_b B_o}\left[V_p \frac{\partial S_o}{\partial t} + S_o \phi \frac{\partial V_p}{\partial t} - \frac{S_o V_p}{B_o}\frac{\partial B_o}{\partial t}\right]$$

Rearranging and using the chain rule in the B_o term,

$$\frac{1}{\alpha_c V_b}\frac{\partial}{\partial t}\left(\frac{\phi V_b S_o}{B_o}\right) = \frac{S_o\phi}{\alpha_c B_o}\left[\frac{1}{S_o}\frac{\partial S_o}{\partial t} + \frac{1}{V_p}\frac{\partial V_p}{\partial t} - \frac{1}{B_o}\frac{\partial B_o}{\partial p_o}\frac{\partial p_o}{\partial t}\right] \quad \text{(A – 53)}$$

Substituting Equation (A – 38) into Equation (A – 53),

$$\frac{1}{\alpha_c V_b}\frac{\partial}{\partial t}\left(\frac{\phi V_b S_o}{B_o}\right) = \frac{S_o\phi}{\alpha_c B_o}\left[\frac{1}{S_o}\frac{\partial S_o}{\partial t} + \frac{1}{V_p}\frac{\partial V_p}{\partial t} + c_o\frac{\partial p_o}{\partial t}\right] \quad \text{(A – 54)}$$

Substituting Equation (A – 54) into Equation (A – 52),

$$\nabla\cdot\left(\beta_c\frac{\boldsymbol{k}_o}{B_o\mu_o}\nabla p_\mathrm{o} - \beta_c\frac{\boldsymbol{k}_o}{B_o\mu_o}\rho_{osc}\gamma_c g\nabla z\right) = \phi\nabla\cdot\mathbf{v}_s + \frac{S_o\phi}{\alpha_c B_o}\left[\frac{1}{S_o}\frac{\partial S_o}{\partial t} + \frac{1}{V_p}\frac{\partial V_p}{\partial t} + c_o\frac{\partial p_o}{\partial t}\right] + q_{osc} \quad \text{(A – 55)}$$

Taking Equation (A – 28) into Equation (A – 55),

$$\nabla\cdot\left(\beta_c\frac{\boldsymbol{k}_o}{B_o\mu_o}\nabla p_\mathrm{o} - \beta_c\frac{\boldsymbol{k}_o}{B_o\mu_o}\rho_{osc}\gamma_c g\nabla z\right) = \frac{q_s\phi}{(1-\phi)} + \frac{S_o\phi}{\alpha_c B_o}\left[\frac{1}{S_o}\frac{\partial S_o}{\partial t} + \frac{1}{V_p}\frac{\partial V_p}{\partial t} + c_o\frac{\partial p_o}{\partial t}\right] + q_{osc} \quad \text{(A – 56)}$$

Developing the term containing the derivative of the pore volume with respect to time:

$$\frac{1}{V_p}\frac{\partial V_p}{\partial t} = \frac{1}{V_p}\frac{\partial V_p}{\partial p_\mathrm{o}}\Big|_{\bar{\sigma}}\frac{\partial p_o}{\partial t} + \frac{1}{V_p}\frac{\partial V_p}{\partial \bar{\sigma}}\Big|_{p_o}\frac{\partial \bar{\sigma}}{\partial t} \quad \text{(A – 57)}$$

Substituting Equation (A – 41) into Equation (A – 57),

$$\frac{1}{V_p}\frac{\partial V_p}{\partial t} = c_p\frac{\partial p_o}{\partial t} - c_{pc}\frac{\partial \bar{\sigma}}{\partial t} \quad \text{(A – 58)}$$

Redefining c_{pp} using Equations (A – 43) into Equation (A – 58):

$$\frac{1}{V_p}\frac{\partial V_p}{\partial t} = \left(c_{pc} - c_s\right)\frac{\partial p_o}{\partial t} - c_{pc}\frac{\partial \bar{\sigma}}{\partial t} \quad \text{(A – 59)}$$

Then, the mean stress can be defined in terms of the volumetric strain using Hooke's law:

$$\bar{\sigma} = \frac{\epsilon_v^e}{c_{bc}} \quad \text{(A – 60)}$$

Differentiating Equation (A – 60) in terms of time and considering as effective mean stress:

$$\frac{\partial \bar{\sigma}}{\partial t} = \frac{1}{c_{bc}}\frac{\partial \epsilon_v^e}{\partial t} + \alpha\frac{\partial p_o}{\partial t} \quad \text{(A – 61)}$$

Replacing Equation (A – 61) into Equation (A – 59) and regrouping:

$$\frac{1}{V_p}\frac{\partial V_p}{\partial t} = \left(c_{pc} - c_s\right)\frac{\partial p_o}{\partial t} - c_{pc}\left(\frac{1}{c_{bc}}\frac{\partial \epsilon_v^e}{\partial t} + \alpha\frac{\partial p_o}{\partial t}\right) \quad \text{(A – 62)}$$

Using Equation (A – 44) in the second term of Equation (A – 62):

$$\frac{1}{V_p}\frac{\partial V_p}{\partial t} = \left[c_{pc}(1-\alpha) - c_s\right]\frac{\partial p_o}{\partial t} - \frac{c_{bc}-c_s}{\phi c_{bc}}\frac{\partial \epsilon_v^e}{\partial t} \quad \text{(A – 63)}$$

Applying the Biot coefficient definition $\alpha = 1 - c_s/c_{bc}$:

$$\frac{1}{V_p}\frac{\partial V_p}{\partial t} = \left[c_{pc}(1-\alpha) - c_s\right]\frac{\partial p_o}{\partial t} - \frac{\alpha}{\phi}\frac{\partial \epsilon_v^e}{\partial t} \quad \text{(A – 64)}$$

The resultant equation is the expression that allows coupling the fluid flow model with the geomechanical model considering elasticity. Plastic deformation can be introduced just by assuming that the pore volume deformation $\left(\partial\epsilon_p = -\partial V_p/V_p\right)$ is composed of an elastic and a plastic part:

$$\frac{1}{V_p}\frac{\partial V_p}{\partial t} = \frac{1}{V_p}\frac{\partial V_p^e}{\partial t} + \frac{1}{V_p}\frac{\partial V_p^p}{\partial t} \quad \text{(A – 65)}$$

Starting from the porosity definition $\left(\phi = V_p/V_b\right)$ and the pore volume definition $\left(V_p = V_b - V_s\right)$:

$$\frac{\partial V_p^p}{dt} = \frac{\partial V_b^p}{dt} - \frac{\partial V_s^p}{dt} \quad \text{(A – 66)}$$

And defining the plastic bulk strain ϵ_v^p and the plastic solid strain ϵ_s^p as:

$$\frac{\partial \epsilon_v^p}{\partial t} = -\frac{1}{V_b}\frac{\partial V_b^p}{\partial t}$$

$$\frac{\partial \epsilon_s^p}{\partial t} = -\frac{1}{V_s}\frac{\partial V_s^p}{\partial t} = -\frac{1}{(1-\phi)V_b}\frac{\partial V_s^p}{\partial t} \quad \text{(A – 67)}$$

Replacing Equations (A – 67) into Equation (A – 66):

$$\frac{\partial V_p^p}{dt} = V_b\left[-\frac{\partial \epsilon_v^p}{\partial t} + (1-\phi)\frac{\partial \epsilon_s^p}{\partial t}\right]$$

Therefore:

$$\frac{1}{V_p}\frac{\partial V_p^p}{\partial t} = -\frac{1}{\phi}\frac{\partial \epsilon_v^p}{\partial t} + \left(\frac{1-\phi}{\phi}\right)\frac{\partial \epsilon_s^p}{\partial t} \quad \text{(A – 68)}$$

The volumetric plastic strain, ϵ_v^p, and the pore plastic strain, ϵ_p^p, are related to phenomena such as rock grains rearrangement, crushing, or micro-fracturing. These variables can be measured in the laboratory; however, the plastic deformation of the rock grains ϵ_s^p is a variable very difficult to measure and it may be small compared to ϵ_v^p and ϵ_p^p. If it is assumed then $\epsilon_s^p = 0$, and Equation (A – 68) can be stated as:

$$\frac{1}{V_p}\frac{\partial V_p^p}{\partial t} = -\frac{1}{\phi}\frac{\partial \epsilon_v^p}{\partial t} \quad (A-69)$$

Replacing Equations (A – 64) and (A – 69) into Equation (A – 65):

$$\frac{1}{V_p}\frac{\partial V_p}{\partial t} = \left[c_{pc}(1-\alpha) - c_s\right]\frac{\partial p_o}{\partial t} - \frac{\alpha}{\phi}\frac{\partial \epsilon_v^e}{\partial t} - \frac{1}{\phi}\frac{\partial \epsilon_v^p}{\partial t} \quad (A-70)$$

Replacing Equation (A – 70) with Equation (A – 56) and regrouping,

$$\nabla\cdot\left(\beta_c\frac{\boldsymbol{k}_o}{B_o\mu_o}\left(\nabla p_o - \rho_{o_{SC}}\gamma_c g\nabla z\right)\right) = \frac{q_s\phi}{(1-\phi)} + \frac{\phi}{\alpha_c B_o}\frac{\partial S_o}{\partial t} + \frac{S_o\phi}{\alpha_c B_o}\left[c_{pc}(1-\alpha) - c_s + c_o\right]\frac{\partial p_o}{\partial t} - \frac{S_o}{\alpha_c B_o}\left(\alpha\frac{\partial \epsilon_v^e}{\partial t} + \frac{\partial \epsilon_v^p}{\partial t}\right) + q_{o_{SC}}$$

In a simplified form:

$$\nabla\cdot\left(\beta_c\frac{\boldsymbol{k}_o}{B_o\mu_o}\left(\nabla p_o - \quad {}_{o_{SC}}\gamma_c g\nabla z\right)\right) = F_o + G_o\frac{\partial S_o}{\partial t} + H_o\frac{\partial S_g}{\partial t} + I_o\frac{\partial p_o}{\partial t} + J_o\left(\alpha\frac{\partial \epsilon_v^e}{\partial t} + \frac{\partial \epsilon_v^p}{\partial t}\right) + q_{o_{SC}} \quad (A-71)$$

where:

$F_o = \frac{q_s\phi}{(1-\phi)}$

$G_o = \frac{\phi}{\alpha_c B_o}$

$H_o = 0$

$I_o = \frac{\phi}{\alpha_c B_o}S_o\left[c_{pc}(1-\alpha) - c_s + c_o\right]$

$J_o = -\frac{S_o}{\alpha_c B_o}$

A1.7.2. Water-phase

Following similar reasoning, as the one applied to obtain Equation (A – 55), the fluid flow governing equation for water can be developed as:

$$\nabla\cdot\left(\beta_c\frac{\boldsymbol{k}_w}{B_w\mu_w}\left(\nabla p_w - \rho_{w_{SC}}\gamma_c g\nabla z\right)\right) = \phi\nabla\cdot\mathbf{v}_s + \frac{1}{\alpha_c V_b}\frac{\partial}{\partial t}\left(\frac{\phi V_b S_w}{B_w}\right) + q_{w_{SC}} \quad (A-72)$$

Taking Equation (A – 28) into Equation (A – 72),

$$\nabla \cdot \left(\beta_c \frac{\boldsymbol{k}_w}{B_w \mu_w} \left(\nabla p_w - \rho_{w_{SC}} \gamma_c g \nabla z \right) \right) = \frac{q_s \phi}{(1-\phi)} + \frac{1}{\alpha_c V_b} \frac{\partial}{\partial t} \left(\frac{\phi V_b S_w}{B_w} \right) + q_{w_{SC}} \quad \text{(A – 73)}$$

Taking Equations (A – 45) and (A – 46) into Equation (A – 73),

$$\nabla \cdot \left(\beta_c \frac{\boldsymbol{k}_w}{B_w \mu_w} \left(\nabla p_o - \nabla p_{cwo} - \rho_{w_{SC}} \gamma_c g \nabla z \right) \right) = \frac{q_s \phi}{(1-\phi)} + \frac{1}{\alpha_c V_b} \frac{\partial}{\partial t} \left[\frac{\phi V_b (1 - S_o - S_g)}{B_w} \right] + q_{w_{SC}} \quad \text{(A – 74)}$$

Developing the derivative of the second term of the right-hand side of Equation (A – 74) and applying the porosity definition, $\phi = V_p / V_b$:

$$\frac{1}{\alpha_c V_b} \frac{\partial}{\partial t} \left[\frac{\phi V_b (1 - S_o - S_g)}{B_w} \right] = \frac{1}{\alpha_c V_b} \frac{\partial}{\partial t} \left[\frac{V_p (1 - S_o - S_g)}{B_w} \right] = \frac{1}{\alpha_c V_b B_w} \left[(1 - S_o - S_g) \left(V_p \frac{\partial \phi}{\partial t} + \phi \frac{\partial V_b}{\partial t} \right) - \phi V_b \left(\frac{\partial S_o}{\partial t} + \frac{\partial S_g}{\partial t} \right) - \phi V_b (1 - S_o - S_g) \frac{1}{B_w} \frac{\partial B_w}{\partial t} \right] \quad \text{(A – 75)}$$

Rearranging and using the chain rule in the B_w term,

$$\frac{1}{\alpha_c V_b} \frac{\partial}{\partial t} \left[\frac{\phi V_b (1 - S_o - S_g)}{B_w} \right] = \frac{\phi}{\alpha_c B_w} \left[(1 - S_o - S_g) \frac{1}{V_p} \frac{\partial V_p}{\partial t} - \left(\frac{\partial S_o}{\partial t} + \frac{\partial S_g}{\partial t} \right) - (1 - S_o - S_g) \frac{1}{B_w} \frac{\partial B_w}{\partial p_w} \frac{\partial p_w}{\partial t} \right] \quad \text{(A – 76)}$$

Taking Equations (A – 39) and (A – 46) into Equation (A – 76),

$$\frac{1}{\alpha_c V_b} \frac{\partial}{\partial t} \left[\frac{\phi V_b (1 - S_o - S_g)}{B_w} \right] = \frac{\phi}{\alpha_c B_w} \left[(1 - S_o - S_g) \frac{1}{V_p} \frac{\partial V_p}{\partial t} - \left(\frac{\partial S_o}{\partial t} + \frac{\partial S_g}{\partial t} \right) + c_w (1 - S_o - S_g) \left(\frac{\partial p_o}{\partial t} - \frac{\partial p_{cwo}}{\partial t} \right) \right] \quad \text{(A – 77)}$$

Substituting Equation (A – 77) into Equation (A – 74) and regrouping and using the chain rule to p_{cwo} terms,

$$\nabla \cdot \left(\beta_c \frac{\boldsymbol{k}_w}{B_w \mu_w} \left(\nabla p_o - \nabla p_{cwo} - \rho_{w_{SC}} \gamma_c g \nabla z \right) \right) = \frac{q_s \phi}{(1-\phi)} - \frac{S_o \phi}{\alpha_c B_w} \left[\frac{1}{S_o} \frac{\partial S_o}{\partial t} + \frac{1}{V_p} \frac{\partial V_p}{\partial t} + c_w \frac{\partial p_o}{\partial t} - c_w \frac{\partial p_{cwo}}{\partial S_w} \frac{\partial S_w}{\partial t} \right] - \frac{S_g \phi}{\alpha_c B_w} \left[\frac{1}{S_g} \frac{\partial S_g}{\partial t} + \frac{1}{V_p} \frac{\partial V_p}{\partial t} + c_w \frac{\partial p_o}{\partial t} - c_w \frac{\partial p_{cwo}}{\partial S_w} \frac{\partial S_w}{\partial t} \right] + \frac{\phi}{\alpha_c B_w} \left[\frac{1}{V_p} \frac{\partial V_p}{\partial t} + c_w \frac{\partial p_o}{\partial t} - c_w \frac{\partial p_{cwo}}{\partial S_w} \frac{\partial S_w}{\partial t} \right] + q_{w_{SC}} \quad \text{(A – 78)}$$

Substituting the derivate of capillary pressure defined at Equation (A – 48) into Equation (A – 78):

$$\nabla \cdot \left(\beta_c \frac{\boldsymbol{k}_w}{B_w \mu_w} \left(\nabla p_o - \nabla p_{cwo} - \rho_{w_{SC}} \gamma_c g \nabla z \right) \right) = \frac{q_s \phi}{(1-\phi)} - \frac{S_o \phi}{\alpha_c B_w} \left[\frac{1}{S_o} \frac{\partial S_o}{\partial t} + c_w p'_{cwo} \left(\frac{\partial S_o}{\partial t} + \frac{\partial S_g}{\partial t} \right) + \frac{1}{V_p} \frac{\partial V_p}{\partial t} + c_w \frac{\partial p_o}{\partial t} \right] - \frac{S_g \phi}{\alpha_c B_w} \left[\frac{1}{S_g} \frac{\partial S_g}{\partial t} + c_w p'_{cwo} \left(\frac{\partial S_o}{\partial t} + \frac{\partial S_g}{\partial t} \right) + \frac{1}{V_p} \frac{\partial V_p}{\partial t} + c_w \frac{\partial p_o}{\partial t} \right] + \frac{\phi}{\alpha_c B_w} \left[c_w p'_{cwo} \left(\frac{\partial S_o}{\partial t} + \frac{\partial S_g}{\partial t} \right) + \frac{1}{V_p} \frac{\partial V_p}{\partial t} + c_w \frac{\partial p_o}{\partial t} \right] + q_{w_{SC}} \quad \text{(A – 79)}$$

Redefining c_{pp} using Equation (A – 43) into Equation (A – 58) for the water phase:

$$\frac{1}{V_p}\frac{\partial V_p}{\partial t} = \left(c_{pc} - c_s\right)\frac{\partial p_w}{\partial t} - c_{pc}\frac{\partial \bar{\sigma}}{\partial t} \quad \text{(A – 80)}$$

Replacing Equation (A – 48) with Equation (A – 80):

$$\frac{1}{V_p}\frac{\partial V_p}{\partial t} = \left(c_{pc} - c_s\right)\left(\frac{\partial p_o}{\partial t} - p'_{cwo}\frac{\partial S_w}{\partial t}\right) - c_{pc}\frac{\partial \bar{\sigma}}{\partial t} \quad \text{(A – 81)}$$

Replacing Equation (A – 61) into Equation (A – 81) and using the Biot coefficient definition $\alpha = 1 - c_s/c_{bc}$:

$$\frac{1}{V_p}\frac{\partial V_p}{\partial t} = \left[c_{pc}(1-\alpha) - c_s\right]\left[\frac{\partial p_o}{\partial t} + p'_{cwo}\left(\frac{\partial S_o}{\partial t} + \frac{\partial S_g}{\partial t}\right)\right] - \frac{\alpha}{\phi}\frac{\partial \epsilon_v^e}{\partial t} \quad \text{(A – 82)}$$

Replacing Equations (A – 82) and (A – 69) into Equation (A – 65):

$$\frac{1}{V_p}\frac{\partial V_p}{\partial t} = \left[c_{pc}(1-\alpha) - c_s\right]\left[\frac{\partial p_o}{\partial t} + p'_{cwo}\left(\frac{\partial S_o}{\partial t} + \frac{\partial S_g}{\partial t}\right)\right] - \frac{\alpha}{\phi}\frac{\partial \epsilon_v^e}{\partial t} - \frac{1}{\phi}\frac{\partial \epsilon_v^p}{\partial t} \quad \text{(A – 83)}$$

Replacing Equation (A – 83) with Equation (A – 79) and regrouping,

$$\nabla\cdot\left(\beta_c\frac{\boldsymbol{k}_w}{B_w\mu_w}\left(\nabla p_o - \nabla p_{cwo} - \rho_{w_{SC}}\gamma_c g\nabla z\right)\right) = \frac{q_s\phi}{(1-\phi)} + \frac{\phi}{\alpha_c B_w}\left\{\left(1-S_o-S_g\right)\left[c_{pc}(1-\alpha) - c_s + c_w\right]p'_{cwo} - 1\right\}\frac{\partial S_o}{\partial t} + \frac{\phi}{\alpha_c B_w}\left\{\left(1-S_o-S_g\right)\left[c_{pc}(1-\alpha) - c_s + c_w\right]p'_{cwo} - 1\right\}\frac{\partial S_g}{\partial t} + \frac{\phi}{\alpha_c B_w}\left\{\left(1-S_o-S_g\right)\left[c_{pc}(1-\alpha) - c_s + c_w\right]\right\}\frac{\partial p_o}{\partial t} - \frac{\phi}{\alpha_c B_w}\left(1-S_o-S_g\right)\left(\alpha\frac{\partial \epsilon_v^e}{\partial t} + \frac{\partial \epsilon_v^p}{\partial t}\right) + q_{w_{SC}} \quad \text{(A – 84)}$$

Differentiating each of the gradient terms and derivate of capillary pressure defined at Equation (A – 48),

$$\nabla\cdot\left(\beta_c\frac{\boldsymbol{k}_w}{B_w\mu_w}\nabla p_{cwo}\right) = \nabla\cdot\left(\beta_c\frac{\boldsymbol{k}_w}{\mu_w B_w}p'_{cwo}\nabla S_w\right) = -\nabla\cdot\left(\beta_c\frac{\boldsymbol{k}_w}{\mu_w B_w}p'_{cwo}\nabla S_o\right) - \nabla\cdot\left(\beta_c\frac{\boldsymbol{k}_w}{\mu_w B_w}p'_{cwo}\nabla S_g\right) \quad \text{(A – 85)}$$

Redefining some variables and introducing Equation (A – 85),

$$\nabla\cdot\left(\beta_c\frac{\boldsymbol{k}_w}{B_w\mu_w}\left(\nabla p_o - \rho_{w_{SC}}\gamma_c g\nabla z\right)\right) + \nabla\cdot\left(\beta_c\frac{\boldsymbol{k}_w}{\mu_w B_w}p'_{cwo}\nabla S_o\right) + \nabla\cdot\left(\beta_c\frac{\boldsymbol{k}_w}{\mu_w B_w}p'_{cwo}\nabla S_g\right) = F_w + G_w\frac{\partial S_o}{\partial t} + H_w\frac{\partial S_g}{\partial t} + I_w\frac{\partial p_o}{\partial t} + J_w\left(\alpha\frac{\partial \epsilon_v^e}{\partial t} + \frac{\partial \epsilon_v^p}{\partial t}\right) + q_{w_{SC}} \quad \text{(A – 86)}$$

where:

$$F_w = \frac{q_s\phi}{(1-\phi)}$$

$$G_w = \frac{\phi}{\alpha_c B_w}\left\{\left(1-S_o-S_g\right)\left[c_{pc}(1-\alpha) - c_s + c_w\right]p'_{cwo} - 1\right\}$$

$$H_w = \frac{\phi}{\alpha_c B_w}\{(1 - S_o - S_g)[c_{pc}(1-\alpha) - c_s + c_w]p'_{cwo} - 1\}$$

$$I_w = \frac{\phi}{\alpha_c B_w}(1 - S_o - S_g)[c_{pc}(1-\alpha) - c_s + c_w]$$

$$J_w = -\frac{1}{\alpha_c B_w}(1 - S_o - S_g)$$

A1.7.3. Gas-phase

Following similar reasoning, as the one applied to obtain the fluid-flow governing equations for oil and water, i.e., Equations (A – 62) and (A – 86), the fluid-flow equation for gas can be developed as:

$$\nabla \cdot \left(\beta_c \frac{\boldsymbol{k}_g}{B_g \mu_g}(\nabla p_g - \rho_{g_{SC}} \gamma_c g \nabla z) + R_{so}\beta_c \frac{\boldsymbol{k}_o}{B_o \mu_o}(\nabla p_o - \rho_{o_{SC}} \gamma_c g \nabla z) + R_{sw}\beta_c \frac{\boldsymbol{k}_w}{B_w \mu_w}(\nabla p_w - \rho_{w_{SC}} \gamma_c g \nabla z) \right) = (1 + R_{so} + R_{sw})\phi \nabla \cdot \mathbf{v}_s + \frac{1}{\alpha_c V_b}\frac{\partial}{\partial t}\left(\frac{\phi V_b S_g}{B_g} + R_{so}\frac{\phi V_b S_o}{B_o} + R_{sw}\frac{\phi V_b S_w}{B_w} \right) + q_{g_{SC}} \quad \text{(A – 87)}$$

Substituting Equation (A – 28) into Equation (A – 87),

$$\nabla \cdot \left(\beta_c \frac{\boldsymbol{k}_g}{B_g \mu_g}(\nabla p_g - \rho_{g_{SC}} \gamma_c g \nabla z) + R_{so}\beta_c \frac{\boldsymbol{k}_o}{B_o \mu_o}(\nabla p_o - \rho_{o_{SC}} \gamma_c g \nabla z) + R_{sw}\beta_c \frac{\boldsymbol{k}_w}{B_w \mu_w}(\nabla p_w - \rho_{w_{SC}} \gamma_c g \nabla z) \right) = (1 + R_{so} + R_{sw})\frac{q_s \phi}{(1-\phi)} + \frac{1}{\alpha_c V_b}\frac{\partial}{\partial t}\left(\frac{\phi V_b S_g}{B_g} + R_{so}\frac{\phi V_b S_o}{B_o} + R_{sw}\frac{\phi V_b S_w}{B_w} \right) + q_{g_{SC}} \quad \text{(A – 88)}$$

Replacing Equations (A – 46) and (A – 47) into Equation (A – 88):

$$\nabla \cdot \left[\beta_c \frac{\boldsymbol{k}_g}{B_g \mu_g}(\nabla p_o + \nabla p_{cgo} - \rho_{g_{SC}} \gamma_c g \nabla z) + \beta_c R_{so}\frac{\boldsymbol{k}_o}{B_o \mu_o}(\nabla p_o - \rho_{o_{SC}} \gamma_c g \nabla z) + \beta_c R_{sw}\frac{\boldsymbol{k}_w}{B_w \mu_w}(\nabla p_o - \nabla p_{cwo} - \rho_{w_{SC}} \gamma_c g \nabla z) \right] = (1 + R_{so} + R_{sw})\frac{q_s \phi}{(1-\phi)} + \frac{1}{\alpha_c V_b}\frac{\partial}{\partial t}\left(\frac{\phi V_b S_g}{B_g} + R_{so}\frac{\phi V_b S_o}{B_o} + R_{sw}\frac{\phi V_b S_w}{B_w} \right) + q_{g_{SC}}$$

Applying the porosity definition, $\phi = V_p / V_b$, and rearranging,

$$\nabla \cdot \left[\beta_c \frac{\boldsymbol{k}_g}{B_g \mu_g}(\nabla p_o + \nabla p_{cgo} - \rho_{g_{SC}} \gamma_c g \nabla z) + \beta_c R_{so}\frac{\boldsymbol{k}_o}{B_o \mu_o}(\nabla p_o - \rho_{o_{SzC}} \gamma_c g \nabla z) + \beta_c R_{sw}\frac{\boldsymbol{k}_w}{B_w \mu_w}(\nabla p_o - \nabla p_{cwo} - \rho_{w_{SC}} \gamma_c g \nabla z) \right] = (1 + R_{so} + R_{sw})\frac{q_s \phi}{(1-\phi)} + \frac{1}{\alpha_c V_b}\frac{\partial}{\partial t}\left(\frac{V_p S_g}{B_g} + R_{so}\frac{V_p S_o}{B_o} + R_{sw}\frac{V_p S_w}{B_w} \right) + q_{g_{SC}} \quad \text{(A – 89)}$$

Deriving the second term of the right-hand side of Equation (A – 89) and replacing Equation (A – 45),

$$\frac{1}{\alpha_c V_b}\frac{\partial}{\partial t}\left(\frac{V_p S_g}{B_g}+R_{so}\frac{V_p S_o}{B_o}+R_{sw}\frac{V_p S_w}{B_w}\right)=\frac{\phi S_g}{\alpha_c B_g}\left(\frac{1}{S_g}\frac{\partial S_g}{\partial t}+\frac{1}{V_p}\frac{\partial V_p}{\partial t}-\frac{1}{B_g}\frac{\partial B_g}{\partial t}\right)+R_{so}\frac{\phi S_o}{\alpha_c B_o}\left(\frac{1}{S_o}\frac{\partial S_o}{\partial t}+\frac{1}{V_p}\frac{\partial V_p}{\partial t}-\frac{1}{B_o}\frac{\partial B_o}{\partial t}+\frac{1}{R_{so}}\frac{\partial R_{so}}{\partial t}\right)+R_{sw}\frac{\phi(1-S_o-S_g)}{\alpha_c B_w}\left[-\frac{1}{(1-S_o-S_g)}\left(\frac{\partial S_o}{\partial t}+\frac{\partial S_g}{\partial t}\right)+\frac{1}{V_p}\frac{\partial V_p}{\partial t}-\frac{1}{B_w}\frac{\partial B_w}{\partial t}+\frac{1}{R_{sw}}\frac{\partial R_{sw}}{\partial t}\right]$$

Applying the chain rule to the volume formation terms, B_o, B_w, and B_g,

$$\frac{1}{\alpha_c V_b}\frac{\partial}{\partial t}\left(\frac{V_p S_g}{B_g}+R_{so}\frac{V_p S_o}{B_o}+R_{sw}\frac{V_p S_w}{B_w}\right)=\frac{\phi S_g}{\alpha_c B_g}\left(\frac{1}{S_g}\frac{\partial S_g}{\partial t}+\frac{1}{V_p}\frac{\partial V_p}{\partial t}-\frac{1}{B_g}\frac{\partial B_g}{\partial p_g}\frac{\partial p_g}{\partial t}\right)+R_{so}\frac{\phi S_o}{\alpha_c B_o}\left(\frac{1}{S_o}\frac{\partial S_o}{\partial t}+\frac{1}{V_p}\frac{\partial V_p}{\partial t}-\frac{1}{B_o}\frac{\partial B_o}{\partial p_o}\frac{\partial p_o}{\partial t}+\frac{1}{R_{so}}\frac{\partial R_{so}}{\partial t}\right)+R_{sw}\frac{\phi(1-S_o-S_g)}{\alpha_c B_w}\left[-\frac{1}{(1-S_o-S_g)}\left(\frac{\partial S_o}{\partial t}+\frac{\partial S_g}{\partial t}\right)+\frac{1}{V_p}\frac{\partial V_p}{\partial t}-\frac{1}{B_w}\frac{\partial B_w}{\partial p_w}\frac{\partial p_w}{\partial t}+\frac{1}{R_{sw}}\frac{\partial R_{sw}}{\partial t}\right] \quad (A-90)$$

Substituting Equations (A – 35) to (A – 37) into Equation (A – 90),

$$\frac{1}{\alpha_c V_b}\frac{\partial}{\partial t}\left(\frac{V_p S_g}{B_g}+R_{so}\frac{V_p S_o}{B_o}+R_{sw}\frac{V_p S_w}{B_w}\right)=\frac{\phi S_g}{\alpha_c B_g}\left(\frac{1}{V_p}\frac{\partial V_p}{\partial t}+\frac{1}{S_g}\frac{\partial S_g}{\partial t}+c_g\frac{\partial p_g}{\partial t}\right)+R_{so}\frac{\phi S_o}{\alpha_c B_o}\left(\frac{1}{V_p}\frac{\partial V_p}{\partial t}+\frac{1}{S_o}\frac{\partial S_o}{\partial t}+c_o\frac{\partial p_o}{\partial t}+\frac{1}{R_{so}}\frac{\partial R_{so}}{\partial t}\right)+R_{sw}\frac{\phi(1-S_o-S_g)}{\alpha_c B_w}\left[\frac{1}{V_p}\frac{\partial V_p}{\partial t}-\frac{1}{(1-S_o-S_g)}\left(\frac{\partial S_o}{\partial t}+\frac{\partial S_g}{\partial t}\right)+c_w\frac{\partial p_w}{\partial t}+\frac{1}{R_{sw}}\frac{\partial R_{sw}}{\partial t}\right] \quad (A-91)$$

Replacing Equations (A – 46) and (A – 44) into Equation (A – 91), and applying the chain rule to the capillary pressures terms p_{cwo} and p_{cgo}, and gas solution terms R_{so} and R_{sw}:

$$\frac{1}{\alpha_c V_b}\frac{\partial}{\partial t}\left(\frac{V_p S_g}{B_g}+R_{so}\frac{V_p S_o}{B_o}+R_{sw}\frac{V_p S_w}{B_w}\right)=\frac{\phi S_g}{\alpha_c B_g}\left[\frac{1}{S_g}\frac{\partial S_g}{\partial t}+\frac{1}{V_p}\frac{\partial V_p}{\partial t}+c_g\frac{\partial p_o}{\partial t}+c_g\frac{\partial p_{cgo}}{\partial S_g}\frac{\partial S_g}{\partial t}\right]+R_{so}\frac{\phi S_o}{\alpha_c B_o}\left[\frac{1}{S_o}\frac{\partial S_o}{\partial t}+\frac{1}{V_p}\frac{\partial V_p}{\partial t}+c_o\frac{\partial p_o}{\partial t}+\frac{1}{R_{so}}\frac{\partial R_{so}}{\partial p_o}\frac{\partial p_o}{\partial t}\right]+R_{sw}\frac{\phi(1-S_o-S_g)}{\alpha_c B_w}\left[-\frac{1}{(1-S_o-S_g)}\left(\frac{\partial S_o}{\partial t}+\frac{\partial S_g}{\partial t}\right)+\frac{1}{V_p}\frac{\partial V_p}{\partial t}+c_w\left(\frac{\partial p_o}{\partial t}-\frac{\partial p_{cwo}}{\partial S_w}\frac{\partial S_w}{\partial t}\right)+\frac{1}{R_{sw}}\frac{\partial R_{sw}}{\partial p_w}\left(\frac{\partial p_o}{\partial t}-\frac{\partial p_{cwo}}{\partial S_w}\frac{\partial S_w}{\partial t}\right)\right] \quad (A-92)$$

Substituting the definition of capillary pressures stated in Equations (A – 46) and (A – 47), and their derivatives stated in Equations (A – 48) and (A – 49) into Equation (A – 92),

$$\frac{1}{\alpha_c V_b}\frac{\partial}{\partial t}\left(\frac{V_p S_g}{B_g}+R_{so}\frac{V_p S_o}{B_o}+R_{sw}\frac{{}_p S_w}{B_w}\right)=\frac{\phi S_g}{\alpha_c B_g}\left[\frac{1}{S_g}\frac{\partial S_g}{\partial t}+\frac{1}{V_p}\frac{\partial V_p}{\partial t}+c_g\frac{\partial p_o}{\partial t}+c_g p'_{cgo}\frac{\partial S_g}{\partial t}\right]+R_{so}\frac{\phi S_o}{\alpha_c B_o}\left[\frac{1}{S_o}\frac{\partial S_o}{\partial t}+\frac{1}{V_p}\frac{\partial V_p}{\partial t}+(R'_{so}+c_o)\frac{\partial p_o}{\partial t}\right]+R_{sw}\frac{\phi(1-S_o-S_g)}{\alpha_c B_w}\left[-\frac{1}{(1-S_o-S_g)}\left(\frac{\partial S_o}{\partial t}+\frac{\partial S_g}{\partial t}\right)+\frac{1}{V_p}\frac{\partial V_p}{\partial t}+(R'_{sw}+c_w)\left[\frac{\partial p_o}{\partial t}-p'_{cwo}\left(\frac{\partial S_o}{\partial t}+\frac{\partial S_g}{\partial t}\right)\right]\right] \quad (A-93)$$

where are defined the variation of gas solubility with oil pressure is:

$$R'_{so}=\frac{1}{R_{so}}\frac{\partial R_{so}}{\partial p_o}$$

$$R'_{sw}=\frac{1}{R_{sw}}\frac{\partial R_{sw}}{\partial p_w}$$

Regrouping,

$$\frac{1}{\alpha_c V_b}\frac{\partial}{\partial t}\left(\frac{V_p S_g}{B_g}+R_{so}\frac{V_p S_o}{B_o}+R_{sw}\frac{V_p S_w}{B_w}\right)=\frac{\phi S_g}{\alpha_c B_g}\left[\left(\frac{1}{S_g}+c_g p'_{cgo}\right)\frac{\partial S_g}{\partial t}+\frac{1}{V_p}\frac{\partial V_p}{\partial t}+c_g\frac{\partial p_o}{\partial t}\right]+R_{so}\frac{\phi S_o}{\alpha_c B_o}\left[\frac{1}{S_o}\frac{\partial S_o}{\partial t}+\frac{1}{V_p}\frac{\partial V_p}{\partial t}+(R'_{so}+c_o)\frac{\partial p_o}{\partial t}\right]+R_{sw}\frac{\phi(1-S_o-S_g)}{\alpha_c B_w}\left[\left[(R'_{sw}+c_w)p'_{cwo}-\frac{1}{(1-S_o-S_g)}\right]\frac{\partial S_g}{\partial t}+\left[(R'_{sw}+c_w)p'_{cwo}-\frac{1}{(1-S_o-S_g)}\right]\frac{\partial S_o}{\partial t}+\frac{1}{V_p}\frac{\partial V_p}{\partial t}+(R'_{sw}+c_w)\frac{\partial p_o}{\partial t}\right] \quad (A-94)$$

Replacing Equation (A – 94) with Equation (A – 89),

$$\nabla\cdot\left[\beta_c\frac{\boldsymbol{k}_g}{B_g\mu_g}\left(\nabla p_o+\nabla p_{cgo}-\rho_{g_{SC}}\gamma_c g\nabla z\right)+\beta_c R_{so}\frac{\boldsymbol{k}_o}{B_o\mu_o}\left(\nabla p_o-\rho_{o_{SzC}}\gamma_c g\nabla z\right)+\beta_c R_{sw}\frac{\boldsymbol{k}_w}{B_w\mu_w}\left(\nabla p_o-\nabla p_{cwo}-\rho_{w_{SC}}\gamma_c g\nabla z\right)\right]=(1+R_{so}+R_{sw})\frac{q_s\phi}{(1-\phi)}+\frac{\phi S_g}{\alpha_c B_g}\left[\left(\frac{1}{S_g}+c_g p'_{cgo}\right)\frac{\partial S_g}{\partial t}+\frac{1}{V_p}\frac{\partial V_p}{\partial t}+c_g\frac{\partial p_o}{\partial t}\right]+R_{so}\frac{\phi S_o}{\alpha_c B_o}\left[\frac{1}{S_o}\frac{\partial S_o}{\partial t}+\frac{1}{V_p}\frac{\partial V_p}{\partial t}+(R'_{so}+c_o)\frac{\partial p_o}{\partial t}\right]+R_{sw}\frac{\phi(1-S_o-S_g)}{\alpha_c B_w}\left[\left[(R'_{sw}+c_w)p'_{cwo}-\frac{1}{(1-S_o-S_g)}\right]\frac{\partial S_g}{\partial t}+\left[(R'_{sw}+c_w)p'_{cwo}-\frac{1}{(1-S_o-S_g)}\right]\frac{\partial S_o}{\partial t}+\frac{1}{V_p}\frac{\partial V_p}{\partial t}+(R'_{sw}+c_w)\frac{\partial p_o}{\partial t}\right]+q_{g_{SC}} \quad (A-95)$$

Redefining c_{pp} using Equation (A – 46) into Equation (A – 57) for the gas phase:

$$\frac{1}{V_p}\frac{\partial V_p}{\partial t}=\left(c_{pc}-c_s\right)\frac{\partial p_g}{\partial t}-c_{pc}\frac{\partial\bar{\sigma}}{\partial t} \quad (A-96)$$

Replacing Equation (A – 49) with Equation (A – 96):

$$\frac{1}{p}\frac{\partial V_p}{\partial t}=\left(c_{pc}-c_s\right)\left(\frac{\partial p_o}{\partial t}+p'_{cgo}\frac{\partial S_g}{\partial t}\right)-c_{pc}\frac{\partial\bar{\sigma}}{\partial t} \quad (A-97)$$

Replacing Equation (A – 61) into Equation (A – 97) and using the Biot coefficient definition $\alpha=1-c_s/c_{bc}$:

$$\frac{1}{V_p}\frac{\partial V_p}{\partial t}=\left[c_{pc}(1-\alpha)-c_s\right]\left[\frac{\partial p_o}{\partial t}+p'_{cgo}\frac{\partial S_g}{\partial t}\right]-\frac{\alpha}{\phi}\frac{\partial\epsilon_v^e}{\partial t} \quad (A-98)$$

Replacing Equations (A – 98) and (A – 69) into Equation (A – 65):

$$\frac{1}{V_p}\frac{\partial V_p}{\partial t}=\left[c_{pc}(1-\alpha)-c_s\right]\left[\frac{\partial p_o}{\partial t}+p'_{cgo}\frac{\partial S_g}{\partial t}\right]-\frac{\alpha}{\phi}\frac{\partial\epsilon_v^e}{\partial t}-\frac{1}{\phi}\frac{\partial\epsilon_v^p}{\partial t} \quad (A-99)$$

Replacing Equation (A – 99) with Equation (A – 95) and regrouping,

$$\nabla\cdot\left[\beta_c\frac{\boldsymbol{k}_g}{B_g\mu_g}\left(\nabla p_o+\nabla p_{cgo}-\rho_{g_{SC}}\gamma_c g\nabla z\right)+\beta_c R_{so}\frac{\boldsymbol{k}_o}{B_o\mu_o}\left(\nabla p_o-\rho_{o_{SzC}}\gamma_c g\nabla z\right)+\beta_c R_{sw}\frac{\boldsymbol{k}_w}{B_w\mu_w}\left(\nabla p_o-\nabla p_{cwo}-\rho_{w_{SC}}\gamma_c g\nabla z\right)\right]=(1+R_{so}+R_{sw})\frac{q_s\phi}{(1-\phi)}+\frac{\phi}{\alpha_c}\frac{\partial S_o}{\partial t}\left\{R_{so}\frac{1}{B_o}+R_{sw}\frac{1}{B_w}\left[\left(1-S_o-S_g\right)(R'_{sw}+c_w)p'_{cwo}-1\right]\right\}+\frac{\phi}{\alpha_c}\frac{\partial S_g}{\partial t}\left\{\frac{1}{B_g}\left[1+S_g p'_{cgo}\left[c_{pc}(1-\alpha)-c_s+c_g\right]\right]+R_{so}\frac{S_o}{B_o}p'_{cgo}\left[c_{pc}(1-\alpha)-c_s\right]+R_{sw}\frac{1}{B_w}\left[\left(1-S_o-S_g\right)\left[p'_{cgo}\left[c_{pc}(1-\alpha)-c_s\right]+(R'_{sw}+c_w)p'_{cwo}\right]-1\right]\right\}+\frac{\phi}{\alpha_c}\frac{\partial p_o}{\partial t}\left\{\frac{S_g}{B_g}\left[c_{pc}(1-\alpha)-c_s+c_g\right]+R_{so}\frac{S_o}{B_o}\left[c_{pc}(1-\alpha)-c_s+c_o+R'_{so}\right]+R_{sw}\frac{(1-S_o-S_g)}{B_w}\left[c_{pc}(1-\alpha)-c_s+c_w+R'_{sw}\right]\right\}-\frac{\phi}{\alpha_c}\left(\alpha\frac{\partial\epsilon_v^e}{\partial t}+\frac{\partial\epsilon_v^p}{\partial t}\right)\left\{\frac{S_g}{B_g}+R_{so}\frac{S_o}{B_o}+R_{sw}\frac{(1-S_o-S_g)}{B_w}\right\}+q_{gsc} \quad \text{(A – 100)}$$

Deriving each of the gradient terms of Equation (A – 89),

$$\nabla\cdot\left(\beta_c\frac{\boldsymbol{k}_g}{B_g\mu_g}\nabla p_{cgo}\right)=\nabla\cdot\left(\beta_c\frac{\boldsymbol{k}_g}{B_g\mu_g}p'_{cgo}\nabla S_g\right) \quad \text{(A – 101)}$$

$$\nabla\cdot\left(R_{sw}\beta_c\frac{\boldsymbol{k}_w}{B_w\mu_w}\nabla p_{cwo}\right)=\nabla\cdot\left(R_{sw}\beta_c\frac{\boldsymbol{k}_w}{B_w\mu_w}p'_{cwo}\nabla S_w\right)=-\nabla\cdot\left(R_{sw}\beta_c\frac{\boldsymbol{k}_w}{B_w\mu_w}p'_{cwo}\nabla S_o\right)-\nabla\cdot\left(R_{sw}\beta_c\frac{\boldsymbol{k}_w}{B_w\mu_w}p'_{cwo}\nabla S_g\right) \quad \text{(A – 102)}$$

Substituting Equations (A – 100) and (A – 101) into Equation (A – 102) and redefining some variables:

$$\nabla\cdot\left[\beta_c\frac{\boldsymbol{k}_g}{B_g\mu_g}\left(\nabla p_o-\rho_{g_{SC}}\gamma_c g\nabla z\right)+\beta_c R_{so}\frac{\boldsymbol{k}_o}{B_o\mu_o}\left(\nabla p_o-\rho_{o_{SC}}\gamma_c g\nabla z\right)+\beta_c R_{sw}\frac{\boldsymbol{k}_w}{B_w\mu_w}\left(\nabla p_o-\rho_{w_{SC}}\gamma_c g\nabla z\right)\right]+\nabla\cdot\left[\left(\beta_c\frac{\boldsymbol{k}_g}{B_g\mu_g}p'_{cgo}+R_{sw}\beta_c\frac{\boldsymbol{k}_w}{B_w\mu_w}p'_{cwo}\right)\nabla S_g\right]+\nabla\cdot\left(R_{sw}\beta_c\frac{\boldsymbol{k}_w}{B_w\mu_w}p'_{cwo}\nabla S_o\right)=F_g+G_g\frac{\partial S_o}{\partial t}+H_g\frac{\partial S_g}{\partial t}+I_g\frac{\partial p_o}{\partial t}+J_g\left[\alpha\frac{\partial\epsilon_v^e}{\partial t}+\frac{\partial\epsilon^p}{\partial t}\right]+q_{gsc} \quad \text{(A – 103)}$$

where:

$$F_g=(1+R_{so}+R_{sw})\frac{q_s\phi}{(1-\phi)}$$

$$G_g=\frac{\phi}{\alpha_c}\left\{R_{so}\frac{1}{B_o}+R_{sw}\frac{1}{B_w}\left[\left(1-S_o-S_g\right)(R'_{sw}+c_w)p'_{cwo}-1\right]\right\}$$

$$H_g=\frac{\phi}{\alpha_c}\left\{\frac{1}{B_g}\left[1+S_g p'_{cgo}\left[c_{pc}(1-\alpha)-c_s+c_g\right]\right]+R_{so}\frac{1}{B_o}S_o p'_{cgo}\left[c_{pc}(1-\alpha)-c_s\right]+R_{sw}\frac{1}{B_w}\left[\left(1-S_o-S_g\right)\left[(R'_{sw}+c_w)p'_{cwo}+\left[c_{pc}(1-\alpha)-c_s\right]p'_{cgo}\right]-1\right]\right\}$$

$$I_g=\frac{\phi}{\alpha_c}\left\{\frac{S_g}{B_g}\left[c_{pc}(1-\alpha)-c_s+c_g\right]+R_{so}\frac{S_o}{B_o}\left[R'_{so}+c_{pc}(1-\alpha)-c_s+c_o\right]+R_{sw}\frac{(1-S_o-S_g)}{B_w}\left[R'_{sw}+c_{pc}(1-\alpha)-c_s+c_w\right]\right\}$$

$$J_g = -\frac{\phi}{\alpha_c}\left[\frac{S_g}{B_g} + R_{so}\frac{S_o}{B_o} + R_{sw}\frac{(1-S_o-S_g)}{B_w}\right]$$

A2. Numerical model

The numerical model of the fluid flow model is displayed in this section, in which the governing equations are discretized in space and time using the finite differences method. The physical model is represented in radial-cylindrical coordinates and is discretized using a block-centered grid. A fully implicit procedure is adopted here for maximum numerical stability. This section presents the description of the simulation grid and the discretization of the governing equation for each phase (oil, water, and gas).

A2.1. Simulation grid

The physical model is a vertical well that passes through several lithological layers. The single-well simulation uses radial-cylindrical coordinates, in which a point in space is identified as the point (r, θ, z). A cylinder well represents the reservoir in a single-well simulation where its longitudinal axis coincides with the vertical well. The reservoir discretization consists of dividing the cylinder into n_r concentric radial segments with the well passing through the center; rays from the center that divide the radial segments into n_θ cake-like slices and planes normal to the longitudinal axis that divide the cake-like slices into n_z segments. Figure A – 2 presents the simulation grid that represents the 3D single-well in radial-cylindrical coordinates.

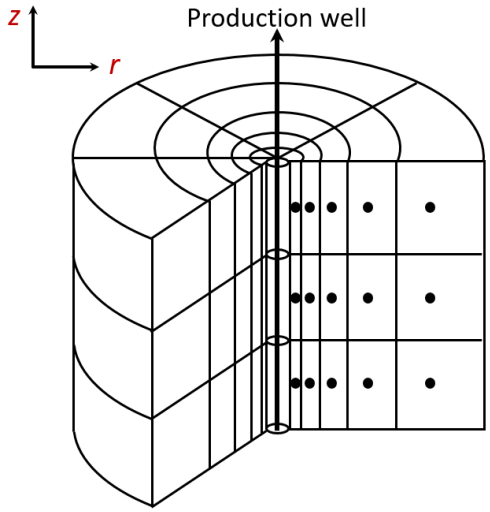

Figure A – 2. Simulation grid representing the 3D single well.

A reservoir block in the discretized reservoir is identified as a block (i, j, k), where $i, j,$ and k are, respectively, the orders of the block in r-, θ-, and z-directions, with $1 \leq i \leq n_r$, $1 \leq j \leq n_\theta$ and $1 \leq k \leq n_z$. Figure A – 3 shows the block (i, j, k) and its neighboring blocks in single-well simulation.

Likewise, a centered block scheme with an irregular grid distribution is used to refine the area around the well, where the most abrupt pressure changes are expected. The grid-block dimensions are designated first, followed by the placement of points in central locations of the blocks and the distance between block boundaries is the defining variable in space.

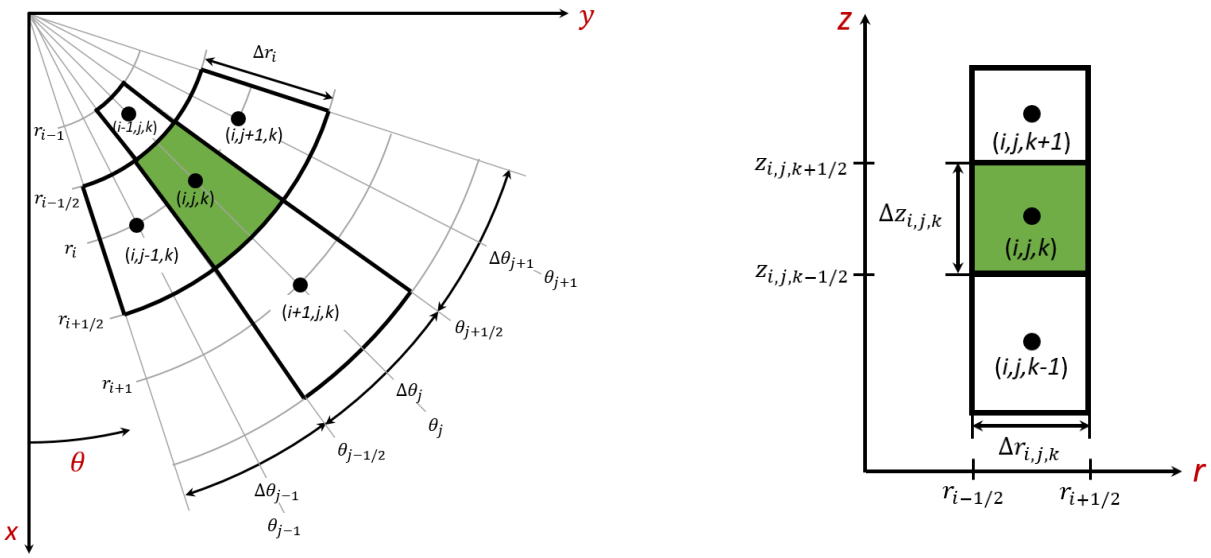

a. b.

Figure A – 3. Block (i, j, k) and its neighboring blocks in single-well simulation. a) Block (i, j, k) and its neighboring blocks in the horizontal plane. b) Block (i, j, k) and its neighboring blocks in the z-direction.

The block boundaries are spaced logarithmically in r to ensure that the radial flow rates between neighboring points using the integrated continuous and discretized forms of Darcy's law are identical. Block boundaries for bulk volume calculations are spaced logarithmically in r^2 to ensure that the actual and discretized bulk volumes of grid blocks are equal.

The dimensions of the block in each direction are given by:

$$\Delta r_{i,j,k} = r_{i+1/2,j,k} - r_{i-1/2,j,k}$$

$$\Delta\theta_{i,j,k} = \theta_{i,j+1/2,k} - \theta_{i,j-1/2,k}$$

$$\Delta z_{i,j,k} = z_{i,j,k+1/2} - z_{i,j,k-1/2} \qquad \text{(A – 104)}$$

The radial distribution is stated in terms of the reservoir's internal boundary or well radius, r_w and the reservoir's external boundary, r_e, by:

$$r_{i+1} = r_i \left(\frac{r_e}{r_w}\right)^{1/n_r} \qquad \text{(A – 105)}$$

The discretized volume of the block (i, j, k) is calculated from:

$$V_{b_{i,j,k}} = \frac{1}{2}\Delta\theta_{i,j,k}\Delta z_{i,j,k}\left(r^2_{i+1/2,j,k} - r^2_{i-1/2,j,k}\right) \quad \text{(A – 106)}$$

where:

$$r^2_{i+1/2,j,k} = \frac{r^2_{i+1,j,k} - r^2_{i,j,k}}{\ln\left(r^2_{i+1,j,k}/r^2_{i,j,k}\right)}$$

$$r^2_{i-1/2,j,k} = \frac{r^2_{i,j,k} - r^2_{i-1,j,k}}{\ln\left(r^2_{i,j,k}/r^2_{i-1,j,k}\right)}$$

A2.2.Governing equations of the fluid flow

A2.2.1. Oil-phase

Equation (A – 73) is the governing equation for the oil phase,

$$\nabla\cdot\left(\beta_c\frac{\boldsymbol{k}_o}{B_o\mu_o}\left(\nabla p_o - \rho_{o_{SC}}\gamma_c g\nabla z\right)\right) = F_o + G_o\frac{\partial S_o}{\partial t} + H_o\frac{\partial S_g}{\partial t} + I_o\frac{\partial p_o}{\partial t} + J_o\left(\alpha\frac{\partial\epsilon^e_v}{\partial t} + \frac{\partial\epsilon^p_v}{\partial t}\right) + q_{o_{SC}} \quad \text{(A – 73)}$$

The finite difference approximation for the left side of the Equation (A – 73) after applying the divergence function for a cylindrical coordinate system, Equation (A – 9), for each direction is given by:

$$\nabla\cdot\left(\beta_c\frac{\boldsymbol{k}_o}{B_o\mu_o}\left(\nabla p_o - \rho_{o_{SC}}\gamma_c g\nabla z\right)\right) = \beta_c\frac{\partial}{r\partial r}\left[r\frac{k_{or}}{B_o\mu_o}\left(\frac{\partial p_o}{\partial r} - \rho_{o_{SC}}\gamma_c g\frac{\partial z}{\partial r}\right)\right] + \beta_c\frac{\partial}{r\partial\theta}\left[\frac{k_{o\theta}}{B_o\mu_o}\left(\frac{\partial p_o}{r\partial\theta} - \rho_{osc}\gamma_c g\frac{\partial z}{r\partial\theta}\right)\right] + \beta_c\frac{\partial}{\partial z}\left[\frac{k_{oz}}{B_o\mu_o}\left(\frac{\partial p_o}{\partial z} - \rho_{o_{SC}}\gamma_c g\frac{\partial z}{\partial z}\right)\right] \quad \text{(A – 107)}$$

To ensure that the discretized equation gives the exact fluid rate for a given constant pressure drawdown, that the discretized volume of the block is equal to the real volume of the block considering the logarithmic radial distribution, and that the material balance is not affected, the governing equation must be multiplied by the discretized volume of the block.

- **For radial direction**

$$\beta_c V_b\frac{\partial}{r\partial r}\left[r\frac{k_{or}}{B_o\mu_o}\left(\frac{\partial p_o}{\partial r} - \rho_{o_{SC}}\gamma_c g\frac{\partial z}{\partial r}\right)\right] = \frac{\beta_c V_{b_{i,j,k}}}{r_{i,j,k}\Delta r_{i,j,k}}\left[\frac{k_{or}}{B_o\mu_o}\Big|_{i+1/2,j,k}\frac{\left(p_{o_{i+1,j,k}} - p_{o_{i,j,k}}\right) - \rho_{osc}\gamma_c g\left(z_{i+1,j,k} - z_{i,j,k}\right)}{\ln\left(r_{i+1,j,k}/r_{i,j,k}\right)} - \frac{k_{or}}{B_o\mu_o}\Big|_{i-1/2,j,k}\frac{\left(p_{o_{i,j,k}} - p_{o_{i-1,j,k}}\right) - \rho_{osc}\gamma_c g\left(z_{i,j,k} - z_{i-1,j,k}\right)}{\ln\left(r_{i,j,k}/r_{i-1,j,k}\right)}\right]$$

Redefining some terms such as transmissibility,

$$\beta_c V_b\frac{\partial}{r\partial r}\left[r\frac{k_{or}}{B_o\mu_o}\left(\frac{\partial p_o}{\partial r} - \rho_{o_{SC}}\gamma_c g\frac{\partial z}{\partial r}\right)\right] = T_{or^+}\left[\left(p_{o_{i+1,j,k}} - p_{o_{i,j,k}}\right) - \rho_{osc}\gamma_c g\left(z_{i+1,j,k} - z_{i,j,k}\right)\right] - T_{or^-}\left[\left(p_{o_{i,j,k}} - p_{o_{i-1,j,k}}\right) - \rho_{o_{SC}}\gamma_c g\left(z_{i,j,k} - z_{i-1,j,k}\right)\right] \quad \text{(A – 108)}$$

where the oil radial transmissibilities are expressed as:

$$T_{or^+} = \frac{\beta_c \Delta\theta_{i,j,k} \Delta z_{i,j,k} \left(r_{i+1/2,j,k}^2 - r_{i-1/2,j,k}^2\right)}{2 r_{i,j,k} \Delta r_{i,j,k} \ln\left(r_{i+1,j,k}/r_{i,j,k}\right)} \frac{k_{or}}{B_o \mu_o}\Big|_{i+1/2,j,k}$$

$$T_{or^-} = \frac{\beta_c \Delta\theta_{i,j,k} \Delta z_{i,j,k} \left(r_{i+1/2,j,k}^2 - r_{i-1/2,j,k}^2\right)}{2 r_{i,j,k} \Delta r_{i,j,k} \ln\left(r_{i,j,k}/r_{i-1,j,k}\right)} \frac{k_{or}}{B_o \mu_o}\Big|_{i-1/2,j,k}$$

Considering the pressure definition of $p_{o_{i,j,k}}$ at the time $n+1$,

$$p_{o_{i,j,k}}{}^{n+1} = p_{o_{i,j,k}}{}^{n} + \Delta p_{o_{i,j,k}}{}^{n+1} \qquad \text{(A – 109)}$$

Replacing Equation (A – 108) with Equation (A – 109):

$$T_{or^+}{}^{n}\left[\left(p_{o_{i+1,j,k}} - p_{o_{i,j,k}}\right)^{n+1} - \rho_{osc}\gamma_c g\left(z_{i+1,j,k} - z_{i,j,k}\right)\right] - T_{or^-}{}^{n}\left[\left(p_{o_{i,j,k}} - p_{o_{i-1,j,k}}\right)^{n+1} - \rho_{osc}\gamma_c g\left(z_{i,j,k} - z_{i-1,j,k}\right)\right] = T_{or^+}{}^{n}\left[\left(p_{o_{i+1,j,k}} - p_{o_{i,j,k}}\right)^{n} + \left(\Delta p_{o_{i+1,j,k}} - \Delta p_{o_{i,j,k}}\right)^{n+1} - \rho_{osc}\gamma_c g\left(z_{i+1,j,k} - z_{i,j,k}\right)\right] - T_{or^-}{}^{n}\left[\left(p_{o_{i,j,k}} - p_{o_{i-1,j,k}}\right)^{n} + \left(\Delta p_{o_{i,j,k}} - \Delta p_{o_{i-1,j,k}}\right)^{n+1} - \rho_{osc}\gamma_c g\left(z_{i,j,k} - z_{i-1,j,k}\right)\right]$$

Finally,

$$\beta_c V_b \frac{\partial}{r\partial r}\left[r \frac{k_{or}}{\mu_o B_o}\left(\frac{\partial p_o}{\partial r} - \rho_{osc}\gamma_c g \frac{\partial z}{\partial r}\right)\right] = T_{or^+}{}^{n}\left(\Delta p_{o_{i+1,j,k}} - \Delta p_{o_{i,j,k}}\right)^{n+1} + T_{or^+}{}^{n}\left(p_{o_{i+1,j,k}} - p_{o_{i,j,k}}\right)^{n} - T_{or^+}{}^{n}\rho_{osc}\gamma_c g\left(z_{i+1,j,k} - z_{i,j,k}\right) - T_{or^-}{}^{n}\left(\Delta p_{o_{i,j,k}} - \Delta p_{o_{i-1,j,k}}\right)^{n+1} - T_{or^-}{}^{n}\left(p_{o_{i,j,k}} - p_{o_{i-1,j,k}}\right)^{n} + T_{or^-}{}^{n}\rho_{osc}\gamma_c g\left(z_{i,j,k} - z_{i-1,j,k}\right) \qquad \text{(A – 110)}$$

- **For tangential direction**

$$\beta_c V_b \frac{\partial}{r\partial\theta}\left[\frac{k_{o\theta}}{B_o\mu_o}\left(\frac{\partial p_o}{r\partial\theta} - \rho_{o_{SC}}\gamma_c g \frac{\partial z}{r\partial\theta}\right)\right] = \frac{2\beta_c V_{b_{i,j,k}}}{r_{i,j,k}^2 \Delta\theta_{i,j,k}}\left[\frac{k_{o\theta}}{B_o\mu_o}\Big|_{i,j+1/2,k} \frac{\left(p_{o_{i,j+1,k}} - p_{o_{i,j,k}}\right) - \rho_{o_{SC}}\gamma_c g\left(z_{i,j+1,k} - z_{i,j,k}\right)}{\Delta\theta_{i,j+1,k} + \Delta\theta_{i,j,k}} - \frac{k_{or}}{B_o\mu_o}\Big|_{i,j-1/2,k} \frac{\left(p_{o_{i,j,k}} - p_{o_{i,j-1,k}}\right) - \rho_{o_{SC}}\gamma_c g\left(z_{i,j,k} - z_{i,j-1,k}\right)}{\Delta\theta_{i,j,k} + \Delta\theta_{i,j-1,j}}\right]$$

Redefining some terms such as transmissibility,

$$\beta_c V_b \frac{\partial}{r\partial\theta}\left[\frac{k_{o\theta}}{B_o\mu_o}\left(\frac{\partial p_o}{r\partial\theta} - \rho_{o_{SC}}\gamma_c g \frac{\partial z}{r\partial\theta}\right)\right] = T_{o\theta^+}\left[\left(p_{o_{i,j+1,k}} - p_{o_{i,j,k}}\right) - \rho_{o_{SC}}\gamma_c g\left(z_{i,j+1,k} - z_{i,j,k}\right)\right] - T_{o\theta^-}\left[\left(p_{o_{i,j,k}} - p_{o_{i,j-1,k}}\right) - \rho_{o_{SC}}\gamma_c g\left(z_{i,j,k} - z_{i,j-1,k}\right)\right] \qquad \text{(A – 111)}$$

where the oil tangential transmissibilities are expressed as:

$$T_{o\theta^+} = \frac{\beta_c \Delta z_{i,j,k}\left(r^2_{i+1/2,j,k} - r^2_{i-1/2,j,k}\right)}{r^2_{i,j,k}\left(\Delta\theta_{i,j,k} + \Delta\theta_{i,j+1,k}\right)} \frac{k_{o\theta}}{B_o \mu_o}\Big|_{i,j+1/2,k}$$

$$T_{or\theta^-} = \frac{\beta_c \Delta z_{i,j,k}\left(r^2_{i+1/2,j,k} - r^2_{i-1/2,j,k}\right)}{r^2_{i,j,k}\left(\Delta\theta_{i,j-1,k} + \Delta\theta_{i,j,k}\right)} \frac{k_{o\theta}}{B_o \mu_o}\Big|_{i,j-1/2,k}$$

Evaluating the pressure $p_{o_{i,j,k}}$ at the time $n+1$ from Equation (A – 109),

$$T_{o\theta^+}{}^n \left[\left(p_{o_{i,j+1,k}} - p_{o_{i,j,k}}\right)^{n+1} - \rho_{o_{SC}} \gamma_c g\left(z_{i,j+1,k} - z_{i,j,k}\right)\right] - T_{o\theta^-}{}^n \left[\left(p_{o_{i,j,k}} - p_{o_{i,j-1,k}}\right)^{n+1} - \rho_{o_{SC}} \gamma_c g\left(z_{i,j,k} - z_{i,j-1,k}\right)\right] = T_{o\theta^+}{}^n \left[\left(p_{o_{i,j+1,k}} - p_{o_{i,j,k}}\right)^{n} + \left(\Delta p_{o_{i,j+1,k}} - \Delta p_{o_{i,j,k}}\right)^{n+1} - \rho_{o_{SC}} \gamma_c g\left(z_{i,j+1,k} - z_{i,j,k}\right)\right] - T_{o\theta^-}{}^n \left[\left(p_{o_{i,j,k}} - p_{o_{i,j-1,k}}\right)^{n} + \left(\Delta p_{o_{i,j,k}} - \Delta p_{o_{i,j-1,k}}\right)^{n+1} - \rho_{o_{SC}} \gamma_c g\left(z_{i,j,k} - z_{i,j-1,k}\right)\right]$$

Finally,

$$\beta_c V_b \frac{\partial}{r\partial\theta}\left[\frac{k_{o\theta}}{\mu_o B_o}\left(\frac{\partial p_o}{r\partial\theta} - \rho_{o_{SC}} \gamma_c g \frac{\partial z}{r\partial\theta}\right)\right] = T_{o\theta^+}{}^n \left(\Delta p_{o_{i,j+1,k}} - \Delta p_{o_{i,j,k}}\right)^{n+1} + T_{o\theta^+}{}^n \left(p_{o_{i,j+1,k}} - p_{o_{i,j,k}}\right)^{n} - T_{o\theta^+}{}^n \rho_{o_{SC}} \gamma_c g\left(z_{i,j+1,k} - z_{i,j,k}\right) - T_{o\theta^-}{}^n \left(\Delta p_{o_{i,j,k}} - \Delta p_{o_{i,j-1,k}}\right)^{n+1} - T_{o\theta^-}{}^n \left(p_{o_{i,j,k}} - p_{o_{i,j-1,k}}\right)^{n} + T_{o\theta^-}{}^n \rho_{o_{SC}} \gamma_c g\left(z_{i,j,k} - z_{i,j-1,k}\right) \quad \text{(A – 112)}$$

- **For vertical direction**

$$\beta_c V_b \frac{\partial}{\partial z}\left[\frac{k_{oz}}{B_o \mu_o}\left(\frac{\partial p_o}{\partial z} - \rho_{o_{SC}} \gamma_c g \frac{\partial z}{\partial z}\right)\right] = \frac{2\beta_c V_{b_{i,j,k}}}{\Delta z_{i,j,k}}\left[\frac{k_{oz}}{B_o \mu_o}\Big|_{i,j,k+1/2} \frac{\left(p_{o_{i,j,k+1}} - p_{o_k}\right) - \rho_{o_{SC}} \gamma_c g\left(z_{i,j,k+1} - z_{i,j,k}\right)}{\Delta z_{i,j,k+1} + \Delta z_{i,j,k}} - \frac{k_{oz}}{B_o \mu_o}\Big|_{i,j,k-1/2} \frac{\left(p_{o_{i,,k}} - p_{o_{i,j,k-1}}\right) - \rho_{o_{SC}} \gamma_c g\left(z_{i,j,k} - z_{i,j,k-1}\right)}{\Delta z_{i,j,k} + \Delta z_{i,j,k-1}}\right]$$

Redefining some terms such as transmissibility,

$$\beta_c V_b \frac{\partial}{\partial z}\left[\frac{k_{oz}}{B_o \mu_o}\left(\frac{\partial p_o}{\partial z} - \rho_{o_{SC}} \gamma_c g \frac{\partial z}{\partial z}\right)\right] = T_{oz^+}\left[\left(p_{o_{i,j,k+1}} - p_{o_{i,j,k}}\right) - \rho_{o_{SC}} \gamma_c g\left(z_{i,j,k+1} - z_{i,j,k}\right)\right] - T_{oz^-}\left[\left(p_{o_{i,j,k}} - p_{o_{i,j,k-1}}\right) - \rho_{o_{SC}} \gamma_c g\left(z_{i,j,k} - z_{i,j,k-1}\right)\right] \quad \text{(A – 113)}$$

where the oil vertical transmissibilities are expressed as:

$$T_{oz^+} = \frac{\beta_c \Delta\theta_{i,j,k}\left(r^2_{i+1/2,j,k} - r^2_{i-1/2,j,k}\right)}{\left(\Delta z_{i,j,k} + \Delta z_{i,j,k+1}\right)} \frac{k_{oz}}{B_o \mu_o}\Big|_{i,j,k+1/2}$$

$$T_{oz^-} = \frac{\beta_c \Delta\theta_{i,j,k}\left(r^2_{i+1/2,j,k} - r^2_{i-1/2,j,k}\right)}{\left(\Delta z_{i,j,k-1} + \Delta z_{i,j,k}\right)} \frac{k_{oz}}{B_o \mu_o}\Big|_{i,j,k-1/2}$$

Evaluating the pressure $p_{o_{i,j,k}}$ at the time $n+1$ from Equation (A – 109),

$$T_{oz^+}{}^n \left(p_{o_{i,j,k+1}} - p_{o_{i,j,k}}\right)^{n+1} - T_{oz^-}{}^n \left(p_{o_{i,j,k}} - p_{o_{i,j,k-1}}\right)^{n+1} = T_{oz^+}{}^n \left[\left(\Delta p_{o_{i,j,k+1}} - \Delta p_{o_{i,j,k}}\right)^{n+1} + \left(p_{o_{i,j,k+1}} - p_{o_{i,j,k}}\right)^{n} - \rho_{o_{SC}} \gamma_c g \left(z_{i,j,k+1} - z_{i,j,k}\right)\right] - T_{oz^-}{}^n \left[\left(\Delta p_{o_{i,j,k}} - \Delta p_{o_{i,j,k-1}}\right)^{n+1} + \left(p_{o_{i,j,k}} - p_{o_{i,j,k-1}}\right)^{n} - \rho_{o_{SC}} \gamma_c g \left(z_{i,j,k} - z_{i,j,k-1}\right)\right]$$

Finally,

$$\beta_c V_b \frac{\partial}{\partial z}\left[\frac{k_{oz}}{B_o \mu_o}\left(\frac{\partial p_o}{\partial z} - \rho_{o_{SC}} \gamma_c g \frac{\partial z}{\partial z}\right)\right] = T_{oz^+}{}^n \left(\Delta p_{o_{i,j,k+1}} - \Delta p_{o_{i,j,k}}\right)^{n+1} + T_{oz^+}{}^n \left(p_{o_{i,j,k+1}} - p_{o_{i,j,k}}\right)^{n} - T_{oz^+}{}^n \rho_{o_{SC}} \gamma_c g \left(z_{i,j,k+1} - z_{i,j,k}\right) - T_{oz^-}{}^n \left(\Delta p_{o_{i,j,k}} - \Delta p_{o_{i,j,k-1}}\right)^{n+1} - T_{oz^-}{}^n \left(p_{o_{i,j,k}} - p_{o_{i,j,k-1}}\right)^{n} + T_{oz^-}{}^n \rho_{o_{SC}} \gamma_c g \left(z_{i,j,k} - z_{i,j,k-1}\right) \quad \text{(A – 114)}$$

Applying these directional relations,

$$\nabla \cdot \left(\beta_c V_{b_{i,j,k}} \frac{\boldsymbol{k}_o}{B_o \mu_o}\left(\nabla p_o - \rho_{o_{SC}} \gamma_c g \nabla z\right)\right) = T_{or^+}{}^n \left(p_{o_{i+1,j,k}} - p_{o_{i,j,k}}\right)^{n} - T_{or^-}{}^n \left(p_{o_{i,j,k}} - p_{o_{i-1,j,k}}\right)^{n} + T_{or^+}{}^n \left(\Delta p_{o_{i+1,j,k}} - \Delta p_{o_{i,j,k}}\right)^{n+1} - T_{or^-}{}^n \left(\Delta p_{o_{i,j,k}} - \Delta p_{o_{i-1,j,k}}\right)^{n+1} - T_{or^+}{}^n \rho_{o_{SC}} \gamma_c g \left(z_{i+1,j,k} - z_{i,j,k}\right) + T_{or^-}{}^n \rho_{o_{SC}} \gamma_c g \left(z_{i,j,k} - z_{i-1,j,k}\right) + T_{o\theta^+}{}^n \left(p_{o_{i,j+1,k}} - p_{o_{i,j,k}}\right)^{n} - T_{o\theta^-}{}^n \left(p_{o_{i,j,k}} - p_{o_{i,j-1,k}}\right)^{n} + T_{o\theta^+}{}^n \left(\Delta p_{o_{i,j+1,k}} - \Delta p_{o_{i,j,k}}\right)^{n+1} - T_{o\theta^-}{}^n \left(\Delta p_{o_{i,j,k}} - \Delta p_{o_{i,j-1,k}}\right)^{n+1} - T_{o\theta^+}{}^n \rho_{o_{SC}} \gamma_c g \left(z_{i,j+1,k} - z_{i,j,k}\right) + T_{o\theta^-}{}^n \rho_{o_{SC}} \gamma_c g \left(z_{i,j,k} - z_{i,j-1,k}\right) + T_{oz^+}{}^n \left(p_{o_{i,j,k+1}} - p_{o_{i,j,k}}\right)^{n} - T_{oz^-}{}^n \left(p_{o_{i,j,k}} - p_{o_{i,j,k-1}}\right)^{n} + T_{oz^+}{}^n \left(\Delta p_{o_{i,j,k+1}} - \Delta p_{o_{i,j,k}}\right)^{n+1} - T_{oz^-}{}^n \left(\Delta p_{o_{i,j,k}} - \Delta p_{o_{i,j,k-1}}\right)^{n+1} - T_{oz^+}{}^n \rho_{o_{SC}} \gamma_c g \left(z_{i,j,k+1} - z_{i,j,k}\right) + T_{oz^-}{}^n \rho_{o_{SC}} \gamma_c g \left(z_{i,j,k} - z_{i,j,k-1}\right) \quad \text{(A – 115)}$$

Substituting Equation (A – 115) into Equation (A – 73),

$$T_{or^+}{}^n \left(p_{o_{i+1,j,k}} - p_{o_{i,j,k}}\right)^{n} - T_{or^-}{}^n \left(p_{o_{i,j,k}} - p_{o_{i-1,j,k}}\right)^{n} + T_{or^+}{}^n \left(\Delta p_{o_{i+1,j,k}} - \Delta p_{o_{i,j,k}}\right)^{n+1} - T_{or^-}{}^n \left(\Delta p_{o_{i,j,k}} - \Delta p_{o_{i-1,j,k}}\right)^{n+1} - T_{or^+}{}^n \rho_{o_{SC}} \gamma_c g \left(z_{i+1,j,k} - z_{i,j,k}\right) + T_{or^-}{}^n \rho_{o_{SC}} \gamma_c g \left(z_{i,j,k} - z_{i-1,j,k}\right) + T_{o\theta^+}{}^n \left(p_{o_{i,j+1,k}} - p_{o_{i,j,k}}\right)^{n} - T_{o\theta^-}{}^n \left(p_{o_{i,j,k}} - p_{o_{i,j-1,k}}\right)^{n} + T_{o\theta^+}{}^n \left(\Delta p_{o_{i,j+1,k}} - \Delta p_{o_{i,j,k}}\right)^{n+1} - T_{o\theta^-}{}^n \left(\Delta p_{o_{i,j,k}} - \Delta p_{o_{i,j-1,k}}\right)^{n+1} - T_{o\theta^+}{}^n \rho_{o_{SC}} \gamma_c g \left(z_{i,j+1,k} - z_{i,j,k}\right) + T_{o\theta^-}{}^n \rho_{o_{SC}} \gamma_c g \left(z_{i,j,k} - z_{i,j-1,k}\right) + T_{oz^+}{}^n \left(p_{o_{i,j,k+1}} - p_{o_{i,j,k}}\right)^{n} - T_{oz^-}{}^n \left(p_{o_{i,j,k}} - p_{o_{i,j,k-1}}\right)^{n} + T_{oz^+}{}^n \left(\Delta p_{o_{i,j,k+1}} - \Delta p_{o_{i,j,k}}\right)^{n+1} -$$

$$T_{oz^-}{}^n\left(\Delta p_{o_{i,j,k}} - \Delta p_{o_{i,j,k-1}}\right)^{n+1} - T_{oz^+}{}^n\rho_{o_{SC}}\gamma_c g\left(z_{i,j,k+1} - z_{i,j,k}\right) + T_{oz^-}{}^n\rho_{o_{SC}}\gamma_c g\left(z_{i,j,k} - z_{i,j,k-1}\right) = F_o + G_o\frac{\Delta S_{o_{i,j,k}}{}^{n+1}}{\Delta t} + H_o\frac{\Delta S_{g_{i,j,k}}{}^{n+1}}{\Delta t} + I_o\frac{\Delta p_{o_{i,j,k}}{}^{n+1}}{\Delta t} + J_o\frac{\left(\alpha_{i,j,k}\Delta\epsilon^e_{v\,i,j,k}{}^{n+1} + \Delta\epsilon^p_{v\,i,j,k}{}^{n+1}\right)}{\Delta t} + q_{o_{SC}}$$

Regrouping and redefining some variables,

$$E_o\Delta p_{o_{i+1,j,k}}{}^{n+1} + \left(C_o - \frac{I_o}{\Delta t}\right)\Delta p_{o_{i,j,k}}{}^{n+1} + W_o\Delta p_{o_{i-1,j,k}}{}^{n+1} + N_o\Delta p_{o_{i,j+1,k}}{}^{n+1} + S_o\Delta p_{o_{i,j-1,k}}{}^{n+1} + U_o\Delta p_{o_{i,j,k+1}}{}^{n+1} + D_o\Delta p_{o_{i,j,k-1}}{}^{n+1} - \frac{G_o}{\Delta t}\Delta S_{o_{i,j,k}}{}^{n+1} - \frac{H_o}{\Delta t}\Delta S_{g_{i,j,k}}{}^{n+1} = -E_o\left(p_{o_{i+1,j,k}}{}^n - \gamma_o z_{i+1,j,k}\right) - C_o\left(p_{o_{i,j,k}}{}^n - \gamma_o z_{i,j,k}\right) - W_o\left(p_{o_{i-1,j,k}}{}^n - \gamma_o z_{i-1,j,k}\right) - N_o\left(p_{o_{i,j+1,k}}{}^n - \gamma_o z_{i,j+1,k}\right) - S_o\left(p_{o_{i,j-1,k}}{}^n - \gamma_o z_{i,j-1,k}\right) - U_o\left(p_{o_{i,j,k+1}}{}^n - \gamma_o z_{i,j,k+1}\right) - D_o\left(p_{o_{i,j,k-1}}{}^n - \gamma_o z_{i,j,k-1}\right) + \frac{J_o}{\Delta t}\left(\alpha_{i,j,k}\Delta\epsilon^e_{v\,i,j,k}{}^{n+1} + \Delta\epsilon^p_{v\,i,j,k}{}^{n+1}\right) + F_o + q_{o_{SC}} \quad \text{(A – 116)}$$

$$\gamma_o = \rho_{o_{SC}}\gamma_c g$$

$$E = T_{or^+}{}^n$$

$$C_o = -(T_{or^+}{}^n + T_{or^-}{}^n + T_{o\theta^+}{}^n + T_{o\theta^-}{}^n + T_{oz^+}{}^n + T_{oz^-}{}^n)$$

$$W_o = T_{or^-}{}^n$$

$$N_o = T_{o\theta^+}{}^n$$

$$S_o = T_{o\theta^-}{}^n$$

$$U_o = T_{oz^+}{}^n$$

$$D_o = T_{oz^-}{}^n$$

$$F_{o_{i,j,k}} = \frac{V_{b_{i,j,k}}q_{s_{i,j,k}}\phi_{i,j,k}}{(1-\phi_{i,j,k})}$$

$$G_{o_{i,j,k}} = \frac{V_{b_{i,j,k}}\phi_{i,j,k}}{\alpha_c B_{o_{i,j,k}}}$$

$$H_{o_{i,j,k}} = 0$$

$$I_{o_{i,j,k}} = \frac{V_{b_{i,j,k}}\phi_{i,j,k}}{\alpha_c B_{o_{i,j,k}}}S_{o_{i,j,k}}\left[c_{pc_{i,j,k}}(1-\alpha_{i,j,k}) - c_{s_{i,j,k}} + c_{o\,i,j,k}\right]$$

$$J_{o_{i,j,k}} = -\frac{V_{b_{i,j,k}}S_{o_{i,j,k}}}{\alpha_c B_{o_{i,j,k}}}$$

A2.2.2. Water-phase

Equation (A – 88) is the governing equation for the water phase,

$$\nabla\cdot\left(\beta_c\frac{\boldsymbol{k}_w}{B_w\mu_w}\left(\nabla p_o-\rho_{w_{SC}}\gamma_c g\nabla z\right)\right)+\nabla\cdot\left(\beta_c\frac{\boldsymbol{k}_w}{B_w\mu_w}p'_{cwo}\nabla S_o\right)+\nabla\cdot\left(\beta_c\frac{\boldsymbol{k}_w}{B_w\mu_w}p'_{cwo}\nabla S_g\right)=F_w+G_w\frac{\partial S_o}{\partial t}+H_w\frac{\partial S_g}{\partial t}+I_w\frac{\partial p_o}{\partial t}+J_w\left(\alpha\frac{\partial\epsilon_v^e}{\partial t}+\frac{\partial\epsilon_v^p}{\partial t}\right)+q_{w_{SC}} \quad (A-88)$$

Similar to the oil phase, the first term of the left-hand side of the Equation (A – 88) can be expanded as:

$$\begin{aligned}&\nabla\cdot\left(\beta_c V_b\frac{\boldsymbol{k}_w}{B_w\mu_w}\left(\nabla p_o-\rho_{w_{SC}}\gamma_c g\nabla z\right)\right)=T_{wr^+}{}^n\left(p_{o_{i+1,j,k}}-p_{o_{i,j,k}}\right)^n-T_{wr^-}{}^n\left(p_{o_{i,j,k}}-p_{o_{i-1,j,k}}\right)^n+\\&T_{wr^+}{}^n\left(\Delta p_{o_{i+1,j,k}}-\Delta p_{o_{i,j,k}}\right)^{n+1}-T_{wr^-}{}^n\left(\Delta p_{o_{i,j,k}}-\Delta p_{o_{i-1,j,k}}\right)^{n+1}-T_{wr^+}{}^n\rho_{w_{SC}}\gamma_c g\left(z_{i+1,j,k}-z_{i,j,k}\right)+\\&T_{wr^-}{}^n\rho_{w_{SC}}\gamma_c g\left(z_{i,j,k}-z_{i-1,j,k}\right)+T_{w\theta^+}{}^n\left(p_{o_{i,j+1,k}}-p_{o_{i,j,k}}\right)^n-T_{w\theta^-}{}^n\left(p_{o_{i,j,k}}-p_{o_{i,j-1,k}}\right)^n+\\&T_{w\theta^+}{}^n\left(\Delta p_{o_{i,j+1,k}}-\Delta p_{o_{i,j,k}}\right)^{n+1}-T_{w\theta^-}{}^n\left(\Delta p_{o_{i,j,k}}-\Delta p_{o_{i,j-1,k}}\right)^{n+1}-T_{w\theta^+}{}^n\rho_{w_{SC}}\gamma_c g\left(z_{i,j+1,k}-z_{i,j,k}\right)+\\&T_{w\theta^-}{}^n\rho_{w_{SC}}\gamma_c g\left(z_{i,j,k}-z_{i,j-1,k}\right)+T_{wz^+}{}^n\left(p_{o_{i,j,k+1}}-p_{o_{i,j,k}}\right)^n-T_{wz^-}{}^n\left(p_{o_{i,j,k}}-p_{o_{i,j,k-1}}\right)^n+\\&T_{wz^+}{}^n\left(\Delta p_{o_{i,j,k+1}}-\Delta p_{o_{i,j,k}}\right)^{n+1}-T_{wz^-}{}^n\left(\Delta p_{o_{i,j,k}}-\Delta p_{o_{i,j,k-1}}\right)^{n+1}-T_{wz^+}{}^n\rho_{w_{SC}}\gamma_c g\left(z_{i,j,k+1}-z_{i,j,k}\right)+\\&T_{wz^-}{}^n\rho_{w_{SC}}\gamma_c g\left(z_{i,j,k}-z_{i,j,k-1}\right)\end{aligned} \quad (A-117)$$

where the water transmissibility relations are expressed as:

$$T_{wr^+}=\frac{\beta_c\Delta\theta_{i,j,k}\Delta z_{i,j,k}\left(r^2_{i+1/2,j,k}-r^2_{i-1/2,j,k}\right)}{2r_{i,j,k}\Delta r_{i,j,k}\ln\left(r_{i+1,j,k}/r_{i,j,k}\right)}\frac{k_{wr}}{B_w\mu_w}\Big|_{i+1/2,j,k}$$

$$T_{wr^-}=\frac{\beta_c\Delta\theta_{i,j,k}\Delta z_{i,j,k}\left(r^2_{i+1/2,j,k}-r^2_{i-1/2,j,k}\right)}{2r_{i,j,k}\Delta r_{i,j,k}\ln\left(r_{i,j,k}/r_{i-1,j,k}\right)}\frac{k_{wr}}{B_w\mu_w}\Big|_{i-1/2,j,k}$$

$$T_{w\theta^+}=\frac{\beta_c\Delta z_{i,j,k}\left(r^2_{i+1/2,j,k}-r^2_{i-1/2,j,k}\right)}{r^2_{i,j,k}\left(\Delta\theta_{i,j,k}+\Delta\theta_{i,j+1,k}\right)}\frac{k_{w\theta}}{B_w\mu_w}\Big|_{i,j+1/2,k}$$

$$T_{wr\theta^-}=\frac{\beta_c\Delta z_{i,j,k}\left(r^2_{i+1/2,j,k}-r^2_{i-1/2,j,k}\right)}{r^2_{i,j,k}\left(\Delta\theta_{i,j-1,k}+\Delta\theta_{i,j,k}\right)}\frac{k_{w\theta}}{B_w\mu_w}\Big|_{i,j-1/2,k}$$

$$T_{wz^+}=\frac{\beta_c\Delta\theta_{i,j,k}\left(r^2_{i+1/2,j,k}-r^2_{i-1/2,j,k}\right)}{\left(\Delta z_{i,j,k}+\Delta z_{i,j,k+1}\right)}\frac{k_{wz}}{B_w\mu_w}\Big|_{i,j,k+1/2}$$

$$T_{wz^-}=\frac{\beta_c\Delta\theta_{i,j,k}\left(r^2_{i+1/2,j,k}-r^2_{i-1/2,j,k}\right)}{\left(\Delta z_{i,j,k-1}+\Delta z_{i,j,k}\right)}\frac{k_{wz}}{B_w\mu_w}\Big|_{i,j,k-1/2}$$

The second term of the left-hand side of Equation (A – 88) can be expanded as:

$$\nabla \cdot \left(\beta_c \frac{\boldsymbol{k}_w}{B_w \mu_w} p'_{cwo} \nabla S_o\right) = \beta_c \frac{\partial}{r\partial r}\left(r \frac{k_{wr}}{B_w \mu_w} p'_{cwo} \frac{\partial S_o}{\partial r}\right) + \beta_c \frac{\partial}{r\partial \theta}\left(\frac{k_{w\theta}}{B_w \mu_w} p'_{cwo} \frac{\partial S_o}{r\partial \theta}\right) + \beta_c \frac{\partial}{\partial z}\left(\frac{k_{wz}}{B_w \mu_w} p'_{cwo} \frac{\partial S_o}{\partial z}\right) \quad \text{(A – 118)}$$

The third term of the left-hand side of Equation (A – 88) can be expanded as:

$$\nabla \cdot \left(\beta_c \frac{\boldsymbol{k}_w}{B_w \mu_w} p'_{cwo} \nabla S_g\right) = \beta_c \frac{\partial}{r\partial r}\left(\frac{r k_{wr}}{B_w \mu_w} p'_{cwo} \frac{\partial S_g}{\partial r}\right) + \beta_c \frac{\partial}{r\partial \theta}\left(\frac{k_{w\theta}}{B_w \mu_w} p'_{cwo} \frac{\partial S_g}{r\partial \theta}\right) + \beta_c \frac{\partial}{\partial z}\left(\frac{k_{wz}}{B_w \mu_w} p'_{cwo} \frac{\partial S_g}{\partial z}\right) \quad \text{(A – 119)}$$

- **For radial direction**

$$\beta_c V_b \frac{\partial}{r\partial r}\left(r \frac{k_{wr}}{B_w \mu_w} p'_{cwo} \frac{\partial S_o}{\partial r}\right) = \frac{\beta_c V_{b_{i,j,k}}}{r_i \Delta r_i}\left(\frac{k_{wr}}{B_w \mu_w} p'_{cwo}\Big|_{i+1/2} \frac{S_{o_{i+1}} - S_{o_i}}{\ln(r_{i+1}/r_i)} - \frac{k_{rw}}{B_w \mu_w} p'_{cwo}\Big|_{i-1/2} \frac{S_{o_i} - S_{o_{i-1}}}{\ln(r_i/r_{i-1})}\right)$$

$$\beta_c V_b \frac{\partial}{r\partial r}\left(r \frac{k_{wr}}{B_w \mu_w} p'_{cwo} \frac{\partial S_o}{\partial r}\right) = T_{wr^+} p'_{cow_{i+1/2}}\left(S_{o_{i+1,j,k}} - S_{o_{i,j,k}}\right) - T_{wr^-} p'_{cwo_{i-1/2}}\left(S_{o_{i,j,k}} - S_{o_{i-1,j,k}}\right) \quad \text{(A – 120)}$$

Considering the saturation definition $S_{o_{i,j,k}}$ at time $n+1$:

$${S_{o_{i,j,k}}}^{n+1} = {S_{o_{i,j,k}}}^{n} + \Delta {S_{o_{i,j,k}}}^{n+1} \quad \text{(A – 121)}$$

Replacing Equation (A – 121) into Equation (A – 120):

$$\begin{aligned}
&{T_{wr^+}}^{n} p'_{cwo_{i+1/2,j,k}}\left(S_{o_{i+1,j,k}} - S_{o_{i,j,k}}\right)^{n+1} - {T_{wr^-}}^{n} p'_{cwo_{i-1/2,j,k}}\left(S_{o_{i,j,k}} - S_{o_{i-1,j,k}}\right)^{n+1} = \\
&{T_{wr^+}}^{n} p'_{cwo_{i+1/2,j,k}}\left(S_{o_{i+1,j,k}} - S_{o_{i,j,k}}\right)^{n} - {T_{wr^-}}^{n} p'_{cwo_{i-1/2,j,k}}\left(S_{o_{i,j,k}} - S_{o_{i-1,j,k}}\right)^{n} + \\
&{T_{wzr^+}}^{n} p'_{cwo_{i+1/2,j,k}}\left(\Delta S_{o_{i+1,j,k}} - \Delta S_{o_{i,j,k}}\right)^{n+1} - {T_{wr^-}}^{n} p'_{cwo_{i-1/2,j,k}}\left(\Delta S_{o_{i,j,k}} - \Delta S_{o_{i-1,j,k}}\right)^{n+1}
\end{aligned}$$

Then,

$$\begin{aligned}
\beta_c V_b \frac{\partial}{r\partial r}\left(\frac{r k_{wr}}{\mu_w B_w} p'_{cwo} \frac{\partial S_o}{\partial r}\right) = {T_{wr^+}}^{n} p'_{cwo_{i+1/2,j,k}}\left(S_{o_{i+1,j,k}} - S_{o_{i,j,k}}\right)^{n} - {T_{wr^-}}^{n} p'_{cwo_{i-1/2,j,k}}\left(S_{o_{i,j,k}} - \right. \\
\left. S_{o_{i-1,j,k}}\right)^{n} + {T_{wr^+}}^{n} p'_{cwo_{i+1/2,j,k}}\left(\Delta S_{o_{i+1,j,k}} - \Delta S_{o_{i,j,k}}\right)^{n+1} - {T_{wr^-}}^{n} p'_{cwo_{i-1/2,j,k}}\left(\Delta S_{o_{i,j,k}} - \Delta S_{o_{i-1,j,k}}\right)^{n+1}
\end{aligned} \quad \text{(A – 122)}$$

- **For tangential direction**

$$\beta_c V_b \frac{\partial}{r\partial \theta}\left(\frac{k_{w\theta}}{B_w \mu_w} p'_{cwo} \frac{\partial S_o}{r\partial \theta}\right) = \frac{2\beta_c V_{b_{i,j,k}}}{r_i^2 \Delta \theta_j}\left(\frac{k_{w\theta}}{B_w \mu_w} p'_{cwo}\Big|_{j+1/2} \frac{S_{o_{j+1}} - S_{o_j}}{\Delta\theta_j + \Delta\theta_{j+1}} - \frac{k_{w\theta}}{B_w \mu_w} p'_{cwo}\Big|_{j-1/2} \frac{S_{o_{j+1}} - S_{o_j}}{\Delta\theta_{j-1} + \Delta\theta_j}\right)$$

Redefining some terms as transmissibility:

$$\beta_c V_b \frac{\partial}{r\partial\theta}\left(\frac{k_{w\theta}}{B_w\mu_w} p'_{cwo} \frac{\partial S_o}{r\partial\theta}\right) = T_{w\theta^+} p'_{cwo_{i,j+1/2,k}} \left(S_{o_{i,j+1,k}} - S_{o_{i,j,k}}\right) - T_{w\theta^-} p'_{cwo_{i,j-1/2,k}} \left(S_{o_{i,j,k}} - S_{o_{i,j-1,k}}\right) \quad \text{(A – 123)}$$

Similarly, evaluating the saturation definition $S_{o_{i,j,k}}$ at time $n+1$ using Equation (A – 121):

$$T_{w\theta^+}{}^n p'_{cwo_{i,j+1/2,k}} \left(S_{o_{i,j+1,k}} - S_{o_{i,j,k}}\right)^{n+1} - T_{w\theta^-}{}^n p'_{cwo_{i,j-1/2,k}} \left(S_{o_{i,j,k}} - S_{o_{i,j-1,k}}\right)^{n+1} =$$
$$T_{w\theta^+}{}^n p'_{cwo_{i,j+1/2,k}} \left(S_{o_{i,j+1,k}} - S_{o_{i,j,k}}\right)^{n} - T_{w\theta^-}{}^n p'_{cwo_{i,j-1/2,k}} \left(S_{o_{i,j,k}} - S_{o_{i,j-1,k}}\right)^{n} +$$
$$T_{w\theta^+}{}^n p'_{cwo_{i,j+1/2,k}} \left(\Delta S_{o_{i,j+1,k}} - \Delta S_{o_{i,j,k}}\right)^{n+1} - T_{w\theta^-}{}^n p'_{cwo_{i,j-1/2,k}} \left(\Delta S_{o_{i,j,k}} - \Delta S_{o_{i,j-1,k}}\right)^{n+1}$$

Then,

$$\beta_c V_b \frac{\partial}{r\partial\theta}\left(\frac{k_{w\theta}}{B_w\mu_w} p'_{cwo} \frac{\partial S_o}{r\partial\theta}\right) = T_{w\theta^+}{}^n p'_{cwo_{i,j+1/2,k}} \left(S_{o_{i,j+1,k}} - S_{o_{i,j,k}}\right)^{n} - T_{w\theta^-}{}^n p'_{cwo_{i,j-1/2,k}} \left(S_{o_{i,j,k}} - S_{o_{i,j-1,k}}\right)^{n} + T_{w\theta^+}{}^n p'_{cwo_{i,j+1/2,k}} \left(\Delta S_{o_{i,j+1,k}} - \Delta S_{o_{i,j,k}}\right)^{n+1} - T_{w\theta^-}{}^n p'_{cwo_{i,j-1/2,k}} \left(\Delta S_{o_{i,j,k}} - \Delta S_{o_{i,j-1,k}}\right)^{n+1} \quad \text{(A – 124)}$$

- **For vertical direction**

$$\beta_c V_b \frac{\partial}{\partial z}\left(\frac{k_{wz}}{B_w\mu_w} p'_{cwo} \frac{\partial S_o}{\partial z}\right) = \frac{2\beta_c V_{b_{i,j,k}}}{\Delta z_k}\left(\frac{k_{wz}}{B_w\mu_w} p'_{cwo}\Big|_{k+1/2} \frac{S_{o_{k+1}} - S_{o_k}}{\Delta z_k + \Delta z_{k+1}} - \frac{k_{wz}}{B_w\mu_w} p'_{cwo}\Big|_{k-1/2} \frac{S_{o_k} - S_{o_{k-1}}}{\Delta z_{k-1} + \Delta z_k}\right)$$

Redefining some terms as transmissibility:

$$\beta_c V_b \frac{\partial}{\partial z}\left(\frac{k_{wz}}{B_w\mu_w} p'_{cwo} \frac{\partial S_o}{\partial z}\right) = T_{wz^+} p'_{cwo_{i,j,k+1/2}} \left(S_{o_{i,j,k+1}} - S_{o_{i,j,k}}\right) - T_{wz^-} p'_{cwo_{i,j,k-1/2}} \left(S_{o_{i,j,k}} - S_{o_{i,j,k-1}}\right) \quad \text{(A – 125)}$$

Similarly, replacing Equation (A – 121) with Equation (A – 125):

$$T_{wr^+}{}^n p'_{cwo_{i,j,k+1/2}} \left(S_{o_{i,j,k+1}} - S_{o_{i,j,k}}\right)^{n+1} - T_{wz^-}{}^n p'_{cwo_{i,j,k-1/2}} \left(S_{o_{i,j,k}} - S_{o_{i,j,k-1}}\right)^{n+1} =$$
$$T_{wz^+}{}^n p'_{cwo_{i,j,k+1/2}} \left(S_{o_{i,j,k+1}} - S_{o_{i,j,k}}\right)^{n} - T_{wz^-}{}^n p'_{cwo_{i,j,k-1/2}} \left(S_{o_{i,j,k}} - S_{o_{i,j,k-1}}\right)^{n} +$$
$$T_{wz^+}{}^n p'_{cwo_{i,j,k+1/2}} \left(\Delta S_{o_{i,j,k+1}} - \Delta S_{o_{i,j,k}}\right)^{n+1} - T_{wz^-}{}^n p'_{cwo_{i,j,k-1/2}} \left(\Delta S_{o_{i,j,k}} - \Delta S_{o_{i,j,k-1}}\right)^{n+1}$$

Then,

$$\beta_c V_b \frac{\partial}{\partial z}\left(\frac{k_{wz}}{B_w\mu_w} p'_{cwo} \frac{\partial S_o}{\partial z}\right) = T_{wz^+}{}^n p'_{cwo_{i,j,k+1/2}} \left(S_{o_{i,j,k+1}} - S_{o_{i,j,k}}\right)^{n} - T_{wz^-}{}^n p'_{cwo_{i,j,k-1/2}} \left(S_{o_{i,j,k}} - S_{o_{i,j,k-1}}\right)^{n} + T_{wz^+}{}^n p'_{cwo_{i,j,k+1/2}} \left(\Delta S_{o_{i,j,k+1}} - \Delta S_{o_{i,j,k}}\right)^{n+1} - T_{wz^-}{}^n p'_{cwo_{i,j,k-1/2}} \left(\Delta S_{o_{i,j,k}} - \Delta S_{o_{i,j,k-1}}\right)^{n+1}$$

Regrouping into the second term of the left-hand side of Equation (A – 88),

$$\nabla \cdot \left(\beta_c V_b \frac{\boldsymbol{k}_w}{B_w \mu_w} p'_{cwo} \nabla S_o\right) = T_{wr^+}{}^n p'_{cwo_{i+1/2,j,k}} \left(S_{o_{i+1,j,k}} - S_{o_{i,j,k}}\right)^n - T_{wr^-}{}^n p'_{cwo_{i-1/2,j,k}} \left(S_{o_{i,j,k}} - S_{o_{i-1,j,k}}\right)^n + T_{wr^+}{}^n p'_{cwo_{i+1/2,j,k}} \left(\Delta S_{o_{i+1,j,k}} - \Delta S_{o_{i,j,k}}\right)^{n+1} - T_{wr^-}{}^n p'_{cwo_{i-1/2,j,k}} \left(\Delta S_{o_{i,j,k}} - \Delta S_{o_{i-1,j,k}}\right)^{n+1} + T_{w\theta^+}{}^n p'_{cwo_{i,j+1/2,k}} \left(S_{o_{i,j+1,k}} - S_{o_{i,j,k}}\right)^n - T_{w\theta^-}{}^n p'_{cwo_{i,j-1/2,k}} \left(S_{o_{i,j,k}} - S_{o_{i,j-1,k}}\right)^n + T_{w\theta^+}{}^n p'_{cwo_{i,j+1/2,k}} \left(\Delta S_{o_{i,j+1,k}} - \Delta S_{o_{i,j,k}}\right)^{n+1} - T_{w\theta^-}{}^n p'_{cwo_{i,j-1/2,k}} \left(\Delta S_{o_{i,j,k}} - \Delta S_{o_{i,j-1,k}}\right)^{n+1} + T_{wz^+}{}^n p'_{cwo_{i,j,k+1/2}} \left(S_{o_{i,j,k+1}} - S_{o_{i,j,k}}\right)^n - T_{wz^-}{}^n p'_{cwo_{i,j,k-1/2}} \left(S_{o_{i,j,k}} - S_{o_{i,j,k-1}}\right)^n + T_{wz^+}{}^n p'_{cwo_{i,j,k+1/2}} \left(\Delta S_{o_{i,j,k+1}} - \Delta S_{o_{i,j,k}}\right)^{n+1} - T_{wz^-}{}^n p'_{cwo_{i,j,k-1/2}} \left(\Delta S_{o_{i,j,k}} - \Delta S_{o_{i,j,k-1}}\right)^{n+1} \quad \text{(A – 126)}$$

Similarly for the third term of the left-hand side of Equation (A – 88),

$$\nabla \cdot \left(\beta_c V_b \frac{\boldsymbol{k}_w}{B_w \mu_w} p'_{cwo} \nabla S_g\right) = T_{wr^+}{}^n p'_{cwo_{i+1/2,j,k}} \left(S_{g_{i+1,j,k}} - S_{g_{i,j,k}}\right)^n - T_{wr^-}{}^n p'_{cwo_{i-1/2,j,k}} \left(S_{g_{i,j,k}} - S_{g_{i-1,j,k}}\right)^n + T_{wr^+}{}^n p'_{cwo_{i+1/2,j,k}} \left(\Delta S_{g_{i+1,j,k}} - \Delta S_{g_{i,j,k}}\right)^{n+1} - T_{wr^-}{}^n p'_{cwo_{i-1/2,j,k}} \left(\Delta S_{g_{i,j,k}} - \Delta S_{g_{i-1,j,k}}\right)^{n+1} + T_{w\theta^+}{}^n p'_{cwo_{i,j+1/2,k}} \left(S_{g_{i,j+1,k}} - S_{g_{i,j,k}}\right)^n - T_{w\theta^-}{}^n p'_{cwo_{i,j-1/2,k}} \left(S_{g_{i,j,k}} - S_{g_{i,j-1,k}}\right)^n + T_{w\theta^+}{}^n p'_{cwo_{i,j+1/2,k}} \left(\Delta S_{g_{i,j+1,k}} - \Delta S_{g_{i,j,k}}\right)^{n+1} - T_{w\theta^-}{}^n p'_{cwo_{i,j-1/2,k}} \left(\Delta S_{g_{i,j,k}} - \Delta S_{g_{i,j-1,k}}\right)^{n+1} + T_{wz^+}{}^n p'_{cwo_{i,j,k+1/2}} \left(S_{g_{i,j,k+1}} - S_{g_{i,j,k}}\right)^n - T_{wz^-}{}^n p'_{cwo_{i,j,k-1/2}} \left(S_{g_{i,j,k}} - S_{g_{i,j,k-1}}\right)^n + T_{wz^+}{}^n p'_{cwo_{i,j,k+1/2}} \left(\Delta S_{g_{i,j,k+1}} - \Delta S_{g_{i,j,k}}\right)^{n+1} - T_{wz^-}{}^n p'_{cwo_{i,j,k-1/2}} \left(\Delta S_{g_{i,j,k}} - \Delta S_{g_{i,j,k-1}}\right)^{n+1} \quad \text{(A – 127)}$$

Substituting Equations (A – 117), (A – 126), (A – 127) into the Equation (A – 88),

$$T_{wr^+}{}^n \left(p_{o_{i+1,j,k}} - p_{o_{i,j,k}}\right)^n - T_{wr^-}{}^n \left(p_{o_{i,j,k}} - p_{o_{i-1,j,k}}\right)^n + T_{wr^+}{}^n \left(\Delta p_{o_{i+1,j,k}} - \Delta p_{o_{i,j,k}}\right)^{n+1} - T_{wr^-}{}^n \left(\Delta p_{o_{i,j,k}} - \Delta p_{o_{i-1,j,k}}\right)^{n+1} - T_{wr^+}{}^n \rho_{w_{SC}} \gamma_c g \left(z_{i+1,j,k} - z_{i,j,k}\right) + T_{wr^-}{}^n \rho_{w_{SC}} \gamma_c g \left(z_{i,j,k} - z_{i-1,j,k}\right) + T_{w\theta^+}{}^n \left(p_{o_{i,j+1,k}} - p_{o_{i,j,k}}\right)^n - T_{w\theta^-}{}^n \left(p_{o_{i,j,k}} - p_{o_{i,j-1,k}}\right)^n + T_{w\theta^+}{}^n \left(\Delta p_{o_{i,j+1,k}} - \Delta p_{o_{i,j,k}}\right)^{n+1} - T_{w\theta^-}{}^n \left(\Delta p_{o_{i,j,k}} - \Delta p_{o_{i,j-1,k}}\right)^{n+1} - T_{w\theta^+}{}^n \rho_{w_{SC}} \gamma_c g \left(z_{i,j+1,k} - z_{i,j,k}\right) + T_{w\theta^-}{}^n \rho_{w_{SC}} \gamma_c g \left(z_{i,j,k} - z_{i,j-1,k}\right) + T_{wz^+}{}^n \left(p_{o_{i,j,k+1}} - p_{o_{i,j,k}}\right)^n - T_{wz^-}{}^n \left(p_{o_{i,j,k}} - p_{o_{i,j,k-1}}\right)^n + T_{wz^+}{}^n \left(\Delta p_{o_{i,j,k+1}} - \Delta p_{o_{i,j,k}}\right)^{n+1} - T_{wz^-}{}^n \left(\Delta p_{o_{i,j,k}} - \Delta p_{o_{i,j,k-1}}\right)^{n+1} - T_{wz^+}{}^n \rho_{w_{SC}} \gamma_c g \left(z_{i,j,k+1} - z_{i,j,k}\right) + T_{wz^-}{}^n \rho_{w_{SC}} \gamma_c g \left(z_{i,j,k} - z_{i,j,k-1}\right) + T_{wr^+}{}^n p'_{cwo_{i+1/2,j,k}} \left(S_{o_{i+1,j,k}} - S_{o_{i,j,k}}\right)^n - T_{wr^-}{}^n p'_{cwo_{i-1/2,j,k}} \left(S_{o_{i,j,k}} - S_{o_{i-1,j,k}}\right)^n + T_{wr^+}{}^n p'_{cwo_{i+1/2,j,k}} \left(\Delta S_{o_{i+1,j,k}} - \Delta S_{o_{i,j,k}}\right)^{n+1} - T_{wr^-}{}^n p'_{cwo_{i-1/2,j,k}} \left(\Delta S_{o_{i,j,k}} - \Delta S_{o_{i-1,j,k}}\right)^{n+1} + T_{w\theta^+}{}^n p'_{cwo_{i,j+1/2,k}} \left(S_{o_{i,j+1,k}} - S_{o_{i,j,k}}\right)^n - T_{w\theta^-}{}^n p'_{cwo_{i,j-1/2,k}} \left(S_{o_{i,j,k}} - S_{o_{i,j-1,k}}\right)^n +$$

$$T_{w\theta^+}{}^n p'_{cwo_{i,j+1/2,k}}\left(\Delta S_{o_{i,j+1,k}}-\Delta S_{o_{i,j,k}}\right)^{n+1}-T_{w\theta^-}{}^n p'_{cwo_{i,j-1/2,k}}\left(\Delta S_{o_{i,j,k}}-\Delta S_{o_{i,j-1,k}}\right)^{n+1}+$$
$$T_{wz^+}{}^n p'_{cwo_{i,j,k+1/2}}\left(S_{o_{i,j,k+1}}-S_{o_{i,j,k}}\right)^{n}-T_{wz^-}{}^n p'_{cwo_{i,j,k-1/2}}\left(S_{o_{i,j,k}}-S_{o_{i,j,k-1}}\right)^{n}+$$
$$T_{wz^+}{}^n p'_{cwo_{i,j,k+1/2}}\left(\Delta S_{o_{i,j,k+1}}-\Delta S_{o_{i,j,k}}\right)^{n+1}-T_{wz^-}{}^n p'_{cwo_{i,j,k-1/2}}\left(\Delta S_{o_{i,j,k}}-\Delta S_{o_{i,j,k-1}}\right)^{n+1}+$$
$$T_{wr^+}{}^n p'_{cwo_{i+1/2,j,k}}\left(S_{g_{i+1,j,k}}-S_{g_{i,j,k}}\right)^{n}-T_{wr^-}{}^n p'_{cwo_{i-1/2,j,k}}\left(S_{g_{i,j,k}}-S_{g_{i-1,j,k}}\right)^{n}+$$
$$T_{wr^+}{}^n p'_{cwo_{i+1/2,j,k}}\left(\Delta S_{g_{i+1,j,k}}-\Delta S_{g_{i,j,k}}\right)^{n+1}-T_{wr^-}{}^n p'_{cwo_{i-1/2,j,k}}\left(\Delta S_{g_{i,j,k}}-\Delta S_{g_{i-1,j,k}}\right)^{n+1}+$$
$$T_{w\theta^+}{}^n p'_{cwo_{i,j+1/2,k}}\left(S_{g_{i,j+1,k}}-S_{g_{i,j,k}}\right)^{n}-T_{w\theta^-}{}^n p'_{cwo_{i,j-1/2,k}}\left(S_{g_{i,j,k}}-S_{g_{i,j-1,k}}\right)^{n}+$$
$$T_{w\theta^+}{}^n p'_{cwo_{i,j+1/2,k}}\left(\Delta S_{g_{i,j+1,k}}-\Delta S_{g_{i,j,k}}\right)^{n+1}-T_{w\theta^-}{}^n p'_{cwo_{i,j-1/2,k}}\left(\Delta S_{g_{i,j,k}}-\Delta S_{g_{i,j-1,k}}\right)^{n+1}+$$
$$T_{wz^+}{}^n p'_{cwo_{i,j,k+1/2}}\left(S_{g_{i,j,k+1}}-S_{g_{i,j,k}}\right)^{n}-T_{wz^-}{}^n p'_{cwo_{i,j,k-1/2}}\left(S_{g_{i,j,k}}-S_{g_{i,j,k-1}}\right)^{n}+$$
$$T_{wz^+}{}^n p'_{cwo_{i,j,k+1/2}}\left(\Delta S_{g_{i,j,k+1}}-\Delta S_{g_{i,j,k}}\right)^{n+1}-T_{wz^-}{}^n p'_{cwo_{i,j,k-1/2}}\left(\Delta S_{g_{i,j,k}}-\Delta S_{g_{i,j,k-1}}\right)^{n+1}=F_w+$$
$$G_w\frac{\Delta S_{o_{i,j,k}}{}^{n+1}}{\Delta t}+H_w\frac{\Delta S_{g_{i,j,k}}{}^{n+1}}{\Delta t}+I_w\frac{\Delta p_{o_{i,j,k}}{}^{n+1}}{\Delta t}+J_w\frac{\left(\alpha_{i,j,k}\Delta\epsilon^e_{v\,i,j,k}{}^{n+1}+\Delta\epsilon^p_{v\,i,j,k}{}^{n+1}\right)}{\Delta t}+q_{w_{SC}}$$

Regrouping and redefining some variables,

$$E_w\Delta p_{o_{i+1,j,k}}{}^{n+1}+\left(C_w-\frac{I_w}{\Delta t}\right)\Delta p_{o_{i,j,k}}{}^{n+1}+W_w\Delta p_{o_{i-1,j,k}}{}^{n+1}+N_w\Delta p_{o_{i,j+1,k}}{}^{n+1}+S_w\Delta p_{o_{i,j-1,k}}{}^{n+1}+$$
$$U_w\Delta p_{o_{i,j,k+1}}{}^{n+1}+D_w\Delta p_{o_{i,j,k-1}}{}^{n+1}+E^*_w\Delta S_{o_{i+1,j,k}}{}^{n+1}+\left(C^*_w-\frac{G_w}{\Delta t}\right)\Delta S_{o_{i,j,k}}{}^{n+1}+W^*_w\Delta S_{o_{i-1,j,k}}{}^{n+1}+$$
$$N^*_w\Delta S_{o_{i,j+1,k}}{}^{n+1}+S^*_w\Delta S_{o_{i,j-1,k}}{}^{n+1}+D^*_w\Delta S_{o_{i,j,k+1}}{}^{n+1}+U^*_w\Delta S_{o_{i,j,k-1}}{}^{n+1}+E^*_w\Delta S_{g_{i+1,j,k}}{}^{n+1}+\left(C^*_w-\right.$$
$$\left.\frac{H_w}{\Delta t}\right)\Delta S_{g_{i,j,k}}{}^{n+1}+W^*_w\Delta S_{g_{i-1,j,k}}{}^{n+1}+N^*_w\Delta S_{g_{i,j+1,k}}{}^{n+1}+S^*_w\Delta S_{g_{i,j-1,k}}{}^{n+1}+U^*_w\Delta S_{g_{i,j,k+1}}{}^{n+1}+$$
$$D^*_w\Delta S_{g_{i,j,k-1}}{}^{n+1}=-E_w\left(p_{o_{i+1,j,k}}{}^n-\gamma_w z_{i+1,j,k}\right)-C_w\left(p_{o_{i,j,k}}{}^n-\gamma_w z_{i,j,k}\right)-W_w\left(p_{o_{i-1,j,k}}{}^n-\right.$$
$$\left.\gamma_w z_{i-1,j,k}\right)-N_w\left(p_{o_{i,j+1,k}}{}^n-\gamma_w z_{i,j+1,k}\right)-S_w\left(p_{o_{i,j-1,k}}{}^n-\gamma_w z_{i,j-1,k}\right)-U_w\left(p_{o_{i,j,k+1}}{}^n-\gamma_w z_{i,j,k+1}\right)-$$
$$D_w\left(p_{o_{i,j,k-1}}-\gamma_w z_{i,j,k-1}\right)^n-E^*_w S_{o_{i+1,j,k}}{}^n-C^*_w S_{o_{i,j,k}}{}^n-W^*_w S_{o_{i-1,j,k}}{}^n-N^*_w S_{o_{i,j+1,k}}{}^n-S^*_w S_{o_{i,j-1,k}}{}^n-$$
$$U^*_w S_{o_{i,j,k+1}}{}^n-D^*_w S_{o_{i,j,k-1}}{}^n-E^*_w S_{g_{i+1,j,k}}{}^n-C^*_w S_{g_{i,j,k}}{}^n-W^*_w S_{g_{i-1,j,k}}{}^n-N^*_w S_{g_{i,j+1,k}}{}^n-S^*_w S_{g_{i,j-1,k}}{}^n-$$
$$^*_w S_{g_{i,j,k+1}}{}^n-D^*_w S_{g_{i,j,k-1}}{}^n+\frac{J_w}{\Delta t}\left(\alpha_{i,j,k}\Delta\epsilon^e_{v\,i,j,k}{}^{n+1}+\Delta\epsilon^p_{v\,i,j,k}{}^{n+1}\right)+F_w+q_{w_{SC}}\qquad(\text{A}-128)$$

$$\gamma_w=\rho_{w_{SC}}\gamma_c g$$

$$E_w=T_{wr^+}{}^n$$

$$E^*_w=T_{wr^+}{}^n p'_{cwo_{i+1/2,j,k}}$$

$$C_w=-(T_{wr^+}{}^n+T_{wr^-}{}^n+T_{w\theta^+}{}^n+T_{w\theta^-}{}^n+T_{wz^+}{}^n+T_{wz^-}{}^n)$$

$$C^*_w=-\left(T_{wr^+}{}^n p'_{cwo_{i+1/2,j,k}}+T_{wr^-}{}^n p'_{cwo_{i-1/2,j,k}}+T_{w\theta^+}{}^n p'_{cwo_{i,j+1/2,k}}+T_{w\theta^-}{}^n p'_{cwo_{i,j-1/2,k}}+\right.$$
$$\left.T_{wz^+}{}^n p'_{cwo_{i,j,k+1/2}}+T_{wz^-}{}^n p'_{cwo_{i,j,k-1/2}}\right)$$

$$W_w = T_{wr^-}{}^n$$

$$W_w^* = T_{wr^-}{}^n p'_{cwo_{i-1/2,j,k}}$$

$$N_w = T_{w\theta^+}{}^n$$

$$N_w^* = T_{w\theta^+}{}^n p'_{cwo_{i,j+1/2,k}}$$

$$S_w = T_{w\theta^-}{}^n$$

$$S_w^* = T_{w\theta^-}{}^n p'_{cwo_{i,j-1/2,k}}$$

$$U_w = T_{wz^+}{}^n$$

$$U_w^* = T_{wz^+}{}^n p'_{cwo_{i,j,k+1/2}}$$

$$D_w = T_{wz^-}{}^n$$

$$D_w^* = T_{wz^-}{}^n p'_{cwo_{i,j,k-1/2}}$$

$$F_{w_{i,j,k}} = \frac{V_{b_{i,j,k}} q_{s_{i,j,k}} \phi_{i,j,k}}{(1-\phi_{i,j,k})}$$

$$G_{w_{i,j,k}} = \frac{V_{b_{i,j,k}} \phi_{i,j,k}}{\alpha_c B_{w_{i,j,k}}} \left\{ \left(1 - S_{o_{i,j,k}} - S_{g_{i,j,k}}\right) \left[c_{pc_{i,j,k}} \left(1 - \alpha_{i,j,k}\right) - c_{s_{i,j,k}} + c_{w_{i,j,k}} \right] p'_{cwo_{i,j,k}} - 1 \right\}$$

$$H_{w_{i,j,k}} = \frac{V_{b_{i,j,k}} \phi_{i,j,k}}{\alpha_c B_{w_{i,j,k}}} \left\{ \left(1 - S_{o_{i,j,k}} - S_{g_{i,j,k}}\right) \left[c_{pc_{i,j,k}} \left(1 - \alpha_{i,j,k}\right) - c_{s_{i,j,k}} + c_{w_{i,j,k}} \right] p'_{cwo_{i,j,k}} - 1 \right\}$$

$$I_{w_{i,j,k}} = \frac{V_{b_{i,j,k}} \phi_{i,j,k}}{\alpha_c B_{w_{i,j,k}}} \left(1 - S_{o_{i,j,k}} - S_{g_{i,j,k}}\right) \left[c_{pc_{i,j,k}} \left(1 - \alpha_{i,j,k}\right) - c_{s_{i,j,k}} + c_{w_{i,j,k}} \right]$$

$$J_{w_{i,j,k}} = -\frac{V_{b_{i,j,k}}}{\alpha_c B_{w_{i,j,k}}} \left(1 - S_{o_{i,j,k}} - S_{g_{i,j,k}}\right)$$

A2.2.3. Gas-phase

Equation (A – 103) is the governing equation for the gas phase:

$$\nabla \cdot \left[\beta_c \frac{\boldsymbol{k}_g}{B_g \mu_g} \left(\nabla p_o - \rho_{g_{SC}} \gamma_c g \nabla z \right) + \beta_c R_{so} \frac{\boldsymbol{k}_o}{B_o \mu_o} \left(\nabla p_o - \rho_{o_{SC}} \gamma_c g \nabla z \right) + \beta_c R_{sw} \frac{\boldsymbol{k}_w}{B_w \mu_w} \left(\nabla p_o - \rho_{w_{SC}} \gamma_c g \nabla z \right) \right] + \nabla \cdot \left[\left(\beta_c \frac{\boldsymbol{k}_g}{B_g \mu_g} p'_{cgo} + R_{sw} \beta_c \frac{\boldsymbol{k}_w}{B_w \mu_w} p'_{cwo} \right) \nabla S_g \right] + \nabla \cdot \left(R_{sw} \beta_c \frac{\boldsymbol{k}_w}{B_w \mu_w} p'_{cwo} \nabla S_o \right) = F_g + G_g \frac{\partial S_o}{\partial t} + H_g \frac{\partial S_g}{\partial t} + I_g \frac{\partial p_o}{\partial t} + J_g \left[\alpha \frac{\partial \epsilon_v^e}{\partial t} + \frac{\partial \epsilon_v^p}{\partial t} \right] + q_{g_{SC}} \quad \text{(A – 103)}$$

The first term of the left-hand side of the Equation (A – 103) can be expanded as:

$$\nabla \cdot \left[\beta_c \frac{\boldsymbol{k}_g}{B_g \mu_g}\left(\nabla p_o - \rho_{g_{SC}} \gamma_c g \nabla z\right) + \beta_c R_{so} \frac{\boldsymbol{k}_o}{B_o \mu_o}\left(\nabla p_o - \rho_{o_{SC}} \gamma_c g \nabla z\right) + \beta_c R_{sw} \frac{\boldsymbol{k}_w}{B_w \mu_w}\left(\nabla p_o - \rho_{w_{SC}} \gamma_c g \nabla z\right)\right] = \nabla \cdot \left(\beta_c \frac{\boldsymbol{k}_g}{B_g \mu_g}\left(\nabla p_o - \rho_{g_{SC}} \gamma_c g \nabla z\right)\right) + \nabla \cdot \left(\beta_c R_{so} \frac{\boldsymbol{k}_o}{B_o \mu_o}\left(\nabla p_o - \rho_{o_{SC}} \gamma_c g \nabla z\right)\right) + \nabla \cdot \left(\beta_c R_{sw} \frac{\boldsymbol{k}_w}{B_w \mu_w}\left(\nabla p_o - \rho_{w_{SC}} \gamma_c g \nabla z\right)\right) \quad \text{(A – 129)}$$

Similar to the oil and water phases, the first term of the right-hand side of Equation (A – 129) can be expanded as:

$$\nabla \cdot \left(\beta_c V_b \frac{\boldsymbol{k}_g}{B_g \mu_g}\left(\nabla p_o - \rho_{g_{SC}} \gamma_c g \nabla z\right)\right) = T_{gr^+}\left(p_{o_{i+1,j,k}} - p_{o_{i,j,k}}\right)^n - T_{gr^-}\left(p_{o_{i,j,k}} - p_{o_{i-1,j,k}}\right)^n + T_{gr^+}\left(\Delta p_{o_{i+1,j,k}} - \Delta p_{o_{i,j,k}}\right)^{n+1} - T_{gr^-}\left(\Delta p_{o_{i,j,k}} - \Delta p_{o_{i-1,j,k}}\right)^{n+1} - T_{gr^+}{}^n \rho_{g_{SC}} \gamma_c g\left(z_{i+1,j,k} - z_{i,j,k}\right) + T_{gr^-}{}^n \rho_{g_{SC}} \gamma_c g\left(z_{i,j,k} - z_{i-1,j,k}\right) + T_{g\theta^+}\left(p_{o_{i,j+1,k}} - p_{o_{i,j,k}}\right)^n - T_{g\theta^-}\left(p_{o_{i,j,k}} - p_{o_{i,j-1,k}}\right)^n + T_{g\theta^+}\left(\Delta p_{o_{i,j+1,k}} - \Delta p_{o_{i,j,k}}\right)^{n+1} - T_{g\theta^-}\left(\Delta p_{o_{i,j,k}} - \Delta p_{o_{i,j-1,k}}\right)^{n+1} - T_{g\theta^+}{}^n \rho_{g_{SC}} \gamma_c g\left(z_{i,j+1,k} - z_{i,j,k}\right) + T_{g\theta^-}{}^n \rho_{g_{SC}} \gamma_c g\left(z_{i,j,k} - z_{i,j-1,k}\right) + T_{gz^+}\left(p_{o_{i,j,k+1}} - p_{o_{i,j,k}}\right)^n - T_{gz^-}\left(p_{o_{i,j,k}} - p_{o_{i,j,k-1}}\right)^n + T_{gz^+}\left(\Delta p_{o_{i,j,k+1}} - \Delta p_{o_{i,j,k}}\right)^{n+1} - T_{gz^-}\left(\Delta p_{o_{i,j,k}} - \Delta p_{o_{i,j,k-1}}\right)^{n+1} - T_{gz^+}{}^n \rho_{g_{SC}} \gamma_c g\left(z_{i,j,k+1} - z_{i,j,k}\right) + T_{gz^-}{}^n \rho_{g_{SC}} \gamma_c g\left(z_{i,j,k} - z_{i,j,k-1}\right) \quad \text{(A – 130)}$$

In Equation (A – 130) the gas transmissibility relations are expressed as:

$$T_{gr^+} = \frac{\beta_c \Delta\theta_{i,j,k} \Delta z_{i,j,k}\left(r^2_{i+1/2,j,k} - r^2_{i-1/2,j,k}\right)}{2 r_{i,j,k} \Delta r_{i,j,k} \ln\left(r_{i+1,j,k}/r_{i,j,k}\right)} \frac{k_g}{B_g \mu_g}\Big|_{i+1/2,j,k}$$

$$T_{gr^-} = \frac{\beta_c \Delta\theta_{i,j,k} \Delta z_{i,j,k}\left(r^2_{i+1/2,j,k} - r^2_{i-1/2,j,k}\right)}{2 r_{i,j,k} \Delta r_{i,j,k} \ln\left(r_{i,j,k}/r_{i-1,j,k}\right)} \frac{k_{gr}}{B_g \mu_g}\Big|_{i-1/2,j,k}$$

$$T_{g\theta^+} = \frac{\beta_c \Delta z_{i,j,k}\left(r^2_{i+1/2,j,k} - r^2_{i-1/2,j,k}\right)}{r^2_{i,j,k}\left(\Delta\theta_{i,j,k} + \Delta\theta_{i,j+1,k}\right)} \frac{k_{g\theta}}{B_g \mu_g}\Big|_{i,j+1/2,k}$$

$$T_{g\theta^-} = \frac{\beta_c \Delta z_{i,j,k}\left(r^2_{i+1/2,j,k} - r^2_{i-1/2,j,k}\right)}{r^2_{i,j,k}\left(\Delta\theta_{i,j-1,k} + \Delta\theta_{i,j,k}\right)} \frac{k_{g\theta}}{B_g \mu_g}\Big|_{i,j-1/2,k}$$

$$T_{gz^+} = \frac{\beta_c \Delta\theta_{i,j,k}\left(r^2_{i+1/2,j,k} - r^2_{i-1/2,j,k}\right)}{\left(\Delta z_{i,j,k} + \Delta z_{i,j,k+1}\right)} \frac{k_{gz}}{B_g \mu_g}\Big|_{i,j,k+1/2}$$

$$T_{gz^-} = \frac{\beta_c \Delta\theta_{i,j,k}\left(r^2_{i+1/2,j,k} - r^2_{i-1/2,j,k}\right)}{\left(\Delta z_{i,j,k-1} + \Delta z_{i,j,k}\right)} \frac{k_{gz}}{B_g \mu_g}\Big|_{i,j,k-1/2}$$

The second term of the right-hand side of Equation (A – 129) can be expanded as:

$$\begin{aligned}
&\nabla \cdot \left(\beta_c V_b R_{so} \frac{\boldsymbol{k}_o}{B_o \mu_o}\left(\nabla p_o - \rho_{o_{SC}} \gamma_c g \nabla z\right)\right) = T_{or^+}{}^n R_{so_{i+1/2,j,k}} \left(p_{o_{i+1,j,k}} - p_{o_{i,j,k}}\right)^n - \\
&T_{or^-}{}^n R_{so_{i-1/2,j,k}} \left(p_{o_{i,j,k}} - p_{o_{i-1,j,k}}\right)^n + T_{or^+}{}^n R_{so_{i+1/2,j,k}} \left(\Delta p_{o_{i+1,j,k}} - \Delta p_{o_{i,j,k}}\right)^{n+1} - \\
&T_{or^-}{}^n R_{so_{i-1/2,j,k}} \left(\Delta p_{o_{i,j,k}} - \Delta p_{o_{i-1,j,k}}\right)^{n+1} - T_{or^+}{}^n R_{so_{i+1/2,j,k}} \rho_{o_{SC}} \gamma_c g \left(z_{i+1,j,k} - z_{i,j,k}\right) + \\
&T_{or^-}{}^n R_{so_{i-1/2,j,k}} \rho_{o_{SC}} \gamma_c g \left(z_{i,j,k} - z_{i-1,j,k}\right) + T_{o\theta^+}{}^n R_{so_{i,j+1/2,k}} \left(p_{o_{i,j+1,k}} - p_{o_{i,j,k}}\right)^n - \\
&T_{o\theta^-}{}^n R_{so_{i,j-1/2,k}} \left(p_{o_{i,j,k}} - p_{o_{i,j-1,k}}\right)^n + T_{o\theta^+}{}^n R_{so_{i,j+1/2,k}} \left(\Delta p_{o_{i,j+1,k}} - \Delta p_{o_{i,j,k}}\right)^{n+1} - \\
&T_{o\theta^-}{}^n R_{so_{i,j-1/2,k}} \left(\Delta p_{o_{i,j,k}} - \Delta p_{o_{i,j-1,k}}\right)^{n+1} - T_{o\theta^+}{}^n R_{so_{i,j+1/2,k}} \rho_{o_{SC}} \gamma_c g \left(z_{i,j+1,k} - z_{i,j,k}\right) + \\
&T_{o\theta^-}{}^n R_{so_{i,j-1/2,k}} \rho_{o_{SC}} \gamma_c g \left(z_{i,j,k} - z_{i,j-1,k}\right) + T_{oz^+}{}^n R_{so_{i,j,k+1/2}} \left(p_{o_{i,j,k+1}} - p_{o_{i,j,k}}\right)^n - \\
&T_{oz^-}{}^n R_{so_{i,j,k-1/2}} \left(p_{o_{i,j,k}} - p_{o_{i,j,k-1}}\right)^n + T_{oz^+}{}^n R_{so_{i,j,k+1/2}} \left(\Delta p_{o_{i,j,k+1}} - \Delta p_{o_{i,j,k}}\right)^{n+1} - \\
&T_{oz^-}{}^n R_{so_{i,j,k-1/2}} \left(\Delta p_{o_{i,j,k}} - \Delta p_{o_{i,j,k-1}}\right)^{n+1} - T_{oz^+}{}^n R_{so_{i,j,k+1/2}} \rho_{o_{SC}} \gamma_c g \left(z_{i,j,k+1} - z_{i,j,k}\right) + \\
&T_{oz^-}{}^n R_{so_{i,j,k-1/2}} \rho_{o_{SC}} \gamma_c g \left(z_{i,j,k} - z_{i,j,k-1}\right)
\end{aligned} \qquad \text{(A – 131)}$$

The third term of the right-hand side of Equation (A – 129) can be expanded

$$\begin{aligned}
&\nabla \cdot \left(\beta_c V_b R_{sw} \frac{\boldsymbol{k}_w}{B_w \mu_w}\left(\nabla p_o - \rho_{w_{SC}} \gamma_c g \nabla z\right)\right) = T_{wr^+}{}^n R_{sw_{i+1/2,j,k}} \left(p_{o_{i+1,j,k}} - p_{o_{i,j,k}}\right)^n - \\
&T_{wr^-}{}^n R_{sw_{i-1/2,j,k}} \left(p_{o_{i,j,k}} - p_{o_{i-1,j,k}}\right)^n + T_{wr^+}{}^n R_{sw_{i+1/2,j,k}} \left(\Delta p_{o_{i+1,j,k}} - \Delta p_{o_{i,j,k}}\right)^{n+1} - \\
&T_{wr^-}{}^n R_{sw_{i-1/2,j,k}} \left(\Delta p_{o_{i,j,k}} - \Delta p_{o_{i-1,j,k}}\right)^{n+1} - T_{wr^+}{}^n R_{sw_{i+1/2,j,k}} \rho_{w_{SC}} \gamma_c g \left(z_{i+1,j,k} - z_{i,j,k}\right) + \\
&T_{wr^-}{}^n R_{sw_{i-1/2,j,k}} \rho_{w_{SC}} \gamma_c g \left(z_{i,j,k} - z_{i-1,j,k}\right) + T_{w\theta^+}{}^n R_{sw_{i,j+1/2,k}} \left(p_{o_{i,j+1,k}} - p_{o_{i,j,k}}\right)^n - \\
&T_{w\theta^-}{}^n R_{sw_{i,j-1/2,k}} \left(p_{o_{i,j,k}} - p_{o_{i,j-1,k}}\right)^n + T_{w\theta^+}{}^n R_{sw_{i,j+1/2,k}} \left(\Delta p_{o_{i,j+1,k}} - \Delta p_{o_{i,j,k}}\right)^{n+1} - \\
&T_{w\theta^-}{}^n R_{sw_{i,j-1/2,k}} \left(\Delta p_{o_{i,j,k}} - \Delta p_{o_{i,j-1,k}}\right)^{n+1} - T_{w\theta^+}{}^n R_{sw_{i,j+1/2,k}} \rho_{w_{SC}} \gamma_c g \left(z_{i,j+1,k} - z_{i,j,k}\right) + \\
&T_{w\theta^-}{}^n R_{sw_{i,j-1/2,k}} \rho_{\ \ SC} \gamma_c g \left(z_{i,j,k} - z_{i,j-1,k}\right) + T_{wz^+}{}^n R_{sw_{i,j,k+1/2}} \left(p_{o_{i,j,k+1}} - p_{o_{i,j,k}}\right)^n - \\
&T_{wz^-}{}^n R_{sw_{i,j,k-1/2}} \left(p_{o_{i,j,k}} - p_{o_{i,j,k-1}}\right)^n + T_{wz^+}{}^n R_{sw_{i,j,k+1/2}} \left(\Delta p_{o_{i,j,k+1}} - \Delta p_{o_{i,j,k}}\right)^{n+1} - \\
&T_{wz^-}{}^n R_{sw_{i,j,k-1/2}} \left(\Delta p_{o_{i,j,k}} - \Delta p_{o_{i,j,k-1}}\right)^{n+1} - T_{wz^+}{}^n R_{sw_{i,j,k+1/2}} \rho_{w_{SC}} \gamma_c g \left(z_{i,j,k+1} - z_{i,j,k}\right) + \\
&T_{wz^-}{}^n R_{sw_{i,j,k-1/2}} \rho_{w_{SC}} \gamma_c g \left(z_{i,j,k} - z_{i,j,k-1}\right)
\end{aligned} \qquad \text{(A – 132)}$$

Similarly, the second term of the left-hand side of the Equation (A – 103) can be expanded as:

$$\nabla \cdot \left[\left(\beta_c V_b \frac{\boldsymbol{k}_g}{B_g \mu_g} p'_{cgo} + \beta_c R_{sw} V_b \frac{\boldsymbol{k}_w}{B_w \mu_w} p'_{cwo}\right) \nabla S_g\right] = \nabla \cdot \left(\beta_c V_b \frac{\boldsymbol{k}_g}{B_g \mu_g} p'_{cgo} \nabla S_g\right) + \nabla \cdot \left(\beta_c R_{sw} V_b \frac{\boldsymbol{k}_w}{B_w \mu_w} p'_{cwo} \nabla S_g\right) \quad \text{(A – 133)}$$

So, the first term of the right-hand side of the Equation (A – 133) can be expanded as:

$$\nabla \cdot \left(\beta_c V_b \frac{\boldsymbol{k}_g}{B_g \mu_g} p'_{cgo} \nabla S_g\right) = T_{gr^+}{}^n p'_{cgo_{i+1/2,j,k}} \left(S_{g_{i+1,j,k}} - S_{g_{i,j,k}}\right)^n - T_{gr^-}{}^n p'_{cgo_{i-1/2,j,k}} \left(S_{g_{i,j,k}} - S_{g_{i-1,j,k}}\right)^n + T_{gr^+}{}^n p'_{cgo_{i+1/2,j,k}} \left(\Delta S_{g_{i+1,j,k}} - \Delta S_{g_{i,j,k}}\right)^{n+1} - T_{gr^-}{}^n p'_{cgo_{i-1/2,j,k}} \left(\Delta S_{g_{i,j,k}} - \Delta S_{g_{i-1,j,k}}\right)^{n+1} + T_{g\theta^+}{}^n p'_{cgo_{i,j+1/2,k}} \left(S_{g_{i,j+1,k}} - S_{g_{i,j,k}}\right)^n - T_{g\theta^-}{}^n p'_{cgo_{i,j-1/2,k}} \left(S_{g_{i,j,k}} - S_{g_{i,j-1,k}}\right)^n + T_{g\theta^+}{}^n p'_{cgo_{i,j+1/2,k}} \left(\Delta S_{g_{i,j+1,k}} - \Delta S_{g_{i,j,k}}\right)^{n+1} - T_{g\theta^-}{}^n p'_{cgo_{i,j-1/2,k}} \left(\Delta S_{g_{i,j,k}} - \Delta S_{g_{i,j-1,k}}\right)^{n+1} + T_{gz^+}{}^n p'_{cgo_{i,j,k+1/2}} \left(S_{g_{i,j,k+1}} - S_{g_{i,j,k}}\right)^n - T_{gz^-}{}^n p'_{cgo_{i,j,k-1/2}} \left(S_{g_{i,j,k}} - S_{g_{i,j,k-1}}\right)^n + T_{gz^+}{}^n p'_{cgo_{i,j,k+1/2}} \left(\Delta S_{g_{i,j,k+1}} - \Delta S_{g_{i,j,k}}\right)^{n+1} - T_{gz^-}{}^n p'_{cgo_{i,j,k-1/2}} \left(\Delta S_{g_{i,j,k}} - \Delta S_{g_{i,j,k-1}}\right)^{n+1} \quad \text{(A – 134)}$$

And the second term of the right-hand side of the Equation (A – 133) can be expanded as:

$$\nabla \cdot \left(\beta_c R_{sw} V_b \frac{\boldsymbol{k}_w}{B_w \mu_w} p'_{cwo} \nabla S_g\right) = T_{wr^+}{}^n p'_{cwo_{i+1/2,j,k}} R_{sw_{i+1/2,j,k}} \left(S_{g_{i+1,j,k}} - S_{g_{i,j,k}}\right)^n - T_{wr^-}{}^n p'_{cwo_{i-1/2,j,k}} R_{sw_{i-1/2,j,k}} \left(S_{g_{i,j,k}} - S_{g_{i-1,j,k}}\right)^n + T_{wr^+}{}^n p'_{cwo_{i+1/2,j,k}} R_{sw_{i+1/2,j,k}} \left(\Delta S_{g_{i+1,j,k}} - \Delta S_{g_{i,j,k}}\right)^{n+1} - T_{wr^-}{}^n p'_{cwo_{i-1/2,j,k}} R_{sw_{i-1/2,j,k}} \left(\Delta S_{g_{i,j,k}} - \Delta S_{g_{i-1,j,k}}\right)^{n+1} + T_{w\theta^+}{}^n p'_{cwo_{i,j+1/2,k}} R_{sw_{i,j+1/2,k}} \left(S_{g_{i,j+1,k}} - S_{g_{i,j,k}}\right)^n - T_{w\theta^-}{}^n p'_{cwo_{i,j-1/2,k}} R_{sw_{i,j-1/2,k}} \left(S_{g_{i,j,k}} - S_{g_{i,j-1,k}}\right)^n + T_{w\theta^+}{}^n p'_{cwo_{i,j+1/2,k}} R_{sw_{i,j+1/2,k}} \left(\Delta S_{g_{i,j+1,k}} - \Delta S_{g_{i,j,k}}\right)^{n+1} - T_{w\theta^-}{}^n p'_{cwo_{i,j-1/2,k}} R_{sw_{i,j-1/2,k}} \left(\Delta S_{g_{i,j,k}} - \Delta S_{g_{i,j-1,k}}\right)^{n+1} + T_{wz^+}{}^n p'_{cwo_{i,j,k+1/2}} R_{sw_{i,j,k+1/2}} \left(S_{g_{i,j,k+1}} - S_{g_{i,j,k}}\right)^n - T_{wz^-}{}^n p'_{cwo_{i,j,k-1/2}} R_{sw_{i,j,k-1/2}} \left(S_{g_{i,j,k}} - S_{g_{i,j,k-1}}\right)^n + T_{wz^+}{}^n p'_{cwo_{i,j,k+1/2}} R_{sw_{i,j,k+1/2}} \left(\Delta S_{g_{i,j,k+1}} - \Delta S_{g_{i,j,k}}\right)^{n+1} - T_{wz^-}{}^n p'_{cwo_{i,j,k-1/2}} R_{sw_{i,j,k-1/2}} \left(\Delta S_{g_{i,j,k}} - \Delta S_{g_{i,j,k-1}}\right)^{n+1} \quad \text{(A – 135)}$$

Similarly, the third term of the left-hand side of the Equation (A – 103) can be expanded as:

$$\nabla \cdot \left(\beta_c R_{sw} V_b \frac{\boldsymbol{k}_w}{B_w \mu_w} p'_{cwo} \nabla S_o\right) = T_{wr^+}{}^n p'_{cwo_{i+1/2,j,k}} R_{sw_{i+1/2,j,k}} \left(S_{o_{i+1,j,k}} - S_{o_{i,j,k}}\right)^n - T_{wr^-}{}^n p'_{cwo_{i-1/2,j,k}} R_{sw_{i-1/2,j,k}} \left(S_{o_{i,j,k}} - S_{o_{i-1,j,k}}\right)^n + T_{wr^+}{}^n p'_{cwo_{i+1/2,j,k}} R_{sw_{i+1/2,j,k}} \left(\Delta S_{o_{i+1,j,k}} - \Delta S_{o_{i,j,k}}\right)^{n+1} - T_{wr^-}{}^n p'_{cwo_{i-1/2,j,k}} R_{sw_{i-1/2,j,k}} \left(\Delta S_{o_{i,j,k}} - \Delta S_{o_{i-1,j,k}}\right)^{n+1} + T_{w\theta^+}{}^n p'_{cwo_{i,j+1/2,k}} R_{sw_{i,j+1/2,k}} \left(S_{o_{i,j+1,k}} - S_{o_{i,j,k}}\right)^n - T_{w\theta^-}{}^n p'_{cwo_{i,j-1/2,k}} R_{sw_{i,j-1/2,k}} \left(S_{o_{i,j,k}} - S_{o_{i,j-1,k}}\right)^n + T_{w\theta^+}{}^n p'_{cwo_{i,j+1/2,k}} R_{sw_{i,j+1/2,k}} \left(\Delta S_{o_{i,j+1,k}} - \Delta S_{o_{i,j,k}}\right)^{n+1} - T_{w\theta^-}{}^n p'_{cwo_{i,j-1/2,k}} R_{sw_{i,j-1/2,k}} \left(\Delta S_{o_{i,j,k}} -$$

$$\Delta S_{o_{i,j-1,k}}\Big)^{n+1} + T_{wz^+}{}^n p'_{cwo_{i,j,k+1/2}} R_{sw_{i,j,k+1/2}} \left(S_{o_{i,j,k+1}} - S_{o_{i,j,k}}\right)^n - T_{wz^-}{}^n p'_{cwo_{i,j,k-1/2}} R_{sw_{i,j,k-1/2}} \left(S_{o_{i,j,k}} - S_{o_{i,j,k-1}}\right)^n + T_{wz^+}{}^n p'_{cwo_{i,j,k+1/2}} R_{sw_{i,j,k+1/2}} \left(\Delta S_{o_{i,j,k+1}} - \Delta S_{o_{i,j,k}}\right)^{n+1} - T_{wz^-}{}^n p'_{cwo_{i,j,k-1/2}} R_{sw_{i,j,k-1/2}} \left(\Delta S_{o_{i,j,k}} - \Delta S_{o_{i,j,k-1}}\right)^{n+1} \quad (A-136)$$

Replacing Equations (A – 129) to (A – 133) into Equation (A – 103),

$$\left(T_{gr^+}{}^n + T_{or^+}{}^n R_{so_{i+1/2,j,k}} + T_{wr^+}{}^n R_{sw_{i+1/2,j,k}}\right) \Delta p_{o_{i+1,j,k}}{}^{n+1} - \left(T_{gr^+}{}^n + T_{gr^-}{}^n + T_{g\theta^+}{}^n + T_{g\theta^-}{}^n + T_{gz^+}{}^n + T_{gz^-}{}^n + T_{or^+}{}^n R_{so_{i+1/2,j,k}} + T_{or^-}{}^n R_{so_{i-1/2,j,k}} + T_{o\theta^+}{}^n R_{so_{i,j+1/2,k}} + T_{o\theta^-}{}^n R_{so_{i,j-1/2,k}} + T_{oz^+}{}^n R_{so_{i,j,k+1/2}} + T_{oz^-}{}^n R_{so_{i,j,k-1/2}} + T_{wr^+}{}^n R_{sw_{i+1/2,j,k}} + T_{wr^-}{}^n R_{sw_{i-1/2,j,k}} + T_{w\theta^+}{}^n R_{sw_{i,j+1/2,k}} + T_{w\theta^-}{}^n R_{sw_{i,j-1/2,k}} + T_{wz^+}{}^n R_{sw_{i,j,k+1/2}} + T_{wz^-}{}^n R_{sw_{i,j,k-1/2}} + \frac{I_g}{\Delta t}\right) \Delta p_{o_{i,j,k}}{}^{n+1} + \left(T_{gr^-}{}^n + T_{or^-}{}^n R_{so_{i-1/2,j,k}} + T_{wr^-}{}^n R_{sw_{i-1/2,j,k}}\right) \Delta p_{o_{i-1,j,k}}{}^{n+1} + \left(T_{g\theta^+}{}^n + T_{o\theta^+}{}^n R_{so_{i,j+1/2,k}} + T_{w\theta^+}{}^n R_{sw_{i,j+1/2,k}}\right) \Delta p_{o_{i,j+1,k}}{}^{n+1} + \left(T_{g\theta^-}{}^n + T_{o\theta^-}{}^n R_{so_{i,j-1/2,k}} + T_{w\theta^-}{}^n R_{sw_{i,j-1/2,k}}\right) \Delta p_{o_{i,j-1,k}}{}^{n+1} + \left(T_{gz^+}{}^n + T_{oz^+}{}^n R_{so_{i,j,k+1/2}} + T_{wz^+}{}^n R_{sw_{i,j,k+1/2}}\right) \Delta p_{o_{i,j,k+1}}{}^{n+1} + \left(T_{gz^-}{}^n + T_{oz^-}{}^n R_{so_{i,j,k-1/2}} + T_{wz^-}{}^n R_{sw_{i,j,k-1/2}}\right) \Delta p_{o_{i,j,k-1}}{}^{n+1} + T_{wr^+}{}^n p'_{cwo_{i+1/2,j,k}} R_{sw_{i+1/2,j,k}} \Delta S_{o_{i+1,j,k}}{}^{n+1} - \left(T_{wr^+}{}^n p'_{cwo_{i+1/2,j,k}} R_{sw_{i+1/2,j,k}} + T_{wr^-}{}^n p'_{cwo_{i-1/2,j,k}} R_{sw_{i-1/2,j,k}} + T_{w\theta^+}{}^n p'_{cwo_{i,j+1/2,k}} R_{sw_{i,j+1/2,k}} + T_{w\theta^-}{}^n p'_{cwo_{i,j-1/2,k}} R_{sw_{i,j-1/2,k}} + T_{wz^+}{}^n p'_{cwo_{i,j,k+1/2}} R_{sw_{i,j,k+1/2}} + T_{wz^-}{}^n p'_{cwo_{i,j,k-1/2}} R_{sw_{i,j,k-1/2}} + \frac{G_g}{\Delta t}\right) \Delta S_{o_{i,j,k}}{}^{n+1} + T_{wr^-}{}^n p'_{cwo_{i-1/2,j,k}} R_{sw_{i-1/2,j,k}} \Delta S_{o_{i-1,j,k}}{}^{n+1} + T_{w\theta^+}{}^n p'_{cwo_{i,j+1/2,k}} R_{sw_{i,j+1/2,k}} \Delta S_{o_{i,j+1,k}}{}^{n+1} + T_{w\theta^-}{}^n p'_{cwo_{i,j-1/2,k}} R_{sw_{i,j-1/2,k}} \Delta S_{o_{i,j-1,k}}{}^{n+1} + T_{wz^+}{}^n p'_{cwo_{i,j,k+1/2}} R_{sw_{i,j,k+1/2}} \Delta S_{o_{i,j,k+1}}{}^{n+1} + T_{wz^-}{}^n p'_{cwo_{i,j,k-1/2}} R_{sw_{i,j,k-1/2}} \Delta S_{o_{i,j,k-1}}{}^{n+1} + \left(T_{gr^+}{}^n p'_{cgo_{i+1/2,j,k}} + T_{wr^+}{}^n p'_{cwo_{i+1/2,j,k}} R_{sw_{i+1/2,j,k}}\right) \Delta S_{g_{i+1,j,k}}{}^{n+1} - \left(T_{gr^+}{}^n p'_{cgo_{i+1/2,j,k}} + T_{gr^-}{}^n p'_{cgo_{i-1/2,j,k}} + T_{g\theta^+}{}^n p'_{cgo_{i,j+1/2,k}} + T_{g\theta^-}{}^n p'_{cgo_{i,j-1/2,k}} + T_{gz^+}{}^n p'_{cgo_{i,j,k+1/2}} + T_{gz^-}{}^n p'_{cgo_{i,j,k-1/2}} + T_{wr^+}{}^n p'_{cwo_{i+1/2,j,k}} R_{sw_{i+1/2,j,k}} + T_{wr^-}{}^n p'_{cwo_{i-1/2,j,k}} R_{sw_{i-1/2,j,k}} + T_{w\theta^+}{}^n p'_{cwo_{i,j+1/2,k}} R_{sw_{i,j+1/2,k}} + T_{w\theta^-}{}^n p'_{cwo_{i,j-1/2,k}} R_{sw_{i,j-1/2,k}} + T_{wz^+}{}^n p'_{cwo_{i,j,k+1/2}} R_{sw_{i,j,k+1/2}} + T_{wz^-}{}^n p'_{cwo_{i,j,k-1/2}} R_{sw_{i,j,k-1/2}} + \frac{H_g}{\Delta t}\right) \Delta S_{g_{i,j,k}}{}^{n+1} + \left(T_{gr^-}{}^n p'_{cgo_{i-1/2,j,k}} + T_{wr^-}{}^n p'_{cwo_{i-1/2,j,k}} R_{sw_{i-1/2,j,k}}\right) \Delta S_{g_{i-1,j,k}}{}^{n+1} + \left(T_{g\theta^+}{}^n p'_{cgo_{j+1/2,j,k}} + T_{w\theta^+}{}^n p'_{cwo_{i,j+1/2,k}} R_{sw_{i,j+1/2,k}}\right) \Delta S_{g_{i,j+1,k}}{}^{n+1} + \left(T_{g\theta^-}{}^n p'_{cgo_{i,j-1/2,k}} + T_{w\theta^-}{}^n p'_{cwo_{i,j-1/2,k}} R_{sw_{i,j-1/2,k}}\right) \Delta S_{g_{i,j-1,k}}{}^{n+1} + \left(T_{gz^+}{}^n p'_{cgo_{i,j,k+1/2}} + T_{wz^+}{}^n p'_{cwo_{i,j,k+1/2}} R_{sw_{i,j,k+1/2}}\right) \Delta S_{g_{i,j,k+1}}{}^{n+1} + \left(T_{gz^-}{}^n p'_{cgo_{i,j,k-1/2}} + T_{wz^-}{}^n p'_{cwo_{i,j,k-1/2}} R_{sw_{i,j,k-1/2}}\right) \Delta S_{g_{i,j,k-1}}{}^{n+1} = -\left(T_{gr^+}{}^n + T_{or^+}{}^n R_{so_{i+1/2,j,k}} + T_{wr^+}{}^n R_{sw_{i+1/2,j,k}}\right) p_{o_{i+1,j,k}}{}^n + \left(T_{gr^+}{}^n \rho_{gSC} \gamma_c g + T_{or^+}{}^n R_{so_{i+1/2,j,k}} \rho_{oSC} \gamma_c g + T_{wr^+}{}^n R_{sw_{i+1/2,j,k}} \rho_{wSC} \gamma_c g\right) z_{i+1,j,k} + \left(T_{gr^+}{}^n + T_{gr^-}{}^n + T_{g\theta^+}{}^n + T_{g\theta^-}{}^n + T_{gz^+}{}^n + T_{gz^-}{}^n + T_{or^+}{}^n R_{so_{i+1/2,j,k}} + T_{or^-}{}^n R_{so_{i-1/2,j,k}} + T_{o\theta^+}{}^n R_{so_{i,j+1/2,k}} + T_{o\theta^-}{}^n R_{so_{i,j-1/2,k}} + T_{oz^+}{}^n R_{so_{i,j,k+1/2}} + T_{oz^-}{}^n R_{so_{i,j,k-1/2}} + T_{wr^+}{}^n R_{sw_{i+1/2,j,k}} + T_{wr^-}{}^n R_{sw_{i-1/2,j,k}} + T_{w\theta^+}{}^n R_{sw_{i,j+1/2,k}} + T_{w\theta^-}{}^n R_{sw_{i,j-1/2,k}} +$$

$$T_{wz^+}{}^{n}R_{sw_{i,j,k+1/2}} + T_{wz^-}{}^{n}R_{sw_{i,j,k-1/2}}\Big)p_{o_{i,j,k}}{}^{n} - \Big[\rho_{g_{SC}}\gamma_c g\big(T_{gr^+}{}^{n} + T_{gr^-}{}^{n} + T_{g\theta^+}{}^{n} + T_{g\theta^-}{}^{n} + T_{gz^+}{}^{n} + T_{gz^-}{}^{n}\big) + \rho_{o_{SC}}\gamma_c g\left(T_{or^+}{}^{n}R_{so_{i+1/2,j,k}} + T_{or^-}{}^{n}R_{so_{i-1/2,j,k}} + T_{o\theta^+}{}^{n}R_{so_{i,j+1/2,k}} + T_{o\theta^-}{}^{n}R_{so_{i,j-1/2,k}} + T_{oz^+}{}^{n}R_{so_{i,j,k+1/2}} + T_{oz^-}{}^{n}R_{so_{i,j,k-1/2}}\right) + \rho_{w_{SC}}\gamma_c g\left(T_{wr^+}{}^{n}R_{sw_{i+1/2,j,k}} + T_{wr^-}{}^{n}R_{sw_{i-1/2,j,k}} + T_{w\theta^+}{}^{n}R_{sw_{i,j+1/2,k}} + T_{w\theta^-}{}^{n}R_{sw_{i,j-1/2,k}} + T_{wz^+}{}^{n}R_{sw_{i,j,k+1/2}} + T_{wz^-}{}^{n}R_{sw_{i,j,k-1/2}}\right)\Big]z_{i,j,k} - \Big(T_{gr^-}{}^{n} + T_{or^-}{}^{n}R_{so_{i-1/2,j,k}} + T_{wr^-}{}^{n}R_{sw_{i-1/2,j,k}}\Big)p_{o_{i-1,j,k}}{}^{n} + \Big(T_{gr^-}{}^{n}\rho_{g_{SC}}\gamma_c g + T_{or^-}{}^{n}R_{so_{i-1/2,j,k}}\rho_{o_{SC}}\gamma_c g + T_{wr^-}{}^{n}R_{sw_{i-1/2,j,k}}\rho_{w_{SC}}\gamma_c g\Big)z_{i-1,j,k} - \Big(T_{g\theta^+}{}^{n} + T_{o\theta^+}{}^{n}R_{so_{i,j+1/2,k}} + T_{w\theta^+}{}^{n}R_{sw_{i,j+1/2,k}}\Big)p_{o_{i,j+1,k}}{}^{n} + \Big(T_{g\theta^+}{}^{n}\rho_{g_{SC}}\gamma_c g + T_{o\theta^+}{}^{n}R_{so_{i,j+1/2,k}}\rho_{o_{SC}}\gamma_c g + T_{w\theta^+}{}^{n}R_{sw_{i,j+1/2,k}}\rho_{w_{SC}}\gamma_c g\Big)z_{i,j+1,k} - \Big(T_{g\theta^-}{}^{n} + T_{o\theta^-}{}^{n}R_{so_{i,j-1/2,k}} + T_{w\theta^-}{}^{n}R_{sw_{i,j-1/2,k}}\Big)p_{o_{i,j-1,k}}{}^{n} + \Big(T_{g\theta^-}{}^{n}\rho_{g_{SC}}\gamma_c g + T_{o\theta^-}{}^{n}R_{so_{i,j-1/2,k}}\rho_{o_{SC}}\gamma_c g + T_{w\theta^-}{}^{n}R_{sw_{i,j-1/2,k}}\rho_{w_{SC}}\gamma_c g\Big)z_{i,j-1,k} - \Big(T_{gz^+}{}^{n} + T_{oz^+}{}^{n}R_{so_{i,j,k+1/2}} + T_{wz^+}{}^{n}R_{sw_{i,j,k+1/2}}\Big)p_{o_{i,j,k+1}}{}^{n} + \Big(T_{gz^+}{}^{n}\rho_{gsc}\gamma_c g + T_{oz^+}{}^{n}R_{so_{i,j,k+1/2}}\rho_{o_{SC}}\gamma_c g + T_{wz^+}{}^{n}R_{sw_{i,j,k+1/2}}\rho_{w_{SC}}\gamma_c g\Big)z_{i,j,k+1} - \Big(T_{gz^-}{}^{n} + T_{oz^-}{}^{n}R_{so_{i,j,k-1/2}} + T_{wz^-}{}^{n}R_{sw_{i,j,k-1/2}}\Big)p_{o_{i,j,k-1}}{}^{n} + \Big(T_{gz^-}{}^{n}\rho_{gsc}\gamma_c g + T_{oz^-}{}^{n}R_{so_{i,j,k-1/2}}\rho_{o_{SC}}\gamma_c g + T_{wz^-}{}^{n}R_{sw_{i,j,k-1/2}}\rho_{w_{SC}}\gamma_c g\Big)z_{i,j,k-1} - T_{wr^+}{}^{n}p'_{cwo_{i+1/2,j,k}}R_{sw_{i+1/2,j,k}}S_{o_{i+1,j,k}}{}^{n} + \Big(T_{wr^+}{}^{n}p'_{cwo_{i+1/2,j,k}}R_{sw_{i+1/2,j,k}} + T_{wr^-}{}^{n}p'_{cwo_{i-1/2,j,k}}R_{sw_{i-1/2,j,k}} + T_{w\theta^+}{}^{n}p'_{cwo_{i,j+1/2,k}}R_{sw_{i,j+1/2,k}} + T_{w\theta^-}{}^{n}p'_{cwo_{i,j-1/2,k}}R_{sw_{i,j-1/2,k}} + T_{wz^+}{}^{n}p'_{cwo_{i,j,k+1/2}}R_{sw_{i,j,k+1/2}} + T_{wz^-}{}^{n}p'_{cwo_{i,j,k-1/2}}R_{sw_{i,j,k-1/2}}\Big)S_{o_{i,j,k}}{}^{n} - T_{wr^-}{}^{n}p'_{cwo_{i-1/2,j,k}}R_{sw_{i-1/2,j,k}}S_{o_{i-1,j,k}}{}^{n} - T_{w\theta^+}{}^{n}p'_{cwo_{i,j+1/2,k}}R_{sw_{i,j+1/2,k}}S_{o_{i,j+1,k}}{}^{n} - T_{w\theta^-}{}^{n}p'_{cwo_{i,j-1/2,k}}R_{sw_{i,j-1/2,k}}S_{o_{i,j-1,k}}{}^{n} - T_{wz^+}{}^{n}p'_{cwo_{i,j,k+1/2}}R_{sw_{i,j,k+1/2}}S_{o_{i,j,k+1}}{}^{n} - T_{wz^-}{}^{n}p'_{cwo_{i,j,k-1/2}}R_{sw_{i,j,k-1/2}}S_{o_{i,j,k-1}}{}^{n} - \Big(T_{gr^+}{}^{n}p'_{cgo_{i+1/2,j,k}} + T_{wr^+}{}^{n}p'_{cwo_{i+1/2,j,k}}R_{sw_{i+1/2,j,k}}\Big)S_{g_{i+1,j,k}}{}^{n} + \Big(T_{gr^+}{}^{n}p'_{cgo_{i+1/2,j,k}} + T_{gr^-}{}^{n}p'_{cgo_{i-1/2,j,k}} + T_{g\theta^+}{}^{n}p'_{cgo_{i,j+1/2,k}} + T_{g\theta^-}{}^{n}p'_{cgo_{i,j-1/2,k}} + T_{gz^+}{}^{n}p'_{cgo_{i,j,k+1/2}} + T_{gz^-}{}^{n}p'_{cgo_{i,j,k-1/2}} + T_{wr^+}{}^{n}p'_{cwo_{i+1/2,j,k}}R_{sw_{i+1/2,j,k}} + T_{wr^-}{}^{n}p'_{cwo_{i-1/2,j,k}}R_{sw_{i-1/2,j,k}} + T_{w\theta^+}{}^{n}p'_{cwo_{i,j+1/2,k}}R_{sw_{i,j+1/2,k}} + T_{w\theta^-}{}^{n}p'_{cwo_{i,j-1/2,k}}R_{sw_{i,j-1/2,k}} + T_{wz^+}{}^{n}p'_{cwo_{i,j,k+1/2}}R_{sw_{i,j,k+1/2}} + T_{wz^-}{}^{n}p'_{cwo_{i,j,k-1/2}}R_{sw_{i,j,k-1/2}}\Big)S_{g_{i,j,k}}{}^{n} - \Big(T_{gr^-}{}^{n}p'_{cgo_{i-1/2,j,k}} + T_{wr^-}{}^{n}p'_{cwo_{i-1/2,j,k}}R_{sw_{i-1/2,j,k}}\Big)S_{g_{i-1,j,k}}{}^{n} - \Big(T_{g\theta^+}{}^{n}p'_{cgo_{i,j+1/2,k}} + T_{w\theta^+}{}^{n}p'_{cwo_{i,j+1/2,k}}R_{sw_{i,j+1/2,k}}\Big)S_{g_{i,j+1,k}}{}^{n} - \Big(T_{g\theta^-}{}^{n}p'_{cgo_{i,j-1/2,k}} + T_{w\theta^-}{}^{n}p'_{cwo_{i,j-1/2,k}}R_{sw_{i,j-1/2,k}}\Big)S_{g_{i,j-1,k}}{}^{n} - \Big(T_{gz^+}{}^{n}p'_{cgo_{i,j,k+1/2}} + T_{wz^+}{}^{n}p'_{cwo_{i,j,k+1/2}}R_{sw_{i,j,k+1/2}}\Big)S_{g_{i,j,k+1}}{}^{n} - \Big(T_{gz^-}{}^{n}p'_{cgo_{i,j,k-1/2}} + T_{wz^-}{}^{n}p'_{cwo_{i,j,k-1/2}}R_{sw_{i,j,k-1/2}}\Big)S_{g_{i,j,k-1}}{}^{n} + \frac{J_g}{\Delta t}\Big(\alpha_{i,j,k}\Delta\epsilon^{e}_{v\,i,j,k}{}^{n+1} + \Delta\epsilon^{p}_{v\,i,j,k}{}^{n+1}\Big) + F_g + q_{g_{SC}}$$

Regrouping and redefining some variables:

$$E_g\Delta p_{o_{i+1,j,k}}{}^{n+1} + \Big(\quad g - \frac{I_g}{\Delta t}\Big)\Delta p_{o_{i,j,k}}{}^{n+1} + W_g\Delta p_{o_{i-1,j,k}}{}^{n+1} + N_g\Delta p_{o_{i,j+1,k}}{}^{n+1} + S_g\Delta p_{o_{i,j-1,k}}{}^{n+1} + U_g\Delta p_{o_{i,j,k+1}}{}^{n+1} + D_g\Delta p_{o_{i,j,k-1}}{}^{n+1} + E^*_g\Delta S_{o_{i+1,j,k}}{}^{n+1} + \Big(C^*_g - \frac{G_g}{\Delta t}\Big)\Delta S_{o_{i,j,k}}{}^{n+1} + W^*_g\Delta S_{o_{i-1,j,k}}{}^{n+1} + N^*_g\Delta S_{o_{i,j+1,k}}{}^{n+1} + S^*_g\Delta S_{o_{i,j-1,k}}{}^{n+1} + U^*_g\Delta S_{o_{i,j,k+1}}{}^{n+1} + D^*_g\Delta S_{o_{i,j,k-1}}{}^{n+1} + E^{**}_g\Delta S_{g_{i+1,j,k}}{}^{n+1} + \Big(C^{**}_g - \frac{H_g}{\Delta t}\Big)\Delta S_{g_{i,j,k}}{}^{n+1} + W^{**}_g\Delta S_{g_{i-1,j,k}}{}^{n+1} + N^{**}_g\Delta S_{g_{i,j+1,k}}{}^{n+1} + S^{**}_g\Delta S_{g_{i,j-1,k}}{}^{n+1} + U^{**}_g\Delta S_{g_{i,j,k+1}}{}^{n+1} +$$

$$D_g^{**}\Delta S_{g_{i,j,k-1}}{}^{n+1} = -E_g p_{o_{i+1,j,k}}{}^{n} - C_g p_{o_{i,j,k}}{}^{n} - W_g p_{o_{i-1,j,k}}{}^{n} - N_g p_{o_{i,j+1,k}}{}^{n} - S_g p_{o_{i,j-1,k}}{}^{n} - U_g p_{o_{i,j,k+1}}{}^{n} - D_g p_{o_{i,j,k-1}}{}^{n} - E_g^* S_{o_{i+1,j,k}}{}^{n} - C_g^* S_{o_{i,j,k}}{}^{n} - W_g^* S_{o_{i-1,j,k}}{}^{n} - N_g^* S_{o_{i,j+1,k}}{}^{n} - S_g^* S_{o_{i,j-1,k}}{}^{n} - U_g^* S_{o_{i,j,k+1}}{}^{n} - D_g^* S_{o_{i,j,k-1}}{}^{n} - E_g^{**} S_{g_{i+1,j,k}}{}^{n} - C_g^{**} S_{g_{i,j,k}}{}^{n} - W_g^{**} S_{g_{i-1,j,k}}{}^{n} - N_g^{**} S_{g_{i,j+1,k}}{}^{n} - S_g^{**} S_{g_{i,j-1,k}}{}^{n} - U_g^{**} S_{g_{i,j,k+1}}{}^{n} - D_g^{**} S_{g_{i,j,k-1}}{}^{n} - E_g' z_{i+1,j,k} + C_g' z_{i,j,k} + W_g' z_{i-1,j,k} + N_g' z_{i,j+1,k} + S_g' z_{i,j-1,k} + U_g' z_{i,j,k+1} + D_g' z_{i,j,k-1} + \frac{J_g}{\Delta t}\left(\alpha_{i,j,k}\Delta\epsilon_{v\,i,j,k}^{e}{}^{n+1} + \Delta\epsilon_{v\,i,j,k}^{p}{}^{n+1}\right) + F_g + q_{g_{SC}} \quad (A-137)$$

$$\gamma_o = \rho_{o_{SC}}\gamma_c g$$

$$\gamma_w = \rho_{w_{SC}}\gamma_c g$$

$$\gamma_g = \rho_{g_{SC}}\gamma_c g$$

$$E_g = T_{gr^+}{}^{n} + T_{or^+}{}^{n} R_{so_{i+1/2,j,k}} + T_{wr^+}{}^{n} R_{sw_{i+1/2,j,k}}$$

$$E_g' = \gamma_g T_{gr^+}{}^{n} + \gamma_o T_{or^+}{}^{n} R_{so_{i+1/2,j,k}} + \gamma_w T_{wr^+}{}^{n} R_{sw_{i+1/2,j,k}}$$

$$E_g^* = T_{wr^+}{}^{n} p'_{cwo_{i+1/2,j,k}} R_{sw_{i+1/2,j,k}}$$

$$E_g^{**} = T_{gr^+}{}^{n} p'_{cgo_{i+1/2,j,k}} + T_{wr^+}{}^{n} p'_{cwo_{i+1/2,j,k}} R_{sw_{i+1/2,j,k}}$$

$$C_g = -\left(T_{gr^+}{}^{n} + T_{gr^-}{}^{n} + T_{g\theta^+}{}^{n} + T_{g\theta^-}{}^{n} + T_{gz^+}{}^{n} + T_{gz^-}{}^{n} + T_{or^+}{}^{n} R_{so_{i+1/2,j,k}} + T_{or^-}{}^{n} R_{so_{i-1/2,j,k}} + T_{o\theta^+}{}^{n} R_{so_{i,j+1/2,k}} + T_{o\theta^-}{}^{n} R_{so_{i,j-1/2,k}} + T_{oz^+}{}^{n} R_{so_{i,j,k+1/2}} + T_{oz^-}{}^{n} R_{so_{i,j,k-1/2}} + T_{wr^+}{}^{n} R_{sw_{i+1/2,j,k}} + T_{wr^-}{}^{n} R_{sw_{i-1/2,j,k}} + T_{w\theta^+}{}^{n} R_{sw_{i,j+1/2,k}} + T_{w\theta^-}{}^{n} R_{sw_{i,j-1/2,k}} + T_{wz^+}{}^{n} R_{sw_{i,j,k+1/2}} + T_{wz^-}{}^{n} R_{sw_{i,j,k-1/2}}\right)$$

$$C_g' = -\Big[\gamma_g\left(T_{gr^+}{}^{n} + T_{gr^-}{}^{n} + T_{g\theta^+}{}^{n} + T_{g\theta^-}{}^{n} + T_{gz^+}{}^{n} + T_{gz^-}{}^{n}\right) + \gamma_o\left(T_{or^+}{}^{n} R_{so_{i+1/2,j,k}} + T_{or^-}{}^{n} R_{so_{i-1/2,j,k}} + T_{o\theta^+}{}^{n} R_{so_{i,j+1/2,k}} + T_{o\theta^-}{}^{n} R_{so_{i,j-1/2,k}} + T_{oz^+}{}^{n} R_{so_{i,j,k+1/2}} + T_{oz^-}{}^{n} R_{so_{i,j,k-1/2}}\right) + \gamma_w\left(T_{wr^+}{}^{n} R_{sw_{i+1/2,j,k}} + T_{wr^-}{}^{n} R_{sw_{i-1/2,j,k}} + T_{w\theta^+}{}^{n} R_{sw_{i,j+1/2,k}} + T_{w\theta^-}{}^{n} R_{sw_{i,j-1/2,k}} + T_{wz^+}{}^{n} R_{sw_{i,j,k+1/2}} + T_{wz^-}{}^{n} R_{sw_{i,j,k-1/2}}\right)\Big]$$

$$C_g^* = -\left(T_{wr^+}{}^{n} p'_{cwo_{i+1/2,j,k}} R_{sw_{i+1/2,j,k}} + T_{wr^-}{}^{n} p'_{cwo_{i-1/2,j,k}} R_{sw_{i-1/2,j,k}} + T_{w\theta^+}{}^{n} p'_{cwo_{i,j+1/2,k}} R_{sw_{i,j+1/2,k}} + T_{w\theta^-}{}^{n} p'_{cwo_{i,j-1/2,k}} R_{sw_{i,j-1/2,k}} + T_{wz^+}{}^{n} p'_{cwo_{i,j,k+1/2}} R_{sw_{i,j,k+1/2}} + T_{wz^-}{}^{n} p'_{cwo_{i,j,k-1/2}} R_{sw_{i,j,k-1/2}}\right)$$

$$C^{**} = -\left(T_{gr^+}{}^{n} p'_{cgo_{i+1/2,j,k}} + T_{gr^-}{}^{n} p'_{cgo_{i-1/2,j,k}} + T_{g\theta^+}{}^{n} p'_{cgo_{i,j+1/2,k}} + T_{g\theta^-}{}^{n} p'_{cgo_{i,j-1/2,k}} + T_{gz^+}{}^{n} p'_{cgo_{i,j,k+1/2}} + T_{gz^-}{}^{n} p'_{cgo_{i,j,k-1/2}} + T_{wr^+}{}^{n} p'_{cwo_{i+1/2,j,k}} R_{sw_{i+1/2,j,k}} + T_{wr^-}{}^{n} p'_{cwo_{i-1/2,j,k}} R_{sw_{i-1/2,j,k}} + T_{w\theta^+}{}^{n} p'_{cwo_{i,j+1/2,k}} R_{sw_{i,j+1/2,k}} + T_{w\theta^-}{}^{n} p'_{cwo_{i,j-1/2,k}} R_{sw_{i,j-1/2,k}} + T_{wz^+}{}^{n} p'_{cwo_{i,j,k+1/2}} R_{sw_{i,j,k+1/2}} + T_{wz^-}{}^{n} p'_{cwo_{i,j,k-1/2}} R_{sw_{i,j,k-1/2}}\right)$$

$$W_g = T_{gr^-}{}^n + T_{or^-}{}^n R_{so_{i-1/2,j,k}} + T_{wr^-}{}^n R_{sw_{i-1/2,j,k}}$$

$$W_g' = \gamma_g T_{gr^-}{}^n + \gamma_o T_{or^-}{}^n R_{so_{i-1/2,j,k}} + \gamma_w T_{wr^-}{}^n R_{sw_{i-1/2,j,k}}$$

$$W_g^* = T_{wr^-}{}^n p'_{cwo_{i-1/2,j,k}} R_{sw_{i-1/2,j,k}}$$

$$W_g^{**} = T_{gr^-}{}^n p'_{cgo_{i-1/2,j,k}} + T_{wr^-}{}^n p'_{cwo_{i-1/2,j,k}} R_{sw_{i-1/2,j,k}}$$

$$N_g = T_{g\theta^+}{}^n + T_{o\theta^+}{}^n R_{so_{i,j+1/2,k}} + T_{w\theta^+}{}^n R_{sw_{i,j+1/2,k}}$$

$$N_g' = \gamma_g T_{g\theta^+}{}^n + \gamma_o T_{o\theta^+}{}^n R_{so_{i,j+1/2,k}} + \gamma_w T_{w\theta^+}{}^n R_{sw_{i,j+1/2,k}}$$

$$N_g^* = T_{w\theta^+}{}^n p'_{cwo_{i,j+1/2,k}} R_{sw_{i,j+1/2,k}}$$

$$N_g^{**} = T_{g\theta^+}{}^n p'_{cgo_{i,j+1/2,k}} + T_{w\theta^+}{}^n p'_{cwo_{i,j+1/2,k}} R_{sw_{i,j+1/2,k}}$$

$$S_g = T_{g\theta^-}{}^n + T_{o\theta^-}{}^n R_{so_{i,j-1/2,k}} + T_{w\theta^-}{}^n R_{sw_{i,j-1/2,k}}$$

$$S_g' = \gamma_g T_{g\theta^-}{}^n + \gamma_o T_{o\theta^-}{}^n R_{so_{i,j-1/2,k}} + \gamma_w T_{w\theta^-}{}^n R_{sw_{i,j-1/2,k}}$$

$$S_g^* = T_{w\theta^-}{}^n p'_{cwo_{i,j-1/2,k}} R_{sw_{i,j-1/2,k}}$$

$$S_g^{**} = T_{g\theta^-}{}^n p'_{cgo_{i,j-1/2,k}} + T_{w\theta^-}{}^n p'_{cwo_{i,j-1/2,k}} R_{sw_{i,j-1/2,k}}$$

$$U_g = T_{gz^+}{}^n + T_{oz^+}{}^n R_{so_{i,j,k+1/2}} + T_{wz^+}{}^n R_{sw_{i,j,k+1/2}}$$

$$U_g' = \gamma_g T_{gz^+}{}^n + \gamma_o T_{oz^+}{}^n R_{so_{i,j,k+1/2}} + \gamma_w T_{wz^+}{}^n R_{sw_{i,j,k+1/2}}$$

$$U_g^* = T_{wz^+}{}^n p'_{cwo_{i,j,k+1/2}} R_{sw_{i,j,k+1/2}}$$

$$U_g^{**} = T_{gz^+}{}^n p'_{cgo_{i,j,k+1/2}} + T_{wz^+}{}^n p'_{cwo_{i,j,k+1/2}} R_{sw_{i,j,k+1/2}}$$

$$D_g = T_{gz^-}{}^n + T_{oz^-}{}^n R_{so_{i,j,k-1/2}} + T_{wz^-}{}^n R_{sw_{i,j,k-1/2}}$$

$$D_g' = \gamma_g T_{gz^-}{}^n + \gamma_o T_{oz^-}{}^n R_{so_{i,j,k-1/2}} + \gamma_w T_{wz^-}{}^n R_{sw_{i,j,k-1/2}}$$

$$D_g^* = T_{wz^-}{}^n p'_{cwo_{i,j,k-1/2}} R_{sw_{i,j,k-1/2}}$$

$$D_g^{**} = T_{gz^-}{}^n p'_{cgo_{i,j,k-1/2}} + T_{wz^-}{}^n p'_{cwo_{i,j,k-1/2}} R_{sw_{i,j,k-1/2}}$$

$$F_{g_{i,j,k}} = \left(1 + R_{so_{i,j,k}} + R_{sw_{i,j,k}}\right) \frac{V_{b_{i,j,k}} q_{s_{i,j,k}} \phi_{i,j,k}}{(1-\phi_{i,j,k})}$$

$$G_{g_{i,j,k}} = \frac{V_{b_{i,j,k}} \phi_{i,j,k}}{\alpha_c} \left\{ \frac{R_{so_{i,j,k}}}{B_{o_{i,j,k}}} + \frac{R_{sw_{i,j,k}}}{B_{w_{i,j,k}}} \left[\left(1 - S_{o_{i,j,k}} - S_{g_{i,j,k}}\right) \left(R'_{sw_{i,j,k}} + c_{w_{i,j,k}}\right) p'_{cwo_{i,j,k}} - 1 \right] \right\}$$

$$H_{g_{i,j,k}} = \frac{V_{b_{i,j,k}} \phi_{i,j,k}}{\alpha_c} \left\{ \frac{1}{B_{g_{i,j,k}}} \left[1 + S_{g_{i,j,k}} p'_{cgo\,i,j,k} \left[c_{pc\,i,j,k}(1 - \alpha_{i,j,k}) - c_{s_{i,j,k}} + c_{g_{i,j,k}} \right] \right] + \right.$$
$$\frac{R_{so_{i,j,k}}}{B_{o_{i,j,k}}} S_{o_{i,j,k}} p'_{cgo\,i,j,k} \left[c_{pc\,i,j,k}(1 - \alpha_{i,j,k}) - c_{s_{i,j,k}} \right] + \frac{R_{sw_{i,j,k}}}{B_{w_{i,j,k}}} \left[\left(1 - S_{o_{i,j,k}} - S_{g_{i,j,k}}\right) \left[\left(R'_{sw_{i,j,k}} + \right.\right.\right.$$
$$\left.\left.\left. c_{w_{i,j,k}} \right) p'_{cwo_{i,j,k}} + \left[c_{pc\,i,j,k}(1 - \alpha_{i,j,k}) - c_{s_{i,j,k}} \right] p'_{cgo\,i,j,k} \right] - 1 \right] \right\}$$

$$I_{g_{i,j,k}} = \frac{V_{b_{i,j,k}} \phi_{i,j,k}}{\alpha_c} \left\{ \frac{S_{g_{i,j,k}}}{B_{g_{i,j,k}}} \left[c_{pc\,i,j,k}(1 - \alpha_{i,j,k}) - c_{s_{i,j,k}} + c_{g_{i,j,k}} \right] + \frac{R_{so_{i,j,k}}}{B_{o_{i,j,k}}} S_{o_{i,j,k}} \left[R'_{so\,i,j,k} + c_{pc\,i,j,k}(1 - \right.\right.$$
$$\left.\left. \alpha_{i,j,k}) - c_{s_{i,j,k}} + c_{o_{i,j,k}} \right] + \frac{R_{sw_{i,j,k}}}{B_{w_{i,j,k}}} \left(1 - S_{o_{i,j,k}} - S_{g_{i,j,k}}\right) \left[R'_{sw\,i,j,k} + c_{pc\,i,j,k}(1 - \alpha_{i,j,k}) - c_{s_{i,j,k}} + c_{w_{i,j,k}} \right] \right\}$$

$$J_{g_{i,j,k}} = -\frac{V_{b_{i,j,k}} \phi_{i,j,k}}{\alpha_c} \left[\frac{1}{B_{g_{i,j,k}}} S_{g_{i,j,k}} + \frac{R_{so_{i,j,k}}}{B_{o_{i,j,k}}} S_{o_{i,j,k}} + \frac{R_{sw_{i,j,k}}}{B_{w_{i,j,k}}} \left(1 - S_{o_{i,j,k}} - S_{g_{i,j,k}}\right) \right]$$

A2.3.Boundary conditions

The governing equations for multiphase flow at the boundaries are affected by pressure and saturation, and the effect of capillary pressure is assumed negligible. This section presents the stated boundary conditions and their discretization.

A2.3.1. Radial direction

- **For the wellbore boundary – internal radial boundary,** $(i = 1)$

Traditionally, wells in the single-well simulation are treated as boundary conditions (Abou-Kassem *et al.*, 2020).

– Pressure condition

The well production is defined as a bottom-hole pressure-constrained well, which states that the wellbore pressure is constant (Dirichlet boundary condition).

$$p_{wf} = constant$$

and its discretization at the boundary can be expressed by:

$$p_{o_{0,j,k}} = \left[1 - \frac{ln(r_1/r_0)}{ln(r_1/r_w)}\right] p_{o_{1,j,k}} + \frac{ln(r_1/r_0)}{ln(r_1/r_w)} \left[p_{wf_{ref}} + \gamma_o\left(z_{1,j,k} - z_{ref}\right)\right] \quad \text{(A – 138)}$$

– Saturation conditions

The well production condition is defined as a non-flow condition, i.e., there is no radial flow between $i = 0$ and $i = 1$, then oil saturation at the radial boundary has no change (Neumann boundary condition type):

$$\frac{\partial S_o}{\partial r} = 0$$

and its discretization at the boundary can be expressed by:

$$S_{o_{0,j,k}} = S_{o_{1,j,k}} \quad \text{(A – 139)}$$

Similarly, for gas saturation (Neumann boundary condition type):

$$\frac{\partial S_g}{\partial r} = 0$$

and its discretization at the boundary can be expressed by:

$$S_{g_{0,j,k}} = S_{g_{1,j,k}} \quad \text{(A – 140)}$$

- **For the external radial boundary,** $(i = n_r)$

– Pressure condition

The external radial pressure condition is defined as a non-flow condition, i.e., there is no radial flow between $i = n_r$ and $i = n_r + 1$ (Neumann boundary condition type):

$$q_o = 0 = -\beta_c \frac{k_{oz}}{\phi B_o \mu_o}\left(\frac{\partial p_o}{\partial r}\right)$$

and its discretization at the boundary can be expressed by:

$$p_{o_{n_r+1,j,k}} = p_{o_{n_r,j,k}} \quad \text{(A – 141)}$$

– Saturation conditions:

The external radial oil saturation condition is defined in terms of the non-flow condition, i.e., there is no radial oil saturation change between $i = n_r$ and $i = n_r + 1$ (Neumann boundary condition type), equal statement of Equation (A – 139), where its discretization at the boundary can be expressed by:

$$S_{o_{n_r+1,j,k}} = S_{o_{n_r,j,k}} \quad \text{(A – 142)}$$

Similarly, gas saturation is a Neumann boundary condition type, an equal statement of Equation (A – 142), where its discretization at the boundary can be expressed by:

$$S_{g_{n_r+1,j,k}} = S_{g_{n_r,j,k}} \quad \text{(A – 143)}$$

A2.3.2. Tangential direction

- **For the first angular boundary,** $(j = 1)$

– Pressure condition

The pressure at the first angular boundary is a Dirichlet boundary condition type that is stated as:

$$p_{o_{i,0,k}} = p_{o_{i,n_\theta,k}} \quad \text{(A – 144)}$$

– Saturation conditions

The oil saturation at the first angular boundary is stated as (Dirichlet boundary condition type):

$$S_{o_{i,0,k}} = S_{o_{i,n_\theta,k}} \quad \text{(A – 145)}$$

Similarly, for the gas saturation (Dirichlet boundary condition type):

$$S_{g_{i,0,k}} = S_{g_{i,n_\theta,k}} \quad \text{(A – 146)}$$

- **For the final angular boundary,** $(j = n_\theta)$

– Pressure condition

The pressure at the final angular boundary is also a Dirichlet boundary condition type that is stated as:

$$p_{o_{i,n_\theta+1,k}} = p_{o_{i,1,k}} \quad \text{(A – 147)}$$

– Saturation conditions

The oil saturation at the final angular boundary is stated as (Dirichlet boundary condition type):

$$S_{o_{i,n_\theta+1,k}} = S_{o_{i,1,k}} \quad \text{(A – 148)}$$

Similarly, for the gas saturation (Dirichlet boundary condition type):

$$S_{g_{i,0,k}} = S_{g_{i,n_\theta,k}} \quad \text{(A – 149)}$$

A2.3.3. Vertical direction

- **For the top boundary,** $(k = 1)$

– **Pressure condition**

The vertical pressure condition at the top is defined as a no-flow condition, i.e., there is no vertical flow between the blocks $k = 0$ and $k = 1$ (Neumann boundary condition type).

$$q_o = 0 = -\beta_c \frac{k_{oz}}{\phi B_o \mu_o}\left(\frac{\partial p_o}{\partial z}\right)$$

and its discretization at the boundary can be expressed by:

$$p_{o_{i,j,0}} = p_{o_{i,j,1}} \qquad \text{(A – 150)}$$

– **Saturation conditions**

The vertical oil saturation condition at the top is defined in terms of the non-flow condition, i.e., there is no vertical oil saturation change between $k = 0$ and $k = 1$ (Neumann boundary condition type) :

$$\frac{\partial S_o}{\partial z} = 0$$

and its discretization at the boundary can be expressed by:

$$S_{o_{i,j,0}} = S_{o_{i,j,1}} \qquad \text{(A – 151)}$$

Similarly, for the gas saturation (Dirichlet boundary condition type):

$$\frac{\partial S_g}{\partial z} = 0$$

and its discretization at the boundary can be expressed by:

$$S_{g_{i,j,0}} = S_{g_{i,j,1}} \qquad \text{(A – 152)}$$

- **For the bottom boundary,** $(k = n_z)$

– **Pressure condition**

The vertical pressure condition at the bottom is defined as a no-flow condition, i.e., there is no vertical flow between the blocks $k = n_z$ and $k = n_z + 1$ (Neumann boundary condition type), and its discretization at the boundary can be expressed by:

$$p_{o_{i,j,n_z+1}} = p_{o_{i,j,n_z}} \quad \text{(A – 153)}$$

– Saturation conditions

The vertical oil saturation condition at the bottom is defined in terms of the non-flow condition, i.e., there is no vertical oil saturation change between the blocks $k = n_z$ and $k = n_z + 1$ (Neumann boundary condition type), and its discretization at the boundary can be expressed by:

$$S_{o_{i,j,n_z+1}} = S_{o_{i,j,n_z}} \quad \text{(A – 154)}$$

Similarly, gas saturation is a Dirichlet boundary condition type, and its discretization at the boundary can be expressed by:

$$S_{g_{i,j,n_z+1}} = S_{g_{i,j,n_z}} \quad \text{(A – 155)}$$

A2.3.Other relations

A2.3.1. Porosity equation

Modeling multiphase fluid flow in reservoirs requires knowledge of basic rock properties such as porosity and permeability. Considering the coupling with the geomechanical and sand production models, porosity depends on reservoir pressure because of solid and pore compressibilities. This section defines a relationship between porosity including the effect of elastoplastic deformation and the sand production process.

From porosity definition $\phi = V_p/V_b$, the porosity change can be expressed as:

$$\frac{\partial \phi}{\phi} = \frac{\partial V_p}{V_p} - \frac{\partial V_b}{V_b} \quad \text{(A – 156)}$$

This definition lets distinguishes in rocks three kinds of compressibility: rock matrix compressibility, rock bulk compressibility, and pore compressibility. Rock matrix compressibility is the fractional change in volume of the solid rock materials (grains) with a unit change in pressure. Rock bulk compressibility is the change in volume of the bulk volume of the rock with a unit change in pressure. Pore compressibility is the fractional change in the pore volume of the rock with a unit change in pressure. However, including the geomechanics effect also the mean stress affects these three compressibilities.

Assuming that V_p and V_b are functions of oil pressure p_o and mean stress $\bar{\sigma}$, the porosity change will therefore be such that:

$$\frac{\partial \phi}{\phi} = \frac{1}{V_p}\left[\left(\frac{\partial V_p}{\partial \bar{p}}\right)\partial p_o + \left(\frac{\partial V_p}{\partial \bar{\sigma}}\right)\partial \bar{\sigma}\right] - \frac{1}{V_b}\left[\left(\frac{\partial V_b}{\partial \bar{p}}\right)\partial p_o + \left(\frac{\partial V_b}{\partial \bar{\sigma}}\right)\partial \bar{\sigma}\right] \quad \text{(A – 157)}$$

Using the definitions of porous compressibilities defined by Zimmerman *et al*. (1986) that are stated in Equations (A – 43) and (A – 44) and replaced them in Equation (A – 157) results:

$$\frac{\partial\phi}{\phi} = \left(c_{bc} - c_{pc}\right)\partial\bar{\sigma} - \left(c_{bp} - c_{pp}\right)\partial p_o$$

Reordering:

$$\partial\phi = -[(1-\phi)c_{bc} - c_s]\partial(\bar{\sigma} - p_o) \qquad \text{(A – 158)}$$

To account for the elastoplasticity, the porosity change in Equation (A – 158) must have a term that is related to the plastic change of porosity. That is, the porosity change can be decomposed into an elastic part, a plastic part, and a sanding part:

$$\partial\phi = \partial\phi^e + \partial\phi^p + \partial\phi^s \qquad \text{(A – 159)}$$

The term $\partial\phi^e$ comes from Equation (A – 159), however an expression for the term $\partial\phi^p$ can be derived assuming that the pore volume and the bulk volume both can be decomposed in an elastic and plastic part too, then:

$$\partial V_p = \partial {V_p}^e + \partial {V_p}^p$$

$$\partial V_b = \partial {V_b}^e + \partial {V_b}^p \qquad \text{(A – 160)}$$

The terms $\partial {V_p}^e$ and $\partial {V_b}^e$ are used to deduce Equation (A – 158), however, to obtain expressions for the terms $\partial {V_p}^p$ and $\partial {V_b}^p$, an assumption that the plastic can be derived assuming that the pore volume is defined as a function of the plastic bulk volume and the plastic solid volume as:

$$\partial {V_p}^p = \partial {V_b}^p - \partial {V_s}^p \qquad \text{(A – 161)}$$

Considering the definition of the plastic strain change as:

$$\partial {\epsilon_v}^p = -\frac{\partial {V_b}^p}{V_b}$$

$$\partial {\epsilon_s}^p = -\frac{\partial {V_s}^p}{V_s} = -\frac{\partial {V_s}^p}{(1-\phi)V_b}$$

$$\partial {\epsilon_p}^p = -\frac{\partial {V_p}^p}{V_p} \qquad \text{(A – 162)}$$

Note that the sign minus in the above definitions means that a strain reduction is assumed to be positive. Replacing these definitions into Equation (A – 161) results in an expression for the plastic pore strain change:

$$\partial {\epsilon_p}^p = \frac{1}{\phi}[\partial {\epsilon_v}^p - (1-\phi)\partial {\epsilon_s}^p] \qquad \text{(A – 163)}$$

Depending on the rock's constitutive behavior and the stress path it experiments, the plastic strains ${\epsilon_v}^p$ and ${\epsilon_p}^p$ will be controlled by phenomena such as grain slippage and rotation, micro-fracturing, and changes in the grain's shape (David, Menendez, Zhu, & Wong, 2001). However, the plastic strain of the grain itself, ${\epsilon_s}^p$, is a variable difficult to measure and model, additionally the compressibility of the grains is very low compared to the pore and bulk compressibilities. Therefore, the contribution of the plastic strain of the grains is assumed to be low and can be ignored, then:

$$\partial {\epsilon_p}^p = \frac{\partial {\epsilon_v}^p}{\phi} \tag{A – 164}$$

Now replace Equations (A – 162) and (A – 164) into Equation (A – 156) resulting in an expression for the porosity change which includes the plastic volumetric strain :

$$\partial \phi^p = \phi \left(\frac{\partial {V_p}^p}{V_p} - \frac{\partial {V_b}^p}{V_b} \right) = \phi \left(- \frac{\partial {\epsilon_v}^p}{\phi} + \partial {\epsilon_v}^p \right)$$

Then:

$$\partial \phi^p = (\phi - 1) \partial {\epsilon_v}^p \tag{A – 165}$$

Replacing Equation (A – 165) into Equation (A – 158) results in an expression for the porosity change that includes the plastic volumetric strain:

$$\partial \phi = [c_s - (1 - \phi) c_{bc}](\partial \bar{\sigma} - \partial p_o) - (1 - \phi) \partial {\epsilon_v}^p \tag{A – 166}$$

Considering the sand production effect on porosity:

$$\partial {V_p}^s = \partial {V_b}^s - \partial {V_s}^s \tag{A – 167}$$

Defining mass sand production as q_s, the solid volume change can be expressed as:

$$\frac{\partial {V_s}^s}{\partial t} = - \frac{q_s}{\rho_s} = \frac{\partial {V_b}^s}{\partial t} - \frac{\partial {V_p}^s}{\partial t} \tag{A – 168}$$

Interpreting Equation (A – 168), the effect of sand production can affect the pore volume as the bulk volume. For consolidated sandstones, the sand production affects directly the pore volume without affecting the bulk volume of the porous media. While for unconsolidated sandstones, sand production affects the pore volume as the bulk volume. The pore compressibility c_p helps to distribute the effect in both volumes acting as a weight variable, where $c_p = 1$, if the sand production comes just from pore volume and $c_p < 1$, if the sand production comes from bulk volume, then the bulk volume change can be defined as:

$$\frac{\partial {V_b}^s}{\partial t} = - \left(\frac{1 - c_p}{1 - \phi} \right) \frac{q_s}{\rho_s}$$

$$\frac{\partial {V_p}^s}{\partial t} = \left(\frac{c_p - \phi}{1-\phi}\right)\frac{q_s}{\rho_s} \qquad \text{(A – 169)}$$

Then, it is possible to express that porosity depends on reservoir pressure because of solid and pore compressibilities.

Replacing Equation (A – 169) into Equation (A – 156), the porosity change due to sand production can be defined as:

$$\frac{\partial \phi^s}{\phi} = \left(\frac{c_p - \phi}{1-\phi}\right)\frac{q_s}{V_p \rho_s}\partial t + \left(\frac{1-c_p}{1-\phi}\right)\frac{q_s}{V_b \rho_s}\partial t$$

Reordering:

$$\partial \phi^s = \frac{c_p q_s}{\rho_s V_b}\partial t$$

Adding this term to the porosity change into Equation (A – 166) and reordering:

$$\partial\phi - \phi c_{bc}(\partial\bar{\sigma} - \partial p_o) - \phi\partial{\epsilon_v}^p - \frac{c_p q_s}{\rho_s V_b}\partial t = [c_s - c_{bc}](\partial\bar{\sigma} - \partial p_o) - \partial{\epsilon_v}^p$$

Integrating with time and reordering:

$$\phi^{n+1}\left[1 - c_{bc}\Delta(\bar{\sigma} - p_o)^{n+1} - \Delta({\epsilon_v}^p)^{n+1} - \frac{q_s c_p}{\rho_s V_b}\Delta t^{n+1}\right] - \phi^n = (c_s - c_{bc})\Delta(\bar{\sigma} - p_o)^{n+1} - \Delta({\epsilon_v}^p)^{n+1}$$

Therefore porosity can be updated with the following equation:

$$\phi^{n+1} = \frac{\phi^n + (c_s - c_{bc})(\Delta\bar{\sigma} - \Delta p_o)^{n+1} - \Delta({\epsilon_v}^p)^{n+1}}{1 - c_{bc}(\Delta\bar{\sigma} - \Delta p_o)^{n+1} - \Delta({\epsilon_v}^p)^{n+1} - \frac{q_s c_p}{\rho_s V_b}\Delta t^{n+1}} \qquad \text{(A – 170)}$$

A2.3.2. Variation of permeability with porosity

A change in the stress state will produce a mechanical modification of the rock's flow capacity. Assuming a homogeneous and isotropic rock, any alteration in the rock's permeability induced by stress is proportional to the modification of its porosity. However, in practice, it is difficult to correlate directly a porosity change with a permeability change, particularly if the constitutive behavior of the rock is no longer elastic after the stress state modification (Davies & Davies, 1999; Wong, 2003; Li & Chalaturnyk, 2006). Acknowledging these aspects, this investigation will use the model proposed by Kozeny-Carman mainly due to its simplicity and its generality, even though it has been demonstrated its lack of accuracy

during elastoplastic processes (Wong, 2003; Li & Chalaturnyk, 2006). It is important to note that the mentioned stress-dependent permeability model does not consider the deviatoric part of the stress tensor, therefore, the changes in the stress-dependent permeability will be a function of volumetric strains rather than shear strains when the constitutive behavior of the rock is elastic.

$$\frac{k}{k_0} = \left(\frac{\phi}{\phi_0}\right)^3 \left(\frac{1-\phi_0}{1-\phi}\right)^2 \quad \text{(A – 171)}$$

A2.3.3. Transmissibility factors

The transmissibility factors correspond to getting the values of $(k/\mu B)$ for each phase at the interface of each grid block in each direction. This calculation is important because this variable is part of the transmissibility term and is a pressure-dependent term, and its treatment can induce nonlinearities. (Abou-Kassem *et al.*, 2020)

- **Radial direction**

There are two interactions between the block, one regressive associated with the block boundary $(i-1/2\,,j,k)$, and other progressive associated with the block boundary $(i+1/2\,,j,k)$.

The rate of fluid flow from the center of grid-block $(i-1,j,k)$ to block boundary $(i-1/2\,,j,k)$ is given by Darcy's law as:

$$q_{o\,(i-1,j,k\to i-1/2,j,k)} = \frac{\beta_c r_{i-1,j,k}\Delta\theta_{i,j,k}\Delta z_{i,j,k}}{(r_{i-1/2,j,k}-r_{i-1,j,k})}\left(\frac{k_{or}}{B_o\mu_o}\right)_{i-1,j,k}\left(p_{o\,i-1,j,k}-p_{o\,i-1/2,j,k}\right) \quad \text{(A – 172)}$$

Similarly, the oil flow rate between the block boundary $(i-1/2,j,k)$ and the center of the grid-block (i,j,k) can be expressed as:

$$q_{o\,(i-1/2,j,k\to i,j,k)} = \frac{\beta_c r_{i,j,k}\Delta\theta_{i,j,k}\Delta z_{i,j,k}}{(r_{i,j,k}-r_{i-1/2,j,k})}\left(\frac{k_{or}}{B_o\mu_o}\right)_{i,j,k}\left(p_{o\,i-1/2,j,k}-p_{o\,i,j,k}\right) \quad \text{(A – 173)}$$

The rate of fluid flow between the centers of grid-blocks $(i-1,j,k\,)$ and (i,j,k), is given by Darcy's law as:

$$q_{o\,(i-1,j,k\to,j,k)} = \frac{\beta_c r_{i-1/2,j,k}\Delta\theta_{i,j,k}\Delta z_{i,j,k}}{(r_{i,j,k}-r_{i-1,j,k})}\left(\frac{k_{or}}{B_o\mu_o}\right)_{i-1/2,j,k}\left(p_{o\,i-1,j,k}-p_{o\,i,j,k}\right) \quad \text{(A – 174)}$$

Assuming in this flow system, there is neither fluid accumulation nor fluid depletion. Therefore, the rate of fluid leaving grid-block $(i-1,j,k)$ has to be equal to the rate of fluid entering grid-block (i,j,k):

$$q_{o\,(i-1,j,k\to i-1/2,j,k)} = q_{o\,(i-1/2,j,k\to i,j,k)} = q_{o\,(i-1,j,k\to i,j,k)} \quad \text{(A – 175)}$$

The pressure drop between the centers of grid-blocks $(i-1,j,k\,)$ and (i,j,k) is equal to the sum of the pressure drops between the block centers and the block boundary between them; that is:

$$\left(p_{o\,i-1,j,k} - p_{o\,i,j,k}\right) = \left(p_{o\,i-1,j,k} - p_{o\,i-1/2,j,k}\right) + \left(p_{o\,i-1/2,j,k} - p_{o\,i,j,k}\right) \quad \text{(A – 176)}$$

Considering the assumptions expressed by Equations (A – 175) and (A – 176) and replacing Equations (A – 172) and (A – 173) with Equation (A – 176), and ensuring compliance with the principle of conservation of mass:

$$\left(\frac{k_{or}}{B_o\mu_o}\right)_{i-1/2,j,k} = \frac{\frac{r_{i,j,k}/r_{i-1,j,k}}{r_{i-1/2,j,k}}}{\frac{r_{i,j,k}/r_{i-1/2,j,k}}{r_{i,j,k}\left(\frac{k_{or}}{B_o\mu_o}\right)_{i,j,k}} + \frac{r_{i-1/2,j,k}/r_{i-1,j,k}}{r_{i-1,j,k}\left(\frac{k_{or}}{B_o\mu_o}\right)_{i-1,j,k}}}$$

Rewriting the previous expression based on the harmonic average recommended by Aziz and Settari (2002) results that the transmissibility factor for the regressive interaction of the grid-block can be stated as:

$$\left(\frac{k_{or}}{B_o\mu_o}\right)_{i-1/2,j,k} = \frac{\ln\left(r_{i,j,k}/r_{i-1,j,k}\right)}{\frac{\ln\left(r_{i,j,k}/r_{i-1/2,j,k}\right)}{\left(\frac{k_{or}}{B_o\mu_o}\right)_{i,j,k}} + \frac{\ln\left(r_{i-1/2,j,k}/r_{i-1,j,k}\right)}{\left(\frac{k_{or}}{B_o\mu_o}\right)_{i-1,j,k}}} \quad \text{(A – 177)}$$

Similarly for the progressive interaction of the grid block:

$$\left(\frac{k_{or}}{B_o\mu_o}\right)_{i+1/2,j,k} = \frac{\ln\left(r_{i+1,j,k}/r_{i,j,k}\right)}{\frac{\ln\left(r_{i+1,j,k}/r_{i+1/2,j,k}\right)}{\left(\frac{k_{or}}{B_o\mu_o}\right)_{i+1,j,k}} + \frac{\ln\left(r_{i+1/2,j,k}/r_{i,j,k}\right)}{\left(\frac{k_{or}}{B_o\mu_o}\right)_{i,j,k}}} \quad \text{(A – 178)}$$

- **Tangential direction**

Similarly to the radial direction, there are two interactions between the block at the tangential direction, one regressive associated with the block boundary $(i, j-1/2\,, k)$, and other progressive associated with the block boundary $(i, j+1/2\,, k)$.

The rate of fluid flow from the center of grid-block$(\,i, j-1, k)$ to block boundary $(i, j-1/2\,, k)$ is given by Darcy's law as:

$$q_{o\,(i,j-1,k\rightarrow i,j-1/2,k)} = \frac{\beta_c \Delta r_{i,j,k}\Delta z_{i,j,k}}{r_{i,j,k}\left(\theta_{i-1/2,j,k}-\theta_{i,j-1,k}\right)}\left(\frac{k_{o\theta}}{B_o\mu_o}\right)_{i,j-1,k}\left(p_{o\,i,j-1,k} - p_{o\,i,j-1/2,k}\right) \quad \text{(A – 179)}$$

Similarly, the oil flow rate between the block boundary $(i, j-1/2, k)$ and the center of the grid-block (i, j, k) can be expressed as:

$$q_{o\,(i,j-1/2,k\rightarrow i,j,k)} = \frac{\beta_c \Delta r_{i,j,k}\Delta z_{i,j,k}}{r_{i,j,k}\left(\theta_{i,j,k}-\theta_{i-1/2,j,k}\right)}\left(\frac{k_{o\theta}}{B_o\mu_o}\right)_{i,j,k}\left(p_{o\,i,j-1/2,k} - p_{o\,i,j,k}\right) \quad \text{(A – 180)}$$

The rate of fluid flow between the centers of grid-blocks $(i, j-1, k)$ and (i, j, k) is given by Darcy's law as:

$$q_{o\,(i,j-1,k\to i,j,k)} = \frac{\beta_c \Delta\theta_{i,j,k} \Delta z_{i,j,k}}{r_{i,j,k}(\theta_{i,j,k}-\theta_{i-1,j,k})} \left(\frac{k_{o\theta}}{B_o}\right)_{i,j-1/2,k} \left(p_{o\,i,j-1,k} - p_{o\,i,j,k}\right) \quad \text{(A – 181)}$$

Assuming in this flow system, there is neither fluid accumulation nor fluid depletion. Therefore, the rate of fluid leaving grid-block $(i, j-1, k)$ has to be equal to the rate of fluid entering grid-block (i, j, k):

$$q_{o\,(i,j-1,k\to i,j-1/2,k)} = q_{o\,(i,j-1/2,k\to i,j,k)} = q_{o\,(i,j-1,k\to i,j,k)} \quad \text{(A – 182)}$$

The pressure drop between the centers of grid-blocks $(i, j-1, k)$ and (i, j, k) is equal to the sum of the pressure drops between the block centers and the block boundary between them; that is:

$$\left(p_{o\,i,j-1,k} - p_{o\,i,j,k}\right) = \left(p_{o\,i,j-1,k} - p_{o\,i,j-1/2,k}\right) + \left(p_{o\,i,j-1/2,k} - p_{o\,i,j,k}\right) \quad \text{(A – 183)}$$

Considering the assumptions expressed by Equations (A – 182) and (A – 183) and replacing Equations (A – 180) and (A – 180) with Equation (A – 183), and ensuring compliance with the principle of conservation of mass:

$$\left(\frac{k_{o\theta}}{B_o\mu_o}\right)_{i,j-1/2,k} = \frac{\theta_{i,j,k}-\theta_{i,j-1,k}}{\frac{\theta_{i,j,k}-\theta_{i,j-1/2,k}}{\left(\frac{k_{o\theta}}{B_o\mu_o}\right)_{i,j,k}} + \frac{\theta_{i,j-1/2,k}-\theta_{i,j-1,k}}{\left(\frac{k_{o\theta}}{B_o\mu_o}\right)_{i,j-1,k}}}$$

Adjusting to the grid features results that the transmissibility factor for the regressive interaction of the grid block can be stated as:

$$\left(\frac{k_{o\theta}}{B_o\mu_o}\right)_{i,j-1/2,k} = \frac{\Delta\theta_{i,j,k}+\Delta\theta_{i,j-1,k}}{\frac{\Delta\theta_{i,j,k}}{\left(\frac{k_{o\theta}}{B_o\mu_o}\right)_{i,j,k}} + \frac{\Delta\theta_{i,j-1,k}}{\left(\frac{k_{o\theta}}{B_o\mu_o}\right)_{i,j-1,k}}}$$

$$\left(\frac{k_{o\theta}}{B_o\mu_o}\right)_{i,j-1/2,k} = \frac{2}{\frac{1}{\left(\frac{k_{o\theta}}{B_o\mu_o}\right)_{i,j,k}} + \frac{1}{\left(\frac{k_{o\theta}}{B_o\mu_o}\right)_{i,j-1,k}}} \quad \text{(A – 184)}$$

Similarly for the progressive interaction of the grid block:

$$\left(\frac{k_{o\theta}}{B_o\mu_o}\right)_{i,j+1/2,k} = \frac{\Delta\theta_{i,j+1,k}+\Delta\theta_{i,j,k}}{\frac{\Delta\theta_{i,j+1,k}}{\left(\frac{k_{o\theta}}{B_o\mu_o}\right)_{i,j+1,k}} + \frac{\Delta\theta_{i,j,k}}{\left(\frac{k_{o\theta}}{B_o\mu_o}\right)_{i,j,k}}}$$

$$\left(\frac{k_{or}}{B_o\mu_o}\right)_{i,j+1/2,k} = \frac{2}{\frac{1}{\left(\frac{k_{o\theta}}{B_o\mu_o}\right)_{i,j+1,k}} + \frac{1}{\left(\frac{k_{o\theta}}{B_o\mu_o}\right)_{i,j,k}}} \quad \text{(A – 185)}$$

- **Vertical direction**

Similarly to the radial direction and tangential direction, there are two interactions between the block in the vertical direction, one regressive associated with the block boundary $(i, j, k-1/2)$, and other progressive associated with the block boundary $(i, j, k+1/2)$.

The rate of fluid flow from the center of grid-block $(i, j, k-1)$ to block boundary $(i, j, k-1/2)$ is given by Darcy's law as:

$$q_{o(i,j,k-1\rightarrow i,j,k-1/2)} = \frac{\beta_c \Delta\theta_{i,j,k}\left(r_{i,j,k+1/2}^2 - r_{i,j,k-1/2}^2\right)}{2\left(z_{i,j,k-1/2} - z_{i,j,k-1}\right)} \left(\frac{k_{oz}}{B_o \mu_o}\right)_{i,j,k-1} \left(p_{o\,i,j,k-1} - p_{o\,i,j,k-1/2}\right) \quad \text{(A – 186)}$$

Similarly, the oil flow rate between the block boundary $i, j, k-1/2$ and the center of the grid-block i, j, k can be expressed as:

$$q_{o(i,j,k-1/2\rightarrow i,j,k)} = \frac{\beta_c \Delta\theta_{i,j,k}\left(r_{i,j,k+1/2}^2 - r_{i,j,k-1/2}^2\right)}{2\left(z_{i,j,k} - z_{i,j,k-1/2}\right)} \left(\frac{k_{oz}}{B_o \mu_o}\right)_{i,j,k} \left(p_{o\,i,j,k-1/2} - p_{o\,i,j,k}\right) \quad \text{(A – 187)}$$

The rate of fluid flow between the centers of grid-blocks $(i, j, k-1)$ and (i, j, k) is given by Darcy's law as:

$$q_{o(i,j,k-1\rightarrow i,j,k)} = \frac{\beta_c \Delta\theta_{i,j,k}\left(r_{i,j,k+1/2}^2 - r_{i,j,k-1/2}^2\right)}{2\left(z_{i,j,k} - z_{i,j,k-1}\right)} \left(\frac{k_{o\theta}}{B_o \mu_o}\right)_{i,j,k-1/2} \left(p_{o\,i,j,k-1} - p_{o\,i,j,k}\right) \quad \text{(A – 188)}$$

Assuming in this flow system, there is neither fluid accumulation nor fluid depletion. Therefore, the rate of fluid leaving grid-block $(i, j, k-1)$ has to be equal to the rate of fluid entering grid-block (i, j, k):

$$q_{o(i,j,k-1\rightarrow i,j,k-1/2)} = q_{o(i,j,k-1/2\rightarrow i,j,k)} = q_{o(i,j,k-1\rightarrow i,j,k)} \quad \text{(A – 189)}$$

The pressure drop between the centers of grid-blocks $(i, j, k-1)$ and (i, j, k) is equal to the sum of the pressure drops between the block centers and the block boundary between them; that is:

$$\left(p_{o\,i,j,k-1} - p_{o\,i,j,k}\right) = \left(p_{o\,i,j,k-1} - p_{o\,i,j,k-1/2}\right) + \left(p_{o\,i,j,k-1/2} - p_{o\,i,j,k}\right) \quad \text{(A – 190)}$$

Considering the assumptions expressed by Equations (A – 189) and (A – 190) and replacing Equations (A – 187) and (A – 188) with Equation (A – 190), and ensuring compliance with the principle of conservation of mass:

$$\left(\frac{k_{oz}}{B_o \mu_o}\right)_{i,j,k-1/2} = \frac{z_{i,j,k} - z_{i,j,k-1}}{\frac{z_{i,j,k} - z_{i,j,k-1/2}}{\left(\frac{k_{oz}}{B_o \mu_o}\right)_{i,j,k}} + \frac{z_{i,j,k-1/2} - z_{i,j,k-1}}{\left(\frac{k_{oz}}{B_o \mu_o}\right)_{i,j,k-1}}}$$

Adjusting to the grid features results that the transmissibility factor for the regressive interaction of the grid block can be stated as:

$$\left(\frac{k_{oz}}{B_o\mu_o}\right)_{i,j,k-1/2} = \frac{\Delta z_{i,j,k}+\Delta z_{i,j,k-1}}{\frac{\Delta z_{i,j,k}}{\left(\frac{k_{oz}}{B_o\mu_o}\right)_{i,j,k}}+\frac{\Delta z_{i,j,k-1}}{\left(\frac{k_{oz}}{B_o\mu_o}\right)_{i,j,k-1}}} \quad \text{(A – 191)}$$

Similarly for the progressive interaction of the grid block:

$$\left(\frac{k_{oz}}{B_o\mu_o}\right)_{i,j,k+1/2} = \frac{\Delta z_{i,j,k+1}+\Delta z_{i,j,k}}{\frac{\Delta z_{i,j,k+1}}{\left(\frac{k_{oz}}{B_o\mu_o}\right)_{i,j,k+1}}+\frac{\Delta z_{i,j,k}}{\left(\frac{k_{oz}}{B_o\mu_o}\right)_{i,j,k}}} \quad \text{(A – 192)}$$

Annex B. Implementation of Finite Element Method (FEM)

B1.Introduction

The Finite Element Method (FEM) is the most often used computational method to solve engineering problems. In this technique, all the complexities of a problem such as a shape, boundary, and loading conditions stay the same and the results obtained are approximate (Sherif, 2012).

The finite element method is the numerical method selected for solving the geomechanical model (elastoplastic stress-strain relation), which requires the solution to the boundary value problem for partial differential equations. The FEM formulation of the problem results in a system of linear algebraic equations and the method yields approximate values of the unknowns at a discrete number of points over the domain. The strategy to solve the problem consists to divide a large problem into smaller ones considering simpler parts that are called finite elements. The simple equations that model these finite elements are then assembled into a larger system of equations that models the entire problem, using variational methods from the calculus of variations to approximate a solution by minimizing the function itself. This section presents the mathematical development as following the basic concepts of FEM proposed by Gockenback (2006), Alberty, Carstensen & Funken (1999), and Alberty, Carstensen, Funken, & Klose (2002).

Any finite element analysis has the following main steps:

- Discretization of the domain: division of the problem domain into finite elements defining a set of elements connected at nodes.
- Element formulation: development of equations for elements.
- Assemble the global system, $\boldsymbol{K}\mathbf{u} = \mathbf{f}$: obtaining the equations of the entire system from the equations of individual elements.
- Boundary conditions: Modify the global system by imposing natural and essential boundary conditions.
- The solution of the system: Solve the global systems and obtain the global displacements, $\mathbf{u}$.
- Post-processing: determining quantities of interest, such as stresses and strains at the nodes for each element, and obtaining visualizations

B2.Discretization of the domain

The discretization of the domain is the first step in finite element analysis that involves the partition of the problem domain or physical model into smaller pieces known as finite elements. This is equivalent

to replacing the domain with an infinite number of degrees of freedom with a system having a finite number of degrees of freedom.

B2.1.Mesh generation

The main purpose of meshing is to make the problem solvable using finite elements. By meshing, the domain is divided into pieces, each piece represents an element, and the element is the basis of the integration that affects directly the accuracy of the solution. So, mesh generation is the process of determining the element and nodal connectivity from a physical model to finite elements. Nodal connectivity is specified by a matrix that contains the coordinates of each node relative to the origin, whereas element connectivity states how the elements are connected and are specified by a matrix with the node identification in each element.

The physical model selected for the fluid flow model has a cylindrical geometry. However, for the geomechanical model, the cylindrical geometry is reduced by a quarter of its original size looking for computational efficiency. Figure (B – 1) presents the physical model in 2D and 3D, which is stated as a quarter of the cylindrical geometry.

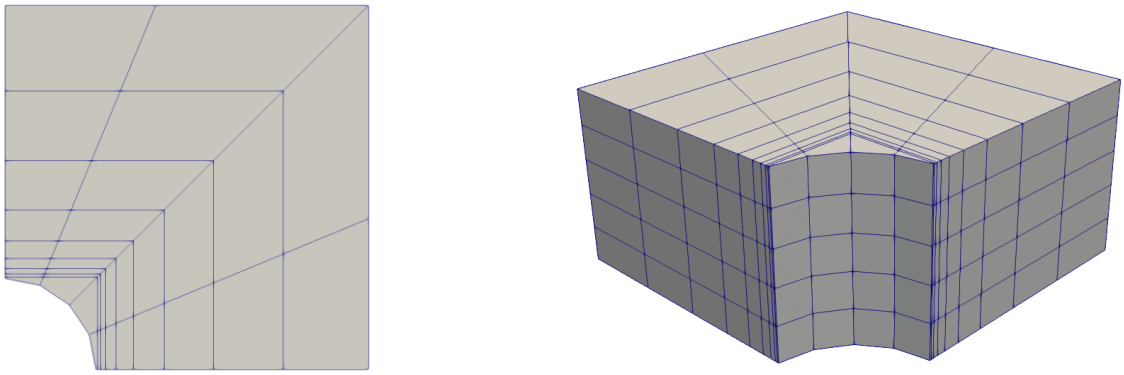

a. b.

Figure B – 1. Physical model. a) Mesh in 2D with the wellbore. b) Mesh in 3D with the wellbore.

B2.2.Element characteristics

The finite element mesh must meet certain conditions to satisfy the interpolation and approximation properties. Ω is a bounded and connected domain of $\mathbb{R}^n, n \epsilon \{2,3\}$, with polyhedral boundary Γ, and $\mathcal{T}_h$ is triangularization of $\overline{\Omega}$. More precisely, $\mathcal{T}_h$ is a finite family of polygons, usually triangles or quadrilaterals (in $\mathbb{R}^2$) or tetrahedral or other (in), such that,

i) $\overline{\Omega} = \cup_{K \epsilon \mathcal{T}_h} K; \mathbb{R}^3$

ii) $\overset{\circ}{K_i} \neq 0 \ \forall K \epsilon \mathcal{T}_h;$

iii) $\overset{\circ}{K_i} \cap \overset{\circ}{K_j} = \emptyset \quad \forall K_i, K_j \epsilon \mathcal{T}_h, \quad K_i \neq K_j;$

iv) If $F = K_i \cap K_j, K_i, K_j \epsilon \mathcal{T}_h, \quad K_i \neq K_j$, then F is a common face, a common side, or a common vertex of K_i and K_j;

v) diam $(K) =: h_K < h \quad \forall K \epsilon \mathcal{T}_h.$

Also, to each $\mathcal{T}_h$ a fixed reference element $\widehat{K}$ is associated, which can or cannot belong to $\mathcal{T}_h$, and a family of affine mappings $\{T_K\}_{K\,\epsilon\,\mathcal{T}_h}$ such that,

i) $T_K: \mathbb{R}^n \rightarrow \mathbb{R}^n$
ii) $K = T_K(\widehat{K}) \quad \forall K\,\epsilon\,\mathcal{T}_h.$

The reference element $\widehat{K}$ is an 8-node hexahedron or 8Hex. A hexahedron is a polyhedron with six faces, eight corners, and twelve edges or sides. This element is often referred to as brick in the FEM literature. Figure B – 2 presents the selected reference element, $\widehat{K}$, which is an 8-node hexahedron in natural coordinates, where the red numbers correspond to the nodes that are locally numbered 1, 2…, 8, to guarantee a positive volume (or, more precisely, a positive Jacobian determinant at every point); and the black numbers correspond to the location in natural coordinates.

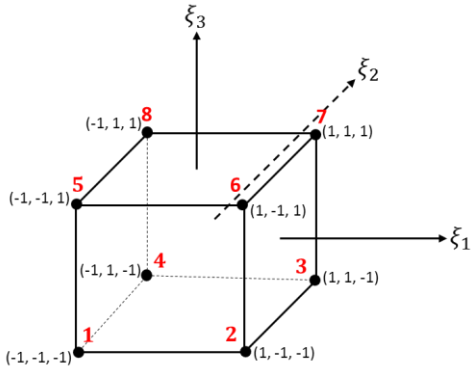

Figure B – 2. Reference element $\widehat{K}$ (8-node hexahedron).

B3.Variational formulation

The variational formulation corresponds to finding a weak form for the value boundary problem to solve. To develop the finite element method, the partial differential equations must be restated in an integral form called the weak form that is corresponding to the differential equation or strong form. The weak form means, that instead of solving a differential equation, an integral function is solved. The integral function implicitly contains the differential equations; however, it is easier to solve an integral function than to solve a differential function. The differential equation of the system poses conditions that must be satisfied by the solution (hence called strong form), whereas, the integral equation states that those conditions need to be satisfied in an average sense (hence weak form). Otherwise, the solution for the strong form is difficult to find because of the conditions that must be met while the weak form reduces the conditions to satisfy to get the solution.

In this section for the geomechanical model (stress-strain relation), the weak form is obtained as a reduced form of the differential equation (strong form) to relax the requirements on solutions to a certain extent.

B3.1.Strong form

The strong form is the conventional differential equation of the physical problem with no mathematical manipulation. The strong form imposes continuity and differentiability requirements on the potential solutions to the equation. In another way, the strong form of the governing equations along with boundary conditions states the conditions at every point over a domain that a solution must satisfy.

Consider the boundary value problem:

$$\text{div}\,\boldsymbol{\sigma} = -\mathbf{f}, \qquad \text{in } \Omega, \qquad \boldsymbol{\sigma} = \mathbb{C}\,\boldsymbol{\epsilon}(\mathbf{u}), \qquad \text{in } \Omega,$$

$$\boldsymbol{\epsilon}(\mathbf{u}) = \frac{1}{2}(\nabla\mathbf{u} + (\nabla\mathbf{u})^T) \tag{B – 1}$$

where $\Omega \subset \mathbb{R}^3$, $\boldsymbol{\sigma}$ is the stress tensor for the tridimensional space, $\mathbb{C}$ is the elasticity operator given by Hooke's law that is,

$$\mathbb{C}\,\boldsymbol{\epsilon}(\mathbf{u}) := \lambda tr\big(\boldsymbol{\epsilon}(\mathbf{u})\big)\boldsymbol{I} + 2G\boldsymbol{\epsilon}(\mathbf{u})$$

where $\boldsymbol{I}$ is the identity matrix, $tr(\cdot)$ is the matrix trace, G and λ are the Lamé parameters.

The features of the boundary value problem require some kind of boundary conditions. Said conditions are established according to the application of the model. In this case, the well-known symmetric boundary conditions are imposed, which are described below. Figure B – 3 presents the symmetric boundary conditions on the quarter cylinder defining each side.

Being Ω the subset of $\mathbb{R}^3$ described by Figure B – 3 whose boundary $\Gamma = \partial\Omega = \Gamma_E \cup \Gamma_W \cup \Gamma_N \cup \Gamma_S \cup \Gamma_T \cup \Gamma_B \cup \Gamma_{W_b}$ with Γ_E, Γ_W, Γ_N, Γ_S, Γ_T and Γ_B that are the boundaries at the east, west, north, south, top, and bottom side respectively, and Γ_{W_b} is the boundary at the wellbore.

For this domain, the symmetric boundary conditions can be stated as:

$$\mathrm{u}_x = 0 \quad \left(\frac{\partial \mathrm{u}_x}{\partial y} + \frac{\partial \mathrm{u}_y}{\partial x}\right) = 0, \quad \left(\frac{\partial \mathrm{u}_x}{\partial z} + \frac{\partial \mathrm{u}_z}{\partial x}\right) = 0, \quad on\ \Gamma_W$$

$$\mathrm{u}_y = 0 \quad \left(\frac{\partial \mathrm{u}_x}{\partial y} + \frac{\partial \mathrm{u}_y}{\partial x}\right) = 0, \quad \left(\frac{\partial \mathrm{u}_y}{\partial z} + \frac{\partial \mathrm{u}_z}{\partial x}\right) = 0, \quad on\ \Gamma_S$$

$$\mathrm{u}_z = 0 \quad \left(\frac{\partial \mathrm{u}_x}{\partial z} + \frac{\partial \mathrm{u}_z}{\partial x}\right) = 0, \quad \left(\frac{\partial \mathrm{u}_y}{\partial z} + \frac{\partial \mathrm{u}_z}{\partial y}\right) = 0, \quad on\ \Gamma_B$$

$$\sigma\,\mathbf{n} = \boldsymbol{\sigma_H} \quad on\ \Gamma_E$$

$$\sigma\,\mathbf{n} = \boldsymbol{\sigma_h} \quad on\ \Gamma_N$$

$$\sigma\,\mathbf{n} = \boldsymbol{\sigma_v} \quad on\ \Gamma_T$$

$$\sigma\,\mathbf{n} = \boldsymbol{p_{wf}} \;\; on\; \Gamma_{W_b} \qquad (B-2)$$

where **n** is the normal unit vector in each face.

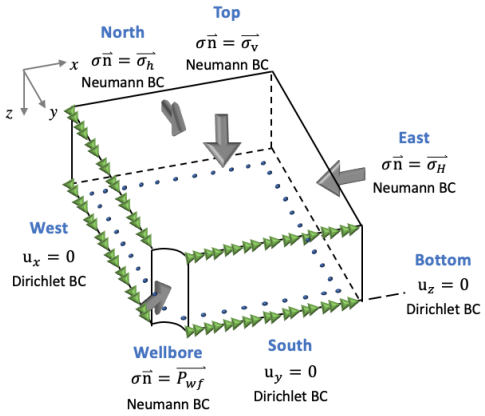

a.

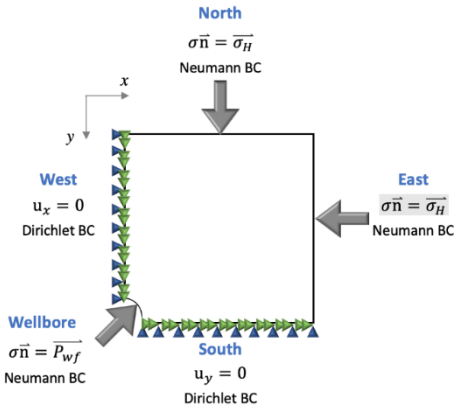

b.

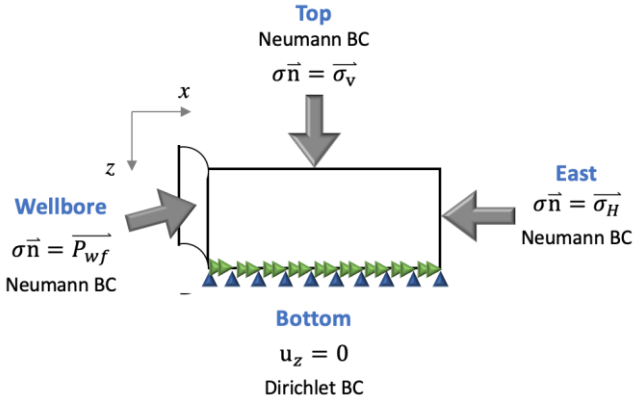

c.

Figure B – 3. Boundary conditions are imposed on the quarter cylinder. a) Sketch of the 3D geometry. b) Sketch of the 2D geometry, plane xy, and c) Sketch of the 2D geometry, plane xz.

B3.2.Weak form

The weak form is an alternate representation of the differential equation and is the basis of the finite element method. The weak form states the conditions that the solution must satisfy in an integral sense.

The symmetric boundary conditions do not allow vector variational formulation for the boundary value problem presented by Equation (B – 1). Equations (B – 2) include the Dirichlet- and Neumann boundary conditions in a general way. This happened because the boundaries cannot be separated as only Dirichlet boundaries or only Neumann boundaries. So, the solution strategy consists to divide the variational formulation into parts in such a way that there is a scalar variational formulation for each direction and thus applying the specific boundary conditions for each direction.

The strong form is expanded in three directions in Cartesian coordinates and applying stress symmetry, the strong form consists to find the scalar fields u_1, u_2 and u_3,

$$\sigma_{ij} = 2G\left(\frac{\partial \mathrm{u}_i}{\partial x_j} + \frac{\partial \mathrm{u}_j}{\partial x_i}\right) + \lambda\delta_{ij}\sum_{k,k}\frac{\partial \mathrm{u}_k}{\partial x_k},\ k = 1,2,3 \quad \text{in } \Omega$$

$$\frac{\partial \sigma_{xx}}{\partial x} + \frac{\partial \sigma_{xy}}{\partial y} + \frac{\partial \sigma_{xz}}{\partial z} = 0, \qquad \text{in } \Omega$$

$$\frac{\partial \sigma_{xy}}{\partial x} + \frac{\partial \sigma_{yy}}{\partial y} + \frac{\partial \sigma_{yz}}{\partial z} = 0, \qquad \text{in } \Omega$$

$$\frac{\partial \sigma_{xz}}{\partial x} + \frac{\partial \sigma_{yz}}{\partial y} + \frac{\partial \sigma_{zz}}{\partial z} = 0, \qquad \text{in } \Omega \qquad \text{(B – 3)}$$

Remark.

In the general case, the stress tensor is described as:

$$\sigma_{ij} = \sum_{kl}\mathbb{C}_{ijkl}\boldsymbol{\epsilon}(\mathbf{u})_{kl} \qquad \text{(B – 4)}$$

where $\mathbb{C}$ is a fourth-order elasticity tensor that is assumed to satisfy the symmetry conditions as:

$$\mathbb{C}_{ijkl} = \mathbb{C}_{ijlk}, \qquad i,j,k,l = 1,2,3$$

$$\mathbb{C}_{ijkl} = \mathbb{C}_{jilk}, \qquad i,j,k,l = 1,2,3$$

$$\mathbb{C}_{ijkl} = \mathbb{C}_{klij} \qquad i,j,k,l = 1,2,3$$

The variational formulation or weak form for this problem is obtained by multiplying Equation (B – 3) by the test functions v_x, v_y, and v_z, and using integration by parts over Ω:

$$\int_\Omega \sigma_{xx}\frac{\partial \mathrm{v}_x}{\partial x} + \int_\Omega \sigma_{xy}\frac{\partial \mathrm{v}_x}{\partial y} + \int_\Omega \sigma_{xz}\frac{\partial \mathrm{v}_x}{\partial z} = \int_\Gamma \left(\gamma_0(\mathrm{v}_x)\gamma_0(\sigma_{xx})n_x + \gamma_0(\mathrm{v}_x)\gamma_0\left(\sigma_{xy}\right)n_y + \gamma_0(\mathrm{v}_x)\gamma_0(\sigma_{xz})n_z\right)$$

$$\int_\Omega \sigma_{xy}\frac{\partial \mathrm{v}}{\partial x} + \int_\Omega \sigma_{yy}\frac{\partial \mathrm{v}_y}{\partial y} + \int_\Omega \sigma_{yz}\frac{\partial \mathrm{v}}{\partial z} = \int_\Gamma \left(\gamma_0\left(\mathrm{v}_y\right)\gamma_0\left(\sigma_{xy}\right)n_x + \gamma_0\left(\mathrm{v}_y\right)\gamma_0\left(\sigma_{yy}\right)n_y + \gamma_0\left(\mathrm{v}_y\right)\gamma_0\left(\sigma_{yz}\right)n_z\right)$$

$$\int_\Omega \sigma_{xz}\frac{\partial \mathrm{v}_z}{\partial x} + \int_\Omega \sigma_{yz}\frac{\partial \mathrm{v}_z}{\partial y} + \int_\Omega \sigma_{zz}\frac{\partial \mathrm{v}_z}{\partial z} = \int_\Gamma \left(\gamma_0(\mathrm{v}_z)\gamma_0(\sigma_{xz})n_x + \gamma_0(\mathrm{v}_z)\gamma_0\left(\sigma_{yz}\right)n_y + \gamma_0(\mathrm{v}_z)\gamma_0(\sigma_{zz})n_z\right) \qquad \text{(B – 5)}$$

The right side of the equation in x direction can be rewritten as:

$$\sum_l \int_{\Gamma_l}\left(\gamma_0(\mathrm{v}_x)\gamma_0(\sigma_{xx})n_x + \gamma_0(\mathrm{v}_x)\gamma_0\left(\sigma_{xy}\right)n_y + \gamma_0(\mathrm{v}_x)\gamma_0(\sigma_{xz})n_z\right) \qquad \text{(B – 6)}$$

where:

$$l = E, W, N, S, T, B, W_b$$

For each boundary condition:

$$\int_{\Gamma_W}\left(\gamma_0(\mathrm{v}_x)\gamma_0(\sigma_{xx})n_x+\gamma_0(\mathrm{v}_x)\gamma_0\left(\sigma_{xy}\right)n_y+\gamma_0(\mathrm{v}_x)\gamma_0(\sigma_{xz})n_z\right)=\int_{\Gamma_W}(\gamma_0(\mathrm{v}_x)\gamma_0(\sigma_{xx})n_x)=0$$

$$\int_{\Gamma_S}\left(\gamma_0(\mathrm{v}_x)\gamma_0(\sigma_{xx})n_x+\gamma_0(\mathrm{v}_x)\gamma_0\left(\sigma_{xy}\right)n_y+\gamma_0(\mathrm{v}_x)\gamma_0(\sigma_{xz})n_z\right)=\int_{\Gamma_S}\left(\gamma_0(\mathrm{v}_x)\gamma_0\left(\sigma_{xy}\right)n_y\right)=0$$

$$\int_{\Gamma_B}\left(\gamma_0(\mathrm{v}_x)\gamma_0(\sigma_{xx})n_x+\gamma_0(\mathrm{v}_x)\gamma_0\left(\sigma_{xy}\right)n_y+\gamma_0(\mathrm{v}_x)\gamma_0(\sigma_{xz})n_z\right)=\int_{\Gamma_B}(\gamma_0(\mathrm{v}_x)\gamma_0(\sigma_{xz})n_z)=0$$

$$\int_{\Gamma_E}\left(\gamma_0(\mathrm{v}_x)\gamma_0(\sigma_{xx})n_x+\gamma_0(\mathrm{v}_x)\gamma_0\left(\sigma_{xy}\right)n_y+\gamma_0(\mathrm{v}_x)\gamma_0(\sigma_{xz})n_z\right)=\int_{\Gamma_E}\left(\gamma_0(\mathrm{v}_x)\sigma_{H_x}\right)=0$$

$$\int_{\Gamma_N}\left(\gamma_0(\mathrm{v}_x)\gamma_0(\sigma_{xx})n_x+\gamma_0(\mathrm{v}_x)\gamma_0\left(\sigma_{xy}\right)n_y+\gamma_0(\mathrm{v}_x)\gamma_0(\sigma_{xz})n_z\right)=\int_{\Gamma_N}\left(\gamma_0(\mathrm{v}_x)\sigma_{h_x}\right)=0$$

$$\int_{\Gamma_T}\left(\gamma_0(\mathrm{v}_x)\gamma_0(\sigma_{xx})n_x+\gamma_0(\mathrm{v}_x)\gamma_0\left(\sigma_{xy}\right)n_y+\gamma_0(\mathrm{v}_x)\gamma_0(\sigma_{xz})n_z\right)=\int_{\Gamma_T}\left(\gamma_0(\mathrm{v}_x)\sigma_{V_x}\right)=0$$

$$\int_{\Gamma_{W_b}}\left(\gamma_0(\mathrm{v}_x)\gamma_0(\sigma_{xx})n_x+\gamma_0(\mathrm{v}_x)\gamma_0\left(\sigma_{xy}\right)n_y+\gamma_0(\mathrm{v}_x)\gamma_0(\sigma_{xz})n_z\right)=\int_{\Gamma_{W_b}}\left(\gamma_0(\mathrm{v}_x)p_{wf_x}\right) \quad \text{(B – 7)}$$

Integrating the solution, Equation (B – 4) would be:

$$\sum_l\int_{\Gamma_l}\left(\gamma_0(\mathrm{v}_x)\gamma_0(\sigma_{xx})n_x+\gamma_0(\mathrm{v}_x)\gamma_0\left(\sigma_{xy}\right)n_y+\gamma_0(\mathrm{v}_x)\gamma_0(\sigma_{xz})n_z\right)=\int_{\Gamma_E}\left(\gamma_0(\mathrm{v}_x)\sigma_{H_x}\right)+$$
$$\int_{\Gamma_N}\left(\gamma_0(\mathrm{v}_x)\sigma_{h_x}\right)+\int_{\Gamma_T}\left(\gamma_0(\mathrm{v}_x)\sigma_{V_x}\right)+\int_{\Gamma_{W_b}}\left(\gamma_0(\mathrm{v}_x)p_{wf_x}\right) \quad \text{(B – 8)}$$

Similarly,

$$\sum_l\int_{\Gamma_l}\left(\gamma_0(\mathrm{v}_y)\gamma_0(\sigma_{xy})n_x+\gamma_0(\mathrm{v}_y)\gamma_0(\sigma_{yy})n_y+\gamma_0(\mathrm{v})\gamma_0(\sigma_{yz})n_z\right)=\int_{\Gamma_E}\left(\gamma_0(\mathrm{v}_y)\sigma_{H_y}\right)+$$
$$\int_{\Gamma_N}\left(\gamma_0(\mathrm{v}_y)\sigma_{h_y}\right)+\int_{\Gamma_T}\left(\gamma_0(\mathrm{v}_y)\sigma_{V_y}\right)+\int_{\Gamma_{W_b}}\left(\gamma_0(\mathrm{v}_y)p_{wf_y}\right) \quad \text{(B – 9)}$$

$$\sum_l\int_{\Gamma_l}\left(\gamma_0(\mathrm{v}_z)\gamma_0(\sigma_{xz})n_x+\gamma_0(\mathrm{v}_z)\gamma_0(\sigma_{yz})n_y+\gamma_0(\mathrm{v}_z)\gamma_0(\sigma_{zz})n_z\right)=\int_{\Gamma_E}\left(\gamma_0(\mathrm{v}_z)\sigma_{H_z}\right)+$$
$$\int_{\Gamma_N}\left(\gamma_0(\mathrm{v}_z)\sigma_{h_z}\right)+\int_{\Gamma_T}\left(\gamma_0(\mathrm{v}_z)\sigma_{V_z}\right)+\int_{\Gamma_{W_b}}\left(\gamma_0(\mathrm{v}_z)p_{wf_z}\right) \quad \text{(B – 10)}$$

$$\int_\Omega\sigma_{xx}\frac{\partial\mathrm{v}_x}{\partial x}+\int_\Omega\sigma_{xy}\frac{\partial\mathrm{v}_x}{\partial y}+\int_\Omega\sigma_{xz}\frac{\partial\mathrm{v}_x}{\partial z}=\int_{\Gamma_E}\left(\gamma_0(\mathrm{v}_x)\sigma_{H_x}\right)+\int_{\Gamma_N}\left(\gamma_0(\mathrm{v}_x)\sigma_{h_x}\right)+\int_{\Gamma_T}\left(\gamma_0(\mathrm{v}_x)\sigma_{V_x}\right)+$$
$$\int_{\Gamma_{W_b}}\left(\gamma_0(\mathrm{v}_x)p_{wf_x}\right) \quad \text{(B – 11)}$$

$$\int_\Omega\sigma_{xy}\frac{\partial\mathrm{v}_y}{\partial x}+\int_\Omega\sigma_{yy}\frac{\partial\mathrm{v}_y}{\partial y}+\int_\Omega\sigma_{yz}\frac{\partial\mathrm{v}_y}{\partial z}=\int_{\Gamma_E}\left(\gamma_0(\mathrm{v}_y)\sigma_{H_y}\right)+\int_{\Gamma_N}\left(\gamma_0(\mathrm{v}_y)\sigma_{h_y}\right)+\int_{\Gamma_T}\left(\gamma_0(\mathrm{v}_y)\sigma_{V_y}\right)+$$
$$\int_{\Gamma_{W_b}}\left(\gamma_0(\mathrm{v}_y)p_{wf_y}\right) \quad \text{(B – 12)}$$

$$\int_{\Omega} \sigma_{xz} \frac{\partial \mathrm{v}_z}{\partial x} + \int_{\Omega} \sigma_{yz} \frac{\partial \mathrm{v}_z}{\partial y} + \int_{\Omega} \sigma_{zz} \frac{\partial \mathrm{v}_z}{\partial z} = \int_{\Gamma_E} \left(\gamma_0(\mathrm{v}_z)\sigma_{H_z}\right) + \int_{\Gamma_N} \left(\gamma_0(\mathrm{v}_z)\sigma_{h_z}\right) + \int_{\Gamma_T} \left(\gamma_0(\mathrm{v}_z)\sigma_{V_z}\right) + \int_{\Gamma_{W_b}} \left(\gamma_0(\mathrm{v}_z)p_{wf_z}\right) \quad \text{(B – 13)}$$

Adding these equations on each side:

$$\int_{\Omega} \sigma_{xx} \frac{\partial \mathrm{v}_x}{\partial x} + \int_{\Omega} \sigma_{xy} \frac{\partial \mathrm{v}_x}{\partial y} + \int_{\Omega} \sigma_{xz} \frac{\partial \mathrm{v}_x}{\partial z} + \int_{\Omega} \sigma_{xy} \frac{\partial \mathrm{v}_y}{\partial x} + \int_{\Omega} \sigma_{yy} \frac{\partial \mathrm{v}_y}{\partial y} + \int_{\Omega} \sigma_{yz} \frac{\partial \mathrm{v}_y}{\partial z} + \int_{\Omega} \sigma_{xz} \frac{\partial \mathrm{v}_z}{\partial x} + \int_{\Omega} \sigma_{yz} \frac{\partial \mathrm{v}_z}{\partial y} + \int_{\Omega} \sigma_{zz} \frac{\partial \mathrm{v}_z}{\partial z} = \int_{\Gamma_E} \left(\gamma_0(\mathrm{v}_x)\sigma_{H_x}\right) + \int_{\Gamma_N} \left(\gamma_0(\mathrm{v}_x)\sigma_{h_x}\right) + \int_{\Gamma_T} \left(\gamma_0(\mathrm{v}_x)\sigma_{V_x}\right) + \int_{\Gamma_{W_b}} \left(\gamma_0(\mathrm{v}_x)p_{wf_x}\right) + \int_{\Gamma_E} \left(\gamma_0(\mathrm{v}_y)\sigma_{H_y}\right) + \int_{\Gamma_N} \left(\gamma_0(\mathrm{v}_y)\sigma_{h_y}\right) + \int_{\Gamma_T} \left(\gamma_0(\mathrm{v}_y)\sigma_{V_y}\right) + \int_{\Gamma_{W_b}} \left(\gamma_0(\mathrm{v}_y)p_{wf_y}\right) + \int_{\Gamma_E} \left(\gamma_0(\mathrm{v}_z)\sigma_{H_z}\right) + \int_{\Gamma_N} \left(\gamma_0(\mathrm{v}_z)\sigma_{h_z}\right) + \int_{\Gamma_T} \left(\gamma_0(\mathrm{v}_z)\sigma_{V_z}\right) + \int_{\Gamma_{W_b}} \left(\gamma_0(\mathrm{v}_z)p_{wf_z}\right) \quad \text{(B – 14)}$$

Equation (B – 14) can be grouped as follows:

$$\int_{\Omega} \boldsymbol{\sigma} : \boldsymbol{\epsilon}(\mathbf{v}) = \int_{\Gamma_E} \mathbf{v} \cdot \boldsymbol{\sigma_H} + \int_{\Gamma_N} \mathbf{v} \cdot \boldsymbol{\sigma_h} + \int_{\Gamma_T} \mathbf{v} \cdot \boldsymbol{\sigma_V} + \int_{\Gamma_{Wb}} \mathbf{v} \cdot \boldsymbol{p_{wf}} \quad \text{(B –15)}$$

The variational formulation for the problem posed by Equation (B – 2) is reduced to a weak form:

Find $\mathbf{w} \in \mathbf{H}$ such that,

$$a(\mathbf{w}, \mathbf{v}) = F(\mathbf{v}), \quad \forall \mathbf{v} \in \mathbf{H} \quad \text{(B – 16)}$$

where $\mathbf{H} := \{\mathbf{v} \in [H^1(\Omega)]^3 :\}$ with the corresponding norm $\|\cdot\|_1$, $a := \mathbf{H} \times \mathbf{H} \to \mathbb{R}$ is the symmetric bilinear form defined by:

$$a(\mathbf{w}, \mathbf{v}) := \int_{\Omega} \mathbb{C}\, \boldsymbol{\epsilon}(\mathbf{w}) : \boldsymbol{\epsilon}(\mathbf{v}) \quad \forall \mathbf{w}, \mathbf{v} \in \mathbf{H},$$

and $F := \mathbf{H} \to \mathbb{R}$ is the linear functional given by:

$$F(\mathbf{v}) := \int_{\Gamma_E} \mathbf{v} \cdot \boldsymbol{\sigma_H} + \int_{\Gamma_S} \mathbf{v} \cdot \boldsymbol{\sigma_h} \int_{\Gamma_T} \mathbf{v} \cdot \boldsymbol{\sigma_V} + \int_{\Gamma_{Wb}} \mathbf{v} \cdot \boldsymbol{p_{wf}} \quad \forall \mathbf{v} \in \mathbf{H}$$

Theorem. The variational problem stated in Equation (B – 7) has a solution and this solution is unique.

B4. Discrete formulation

The discrete formulation assembles the global system to obtain the approximation for the solution of the variational problem, obtaining the equations of the entire system from the equations of each element and defining the shape functions.

For implementation, the value problem presented in Equation (B – 7) is discretized using the standard Galerkin method and requires the construction of a finite-dimensional subspace of **H**, i.e., space $H^1(\boldsymbol{\Omega})$ is replaced by the finite-dimensional subspace **H**. For the general form, the finite element discretization can be expressed as:

$$\int_{\Omega} \boldsymbol{\epsilon}(\boldsymbol{\eta_k}) : \mathbb{C}\, \boldsymbol{\epsilon}(\mathbf{u}_h) dx = \int_{\Omega} \mathbf{f} \cdot \boldsymbol{\eta_k}\, dx + \int_{\Gamma_N} \mathbf{g} \cdot \boldsymbol{\eta_k}\, dS \qquad (k = 1, \dots, N_{\mathrm{e}}) \qquad \text{(B – 17)}$$

The approximation for the solution of the variational problem stated in Equation (B – 16) requires similar construction of a finite-dimensional subspace of **H** and, the mesh displayed in Figure B – 1 as a mesh $\mathcal{M}_h$ of 8-node hexahedrons defined on $\boldsymbol{\Omega}$ and composed by N_{e} elements: $m_1, m_2, \dots, m_{N_{\mathrm{e}}}$ and the collection of vertices: $\{\boldsymbol{x}_i\}_{i=1}^{N_{\mathrm{v}}} \in \mathbb{R}^3$, where N_{v} is the vertice number. Additionally, for the set of vertices on $\mathcal{M}_h$, a subset of free nodes is defined as $\Lambda = \left\{\boldsymbol{x}_{\mathrm{f}_1}, \boldsymbol{x}_{\mathrm{f}_2}, \dots, \boldsymbol{x}_{\mathrm{f}_{N_{\mathrm{f}}}}\right\}$, where a free node is a vertex that does not lies in the frontier Γ_D of $\boldsymbol{\Omega}$ and N_{f} is the free node number.

B4.1.The basic functions

It is well known that a finite set of real numbers with one-to-one correspondence with the set of nodes of the mesh, $\mathcal{M}_h$, determinates a unique function defined piece-wise, continuous, and trilinear on $\mathcal{M}_h$. The space of these functions can be denoted as $T_h^{(1)}$ and a finite-dimensional subspace can be defined as $\mathbf{v}_h \subset H^1(\Omega)$:

$$\mathbf{v}_h \coloneqq \left\{\mathrm{v} \in T_h^{(1)}\right\} \qquad \text{(B – 18)}$$

which dimension is $\#\Lambda = N_f$ and has a nodal basis $\left\{\boldsymbol{\eta}_1, \boldsymbol{\eta}_2, \dots, \boldsymbol{\eta}_{N_{\mathrm{f}}}\right\}$, where:

$$\boldsymbol{\eta}_i(\boldsymbol{x}_j) = \begin{cases} 1, & i = j \\ 0, & i \neq j \end{cases}, \ \forall\, \boldsymbol{x}_j \in \Lambda$$

For this space, its vector version can be generated as:

$$\mathbf{v}_h = \left\{\mathbf{v} = \begin{pmatrix} \mathrm{v}_1 \\ \mathrm{v}_2 \\ \mathrm{v}_3 \end{pmatrix} : \mathrm{v}_1, \mathrm{v}_3, \mathrm{v}_3 \in \mathbf{v}_h\right\} \subset \mathbf{H} \qquad \text{(B – 19)}$$

which basis is $\left\{\boldsymbol{\eta}_1, \boldsymbol{\eta}_2, \dots, \boldsymbol{\eta}_{3N_{\mathrm{f}}}\right\}$ and each component can be stated as:

$$\boldsymbol{\eta}_i = \begin{pmatrix} \eta_i \\ 0 \\ 0 \end{pmatrix}, \qquad \boldsymbol{\eta}_{N_{\mathrm{f}}+i} = \begin{pmatrix} 0 \\ \eta_i \\ 0 \end{pmatrix}, \qquad \boldsymbol{\eta}_{2N_{\mathrm{f}}+i} = \begin{pmatrix} 0 \\ 0 \\ \eta_i \end{pmatrix}, \qquad i = 1,2, \dots, N_{\mathrm{f}}$$

The variational problem that is restated in Equation (B – 14) can be considered a Galerkin problem:

Find $\mathbf{u}_h \in \mathbf{v}_h$ such that,

$$a(\mathbf{u}_h, \mathbf{v}) = F(\mathbf{v}), \ \ \forall \in \ \mathbf{v}_h \tag{B – 20}$$

In Equation (B – 20), the discrete displacement vector $\mathbf{u}_h$, since $\mathbf{u}_h \in \ \mathbf{v}_h$, can be written as:

$$\mathbf{u}_h = \ \sum_{l=1}^{N_\mathrm{e}} U_l \boldsymbol{\eta}_l \tag{B – 21}$$

And thus Equation ((B – 1) yields the linear system of equations:

$$\sum_{l=1}^{N_\mathrm{f}} \left(\int_\Omega \boldsymbol{\epsilon}(\boldsymbol{\eta}_k) : \mathbb{C}\boldsymbol{\epsilon}(\boldsymbol{\eta}_l) dx \right) U_l = \int_{\boldsymbol{\Omega}} \mathbf{f} \cdot \boldsymbol{\eta}_k \, dx + \int_{\boldsymbol{\Gamma_N}} \mathbf{g} \cdot \boldsymbol{\eta}_k \, dS \quad (k = 1, \dots, N_\mathrm{e}) \tag{B – 22}$$

The coefficient matrix (global stiffness matrix) $K = (K_{kl}) \in \mathbb{R}^{N_\mathrm{e} \times N_\mathrm{e}}$ and the right-side $F = (F_k)$ are defined as:

$$\mathrm{K}_{k\ell} = \int_\Omega \epsilon\,(\boldsymbol{\eta}_k) \mathbb{C}\boldsymbol{\epsilon}(\boldsymbol{\eta}_l) dx$$

$$\int_{\boldsymbol{\Omega}} \mathbf{f} \cdot \boldsymbol{\eta}_k \, dx + \int_{\boldsymbol{\Gamma_N}} \mathbf{g} \cdot \boldsymbol{\eta}_k \, dS \tag{B – 23}$$

B4.2.The shape functions

As mentioned above, the shape functions relate the field variable at any point within the element to the field variables at nodes. Galerkin's method is usually to choose $\eta_i \in \ \mathbb{P}_n^m$, which is the space of the n −variate polynomials of degree at most m with dimension defined as:

$$d = \binom{n+m}{m}$$

However, in the case of a mesh of 8-node hexahedrons, this kind of function is not straightforward to determine a base for the functions defined piece-wise, continuous, and trilinear. A common practice, in this case, is to describe the shape functions in a reference element, $\widehat{K}$, in which, a correspondence with each general hexahedron can be established. For this purpose, let $\mathcal{F}$ be a mapping between a reference cube $\widehat{K}$ and a hexahedron $m_k \in \ \mathcal{M}_h$.

$$\mathcal{F} : \ \widehat{K} \longrightarrow \ m_k$$

$$\mathbf{u} = (\ \xi_1, \xi_2, \xi_3) \ \longrightarrow \boldsymbol{x} = (x, y, z)$$

$$x = a_1 + a_2\xi_1 + a_3\xi_2 + a_4\xi_3 + a_5\xi_1\xi_2 + a_6\xi_1\xi_3 + a_7\xi_2\xi_3 + a_8\xi_1\xi_2\xi_3$$

$$y = b_1 + b_2\xi_1 + b_3\xi_2 + b_4\xi_3 + b_5\xi_1\xi_2 + b_6\xi_1\xi_3 + b_7\xi_2\xi_3 + b_8\xi_1\xi_2\xi_3$$

$$z = c_1 + c_2\xi_1 + c_3\xi_2 + c_4\xi_3 + c_5\xi_1\xi_2 + c_6\xi_1\xi_3 + c_7\xi_2\xi_3 + c_8\xi_1\xi_2\xi_3 \tag{B – 24}$$

Being $\{a_i\}_{i=1}^8$, $\{b_i\}_{i=1}^8$,$\{c_i\}_{i=1}^8 \in \ \mathbb{R}$, $\widehat{K} = [-1,1]^3$ and m_k has the vertices:

$$V_1 = (x_1, y_1, z_1)$$

$$V_2 = (x_2, y_2, z_1)$$

$$V_3 = (x_3, y_3, z_1)$$

$$V_4 = (x_4, y_4, z_1)$$

$$V_5 = (x_1, y_1, z_2)$$

$$V_6 = (x_2, y_2, z_2)$$

$$V_7 = (x_3, y_3, z_2)$$

$$V_8 = (x_4, y_4, z_2) \qquad \text{(B – 25)}$$

These vertices are labeled bottom-up and in a counter-clockwise sense from the minor base, as seen in Figure B – 1.

For $\mathcal{F}$, the next relations can be stated for these vertices:

$$V_1^R = (-1, -1, -1) \longrightarrow V_1 = (x_1, y_1, z_1)$$

$$V_2^R = (1, -1, -1) \longrightarrow V_2 = (x_2, y_2, z_1)$$

$$V_3^R = (1,1, -1) \longrightarrow V_3 = (x_3, y_3, z_1)$$

$$V_4^R = (-1,1, -1) \longrightarrow V_4 = (x_4, y_4, z_1)$$

$$V_5^R = (-1, -1,1) \longrightarrow V_5 = (x_1, y_1, z_2)$$

$$V_6^R = (1, -1,1) \longrightarrow V_6 = (x_2, y_2, z_2)$$

$$V_7^R = (1,1,1) \longrightarrow V_7 = (x_3, y_3, z_2)$$

$$V_8^R = (-1,1,1) \longrightarrow V_8 = (x_4, y_4, z_2) \qquad \text{(B – 26)}$$

These relations yield the next systems of linear equations:

$$\boldsymbol{Ma} = \boldsymbol{x}$$

$$\boldsymbol{Mb} = \boldsymbol{y}$$

$$\boldsymbol{Mc} = \boldsymbol{z} \qquad \text{(B – 27)}$$

where each component can be expressed by:

$$\boldsymbol{M} = \begin{pmatrix} 1 & -1 & -1 & -1 & 1 & 1 & 1 & -1 \\ 1 & 1 & -1 & -1 & -1 & -1 & 1 & 1 \\ 1 & 1 & 1 & -1 & 1 & -1 & -1 & -1 \\ 1 & -1 & 1 & -1 & -1 & 1 & -1 & 1 \\ 1 & -1 & -1 & 1 & 1 & -1 & -1 & 1 \\ 1 & 1 & -1 & 1 & -1 & 1 & -1 & -1 \\ 1 & 1 & 1 & 1 & 1 & 1 & 1 & 1 \\ 1 & -1 & 1 & 1 & -1 & -1 & 1 & -1 \end{pmatrix}$$

$\boldsymbol{a} = (a_1, \dots, a_8)^T$

$\boldsymbol{b} = (b_1, \dots, b_8)^T$

$\boldsymbol{c} = (c_1, \dots, c_8)^T$

$\boldsymbol{x} = (x_1, \dots, x_4, x_1, \dots, x_4)^T$

$\boldsymbol{y} = (y_1, \dots, y_4, y_1, \dots, y_4)^T$

$\boldsymbol{z} = (z_1, z_1, z_1, z_1, z_2, z_2, z_2, z_2)^T$

It can build a set of functions $\gamma_i : \widehat{K} \rightarrow \mathbb{R}$ such that,

$$\gamma_i\left(V_j^R\right) = \begin{cases} 1, & i = j \\ 0, & i \neq j \end{cases} \quad \text{(B – 28)}$$

and it can be set as:

$$\gamma_i(\xi_1, \xi_2, \xi_3) \coloneqq \beta_1^i + \beta_2^i\xi_1 + \beta_3^i\xi_2 + \beta_4^i\xi_3 + \beta_5^i\xi_1\xi_2 + \beta_6^i\xi_1\xi_3 + \beta_7^i\xi_2\xi_3 + \beta_8^i\xi_1\xi_2\xi_3\,, \ \left\{\beta_k^i\right\}_{k=1}^8 \in \mathbb{R} \quad \text{(B – 29)}$$

Imposing the condition stated by Equation (B – 29) for each V_j^R generating the following systems of linear equations:

$$\boldsymbol{M}\boldsymbol{\beta}^i = \boldsymbol{e}_i, \ i = 1, \dots, 8 \quad \text{(B – 30)}$$

where $\boldsymbol{e}_i$ is the canonical vector of $\mathbb{R}^8$ and $\boldsymbol{\beta}^i = \left(\beta_1^i, \dots, \beta_8^i\right)^{\boldsymbol{T}}$.

With the solution of the previous systems, the shape functions are the following:

$$\gamma_1(\xi_1, \xi_2, \xi_3) = \frac{1}{8}(1 - \xi_1 - \xi_2 - \xi_3 + \xi_1\xi_2 + \xi_1\xi_3 + \xi_2\xi_3 - \xi_1\xi_2\xi_3)$$

$$\gamma_2(\xi_1, \xi_2, \xi_3) = \frac{1}{8}(1 + \xi_1 - \xi_2 - \xi_3 - \xi_1\xi_2 - \xi_1\xi_3 + \xi_2\xi_3 + \xi_1\xi_2\xi_3)$$

$$\gamma_3(\xi_1,\xi_2,\xi_3) = \frac{1}{8}(1+\xi_1+\xi_2-\xi_3+\xi_1\xi_2-\xi_1\xi_3-\xi_2\xi_3-\xi_1\xi_2\xi_3)$$

$$\gamma_4(\xi_1,\xi_2,\xi_3) = \frac{1}{8}(1-\xi_1+\xi_2-\xi_3-\xi_1\xi_2+\xi_1\xi_3-\xi_2\xi_3+\xi_1\xi_2\xi_3)$$

$$\gamma_5(\xi_1,\xi_2,\xi_3) = \frac{1}{8}(1-\xi_1-\xi_2+\xi_3+\xi_1\xi_2-\xi_1\xi_3-\xi_2\xi_3+\xi_1\xi_2\xi_3)$$

$$\gamma_6(\xi_1,\xi_2,\xi_3) = \frac{1}{8}(1+\xi_1-\xi_2+\xi_3-\xi_1\xi_2+\xi_1\xi_3-\xi_2\xi_3-\xi_1\xi_2\xi_3)$$

$$\gamma_7(\xi_1,\xi_2,\xi_3) = \frac{1}{8}(1+\xi_1+\xi_2+\xi_3+\xi_1\xi_2+\xi_1\xi_3+\xi_2\xi_3+\xi_1\xi_2\xi_3)$$

$$\gamma_8(\xi_1,\xi_2,\xi_3) = \frac{1}{8}(1-\xi_1+\xi_2+\xi_3-\xi_1\xi_2-\xi_1\xi_3+\xi_2\xi_3-\xi_1\xi_2\xi_3)$$

$$\eta_i = \gamma_i \circ \mathcal{F}^{-1} \qquad \text{(B – 31)}$$

B5. Integration

In a general case, for some integrable function f defined on Ω, it can be stated that,

$$\int_\Omega f = \int_{m_1 \cup \cdots \cup m_{N_e}} f = \sum_k \int_{m_k} f \qquad \text{(B – 32)}$$

In this context, the term $\partial \mathrm{m}_{N_i}$ only refers to the faces of m_{N_i} that have Neumann conditions.

For the matrix **K** (previously described), each of the entries $\mathbf{K}_{ij}$ involves the integration over Ω of the derivatives of $\boldsymbol{\eta_i}$. However, a priori, there is no explicit expression for these functions. To sort out this problem, instead of carrying out each integral $\int_{m_k}$ an equivalent integration $\int_{\widehat{K}}$ can be computed, where $\widehat{K}$ is the reference element described in the previous section. This transformation requires an adequate change of variables and also considers the previous mapping $\mathcal{F}$, then:

$$\mathcal{F}(\mathbf{u}) = \begin{pmatrix} a_1+a_2\xi_1+a_3\xi_2+a_4\xi_3+a_5\xi_1\xi_2+a_6\xi_1\xi_3+a_7\xi_2\xi_3+a_8\xi_1\xi_2\xi_3 \\ b_1+b_2\xi_1+b_3\xi_2+b_4\xi_3+b_5\xi_1\xi_2+b_6\xi_1\xi_3+b_7\xi_2\xi_3+b_8\xi_1\xi_2\xi_3 \\ c_1+c_2\xi_1+c_3\xi_2+c_4\xi_3+c_5\xi_1\xi_2+c_6\xi_1\xi_3+c_7\xi_2\xi_3+c_8\xi_1\xi_2\xi_3 \end{pmatrix} \qquad \text{(B – 33)}$$

The Jacobian for this transformation is the matrix:

$$J(\mathbf{u}) = \mathcal{F}'(\mathbf{u}) = \begin{pmatrix} a_2+a_5\xi_2+a_6\xi_3+a_8\xi_2\xi_3 & a_3+a_5\xi_1+a_7\xi_3+a_8\xi_1\xi_3 & a_4+a_6\xi_1+a_7\xi_2+a_8\xi_1\xi_2 \\ b_2+b_5\xi_2+b_6\xi_3+b_8\xi_2\xi_3 & b_3+b_5\xi_1+b_7\xi_3+b_8\xi_1\xi_3 & b_4+b_6\xi_1+b_7\xi_2+b_8\xi_1\xi_2 \\ c_2+c_5\xi_2+c_6\xi_3+c_8\xi_2\xi_3 & c_3+c_5\xi_1+c_7\xi_3+c_8\xi_1\xi_3 & c_4+c_6\xi_1+c_7\xi_2+c_8\xi_1\xi_2 \end{pmatrix} \qquad \text{(B – 34)}$$

For the transformation:

$\gamma_i(\mathbf{u}) = \boldsymbol{\eta_i}(\mathcal{F}(\mathbf{u}))$

Applying the chain rule:

$\nabla\gamma_i(\mathbf{u}) = \mathcal{F}'(\mathbf{u})^T \nabla\boldsymbol{\eta}_i(\mathcal{F}(\mathbf{u}))$

$\Rightarrow \nabla\boldsymbol{\eta}_i\left(\mathcal{F}(\mathbf{u})\right) = \mathcal{F}'(\mathbf{u})^{-T}\nabla\gamma_i(\mathbf{u})$ (B – 35)

B6.Multi-layer model

The physical model would include various layers or formations with different properties to simulate a CHOPS well. Figure B – 4 (a) presents the physical model for the multi-layer model. This configuration affects the geomechanical model because of the interface between the layer considering that each layer has different petrophysical and mechanical properties. For this reason, the domain changes and is composed of different domains separated by interfaces. Figure B – 4 (b) schematizes the new domain that intends to modify the mathematical model to skate out the geomechanical model with multiple layers.

Being $\boldsymbol{\Omega} \subset \mathbb{R}^3$ in a domain composed of $n+1$ disjoint domains, separated by n interfaces Γ, this is:

$\Omega = \Omega_1 \cup \ldots \cup \Omega_{n+1} \cup \Gamma_1 \cup \ldots \cup \Gamma_n$ (B – 36)

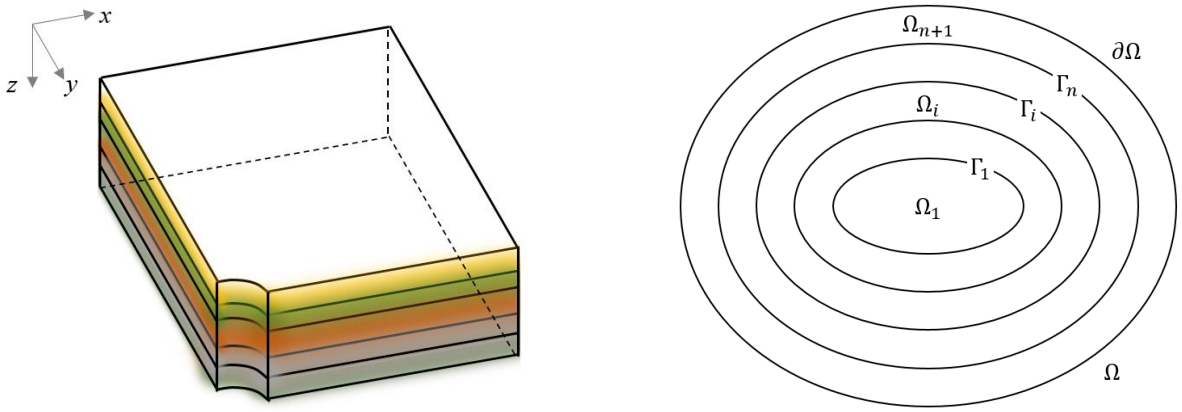

a. b.

Figure B – 4. Model representation for the multi-layer model. a) Physical model. b) Mathematical representation.

The problem to solve is given by the following differential equation:

$\boldsymbol{\sigma} = \mathbb{C}\,\boldsymbol{\epsilon}(\mathbf{u})$ in $\Omega \setminus \Gamma_1 \cup \ldots \cup \Gamma_n$

$\text{div}\,\boldsymbol{\sigma} = -f$ in $\Omega \setminus \Gamma_1 \cup \ldots \cup \Gamma_n$ (B – 37)

with the boundary conditions:

$\mathbf{M}\,\mathbf{u} = \mathrm{w}$ in $\partial\Omega_D$

$\sigma\,\mathbf{n} = g$ in $\partial\Omega_N$

and with the jump conditions:

$[\mathbf{u}\,(\boldsymbol{x})]_{\Gamma_1} = \mathbf{0}, \quad \boldsymbol{x} \in \Gamma_1, i = 1, \dots, n$

where:

$[\mathbf{u}\,(\boldsymbol{x})]_{\Gamma_i} = \mathbf{0}, \quad \mathbf{u}_{i+1}\,(\boldsymbol{x}) - \mathbf{u}_i\,(\boldsymbol{x}),\ i = 1, \dots, n$

and $\mathbb{C}$ remains the elasticity tensor given by:

$\mathbb{C}\,\xi = \lambda(\vec{x})\ tr(\xi)\boldsymbol{I} + 2\,\mu(\vec{x})\,\xi$

where $\lambda(\boldsymbol{x}), \mu(\boldsymbol{x}) : \mathbb{R}^3 \to \mathbb{R}$, with positive functions defined by:

$$\lambda(\boldsymbol{x}) = \begin{cases} \lambda_1(\boldsymbol{x}), & \boldsymbol{x} \in \Omega_1, \\ \vdots & \vdots \\ \lambda_{n+1}(\boldsymbol{x}), & \boldsymbol{x} \in \Omega_{n+1} \end{cases}$$

$$\mu(\boldsymbol{x}) = \begin{cases} \mu_1(\boldsymbol{x}), & \boldsymbol{x} \in \Omega_1, \\ \vdots & \vdots \\ \mu_{n+1}(\boldsymbol{x}), & \boldsymbol{x} \in \Omega_{n+1} \end{cases}$$

B7.Visco-plastic method

If the formation or rock is elastic, the constitutive matrix is therefore constant. If the formation or rock behaves as nonlinear elastic or elasto-plastic, the equivalent constitutive matrix is no longer constant and varies with stress and strain and consequently changes during a finite element analysis. Therefore, a solution strategy is needed to account for this change in material behavior.

The analysis of any boundary value problem must satisfy four basic solution requirements: equilibrium, compatibility, constitutive behavior, and boundary conditions. The nonlinearity given by the constitutive behavior of the material causes the finite element equations to be reduced to the following incremental form:

$$[K]^i\{\Delta u\}^i = \{\Delta f\}^i \qquad \text{(B – 38)}$$

where $[K]^i$ is the incremental global system stiffness matrix, $\{\Delta u\}^i$ is the vector of incremental nodal displacements, $\{\Delta f\}^i$ is the vector of incremental nodal forces or load vector, and i is the increment number.

The solution to the boundary value problem is obtained by applying the change in boundary conditions in a series of increments and for each increment, the global system must be solved. The incremental global stiffness matrix depends on the current stress and strain due to the nonlinear constitutive behavior; hence, it is not constant and varies over an increment. In general, if the solution increments are sufficiently small all solution strategies would give comparable predictions. Nevertheless, as the increment size increases, some solution schemes can result in particularly inaccurate predictions. The final solution is given by the sum of the results of each increment. Also, the solution strategies aim that the solution of the incremental global system satisfies the four basic requirements mentioned above (Potts & Zdravkovic, 1999).

For finite element analysis, two main types of solution strategies can be used to solve the basic equation, which corresponds to Equation (B – 38). The first strategy is the tangent stiffness method, which consists to reduce the material stiffness as failure is approached so that the global stiffness matrix is updated at each iteration to reach convergence. This method requires a relatively small number of iterations to reach convergence but the cost of computer memory is very large because of the creation of the global stiffness matrix at each iteration. The second strategy is the constant stiffness method, in which the stiffness matrix is made only once and stays constant throughout, doing that the memory cost is small. In general, the constant stiffness methods use repeated elastic solutions to reach convergence by iteratively changing the loads (Sherif, 2012). Figure B – 5 presents the two nonlinear solutions strategies.

There are two popular solutions methods considered as constant stiffness methods: the modified Newton Raphson and visco-plastic schemes, which are usually used in geotechnical boundary value problems. The visco-plastic method equal to the tangent stiffness method is sensitive to increment size and can lead to inaccurate predictions unless many small solution increments are adopted. The modified Newton-Raphson scheme is the most robust and most economical, in terms of memory cost (Potts & Zdravkovic, 1999).

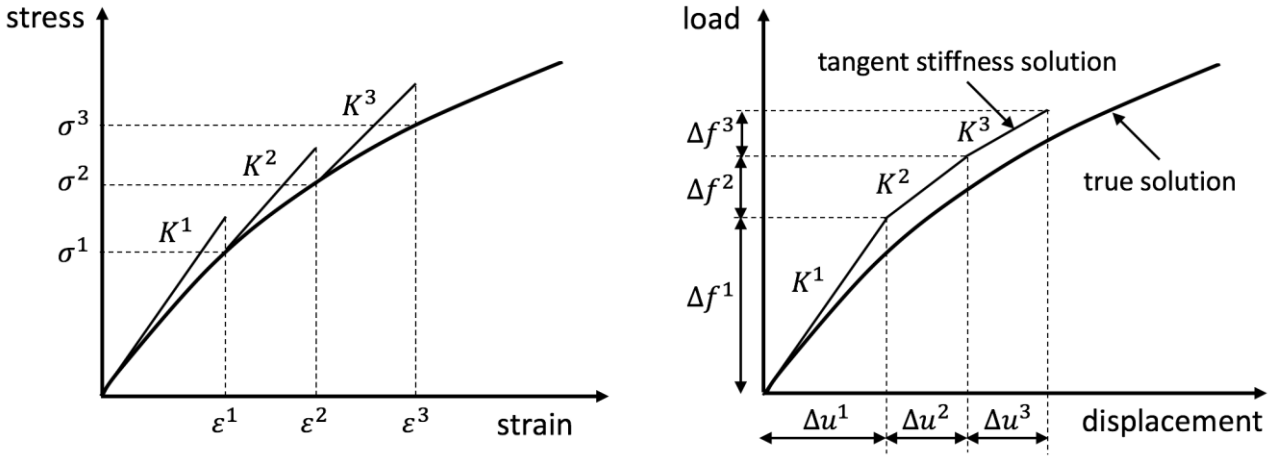

a. b.

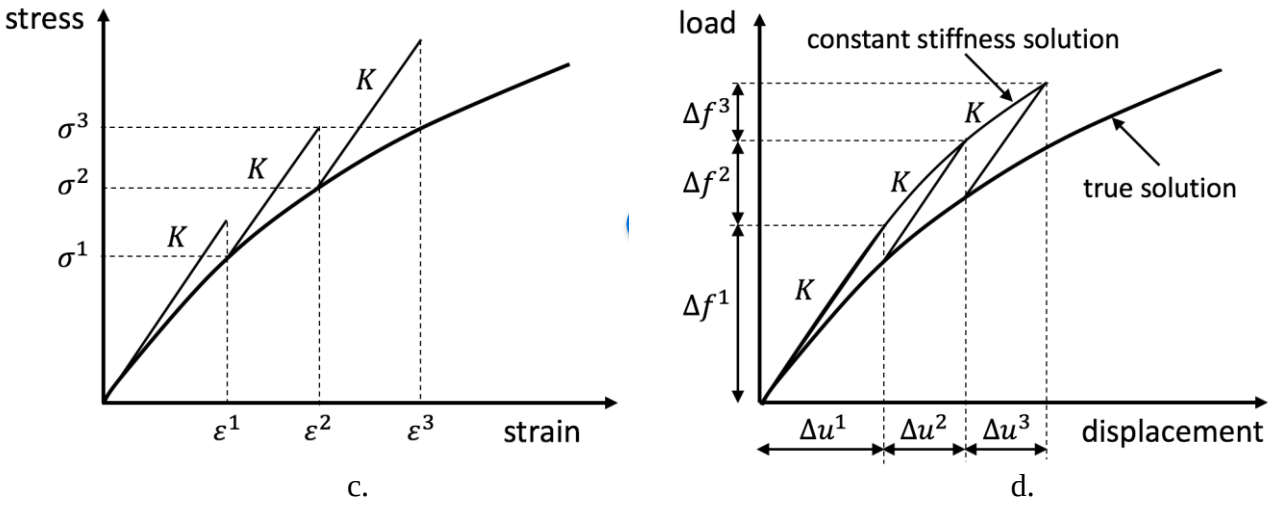

c. d.

Figure B – 5. Nonlinear solutions strategies for finite element analysis. a) Tangent stiffness method in the plane (ε, σ); b) Tangent stiffness method in the plane (u, f); c) Constant stiffness method in the plane (ε, σ); and, d) Constant stiffness method in the plane (u, f) (Potts & Zdravkovic, 1999; Sherif, 2012).

B7.1.Implementation of the method to the elasto-plastic model

This scheme uses the equations of visco-plastic behavior and time as a trick to determine the behavior of nonlinear, elasto-plastic, and time-independent materials. This method was initially developed for linear elastic visco-plastic, i.e., time-dependent material behavior. Due to its simplicity, the visco-plastic algorithm has been widely used. In this scheme, the elasto-plastic behavior can be characterized by two parts: an elastic and a plastic component (Potts & Zdravkovic, 1999). Figure B – 7 illustrates this strategy.

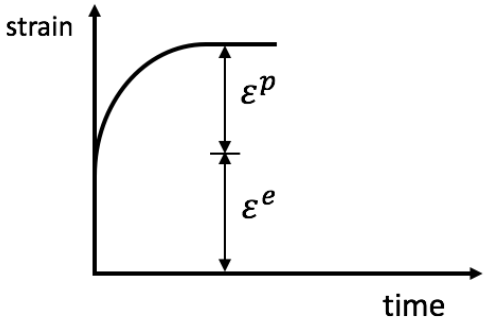

Figure B – 7. The visco-plastic method is applied to an elasto-plastic material (Potts & Zdravkovic, 1999).

When a solution increment is applied, the system is assumed to instantly behave linearly elastically. If the resultant stress state lies within the yield surface, the incremental behavior is elastic and the determined displacements are correct. If the resultant stress state violates yield, the stress state can only be supported temporarily and visco-plastic strain happens. The magnitude of the visco-plastic strain rate is estimated by the value of the yield function, which is a measure of the amount by which the current stress state exceeds the yield condition. The visco-plastic strains rise with time, relaxing the material with

a decrease in the yield function and hence the visco-plastic strain rate. A marching technique led to a step forward in time until the visco-plastic strain rate is insignificant. Here, the cumulative visco-plastic strain and the associated stress change are equal to the incremental plastic strain and stress change respectively. Figure B – 8 represents the application of the visco-plastic method (Potts & Zdravkovic, 1999).

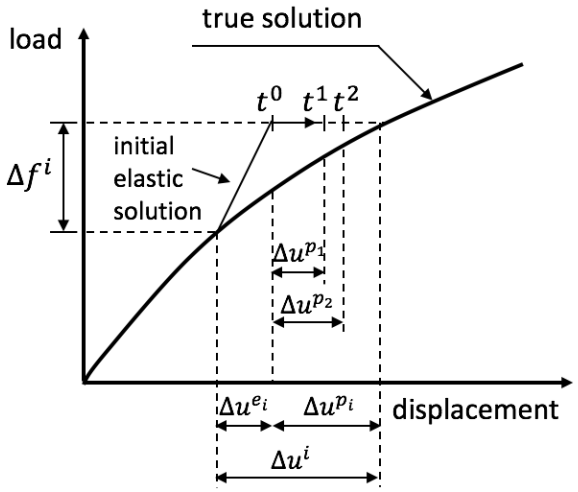

Figure B – 8. Application of the visco-plastic scheme for a uniaxial loading for a non-linear material (Potts & Zdravkovic, 1999).

As a constant stiffness method, the visco-plastic method uses repeated elastic solutions to reach convergence by iteratively varying the loads on the system. The displacement increment must be solved for each load increment and is used to calculate the total strain increments using the strain-displacement matrix:

$$\{\Delta u\}^i = [K]^{-1}\{\Delta f\}^i \quad \text{(B – 39)}$$

$$\{\Delta \varepsilon^T\}^i = [B]\{\Delta u\}^i \quad \text{(B – 40)}$$

where $\{\Delta\varepsilon\}^i$ is strain increment vector and $[B]$ is the strain-displacement matrix.

If the material is yielding, the strain will include both elastic and plastic components:

$$\{\Delta \varepsilon^T\}^i = \{\Delta \varepsilon^e\}^i + \{\Delta \varepsilon^p\}^i \quad \text{(B – 41)}$$

But it is only the elastic strains that produce stresses through the elastic constitutive matrix $[C]$,

$$\{\Delta\sigma\}^i = [C]\{\Delta \varepsilon^e\}^i \quad \text{(B – 42)}$$

These stresses are then added to the existing stresses and the resulting stresses are used to check whether the yield is violated or not.

$$\{\sigma\}^i = \{\sigma\}^{i-1} + \{\Delta\sigma\}^i \quad \text{(B – 43)}$$

This stress is then used to evaluate the yield function. If the stress is below the yield surface ($F \leq 0$) then the material behaves elastically and the complete process is repeated with an increased load in Equation (B – 39). Instead, if the stress is above the yield surface ($F > 0$), the stress is overvalued and it should be redistributed so that it can be brought back as close as possible to the yield surface ($F = 0$). This means that the material behaves plastically and the plastic strains should be calculated. This calculation requires the differentiation of the yield and plastic potential derivatives with respect to stress:

$$\{\Delta\varepsilon^p\}^i = \Delta\Lambda\left[(1-\omega)\left(\frac{\partial g}{\partial\sigma}\right)^{i-1} + \omega\left(\frac{\partial g}{\partial\sigma}\right)^{i}\right] \quad \text{(B – 44)}$$

Where $\Delta\Lambda$ is the increment of the plastic multiplier and ω is a parameter that depends on the integration time used to introduce an explicit ($\omega = 0$) or implicit ($\omega = 1$). For implicit integration, the derivative of the plastic potential function has to be calculated at the current stress, which is unknown and complicates the coding process but it is beneficial. For explicit integration, the differentials are calculated at the previously known stress, and Equation (B – 44) can be expressed as:

$$\{\Delta\varepsilon^p\}^i = \Delta\Lambda\left(\frac{\partial g}{\partial\sigma}\right)^{i-1} \quad \text{(B – 45)}$$

The plastic strains led to an estimate of the excess load at the nodes and these loads are used also for the external load increment for the next iteration. These loads can be generated using two methods, the visco-plastic method, and the initial stress method. The visco-plastic method is used here.

B7.2.Explicit integration with the visco-plastic method

As described above, if the stress state violates yield, the stress state can only be sustained momentarily and plastic straining occurs, which is referred to as visco-plastic strains in this method. The visco-plastic strain rate is determined by the value of the yield function, which is a measure of the degree to which the current stress state exceeds the yield condition. The visco-plastic strains increase with time or iteration, causing the formation to relax with a reduction in the yield function and therefore in the visco-plastic strain rate.

For time-independent elasto-plastic materials, the visco-plastic strain rate is given by,

$$\left\{\frac{\partial\varepsilon^{vp}}{\partial t}\right\}^i = \Delta t * F * \left\{\frac{\partial g}{\partial\sigma}\right\} \quad \text{(B – 46)}$$

where Δt is a pseudo time step, F is the value of the yield function at the current stress and $\{\partial g/\partial\sigma\}$ is the plastic potential derivative of the current stress.

The strain is accumulated from one iteration to the next as:

$$\{\Delta\varepsilon^{vp}\}^i = \{\Delta\varepsilon^{vp}\}^i + \left\{\frac{\partial\varepsilon^{vp}}{\partial t}\right\}^i \quad \text{(B – 47)}$$

When the visco-plastic strain rate from Equation (B – 46) becomes very small (at convergence), the cumulative visco-plastic strain and the associated stress change are equal to the incremental plastic strain and stress change respectively.

The stress increment associated with the visco-plastic strain rate is given by:

$$\{\Delta\sigma^{vp}\}^i = [C]\left\{\frac{\partial\varepsilon^{vp}}{\partial t}\right\}^i \quad \text{(B – 48)}$$

Calculate the associated nodal loads, $\{\Delta r\}^i$, :

$$\{\Delta r\}^i = \int_{vol} B^T[C]\left\{\frac{\partial\varepsilon^{vp}}{\partial t}\right\}^i dV \quad \text{(B – 49)}$$

The incremental global load vector becomes

$$\{\Delta f\}^i = \{\Delta f\}^{i-1} + \sum_{all\ elements}\int_{vol} B^T[C]\left\{\frac{\partial\varepsilon^{vp}}{\partial t}\right\}^i dV \quad \text{(B – 50)}$$

Once convergence has been achieved the displacements, stresses, and strains are updated, and ready for the next load increment:

$$\{u\}^j = \{u\}^{j-1} + \{\Delta u\}^i$$

$$\{\varepsilon\}^j = \{\varepsilon\}^{j-1} + \{\Delta\varepsilon\}^i$$

$$\{\varepsilon^p\}^j = \{\varepsilon^p\}^{j-1} + \{\Delta\varepsilon^{vp}\}^i$$

$$\{\sigma\}^j = \{\sigma\}^{j-1} + \{\Delta\sigma\}^i \quad \text{(B – 51)}$$

B7.3.Convergence

During the iteration process from Equation (B – 39) through (B – 51) the process is repeated until the stresses are close enough to the yield surface within a certain error which should be less than a pre-established tolerance that is set to be 0.01. When this criterion is reached, the solution is said to be converged. Convergence is indicated by either of the following:

- The increment in displacements from Equation (B – 39) is closely the same from one iteration to the next.
- The yield function F is too small.
- The visco-plastic strain rate is too small.
- The stress increment from Equation (B – 42) is closely the same from one iteration to the next.

The displacement conditions are used to calculate the error. In this condition, the difference between the absolute maximum of the incremental displacements in iteration i and iteration $i-1$ should be less than the pre-established tolerance. The complete load stepping is shown in the flow chart on the next page.

Annex C. PVT properties for heavy oil

The fluid flow model is a black-oil model as a simplified model to describe the multiphase flow with mass interchange between phases in a porous medium. In the black-oil model, it is assumed that the fluid consists of a water component and two hydrocarbons, oil and gas. The fluid flows in three phases that are gas, oil, and water phases. The pressure-volume-temperature PVT properties describe the reservoir fluids and appraise their volumetric behavior at several pressure stages. This annex summarizes the PVT properties for a black-oil fluid composed of three phases: gas, oil, and water and reviews the most common empirical correlations used for determining reservoir properties for gas, oil, and water whenever laboratory PVT data are not available. The main properties, which are determined from empirical correlations, are density, bubble-point pressure, gas solubility, volume, compressibility, and viscosity. The oil correlations from this section are selected to model the phase behavior of heavy oils (10 – 22°API) and extra-heavy oils (1 – 9.9°API), both treated as black oils.

C1.Gas

Natural petroleum gases have varying quantities of different hydrocarbon compounds and inorganic compounds, such as hydrogen sulfide, carbon dioxide, nitrogen, and water. Characterizing, measuring, and correlating the physical properties of natural gases must take into account this variety of components. This section summarizes the following pressure volume temperature (PVT) properties for gas: density, isothermal compressibility, formation-volume factor (FVF), and viscosity, among others. (Sutton, 2006)

C1.1.General relation

The gas PVT behavior is based on the real gas law,

$$pV = nZRT \qquad \text{(C – 1)}$$

In Equation (C – 1), p is pressure, n is the molar volume, Z is the gas deviation factor, T is the absolute temperature and R is the universal constant,

$$R = 10.7315 \ \frac{psia \cdot \text{ft}^3}{\text{lbmol} \cdot {}^\circ R}$$

C1.2. Gas deviation factor

The gas deviation factor is a dimensionless quantity used for gas correction at higher pressures and temperatures. It is also known as the gas compressibility factor.

Brill & Beggs (1974) propose a correlation to calculate the Z-factor as,

$$Z = A + \frac{1-A}{e^B} + Cp_{pr}^D \qquad \text{(C – 2)}$$

In Equation (C – 2) A, B, C, and D are defined as follows:

$$A = 1.39\left(T_{pr} - 0.92\right)^{0.5} - 0.36T_{pr} - 0.1$$

$$B = \left(0.62 - 0.23T_{pr}\right)p_{pr} + \left[\frac{0.066}{T_{pr}-0.86} - 0.037\right]{p_{pr}}^2 + \frac{0.32}{10^{9(T_{pr}-1)}}{p_{pr}}^6$$

$$C = 0.132 - 0.32\log T_{pr}$$

$$D = 10^{\left(0.3106-0.49T_{pr}+0.1824{T_{pr}}^2\right)}$$

In these latter equations, p_{pr} and T_{pr} are the pseudo-reduced pressure and temperature, respectively:

$$p_{pr} = p/p_{pc}$$

$$T_{pr} = T/T_{pc}$$

where p and T are absolute pressure and temperature and p_{pc} and T_{pc} are the pseudo-critical pressure and temperature, respectively.

Sutton (1985) suggests the following correlations to estimate the pseudo-critical properties of gas mixtures:

$$p_{pcHC} = 756.8 - 131\gamma_{gHC} - 3.6\gamma_{gHC}^2$$

$$T_{pcHC} = 169.2 + 349.5\gamma_{gHC} - 74.0\gamma_{gHC}^2 \qquad \text{(C – 3)}$$

p_{pcHC} and T_{pcHC} are the pseudo-critical pressure and temperature of the hydrocarbon gas mixtures, and γ_{gHC} is the specific gravity of the hydrocarbon gas mixtures.

Standing (1947, 1981) develops two sets of correlations for pseudo-critical properties. The first correlation applies to dry hydrocarbon gas $\left(\gamma_{gHC} < 0.75\right)$:

$$p_{pcHC} = 667 + 15\gamma_{gHC} - 37.5\gamma_{gHC}^2$$

$$T_{pcHC} = 168 + 325\gamma_{gHC} - 12.5\gamma_{gHC}^2 \qquad \text{(C – 4)}$$

The second correlation applies to wet-gas mixtures $\left(\gamma_{gHC} \geq 0.75\right)$:

$$p_{pcHC} = 706 - 51.7\gamma_{gHC} - 11.1\gamma_{gHC}^2 \qquad \text{(C – 5)}$$

$$T_{pcHC} = 187 + 330\gamma_{gHC} - 71.5\gamma_{gHC}^2$$

C1.3.Corrected gas gravity

Vazquez & Beggs (1980) present the correlation to calculate the corrected gas-specific gravity at separator conditions, γ_{gc}, as,

$$\gamma_{gc} = \gamma_g \left[1 + (0.5912 \times 10^{-4})\gamma_{API} T_{sp} log\left(\frac{p_{sp}}{114.7}\right)\right] \quad \text{(C – 6)}$$

In Equation (C – 6), T_{sp} and p_{sp} are temperature and pressure at separator conditions, respectively.

Kartoatmodjo & Schmidt (1991) present a modification of the Vazquez & Beggs correlation,

$$\gamma_{gc} = \gamma_g \left[1 + 0.1595 \frac{\gamma_{API}^{0.4078}}{T_{sp}^{0.2466}} log\left(\frac{p_{sp}}{114.7}\right)\right] \quad \text{(C – 7)}$$

Kartoatmodjo & Schmidt correlation is useful to calculate other PVT properties at bubble-point conditions (Equation (C – 7)).

C1.4.Gas formation-volume factor

The gas formation-volume factor B_g is defined as the ratio of the gas volume at the temperature and pressure of any stage below the bubble point and the volume of the same gas at standard conditions through differential liberation (El-Hoshoudy & Desouky, 2019). Applying the real gas law at standard conditions and reservoir conditions:

$$B_g = \frac{p_{SC}}{T_{SC}} \frac{ZT}{p} \quad \text{(C – 8)}$$

For field units ($p_{SC} = 14.7\ psia$ and $T_{SC} = 60°F$), therefore:

$$B_g = 28.279 \frac{ZT}{p} [\text{ft}^3/\text{scf}] = 5.0368 \frac{ZT}{p} [\text{bbl/scf}] \quad \text{(C – 9)}$$

Figure C – 2 presents the behavior of a typical gas formation-volume factor at a constant temperature. As pressure increases the gas is compressed and the gas formation-volume factor becomes smaller.

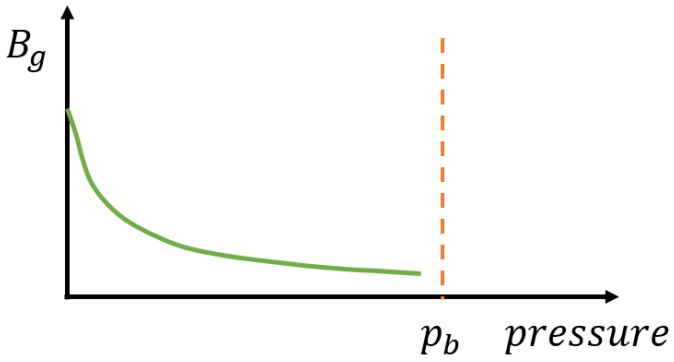

Figure C – 3. The behavior of a typical gas formation-volume factor at a constant temperature.

C1.5.Isothermal gas compressibility

The isothermal gas compressibility c_g is defined as the relative change in the volume of the gas with respect to the change in pressure at constant temperature (El-Banbi, Alzahabi, & El-Maraghi, 2018):

$$c_g = -\frac{1}{V_g}\left(\frac{\partial V_g}{\partial p}\right) = \frac{1}{p} - \frac{1}{Z}\left(\frac{\partial Z}{\partial p}\right)_T \quad \text{(C – 10)}$$

For sweet natural gas (i.e., not containing H_2S) at pressures less than $1000\,psia$, the second term in Equation (C – 10) is negligible and $c_g = 1/p$ is a reasonable approximation.

This approach uses gas compressibility c_g in psi^{-1}.

C1.6.Gas density

Gas density is defined as the mass of the gas occupying a certain volume at a specified pressure and temperature. The gas density at standard conditions is calculated using the gas gravity definition:

$$\rho_{g_{sc}} = 0.0763\gamma_g \quad \text{(C – 11)}$$

where density in lbm/ft^3.

The gas density at different pressure and temperature conditions can be obtained from the real gas law:

$$\rho_g = pM_g/ZRT \quad \text{(C – 12)}$$

In Equation (C – 12), M_g is the gas's molecular weight.

Also, gas density can be obtained in terms of gas-specific gravity by:

$$\rho_g = 28.97p\gamma_g/ZRT \quad \text{(C – 13)}$$

Another way to calculate the gas density is using the gas formation-volume factor as:

$$\rho_g = \frac{\rho_{g_{SC}}}{B_g} \quad \text{(C – 14)}$$

C1.7.Gas viscosity

The gas viscosity is defined as the resistance of the gas as fluid to flow. The viscosity of hydrocarbon gases generally ranges from 0.01 to 0.03 cP at standard and reservoir conditions, reaching up to 0.1 cP for near-critical gas condensates (Brulé & Whitson, 2000).

Lee, Gonzalez & Eakin (1966) propose a correlation for gas viscosity:

$$\mu_g = A_1 \times 10^{-4} e^{\left(A_2 \rho_g^{A_3}\right)} \quad \text{(C – 15)}$$

In Equation (C – 15), A_1, A_2 and A_3 are defined as:

$$A_1 = \frac{\left(9.379 + 0.01607 M_g\right) T^{1.5}}{209.2 + 19.26 M_g + T}$$

$$A_2 = 3.448 + (986.4/T) + 0.01009 M_g$$

$$A_3 = 2.447 - 0.2224 A_2$$

where μ_g is gas viscosity in cP, gas density ρ_g in $\mathrm{g/cm^3}$ and temperature T at $°R$.

C2.Oil

This section provides correlations for PVT properties of reservoir oils, including bubble-point pressure, oil density, compressibility, formation-volume factor, and viscosity. With only a few exceptions, oil properties have been correlated in terms of surface oil and gas properties, including solution gas-oil ratio, oil and gas gravity, and temperature.

In a black oil reservoir, the oil and gas formation-volume factors, gas densities, solution gas-oil ratio, and the oil and gas viscosities are measured at reservoir temperature as a function of pressure. Once these measurements are performed, they can be applied in empirical correlations to obtain the relative in-situ amounts of oil and gas during the production life of the reservoir (El-Hoshoudy & Desouky, 2019).

Crude oils usually contain dissolved gas consisting mainly of light components such as methane and ethane, some intermediates, and smaller amounts of non-hydrocarbons. The quantity of dissolved gas has a significant effect on oil properties. Oil properties can be grouped into two categories: saturated and under-saturated conditions. The saturated condition is defined at pressures at or below the bubble point, and the under-saturated condition is defined at pressures greater than the bubble point.

Table C – 1 enlists the recommended PVT correlations for conventional oils, which give the best results with errors reduced for each oil property. The development of these correlations uses crude oils from

various oil-producing regions of the world. Table C – 2 presents the data ranges of oil properties correlations for general use.

Table C – 1. PVT correlations for conventional oils (Sutton, 2006)

PROPERTY	CORRELATION
Bubble-point pressure	Lasater (1958), Al-Shammasi (2001) or Velarde, Blasingame & McCaine Jr. (1997)
Solution gas-oil ratio	Standing (1947,1981) and Vazquez & Beggs (1980).
Formation-volume factor	Al-Marhoun (1992), Al-Shammasi (2001), Frashad, LeBlanc, Garber & Osorio (1996),
Isothermal compressibility	Dindoruk & Christman (2001), Petrosky (1990) and Frashad *et al*. (1996).
Dead oil viscosity	Glasø (1980), Bergman (2004) and Fitzgerald (1994).
Gas-saturated oil viscosity	Chew & Connally (1959) and Beggs & Robinson (1975)
Under-saturated oil viscosity	Beal (1970), Kouzel (1965) and Vazquez & Beggs (1980)

Table C – 2. Data ranges used for oil properties correlations for conventional oil (Sutton, 2006).

PROPERTY	MINIMUM	MAXIMUM	AVERAGE
Bubble-point pressure, psia	32	10,326	2,041
Temperature, °F	58	342	185
Solution gas-oil ratio, GOR, scf/STB	6	3,448	592
Formation-volume factor, FVF, bbl/STB	1.023	2.952	1.349
Crude oil gravity, °API	6.0	63.7	34.1
Gas specific gravity	0.511	3.445	1.005

C2.1.Oil gravity

The oil gravity is a dimensionless property that represents the oil density at stock tank conditions. The crude oil density is defined as the mass of a unit volume of crude at a specified pressure and temperature (El-Hoshoudy & Desouky, 2019).

The crude oil specific gravity, γ_o, is calculated as:

$$\gamma_o = \frac{141.5}{\gamma_{API}+131.5} \quad \text{(C – 16)}$$

In Equation (C – 16), γ_{API} is the API gravity.

C2.2.API gravity

The petroleum industry uses API gravity as the preferred oil gravity scale and can be solved from Equation (C – 16) as:

$$\gamma_{API} = \frac{141.5}{\gamma_o} - 131.5 \quad \text{(C – 17)}$$

C2.3.Characterization factor

The use of the Watson characterization factor is a way of further characterizing crude oils and components, which is the ratio between the mean average boiling point, T_b, and oil-specific gravity, γ_o,

that could be used to indicate the chemical nature of hydrocarbon fractions and, therefore, could be used as a correlative factor. (Watson & Nelson, 1933; Watson, Nelson & Murphy, 1935)

Characterization factor K_W is calculated as:

$$K_W = \frac{{T_b}^{1/3}}{\gamma_o} \tag{C – 18}$$

Characterization factors are useful because they stay reasonably constant for chemically similar hydrocarbons. A characterization factor of 12.5 or greater denotes a hydrocarbon compound predominantly paraffinic in nature. Lower values of this factor denote hydrocarbons with more naphthenic or aromatic components. Highly aromatic hydrocarbons exhibit values of 10.0 or less; therefore, the Watson characterization factor offers a means of determining the paraffinicity of crude oil. Whitson (1983) established the following relationship in terms of oil molecular weight, M_o and oil-specific gravity, γ_o.

$$K_W = 4.5590\, M_o^{0.15178}\, {\gamma_o}^{0.84573} \tag{C – 19}$$

C2.4.Molecular weight

Whitson (1983) establishes a correlation to compute the crude oil molecular weight,

$$M_o = \left(\frac{K_W\, {\gamma_o}^{0.84573}}{4.5579}\right)^{6.58848} \tag{C – 20}$$

C2.5.Bubble-point pressure

The bubble-point pressure is defined as the highest pressure at which a bubble of gas is first liberated from the oil, and is determined experimentally by conducting a constant mass depletion test or estimated from empirical correlations (El-Hoshoudy & Desouky, 2019).

The empirical correlations of bubble-point pressure for general use are presented in Table C – 3.

For heavy oils, De Ghetto, Paone & Villa (1995) proposed a modification of the Standing correlation,

$$p_b = 15.7286 \left[\left(\frac{R_{so}}{\gamma_g}\right)^{0.7885} 10^{(0.0020T - 0.0142\gamma_{API})}\right] \tag{C – 21}$$

with temperature T in $°F$, gas-oil ratio R_{so} in scf/STB, and bubble-point pressure p_b in $psia$.

Table C – 3. Correlations of bubble-point pressure for general use.

AUTHOR	CORRELATION
Lasater (1958)	$p_b = \frac{A(T+459.67)}{\gamma_g}$ where: $A = e^{\left(\frac{\gamma_g - 0.15649}{0.33705}\right)} - 0.59162$ $y_g = \left[1 + \frac{\gamma_o}{7.521 \times 10^{-6} R_{so} M_o}\right]^{-1}$
Al-Shammasi (2001)	$p_b = \frac{\gamma_o^{5.527215}[\gamma_g R_{so}(T+459.67)]^{0.783716}}{e^{1.841408\gamma_o\gamma_g}}$ $p_b = 1091.47\left[\frac{R_{so}^{0.081465} 10^{\left(0.013098T^{0.282372} - 8.2\times10^{-6}\gamma_{API}^{2.176124}\right)}}{\gamma_g^{0.161488}} - 0.740152\right]^{5.354891}$
Velarde *et al*. (1997)	where: $R_{so} = R_{sob}[A(p/p_b)^B + (1-A)(p/p_b)^C]$ $A = 9.73 \times 10^{-7}\gamma_g^{1.1672608}\gamma_{API}^{0.929870}T^{0.247235}p_b^{1.056052}$ $B = 0.022339\gamma_g^{-1.004750}\gamma_{API}^{0.337711}T^{0.132795}p_b^{0.302065}$ $C = 0.725167\gamma_g^{-1.485480}\gamma_{API}^{-0.164741}T^{-0.091330}p_b^{0.047094}$
Standing (1947, 1981)	$p_b = 18.2\left[\left(\frac{R_{so}}{\gamma_g}\right)^{0.83} 10^{(0.00091T - 0.0125\gamma_{API})} - 1.4\right]$
Glasø (1980)	$p_b = 1.7679 + 1.7447\log A - 0.30218(\log A)^2$ where: $A = \left(\frac{R_{so}}{\gamma_g}\right)^{0.816}\left(\frac{T^B}{\gamma_{API}^{0.989}}\right)$ For nonvolatile oils: $B = 0.172$ For volatile oils: $B = 0.130$
Vazquez & Beggs (1980)	$p_b = \left[A\left(\frac{R_{so}}{\gamma_{gc}}\right)10^{\left(\frac{B\gamma_{API}}{T+459.67}\right)}\right]^C$ where: For $\gamma_{API} \leq 30$: $A = 27.64$, $B = -11.172$, and $C = 0.9143$. For $\gamma_{API} > 30$: $A = 56.06$, $B = -10.393$, and $C = 0.8425$.

C2.6.Solution gas-oil ratio

The solution gas-oil ratio is the same gas solubility and is defined as the number of standard cubic feet of gas that dissolve in one stock-tank barrel of crude oil at a certain pressure and temperature and defined in scf/STB (El-Hoshoudy & Desouky, 2019).

$$R_{so} = \frac{(V_g)_{SC}}{(V_o)_{SC}} \tag{C – 22}$$

Equation (C – 22) defines the solution gas-oil ratio where $(V_g)_{SC}$ and $(V_o)_{SC}$ are the gas and oil volumes at standard conditions.

Following the definition, at standard conditions, dissolved gas is completely released from the oil, and therefore the oil contains no gas. Gas solubility increases with pressure until it reaches the maximum value at saturation pressure. Below the bubble point pressure, gas is evolved with a reduction in pressure and the gas solubility also decreases. Generally, the lighter the oil the higher the gas solubility, therefore volatile oils often have a higher solution GOR than black oils (El-Hoshoudy & Desouky, 2019).

Figure C – 2 presents the behavior of a typical solution gas-oil ratio at a constant temperature. As the pressure increases, more and more gas can be forced into the liquid phase. The pressure when the liquid phase cannot hold any more gas is the bubble point pressure.

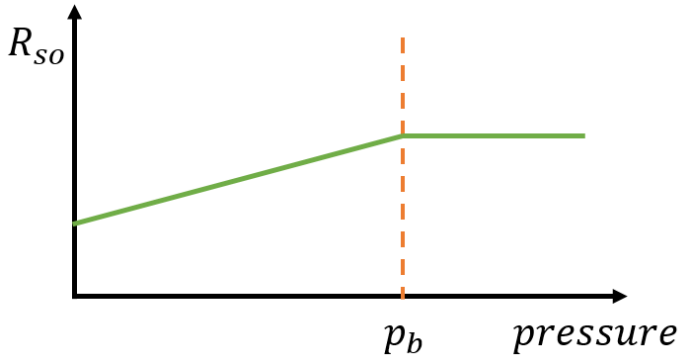

Figure C – 2. The behavior of a typical solution gas-oil ratio at a constant temperature.

Sometimes the solution gas-oil ratio, R_{so}, is required at a given pressure, and this is readily calculated by solving the bubble-point correlation. Table C – 4 summarizes the solution gas-oil ratio correlations for general use.

Table C – 4. Correlations of solution gas-oil ratio for general use.

AUTHOR	CORRELATION
Standing (1947, 1981)	$R_{so} = \gamma_g\left[(0.055 p_b + 1.4)10^{(0.0125\gamma_{API} - 0.00091T)}\right]^{1.205}$
Vazquez & Beggs (1980)	$R_{so} = A\gamma_{gc} p^B e^{[C(\gamma_o/(T+460))]}$ where: For $\gamma_{API} \leq 30$: $A = 0.0362$, $B = 1.0937$, and $C = 25.7240$. For $\gamma_{API} > 30$: $A = 0.0178$, $B = 1.1870$, and $C = 23.9310$.

For heavy oils, De Ghetto *et al.* (1995) propose a modification of the Vazquez-Beggs correlation,

$$R_{so} = A\,\gamma_{gc}\,{p_b}^B 10^{[C(\gamma_{API}/(T+460))]} \qquad \text{(C – 23)}$$

with,

$A = 0.01772$, $B = 1.2057$, and $C = 10.9267$.

$$\gamma_{gc} = \gamma_{g_{sp}}\left[1 + 0.5912\,\gamma_{API}\,T_{sp}\,\log\left(\frac{p_{sp}}{114.7}\right) \times 10^{-4}\right]$$

For extra-heavy oils, De Ghetto *et al.* (1995) propose a modification of the Standing correlation,

$$R_{so} = \gamma_g\left[0.0934\,p_b\,10^{(0.0169\,\gamma_{API} - 0.00156T)}\right]^{1.1128} \qquad \text{(C – 24)}$$

with temperature T in $°F$, bubble-point pressure p_b in $psia$, the gas-oil ratio R_{so} in scf/STB, and $\gamma_{g_{sp}}$, p_{sp} and T_{sp} are specific gravity, pressure, and temperature at separator conditions, respectively.

C2.7.Oil formation-volume factor

The oil formation-volume factor (FVF), B_o, is the ratio of the volume occupied in the reservoir by a volume of oil measured at standard conditions. In other words, it relates the volume of oil at stock-tank conditions to the volume of oil at elevated pressure and temperature in the reservoir. Values typically vary from approximately 1.0 bbl/STB for crude oil systems containing little or no solution gas to nearly 3.0 bbl/STB for highly volatile oils.

Figure C – 3 presents the behavior of a typical oil formation-volume factor at a constant temperature. As the pressure increases, more and more gas goes into the liquid phase resulting in an increased formation-volume factor. Once the bubble-point pressure is reached, no more gas can be forced into the solution and the formation-volume factor begins a gradual decline as the liquid is compressed.

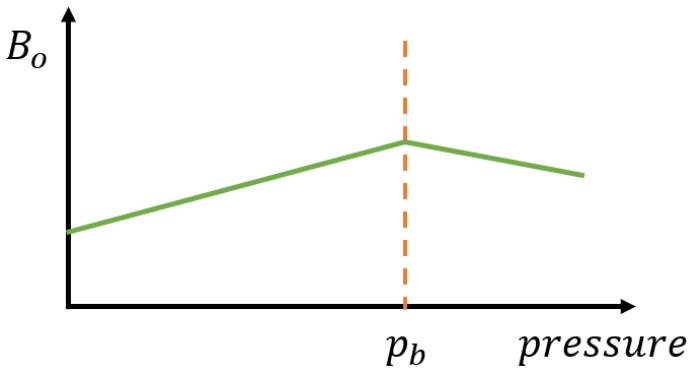

Figure C – 3. The behavior of a typical oil formation-volume factor at a constant temperature.

C2.7.1. Under-saturated oil

The FVF below the bubble-point pressure is affected by both gas solubility and compressibility, while above the bubble-point the gas solubility is constant, and therefore only compressibility influences. Therefore, knowing the isothermal compressibility, the under-saturated oil FVF is given by,

$$B_o = B_{ob} e^{[c_o(p_b - p)]} \qquad \text{(C – 25)}$$

with pressures p_b and p in $psia$, oil compressibility c_o in psi^{-1} and oil formation-volume factors B_{ob} and B_o in RB/STB.

C2.7.2. Gas-saturated oil

For gas-saturated systems $(p \leq p_b)$, gas is liberated as pressure is reduced below the bubble point. The bubble-point pressure is a reference to observing the behavior of the oil formation-volume factor.

Table C – 5 presents other correlations of oil formation-volume factor in gas-saturated oil known as bubble-point oil FVF.

Table C – 5. Correlations of oil formation-volume factor at gas-saturated oil.

AUTHOR	CORRELATION
Al-Shammasi (2001)	$B_{ob} = 1 + 5.53 \times 10^{-7} R_s (T - 60) + \frac{1.81 \times 10^{-7} R_{so}}{\gamma_o} + \frac{4.49 \times 10^{-4} (T-60)}{\gamma_o} + \frac{2.06 \times 10^{-4} R_{so} \gamma_g}{\gamma_o}$
Al-Marhoun (1992)	$B_{ob} = 1 + (0.177342 \times 10^{-3}) R_{so} + (0.220163 \times 10^{-3}) R_{so} \left(\frac{\gamma_g}{\gamma_o}\right) + (4.292580 \times 10^{-6}) R_{so} (T - 60)(1 - \gamma_o) + (0.528707 \times 10^{-3})(T - 60)$
Frashad *et al.* (1996)	$B_{ob} = 1 + 10^{[-2.6541 + 0.5576\, logA + 0.3331\, logA^2]}$ where: $A = R_{so}^{0.5956} \frac{\gamma_g^{0.2369}}{\gamma_o^{1.3282}} + 0.0976T$
Kartoatmodjo & Schmidt (1991)	$B_{ob} = 0.98496 + 1.0 \times 10^{-4} \left(\frac{R_{so}^{0.755} \gamma_{gc}^{0.25}}{\gamma_o^{1.5}} + 0.45T\right)^{1.5}$
Standing (1947,1981)	$B_{ob} = 0.9759 + (12 \times 10^{-5}) A^{1.2}$ where: $A = R_{so} \left(\frac{\gamma_g}{\gamma_o}\right)^{0.5} + 1.25T$
Glasø (1980)	$\log(B_{ob} - 1) = -6.585 + 2.9133 \log A - 0.2768 (\log A)^2$ where: $A = R_{so} \left(\frac{\gamma_g}{\gamma_o}\right)^{0.526} + 0.968T$
Vazquez & Beggs (1980)	$B_{ob} = 1 + AR_{so} + B(T - 60)\left(\frac{\gamma_{API}}{\gamma_{gc}}\right) - CR_{so}(T - 60)\left(\frac{\gamma_{API}}{\gamma_{gc}}\right)$ For $\gamma_{API} \leq 30$: $A = 4.677 \times 10^{-4}$, $B = 0.1751 \times 10^{-4}$ and $C = 1.8106 \times 10^{-8}$. For $\gamma_{API} > 30$: $A = 4.67 \times 10^{-4}$, $B = 0.11 \times 10^{-4}$ and $C = 0.1337 \times 10^{-8}$.

The empirical correlation for the formation-volume factor proposed by Vazquez & Beggs (1980) presents better results for heavy oils and extra-heavy oils. Later, Romero, Fernandez & Rojas (2001) report the Standing and Beggs correlation as the most adequate correlation to calculate the oil formation-volume factor for heavy oils:

$$B_o = 0.972 + 0.000147\, F^{1.175} \qquad \text{(C – 26)}$$

where:

$$F = R_s \left(\frac{\gamma_g}{\gamma_o}\right)^{0.5} + 1.25T$$

with temperatures T in $°F$, gas-oil ratio R_{so} in scf/STB, and oil formation-volume factor B_o in RB/STB.

C2.8.Isothermal oil compressibility

Isothermal oil compressibility is defined as the change in fluid volume with respect to the change in pressure at isothermal conditions. The oil compressibility is a source of energy for fluid flow in the reservoir. In an under-saturated reservoir, the oil compressibility is a dominant drive mechanism, but for

a saturated reservoir it is dominated by the much larger gas compressibility, c_g, effects due to dissolved gas evolving from the solution (El-Banbi *et al*., 2018).

C2.8.1. Under-saturated oil

The oil isothermal compressibility, c_o in psi^{-1}, for $(p > p_b)$ is given as:

$$c_o = -\frac{1}{V_o}\left(\frac{\partial V_o}{\partial p}\right)_T = -\frac{1}{B_o}\left(\frac{\partial B_o}{\partial p}\right)_T \qquad \text{(C – 27)}$$

which expresses how the volume changes with pressure change under constant temperature conditions.

Above bubble-point pressure, oil volume changes as a function of isothermal compressibility only.

C2.8.2. Gas-saturated oil

Below the bubble-point pressure $(p \le p_b)$, oil isothermal compressibility is defined by oil and gas properties to account for gas coming out of solution. The corresponding saturated oil compressibility c_o in $psi^{-1}$is calculated as:

$$c_o = -\frac{1}{B_o}\left[\left(\frac{\partial B_o}{\partial p}\right)_T - B_g\left(\frac{\partial R_{so}}{\partial p}\right)_T\right] \qquad \text{(C – 28)}$$

The empirical correlations to predict isothermal compressibility for gas-saturated oil are summarized in Table C – 6.

Table C – 6. Correlations of isothermal compressibility at gas-saturated oil.

AUTHOR	CORRELATION
Frashad *et al.* (1996)	$c_{ob} = 10^{(-5.4531+5.03\times10^{-4}A-3.5\times10^{-8}A^2)}$ where: $A = R_{so}^{0.1982}T^{0.6685}\gamma_g^{-0.21435}\gamma_{API}^{1.0116}p^{-0.1616}$
Petrosky (1990)	$c_o = \frac{1.705\times10^{-7}R_{so}^{0.69357}\gamma_g^{0.1885}\gamma_{API}^{0.3272}T^{0.6729}}{p^{0.5906}}$
Dindoruk & Chistman (2001)	$c_o = 10^{-6}(4.487462348 + 0.005197040A + 1.258\times10^{-5}A^2)$ where: $A = \frac{B^{1.759732076}}{\left(2.749114986+\frac{2R_{so}^{-1.713572145}}{\gamma_g^{9.999932841}}(T-60)\right)^2}$ $B = \frac{R_{so}^{0.980922372}\gamma_g^{0.0021003077}}{\gamma_o^{0.338486128}} + 20.00006358(T-60)^{0.300001059} - 0.876813622R_s$
Standing (1947, 1981)	$c_o = 10^{-6}e^{\left[\frac{\rho_o+4.347\times10^{-3}(p-p_b)-79.1}{7.141\times10^{-4}(p-p_b)-12.938}\right]}$
Vazquez & Beggs (1980)	$c_o = \frac{5R_{so}+17.2T-1180\gamma_{gc}+12.61\gamma_{API}-1.433}{10^5 p}$
Kartoatmodjo & Schmidt (1991)	$c_o = \frac{10^{[0.83415+0.5002\,log(R_{so})+0.3613\,log(\gamma_{API})+0.7606\log(T)-0.35505\log(\gamma_{gc})]}}{10^5 p}$

Oil compressibility is used to calculate the variation in under-saturated density and formation-volume factor with pressure.

De Ghetto *et al.* (1995) propose a modification of the Vazquez & Beggs correlation to compute the oil compressibility for a gas-saturated oil.

For heavy oil,

$$c_o = \frac{-2841.8+2.96465R_{so}+25.5439T-1230.5\gamma_{gc}+41.91\gamma_{API}}{10^5 p} \quad \text{(C – 29)}$$

and for extra-heavy oils,

$$c_o = \frac{-889.6+3.1374R_{so}+20T-627.3\gamma_{gc}-81.4476\gamma_{API}}{10^5 p} \quad \text{(C – 30)}$$

with pressure p in $psia$, gas-oil ratio R_{so} in scf/STB and oil compressibility c_o in psi^{-1}.

C2.9.Oil density

The crude oil density is defined as the mass of a unit volume of crude at a specified pressure and temperature. The oil density at standard conditions can be calculated from oil gravity as:

$$\rho_{oSC} = 62.42796 \frac{141.5}{\gamma_{API}+131.5} \quad \text{(C – 31)}$$

where density in lbm/ft^3.

In typical oil reservoirs, the oil density decreases with pressure depletion until it reaches the lowest value at the bubble-point pressure (El-Hoshoudy & Desouky, 2019).

C2.9.1. Under-saturated oil

Following (Abou-Kassem, Rafiqul Islam, & Farouq Ali, 2020), the oil density above the bubble-point pressure $(p > p_b)$ is calculated as:

$$\rho_o = \rho_{ob}[1 + c_o(p - p_b)] \quad \text{(C – 32)}$$

(Brulé & Whitson, 2000) present another form to calculate oil density for an under-saturated oil:

$$\rho_o = \frac{62.42796\,\gamma_o+0.0136\,\gamma_g\,R_{so}}{B_o} \quad \text{(C – 33)}$$

where density in lbm/ft^3.

C2.9.2. Gas-saturated oil

The oil density below the bubble-point pressure $(p \leq p_b)$ is calculated as (Abou-Kassem *et al.*, 2020):

$$\rho_o = \frac{\rho_{o_{SC}} + \rho_{g_{SC}} R_{so}/5.615}{B_{ob}} \qquad \text{(C – 34)}$$

C2.10. Oil viscosity

The oil viscosity is defined as the resistance of the fluid to flow. The correlations for oil viscosity are stated for dead, gas-saturated, and under-saturated oil viscosities.

C2.10.1. Dead-oil viscosity

The empirical correlations of the dead oil viscosity for general use are presented in Table C – 7.

Table C – 7. Correlations of dead-oil viscosity.

AUTHOR	CORRELATION
Glasø (1980)	$\mu_{do} = \left(\frac{3.141\times10^{10}}{T^{3.444}}\right)\log(\gamma_{API})^{[10.313\log T - 36.447]}$
Bergman (2004)	$\mu_{do} = e^{A} - 1.0$ where: $A = e^{[22.33 - 0.194\gamma_{API} + 0.00033\gamma_{API}^2 - (3.2 - 0.0185\gamma_{API})\log(T+310)]}$
Fitzgerald (1997)	$\mu_{do} = [\gamma_o - 4.6\times10^{-4}(T-60)]\langle X_6 - 0.7 - e^{[-0.7487 - 3.295(X_6-0.7) + 0.6119(X_6-0.7)^2 - 0.3193(X_6-0.7)^3]}\rangle$ where: $\log(X_6) = 10^{[\log\log(X_3) + X_5(\log(T+459.67) - \log(559.67))]}$ $X_5 = \frac{[\log\log(X_3) - \log\log(X_4)]}{\log(559.67) - \log(669.67)}$ $X_4 = \nu_{210} + 0.7 + e^{(-1.47 - 1.84\nu_{210} - 0.5\nu_{210}^2)}$ $X_3 = \nu_{100} + 0.7 + e^{(-1.47 - 1.84\nu_{100} - 0.5\nu_{100}^2)}$ $\log\nu_{210} = -1.92353 + 2.41071\times10^{-4}T_b + 0.51130\log(T_b\nu_{100})$ $\nu_{100} = X_1 + X_2$ $\log X_2 = 1.35579 + 8.16059\times10^{-4}T_b + 8.38505\times10^{-7}T_b^2$ $\log X_1 = A_1 + A_2K_W$ $A_1 = 34.931 - 8.84387\times10^{-2}T_b + 6.73513\times10^{-5}T_b^2 - 1.01394\times10^{-8}T_b^3$ $A_2 = -2.92649 + 6.98405\times10^{-3}T_b + 5.09947\times10^{-6}T_b^2 + 17.49378\times10^{-10}T_b^3$
Standing (1947, 1981)	$\log(\mu_{do}/\rho_o) = \frac{1}{C[K_W - (8.24/\gamma_O)] + 1.639B - 1.059} - 2.17$ where: $A = 1 + 8.69\log[(T+459.67)/559.67]$ $B = 1 + 0.544\log[(T+459.67)/559.67]$ $C = -0.1285\frac{(2.87A-1)\gamma_o}{2.87A-\gamma_o}$ $\rho_o = \frac{\gamma_o}{1 + 0.000321(T-60)10^{(0.00462\gamma_{API})}}$
Kartoatmodjo & Schmidt (1991)	$\mu_{do} = \left(\frac{3.141\times10^{10}}{T^{3.444}}\right)\log(\gamma_{API})^{[10.313\log T - 36.447]}$

For heavy oils, De Ghetto *et al.* (1995) propose a modification of the Egbogah-Jack correlation,

$$\log\log(\mu_{do}+1) = 2.06492 - 0.0179\gamma_{API} - 0.70226\ \log(T) \quad \text{(C – 35)}$$

For extra-heavy oils, De Ghetto *et al.* (1995) proposed a modification of the Egbogah-Jack correlation,

$$\log\log(\mu_{do}+1) = 1.90296 - 0.012619\ \gamma_{API} - 0.61748\ \log(T) \quad \text{(C – 36)}$$

In general, all the correlations for oil viscosity use the T in $°F$ and μ_{do} in cP.

C2.10.2. Under-saturated oil

Table C – 8 presents the empirical correlations to calculate the viscosity of an under-saturated oil.

Table C – 8. Correlations of under-saturated oil viscosity.

AUTHOR	CORRELATION
Vazquez & Beggs (1980)	$\mu_o = \mu_{ob}(p/p_b)^A$ where: $A = 2.6p^{1.187}e^{[-11.513-(8.98\times10^{-5})p]}$
Beal (1970)	$\frac{\mu_o-\mu_{ob}}{0.001(p-p_b)} = 0.0024\mu_{ob}^{1.6} + 0.038\mu_{ob}^{0.56}$
Kouzel (1965)	$\mu_o = \mu_{ob}10^{\left[\frac{(p-p_b)\left(-0.0102+0.04042\mu_{ob}^{0.181}\right)}{1000}\right]}$
Kartoatmodjo & Schmidt (1991)	$\mu_o = 1.00081\mu_{ob} + 1.127\times10^{-3}(p-p_b)(-6.517\times10^{-3}\mu_{ob}^{1.8148} + 0.0038\mu_{ob}^{1.59})$
Labedi (1990)	$\mu_o = \mu_{ob} - \left[\left(1-\frac{P}{p_b}\right)\left(\frac{10^{-2.488}\mu_{od}^{0.9036}p_b^{0.6151}}{10^{0.01976\gamma_{API}}}\right)\right]$

For heavy oils, De Ghetto *et al.* (1995) propose a modification of the Kartoatmodjo & Schmidt correlation,

$$\mu_o = 0.9886\mu_{ob} + 0.002763\ (p-p_b)\left(-0.01153\ \mu_{ob}^{1.7933} + 0.00316\ \mu_{ob}^{1.5939}\right) \quad \text{(C – 37)}$$

For extra-heavy oils, De Ghetto *et al.* (1995) propose a modification of Labedi's correlation,

$$\mu_o = \mu_{ob} - \left[\left(1-\frac{p}{p_b}\right)\left(\frac{10^{-2.19}\mu_{oD}^{1.055}p_b^{0.3132}}{10^{0.0099\gamma_{API}}}\right)\right] \quad \text{(C – 38)}$$

These correlations for oil viscosity at under-saturated conditions use pressures p and p_b in $psia$, and viscosities μ_o, μ_{ob} and μ_{do} in cP.

C2.10.3. Gas-saturated oil

The oil viscosity of a gas-saturated oil ($p \le p_b$) is useful to calculate the under-saturated oil viscosity. Table C – 9 presents the empirical correlations to calculate the oil viscosity at gas-saturated conditions known as bubble-point oil viscosity.

Table C – 9. Correlations of bubble-point oil viscosity.

AUTHOR	CORRELATION
Chew & Connally (1959)	$\mu_{ob} = A\mu_{od}^{B}$ where: $A = 0.20 + \frac{0.80}{10^{0.00072R_{so}}}$ $B = 0.43 + \frac{0.57}{10^{0.00072R_{so}}}$
Beggs & Robinson (1975)	$\mu_{ob} = A\mu_{od}^{B}$ where: $\mathrm{A} = 10.715(R_{so} + 100)^{-0.515}$ $B = 5.44(R_{so} + 100)^{-0.338}$
Standing (1947, 1981)	$\mu_{ob} = A\mu_{od}^{B}$ where: $\mathrm{A} = 10^{-(7.4\times10^{-4})R_{so}+(2.2\times10^{-7})R_{so}^{2}}$ $B = \frac{0.68}{10^{(8.62\times10^{-5})R_{so}}} + \frac{0.25}{10^{(1.1\times10^{-3})R_{so}}} + \frac{0.062}{10^{(3.74\times10^{-3})R_{so}}}$
Kartoatmodjo & Schmidt (1991)	$\mu_{ob} = -0.06821 + 0.9824A + 4.034\times10^{-4}A^{2}$ where: $\mathrm{A} = \left[0.2001 + 0.8428\times10^{(-8.45\times10^{-4}R_{so})}\right]\mu_{od}^{B}$ $B = 0.43 + 0.5165\times10^{(-8.1\times10^{-4}R_{so})}$

For heavy oils, De Ghetto *et al.* (1995) propose a modification of the Kartoatmodjo & Schmidt correlation,

$$\mu_{ob} = -0.6311 + 1.078\,A - 3.653\times10^{-3}\,A^{2} \qquad \text{(C – 39)}$$

$$A = \left[0.2478 + 0.6114\times10^{(-8.45\times10^{-4}R_{so})}\right]\mu_{od}^{B}$$

$$B = 0.4731 + 0.5158\times10^{(-8.1\times10^{-4}R_{so})}$$

For extra-heavy oils, De Ghetto *et al.* (1995) propose a modification of the Kartoatmodjo & Schmidt correlation,

$$\mu_{ob} = 2.3945 + 0.8927\,A + 1.567\times10^{-3}\,A^{2} \qquad \text{(C – 40)}$$

$$A = \left[-0.0335 + 1.0785\times10^{(-8.45\times10^{-4}R_{so})}\right]\mu_{od}^{B}$$

$$B = 0.5798 + 0.3432\times10^{(-8.1\times10^{-4}R_{so})}$$

These correlations for oil viscosity at saturated conditions use the gas-oil ratio R_{so} in scf/STB and oil viscosities μ_{ob} and μ_{od} in cP.

C3.Water

Water is normally present in hydrocarbon reservoirs. Consequently, knowledge of certain physical properties of connate, interstitial, or formation water is important. These properties, as for oil, are affected by pressure, temperature, and amount of gas in solution and dissolved solids.

C3.1.Water specific gravity

The water-specific gravity, γ_w can be computed as (Banzer, 1996),

$$\gamma_w = 1.0 + 0.695 \times 10^{-6} S \quad \text{(C – 41)}$$

where S is the salinity as dissolved solids concentration in mg/l.

C3.2.Solution gas-water ratio

The solution gas-water ratio, R_{sw} or gas in water solubility can be defined as the gas volume in scf that can be dissolved in a water volume of 1 STB at reservoir conditions.

McCoy's correlation is the most useful correlation to compute the solution gas-water ratio (Banzer, 1996),

$$R_{sw} = R_{swp}[1 - (0.0753 - 1.73 \times 10^{-4} T)S] \quad \text{(C – 42)}$$

In Equation (C – 42), R_{swp}, A, B, and C can be calculated as:

$$R_{swp} = A + Bp + Cp^2 \quad \text{(C – 43)}$$

$$A = 2.12 + 3.45 \times 10^{-3} T - 3.59 \times 10^{-5} T^2$$

$$B = 0.0107 - 5.26 \times 10^{-5} T + 1.48 \times 10^{-7} T^2$$

$$C = -8.75 \times 10^{-7} + 3.9 \times 10^{-9} T - 1.02 \times 10^{-11} T^2$$

where pressure p in $psia$, temperature T in $°F$, and S is salinity in percentage by weight of dissolved solids ($1\% \cong 10{,}000$ ppm).

C3.3.Isothermal water compressibility

The isothermal compressibility of a fluid is a measure of the relative volume change as a response to a pressure (or mean stress) change.

C3.3.1. Under-saturated water

The isothermal water compressibility, c_w, for $(p > p_b)$ is stated in a similar way to the oil,

$$c_w = -\frac{1}{V_w}\left(\frac{\partial V_w}{\partial p}\right)_T = -\frac{1}{B_w}\left(\frac{\partial B_w}{\partial p}\right)_T \quad \text{(C – 44)}$$

Dodson & Standing (1944) present a correlation for isothermal water compressibility, c_w, for $(p > p_b)$:

$$c_w = c_{wp}[1 + 8.9 \times 10^{-3} R_{sw}] \quad \text{(C – 45)}$$

In Equation (C – 45), c_{wp}, A, B, and C can be calculated as:

$$c_{wp} = \frac{(A + BT + CT^2)}{10^6}$$

$$A = 3.8546 - 1.34 \times 10^{-4} p$$

$$B = -0.01052 + 4.77 \times 10^{-7} p$$

$$C = 3.9267 \times 10^{-5} - 8.8 \times 10^{-10} p$$

where pressure p in $psia$, temperature T in $°F$, and salinity S in percentage by weight of dissolved solids.

C3.3.2. Gas-saturated water

The isothermal water compressibility, c_w, for $(p \leq p_b)$ is defined in a similar way to the oil definition,

$$c_w = -\frac{1}{B_w}\left[\left(\frac{\partial B_w}{\partial p}\right)_T - B_g \left(\frac{\partial R_{sw}}{\partial p}\right)_T\right] \quad \text{(C – 46)}$$

In Equation (C – 46), the first term on the right-hand side is simply the water compressibility for an under-saturated oil, i.e., c_w for $(p > p_b)$ and is estimated by the correlation presented in Equation (C – 45). The second term on the right-hand side is determined by separating it into three parts: the gas formation-volume factor, B_g, that is determined by Equation (C – 9); the water formation-volume factor, B_w, which is determined by the correlations presented in the next section; and, the derivative $(\partial R_{sw}/\partial p)_T$, which is determined by the following correlations developed by Ramey (Ramey Jr., 1964; Banzer, 1996):

$$\left(\frac{\partial R_{sw}}{\partial p}\right)_T = B + 2Cp \quad \text{(C – 47)}$$

Equation (C – 47) is obtained by deriving Equation (C – 40) from McCoy's correlation for the solution gas-water ratio, R_{sw}.

This correlation uses pressure p in $psia$, gas-water ratio R_{sw} in $\mathrm{scf/STB}$ and water compressibility c_w in psi^{-1}.

C3.4.Water formation-volume factor

The water formation-volume factor, B_w, similarly to the oil, is the variation of the water volume at stock-tank conditions to the water volume at elevated pressure and temperature in the reservoir including the gas in solution.

C3.4.1. Under-saturated water

Similar to oil, the water formation-volume factor, B_w at under-saturated condition $(p > p_b)$ is defined as:

$$B_w = B_{wb} e^{c_w(p_b - p)} \quad \text{(C – 48)}$$

with pressures p_b and p in $psia$, water compressibility c_w in psi^{-1} and water formation-volume factors B_{wb} and B_w in RB/STB. B_{wb} is defined by the following correlation.

C3.4.2. Gas-saturated water

McCain (1990) proposes a correlation to calculate the water formation-volume factor at gas-saturated conditions, $(p \leq p_b)$, B_{wb},

$$B_{wb} = (1 + \Delta V_{wp})(1 + \Delta V_{wT}) \quad \text{(C – 49)}$$

In Equation (C – 46), ΔV_{wp} and ΔV_{wT}, can be calculated as:

$$\Delta V_{wp} = -1.95301 \times 10^{-9} pT - 1.72834 \times 10^{-13} p^2 T - 3.58922 \times 10^{-7} p - 2.25341 \times 10^{-10} p^2$$

$$\Delta V_{wT} = -1.0001 \times 10^{-2} + 1.33391 \times 10^{-4} T + 5.50654 \times 10^{-7} T^2$$

With pressure p in $psia$, temperature T in $°F$, and water formation-volume factor at bubble-point pressure B_{wb} in RB/STB.

C3.5.Water viscosity

The water viscosity depends on pressure, temperature, and dissolved solids. Thus, the water viscosity increases as pressure increases and decreases as temperature increases and increases as dissolved solids concentration increases. The Matthews and Russel correlation gives adequate results (Banzer,1996):

$$\mu_w = [1 + 3.5 \times 10^{-12} p^2 (T - 40)] \left(A + \frac{B}{T}\right) \quad \text{(C – 50)}$$

In Equation (C – 50), A and B can be calculated as:

$$A = -0.04518 + 0.009313S - 0.000393S^2$$

$$B = 70.634 + 0.09576S^2$$

with pressure p in $psia$, temperature T in $°F$, and salinity S in percentage by weight of dissolved solids. The ranges for this correlation: $p \leq 10000$, $60 \leq T \leq 400$, and $S \leq 26$.

C3.6.Water density

The water density at standard conditions is calculated using the McCain correlation (Banzer,1996):

$$\rho_{w_{SC}} = 62.368 + 0.438603S + 1.60074 \times 10^{-3}S^2 \quad \text{(C – 51)}$$

with S is salinity in percentage by weight of dissolved solids ($1\% \cong 10{,}000$ ppm).

The water density at different pressure and temperature conditions can be calculated similarly to the oil (Banzer,1996),

$$\rho_w = \frac{64.368\gamma_w}{B_w} \quad \text{(C – 52)}$$

where density in lbm/ft^3.

References

Abivin, P., Hénaut, I. Argillier, J. F. & Moan, M. (2008). Viscosity behavior of foamy oil: Experimental study and modeling. *Petroleum Science and Technology, 26* (13): 1545-1558. https://doi.org/10.1080/10916460701208850.

Abou-Kassem, J. H., Rafiqul Islam, M. & Farouq Ali, S. M. (2020). *Petroleum Reservoir Simulation (Second Edition)*. Gulf Professional Publishing. ISBN 9780128191507, https://doi.org/10.1016/B978-0-12-819150-7.00001-3.

Adil, I., & Maini, B. B. (2007). Role of Asphaltenes in Foamy Oil Reservoir. *Journal of Canadian Petroleum Technology*, *46*(4).

Alappat, C., Hager, G., Schenk, O., Thies, J., Basermann, A., Bischop, A., Fehske, H., & Wellein, G. (2020). A recursive algebraic coloring technique for hardware-efficient symmetric sparse matrix-vector multiplication. *ACM Transactions on Parallel Computing*, Vol. 7, No. *3*(19).

Alberty, J., Carstensen, C., & Funken, S. A. (1999). Remarks around 50 lines of Matlab: short finite element implementation. *Numerical Algorithms*, *20*(2-3), 117-137. https://doi.org/10.1023/A:1019155918070.

Alberty, J., Carstensen, C., Funken, S. A., & Klose, R. (2002). Matlab implementation of the finite element methods in elasticity. *Computing*, *69*(3), 239-263. https://doi.org/10.1007/s00607-002-1459-8.

Alejano, L.R., & Bobet, A. (2012). Drucker–Prager Criterion. *Rock Mechanics and Rock Engineering, 45*, 995-999. http://doi.org/10.1007/s00603-012-0278-2.

Al-Marhoun, M. A. (1992). New correlations for formation volume factors of oil and gas mixtures. *Journal Canadian Petroleum Technology*, *31*(3): 22. http://dx.doi.org/10.2118/92-03-02.

Al-Shammasi, A. A. (2001). A review of bubble point pressure and oil formation volume factor correlations. *SPE Reservoir Evaluation & Engineering*, *4*(2): 146-160. http://dx.doi.org/10.2118/71302-PA.

Ahmed, T. H. (2010). *Reservoir Engineering Handbook (Fourth Edition)*. Gulf Professional Publishing. ISBN 978-1-85617-803-7.

Araujo, E. F., Alzate-Espinosa G. A. & Arbelaez-Londoño, A., (2015, September). A Prediction and Quantification Model of Sand Production. In *2015 Heavy Oil Latin America Conference & Exhibition*, Bogota, Colombia.

Araujo-Guerrero, E. F. (2015). *Modelo de predicción y cuantificación de la producción de arena en yacimientos de crudo pesado.* (M.Sc. thesis). Universidad Nacional de Colombia, Medellin, Colombia. https://repositorio.unal.edu.co/handle/unal/59770.

Araujo Guerrero, E. F., Alzate, G. A., Arbelaez-Londono, A., Pena, S., Cardona, A., & Naranjo, A. (2014, September). Analytical prediction model of sand production integrating geomechanics for open

hole and cased–perforated wells. In *SPE heavy and extra heavy oil conference: Latin America*, Medellín, Colombia. https://doi.org/10.2118/171107-MS.

Araujo-Guerrero, E. F., Alzate-Espinosa, G. A., Arbelaez-Londoño, A., & Morales-Monsalve, C. B. (2018, August). An Analytical Model for the Sand Production Potential Quantification. In *ISRM VIII Brazilian Symposium on Rock Mechanics-SBMR 2018*, Salvador, Bahia, Brazil.

Aziz, K. & Settari, A. (2002) Petroleum Reservoir Simulation. Applied Science Publishers, London, 135-139. ISBN: 0973061405.

Banzer, C. (1996). Correlaciones numéricas PVT. INPELUZ, Maracaibo, Venezuela.

Basilio, E., & Babadagli, T. (2020). Mechanics of foamy oil during methane-based cyclic solvent injection process for enhanced heavy oil recovery: A comprehensive review. *SPE Reservoir Evaluation & Engineering*, *23* (03): 1077-1092. https://doi.org/10.2118/200492-PA.

Bayon, Y. M., Cordelier, P. R., Coates, R. M., Lillico, D. A., & Sawatzky, R. P. (2002, November). Application and comparison of two models of foamy oil behavior of long core depletion experiments. In *SPE International Thermal Operations and Heavy Oil Symposium and International Horizontal Well Technology Conference*. Calgary, Alberta, Canada. https://doi.org/10.2118/78961-MS.

Beal, C. (1970). The viscosity of air, water, natural gas, crude oil, and its associated gases at oil field temperatures and pressures. Richardson, Texas, US. *Reprint Series SPE (Oil and Gas Property Evaluation and Reserve Estimates)*, No. 3, 114–127.

Beggs, H. D. & Robinson, J. R. (1975). Estimating the viscosity of crude oil systems. *Journal Petroleum Technology*, 27 (9): 1140-1141. http://dx.doi.org/10.2118/5434-PA.

Bergman, D. F. (2004). Don't forget viscosity. In *Petroleum Technology Transfer Council 2nd Annual Reservoir Engineering Symposium*, 28 July, Lafayette, Louisiana, US.

Bratli, R. K., & Risnes, R. (1981). Stability and failure of sand arches. *Society of Petroleum Engineers Journal*, *21*(02), 236-248. https://doi.org/10.2118/8427-PA.

Brill, J. P. & Beggs, H. D. (1974). Two-phase flow in pipes. In *U. Tulsa INTERCOM Course*, The Hague.

Brill, J. P. & Mukherjee, H. (1999). *Multiphase Flow in Wells*, No. 17. Richardson, Texas: Monograph

Brulé, M. R. & Whitson, C. H. (2000). Phase Behavior. SPE Monograph Series, Vol. 20, 233 pp., ISBN: 978-1-55563-087-4.

Burton, R. C., Davis, E. R., & Morita, N. (1998, September). Application of reservoir strength characterization and formation failure modeling to analyze sand production potential and formulate sand control strategies for a series of North Sea gas reservoirs. In *SPE Annual Technical Conference and Exhibition*, New Orleans, LA, US. https://doi.org/10.2118/48979-MS.

Bybee, K. (2011). Alaskan Heavy Oil: First CHOPS at an Untapped Arctic Resource. *Journal of Petroleum Technology*, 63 (3), pp.87 – 88. https://doi.org/10.2118/0311-0087-JPT.

Cerasi, P. R., & Vardoulakis, I. (2012, June). Sand production model based on episodic functions. In *46th US Rock Mechanics/Geomechanics Symposium*. Chicago, Illinois, US.

Chen, W. F. & Baladi, G. Y. (1985). *Soil Plasticity: Theory and Implementation*. Elsevier, New York, ISBN 0444565353.

Chen, W.F. & Han, D.J. (1988). *Plasticity for Structural Engineers*. Springer, New York, US.

Chen, T., & Leung, J. Y. (2021). Numerical Simulation of Nonequilibrium Foamy Oil for Cyclic Solvent Injection in Reservoirs after Cold Heavy Oil Production with Sand. *SPE Reservoir Evaluation & Engineering*, *24* (03): 675-691. https://doi.org/10.2118/205504-PA.

Chen, J. Z., & Maini, B. (2005, June). Numerical simulation of foamy oil depletion tests. In *Canadian International Petroleum Conference*, Calgary, Alberta, Canada. https://doi.org/10.2118/78961-MS.

Chen, H. Y., Teufel, L. W. & Lee, R. L. (1995). Coupled fluid flow and geomechanics in reservoir study - I. Theory and governing equations. http://dx.doi.org/10.2118/30752-MS.

Chen, Z., Sun, J., Wang, R., & Wu, X. (2015). A pseudobubblepoint model and its simulation for foamy oil in porous media. *SPE Journal*, *20* (02): 239-247. https://doi.org/10.2118/172345-PA.

Chew, J. & Connally, C. A. Jr. (1959). A viscosity correlation for gas-saturated crude oils. In *Transactions of the American Institute of Mining, Metallurgical, and Petroleum Engineers*, Vol. 216, 23. Dallas, Texas, US. Society of Petroleum Engineers of AIME.

Cividini, A. (1993) Constitutive behaviour and numerical modelling. *Hudson J (ed) Comprehensive rock engineering*, vol 1. Pergamon Press, Oxford, pp 395–426.

Claridge, E. L. & Prats, M. (1995, July). A proposed model and mechanism for anomalous foamy heavy oil behavior. In *1995 International Heavy Oil Symposium*, Calgary, Canada.

Dassault Systémes Simulia Corporation (2014). *Abaqus / CAE User's Manual*, Version 6.14. Providence, RI, USA.

David, C., Menendez, B., Zhu, W., & Wong, T.F. (2001). Mechanical compaction, microstructures and permeability evolution in sandstones. *Physics and Chemistry of the Earth, Part A: Solid Earth and Geodesy*, 26, 45-51. https://doi.org/10.1016/S1464-1895(01)00021-7.

Davies, J. & Davies, D. (1999). Stress-dependent permeability: Characterization and modeling. In *SPE Annual Technical Conference and Exhibition*, 3-6 October, Houston, Texas, US. https://doi.org/10.2118/71750-PA.

Davis, R. O. & Selvadurai, A. P. S. (2002). *Plasticity and Geomechanics*. Cambridge University Press, Cambridge, UK. ISBN 9780511614958. https://doi.org/10.1017/CBO9780511614958.

De Ghetto, G., Paone, F. & Villa, M. (1995). Pressure-Volume-Temperature correlations for heavy and extra heavy oils. SPE International Heavy Oil Symposium, 19-21 June, Calgary, Alberta, Canada. https://doi.org/10.2118/30316-MS.

De Mirabal, M., Rodriguez, H., & Gordillo, R. (1997). Production improvement strategy for foamy Hamaca crude oil: a field case. In *International Thermal Operations and Heavy Oil Symposium*, Bakersfield, California. https://doi.org/10.2118/37544-MS.

Denbina, E. S., Baker, R. O., Gegunde, G. G., Klesken, A. J., & Sodero, S. F. (2001). Modelling cold production for heavy oil reservoirs. *Journal of Canadian Petroleum Technology*, *40*(03). https://doi.org/10.2118/01-03-01.

Detournay, C. (2009). Numerical modeling of the slit mode of cavity evolution associated with sand production. *SPE Journal*, *14*(04), 797-804. https://doi.org/10.2118/116168-PA.

Dindoruk, B., & Christman, P. G. (2001). PVT properties and viscosity correlations for Gulf of Mexico oils. In *SPE Annual Technical Conference and Exhibition*, September 30 – October 3, New Orleans, Louisiana, US. https://doi.org/10.2118/71633-MS.

Ding, X. & Zhang, G. (2017). Coefficient of equivalent plastic strain based on the associated flow of the Drucker-Prager criterion. *International Journal of Non-Linear Mechanics*, Vol., pp. 15-20. ISSN 0020-7462. https://doi.org/10.1016/j.ijnonlinmec.2017.04.018.

Dodson, C. R. & Standing, M. B. (1944). Pressure-Volume-Temperature and solubility relations for natural gas-water-mixtures. *Drilling and Production Practice, API,* 173-179. API-44-173.

Drucker, D. C., & Prager, W. (1952). Soil mechanics and plastic analysis or limit design. *Quarterly of Applied Mathematics*. Vol. 10, pp. 157−165.

Du, Z., Jiang, W., & Chen, Z. (2009, April). A new integrated model to simulate the disturbed zone in CHOPS: spread and erosion. *SPE Production and Operations Symposium*, Oklahoma City, Oklahoma, USA. https://doi.org/10.2118/119587-MS.

Dusseault, M. B. (2002). *CHOPS: Cold Heavy Oil Production with Sand in the Canadian heavy oil industry*. Alberta Department of Energy.

Dusseault, M. B. (2009). Monitoring and modelling in coupled geomechanics processes. *Journal of Canadian Petroleum Technology*, Vol. 48, No. 7.

Dusseault, M. B., & El-Sayed, S. (2000, April). Heavy-oil production enhancement by encouraging sand production. In *SPE/DOE Improved Oil Recovery Symposium*. https://doi.org/10.2118/59276-MS.

Eshiet, K.I.-I.I & Sheng, Y. (2021) Investigating Sand Production Phenomena: An Appraisal of Past and Emerging Laboratory Experiments and Analytical Models. *Geotechnics 2021*, 1, 492–533. https://doi.org/10.3390/geotechnics1020023.

El-Banbi, A., Alzahabi, A. & El-Maraghi, A (2018). *PVT Property Correlations Selection and Estimation*. Saint Louis: Elsevier Science & Technology, pp. 432. https://doi.org/10.1016/C2016-0-01806-5.

El-Hoshoudy, A. & Desouky, S. (2019). *PVT Properties of Black Crude Oil*. Chapter 3. Processing of Heavy Crude Oils. IntechOpen. Ramasamy Marappa Gounder. https://doi.org/10.5772/intechopen.82278.

Fan, Z., & Yang, D. (2016, April). Characterization of wormhole growth and its applications for CHOPS wells using history matching. In *SPE Improved Oil Recovery Conference,* Tulsa, Oklahoma, US. https://doi.org/10.2118/179617-MS.

Fan, Z., Yang, D., & Li, X. (2020). Characterization of Multiphase Flow in CHOPS Processes Using a Systematic Framework. *SPE Reservoir Evaluation & Engineering*, *23*(03), 0930-0942. https://doi.org/10.2118/186080-PA.

Foo, Y. Y., Chee, S. C., Zain, Z. M., & Mamora, D. D. (2011, July). Recovery Processes of Extra Heavy Oil-Mechanistic Modelling and Simulation Approach. *SPE Enhanced Oil Recovery Conference*, Kuala Lumpur, Malaysia. https://doi.org/10.2118/143390-MS.

Firoozabadi, A. (2001). Mechanisms of solution gas drive in heavy oil reservoirs. *Journal of Canadian Petroleum Technology*, Vol. 40, No. 3, pp. 15-20.

Fitzgerald, D. J. (1994). A predictive method for estimating the viscosity of undefined hydrocarbon liquid mixtures. MS thesis, *Pennsylvania State University*, Pennsylvania, US.

Frashad, F., LeBlanc, J. L., Garber, J. D. & Osorio, J. G. (1996). Empirical PVT correlations for Colombian crude oils. In *SPE Latin American and Caribbean Petroleum Engineering Conference*, Port of Spain, Trinidad and Tobago, 23–26 April. http://dx.doi.org/10.2118/36105-MS.

Geilikman, M. B., Dusseault, M. B., & Dullien, F. A. (1994, February). Sand production as a viscoplastic granular flow. In *SPE formation damage control symposium*, Lafayette, Louisiana, US. https://doi.org/10.2118/27343-MS.

Geilikman, M. B., Dusseault, M. B., & Dullien, F. A. (1994, April). Fluid production enhancement by exploiting sand production. In *SPE/DOE Improved Oil Recovery Symposium*, Tulsa, Oklahoma, US. https://doi.org/10.2118/27797-MS.

Glasø, Ø. (1980). Generalized Pressure-Volume-Temperature correlations. *Journal Petroleum Technology*, *32*(5): 785-795.http://dx.doi.org/10.2118/8016-PA.

Gockenbach, M.S. (2006).*Understanding and implementing the finite element method.* Siam. pp. 363. ISBN:978-0-898716-14-6. https://digitalcommons.mtu.edu/math-fp/23.

Goodarzi, N., Bryan, J. L., Mai, A. T. & Kantzas, A. (2005). Heavy oil fluid testing with conventional and novel techniques. *SPE International Thermal Operations and Heavy Oil Symposium*, 1-3 November, Calgary, Alberta, Canada. http://dx.doi.org/10.2118/97803-MS.

Guo, B., Gao, D., Ai, C., & Qu, J. (2012). Critical oil rate and well productivity in cold production from heavy-oil reservoirs. *SPE Production & Operations*, *27*(01), 87-93. https://doi.org/10.2118/133172-PA.

Han, G., Stone, T., Liu, Q., Cook, J., & Papanastasiou, P. (2005, January). 3D elastoplastic fem modelling in a reservoir simulator. In *SPE Reservoir Simulation Symposium*, The Woodlands, Texas, USA. https://doi.org/10.2118/91891-MS.

Handy, L.L. (1957). Effect of Local High Gas Saturations on Productivity Indices. *API Drilling and Production Practice*. Paper No. 57–111.

Hayatdavoudi, A. (1999, March). Formation sand liquefaction: A new mechanism for explaining fines migration and well sanding. In *SPE Mid-Continent Operations Symposium,* Oklahoma City, Oklahoma, USA. https://doi.org/10.2118/52137-MS.

Istchenko, C. M., & Gates, I. D. (2011, December). The Well-Wormhole Model of Cold Production of Heavy Oil Reservoirs. In *SPE Heavy Oil Conference and Exhibition,* Kuwait City, Kuwait. https://doi.org/10.2118/150633-MS.

Istchenko, C. M., & Gates, I. D. (2014). Well/wormhole model of cold heavy-oil production with sand. *SPE Journal*, *19*(02), 260-269. https://doi.org/10.2118/150633-PA.

Itasca Consulting Group, Inc. (2005). *Fast Lagrangian Analysis of Continua (FLAC).* Online Version. FLAC Version 5.0. 3th Ed. Minneapolis, MN, US.

Joseph, D. D., Kamp, A. M., & Bai, R. (2002). Modeling foamy oil flow in porous media. *International Journal of Multiphase Flow*, *28*(10), 1659-1686. http://dx.doi.org/10.1016/s0301-9322(02)00051-4.

Kamp, A. M., Heny, C., Andarcia, L., Lago, M., & Rodriguez, A. (2001). Experimental Investigation of Foamy Oil Solution Gas Drive. In SPE *International Thermal Operations and Heavy Oil Symposium*, Porlamar, Margarita Island, Venezuela. https://doi.org/10.2118/69725-MS.

Kartoatmodjo, T. R. S. & Schmidt, Z. (1991). New correlations for crude oil physical properties. SPE-23556-MS (unsolicited paper).

Kim, A. S., & Sharma, M. M. (2012, June). A Predictive Model for Sand Production in Realistic Downhole Condition. In *46th US Rock Mechanics/Geomechanics Symposium*, Chicago, Illinois, US.

Klar, G., Gast, T., Pradhana, A., Fu, C., Schroeder, C., Chenfanfu, J., & Teran, J. (2016). Drucker-Prager elastoplasticity for sand animation. *ACM Transactions on Graphics*. *(35)*1-12. https://doi.org/10.1145/2897824.2925906.

Kouzel, B. (1965). How pressure affects liquid viscosity. *Hydrocarbon Process*. March: 120.

Kraus, W. P., McCaffrey, W. J., & Boyd, G. W. (1993). PseudoBubble Point Model For Foamy Oils. In *1993 Annual Technical Meeting*, May, Calgary, Alberta. https://doi.org/10.2118/93-45.

Kumar, R., & Mahadevan, J. (2012). Well-performance relationships in heavy-foamy-oil reservoirs. *SPE Production & Operations*, *27*(01), 94-105. https://doi.org/10.2118/117447-PA.

Labedi, R. M. (1990, October). Use of production data to estimate the saturation pressure, solution GOR, and chemical composition of reservoir fluids. *SPE Latin America Petroleum Engineering Conference*, Rio de Janeiro, Brazil. https://doi.org/10.2118/21164-MS.

Lasater, J.A. (1958). Bubble point pressure correlations. *Journal Petroleum Technology*, *10*(5): 65–67. http://dx.doi.org/10.2118/957-G.

Lebel, J. P. (1994, March). Performance implications of various reservoir access geometries. In *11th Annual Heavy Oil & Oil Sands Technology Symposium*, Calgary, Canada.

Lee, A. L., Gonzalez, M. H., & Eakin, B. E. (1966). The viscosity of natural gases. *Journal Petroleum Technology*, 997. Trans., AIME, 237. https://doi.org/10.2118/1340-PA.

Li, P. & Chalaturnyk, R. J. (2006). Permeability variations associated with shearing and isotropic unloading during the SAGD process. *Journal of Canadian Petroleum Technology*, *45*(01) https://doi.org/10.2118/06-01-05.

Liu, P., Mu, Z., Li, W., Wu, Y., & Li, X. (2017). A new mathematical model and experimental validation on foamy-oil flow in developing heavy oil reservoirs. *Scientific Reports*, *7* (1): 1-13. https://doi.org/10.1038/s41598-017-08882-2.

Liu, X., & Zhao, G. (2004, June). Effects of wormholes on cold heavy oil production. In *Canadian International Petroleum Conference*, Calgary, Alberta, Canada. https://doi.org/10.2118/2004-048.

Liu, X., & Zhao, G. (2005). A fractal wormhole model for cold heavy oil production. *Journal of Canadian Petroleum Technology*, *44*(09). https://doi.org/10.2118/05-09-03.

Loughead, D. J., & Saltuklaroglu, M. (1992, March). Lloydminster heavy oil production: why so unusual. In *9th Annual Heavy Oil and Oil Sands Technology Symposium*, Calgary, Canada.

Lu, X., Zhou, X., Luo, J., Zeng, F., & Peng, X. (2019). Characterization of foamy oil and gas/oil two-phase flow in porous media for a heavy oil/methane system. *Journal of Energy Resources Technology*, *141* (3). https://doi.org/10.1115/1.4041662.

Maini, B. (1996). Foamy oil flow in heavy oil production. *Journal of Canadian Petroleum Technology*, *35* (06). https://doi.org/10.2118/96-06-01

Maini, B. B. (2001). Foamy-oil flow. *Journal of Petroleum Technology*, *53*(10), 54-64. https://doi.org/10.2118/68885-JPT.

Maini, B. B., Sarma, H. K., & George, A. E. (1993). Significance of foamy-oil behaviour in primary production of heavy oils. *Journal of Canadian petroleum technology*, *32*(09). https://doi.org/10.2118/93-09-07.

Mastmann, M., Moustakis, M. L. & Bennion, D. B. (2001). Predicting foamy oil recovery. *SPE Western Regional Meeting*, 26-30 March, Bakersfield, California, US. https://doi.org/10.2118/68860-MS.

Mehrotra, A.K. (1991a). A generalized viscosity equation for pure heavy hydrocarbons. *Ind. Eng. Chem. Res., 30* (1991), pp. 420-427. https://doi.org/10.1021/ie00050a021.

Mehrotra, A.K. (1991b). Generalized one-parameter viscosity equation for light and medium hydrocarbons. Ind. Eng. Chem. Res., 30, pp. 1367-1372. https://doi.org/10.1021/ie00054a044.

McCain, W. D., Jr. (1990). The properties of petroleum fluids. *PennWell Books*. 2nd. Ed. Tulsa, OK, US.

Mohamad-Hussein, A., Mendoza, P. E. V., Delbosco, P. F., Sorgi, C., De Gennaro, V., Subbiah, S. K., … & Daniels, R. (2021). Geomechanical modelling of cold heavy oil production with sand. *Petroleum*. https://doi.org/10.1016/j.petlm.2021.02.002.

Morita, N., Whitfill, D. L., Fedde, Ø. P., & Løvik, T. H. (1989). Parametric Study of Sand-Production Prediction: Analytical Approach. *SPE Production Engineering* 4 (1): 25–33. *Trans., AIME, 287*. https://doi.org/10.2118/16990-PA.

Morita, N., Whitfill, D. L., Massie, I., & Knudsen, T. W. (1989). Realistic sand-production prediction: numerical approach. *SPE Production Engineering*, *4*(01), 15-24. https://doi.org/10.2118/16989-PA.

Nouri, A., Vaziri, H. H., Belhaj, H. A., & Islam, M. R. (2006). Sand-production prediction: a new set of criteria for modeling based on large-scale transient experiments and numerical investigation. *SPE Journal*. https://doi.org/10.2118/90273-PA.

Osorio, J.G. (1999). *Numerical modeling of coupled fluid-flow/geomechanical behavior of reservoirs with stress-sensitive permeability*. (Ph. D. Dissertation). New Mexico Institute of Mining and Technology, Socorro, New Mexico, US. 1999.

Olatunji, O. O & Micheal, O. (July, 2017). Prediction of sand production from oil and gas reservoirs in the Niger Delta using Support Vector Machines SVMS: A binary classification approach. In *SPE Nigeria Annual International Conference and Exhibition*, Lagos, Nigeria. https://doi.org/10.2118/189118-MS.

Pan, Y., Chen, Z., Sun, J., Bao, X., Xiao, L., & Wang, R. (2010, May). Research progress of modelling on cold heavy oil production with sand. In *SPE Western Regional Meeting*, Anaheim, California, US. https://doi.org/10.2118/133587-MS.

Papamichos, E., & Stavropoulou, M. (1998). An erosion-mechanical model for sand production rate prediction. *International Journal of Rock Mechanics and Mining Sciences*, *4*(35), 531-532. http://dx.doi.org/10.1016%2FS0148-9062(98)00106-5.

Papamichos, E., Vardoulakis, I., Tronvoll, J. & Skjærstein, A. (2001). Volumetric sand production model and experiment. *International Journal for Numerical and Analytical Methods in Geomechanics*. *(25)* 789-808. https://doi.org/10.1002/nag.154.

Papanastasiou, P. C., & Vardoulakis, I. G. (1992). Numerical treatment of progressive localization in relation to borehole stability. *International Journal for Numerical and Analytical Methods in Geomechanics*, *16* (6), 389-424. https://doi.org/10.1002/nag.1610160602.

Perkins, T. K., & Weingarten, J. S. (1988, October). Stability and failure of spherical cavities in unconsolidated sand and weakly consolidated rock. In *SPE Annual Technical Conference and Exhibition*, Houston, Texas, USA. https://doi.org/10.2118/18244-MS.

Petrosky, G. E. Jr. (1990). PVT Correlations for Gulf of Mexico crude oils. (M.Sc. thesis). *University of Southwestern Louisiana*, Lafayette, Louisiana, US.

Pooladi-Darvish, M., & Firoozabadi, A. (1999). Solution-gas drive in heavy oil reservoirs. *Journal of Canadian Petroleum Technology*, *38*(04). https://doi.org/10.2118/99-04-06.

Potts, D.M & Zdravkovic, L. (1999). *Finite element analysis in geotechnical engineering, Theory.* pp. 440. Thomas Telford Publishing. London, UK. ISBN 10: 0727727532.

Puttagunta, V. R., Miadonye, A., & Singh, B. (1992). Viscosity-temperature correlation for prediction of kinematic viscosity of conventional petroleum liquid. United Kingdom.

Puttagunta, V. R., Singh, B., & Miadonye, A. (1993). Correlation of bitumen viscosity with temperature and pressure. *The Canadian Journal of Chemical Engineering.* https://doi.org/10.1002/cjce.5450710315.

Rahmati, H., Jafarpour, M., Azadbakht, S., Nouri, A., Vaziri, H., Chan, D., & Xiao, Y. (2013). Review of sand production prediction models. *Journal of Petroleum Engineering*. http://dx.doi.org/10.1155/2013/864981.

Ramey Jr., H.J. (1964). Rapid Methods for Estimating Reservoir Compressibilities. *J Pet Technol* 16: 447–454.https://doi.org/10.2118/772-PA.

Ramos, G. G., Katahara, K. W., Gray, J. D., & Knox, D. J. W. (1994, August). Sand production in vertical and horizontal wells in a friable sandstone formation, North Sea. In *Rock Mechanics in Petroleum Engineering*, Delft, Netherlands. https://doi.org/10.2118/28065-MS.

Rangrizshokri, A. (2015). *Evaluation of post-CHOPS (Cold Heavy Oil Production with Sands) Enhanced Oil Recovery Methods*. (Ph.D. Dissertation). University of Alberta, Edmonton, Alberta, Canada. https://doi.org/10.7939/R3HX15Z95.

Risnes, R. & Bratli, R. K. (1979). Stability and failure of sand arches. In *the 54th Annual Technical Conference and Exhibition of the Society of Petroleum Engineers of AIME*, Las Vegas, Nevada, US, September.

Risnes, R., Bratli, R. K., & Horsrud, P. (1982). Sand stresses around a wellbore. *Society of Petroleum Engineers Journal*, *22*(06), 883-898. https://doi.org/10.2118/9650-PA.

Rivero, J. A., Coskuner, G., Asghari, K., Law, D. H.-S., Pearce, A., Newman, R., Birchwood, R., Zhao, J. & Ingham, J. (2010, September). Modeling CHOPS using a coupled flow-geomechanics simulator with nonequilibrium foamy-oil reactions: A multiwell history matching study. In *SPE Annual Technical Conference and Exhibition*. Florence, Italy. https://doi.org/10.2118/135490-MS.

Robertson, P. K., & Fear, C. E. (1997). Cyclic liquefaction and its evaluation based on the SPT and CPT. In *Proceeding of the NCEER workshop on evaluation of liquefaction resistance of soils,* pp. 41-87.

Romero, D. J., Fernandez, B., & Rojas, G. (2001). Thermodynamic Characterization of a PVT of Foamy Oil. SPE International Thermal Operations and Heavy Oil Symposium, 12-14 March, Porlamar, Margarita Island, Venezuela. https://doi.org/10.2118/69724-MS.

Ruifeng, W., Xintao, Y., Xueqing, T., Xianghong, W., Xinzheng, Z., Li, W., & Xiaoling, Y. (2011, December). Successful cold heavy oil production with sand (CHOPS) application in massive heavy oil reservoir in Sudan: A case study. In *SPE Heavy Oil Conference and Exhibition*, Kuwait City, Kuwait. https://doi.org/10.2118/150540-MS.

Sahni, A., Gadelle, F., Kumar, M., Tomutsa, L., & A. R. Kovscek (2006). Experiments and Analysis of Heavy-Oil Solution-Gas Drive. *SPE Res Evaluation & Engineering, 7*(3): 217–229. https://doi.org/10.2118/88442-PA.

Salama, M. M., & Venkatesh, E. S. (1983, May). Evaluation of API RP 14E erosional velocity limitations for offshore gas wells. In *Offshore Technology Conference*, Houston, Texas, US. https://doi.org/10.4043/4485-MS.

Sanyal, T., & Al-Sammak, I. (2011; November). Analysis of the First CHOPS Pilot for Heavy Oil Production in Kuwait. In *Canadian Unconventional Resources Conference*, Calgary, Alberta, Canada. https://doi.org/10.2118/148966-MS.

Shafiei, A. & Dusseault, M. B. (2013). Geomechanics of thermal viscous oil production in sandstones. *Journal of Petroleum Science and Engineering*, 103: 121-139, ISSN 0920-4105. https://doi.org/10.1016/j.petrol.2013.02.001.

Sheng, J.J., Hayes, R.E., Maini, B.B., & Tortike, W.S. (1999) Modeling foamy oil flow in porous media. *Transport in Porous Media,* 35: 227–258. https://doi.org/10.1023/A:1006523526802.

Sherif, F.N. (2012). *MATLAB FEM Code – From elasticity to plasticity. Master thesis. Norwegian University of Science and Technology*. Trondheim, Norway.

Sheng, J. J., Maini, B. B., Hayes, R. E., & Tortike, W. S. (1999a). Critical review of foamy oil flow. *Transport in Porous Media*, *35* (2): 157-187. https://doi.org/10.1023/A:1006575510872.

Sheng, J. J., Hayes, R. E., Maini, B. B., & Tortike, W. S. (1999b). Modelling foamy oil flow in porous media. *Transport in Porous Media*, *35* (2): 227-258. https://doi.org/10.1023/A:1006523526802.

Sheng, J. J., Maini, B. B., Hayes, R. E., & Tortike, W. S. (1999c). A non-equilibrium model to calculate foamy oil properties. *Journal of Canadian Petroleum Technology*, *38* (04). https://doi.org/10.2118/99-04-04.

Smith, G. E. (1988). Fluid flow and sand production in heavy-oil reservoirs under solution-gas drive. *SPE Production Engineering*, *3* (02): 169-180. https://doi.org/10.2118/15094-PA.

Squires, A. (1993, March). Inter-well tracer results and gel blocking program. In *10th Annual Heavy Oil and Oil Sands Technical Symposium*, Calgary, Alberta, Canada.

Standing, M. B. (1947). A Pressure-Volume-Temperature correlation for mixtures of California oils and gases. *API Drilling and Production Practice*, 275-287.

Standing, M. B. (1981). *Volumetric and phase behavior of oil field hydrocarbon systems*. 9th edition. Richardson, Texas, US. Society of Petroleum Engineers of AIME.

Sutton, R. P. (1985). Compressibility factors for high-molecular-weight reservoir gases. *Presented at 1985 SPE Annual Technical Conference and Exhibition*, Las Vegas, Nevada, US. 22–25 September. https://doi.org/10.2118/14265-MS.

Sutton, R. P. (2006). Oil system correlations. *Petroleum Engineering Handbook, Volume I – General Engineering*, Chapter 6, Ed. John R. Fanchi: 257 – 331. *Society of Petroleum Engineers*. ISBN: 978-1-55563-108-6.

Tan, T., Slevinsky, R., & Jonasson, H. (2005). A new methodology for modelling of sand wormholes in field scale thermal simulation. *Journal of Canadian Petroleum Technology*, *44*(04). https://doi.org/10.2118/05-04-01.

Tang, G. Q., Sahni, A., Gadelle, F., Kumar, M., & Kovscek, A. R. (2006). Heavy-oil solution gas drive in consolidated and unconsolidated rock. *SPE Journal*, *11* (02): 259-268. https://doi.org/10.2118/87226-PA.

Tang, G. Q., Temizel, C., & Kovscek, A. R. (2006, September). The Role of Oil Chemistry on Cold Production of Heavy Oils. In *SPE Annual Technical Conference and Exhibition*, San Antonio, Texas, US. https://doi.org/10.2118/102365-MS.

Terzaghi, K., Peck, R. B., & Mesri, G. (1996). *Soil mechanics in engineering practice*. John Wiley & Sons.

Tremblay, B., Sedgwick, G., & Vu, D. (1999). CT imaging of wormhole growth under solution-gas drive. *SPE Res Eval & Eng* 2 (1999): 37-45. https://doi.org/10.2118/54658-PA.

Tremblay, B., & Oldakowski, K. (2003). Modeling of wormhole growth in cold production. *Transport in porous media*, *53*(2): 197-214. https://doi.org/10.1023/A:1024017622009.

Tremblay, B. (2005). Modelling of sand transport through wormholes. *Journal of Canadian Petroleum Technology*, *44* (4). https://doi.org/10.2118/05-04-06.

Uddin, M. (2005). Numerical studies of gas exsolution in a live heavy oil reservoir. In *SPE International Thermal Operations and Heavy Oil Symposium*, Calgary, Alberta, Canada. https://doi.org/10.2118/97739-MS.

Van den Hoek, P.J., Kooijman, A.P., De Bree, P.H., Kenter, C.J., Sellmeyer, C.J., & Willson, S.M. (2000). Mechanisms of downhole sand cavity re-stabilization in weakly consolidated sandstones. In *SPE European Petroleum Conference.* Paris, France. https://doi.org/10.2118/65183-MS.

Van den Hoek, P. J., Hertogh, G. M. M., Kooijman, A. P., De Bree, P., Kenter, C. J., & Papamichos, E. (2000). A new concept of sand production prediction: theory and laboratory experiments. *SPE Drilling & Completion*, *15*(04), 261-273. https://doi.org/10.2118/65756-PA.

Vanderheyden, B., Jayaraman, B., Ma, X., & Zhang, D. (2013, February). Multiscale simulation of CHOPS wormhole networks. In *SPE Reservoir Simulation Symposium*, The Woodlands, Texas, US. https://doi.org/10.2118/163603-MS.

Vardoulakis, I., Stavropoulou, M., & Papanastasiou, P. (1996). Hydro-mechanical aspects of the sand production problem. *Transport in porous media*, *22* (2): 225-244. https://doi.org/10.1007/BF01143517.

Vazquez, M. & Beggs, H. D. (1980). Correlations for fluid physical property prediction. *Journal Petroleum Technology*, *32*(6): 968-970. http://dx.doi.org/10.2118/6719-PA.

Veeken, C. A. M., Davies, D. R., Kenter, C. J., & Kooijman, A. P. (1991, October). Sand production prediction review: developing an integrated approach. In *SPE annual technical conference and exhibition*, Dallas, Texas, USA. https://doi.org/10.2118/22792-MS.

Velarde, J., Blasingame, T.A., & McCain Jr., W.D. (1997). Correlation of black oil properties at pressures below bubble point pressure - A new approach. In *Annual Technical Meeting of CIM*, Calgary, Alberta, Canada, 8–11 June. http://dx.doi.org/10.2118/97-93.

Walton, I.C., Atwood, D.C., Halleck, P.M. & Bianco, L.C.B. (2002). Perforating unconsolidated sands: An experimental and theoretical investigation. *SPE Drilling & Completion*, *17*(03): 141–150. https://doi.org/10.2118/79041-PA.

Wan, R.G., Chan, D.H., & Kosar, K.M. (1991). A constitutive model for the effective stress-strain behaviour of oil sands. *Journal of Canadian Petroleum Technology*, *30* (04): 89-98. https://doi.org/10.2118/91-04-08.

Wan, R. G., Liu, Y., & Wang, J. (2006). Prediction of volumetric sand production using a coupled geomechanics-hydrodynamic erosion model. *Journal of Canadian Petroleum Technology*, *45* (04). https://doi.org/10.2118/06-04-01.

Wan, R.G. & Wang, J. (2004a). Analysis of sand production in unconsolidated oil sand using a coupled erosional-stress-deformation model. *Journal of Canadian Petroleum Technology*, 43: 47–53. https://doi.org/10.2118/04-02-04.

Wan, R. G., & Wang, J. (2004b). Modelling of sand production and wormhole propagation in an oil saturated sand pack using stabilized finite element methods. *Journal Canadian International Petroleum Conference*, *43* (04). https://doi.org/10.2118/04-04-04.

Wang, Y., & Chen, C. Z. (2004). Simulating cold heavy oil production with sand by reservoir-wormhole model. *Journal of Canadian Petroleum Technology*, *43*(04). https://doi.org/10.2118/04-04-03.

Wang, H., & Sharma, M.M. (2016, September). A fully 3-D, multi-phase, poro-elasto-plastic model for sand production. In *SPE Annual Technical Conference and Exhibition*, Dubai, UAE. https://doi.org/10.2118/181566-MS.

Wang, J., Walters, D., Wan, R.G., & Settari, A. (2005, June). Prediction of volumetric sand production and wellbore stability analysis of a well at different completion schemes. In *Alaska Rocks 2005, The 40th US Symposium on Rock Mechanics (USRMS)*, Anchorage, Alaska, US.

Wang, J., Walters, D.A., Settari, A., & Wan, R.G. (2006, November). Simulation of cold heavy oil production using an integrated modular approach with emphasis on foamy oil flow and sand production effects. In *1ST Heavy Oil Conference*, Beijing, China.

Wang, J., Walters, D., Settari, A., Wan, R.G., & Liu, Y.N. (2004, June). Sand production and instability analysis in a wellbore using a fully coupled reservoir-geomechanics model, Gulf rocks. In *6th North America Rock Mechanics Symposium (NARMS)*, Houston, Texas, US.

Wang, Y., Chen, C. C., & Dusseault, M. B. (2001, March). An integrated reservoir model for sand production and foamy oil flow during cold heavy oil production. In *SPE International Thermal Operations and Heavy Oil Symposium*. Porlamar, Margarita Island, Venezuela. https://doi.org/10.2118/69714-MS.

Wang, R., Qin, J., Chen, Z., & Zhao, M. (2008). Performance of drainage experiments with Orinoco Belt heavy oil in a long laboratory core in simulated reservoir conditions. *SPE Journal*, *13*(04), 474-479. https://doi.org/10.2118/104377-PA.

Wang, J., Yale, D., & Dasari, G. (2011). Numerical modeling of massive sand production. In *SPE Annual Technical Conference and Exhibition*, October. Denver, Colorado, US. https://doi.org/10.2118/147110-MS.

Wang, Y., & Xue, S. (2004). Simulating cold production by a coupled reservoir-geomechanics model with sand erosion. *Journal of Canadian Petroleum Technology*, *43*(05). https://doi.org/10.2118/04-05-03.

Watson, K. M. & Nelson, E. F. (1933). Improved methods for approximating critical and thermal properties of petroleum. *Industrial and Engineering Chemistry*, *25*: 880.

Watson, K. M., Nelson, E. F., & Murphy, G. B. (1935). Characterization of petroleum fractions. *Industrial and Engineering Chemistry*, *7*: 1460–1464.

Weingarten, J. S., & Perkins, T. K. (1995). Prediction of sand production in gas wells: methods and Gulf of Mexico case studies. *Journal of Petroleum Technology*, *47*(07), 596-600. https://doi.org/10.2118/24797-PA.

Whitson, C. H. (1983). Characterizing hydrocarbon plus fractions. *SPE Journal*, *23*(4): 683-694. http://dx.doi.org/10.2118/12233-PA.

Wong, R. C. K (2003). A model for strain-induced permeability anisotropy in deformable granular media. Canadian Geotechnical Journal, 40(1), 95–106. https://doi.org/10.1139/t02-088.

Wu, B., Choi, S. K., Denke, R., Barton, T., Viswanathan, C., Lim, S., Zamberi, M., Shaffee, S., Fadhlan, N., Johar, Z., Jadid, M. B., & Madon, B. B. (2016, March). A new and practical model for amount and rate of sand production estimation. In *Offshore Technology Conference Asia*, Kuala Lumpur, Malaysia. https://doi.org/10.4043/26508-MS.

Xiao, L. (2012). *Study on wormhole coverage, foamy oil phenomenon, and well interference of cold heavy oil production with sand wells*. (Master thesis). The University of Regina,

Xiao, L., & Zhao, G. (2012, June). A novel approach for determining wormhole coverage in CHOPS wells. In *SPE Heavy Oil Conference Canada*, Calgary, Alberta, Canada. https://doi.org/10.2118/157935-MS.

Xiao, L., & Zhao, G. (2013, June). Integrated study of foamy oil flow and wormhole structure in CHOPS through transient pressure analysis. In *SPE Heavy Oil Conference-Canada*, Calgary, Alberta, Canada. https://doi.org/10.2118/165538-MS.

Xiao, L., & Zhao, G. (2017). Estimation of CHOPS wormhole coverage from rate/time flow behaviors. *SPE Reservoir Evaluation & Engineering*, *20* (04), 0957-0973. https://doi.org/10.2118/157935-PA.

Yang, Z., Li, X., Xu, X., Shen, Y., & Shi, X. (2021, June). Development Features of Cold Production with Horizontal Wells in a Foamy Extra-Heavy Oil Reservoir. In *SPE Trinidad and Tobago Section Energy Resources Conference*, Virtual. https://doi.org/10.2118/200974-MS.

Yang, J. Y., Tremblay, B., & Babchin, A. (1999, March). A wormhole network model of cold production in heavy oil. In *International Thermal Operations/Heavy Oil Symposium*, Bakersfield, California, US. https://doi.org/10.2118/54097-MS.

Yeung, K. C. (1995, February). Cold Flow Production of Crude Bitumen at the Burnt Lake Project, Northeastern Alberta. In *6th UNITAR conference on heavy crude and tar sands on fueling for a clean and safe environment*, Houston, Texas, US.

Yi, X. (2001, June). Gas Well Sand Production Modelling With Coupled Geomechanical-Gas/Sand Flow Model. In *Canadian International Petroleum Conference*, Calgary, Alberta, Canada. https://doi.org/10.2118/2001-050.

Yi, X., Valkó, P. P. & Russell, J. E. (2005). Effect of Rock Strength Criterion on the Predicted Onset of Sand Production. *International Journal of Geomechanics*. Vol. 5, Issue 1. https://doi.org/10.1061/(ASCE)1532-3641(2005)5:1(66).

Young, J. P., Mathews, W. L., & Hulm, E. (2010). Alaskan Heavy Oil: First CHOPS at a vast, untapped arctic resource. In *SPE Western Regional Meeting*, 27-29 May, Anaheim, California, USA. https://doi.org/10.2118/133592-MS.

Yu, H., & Leung, J. Y. (2020). A Sand-Arch Stability Constrained Dynamic Fractal Wormhole Growth Model for Simulating Cold Heavy-Oil Production with Sand. *SPE Journal*, *25* (06): 3440-3456. https://doi.org/10.2118/193893-PA.

Zhou, X., Yuan, Q., Zeng, F, Zhang, L. & Jiang, S. (2017) Experimental study on foamy oil behavior using a heavy oil–methane system in the bulk phase. Journal of Petroleum Science and Engineering, Vol.158, pp 309-321. ISSN 0920-4105. https://doi.org/10.1016/j.petrol.2017.07.070.

Zimmerman, W., Somerton, W. H., & King, M. S. (1986). Compressibility of porous rocks. *Journal of Geophysical Research*, 91(6), 765–777. https://doi.org/10.1029/JB091iB12p12765.